Finnie, Michael (2010) *An interfacial study of III-V materials.* PhD thesis.

http://theses.gla.ac.uk/1941/

Copyright and moral rights for this thesis are retained by the author

A copy can be downloaded for personal non-commercial research or study, without prior permission or charge

This thesis cannot be reproduced or quoted extensively from without first obtaining permission in writing from the Author

The content must not be changed in any way or sold commercially in any format or medium without the formal permission of the Author

When referring to this work, full bibliographic details including the author, title, awarding institution and date of the thesis must be given

Glasgow Theses Service
http://theses.gla.ac.uk/
theses@gla.ac.uk

An Interfacial Study of III-V Materials

Michael P. Finnie

A Thesis submitted for the degree of Doctor of Philosophy at the University of Glasgow.

June 2010

© Michael Finnie, 2010

Abstract

Z-contrast imaging, using a high-angle annular dark field detector, can be used to characterise III-V heterostructures. GaAs/AlAs heterostructures were grown using MBE and prepared for TEM using a cross-sectional method. SuperSTEM 1 was used to investigate both the GaAs-on-AlAs and the AlAs-on-GaAs interfaces as a function of specimen thickness. The analysis of the images showed that the apparent interface widths varied with thickness in an unexpected manner. The measured GaAs-on-AlAs interface widths remained constant with thickness while the AlAs-on-GaAs interface widths increased. Furthermore, the apparent width of the GaAs layer increased with increasing thickness. The actual interfacial width can be a result of either surface stepping during MBE growth or inter-diffusion of the Type-3 atoms. To assist the interpretation of these results, a series of interfacial models were created and explored using a modified version of the frozen phonon multislice simulation. The models consisted of terraced, vicinal and diffused interfaces. The model results indicate that a diffuse interface can be used to describe the characteristics observed in the experimental images. However, probe scattering from the interfacial region can be counter intuitive. A systematic study of these effects is presented outlining complications that can occur when interpreting interfacial structures using HAADF imaging.

Acknowledgments

I am very grateful for having had the opportunity to be a student under the supervision of Prof. Alan Craven. His guidance during this project has made my time as a graduate student exciting and challenging. I would also like to thank Dr. Ian Maclaren and Dr. Maureen MacKenzie, my second supervisors, who provided many stimulating discussions and much needed advice. This project followed on from research carried out at SuperSTEM by Dr. Paul Robb to whom I am indebted for his support and for his experimental work that made this project possible. I am also very grateful of the environment provided by the academic staff within the Solid State Physics Group who were always willing to give advice and helpful discussions.

The support given by the technical staff has been first class and I am very grateful to Dr. Sam McFadzean, Mr. Brian Miller, Mr. Colin How and Mr. William Smith for their training and expert advice. Much of the modeling work described in the following chapters has been possible because of the support provided by the ScotGRID and departmental IT teams. In particular I would like to thank Dr. Stuart Purdie and Dr. Douglas McNab for their assistance when using the GRID and Mr. Iain Sim for his support with the departmental clusters.

I would also like to thank all the members of SSP for making my time within the group very enjoyable. In particular I would like to thank Gary, Paul, Paolo and Rafael for their friendship and for taking my money during poker. My family have been very supportive during my studies and I would especially like to thank my parents for their kind words of wisdom. I would like to thank my daughter Holly who, during the most difficult periods of this project, has been a source of joy. Finally, and most importantly, I want to thank Laura for her love and support in times when I needed it most.

Declaration

This thesis has been written solely by myself and details the research I have carried out within the Solid State Physics Group in the Department of Physics and Astronomy at the University of Glasgow. The work described is my own except where otherwise stated.

This thesis has not been submitted in any previous application for a higher degree.

....

M P Finnie

Contents

1 Introduction **1**

1.1 Semiconductor Device Development 1

1.1.1 Semiconducting Materials 1

1.1.2 Device Growth 2

1.1.3 Field Effect Transistor 3

1.1.4 MOSFET 3

1.1.5 High-k 6

1.1.6 MODFET 6

1.2 Interfacial Roughness 8

1.2.1 Electron Microscopy 8

1.2.2 The SuperSTEM Project 9

1.3 Thesis Outline 11

2 Background, Instrumentation and Methods **13**

2.1 Imaging with the Electron 13

2.2 Beam Specimen Interaction 14

2.2.1 Elastic Scattering 15

2.2.1.1 The Scattering Cross-Section 15

2.2.1.2 Bragg Scattering 18

2.2.2 Inelastic Scattering 18

2.2.2.1 Plasmons and Phonons 18

2.2.2.2 Single Electron Scattering 20

2.2.2.3 X-ray Emission 20

2.2.2.4 Beam Damage 20

2.3 Electron Microscopy 22

2.3.1 Electron Sources 22
2.3.1.1 Thermionic Sources 23
2.3.1.2 Field-Emission Sources 23
2.3.2 Electron Lenses 24
2.3.3 Aberrations 25
2.3.3.1 Higher Order Aberrations 27
2.3.3.2 Balancing Aberrations 28
2.4 Instrumentation and Techniques 31
2.4.1 FEI Tecnai T20 31
2.4.1.1 Gatan Image Filter 31
2.4.1.2 Convergent Beam Electron Diffraction 33
2.4.2 Tecnai TF20 34
2.4.2.1 High Angle Annular Dark Field Imaging 36
2.4.2.2 EELS 36
2.4.3 SuperSTEM 37
2.5 Sample Preparation 39
2.5.1 Cross Sectioning Method 39
2.6 Summary 41

3 Computational Software: Modification and Single Crystal Calculation 42

3.1 Multislice Image Simulation 42
3.1.1 HAADF signal 45
3.1.2 Electron Intensity Distribution 45
3.1.3 Frozen Phonon Method 46
3.2 Software Modifications 47
3.2.1 Probe Forming Software 48
3.2.2 Multislice Code 48
3.3 Simulated Image Calculation 50
3.3.1 Cluster Computing 50
3.3.2 GRID Computing 51
3.4 Data Processing 54
3.4.1 Matlab 54

3.4.2 Atomeye . . . 56
3.5 Simulated Probes . . . 56
3.5.1 T20 Probe . . . 56
3.5.2 SuperSTEM 1 Probe . . . 58
3.6 Simulated Single Crystals . . . 60
3.6.1 GaAs Single Crystal . . . 60
3.6.1.1 Calculation Parameters . . . 60
3.6.1.2 GaAs EELS Signal . . . 62
3.6.1.3 GaAs HAADF Signal . . . 63
3.6.1.4 GaAs Column Ratio . . . 65
3.6.2 AlAs Single Crystal . . . 66
3.6.2.1 Calculation Parameters . . . 66
3.6.2.2 AlAs EELS Signal . . . 67
3.6.2.3 AlAs HAADF Signal . . . 68
3.6.2.4 AlAs Column Ratio . . . 70
3.7 Summary . . . 70

4 Debye Waller Factor Validation **73**
4.1 Background Theory . . . 73
4.2 Specimen Thickness Measurement . . . 76
4.2.1 Two-Beam Condition . . . 78
4.2.2 t/λ Measurement . . . 81
4.2.3 Mean Free Path Approximation . . . 81
4.2.4 Mean Free Path Determination for GaAs . . . 82
4.2.4.1 Mean Free Path Measurement for GaAs [310] . . . 82
4.2.4.2 Mean Free Path Measurement for GaAs [110] . . . 83
4.3 Experimentally Derived Mean Square Displacement . . . 84
4.4 Effect of $< u^2 >$ on HAADF Signal . . . 89
4.4.1 T20 Probe . . . 89
4.4.2 SuperSTEM Probe . . . 90
4.5 Discussion and Conclusions . . . 91

5 Experimental GaAs - AlAs Interface **95**
5.1 Introduction . . . 95

5.2 Column Ratio Mapping . . . 96
5.2.1 Background HAADF Signal Removal . . . 96
5.2.1.1 Frequency Filter Method . . . 98
5.2.1.2 Positional Mask Method . . . 99
5.2.2 Automated Signal Measurement . . . 104
5.3 Interface Width Measurement . . . 105
5.3.1 Column Ratio Threshold . . . 107
5.3.2 Analytical Function Fitting . . . 108
5.4 Experimental SuperSTEM Images . . . 110
5.4.1 Local Roughness . . . 112
5.4.2 Experimental Measurements . . . 113
5.5 Background Signal Analysis . . . 117
5.6 Discussion and Conclusions . . . 120

6 Simulated GaAs - AlAs Interface 123
6.1 Modelling Proposals . . . 123
6.2 Simulated GaAs - AlAs Interface . . . 126
6.2.1 Model Configuration . . . 126
6.2.2 Perfect Interface . . . 128
6.2.3 Sawtooth Interface . . . 134
6.2.3.1 110nm Repeat Length (AlAs Projection) . . . 137
6.2.3.2 110nm Repeat Length (GaAs Projection) . . . 142
6.2.3.3 18nm Repeat Length (AlAs Projection) . . . 151
6.2.3.4 18nm Repeat Length (GaAs Projection) . . . 153
6.2.4 Diffused Interface . . . 157
6.2.4.1 Linear Diffusion Model . . . 159
6.2.4.2 Segregation Model . . . 160
6.2.5 Simple Vicinal Interface . . . 167
6.2.5.1 AlAs Projection . . . 171
6.2.5.2 GaAs Projection . . . 179
6.2.6 Random Step Vicinal Interface . . . 188
6.2.6.1 Type-A ($\theta = 0.2°$) . . . 189
6.2.6.2 Type-A ($\theta = 0.3°$) . . . 191

6.2.6.3 Type-A ($\theta = 0.6°$) 192
6.2.6.4 Type-G ($\theta = 0.2°$) 196
6.2.6.5 Type-G ($\theta = 0.6°$) 197
6.3 Discussion and Conclusions 198

7 Atomic Column Scattering **204**
7.1 AlAs - GaAs 207
7.1.1 AlAs - GaAs $_{4.3nm}$ 207
7.1.2 AlAs - GaAs $_{14.3nm}$ 209
7.1.3 AlAs - GaAs $_{30.8nm}$ 213
7.1.4 AlAs - GaAs $_{100nm}$ 215
7.1.5 Electron Re-Scattering 217
7.2 GaAs - AlAs 229
7.2.1 GaAs - AlAs $_{3.9nm}$ 229
7.3 InAs - AlAs 231
7.3.1 InAs - AlAs $_{1.7nm}$ 234
7.4 Implications for Quantitative HAADF Imaging 237
7.4.1 Quantitative HAADF Imaging 237
7.4.1.1 Thin Specimen - 30nm 238
7.4.1.2 Thick Specimen - 60nm 239
7.5 Discussion and Conclusions 241

8 Conclusions and Future Work **242**
8.1 Introduction 242
8.2 Conclusions 243
8.3 Future Work 248

List of Figures

1.1 MBE Growth Chamber . . . 3
1.2 A Cross-Section of a MOSFET & MODFET. . . . 4
1.3 MOSFET Output . . . 5
1.4 Heterojunction Band Diagram . . . 7

2.1 Beam Specimen Interactions . . . 14
2.2 Elastic Interaction . . . 15
2.3 Von Laue Equation . . . 17
2.4 Coherent Scattering . . . 19
2.5 Magnetic Lens Schematic . . . 25
2.6 Magnetic Lens Aberrations . . . 26
2.7 Aberration Function, $\chi(\alpha)$ . . . 28
2.8 Contrast Transfer Function, $Sin(\chi)$ . . . 29
2.9 The Optical Transfer Function, OTF . . . 30
2.10 FEI Tecnai $T20$ . . . 32
2.11 Gatan Image Filter, GIF . . . 33
2.12 Two Beam Condition . . . 34
2.13 FEI Tecnai $TF20$ . . . 35
2.14 SuperSTEM 1 . . . 38

3.1 Multislice Wavefunction Propagation . . . 44
3.2 CBED and Electron Intensity Distribution . . . 50
3.3 Script Control Process . . . 52
3.4 Glasgow ScotGRID Cluster Nodes . . . 53
3.5 GaAs [110] Projected View . . . 61
3.6 Slicing and Probe Positioning for [110] GaAs . . . 62
3.7 GaAs - Primary Column Intensity . . . 63

3.8 GaAs - HAADF Signal 64
3.9 GaAs - Background Subtracted HAADF Signal 65
3.10 GaAs - Column Ratio 67
3.11 AlAs - Primary Column Intensity 68
3.12 AlAs - HAADF Signal 69
3.13 AlAs - Background Subtracted HAADF Signal 69
3.14 AlAs - Column Ratio 71

4.1 Line Profile of EF-CBED, GaAs [310] 75
4.2 GIF - Energy Filtered Images 76
4.3 Energy Filtered CBED, GaAs [310] 77
4.4 Two-Beam Condition using GaAs 000 and 400 Reflections 79
4.5 Two-beam Condition Measurements 79
4.6 Specimen Thickness Determination 80
4.7 EELS Spectrum 81
4.8 Specimen Thickness Regression [310] 83
4.9 Specimen Thickness Regression [110] 84
4.10 GaAs [310] Unit Cell 86
4.11 Experimental and Simulated GaAs [310] CBED Pattern 87
4.12 FOLZ Ratio for the [310] Orientation 88
4.13 FOLZ Ratio for the [110] Orientation 88
4.14 T20 HAADF Signal Dependence on $< u^2 >$, [110] 90
4.15 T20 HAADF Signal Dependence on $< u^2 >$, [310] 91
4.16 SuperSTEM HAADF Signal Dependence on $< u^2 >$, [110] 92
4.17 SuperSTEM Column Ratio Dependence on $< u^2 >$, [110] 92
4.18 Radial Variation of FOLZ Ring Intensity 94

5.1 A HAADF Image of a [110] Orientated GaAs - AlAs Interface. 97
5.2 FT Residual Background 100
5.3 Single and Interpolated Background Estimation. 102
5.4 Background Effect on Column Ratio 103
5.5 Automated Data Extraction Process 106
5.6 Column Ratio Map of GaAs - AlAs Superlattice 107
5.7 Column Ratio - Thresholding 108

5.8 Column Ratio - Analytical Function 109
5.9 MBE Sample - C102 111
5.10 Estimation of Local Interfacial Roughness 113
5.11 Column Ratio Map with Fit 114
5.12 Histogram of Fit Variation 114
5.13 Variation of the Local Roughness 115
5.14 Column Ratio Profile from the Deep Superlattice Region 117
5.15 Experimental Interface Width - Average 118
5.16 Type-A Interface Width - Line By Line 118
5.17 Type-G Interface Width - Line By Line 119
5.18 Background HAADF Signal Analysis 121
5.19 Experimental Interface Width - Background 122

6.1 GaAs - AlAs Model Configuration 127
6.2 Ideal Interface - Schematic 128
6.3 Ideal Interface - Dumbbell 8 HAADF 131
6.4 Ideal Interface - Dumbbell 8 Primary Column Intensity 131
6.5 Ideal Interface - Probe Positioning. 132
6.6 Ideal Interface - Dumbbell 9 HAADF 133
6.7 Ideal Interface - Variation of Column Ratio with Thickness 135
6.8 Ideal Interface - Column Ratio 135
6.9 Ideal Interface - Interface Width. 136
6.10 Ideal Interface - Interface Position 136
6.11 Sawtooth Interface (110nm AlAs Projection) - Schematic 139
6.12 Sawtooth Interface (110nm AlAs Projection) - Column Ratio 139
6.13 Sawtooth Interface (110nm AlAs Projection) - Interface Position 140
6.14 Sawtooth Interface (110nm AlAs Projection) - Dumbbell 6 HAADF . . 142
6.15 Sawtooth Interface (110nm AlAs Projection) - Dumbbell 6 Primary Column Intensity 143
6.16 Sawtooth Interface (110nm AlAs Projection) - Dumbbell 7 HAADF . . 143
6.17 Sawtooth Interface (110nm AlAs Projection) - Dumbbell 7 Primary Column Intensity 144
6.18 Sawtooth Interface (110nm AlAs Projection) - Interface Width 144

6.19 Sawtooth Interface (110nm GaAs Projection) - Interface Position . . . 146
6.20 Sawtooth Interface (110nm GaAs Projection) - Interface Width 146
6.21 Sawtooth Interface (110nm GaAs Projection) - Column Ratio 147
6.22 Sawtooth Interface (110nm GaAs Projection) - Dumbbell 10 HAADF . 148
6.23 Sawtooth Interface (110nm GaAs Projection) - Dumbbell 10 Primary Column Intensity 149
6.24 Sawtooth Interface (110nm GaAs Projection) - Dumbbell 11 HAADF . 149
6.25 Sawtooth Interface (110nm GaAs Projection) - Dumbbell 11 Primary Column Intensity 150
6.26 Sawtooth Interface (18nm AlAs Projection) - Interface Position 152
6.27 Sawtooth Interface (18nm AlAs Projection) - Interface Width 152
6.28 Sawtooth Interface (18nm AlAs Projection) -Column Ratio 153
6.29 Sawtooth Interface (18nm GaAs Projection) - Interface Position 154
6.30 Sawtooth Interface (18nm GaAs Projection) - Interface Width 155
6.31 Sawtooth Interface (18nm GaAs Projection) - Column Ratio 156
6.32 Sawtooth Interface (18nm GaAs Projection) - Dumbbell 5 HAADF . . 157
6.33 Sawtooth Interface (18nm GaAs Projection) - Dumbbell 7 HAADF . . 158
6.34 Sawtooth Interface (18nm GaAs Projection) - Dumbbell 10 HAADF . 158
6.35 Linear Diffusion Model - Concentration 160
6.36 Linear Diffusion Model - Schematic 161
6.37 Linear Diffusion Model - Column Ratio 161
6.38 Linear Diffusion Model - Interface Position 162
6.39 Linear Diffusion Model - Interface Width 163
6.40 Type-A Diffusion Model - Concentration 165
6.41 Type-A Diffusion Model - Schematic 166
6.42 Type-A Diffusion Model - Column Ratio 166
6.43 Type-A Diffusion Model - Interface Position 167
6.44 Type-A Diffusion Model - Interface Width 168
6.45 Type-G Diffusion Model - Concentration 169
6.46 Type-G Diffusion Model - Schematic 169
6.47 Type-G Diffusion Model - Interface Position 170
6.48 Type-G Diffusion Model - Interface Width 170
6.49 Simple Vicinal Interface - Overview 172

6.50 Vicinal Interface - AlAs Projection - 8nm Entry - Schematic 172
6.51 Vicinal Interface - AlAs Projection - 8nm Entry - Column Ratio 173
6.52 Vicinal Interface - AlAs Projection - 8nm Entry - Interface Position . . 173
6.53 Vicinal Interface - AlAs Projection - 8nm Entry - Interface Width . . . 174
6.54 Vicinal Interface - AlAs Projection - 2nm Entry - Schematic 176
6.55 Vicinal Interface - AlAs Projection - 2nm Entry - Column Ratio 177
6.56 Vicinal Interface - AlAs Projection - 2nm Entry - Interface Position . . 177
6.57 Vicinal Interface - AlAs Projection - 2nm Entry - Interface Width . . . 178
6.58 Vicinal Interface - AlAs Projection - 2nm Entry - Dumbbell 6 180
6.59 Vicinal Interface - AlAs Projection - 8nm Entry - Dumbbell 6 180
6.60 Vicinal Interface - GaAs Projection - 2nm Entry - Schematic 181
6.61 Vicinal Interface - GaAs Projection - 12nm Entry - Schematic 181
6.62 Vicinal Interface - GaAs Projection - 2nm Entry - Column Ratio 183
6.63 Vicinal Interface - GaAs Projection - 12nm Entry - Column Ratio . . . 184
6.64 Vicinal Interface - GaAs Projection - 2nm Entry - Interface Position . . 185
6.65 Vicinal Interface - GaAs Projection - 12nm Entry - Interface Position . 186
6.66 Vicinal Interface - GaAs Projection - 2nm Entry - Interface Width . . . 186
6.67 Vicinal Interface - GaAs Projection - 12nm Entry - Interface Width . . 187
6.68 Vicinal Interface - GaAs Projection - 2nm Entry - Dumbbell 12 187
6.69 Vicinal Interface - GaAs Projection - 12nm Entry - Dumbbell 12 188
6.70 Random Vicinal Type-A Interface - Overview 190
6.71 Random Vicinal Step Length. 190
6.72 Random Vicinal Interface - Type-A - $\theta = 0.2°$ - Interface Position . . . 191
6.73 Random Vicinal Interface - Type-A - $\theta = 0.2°$ - Interface Width 192
6.74 Random Vicinal Interface - Type-A - $\theta = 0.3°$ - Interface Position . . . 193
6.75 Random Vicinal Interface - Type-A - $\theta = 0.3°$ - Interface Width 193
6.76 Random Vicinal Interface - Type-A - $\theta = 0.6°$ - Interface Position . . . 195
6.77 Random Vicinal Interface - Type-A - $\theta = 0.6°$ - Interface Width 195
6.78 Diffuse Vicinal Interface - Type-G - $\theta = 0.2°$ - Interface Position 196
6.79 Diffuse Vicinal Interface - Type-G - $\theta = 0.2°$ - Interface Width 197
6.80 Diffuse Vicinal Interface - Type-G - $\theta = 0.6°$ - Interface Position 198
6.81 Diffuse Vicinal Interface - Type-G - $\theta = 0.6°$ - Interface Width 200
6.82 Experimental and Model Comparison - Vicinal 202

6.83 Experimental and Model Comparison - Diffused 203

7.1 Interfacial Change of Lattice Parameter 208
7.2 AlAs into GaAs $_{4.3nm}$ 210
7.3 AlAs into GaAs $_{14.3nm}$ 212
7.4 Intensity Integration Profile - Overview 213
7.5 Intensity Integration - Single Crystal AlAs 214
7.6 AlAs into GaAs $_{30.8nm}$ 216
7.7 AlAs into GaAs $_{100nm}$ 218
7.8 Electron Re-Scattering - Overview 219
7.9 Electron Re-Scattering Matrix. 221
7.10 Re-Scattering Comparison - Single Crystal GaAs 222
7.11 Re-Scattering Comparison - Single Crystal AlAs 223
7.12 Re-Scattering Comparison - AlAs into GaAs $_{4.3nm}$ 225
7.13 Re-Scattering Comparison - AlAs into GaAs $_{14.3nm}$ 226
7.14 Re-Scattering Comparison - AlAs into GaAs $_{30.8nm}$ 227
7.15 Re-Scattering Comparison - AlAs into GaAs $_{100nm}$ 228
7.16 Intensity Integration - Single Crystal GaAs 230
7.17 GaAs into AlAs $_{3.9nm}$ 232
7.18 Single Crystal InAs 235
7.19 InAs into AlAs $_{1.7nm}$ 236
7.20 Quantitative Complications - Thin Specimen - Low Z to High Z 238
7.21 Quantitative Complications - Thin Specimen- High Z to Low Z 239
7.22 Quantitative Complications - Thick Specimen - Low Z to High Z . . . 240
7.23 Quantitative Complications - Thick Specimen - High Z to Low Z . . . 240

8.1 Input Parameters for autoslic_interface.c 267

List of Tables

2.1 Atomic Screening Parameters 16
2.2 Atomic Displacement Energies for III-V materials 21
2.3 Maximum Energy Transfer 22

3.1 Simulated Probe Parameters: FEI Tecnai $T20$ 57
3.2 Simulated Probe Parameters: SuperSTEM 1 58
3.3 Simulated Aberrations: SuperSTEM 1 24mrad 59
3.4 III-V Crystal Simulation Parameters 71

4.1 Energy Filtered CBED & EELS - Experimental Parameters 77
4.2 Mean Free Path Approximation 82

6.1 Simulation Model Overview 199

List of Symbols

$< u^2 >$ mean square displacement amplitude

$< u^2 >_{current}$ current mean square displacement amplitude

α re-scattering coefficient

α semiangle of incidence

α/β goniometer tilt

β collection angle

χ phase distortion function

Δz slice thickness

d interplanar spacing

t specimen thickness

$\boldsymbol{g}$ diffraction vector

$\boldsymbol{v}$ velocity

$a,\ b$ unit cell dimensions

A amperes

c velocity of light

dx image size, x

dy image size, y

e charge on the electron

F relativistic factor

G angular radius of the FOLZ ring

G giga

H lattice spacing parallel to the beam direction

h Planck's constant

k dielectric constant

k kilo

M Debye-Waller factor

M mega

m aberration azimuthal symmetry

m meter

m milli

Nx image sampling, x

Ny image sampling, y

n nano

n order of aberration

P propagator function

p	pico
q	electron charge
sr	steradians
t	transmission function
V	accelerating voltage
X	atomic species
x	distance
x_{pp}	probe position
Z	Atomic Number
η	re-scattering index
λ	mean free path
λ	wavelength
μ	micro
$\otimes$	convolution
$\overrightarrow{k}$	wave vector
$\overrightarrow{n}$	integer vector
$\overrightarrow{r}$	atom separation vector
ϕ	azimuthal angle
ψ	wavefunction amplitude
$\psi_{transmitted}$	transmitted wavefunction amplitude
$\mathbf{B}$	magnetic induction strength
$\mathbf{F}$	Lorentz force
θ	scattering semiangle
θ	vicinal interface angle
θ_0	screening parameter
θ_B	Bragg angle
θ_i	distance between K-M fringes
ξ_g	extinction distance
a_0	the Bohr radius
B_L	longitudinal component of induction field
B_R	radial component of induction field
C_1	defocus
C_3	spherical aberration
C_5	fifth order aberration
E_0	beam energy
E_{max}	maximum energy transfer
E_m	average energy loss
$E_{transfer}$	transfer energy
E_d	displacement energy
$f(\theta)$	atomic scattering factor
f_{B_j}	electron scattering factor
f_i	atomic fraction
f_x	scattering factor for X-rays
$FOLZ_{ratio}$	ratio of FOLZ intenisty

I_0 zero-loss peak intensity

$I_{background}$ FOLZ background intensity

I_{FOLZ} FOLZ intensity

I_P interface position

I_t total spectrum intensity

I_W interface width

k_{max} maximum wave vector

m_0 rest mass of the electron

N_X number of atoms

$r_{diffraction}$ theoretical disk radius

$r_{spherical}$ spherical aberration disk radius

s_i deviation parameter

v_z projected potential

V_d device drain voltage

V_g device gate voltage

V_t device threshold voltage

a error function amplitude coefficient

b error function width coefficient

c error function position coefficient

K Kelvin

M scattering atom mass

m mean

ML mono-layer

R device scaling constant

v variance

Å Ångström

Chapter 1

Introduction

1.1 Semiconductor Device Development

1.1.1 Semiconducting Materials

Semiconductor devices are the key components for many electronic systems [1]. Components such as resistors, diodes and transistors form the foundations of modern computing and can be fabricated from semiconducting materials [1, 2, 3]. A semiconductor's ability to conduct can be drastically changed by exposure to light, heat, magnetic or electric fields [4]. This sensitivity of conductivity make semiconductors one of the most important materials for electronic applications.

The conduction current within a semiconductor can be carried either by the flow of electrons or by the flow of positively charged "holes". The concentration of these charge carriers can be increased by the addition of impurities to the semiconductor which is known as doping [4, 1]. When the doped semiconductor contains excess holes it is called a "p-type" semiconductor, and when it contains excess free electrons it is known as "n-type" [4, 1]. An ideal high-speed semiconductor should have at least one type of charge carrier that responds rapidly to changes in an applied electric field [4].

By far the most important semiconductor is silicon, Si, found in column IV in the periodic table. High-quality layers can be grown thermally and the cost of "device grade" silicon is low making the material ideal for device fabrication. Semiconductors can also be composed of two elements and many of these important compounds are derived from elements found in columns III and V and are called III-V compounds. These binary III-V compounds exhibit properties, such as a direct band gap, that are

absent in silicon [3]. More complex ternary III-V compounds such as $Al_xGa_{1-x}As$ (where $0 \leqslant x \leqslant 1$) provide a range of compounds that allow specific material characteristics to be controlled by careful doping. III-V compounds have certain advantages over silicon due to their higher carrier mobilities and higher carrier velocities which are vital when fabricating high speed switching devices [4].

1.1.2 Device Growth

Molecular Beam Epitaxy (MBE) is a method of growing high quality multilayer systems [5]. Developments in MBE have allowed exceptional control over growth parameters such as doping concentration and layer thickness [6]. MBE growth is achieved in a high vacuum (10^{-13} Bar) chamber and a typical MBE setup is shown in figure 1.1. The growth materials are produced by heating high-purity solid sources of the lattice elements in a series of effusion cells. The temperature of the cells are controlled to give the required evaporation rate and a series of shutters control the thermal beams. The beams are directed onto a heated substrate causing a reaction with the crystalline surface producing epitaxial growth [4, 1, 7]. The chamber also typically contains in-situ diagnostic tools and figure 1.1 shows a Reflection High-Energy Electron Diffraction (RHEED) system. This system uses electrons reflected off the growth surface of the crystal to form a diffraction pattern on a screen. During MBE growth, the intensity of the pattern oscillates allowing accurate measurement of growth rates and surface quality [8, 3, 2, 9]. The process of MBE is used to grow high quality multilayer systems from which many electrical components are formed such as transistors, photonic devices and microwave devices.

The quality of the interfacial layers grown using MBE can greatly affect the usability and performance of the final fabricated devices [1, 4]. In the case of MODFETs, a 2D electron gas forms at the interfacial region and carrier motion along this interface will be impeded if the interface has a degree of roughness [10]. In this case, the interfacial roughness can cause increased scattering of the charge carriers reducing the operating current of the device. This, in turn, reduces the overall device performance [4].

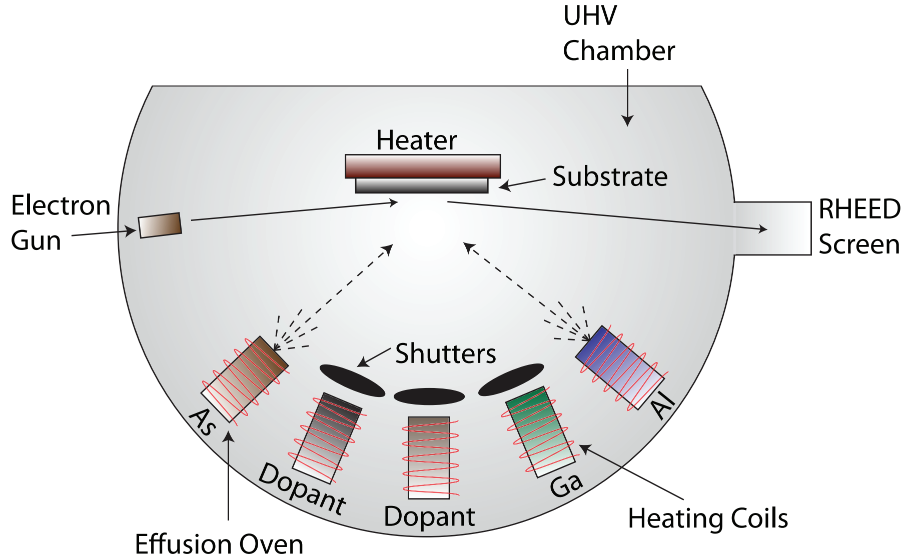

Figure 1.1 – A schematic of a typical MBE growth chamber. The effusion cells, shutters, substrate and RHEED monitoring system are indicated.

1.1.3 Field Effect Transistor

A field effect transistor (FET) is a voltage controlled device and consists of a gate, drain and a source [11]. The gate can be used to control the current that flows within the semiconductor between the source and the drain. The application of a voltage to the gate produces an electric field within the semiconducting material that can create or eliminate a conduction channel between the source and drain [1]. The FETs are distinguished by the method of insulating the gate from the conduction channel. A metal-oxide semiconductor FET (MOSFET), shown in figure 1.2(1), utilises an oxide insulator, typically SiO_2. In a modulated-doping field effect transistor (MODFET), shown in figure 1.2(2), this is achieved using a semi-insulating AlGaAs layer [4].

1.1.4 MOSFET

The operation of the MOSFET is dependent on the threshold voltage of the device, V_t. Two different operational modes are controlled using V_t and define the normal state of the device where the device is either normally off (enhancement mode) or normally on (depletion mode) [5]. The value of V_t can be controlled via substrate doping or the thickness of the oxide layer. The n-type MOSFET, shown in figure 1.2(1), operating in enhancement mode, can be categorised into three different classes. The three classes

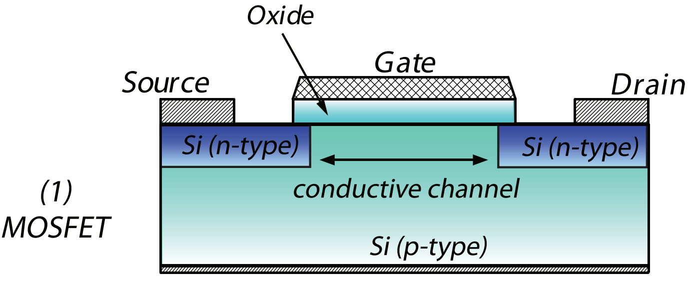

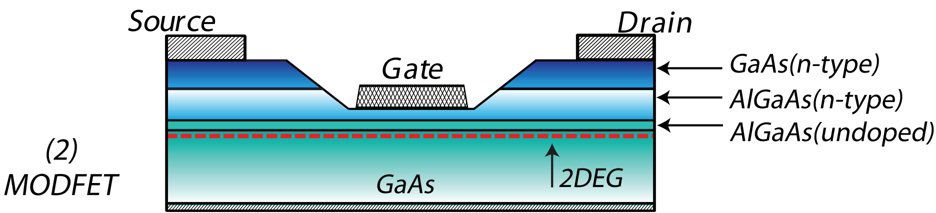

Figure 1.2 – A cross-section of (1) an n-type metal-oxide semiconductor field effect transistor (MOSFET) device and (2) a modulated-doped field effect transistor (MODFET).

are dependent on the threshold voltage V_t , the applied gate voltage V_g and the drain voltage V_d [1, 4, 5].

$V_g < V_t$ Where the applied gate voltage is less than the device threshold voltage the device is off and there is **no** conduction between the source and the drain (except a small leakage current).

$V_g > V_t$ & $V_d < (V_g - V_t)$ When the applied gate voltage is greater than the device threshold voltage and the drain voltage is less than $V_g - V_t$ the device is on and operating like a resistor.

$V_g > V_t$ & $V_d > (V_g - V_t)$ When the applied gate voltage is greater than the device threshold voltage and the drain voltage is greater than $V_g - V_t$ the device is on and conduction is now operating in saturation mode. In this mode the conduction of electrons between the source and drain is not confined to a thin channel but extends deeper into the substrate. The device is operating in the ***active*** region.

The output and transfer characteristics summarised in the I-V plots of figure 1.3 indicate that a positive gate bias that is larger than the threshold voltage, V_t, must be applied before a significant drain current will flow.

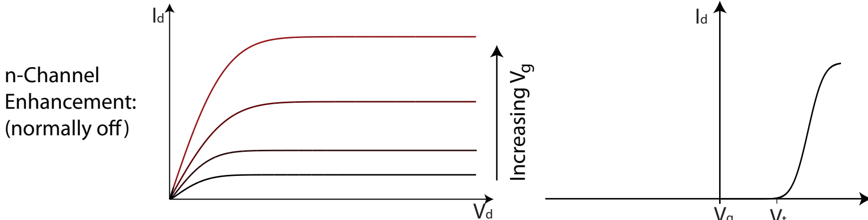

Figure 1.3 – The above plots detail the transfer characteristics of the n-channel MOSFET operating in enhancements mode. The left graph shows the relationship between the drain current, I_d, and the drain to source voltage, $v_g - v_{th}$. The graph on the right indicates that a significant drain current, I_d, will only flow when $v_g > v_{th}$.

Crystalline silicon, and the native oxide that naturally forms, provided a simple low cost system for the development of MOSFET devices. This allowed silicon to become the most widely used material in integrated devices. The first MOSFET was fabricated using a thermally oxidised silicon substrate. This produced a device with a channel length $20\mu m$ long and a gate oxide over $100nm$ thick [3].

The scaling of such a device to smaller sizes is desirable for many reasons. Firstly, with smaller device dimensions more devices can be fabricated within a single wafer. This results in devices with consistent functionality [1, 4]. The fabrication cost of a semiconductor wafer is relatively fixed therefore producing more devices per wafer is cost efficient. Furthermore, by scaling the device dimensions (and operating voltages) by a constant, R, many physical properties of the devices are improved. The switching speeds scale linearly with R, the switching power is reduced by R^2 and the switching energy reduced by R^3 [11]. However, as the scaling constant R decreases, the maximum voltage that may be applied to the gate reduces [1, 4]. This sets a limit to the threshold voltage which must also be scaled accordingly. The threshold voltage reaches a point where the transistor cannot be switched completely on or off resulting in a significant leakage current [1]. Furthermore, with a reducing R, the thickness of the insulating gate oxide reduces to a level where electron tunneling between the gate and channel will affect the operation of the device [4].

Another significant issue with device miniaturisation is the increase in device variability. One of the key requirements of fabrication is the ability to mass produce devices with specific electrical, mechanical or optical characteristics. As the size of the devices are reduced, substrate defects and growth defects can strongly influence the characteristics of the device, to a point that the variability of the devices over a single wafer is significant [1, 5].

With these fundamental limitations on the minutarisation of MOSFET devices, the search has turned to other semiconducting materials to continue the improvement in device operation [11, 1, 4].

1.1.5 High-k

The term high-k refers to a material with a high dielectric constant, k, that can be used in semiconductor fabrication to replace the silicon dioxide insulating layer. The implementation of high-k gate dielectrics is one strategy developed to allow the continued miniaturisation of semiconductor devices. Replacing the insulating layer with a high-k material allows increased gate capacitance without the leakage effects. This does, however, add complexity to the manufacturing process. Silicon dioxide can be formed by oxidizing silicon and results in a uniform oxide and a high quality interface and has a dielectric constant (k value) of $\sim$4. Where the k value is the ratio of the permittivity of the medium to the permittivity of free space. Therefore, research is focused on finding a material with a high dielectric constant that can be easily integrated into current manufacturing processes. Another consideration is how the high-k material will change the electrical properties of the device. Current research is focused on hafnium silicate, zirconium silicate, hafnium dioxide and zirconium dioxide, and these high-k materials are typically deposited using atomic layer deposition. High-k materials will typically have a k value of around 30.

1.1.6 MODFET

Advances in epitaxial-growth techniques during the 1970s allowed the fabrication of high quality multilayer structures [9]. The development of high precision growth techniques allowed the fabrication of high quality III-V heterostructures which consisted of semiconductors with differing band gaps. When two semiconducting materials with different band gaps are joined together to form a heterojunction, a discontinuity forms in both the conduction and the valence band edges [4]. For the MODFET, figure 1.2(2), the discontinuity is between a wide band gap n-type, AlGaAs, and a lower band gap material, GaAs. Figure 1.4 shows a conduction-band diagram for the MODFET under positive gate bias (i.e. depletion mode). In this case, the additional charges from the n-doped AlGaAs modify the band edges at the junction creating a triangular poten-

tial well in the conduction band of GaAs [1]. Electrons accumulate within this well, creating a sheet of charge that is analogous to the conduction channel in a MOSFET device. This 2D electron gas can be used as the active channel of the device and can be modulated by the field from the gate [4, 1].

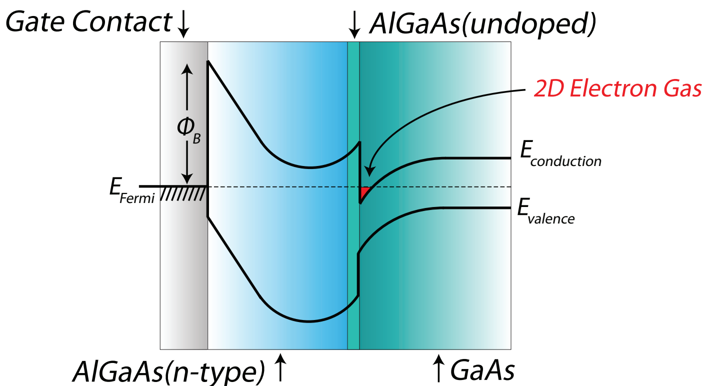

Figure 1.4 – Energy band diagram of a heterojunction between a high band gap material (AlGaAs) and a low band gap material (GaAs). Indicated is the formation of a high conductivity inversion layer at the junction interface.

An important consideration when forming a heterojunction between two materials is the difference in the lattice parameter [1]. For example, GaAs has a lattice parameter of 5.6533$\mathring{A}$ while the lattice parameter for AlAs is 5.6605$\mathring{A}$ which corresponds to a lattice mismatch of 0.12%. As the MBE growth of the lattice mismatched material commences, the lattice misfit is accommodated by elastic strain. However, when the layer thickness exceeds a critical value, the strain is relieved through the formation of a dislocation at the interface. As the lattice mismatch increases, this critical thickness reduces, and the ability to grow low defect layers becomes increasingly difficult [4, 5]. For example, the growth of InAs films on a GaAs substrate results in a lattice mismatch of $> 7\%$ which produces extensive dislocation formation for layer thicknesses greater than a few monolayers. The strain that forms at an interface results in compression and dilation forces that can affect inter atomic bonding. This can, in turn, drastically modify the band structure of the material [4]. The dislocations are potential trapping sites that cause scattering of the charge carriers, this reduces the overall charge mobility affecting the performance of the device. The lattice mismatch can be reduced by doping of the growth material [1]. Furthermore, the implementation of periodic potentials (superlattices) by doping modulation offers the ability to tune the optical and electronic properties of these devices [9].

1.2 Interfacial Roughness

The ability to characterise the abruptness of the interfacial region is vital if a full understanding of the growth mechanisms during MBE is to be developed. A variety of techniques have been developed to determine the degree of interfacial roughness. The MBE growth can be monitored using an *in situ* technique called Reflection High Energy Electron Diffraction, RHEED [12, 13]. An electron beam is reflected from the growth surface producing a diffraction pattern on a viewing screen. The intensity oscillations of the pattern can be used as an accurate direct measure of the MBE growth rate [14]. When MBE growth is initiated on a smooth surface the intensity of the RHEED pattern begins to oscillate. The frequency of the oscillation corresponds directly to the monolayer growth rate (where in the case of GaAs a monolayer is the thickness of one full layer of Ga and one full layer of As atoms). The intensity oscillations are a direct result of the layer by layer growth. Before growth begins the substrate is initially smooth and the reflected intensity is bright. As the layer nucleates islands form on the surface and the intensity is reduced. As the layer growth finishes the islands coalesce into a complete layer and the intensity increases again. These intensity oscillations can therefore been attributed to the degree of roughness [14]. While RHEED can be used to monitor the growth of each mono-layer, estimating the interfacial roughness using this technique can be difficult.

1.2.1 Electron Microscopy

As the scale of devices has reduced significantly, it is becoming increasingly important to have the ability to characterise interfacial structures at the atomic scale. Furthermore, to know exactly where each atom is and how it is bonded is vital for complete characterisation. For heterostructures formed between two semiconductors, this means obtaining information from within the bulk of the solid [15]. In Scanning Transmission Electron Microscopy (STEM) an electron beam is focused to a very small probe and scanned across the surface of a thin specimen. If the sample is thin enough, transmitted electrons can be collected using a detector. If the output signal from the detector is proportional to the intensity incident onto the detector then an image can be formed. An overall image is built up point by point as the probe is scanned across the surface of the specimen. An image can be formed by selecting transmitted electrons that are

scattered into a specific solid angle. For example, a bright field detector placed on the optic axis produces images that has phase contrast. In this case, electrons that are coherently scattered outwith the detector angles will not contribute. Collecting only the high angle scattered electrons, typically greater than $50mrad$, produces an image with atomic number sensitivity. The transmitted electrons can also be dispersed using a magnetic prism, allowing electrons of a specific energy range to contribute to the image. In practice, the resolution of the images depends on the size of the probe. This, in turn, is limited by diffraction at the probe forming aperture and lens aberrations. With the development of aberration correction, electron microscopes now have the ability to form sub-Ångström probes. These probes can be used to analyse structures at the atomic scale [16, 17].

The principles of aberration correction have been known since 1947. It was Scherzer who recognised that round electron lenses would suffer from spherical aberration, limiting the probe size to $\sim 2\mathring{A}$ for electrons between 100-200kV [18]. Scherzer also discussed the use of non-round lenses as a possible way of correcting the lens aberrations. Aberration correctors that are comprised of multipole lens combinations can be used to correct for lens aberrations. However, the complexity of the lens alignment and operation requires the components to be computer controlled. This control has only been available with recent developments in computer processing power. These recent developments in aberration correction have revolutionised the field of microscopy and micro-analysis [19].

1.2.2 The SuperSTEM Project

The SuperSTEM project began in 1997 after Professor L. M. Brown presented a paper entitled “A Synchrotron in a Microscope” [20] to the EMAG conference. This paper proposed a challenge to the microscopy community to exploit the emerging research on aberration correction. The SuperSTEM project was then funded in 2001 by the Engineering and Physical Sciences Research Council (EPSRC) and is based in Daresbury, UK. The SuperSTEM management committee consists of members from the four collaborating universities (Glasgow, Cambridge, Leeds and Liverpool). The first microscope, SuperSTEM 1, is based on a VG Instruments HB501 100kV (cold FEG emitter) dedicated STEM retrofitted with a Mark II quadrupole-octupole aberration

corrector supplied by Nion[1]. The aberrations are corrected to third order providing a resolution better than 1 Ångström. The microscope is also fitted with a UHV ENFINA spectrometer with an energy resolution of 0.3eV [21, 22]. SuperSTEM 2 is a Nion UltraSTEM 100, which has been specially designed as an aberration corrected instrument, is also a 100kV (cold FEG emitter) STEM (with CTEM capabilities). It corrects up to fifth order electron-optic aberrations using a quadrupole-octupole design. Using a 3 lens condenser system, the microscope can achieve a small probe with a very high current improving analytical signal to noise. The larger convergence angle and higher order correction improves the theoretical image resolution and a probe size of < 0.7 Ångströms should be achievable [21, 22].

Recent research at the University of Glasgow used SuperSTEM 1, combined with HAADF imaging, to investigate several MBE grown III-V semiconductor structures [23]. The aim of the project was to characterise the composition and interfacial sharpness of the various layers that were present in the MBE grown sample. This required the development of a consistent method for extracting the atomic column information from the STEM images. The image processing technique is termed Column Ratio Mapping and involves the automated process of measuring atomic column intensity ratios in high-resolution HAADF images. The Column Ratio Mapping reveals compositional variations across the HAADF image and allows a statistical analysis of interfacial regions. The interpretation of these Column Ratio Maps required the understanding of sub-Ångström probe scattering in III-V materials. This understanding was developed through the use of computer modelling where the interaction of the probe within single crystal III-V materials was studied in detail [23].

In this current project, the investigation aimed towards interpreting the HAADF STEM images and in particular understanding the interaction of the sub-Ångström probe at an interfacial region. HAADF imaging makes use of the strong channelling effects that occur when a sub-Ångström probe illuminates an atomic column within a crystal. The interpretation of these images require careful consideration as they may not represent a full projection of the crystal structure, but rather a section of a thin region within the sample. The aim of this project was to develop a series of interfacial models that could be evaluated and directly compared to experimental images providing an understanding of the mechanisms that contribute to image contrast. The results

[1]Nion R&D, 1102 8th St., Kirkland, WA 98033, USA

of this investigation allowed an informed interpretation of the SuperSTEM 1 images. Furthermore, the understanding of probe scattering at interfacial regions provides a foundation for the development of future HAADF-STEM experiments.

1.3 Thesis Outline

Chapter two develops the background theory of electron-specimen interactions and the imaging theory that is required for the interpretation of the experimental images. Furthermore, a basic overview of the layout and operational modes of the microscopes used to obtain the experimental images is presented. The imaging and analytical microscopy techniques used throught this work are also discussed. Chapter two also outlines the methods used to prepare the TEM samples using a cross-sectional method.

Chapter three deals with the theory of image simulation and discusses the computational code that was employed to calculate the simulated images. The chapter also details the main modifications made to the original code and, more specifically, why these modifications were necessary. In addition to discussing the modified simulation code, chapter three outlines the development of the scripts that were required to operate, distribute, collate and analyse the simulation output. The use of GRID computing is also discussed and the progression from small scale cluster computing to large scale GRID computation is presented. The last section in chapter three details the calculation results from single III-V crystals which provides a basic understanding of probe scattering in bulk material that can be used as a comparison to the complex interfacial structures.

Chapter four presents an investigation into the effect of a parameter used in the calculation of the simulated HAADF images. This parameter is the lattice vibrational energy of the atoms within the crystal structure and can be controlled in the simulations using a single value $< u^2 >$. This parameter corresponds to the mean square displacement of the atomic vibration amplitude and the values are commonly taken from diffraction studies [24, 25]. This chapter is concerned with verifying that the parameters used in the multislice calculations produce results that are consistent with the conditions used in the microscope.

Chapter five outlines the Column Ratio Mapping method and develops a process to reduce image artifacts that are associated with the background removal process. A

robust pattern matching system is described that can be used to quickly extract the atomic column information from potentially noisy image data. An objective method for measuring the interfacial characteristics is then described, where the fitting of an analytical function can be used to measure both the interface width and the interface position. The MBE grown multilayer system is introduced and the areas that were the focus of the study are described. This data extraction method is then used to perform a line by line analysis on the HAADF images and the results are presented.

Chapter six describes the formation of a series of simple interfacial models that could be used to describe the experimental results from chapter five. The simple models are systematically evolved in an attempt to fully understand the experimental results. The characteristics of each model is described in turn and a comparison is made with the experimental measurements. The results ultimately indicate which interfacial models could be used to describe the experimental interface.

Chapter seven details the results from an investigation into the HAADF signal generated from partially populated III-V atomic columns. This was prompted by the results from chapter six that indicated that the HAADF signal generated from a particular atomic column can be greatly affected by the distribution of atoms. For instance, two atomic columns can have a very similar compositional content but the resulting HAADF signal will depend strongly on the depths of the compositional changes. The results from this chapter identify complexities associated with the interpretation of HAADF STEM images.

Chapter eight presents a summary of the main conclusions drawn from chapters four to seven. This chapter also describes future experimental and simulated work that can be performed to develop an improved understanding of HAADF image contrast.

Chapter 2

Background, Instrumentation and Methods

2.1 Imaging with the Electron

In 1897 J.J. Thomson discovered the electron and for this he was awarded the 1906 Nobel prize [26]. Eighteen years later the French physicist Louis De Broglie first postulated wave-particle duality [27]. This theory describes electrons as both particulate and wavelike in nature and relates the electron momentum to its wavelength. Equation 2.1 shows this relation with a relativistic correction factor included.

$$\lambda = \frac{h}{[2m_0 eV(1+\frac{eV}{2m_0c^2})]^{\frac{1}{2}}} \tag{2.1}$$

In this equation h is Plank's constant, eV is the electron energy, c is the speed of light in vacuum and m_0 is the rest mass of the electron. This relation shows that increasing the energy of the electron reduces the associated wavelength.

The wave nature of electrons was confirmed in 1927 by Davisson and Germer when interference effects were observed during electron scattering experiments from a crystal of nickel [28]. The concept of using electrons for imaging was then developed by Ruska and Knoll in the form of the first electron microscope. Their paper of 1932 showed images taken on the instrument [29] and, within a short time, the resolution limit of optical microscopes had been surpassed [26].

A typical modern electron microscope uses 100-300kV electrons, corresponding to a wavelength of 3.7-1.9pm. The practical resolution of the microscope is considerably

lower than this due to electron lens aberrations and the fundamental diffraction limitations of the imaging system [30, 31]. Advances in electron lens correctors are now increasing the performance of microscopes and current state of the art instruments can resolve features at the sub-Ångström scale [32, 16, 19].

The following section, 2.2, describes the main electron-specimen interactions that can be detected in a modern electron microscope. These interactions can reveal a wealth of information about the sample including the crystal structure, atomic bonding, chemical composition and local thickness variations [33].

2.2 Beam Specimen Interaction

When high energy electrons interact with matter a number of signals are generated. Most of these signals can be detected and measured in a modern electron microscope [34, 35, 26, 36]. Some of the important electron-specimen interactions are shown in figure 2.1. The cross section for each process depends greatly on both the microscope parameters used (such as the energy of the incident electrons) and the specimen being investigated [34, 26].

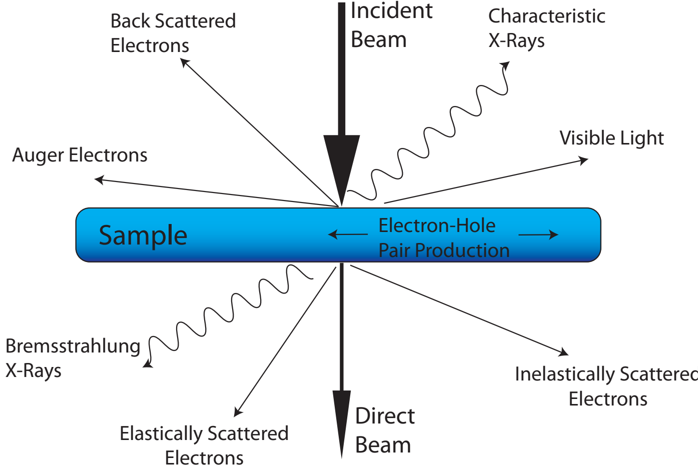

Figure 2.1 – Beam Specimen Interaction shows the relative directions of the peak secondary signals when high energy electrons interact with a microscope sample.

Two important processes are outlined below and can be classified as elastic and inelastic interaction. An inelastic process occurs when the electron passes through the sample and loses an amount of energy. An elastic interaction occurs when the electron does not lose energy during the interaction [36, 37, 38]. Both of these interaction processes are discussed in the following sections.

2.2.1 Elastic Scattering

Elastically scattered electrons are those which are transmitted through the specimen with no (or virtually no) energy loss [37]. Figure 2.2 shows two possible interaction mechanisms [38, 37]. The first mechanism is where the scattering is associated with the incident electron interacting with the nucleus of the atom. As the incident electron passes close to the nucleus, the effects from the electron cloud are reduced producing high angles of scattering [34, 39]. When the incident electron interacts with the atom from some distance away, the electron cloud partially screens the potential from the nucleus and, as a result, the scattering is predominantly at low angles. It is possible for both these processes to be fully elastic. The simplest consideration of elastic scattering is from an isolated nucleus which is discussed in section 2.2.1.1 below.

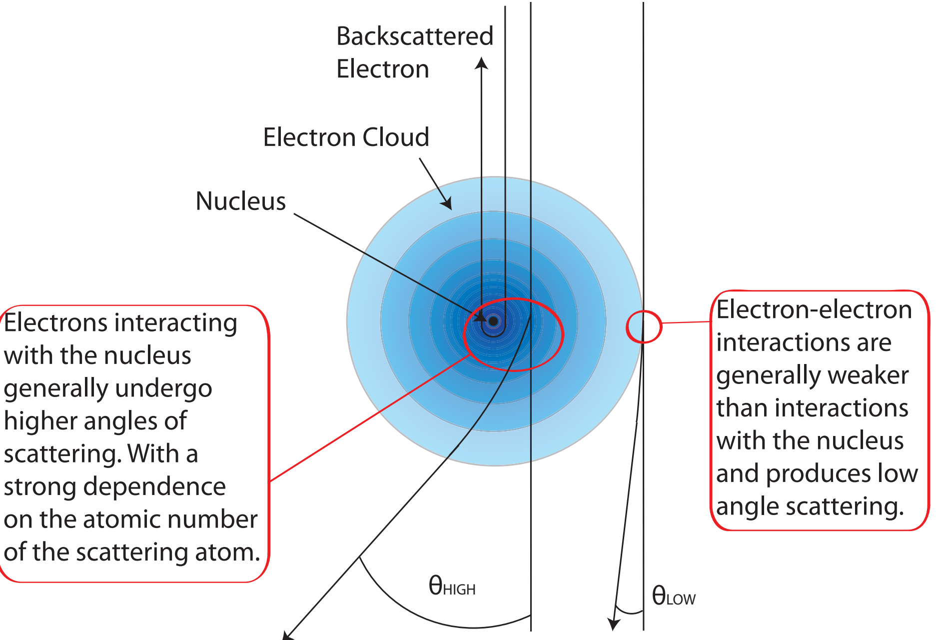

Figure 2.2 – A schematic diagram indicating the difference between low and high angle scattering. Scattering from the electron cloud contributes significantly to low angles of scattering while scattering from the nucleus is dominant at higher angles of scattering.

2.2.1.1 The Scattering Cross-Section

The atomic nucleus was studied extensively by Rutherford and he derived an expression for the probability of scattering from an isolated nucleus into a given solid angle. The angular probability of scattering is dependent on both the incident electron energy E_0 and the atomic number Z of the nucleus and is strongly forward biased [34]. If the

incident electron does not pass close to the nucleus, the surrounding electron cloud can have a screening effect, reducing the interaction cross section. The effect of screening can be assessed by the screening parameter (equation 2.2) where θ_0 defines an angle below which the electron cloud screening is significant [34, 26, 37].

$$\theta_0 = \frac{0.117 Z^{\frac{1}{3}}}{E_0^{\frac{1}{2}}} \tag{2.2}$$

Material	**Atomic Number**	**Screening Parameter** (mrad)
Al	13	27.506
Si	14	28.187
P	15	28.850
Ga	31	36.740
Ge	32	37.141
As	33	37.525
In	49	42.813
Sn	50	43.092
Sb	51	43.389

Table 2.1 – The screening parameter is an indication of the scattering angles below which the screening effects of the electron cloud can be neglected. This is important when considering the solid angle of the detector collecting the electrons (such as in HAADF imaging, see: 2.4.2.1 on page 36).

Table 2.1 lists some screening parameters for common semiconductor materials. The values in this table indicate that for high angles of scattering (i.e. above $50mrad$) the screening effects of the electron cloud can be neglected and it is predominantly the nucleus that contributes to the scattering interaction. This has important consequence when considering High-Angle Annular Dark Field imaging (see section 2.4.2.1 on page 36).

The wave nature of the electron can be included using an atomic scattering factor. This is a measure of the scattered electron wavefunction amplitude [34, 26] and is defined in equation 2.3.

$$f(\theta) = \frac{(1 + \frac{E_0}{m_0 c^2})}{8\pi^2 a_0} \left(\frac{\lambda}{sin\frac{\theta}{2}} \right)^2 (Z - f_x) \tag{2.3}$$

In this equation, a_0 is the Bohr radius, λ is the incident electron wavelength, E_0 is the incident beam energy, θ is the scattering semiangle, m_0 is the mass of the electron, Z is the atomic number of the scattering atom and f_x is the scattering factor for X-rays [34]. The scattering factor is a measure of the angular variation of scattering from an

isolated atom [34]. The expression indicates that the elastic scattering is lower for lower incident electron wavelengths, λ. The scattering also reduces as the scattering semiangle, θ, increases. However, the elastic scattering increases as the atomic number of the scattering atom, Z, increases [34].

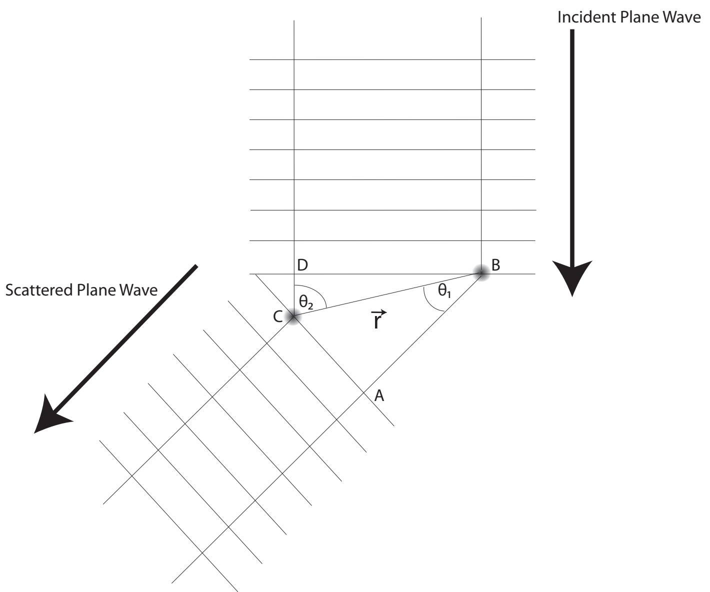

Figure 2.3 – the Von Laue equation details the geometrical relationship of scattering from two atoms and the phase difference between the incident and scattered waves.

This concept of the scattering factor can be extended to include scattering from multiple atoms contained within a regular crystal structure. Von Laue developed the geometrical arguments to calculate the path difference for a plane wave incident on two atoms a distance, $\overrightarrow{r}$, apart [40, 26]. Figure 2.3 shows the approach used by Von Laue where the path length between two scattering centre can be calculated using the atom separation and the angle of the incident and scattered waves.

$$\overrightarrow{r}(cos\theta_1 - cos\theta_2) = \overrightarrow{n}\lambda \tag{2.4}$$

Equation 2.4 shows that the path length changes with scattering angle and that at specific angles of θ_1 and θ_2, the path difference between the scattered waves is a whole number of wavelengths, $\overrightarrow{n}$, resulting in constructive interference. At other specific scattering angles the path difference between the scattered waves is a half number of wavelengths causing destructive interference. Between these two extremes a range of scattering amplitudes exist.

2.2.1.2 Bragg Scattering

Bragg simplified this approach by generalising the scattering from two isolated atoms to a plane of atoms [34]. Bragg developed the concept that the waves were reflected from the atomic planes and that the path length must have an integral number of wavelengths to remain in phase. The left hand diagram in figure 2.4 shows the generalised case where atoms are distributed along a single plane and an incident plane wave is incident at an angle theta (from the surface). Waves, ψ_1 & ψ_2, are scattered by adjacent scattering centers at positions a and c. The overall path length is the same because the triangles formed from adc and cba are identical. This indicates that the distribution of atoms over a particular plane will not affect the overall path length. Therefore, the phase relationship between the scattered beams will remain constant [41]. This result can be extended to a set of parallel planes each a distance d from each other (shown on the right side of figure 2.4). The path difference for scattered beams, ψ_3 & ψ_4, is $2d \sin \theta$ and therefore the scattering will be in phase when $2d \sin \theta = n\lambda$, where n is an integer. When this condition is satisfied $\theta = \theta_B$ and the planes are said to be orientated to meet the Bragg condition (where the Bragg angle, θ_B, is the incident angle) [42]. This coherent scattering produces strong reflections at well defined directions which are dependent on the crystallographic nature of the specimen. Each diffracted beam in the pattern is the result of coherent scattering from a set of atomic planes within the crystal. Therefore, the diffraction pattern can be used to gain information about the crystal structure of the specimen [42, 26, 34].

2.2.2 Inelastic Scattering

Electrons that lose energy when they interact with matter are described as being inelastically scattered. The mechanisms for energy loss fall into four categories which are electron-phonon interaction, plasmon scattering, single electron scattering and direct radiation loss [34, 37]. These four inelastic interactions are described below in sections 2.2.2.1-2.2.2.3.

2.2.2.1 Plasmons and Phonons

The atoms within a crystal are not stationary, instead, they oscillate around their mean position with a certain amplitude [42, 26, 39, 34]. These modes of vibration play

Figure 2.4 – Coherent scattering produces strong reflections at well defined directions which are dependent on the crystallographic nature of the specimen. Each diffracted beam in the pattern is the result of coherent scattering from a set of atomic planes within the crystal a distance d apart.

a vital role in determining the physical properties of the material [43, 44]. An incident electron can interact with the crystal lattice and gain or lose energy by transferring energy to the lattice. This transfer of energy can change the trajectory of the electron from the specific Bragg conditions and although the energy loss is small the scattering angle can be large [34]. Phonons therefore cause a diffuse background of scattering between the Bragg diffracted beams. The reduction of intensity in the Bragg beams can be described using the Debye Waller Factor (see section 4 on page 73) [36].

Incident electrons can interact with the valence electrons in matter via the Coulomb potential to produce collective oscillations. This plasmon energy loss has the greatest cross-section of all the inelastic processes, the typical loss is in the order of $15eV$ [38, 37]. The mean free path for plasmon excitation is generally $50-150nm$ and so the measurements of the plasmon losses can be used to give an estimate of the specimen thickness [45, 46].

2.2.2.2 Single Electron Scattering

The incident electron can also transfer energy to single electrons. A lightly bound valence electron can be ejected to produce a secondary electron [34, 37]. These secondary electrons typically have energies up to $50eV$ and can be used to form Scanning Electron Microscopy (SEM) images. The incident electron can eject an inner shell electron resulting in an ionised atom [47, 34]. The ionisation will occur at a specific energy corresponding to the inner shell electron that has been ejected. This characteristic energy will be lost by the incident electron which can then be detected using Electron Energy Loss Spectroscopy (EELS) identifying the atomic species (see 2.4.2.2 on page 36) [47].

2.2.2.3 X-ray Emission

Incident electrons traversing the specimen will emit energy if they are decelerated producing a background X-ray signal called bremsstrahlung [48]. This radiation is emitted as a continuous spectrum and the maximum X-ray energy is limited by the incident electron energy [34, 37]. This emission is associated with the slowing down of the incident electrons as they interact with the electrons and nuclei within the sample [48, 26, 34]. With 100-300kV electrons the energy is high enough to eject an inner shell electron producing characteristic X-rays and Auger electrons [37]. The incident electron can transfer energy to an inner-shell electron, exciting it into the conduction band, producing an inner-shell vacancy [39]. This vacancy can be filled by an electron from the outer shell which releases energy radiated as an X-ray. The frequency of the emitted X-ray is dependent on the energy change of the outer-shell electron and is therefore characteristic to that transition [48, 34, 37]. The energy transitions available within an isolated atom are dependent on the atomic number, Z, of the atom. Detecting the energy of the emitted X-ray allows the material being excited to be determined unambiguously [48, 34, 37]. The ionised atom may also de-excite, via a competing process, resulting in the emission of an Auger electron. The Auger electrons also have a characteristic energy and can therefore be used in analytical studies [49].

2.2.2.4 Beam Damage

Using high kV electrons for imaging and analysis means there is a possibility of damaging the specimen under investigation [35, 34]. There are two main types of damage

that a specimen will sustain when in the microscope. The damage can be classed as atom displacement and ionisation [50]. If the electron beam modifies the specimen this can throw into question the validity of any results acquired. The effects of the high kV beam will vary depending on the elemental composition of each compound. An important measure for beam damage is the displacement energy E_d. This is the minimum energy an atom within the solid requires to be permanently displaced from its lattice site to a defect position. The value of E_d will vary depending on the bonding, however, these values have been tabulated for many III-V compounds by Bryant and Cox [51]. These values were determined using electron irradiation experiments and are listed in table 2.2.

The maximum energy transfer can also be calculated, this will give an indication of the materials that are sensitive to the high energy electrons used in the experiments. For a given scattering angle θ, the energy transferred from the incident electron to the atom can be calculated using equation 2.5. E_{max} is a function of the scattering atom mass, M, the rest mass of the electron, m_0c^2 (511keV) and the incident electron energy, E_0. The maximum transfer of energy occurs when the incident electrons are back scattered and θ=π.

$$E_{transfer} = E_{max} sin^2 \frac{\theta}{2} \tag{2.5}$$

$$E_{max} = \frac{2E_0(E_0 + 2m_0c^2)}{Mc^2} \tag{2.6}$$

Table 2.2 details the displacement energy for some of the III-V materials investigated. Table 2.3 indicates values for $E_{transfer}$ for the elements in the III-V compounds calculated for 100 and 200kV electrons as these were the range of incident electron energies used experimentally.

Compound	Type-3 E_d(eV)	Type-5 E_d(eV)
InP	6.7	8.7
InAs	6.7	8.3
InSb	5.7	6.6
GaAs	9.0	9.4

Table 2.2 – The table above lists the displacement energy for both the Type-3 and Type-5 atoms for a variety of III-V compounds [51].

Element	100kV E_{max}(eV)	200kV E_{max}(eV)
Al	8.930	19.50
P	8.015	17.465
Ga	3.8790	8.451
As	3.644	7.939
In	2.454	5.346
Sb	2.358	5.137

Table 2.3 – The Transfer Energies above show the maximum energy that can be transferred to the atom, to avoid atom displacement damage the kV should be operated to ensure the transfer energy is less than the threshold energy for displacement.

It is clear from table 2.3 that only the compounds containing the lightest elements are at risk of being seriously affected by displacement damage. This gives an indication that working energies of 100kV should not affect most of the III-V compounds listed in table 2.2. However, compounds containing lighter elements (e.g. P) could be affected when working at energies approaching 200kV.

2.3 Electron Microscopy

During this project images and measurements were taken with a Tecnai TF20, Tecnai T20 and SuperSTEM1[1]. Sections 2.3.1 - 2.3.2 give an overview of characteristics that are common to all these instruments. A review of each microscope and specific operating conditions are detailed in sections 2.4.1, 2.4.2 & 2.4.3 .

2.3.1 Electron Sources

All microscopes require a source of electrons with which to illuminate the specimen. The brightness, beam current, energy spread and stability are all dependent on the type of source used in the microscope [52]. Electrons are extracted and accelerated to the operational energy of the microscope using an electron gun assembly. A series of lenses and apertures then control the electron beam convergence angle, α. In some imaging modes this should (ideally) be zero when parallel illumination is required. This is the case in conventional transmission electron microscopy (CTEM). Other techniques require a non-zero α where the electrons are focused to a very fine probe. This is the type of illumination used in scanning transmission electron microscopy (STEM) where

[1]Images taken by P.Robb, University of Glasgow.

a small probe is formed and scanned across a sample surface.

Generally, there are only two types of electron source used, a thermionic or a field-emission source [34, 40]. Thermionic sources can be made from either a tungsten filament or a lanthanum hexaboride crystal (LaB_6). A FEG sources is formed using a fine tungsten needle. These sources are discussed in the following sections.

2.3.1.1 Thermionic Sources

The Tecnai T20 uses a thermionic emission LaB_6 source. This type of source uses a rare earth boride crystal that is grown in a [110] orientation to enhance electron emission. Lanthanum hexaboride has a low work function of $2.4eV$ [37] and the source can be heated indirectly to an operating temperature of $1700K$ which provides the electrons with enough energy to leave the surface [34]. Once past the surface potential barrier, the electrons can be accelerated through a potential to achieve the operating energy of the microscope. The typical energy spread and brightness of a LaB_6 source are $1.5eV$ and $10^{10}A/m^2sr$ respectively (@ 100kV) [40, 34].

2.3.1.2 Field-Emission Sources

A cold field-emission gun (cold FEG) consists of a very fine tungsten filament which is mounted close to an extraction anode [34]. This anode is positively charged with a few thousand volts producing a very strong electric field at the tip of the filament [37]. This “extraction voltage” reduces the potential barrier at the surface of the filament allowing electrons to tunnel through and escape [34, 26]. A second anode is used to accelerate the electrons through the required operating energy. A FEG source is considerably brighter than a LaB_6, typically by a factor of 1000 [34]. The fine emission tip of the tungsten filament also allows the formation of a very small probe at the surface of the sample [34, 53]. The high brightness of the FEG is useful when operating in STEM as it provides a large current within a very small probe. This improves the signal to noise ratio of both imaging and analysis [40]. A FEG source does, however, require ultra high vacuum (UHV) conditions primarily to minimise contamination building up on the tip [34].

The electron source in SuperSTEM 1 is a $100kV$ cold FEG with an extraction voltage $<4kV$. The source has an energy spread of $0.3eV$ and a brightness of $10^{13}A/m^2sr$. Under UHV conditions surface contamination still builds on the tip gradually reducing

the emission current. This reduction in current can be compensated for by increasing the extraction voltage [37] but must eventually be removed by quickly heating the tip [34, 26]. This gradual build up of contamination therefore causes a reduction in the overall emission stability.

The electron source in the Tecnai TF20 is a $200kV$ thermally assisted Schottky FEG which consists of a tungsten filament coated with a thin film of zirconia. The thin film has the effect of lowering the surface work function and results in a filament with a greater overall emission stability [34]. A thermally assisted FEG does not suffer with surface contamination to the same degree, however, the increased tip temperature results in an larger energy spread [34].

2.3.2 Electron Lenses

A magnetic lens consists of two main parts and a schematic can be seen in figure 2.5. The first part is the pole piece which is a cylinder formed from a soft magnetic material (typically iron) that has a hole drilled through it called the bore. The bore allows the electron beam to pass through the center of the lens. The pole piece can be split into an upper and lower section and separated by a gap. The second part of the lens is a series of copper coils that surround the polepiece [54]. When a current is passed through the copper coils a magnetic field is created in the polepiece. The strength of the magnetic field is dependent on the current passed through the coils [54]. When an electron passes through the field axially the electrons experience a force that is proportional to the radial displacement from the optic axis [55, 54]. Figure 2.5 shows the schematic of the magnetic lens and the magnetic field lines within the bore hole.

When an electron with charge q enters a magnetic induction strength, B, it experiences a Lorentz force , F, which depends on the velocity, v, of the electron. These are related through equation 2.7.

$$F = q(v \times B) \tag{2.7}$$

An electron passing through the lens along the optic axis will experience no force. Whereas an electron passing a distance r from the optic axis will interact with the radial component,B_R, of the field initially. The subsequent change in direction causes the electron to interact with both the longitudinal and radial components, B_L and B_R

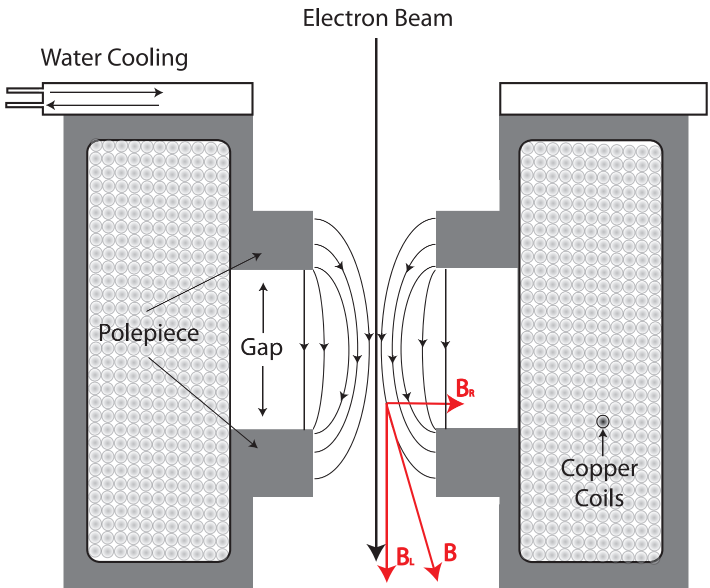

Figure 2.5 – An electron passing through the lens on the optic axis will experience no force, one passing a distance r from the optic axis will interact with the radial component of the lens initially B_R, the change in direction causes the electron to then interact with both the longitudinal and radial components, B_L and B_R.

[55, 54]. This interaction causes the electron to spiral through the lens field with a helical path. The strength of the field in the lens therefore controls the path of the electrons and, therefore, controls the focal length of the lens.

2.3.3 Aberrations

In 1949 Scherzer recognized that all round electron lenses would suffer from spherical aberration [18]. The magentic field created by a round electron lens can be described using Maxwell's equations and Scherzer discovered that the field could not be formmed into a perfect lens. This places a fundamental limitation on the spatial resolution of an electron microscope to about 2Å for electrons of energy 100–200keV [37]. Furthermore, the inhomogeneity of the construction material, misalignment of components and thermal drift all contribute further to lens aberrations and reduce the performance of the imaging system [55]. With the advent of aberration correction many of these aberrations can be measured and some can be compensated for, giving considerable improvement to the operating resolution [32, 19]. This correction can be achieved using a combination of multi-pole, non-round, lenses.

Prior to aberration correction, spherical aberration, C_3, was the dominant aberration that limited the practical resolution of a microscope [32, 19]. The effect of

spherical aberration is to increase the curvature of the transmitted wavefront. Figure 2.6 shows an ideal lens system (left) which takes a point object and brings the image to focus at the Gaussian plane. The right hand side of figure 2.6 shows the effect of spherical aberration on the same wavefront. Spherical aberration is a result of the lens strength varying with radial distance, r. Paraxial electrons are brought to focus near the Gaussian plane while electrons far from the optic axis are brought to focus before the Gaussian image plane. This causes a reduction in the resolution of the lens and the point image is spread over a larger area [52, 31, 54]. The point source is therefore imaged as a disk of radius $r_{spherical}$ as in equation 2.8.

$$r_{spherical} = C_3\alpha^3 \tag{2.8}$$

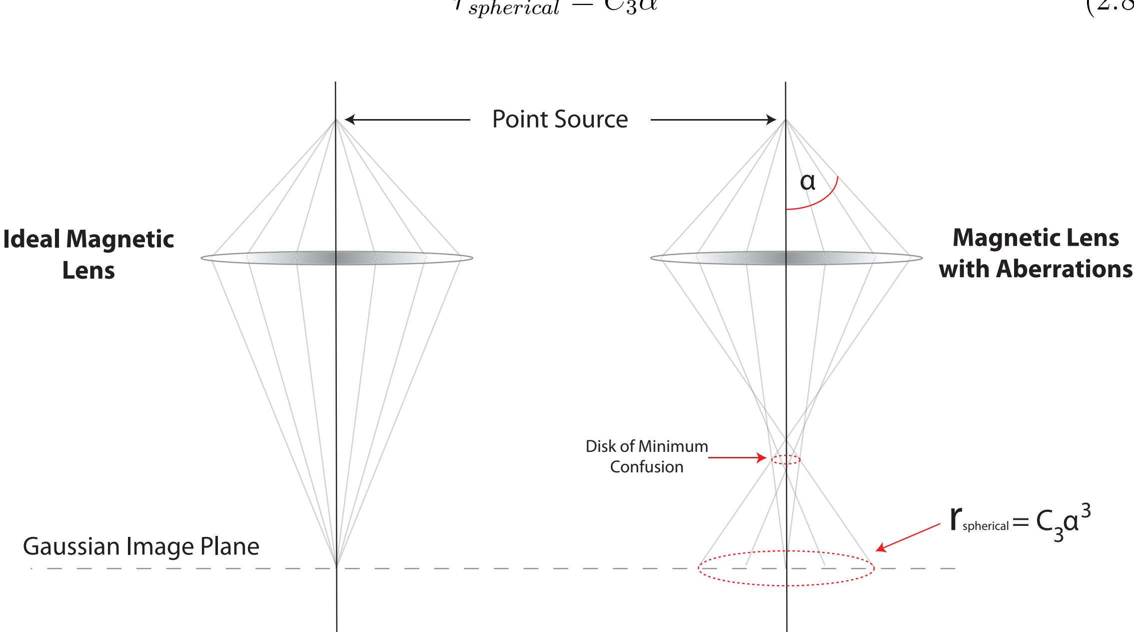

Figure 2.6 – All magnetic lenses suffer from aberrations. These aberrations modify the phase of the electron wavefront in an unpredictable way. However, many aberrations can be measured and corrected for.

If there are no lens aberrations at all, diffraction will occur at the probe defining aperture and the perfect lens system will take two coherent point sources and produce two Airy disks in the corresponding image plane [56]. The Rayleigh Criterion defines that two points are resolved if the minimum between the overlapping peaks drops to at least 80% of the maximum value [34, 56]. The separation distance of the peaks can be considered to be a measure of the resolution of the lens system. This theoretical resolution of an ideal lens occurs when the maxima of one peak is aligned with the minima of the other peak. This is the radius of the Airy disk and is the diffraction

limited resolution, $r_{diffraction}$, given by equation 2.8 [34, 56].

$$r_{diffraction} = 0.61\frac{\lambda}{\alpha} \tag{2.9}$$

The practical resolution of the microscope is, however, limited by the spherical aberration, $r_{spherical}$, which is proportional to α^3 and limited by diffraction which is proportional to $\frac{1}{\alpha}$. Taking a combination of both limiting factors in quadrature provides a value for the practical resolution of an un-corrected microscope which is given in equation 2.10.

$$r_{practical} \approx (C_3\lambda^3)^{\frac{1}{4}} \tag{2.10}$$

In practice there are many more aberrations that affect the lens system and these are described in the following section.

2.3.3.1 Higher Order Aberrations

The equation in 2.11 can be used to describe all aberrations. The aberration function, $\chi(\alpha, \phi)$, is a double sum, where $\frac{2\pi}{\lambda}$ is the incident electron wavevector, ϕ is the azimuthal angle and α is the convergence angle [19, 57, 32].

$$\chi(\alpha, \phi) = \frac{2\pi}{\lambda}\sum_{i=1}\frac{\alpha^{(n+1)}}{n+1}\sum_{m+nodd, m\leq n+1}[C_{nma}cos(m\phi) + C_{nmb}sin(m\phi)] \tag{2.11}$$

In equation 2.11 the aberration coefficients, C_{nmx}, have subscripts that indicate the type of aberrations. The first subscript, n, gives the order of the aberration, the second, m, is the aberration azimuthal symmetry where $\frac{2\pi}{m}$ radians is the minimum rotational symmetry. The two orthogonal contributions of the same aberration that arise for all non-rotationally symmetric aberrations are denoted by subscripts a and b [19, 57, 32]. Expanding equation 2.11 and substituting $\theta_x = \alpha cos(\phi)$ and $\theta_y = \alpha sin(\phi)$ gives the aberration function in the form shown in 2.12.

$$\chi(\theta_x, \theta_y) = \frac{2\pi}{\lambda}[C_1\frac{\theta_x^2 + \theta_y^2}{2} + C_{12a}\frac{\theta_x^2 - \theta_y^2}{2} + C_{12b}\theta_x^2\theta_y^2 + C_{21a}\theta_x\frac{\theta_x^2 + \theta_y^2}{3} + \ldots] \tag{2.12}$$

The $\theta_x^2 + \theta_y^2$ term is equal to α^2 and highlights the rotationally symmetric nature of the C_1 aberration as it has no azimuthal dependence. This is also the case for the C_3 and C_5 aberrations [19, 57, 32].

2.3.3.2 Balancing Aberrations

Scherzer first proposed offsetting the effects of one aberration with another when he discovered that the effects of spherical aberration could be reduced by optimising the defocus [18]. The aberration function including C_1 and C_3 (defocus and spherical aberration) is plotted in figure 2.7 showing how this function varies with α for $200kV$ electrons. The solid blue line indicates the aberration function when C_3 is equal to $1.2mm$ and with zero C_1 (Gaussian defocus). The solid red line indicates the aberration function when the defocus is used to offset the spherical aberration and C_1 taking a value of $-60nm$ (Scherzer defocus). The graph clearly shows that by changing the defocus the phase change of the wavefunction across the lens is modified.

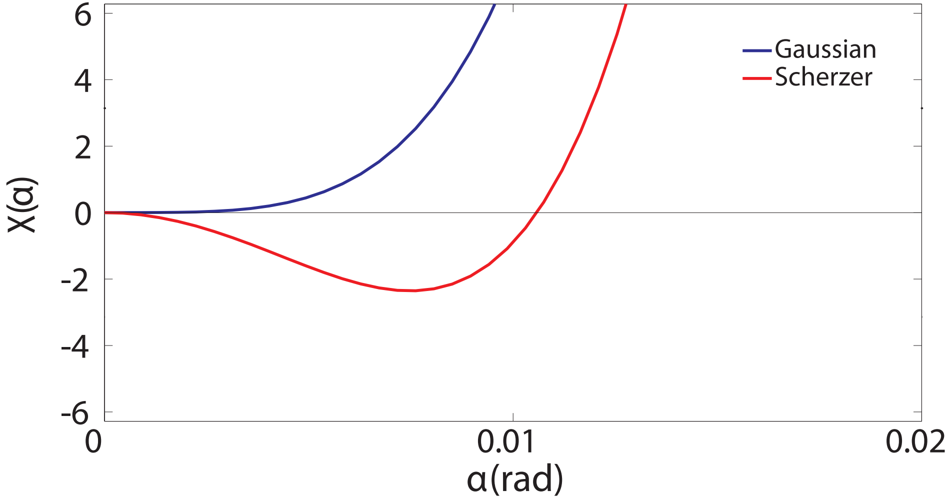

Figure 2.7 – A comparison plot of how the aberration function varies with convergence angle, α. The blue line indicates the phase using Gaussian defocus. The red line indicates a defocus value calculated from Scherzer's relation $C_1 = \sqrt{1.5 C_3 \lambda}$.

Two cases are important to consider when investigating the effect of the lens aberrations. The first is coherent imaging where the Contrast Transfer Function (CTF) provides an intuitive representation of the transfer properties of the optical system [40, 55]. The CTF is defined as $sin(\chi)$ and a plot of $sin(\chi)$ against α shows the contrast transfer as a function of spatial frequency within the image [26]. A CTF value of one indicates positive transfer of contrast (i.e. atoms appear bright) while a value of

minus one would indicate negative image contrast (i.e. atoms appear dark). A value of zero indicates that no image contrast would be seen at that spatial frequency [34]. Due to the contrast transfer changing with frequency, information from the sample will not be translated to the image consistently, thus confusing image interpretation. Specific frequency components above a certain value can be removed using an aperture. The CTF gives an indication of the maximum allowable frequency to ensure intuitive image interpretation. Consistent image contrast transfer can be achieved by placing the aperture at the first crossover in the CTF. Figure 2.8 is the CTF for the aberration function in figure 2.7 and clearly indicates that the location of the first crossover is at a higher spatial frequency when operating at Scherzer defocus. In practice the oscillations in the CTF function are damped by the spatial coherence and chromatic aberration of the source. This results in the higher spatial frequencies that may have passed through the system to be damped out. As a result, this damping places an "information limit" onto the accessible high frequency image information.

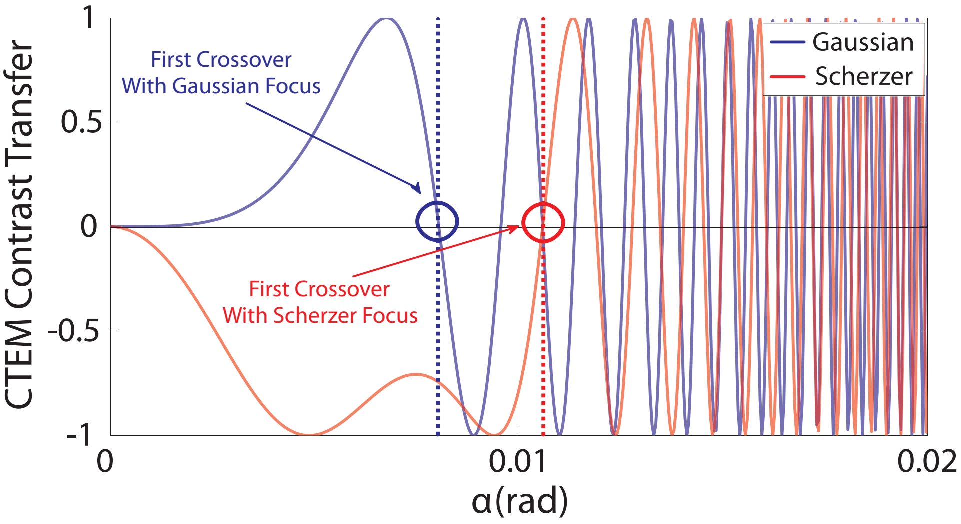

Figure 2.8 – The CTF, $sin(\chi)$, gives an intuitive representation of the coherent transfer properties of the phase information in an optical system. Reversals in the function correspond to reversals in the contrast transfer in a CTEM image at specific spatial frequencies. The red and blue circles indicate where the aberration function, $\chi(\alpha)$, crosses the x-axis and therefore the frequency at which the first contrast reversal takes place.

The next case is incoherent imaging where the phase dependent contrast transfer is described by the Optical Transfer Function (OTF). This function is defined as the Fourier Transform (FT) of the STEM probe, $OTF(\vec{\alpha}) = FT[I(\vec{r})]$ [56, 26]. This characterises the transfer strength of specific spatial frequencies. For a very fine STEM

probe, the OTF is wide indicating that information out to high spatial frequencies can be resolved in the image. Likewise, a large probe will have a narrow OTF reducing the maximum spatial frequency that will be transferred from the specimen to the image. Figure 2.9 indicates the OTF for identical parameters used in the formation of the CTF in figure 2.7 [34].

Both figures 2.8 & 2.9 indicate the clear improvements in the imaging conditions when using Scherzer rather than Gaussian defocus. This is the simplest form of aberration optimisation. With the advent of aberration correction, it is now possible to correct the lower order aberrations and compensate for the higher order aberrations [32, 57, 19]. The experimental method for aberration diagnosis and correction for SuperSTEM 1 is discussed in section 2.4.3. Section 3.5 details typical measured aberration coefficients for SuperSTEM 1.

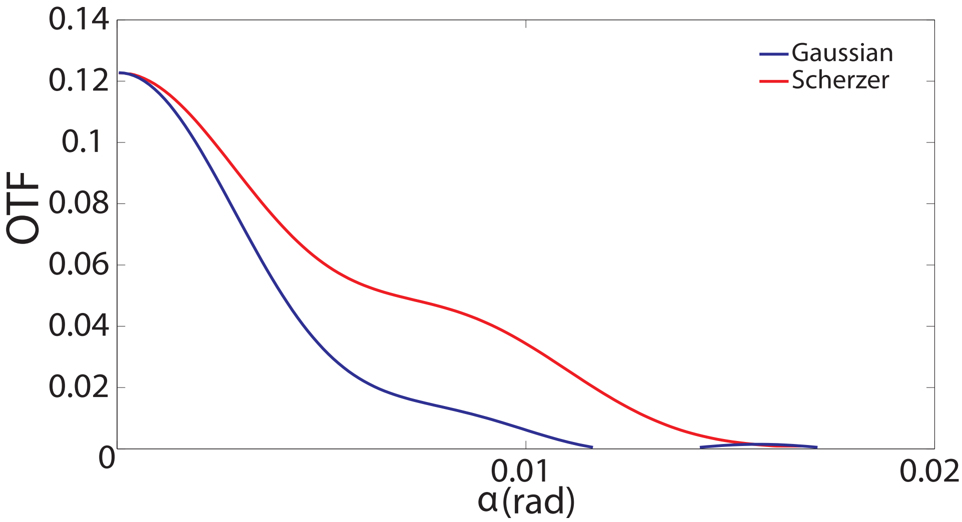

Figure 2.9 – The Optical Transfer Function, OTF, describes the incoherent transfer of phase information as a function of spatial frequency from the object function (specimen) to the image.

Therefore, the lens aberrations can greatly affect the quality of STEM probe that can be formed by the lens system. The overall probe size is determined by the source size, diffraction at the probe forming aperture, the energy spread of the source and the lens aberrations. All of these factors have an influence on the final image resolution.

If the specimen is very thin, then the incident electrons pass through the specimen with only a small deviation in their path. In this case the effect of the sample can be considered to be a “weak phase object”. In practice, the sample will be too thick to be considered as a weak phase object. With increasing sample thickness the effects

of dynamical scattering becomes important as the incident electrons can scatter more than once as they traverse the specimen.

2.4 Instrumentation and Techniques

2.4.1 FEI Tecnai T20

In the Kelvin Nanocharacterisation Center (KNC), which is based in the Department of Physics at Glasgow University, the FEI Tecnai T20 is operated as a conventional transmission electron microscope (CTEM) instrument and a schematic is shown in figure 2.10. The $200kV$ LaB_6 electron source is housed at the top of the microscope and a condenser system is used to modify the path of the electron flux to illuminate the specimen. A multiple lens condenser system allows greater flexibility and control over the beam where the C1 lens is used to demagnify the source and the C2 lens produces an image of the C1 crossover at the specimen plane [52, 31, 54]. The sample can be mounted in a low background double tilt rod with an allowable goniometer tilt of $40°/30°$ (α/β). The microscope is fitted with a Soft Imaging System (SIS camera) that can be used to acquire high rate data from a wide field of view. Below the SIS is a Gatan Image Filter (GIF) which can be used to record energy filtered images and EELS spectra.

2.4.1.1 Gatan Image Filter

A Gatan Image Filter (GIF) is positioned after the post specimen optics on the T20, below the microscope viewing screen. The GIF contains a spectrometer designed to disperse the electrons allowing the CCD camera to record an energy filtered image. The GIF was developed by Krivanek et al. [57] and a schematic of the system is shown in figure 2.11. The GIF is essentially a PEELS (parallel EELS) with an energy-selecting slit after the magnetic sector [57, 34]. There are then a series of quadrupoles and sextupoles, a TV-rate CCD camera and a slow scan CCD imaging camera. The first two quadrupoles, $Q_{a,b}$, increase the dispersion of the spectrometer at the slit entrance [57]. The remaining optics allow the GIF to operate in two different modes. The first mode is where the optics project an image of the energy loss spectrum at the slit onto the CCD. This allows the unit to operate like a standard PEELS. The second mode is

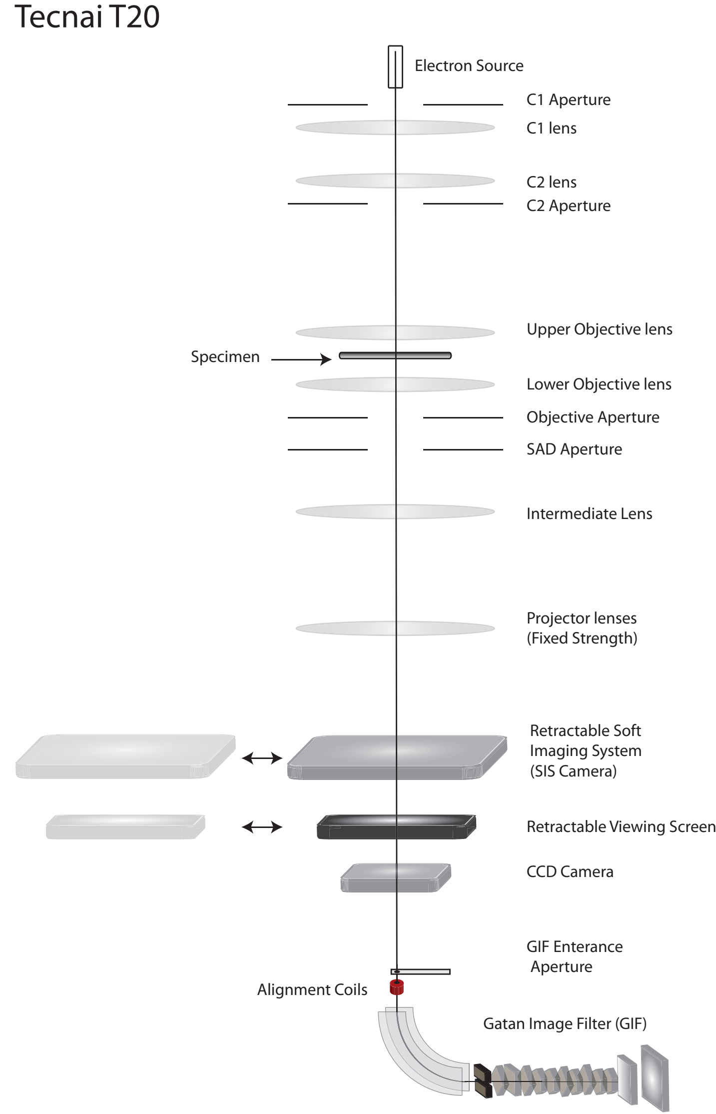

Figure 2.10 – A schematic indicating the relative positions of the lenses within the FEI Tecnai $T20$. The relative arrangement of the electron detectors are also shown. The intermediate lens strength can be varied to focus either the diffraction plane or the specimen back focal plane onto the object plane of the projector system. This allows both diffraction patterns and images to be viewed or recorded on the SIS camera. Below the SIS camera is the Gatan Image Filter (GIF) which can be used to produce energy filtered images and EELS spectra.

where the optics are used to project a magnified image at the CCD. This image contains only electrons of a specific energy selected by the slit forming an energy filtered image. The large number of quadrupoles and sextupoles within the GIF require a complex alignment procedure that necessitates computer control to operate.

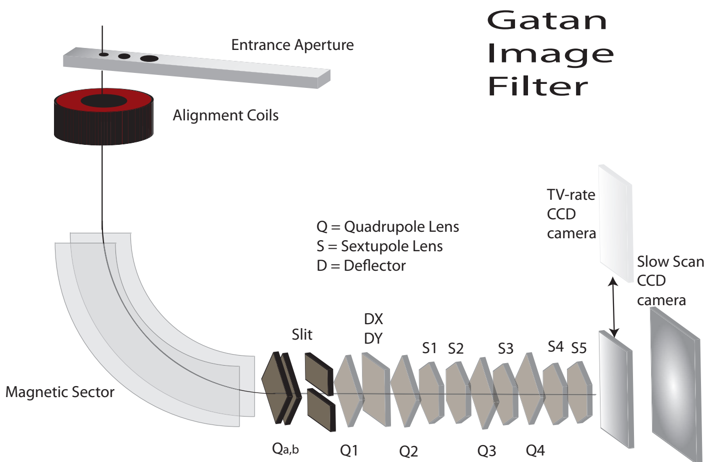

Figure 2.11 – The *GIF* is capable of performing electron energy loss spectroscopy by collecting a dispersed electron spectra on a CCD camera. The electrons are chromatically dispersed by a magnetic prism. The optics allow a projected image or an energy loss spectrum to be collected.

2.4.1.2 Convergent Beam Electron Diffraction

The data recorded for chapter 4 required the use of the T20 in convergent beam mode. Energy Filtered Convergent Beam Electron Diffraction (EF-CBED) patterns typically yield more information than diffraction patterns using parallel illumination [34, 37]. CBED images can be used to investigate the specimen thickness and electron-phonon interactions. A convergent beam electron diffraction pattern is formed in the back focal plane of the objective lens when the illumination is focused to a spot on the sample [37]. The resulting diffraction image consists of intensity disks that contain localised information about the sample. The information that can be extracted from the resulting patterns include the illumination convergence angle, specimen thickness, the crystal symmetry and specimen orientation [37, 34]. A further advantage when using a convergent beam is the improvement in the spatial resolution, with parallel illumination the operator is limited by the selected area aperture. With a convergent beam the CBED resolution is only limited by the smallest probe diameter [58]. This improvement in resolution is vital if small regions of the sample are to be characterised.

Chapter 4 details the use of CBED patterns to measure the specimen thickness

at local regions of the sample. This method was first described by Kelly *et al.* [59] and further developed by S.M.Allen [60]. The method involves measuring intensity oscillations in energy filtered diffraction patterns taken at a two beam condition. The two beam condition is satisfied when the specimen is orientated to strongly excite just one of the diffracted beams [34, 59]. This condition ensures that strong diffraction is occurring from a specific set of atomic planes. The left of figure 2.12 shows a schematic of a standard convergent beam pattern with the $\pm g$ reflections. By tilting the sample, a two beam condition can be created where only the direct (000) beam and one other reflection is strongly excited (in this case the $-g$ reflection). The separation of the intensity oscillations are sensitive to the local specimen thickness and can be measured to estimate the thickness of the specimen to an accuracy of $\pm 5\%$ [61, 62].

Figure 2.12 – A two beam condition ensures that strong diffraction is occurring from a specific set of atomic planes. The left schematic shows a standard convergent beam with the $\pm g$ reflections. By tilting the sample a two beam condition can be created where only the direct (000) beam and the $-g$ reflection are excited.

2.4.2 Tecnai TF20

The Tecnai TF20 is a $200kV$ instrument with a Field Emission Gun housed at the top of the microscope. Apart from the electron source, the primary difference from the T20 is the STEM capability of the TF20. A set of scan coils above the objective lens sys-

tem allows the illumination to be scanned across the specimen surface. During STEM imaging, the data can be collected in series with each probe position corresponding to one pixel in the final STEM image [53]. It is the probe size that defines the resolution of the microscope in STEM which is, in turn, governed by the lens aberrations [34]. The schematic in 2.13 gives an overview of the TF20 and details the relative positions of the lens and detectors. The post specimen detectors consist of a Gatan Multiscan CCD Camera which is used for imaging, a Gatan HAADF detector, a Gatan Bright Field detector and a Gatan ENFINA Electron Energy Loss Spectrometer (EELS). The detector arrangement is flexible and allows multiple signals to be detected simultaneously.

Tecnai TF20

Electron Source
C1 Aperture
C1 lens
C2 lens
C2 Aperture
Deflection Coils
Upper Objective lens
Specimen
Lower Objective lens
Objective Aperture
SAD Aperture
Diffraction lens
Intermediate lens
Projector lenses
CCD Detector
HAADF Detector
Bright Field Detector
Spectrometer Aperture
EELS Spectrometer
Magnetic Sector
Post spectrometer optics
YAG
CCD

Figure 2.13 – Schematic of the Tecnai F20 instrument. In STEM the condenser and upper objective lenses form a fine probe. A set of deflection coils scan the probe across the surface of the specimen. The transmitted electrons can be collected using a bright field or HAADF detector. The TF20 also has a Gatan ENFINA Spectrometer allowing spectrum imaging.

2.4.2.1 High Angle Annular Dark Field Imaging

High-angle annular dark-field (HAADF) imaging is very sensitive to the atomic number of the specimen [63, 64, 65]. This imaging technique uses an annular detector positioned concentrically about the optic axis [15]. This type of detector allows only electrons falling into a specific solid angle to contribute to the final image and typically collects electrons scattered through angles greater than $50mrad$ [34]. High angle scattering is "Rutherford like" in its simplest approximation and the probability of scattering is proportional to the square of the atomic number, Z^2 [65]. For low collection angles, coherent scattering is dominant due to the periodic nature of the crystal structure. As the scattering angle increases, the "apparent" inter-planar spacing of the crystal lattice becomes comparable to the thermal vibrations of the lattice and the scattering becomes incoherent. For incoherent scattering, the phase relationship between the scattered electrons is no longer dominant and it is the scattered intensity that forms the measured signal. This results in images that can be directly interpreted and have no contrast reversals [34, 64]. The HAADF images do not uniquely identify the atoms giving rise to the contrast in the image. However, a very small probe can be scanned across the sample surface producing intensity changes in the image that can indicate compositional changes at the atomic scale [64, 66, 65].

2.4.2.2 EELS

The EELS spectrometer allows the analysis of the energy distribution that occurs when electrons interact with a specimen [35]. The EELS spectrum contains both elastically and inelastically scattered electrons [35, 34] and reveals details of the atomic bonding, atom distribution and electronic structure of the sample [67]. The spectrometer utilises a magnetic prism which consists of a homogeneous magnetic field normal to the electron beam [68]. This field causes electrons of different energies to follow different trajectories [35]. The electrons emerge dispersed producing a spectrum at the focal plane of the spectrometer. The interaction of the incident electrons with the specimen can be described in terms of a mean free path (MFP) for inelastic interaction [34]. This is the average distance an electron will travel within the specimen before suffering an inelastic interaction. If the specimen is very thin (i.e. < 0.2 MFP) then most electrons will traverse the specimen without losing energy and will therefore contribute to the zero

loss peak. Electrons losing a small amount of energy ($<50eV$), contribute to the low loss region of the spectrum and generally consist of electrons that have either set up plasmon oscillations (2.2.2.1 on page 18) or have interacted with the weakly bound outer shell electrons [34, 35]. The high loss part of the spectrum (energy loss $>50eV$), contains information from the inelastic interactions with the tightly bound core shell electrons [34]. The whole energy spectrum can be collected in parallel (PEELS) as the detector is comprised of a yttrium aluminium garnet (YAG) detector that is coupled to a photo diode array in the dispersion plane. Each diode in the array is electrically isolated and the signal accumulates across the full spectrum over a specified integration time [35, 57]. The dispersion of the spectrum is defined as the distance between electrons having an energy difference of dE and is usually measured in $\mu m/eV$. The dispersion can therefore be varied, allowing a specific energy range of the spectrum to be recorded. The EELS spectra were used in the Mean Free Path calculation in chapter 4.

2.4.3 SuperSTEM

SuperSTEM 1 is a modified VG HB501 dedicated STEM instrument and a schematic can be seen in figure 2.14 [53]. The entire column is inverted with the gun at the bottom and the specimen and detectors above. This improves the overall stability of the instrument which can achieve specimen drift rates of less than $10nm$ per hour [16, 22]. The overall stability is vital to the operation of the microscope [53]. The facility is based at the Daresbury Laboratory and the site provides an optimised environment for the microscope working conditions [53, 16].

The pre-specimen optics consist of a twin condenser lens system and a set of deflection coils for scanning the STEM probe. The column has been modified to house a second generation Nion aberration corrector between these components [69]. This change to the microscope column combined with a large probe semi-angle ($24mrad$) requires the use of a coupling module to compress the angular range of electrons into the ENFINA spectrometer [16]. This module forms part of the post-specimen system and the other components include a HAADF detector, a Gatan ENFINA spectrometer and an on-axis CCD. The CCD is vital for aberration diagnosis, it is used to image the far field diffraction pattern which is used during the automated aberration correction procedure.

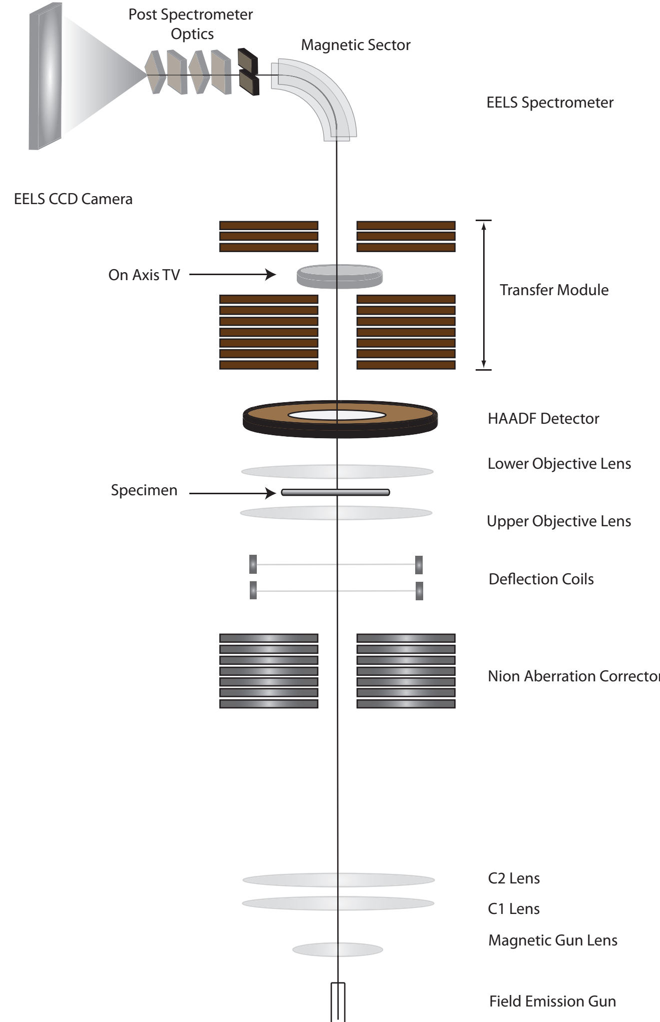

Figure 2.14 – A schematic of SuperSTEM 1, showing the relative positions of the lens system, aberration corrector and electron detectors. This dedicated STEM has the column inverted with the gun at the bottom and the detectors above which improves the instruments overall stability. The Nion corrector corrects the pre specimen lens aberrations. The transfer module is also necessary to couple the larger convergence angles of the probe to the acceptance angles of the spectrometer.

2.5 Sample Preparation

2.5.1 Cross Sectioning Method

A cross sectioning method was used to prepare the microscope samples investigated in chapters 4 and 5. This method can produce very thin ($<30nm$) crystallographically orientated TEM samples [70]. The process begins with the MBE grown structures on a substrate wafer. A small section of this sample is cleaved along a specific crystallographic direction, mounted in an encapsulation process and then thinned to electron transparency using mechanical grinding and ion milling [34, 70]. The final specimen should be representative of the original material allowing the structure and composition to be investigated. The samples investigated in this thesis were grown on [001] orientated GaAs and the cross sections are prepared such that when placed into the microscope the beam direction is aligned to the crystallographic [110] direction.

The main stages of the cross sectional preparation method are as detailed below:

1. Cleaving

   The first stage of the preparation process involves using a diamond tipped scribe to mark and cleave two rectangular sections (typically 20 by 2 mm) with the long edges orientated to the [110] direction (indicated by the flat edge on the substrate wafer). These sections are cleaned using solvent in preparation for encapsulation.

2. Encapsulation

   In preparation for the encapsulation process a slot is cut into a molybdenum rod ready to accept the cleaved sections. A thin layer of epoxy resin is placed on the upper surface of both prepared sections (i.e. the face with the growth layers) and they are placed together into the slotted rod. To complete the encapsulation process a tightly fitting brass tube is slid over the rod to hold the sections together. This encapsulation is then placed into an oven to cure the resin for a minimum of 1 hour at $130°C$.

3. Disk Cutting

   After encapsulation a diamond saw is used to cut the encapsulation into individual disks $600 - 800\mu m$ wide.

4. Dimpling

These individual disks are thinned using a hand grinder until approximately $80 - 100\mu m$. A Gatan dimple grinder is then used to thin the centre of the disk to a thickness of $20\mu m$. The dimpler uses diamond paste to grind material from the surface of the disk. A rotating steel wheel is coated with the diamond paste and specific rotational speed and weight can be applied to the wheel to accurately thin the disk on both sides. A higher grade diamond paste is also used with a soft felt wheel for a final polish.

5. Ion Milling

   A Gatan Precision Ion Polishing System (PIPS) is then used to mill the specimen to electron transparency. The PIPS uses two argon ion guns that can be directed with specific angles of incidence onto the sample surface. Using a small angle of incidence (from surface) is preferable for two reasons, firstly, ion implantation is greatly reduced at glancing angles, furthermore, any preferential thinning of different materials is minimised [71]. The ion guns were orientated at $\pm 4°$ incident angles. This configuration allows the simultaneous milling of both sample faces. The samples were milled at an acceleration voltage of 4kV while being rotated at 2rpm for approximately 2 hours. The milling was stopped when light was visible through a small hole formed at the centre of the sample.

6. Ion Polish

   The final ion polish was performed using a Technoorg Linda Gentle Mill. This low kV ion mill was operated at 300eV with an ion incidence angle of 10°. This final polish improves the surface quality of the prepared sample by minimising any amorphous layer produced by earlier stages of preparation.

7. Sample Storage

   The environment the samples are stored in has to be controlled to minimise oxidisation and contamination. The samples are therefore stored in a desiccator under vacuum ($< 10^{-1} Bar$).

Many stages require the samples to be temporarily attached to glass slides for grinding and handling. This is achieved using a variety of bonding substances and the removal of such substances requires the use of solvents (chloroform, ethanol and propanol) which are used between many of the preparation stages.

2.6 Summary

This chapter presented the fundamental theory of electron microscopy which included electron specimen interaction and scattering theory. An evaluation of the potential specimen damage was given specifically for the III-V materials investigated and the incident electron energies used. An outline of the electron microscope which included electron sources, electromagnetic lenses and the electron detectors was presented. The instrumentation used for the collection of data in the following chapters. Background information on both CTEM and STEM instruments was also provided along with the specific imaging techniques used throughout this work, such as HAADF-STEM imaging and aberration correction. The final section described the method used to prepare the TEM sample for investigation in the microscope.

Chapter 3

Computational Software: Modification and Single Crystal Calculation

To confidently interpret high resolution electron microscope images it is necessary to compare any experimental measurements with accurate image simulations [72, 73]. In crystalline samples, complex dynamical effects can be very important, producing image contrast that is counter intuitive [74]. The multislice code is a well established method of generating simulated electron microscope images and is an essential tool for image interpretation. The results presented in the following chapters were calculated using a modified version of the software distributed by E. J. Kirkland [72]. The main modifications are outlined in section 3.2.

3.1 Multislice Image Simulation

The multislice code was originally developed to simulate CTEM images where the incident wave function is a plane wave [34]. The code was subsequently extended to simulate convergent beam diffraction patterns and finally used to simulate STEM images [75]. The multislice algorithm is based on the optical theory developed by Cowley and Moodie [76] and uses numerical integration to solve the Schrödinger equation. A summary of the image formation is detailed below.

A STEM image is formed by sequentially scanning a probe across the surface of a sample and generating a signal at each probe position. To calculate the HAADF signal, the integrated intensity of electrons that are scattered from the sample into a specific solid angle is measured. The probe wavefunction at the entrance face of the

specimen is given by equation 3.1.

$$\psi(\overrightarrow{x},\, x_{pp}) = \int_{aperture} exp\Big[-i\chi(\overrightarrow{k}) - 2\pi i \overrightarrow{k} \cdot (\overrightarrow{x} - x_{pp})\Big] d\overrightarrow{k} \qquad (3.1)$$

where x_{pp} is the deflected probe position and $\chi(\overrightarrow{k})$ is the aberration function given in equation 2.11 and the integration is over the aperture for $\overrightarrow{k} \leqslant k_{max}$.

If the specimen is very thin, then the incident electrons pass through the specimen with only a small deviation in their path. In this case the effect of the sample can be considered to be a "weak phase object" and can be modelled as a simple transmission function, $t(x)$. The resulting transmitted wavefunction is $\psi_{transmitted} = t(x)\psi(\overrightarrow{x},\, x_{pp})$.

In practice, the sample will be too thick to be considered as a weak phase object. With increasing sample thickness the effects of dynamical scattering becomes important as the incident electrons can scatter more than once as they traverse the specimen. When dynamical scattering is important the transmission function must be calculated one step at a time. The specimen is divided into many thin slices each of which is perpendicular to the optic axis. Ideally, each slice is thin enough to be treated as a weak phase object and then the effect of each layer can then be calculated as a small, position dependent phase shift. This allows the calculation to proceed using a two step approach. The wavefunction is first transmitted through a slice and then propagated through vacuum to the next slice.

The first step is to calculate the transmission function, which is performed using the projected atomic potential of the slice. The projected potential in reciprocal space is calculated using electron scattering amplitudes and is defined in equation 3.2 for a cubic material. In this expression a and b are the unit cell dimensions, f_{B_j} is the electron scattering factor and $\frac{m}{m_o}$ is a relativistic correction. This summation is over all the atoms in the slice (where x_j is the relative position of the jth atom).

$$V_z(\overrightarrow{k}) = \frac{\lambda}{ab}(\frac{m}{m_o})\sum_j f_{B_j}(k) exp\big[2\pi i k \cdot (x_j)\big] \qquad (3.2)$$

The inverse Fourier Transform produces the projected potential in real space, $v_z(x)$, that relates to the transmission function such that $t_{slice} = exp\big[iv_z(x)\big]$. After transmission, the wavefunction is propagated through free space to the next slice via convolution

in real space (or multiplication in reciprocal space) with the propagator function defined in equation 3.3.

$$FT\left[p(x, \Delta z)\right] = P(k, \Delta z) = e^{(-i\pi\Delta z\lambda k^2)} \tag{3.3}$$

The propagation of the wavefunction through the specimen can be described using a recursion relation. This relates the wavefunction at a slice n+1 to that of slice n. These steps are shown in figure 3.1. The initial incident probe wavefunction at the entrance face of the specimen is given in equation 3.1 and the incident wavefunction incident on the $(n+1)^{th}$ slice can be calculated using equation 3.4.

$$\psi_{t_{n+1}}(x,\, x_{pp}) = \left[t(x)_n\psi_n(x,\, x_{pp})\right] \otimes p(x,\, \Delta z) \tag{3.4}$$

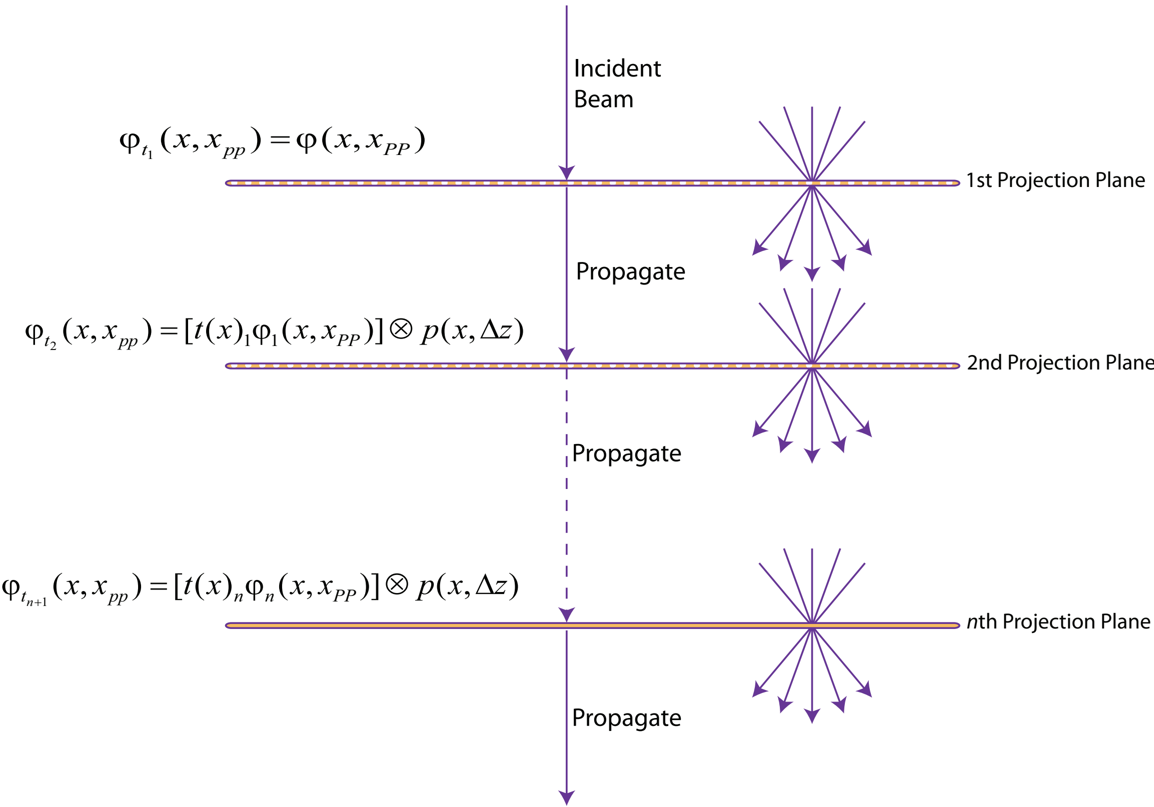

Figure 3.1 – The potential within each slice of the crystal can be approximated to a phase grating. The amplitudes and phases of all the beams interacting with the slice are calculated. They are then propagated through free space to the next slice. This allows the multislice code to proceed using a repeating two step process.

It is important to limit the spatial frequencies present in both the propagator function and the transmission function otherwise artifacts can enter into the calculation. The propagator and transmission functions should therefore be limited to 2/3 of the

maximum spatial frequencies present and also be cylindrically symmetric.

3.1.1 HAADF signal

Experimentally a HAADF detector is placed in the diffraction plane of the objective lens system. The detector subtends a specific solid angle and collects electrons that have scattered out to large angles. In the simplest approximation, these are the electrons that have interacted directly with the atomic nuclei within the sample [34]. The resulting images can be interpreted intuitively as they do not have contrast reversals with changes in focus or specimen thickness [37]. Therefore brighter areas in the image correspond to areas within the specimen which have a higher average atomic number [34]. These Z-contrast images can be simulated using the multislice method from the calculated wavefunction at the exit face of the crystal. This is done by first calculating the two dimensional Fourier Transform (FT) of the exit wavefunction. Taking the square modulus gives the electron intensity distribution in reciprocal space [34]. This intensity distribution represents the scattering at the diffraction plane of the objective lens. The intensity distribution can be integrated over the solid angle of the HAADF detector by summing the intensity within the appropriate area of the transformed image. This integrated intensity is then normalised to the incident probe intensity to give the simulated HAADF signal for that particular probe position [72, 75, 77]. A complete HAADF image can be created by detecting the scattered intensity at a number of probe positions across the crystal surface. The simulated intensity falling onto the HAADF detector can be seen on the left side of figure 3.2.

3.1.2 Electron Intensity Distribution

The accurate calculation of the EELS signal generated from a crystal structure would require inelastic scattering events to be incorporated into the multislice code. A method for including inelastic scattering was developed by Rossouw and Maslen and applied by a number of authors [78, 79, 80]. A simplified estimation of the EELS signal can be calculated from the intensity distribution within the simulated crystal. The probability for inner-shell ionisation can then be described using a matrix element which is only significant close to the atomic nucleus [73, 81]. Furthermore, the amplitude of the inelastic wave function is proportional to the amplitude of the elastic wave function

[78]. Cosgriff et. al calculated the K-shell EELS object function for a variety of atomic numbers and collector apertures [81]. From this data the radial extent of the object function for gallium and arsenic can be estimated to be approximately $0.2\AA$ [73]. The electron intensity can therefore be calculated at every slice within the specimen and an integration window of $0.4\AA$ x $0.4\AA$ placed around each atomic position. By integrating the total intensity for each atomic species the strength of each particular signal can be estimated [82, 83, 84]. Investigating the total EELS signal for each species can provide insight into how the signal changes with probe conditions and specimen thickness. In addition to the total EELS signal, it is instructive to calculate the EELS signal generated from only the atomic column beneath the probe position. This can give a clear indication of where, within the primary column, the EELS signal is being generated. This can be useful in optimising experimental EELS acquisition and investigating limiting factors due to specimen thickness and microscope operating conditions [78]. This simplified approximation only holds for large EELS collector apertures but can, however, provide an estimation of the spatial origin of the EELS signal [73, 78].

3.1.3 Frozen Phonon Method

A HAADF detector measures the time averaged incident electron flux scattered from the incident beam [26]. The atoms within a crystal lattice are not stationary but rather vibrate about their equilibrium positions, the magnitude of the vibration is dependent on both the chemistry and temperature of the material [75, 26]. These quantised modes of vibration, called phonons, can also be excited by the interaction of the high energy electrons with the crystal lattice [85]. This thermal diffuse scattering (TDS) contributes significantly to the HAADF signal [72, 73, 82] and therefore must be included in HAADF image simulations [72]. The frozen phonon method was developed as a means of including TDS effects into multislice simulations. This method is based on the premise that the velocity at which the incident electron traverses the specimen is considerably greater than the vibration of the atoms within the crystal [34]. This being the case, the atomic positions within the crystal 'appear' stationary to the incident electron as it propagates through the specimen [86]. This stationary configuration can be simulated by applying a small random offset to each atom position within the simulated crystal. The magnitude of the offset is calculated using the Debye Waller Factor

[73]. The time averaging of the experimental detector is modelled by incoherently summing the simulated HAADF signal from many different random atomic configurations. The configurations generated in this way are based on a simple Einstein model where each atom within the crystal is described as an independent oscillator [87]. In reality, the vibration of neighboring atoms in the lattice may exhibit coupling effects. These can be included in more advanced phonon models, such as the Debye model [88].

The required number of phonon configurations greatly depends on the measurements being made and the accuracy required [72]. The Einstein model accurately reproduces many first-order effects seen in an experimental CBED image, such as the Kikuchi lines [89]. A detailed phonon model, such as the Debye model, includes a correlation between the atom vibrations and is required to accurately reproduce other detail, such as the intensity banding seen perpendicular to the Kikuchi lines [86]. While these correlations are vital to reproduce some features in the CBED patterns, they are not as important when calculating the HAADF signal [86]. In this case, it is the integrated signal, and not the structure within the pattern, that contributes to the generated HAADF signal. To this end the software used in the following chapters incorporated TDS effects using an uncorrelated oscillatory pattern following the Einstein model.

The frozen phonon method was chosen over other methods (such as a absorption potential) as it accurately includes the effects of electron re-scattering (whereas the absorption potential does not). The effects of electron re-scattering becomes important as the thickness of the sample increases and if not included can result in calculation errors.

3.2 Software Modifications

The simulation process is computationally very expensive and to simulate HAADF images of large structures requires many hours of processing time. The original software code supplied with Kirkland's book includes two source files *probe.c* and *autoslic.c* [72]. The former is used to create the probe wavefunction at the entrance face of the specimen and the latter is used to propagate the wavefunction through the crystal structure. The probe code is limited to including the effects from spherical aberration, defocus and convergence angle. The autoslic code is limited to calculating one exit face wavefunction for one input wavefunction at one specified thickness. An investigation will

typically require many probe positions and a thickness series requires the calculation of a large range of specimen thicknesses. Furthermore, for aberration corrected probes it is vital to include higher order aberrations to obtain an initial probe shape that is representative of the experimental probe [73]. To allow investigation of large interface structures using aberration corrected probes required the modification of this original source code which was written in *c*. The details of the significant modifications are described below.

3.2.1 Probe Forming Software

It is important that the starting point of the multislice calculations, the initial probe wavefunction, is an accurate representation of the experimental microscope conditions [73]. The original Kirkland code included Defocus and Spherical Aberration to describe the initial probe conditions. This was sufficient to describe an un-corrected STEM probe where spherical aberration is the limiting factor [19]. With SuperSTEM 1, the third order aberrations can be corrected and aberrations up to fifth order can be measured. This measurement provides the necessary aberration coefficients to reproduce the incident probe [53]. These higher order aberrations can be incorporated into the original probe code to allow an accurate representation of the experimental probe wavefunction for SuperSTEM 1. The modified probe software is detailed in appendix 8.3 on page 263.

3.2.2 Multislice Code

The multislice code has a high demand on processing power as each slice of the simulation requires both a Fourier Transform, FT, and an Inverse Fourier Transform, FT^{-1}. This is compounded by the need to run multiple atomic configurations for multiple probe positions. The standard software calculates the exit wavefunction for one phonon configuration for one probe position at one specified crystal thickness. For this single calculation the user must manually input the details of the probe wavefunction file, the crystal structure file and other starting parameters. The output wavefunction is then calculated and recorded as a TIFF file ($typically\ 42Mb$) which must then be processed to calculate either the electron density distribution or the HAADF signal (requiring another FT). The size of these output files poses another problem, incoherently

summing the HAADF signal must be done in the detector plane, requiring the images to be stored until processed. As the computing clusters are accessed across a network, the allocated storage space is often limited and the writing speed or transfer of these image files across a network can also be a factor. The range and accuracy (i.e. number of phonons) of the simulation is therefore limited by the calculation and processing time. This, in turn, limits the number and complexity of models that can practically be investigated. Modifications to the original software and new control software was required to reduce both the calculation and processing times.

The first stage was to remove the need to work with many large TIFF files. This was achieved by processing the data at run time, within the multislice code, by utilising the FT & FT^{-1} used in the transmission and propagation of the wavefunction. Using this method, the HAADF signal can be calculated for each slice of the simulation and recorded using a single value without any significant computational overhead. This signal value corresponds to the total integrated intensity incident on the HAADF detector, normalised to the incident probe intensity [73, 72]. The left hand side of figure 3.2 indicates the electron intensity incident on the solid angle of the HAADF detector calculated for a [110] orientated GaAs single crystal using the SuperSTEM 1 probe conditions.

The total EELS signal and the primary column EELS signal generated from each slice within the simulation are also extracted sequentially during the calculation. This is achieved through the use of integration masks around each atomic position. The first mask selects only the atomic column that the probe is focused onto (i.e. the primary column). The random atomic displacement must also be taken into consideration when placing the integration mask, the RMS displacement can typically be $0.1\AA$, which is comparable to the size of the integration window. The location of each integration window is therefore calculated by referencing the RMS displacement array generated for each slice.

The next set of masks are specific to each atomic species in the supercell. A separate mask is created locating and masking only one type of atom. These masks then allow the intensity around the primary column and the intensity around each atomic species to be measured for each slice of the simulation. The right hand side of figure 3.2 indicates the placement of some of the atomic positions (red) and integration windows (yellow). Processing the data at runtime reduces the typical storage requirements from

600 images at $42Mb$ each to a single text file containing 600 values. However, one significant drawback to this method is the inability to interrogate the original data set using a new set of parameters, such as the integration window size or the HAADF detector solid angle.

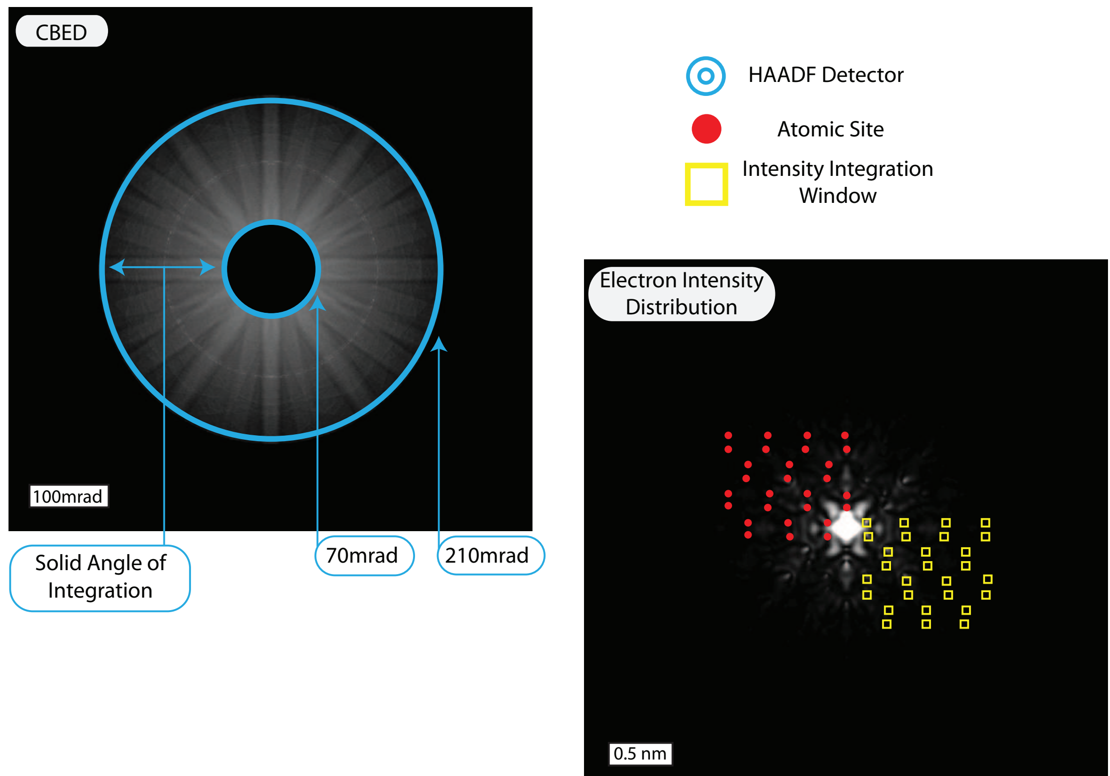

Figure 3.2 – The diagram on the left shows the fraction of the convergent beam diffraction pattern that is incident onto the HAADF detector. The position of the inner and outer edges of the HAADF detector are shown in blue. The diagram on the right shows an image of the real space electron intensity map. This image shows the intensity distribution at a specific depth in the crystal structure. In this case the image shows the intensity at a depth of 20nm from the crystal surface. The locations of some of the atomic sites are indicated (red) along with some of the masked integration regions (yellow).

3.3 Simulated Image Calculation

3.3.1 Cluster Computing

The second stage was to introduce a degree of automation. The aim was to reduce the time required to calculate a large crystal interface with many probe positions and to simplify the naming, storage and processing of the large quantities of data that this type of simulation produces. A single line trace across an interface would require the

calculation of 48 probe positions and 100 phonon configurations which results in 14,400 output text files containing the HAADF, Primary Column and Integrated Intensity data. As the simulations can be running independently on separate clusters, custom written code was required that would distribute the simulations over a series of nodes within a cluster, modify the input parameters and then organise and process the output files. This distribution code was written in Bash and the subsequent processing was performed using Matlab[1]. Figure 3.3 is a flow chart describing the control software.

Cluster one is a rack of eight, Sunfire Dual Core processors, operating Linux and is a dedicated cluster for use within the Solid State Physics group. Cluster two consists of 23 desktops (dual core AMD) partitioned to operate in a Windows or Linux environment. Running the multislice codes on cluster one is straightforward and jobs can be distributed across the nodes and run to completion without any interruption. Cluster two requires the status of each node to be checked before attempting to distribute, as each node can operate in wither a Windows or Linux environment. The Distribution script therefore locates a suitable node to run the job and transfers the appropriate probe position script to the node. The Probe Position Script then controls the modified multislice code, generates the input parameter files and organises the output files. This script takes a skeleton input file containing all the constant parameters (image sizes, specimen temperature...) and overlays the variable parameters (phonon number, probe position...). The input file is then fed into the multislice code which generates the calculation output as a series of text files. These files are then renamed and transferred across the network to be processed using Matlab (see section 3.4.1 below).

3.3.2 GRID Computing

During this project, access to the Grid facility was negotiated providing a substantial increase in computing power. GridPP is a STFC funded collaboration of computer scientists who are building a Grid for particle physics. The Grid is the next step in computer inter-connectivity where processing power and storage can be shared over a global network. GridPP manages the UK's involvement in the CERN LHC Grid Computing Project (LCG). ScotGRID which consists of Durham University, University of Edinburgh and the University of Glasgow is overseen by GridPP. Glasgow hosts a grid computing site dedicated to promoting grid computing within the University and

[1]The MathWorks Inc.

Script Control Process:

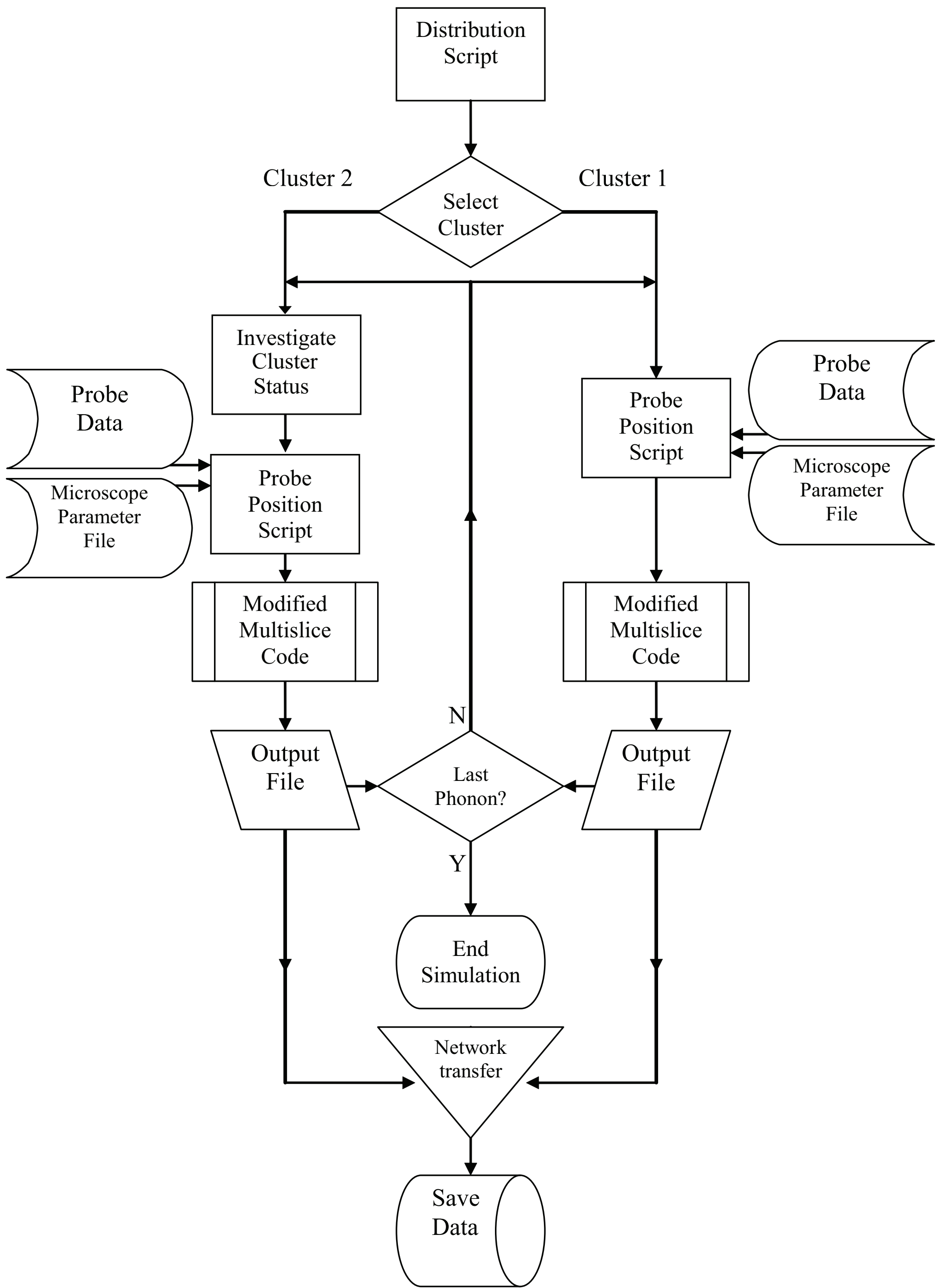

Figure 3.3 – This flow chart describes the control scripts that simplify the calculation of complete series of simulations.

supporting the wider ScotGrid project. The Glasgow based cluster has 310 worker nodes consisting of 140 x Twin CPU; Dual Core Opteron 280 Processors; 2.4GHz capable of running running 4 jobs per node and 170 x Twin CPU; Quad Core Xeon E5420 Processors; 2.5GHz capable of running 8 jobs per node (see: figure 3.4) As direct access to the Grid nodes is not possible, the simulation "jobs" must be packaged up and submitted via the submission system using a scripting language similar to Python. The job is then added to one of the submission queues which is chosen to match the simulation running time. The queues available are a 6 hour, 1 day and a 2 day queue. The queue name defines the maximum time allocated to the job. For example, a job submitted to the 1 day queue will wait until the allocated node becomes available, at which point the node can be used by the user for a full 24 hours. It is therefore vital that the full node time is used to maximize the total throughput of the simulations. A single multislice simulation for one probe position requires 80 minutes for completion and therefore the allocated Grid time is optimised by running a series of jobs sequentially on each node.

Figure 3.4 – Glasgow hosts a grid computing site dedicated to promoting grid computing within the University and supporting the wider ScotGRID project. The Glasgow ScotGRID Cluster Worker Nodes are shown above.

3.4 Data Processing

3.4.1 Matlab

Matlab scripting provides a very flexible platform with which to interrogate the simulation data set and greatly simplifies the post calculation analysis and visualisation process. All of the graphs and many of the interface schematics were created using Matlab. The main processing scripts were used to form the crystal structure input file, check the simulation status, read and average the output files and then interrogate the resulting data sets allowing the interfacial characteristics to be measured. The code for these scripts are detailed in Appendix B on page 284 and a brief outline of the script functions are described below.

Model Formation Script

This script is used to create the crystal structure files used as the input for the multislice simulation. The script can be used to generate single crystal or interfacial structures. The interface can be orientated to be perpendicular to the crystal surface or have a specific vicinal angle (i.e. the interface normal is not parallel to the crystal surface). The interface can have an abrupt change over one atomic monolayer or have a graduated change, simulating inter-diffusion. The diffuse interface is generated using a random number generator with control over the concentration of the segregation element in each atomic column. This script allows the development of the interfacial structures which are discussed in detail in section 6.1.

Sim-Status

The progress of the running simulations is verified by firstly reading each generated text file and ensuring that the text file content is consistent with the expected data (i.e a single column or multiple columns of floating point numbers). The file size is checked to ensure that the simulation has generated the correct volume of data. This information is then displayed graphically, indicating any simulation batches that are incomplete or have been generated incorrectly. This script is required when submitting jobs to cluster 2, as individual nodes can be reset resulting in incomplete batches of simulations that must be reset and re-calculated. It is also required for Grid jobs as

some jobs may be rejected when the submission clusters are very busy resulting in incomplete batches of simulations.

Sim-Reset

This script uses Sim-Status to first identify the specific jobs that are incomplete. The script then removes all the partially complete output text files and modifies the submission script to re-run the incomplete jobs.

Sim-Read

The Sim-read script performs the averaging of the Intensity and HAADF data. The script starts with the first probe position and calculates the mean and standard deviation of the HAADF and Intensity data before moving onto the next probe position. The completed data set contains the averaged HAADF data, EELS data and measurement error. The total number of averaged files are recorded ensuring that a minimum required phonon count has been reached.

Data Set Interrogation

The simulation data set formed by Sim-Read can be interrogated using an additional set of scripts. These allow measurement of the HAADF signal and Intensity line profiles on a slice by slice basis. This allows trends in the data to be ascertained.

Interface Interpolate

This script was used for the analysis in chapters 5 and 6. For the simulated data the script first uses the Data Set Interrogation script to extract the HAADF data generated from an interface. The data is then converted into a series of column ratio profiles, allowing the width of the interface at every slice to be measured. For the experimental data, the column ratio maps are converted into a series of column ratio profiles. The same measurement method is again applied. The width measurement is made by fitting an analytical function to the data, the optimum fit is achieved using a *least squares method*. It is from the analytical function that all the measurements are made. The benefit of this automated approach ensures an objective measurement for each fit and reduces the processing time required for each model.

3.4.2 Atomeye

Atomeye[2] is visualisation software developed by J. Li [90]. This was specifically developed for interactive viewing of large crystal structures ($> 10^6$ atoms). Atomeye was used to view the interfacial models that were developed, providing a method for verifying the simulated crystal structure. The simulation structure files are generated through the Model Formation Script and consist of a text file containing the atomic species and positions. The interface text files are large and it would be impossible to verify the structure from the text file alone. Atomeye is therefore a valuable tool when cross-checking the structure files. The crystal structure figures (such as figure 3.5) were also created using Atomeye. The images were subsequently annotated using Adobe Illustrator[3].

3.5 Simulated Probes

The calculation of the starting probe wavefunction requires the knowledge of several parameters which include the incident electron wavelength, λ, illumination convergence semiangle, α, image size and sampling, $dx\&Nx$, and the objective lens aberration coefficients [72]. The measured values of these parameters all have a degree of uncertainty. However, a reasonable representation of the incident probe can usually be formed using an estimation of these parameters. Focused probe wavefunctions were calculated for for the Tecnai T20 and SuperSTEM 1. These were used as the starting point for the simulations in section 3.6 and chapters 4, 6 and 7. The input parameters used and the resulting probe characteristics are detailed in the following sections.

3.5.1 T20 Probe

For the investigations in chapter 4 a direct comparison between the simulated and experimental energy filtered images was required. A simulated convergent beam that represented the Tecnai T20 convergent probe was formed using the parameters outlined in table 3.1. As the T20 probe is un-corrected, the dominant lens aberration is C_3. Therefore, the probe was formed using the published C_3 value and a C_1 value corresponding to Scherzer defocus.

[2]http://mt.seas.upenn.edu/Archive/Graphics/A
[3]Adobe Systems Inc.

T20 Probe Parameters:	
Wavelength, λ	$0.0251\mathring{A}$
Convergence Angle, α	4 mrad
Image Size, dx x dy	$62.183\mathring{A}$ x $62.567\mathring{A}$
Image Sampling, Nx x Ny	2048 x 2048 pixels
C_1	$235.6\mathring{A}$
C_3	$1.2\text{x}10^7\mathring{A}$
FWHM	$3.405\mathring{A}$
Diameter of central max	$7.266\mathring{A}$
Probe density of central max (fraction of total intensity / $\mathring{A}^2$)	0.0178
Beam Diameter containing 90% of total probe intensity	$14.4\mathring{A}$
Percentage of beam current contained in central max	73.91

Table 3.1 – Simulated Probe Parameters: FEI Tecnai $T20$. The image size, dx and dy, is selected to correspond to the size of the crystal structure being simulated.

3.5.2 SuperSTEM 1 Probe

SuperSTEM 1 can measure aberrations up to fifth order. It is a straightforward process to record the post-correction coefficients to use in the corresponding simulations. Table 3.2 details the parameters used to form the SuperSTEM 1 probe. This table also details the measured characteristics from the simulated probe, such as the FWHM. The simulated aberration coefficients that were used to replicate the 24mrad SuperSTEM 1 probe are detailed in table 3.3. These aberration coefficients were recorded from a VG Microscopes HB501 STEM, fitted with the first Nion quadrupole-octupole aberration corrector [69]. This simulated probe was used in the calculations for chapter 6, where the simulated results are compared to the experimental images taken using SuperSTEM 1. The same probe was used for the calculations in section 3.6, where the behavior of the 24mrad probe was investigated when propagating through various bulk III-V materials. The results presented in section 3.6 are also used for reference when interpreting more complex interfacial simulations in chapter 6.

SuperSTEM 1 Probe Parameters	
Wavelength, λ	$0.0370\mathring{A}$
Convergence Angle, α	24 mrad
Image Size, dx x dy	$55.965\mathring{A}$ x $56.533\mathring{A}$
Image Sampling, Nx x Ny	2048 x 2048 pixels
Aberration Coefficients	see table 3.3
FWHM	$0.981\mathring{A}$
Diameter of central max	$1.529\mathring{A}$
Probe density of central max (fraction of total intensity / $\mathring{A}^2$)	0.3085
Beam Diameter containing 90% of total probe intensity	$6.12\mathring{A}$
Percentage of beam current contained in central max	56.64

Table 3.2 – Simulated Probe Parameters: SuperSTEM 1.

Aberration Coefficient	**Description**	$\mathring{A}$
C_1=	defocus	8.4
$C_{1,2a}$=	astigmatism	3.7
$C_{1,2b}$=		0.5
$C_{2,1a}$=	coma	308
$C_{2,1b}$=		-3736
$C_{2,3a}$=	3-fold astigmatism	-483
$C_{2,3b}$=		-973
C_3=	spherical	-199448
$C_{3,2a}$=		-66272
$C_{3,2b}$=		-8710
$C_{3,4a}$=		-65613
$C_{3,4b}$=		69533
$C_{4,1a}$=		-1007440
$C_{4,1b}$=		12199870
$C_{4,3a}$=		1576470
$C_{4,3b}$=		3177760
$C_{4,5a}$=		232570
$C_{4,5b}$=		145810
C_5=	5th order rotational	440365700
$C_{5,2a}$=		140835390
$C_{5,2b}$=		18510170
$C_{5,4a}$=		186631310
$C_{5,4b}$=		-197781720
$C_{5,6a}$=		-5748520
$C_{5,6b}$=		47644720

Table 3.3 – Simulated Aberrations: SuperSTEM 1 24mrad.

3.6 Simulated Single Crystals

This section details the parameters used to create the crystal structure for the [110] orientated III-V single crystals. The results from the multislice calculations that outline the scattering behavior of the 24mrad SuperSTEM1 probe within these structures is presented. For each single crystal, both the distribution of scattered intensity in real space and the integrated HAADF signal were calculated as a function of crystal thickness and probe position.

The III-V materials investigated all have a face centered cubic (FCC) zinc-blende structure. When orientated in the [110] direction, the atomic columns align to give a characteristic dumbbell configuration. For a single crystal in this orientation, each dumbbell consists of two atomic columns where each column contains atoms of only one atomic species. Figure 3.5 shows an example of this projection for GaAs, both the unit cell and the atomic columns are indicated. The growth direction is in the [001] orientation, which means that when orientated to [110], the changes of composition are perpendicular to the beam direction, allowing the interface to be studied in detail. For example, if a perfect interface is formed during [001] growth, the [110] atomic columns are parallel to the interfacial plane and the change in composition would be atomically abrupt over a mono-layer (Δy direction in figure 3.5).

3.6.1 GaAs Single Crystal

3.6.1.1 Calculation Parameters

The unit cell for [110] orientated GaAs can be broken down into two repeating slices in the Δz direction. Each slice contains two atoms and figure 3.6 shows these slices with the relative positions of each atom within the unit cell. This unit cell can be replicated in the x and y directions to create each slice of the structure. Each slice is then stacked in a repeating A-B-A-B-A... pattern with a Δz separation of $1.99875\AA$. Before the probe wavefunction can be transmitted through the crystal structure the atomic potential must be calculated for each slice of the model [72, 75, 77]. The multislice code can then be used to propagate the probe wavefunction though the crystal in a series of steps until the exit face wavefunction is calculated (see section 3.1). To simulate a full STEM image containing many pixels, requires many different probe positions and long calculation times. This greatly limits the range of models that can be investigated.

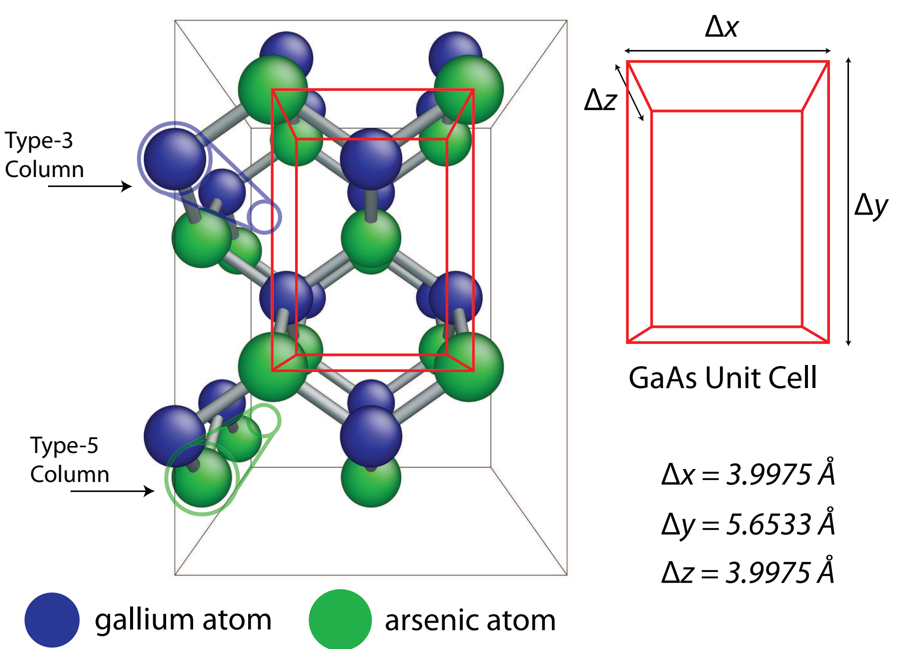

Figure 3.5 – The [110] projection of a GaAs single crystal where the unit cell is indicated by the red cube. The alignment of the atomic columns is shown on the left where each column contains only one atomic species.

By carefully selecting discrete probe positions, the calculation times can be reduced by many orders of magnitude while still providing vital data about the simulated signals. There are three specific probe positions for each dumbbell that produce important signals. These are when the probe is positioned on the Type-3 column, the Type-5 column and when the probe is placed between the dumbbells. This background probe position allows a measurement of the background reference signal. The signal from the background position can be subtracted from the "on-column" signals allowing an estimation of the signal generated from the primary column (i.e. the atomic column that the probe is focused onto). The right hand side of figure 3.6 indicates the Type-3, Type-5 and background probe positions.

The generated signals vary with specimen thickness. This variation is of particular interest, so the signal calculation is performed at each slice to a depth of $120nm$. This thickness limit was selected as it is greater than the thickest experimental image examined in chapter 5. Furthermore, STEM specimens are rarely thicker than this as beam broadening degrades the image (and analytical) resolution [53]. The HAADF signal generation from a sub-Ångström STEM probe in bulk III-V material has been studied extensively in a previous project [23]. However, higher order aberrations were

not included in the initial probe wavefunction and the number of phonon configurations was limited to eight. These single crystal calculations should, therefore, provide a reference for the interfacial models using the same calculation parameters.

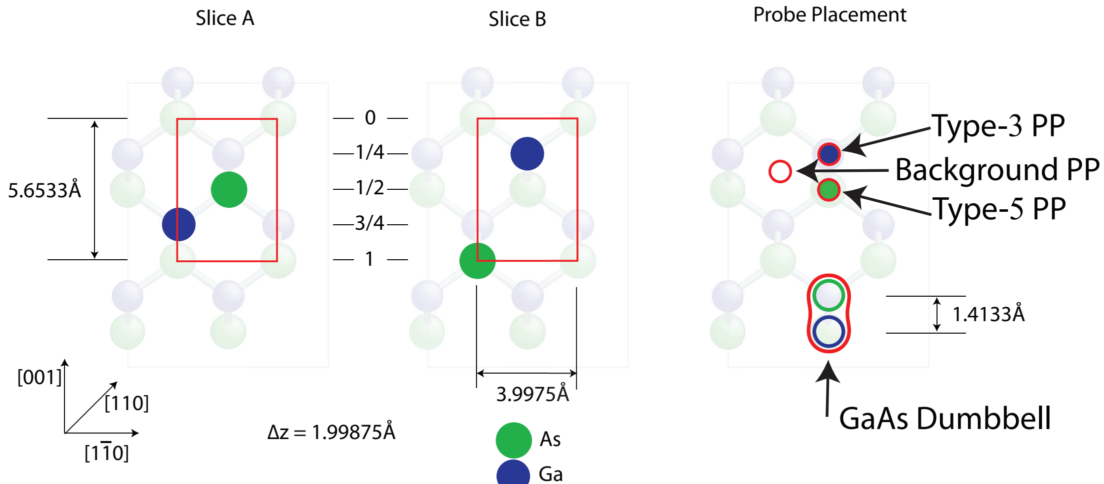

Figure 3.6 – The [110] GaAs unit cell can be reduced to two repeating slices in the Δz direction. Simulating discreet probe positions greatly reduces the calculation time. For each dumbbell the three probe positions indicated above are important. The probe is placed in turn on the Type-3 & Type-5 columns. The background signal (BG) is calculated when the probe is placed between the dumbbells.

3.6.1.2 GaAs EELS Signal

Section 3.1.2 described a method for estimating the EELS signal from a crystal using a series of integration masks. These masks select only the electron intensity close to the atomic positions. Figure 3.7 shows how the intensity that exists on the primary column varies as a function of specimen thickness. At each slice, the intensity on the primary atomic column (i.e. the column directly beneath the focused probe position) is calculated and then normalised to the total intensity in the incident probe (see section 3.1.2 on page 45). The data labeled 'Ga Column Intensity' (blue) corresponds to the variation of the intensity down the Type-3 column when the probe is focused on the Type-3 column. Likewise the data labeled 'As Column Intensity' (green) is the variation of the intensity down the Type-5 column when the probe is focused on the Type-5 column. The gallium and arsenic columns have a similar average atomic number and therefore the electrons scatter in a similar way, this is evident from figure 3.7. The intensity fluctuations are similar and the maximum intensity on the primary column occurrs at a crystal depth of approximately $2nm$. This peak can be attributed to the potential of the atomic column drawing in intensity from the probe and can be

described as a "channelling" effect. During channelling the atomic column acts like a waveguide and the electron wavefunction couples to the atomic potential. It is while the probe is channelling that a significant HAADF signal is produced. The depth at which the on column intensity drops to below 5% of the peak value is one possible measure of the channelling depth of the atomic column. This is indicated in figure 3.7 by the vertical broken lines. It is clear that the intensity on the Type-5 column has a shorter channelling depth than the Type-3 column due to the slightly higher average atomic number of the Type-5 column.

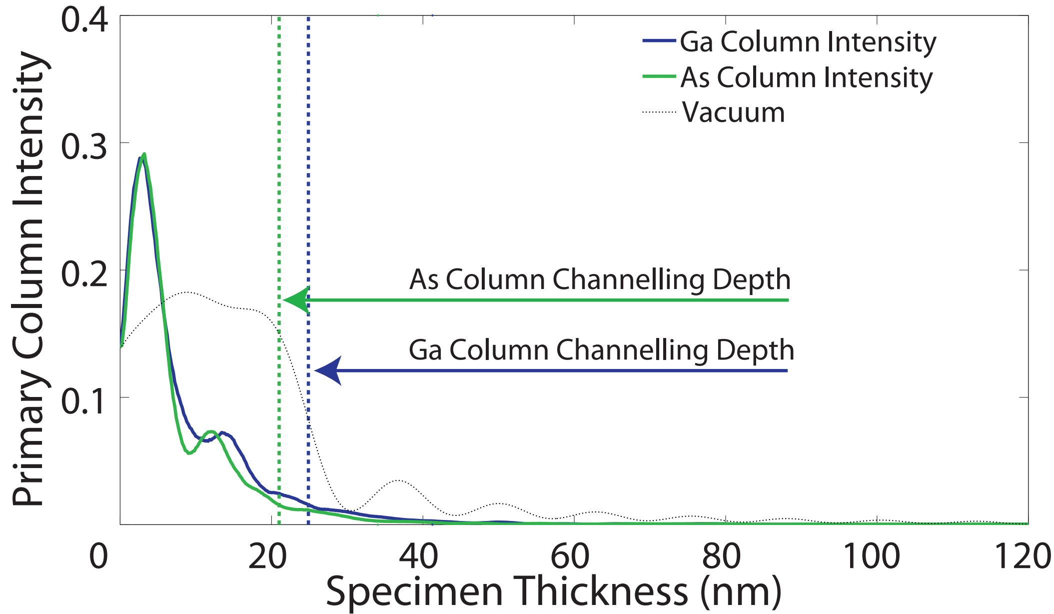

Figure 3.7 – The GaAs Primary Column Intensity as a function of specimen thickness for the Type-3 and Type-5 atomic columns. The broken black line shows an identical integration column when the STEM probe is propagating through vacuum. This line trace gives an indication of the depth of focus of the 24mrad superSTEM probe.

3.6.1.3 GaAs HAADF Signal

Section 3.1.1 describes the procedure for calculating the HAADF signal from a simulated exit wavefuction. This is achieved by masking the solid angle subtended by the detector within the Fourier Transform of the electron wavefunction. Figure 3.8 indicates how the HAADF signal varies with crystal thickness for a GaAs single crystal where the 'Ga HAADF Signal' and 'As HAADF Signal' correspond to the calculated HAADF signal when the probe is positioned on the Type-3 and Type-5 column respectively. The 'Background HAADF Signal' is collected when the probe is positioned

between the dumbbells. Both the Type-3 and Type-5 HAADF signals show a similar trend and increase over the full crystal thickness. The top 25nm of the crystal, however, shows the greatest increase in signal. This can be directly attributed to the high electron density around the primary scattering column in this region. Figure 3.7 shows that the intensity around the Type-3 and Type-5 columns is maintained until a depth of approximately 25nm. At this point most electrons have been scattered off the primary column. It is this scattering that generates the large change in the HAADF signal in the top section of the crystal. The HAADF signal generated from 25nm onwards can be attributed to background scattering which occurs when the probe has de-channeled. In this case, the signal is generated predominantly from the non-primary columns. The increase in the background HAADF signal (indicated in red on figure 3.8) is approximately linear with thickness. The background can be subtracted from the on-column HAADF signals to give an estimation of the signal generated from the primary column.

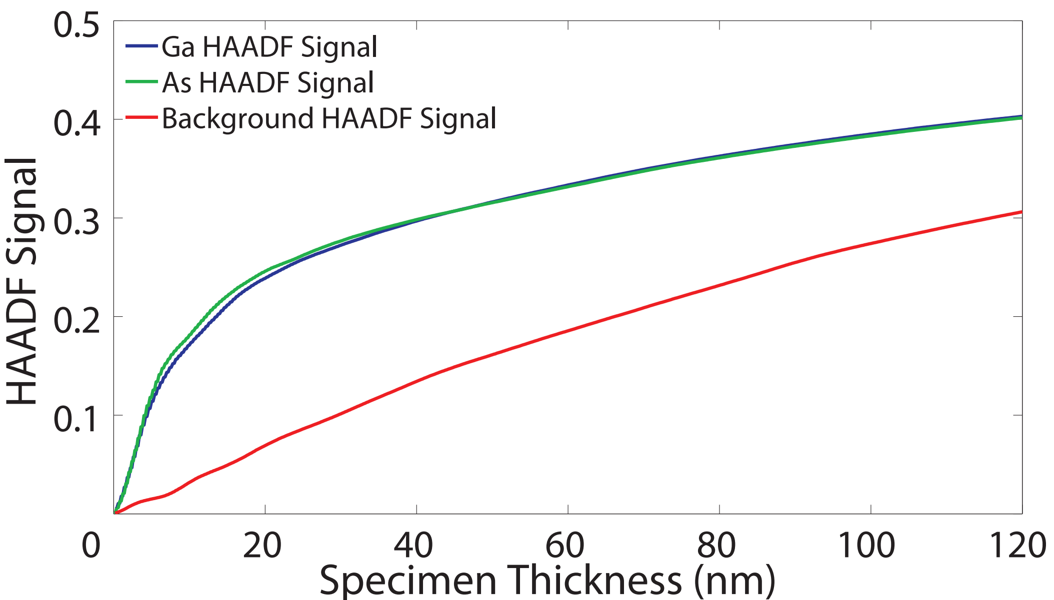

Figure 3.8 – The GaAs HAADF signal as a function of specimen thickness for probe placed on the Type-3, Type-5 and background positions.

Figure 3.9 is a plot of the background subtracted (BGS) HAADF signals from the Type-3 and Type-5 columns in single crystal GaAs. The data is plotted as a function of specimen thickness and the vertical broken lines indicate the channelling depth

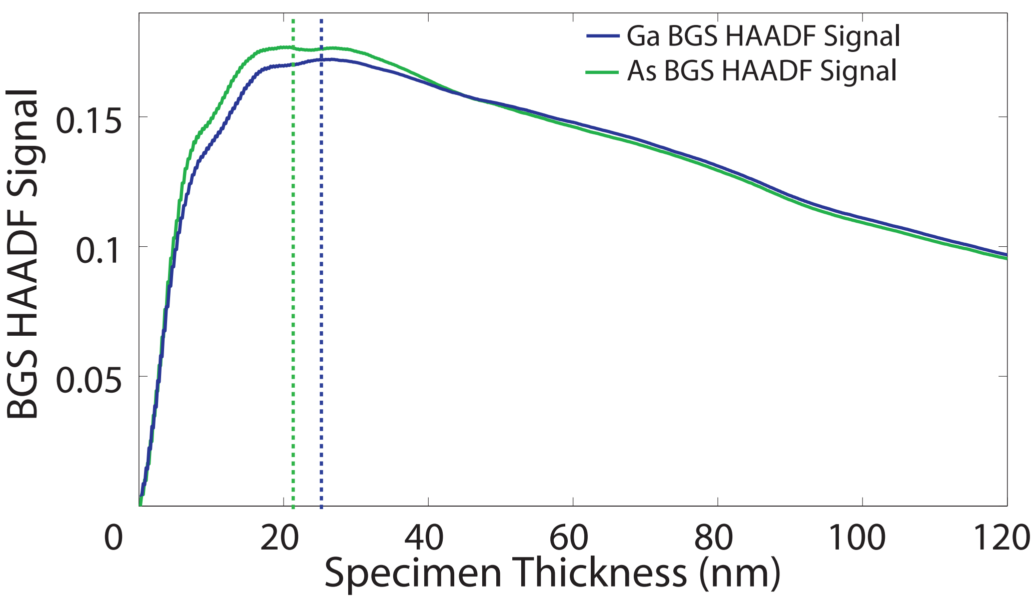

Figure 3.9 – The GaAs Background subtracted HAADF signal as a function of specimen thickness for probe placed on the Type-3 and Type-5 positions.

(overlaid from figure 3.7). The BGS signal gives a clear indication of the optimum specimen thickness for HAADF signal generation. The maximum HAADF signals generated by the primary columns occur at a crystal thickness of approximately $20 - 25nm$. This again corresponds to the depth at which the probe de-channels from the primary column. The drop in BGS signal above $30nm$ can be attributed to a dynamical scattering effect. Electrons that are scattered in the upper region of the crystal, are re-scattered out-with the solid angle of the HAADF detector as the thickness increases.

3.6.1.4 GaAs Column Ratio

A quantitative comparison of simulated and experimental images would require the experimental images to be normalised to the intensity of the incident probe. This would allow the experimental images to be placed on an absolute scale [66]. This would be possible using an annular dark-field detector that has an output voltage that is directly proportional to the electron flux averaged over time (i.e. the measured intensity) [66]. Without this type of system, comparisons are limited to those using ratios of scattered intensity within the simulated and experimental images. One such measure is the column ratio. This is defined as the ratio of the BGS HAADF signal from the Type-3 column to that of the Type-5 column. The column ratio is defined in equation 3.5.

$$Column\ Ratio = \frac{BGS\ HAADF\ Signal_{Type-III}}{BGS\ HAADF\ Signal_{Type-V}} = \frac{I_{Type-III} - I_{BG}}{I_{Type-V} - I_{BG}} \tag{3.5}$$

Figure 3.10 shows the variation of the column ratio as a function of specimen thickness for GaAs. From the basic theory of HAADF imaging outlined in section 2.4.2.1, high angle scattering can be approximated to Z^2 and the column ratio for GaAs can be estimated using equation 3.6.

$$Column\ Ratio_{GaAs} = \frac{Z_{Type-III}}{Z_{Type-V}} = \frac{31^2}{33^2} = 0.8825 \tag{3.6}$$

The theoretical value for the column ratio of GaAs is indicated in figure 3.10 by the horizontal red broken line. The plot also indicates that for very thin specimens the column ratio agrees with this Rutherford type scattering model. As the thickness of the specimen increases, the column ratio quickly tends to unity. At this point it would be impossible to differentiate between the Type-3 and Type-5 atomic columns in the HAADF image. The plot also shows some experimental column ratio values calculated over a range of specimen thicknesses, these are indicated using a black dot. These experimental column ratios were calculated from experimental images of bulk GaAs taken using SuperSTEM 1. The imaging and processing techniques used to measure the experimental column ratio are described in chapter 5. However, figure 3.10 indicates that there is a good agreement with the simulated and experimental column ratio values.

3.6.2 AlAs Single Crystal

3.6.2.1 Calculation Parameters

The same simulated SuperSTEM 1 probe was used to characterise the HAADF and EELS signal generated from a single AlAs crystal. When orientated in the [110] direction AlAs also exhibits the dumbbell structure. However, the change in the Type-3 atom requires the modification of some of the simulation parameters including the unit cell dimensions and the magnitude of the Type-3 RMS displacement. The simulation parameters for AlAs are detailed in table 3.4.

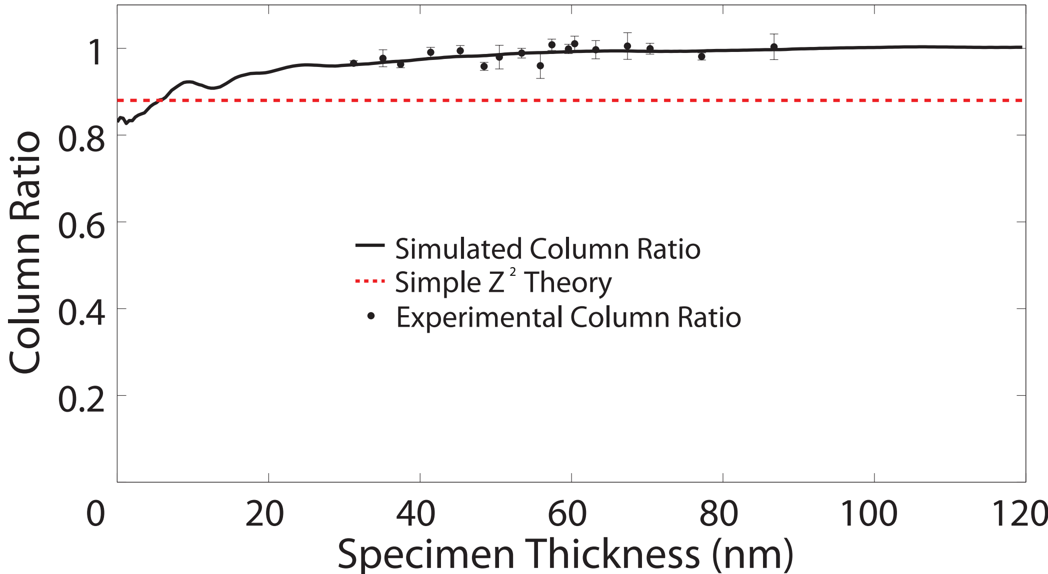

Figure 3.10 – The graph above shows the column ratio as a function of specimen thickness for single crystal GaAs. The solid black line indicates the simulated column ratio values. The red broken line shows the theoretical column ratio using a simple Z^2 model. The data points correspond to experimental column ratio values calculated from a SuperSTEM 1 image. Chapter 5 describes the experimental column ratio calculation process in detail.

3.6.2.2 AlAs EELS Signal

Figure 3.11 shows the variation of the primary column intensity as a function of specimen thickness for an AlAs single crystal. The data labeled 'Al Column Intensity' (blue) corresponds to the variation of the intensity down the Type-3 column when the probe is focused on that column. The data labeled 'As Column Intensity' (green) is the variation of the intensity down the Type-5 column when the probe is focused on that column. The Type-5 column intensity peaks show no appreciable difference in the position or magnitude of the intensity oscillations when compared to the Type-5 column intensity in GaAs. The Type-3 column in the AlAs case exhibits different characteristics. In particular, the first intensity peak is at a depth of $4nm$ and the depth of channelling is considerably greater. The channelling depth is greater than the $120nm$ simulation depth (indicated by the blue arrow) and is due to the lower scattering potential of the Type-3 column in AlAs.

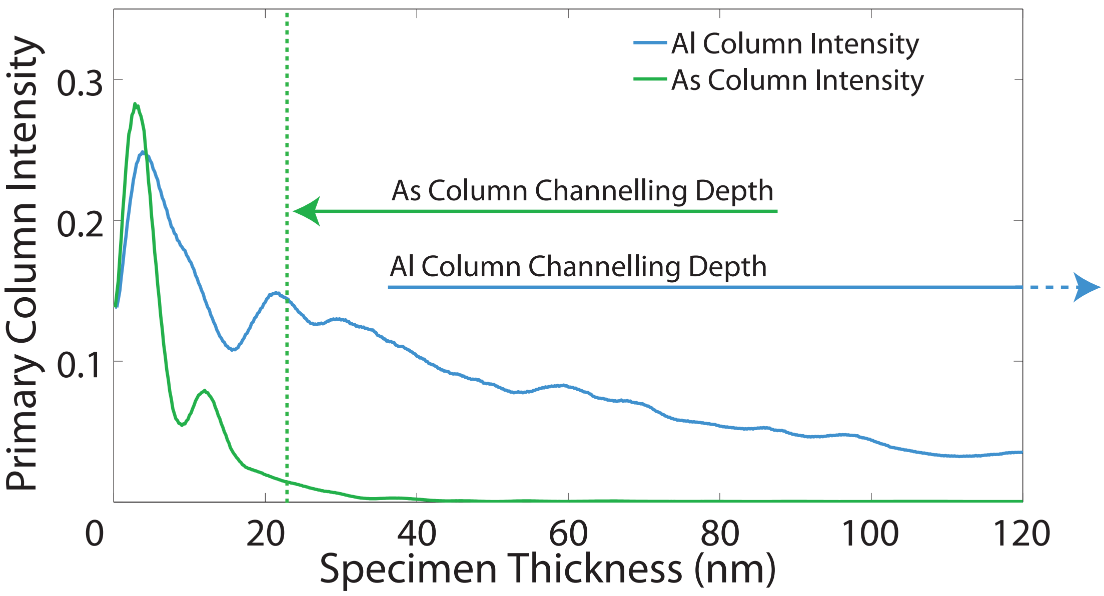

Figure 3.11 – The AlAs Primary Column Intensity as a function of specimen thickness for the Type-3 and Type-5 atomic columns. The vertical broken green line indicates the channelling depth of the Type-5 column. The channelling depth of the Type-3 column exceeds the simulation depth.

3.6.2.3 AlAs HAADF Signal

The AlAs HAADF signals, shown in figure 3.12, also exhibit a clear difference from those of single crystal GaAs. The Type-5 HAADF signal (green) again has a sharp gradient in the top $20nm$ of the crystal. Beyond the channelling depth, the HAADF signal increase is approximately linear with thickness. The HAADF signal generated from the Type-3 column (blue) shows a gradual increase, although the probe is incident on the atomic column, the lower potential of the aluminium column produces a lower rate of scattering. The background signal (red) has a smaller gradient than the background generated from the GaAs crystal. This is due to the lower average atomic number of the AlAs crystal. The background signal can again be subtracted from the on-column signals and the plot of the background subtracted HAADF signal is shown in figure 3.13. This graph highlights the different scattering mechanisms of the Type-3 and Type-5 columns in AlAs. While the HAADF signal from the Type-5 column is predominantly generated from the top $20nm$ of the crystal the Type-3 HAADF signal continues to build over the full depth of the simulation ($> 120nm$).

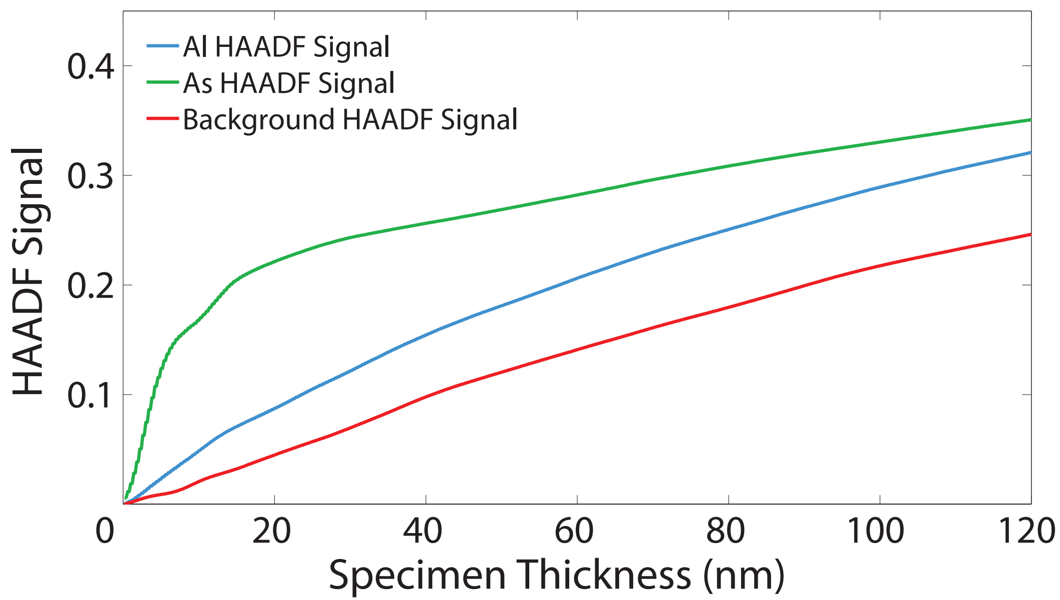

Figure 3.12 – The AlAs HAADF signal as a function of specimen thickness for probe placed on the Type-3, Type-5 and background positions.

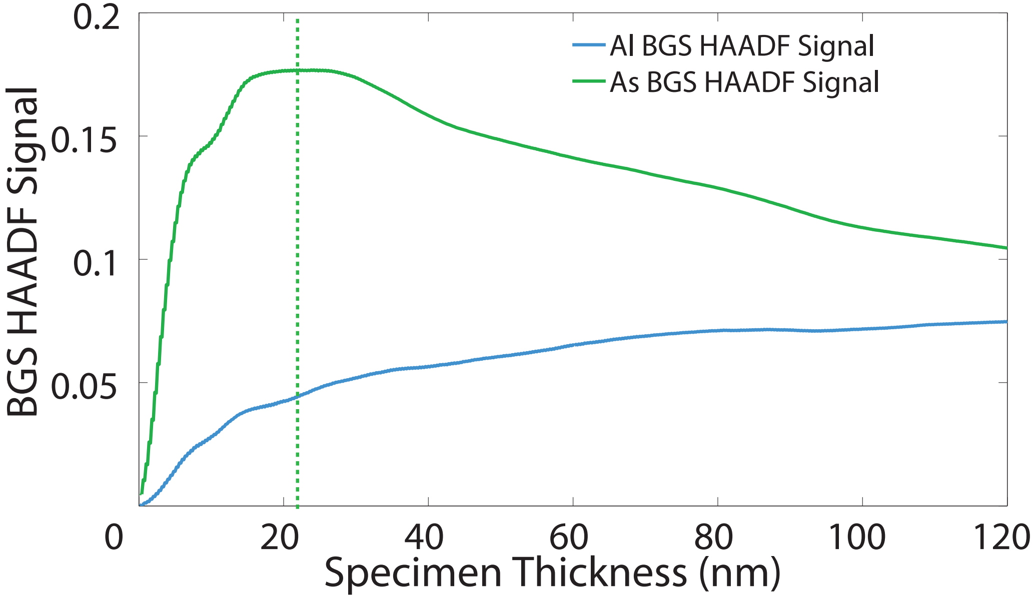

Figure 3.13 – AlAs: Background subtracted HAADF signal as a function of specimen thickness for probe placed on the Type-3 and Type-5 positions.

3.6.2.4 AlAs Column Ratio

The column ratio for the AlAs single crystal can be calculated by taking the ratio of the BGS HAADF signals. A plot of the column ratio variation with specimen thickness is shown in figure 3.14. The red broken line indicates the column ratio for AlAs calculated using a simple Z^2 approximation which again holds for very thin crystals. As the thickness of the specimen increases the probe de-channels and the measured HAADF signal is then the result of de-localised scattering. The black dots represent experimental column ratio values which were measured from a series of SuperSTEM 1 image. These images were of single crystal AlAs and were recorded over a wide range of specimen thicknesses. There is clearly good agreement between the simulated and experimental column ratio measurement. Figures 3.10 & 3.14 indicate that the measured dumbbell column ratio varies considerably depending on the atomic species and the specimen thickness. The column ratio values do, however, change in a predictable way for single crystals. Furthermore, the simulations accurately reproduce the experimental column ratio values. The multislice calculations, therefore, reproduce the scattering effects of high energy electrons from single crystal III-V materials. It can be assumed that scattering from atomic columns partially populated with different atomic species will also be faithfully reproduced. The multislice calculations provide an opportunity of investigating the variation of the HAADF signal at a variety of interfacial structures. Furthermore, the simulations can be directly compared to experimental column ratio maps. These column ratio maps are formed by processing raw HAADF images and the process is outlined in section 5.2.

A comparative table of the simulated parameters used in the calculations for single crystal GaAs and AlAs are collected in table 3.4.

3.7 Summary

This chapter presents the background theory of multislice image calculation, the multislice code modifications and a discussion of the signals generated from single crystal III-V materials. Section 3.1 described how the electron wavefunction at the exit face of a crystal can be used to calculate the HAADF signal. This section also details the use of the electron wavefunction within the crystal to estimate the spatial origin of the EELS signal. The calculation of both these signals for large interfacial structures

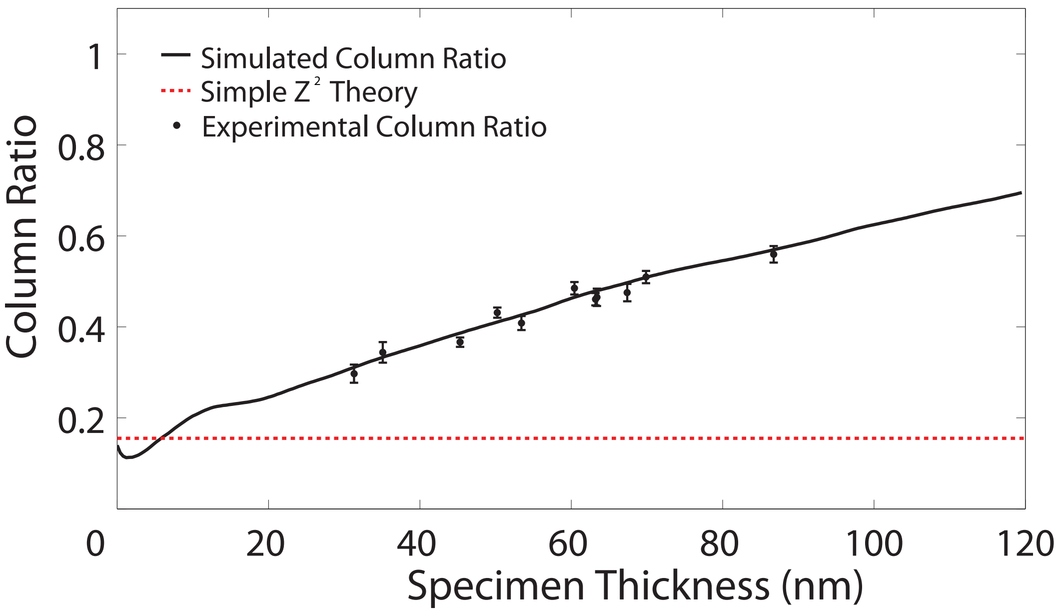

Figure 3.14 – The graph above shows the column ratio as a function of specimen thickness for single crystal AlAs. The solid black line indicates the simulated column ratio values, the red broken line shows the theoretical column ratio using a simple Z^2 model. The data points correspond to experimental column ratio values calculated from a SuperSTEM 1 image. Chapter 5 on page 95 describes the experimental column ratio calculation process in detail.

III-V Material	AlAs		GaAs		InAs	
$Z_{average}$	23		32		41	
Lattice Constant (@300K)	5.660$\AA$		5.653$\AA$		6.058 $\AA$	
Δz	2.001$\AA$		1.999$\AA$		2.142$\AA$	
Dumbbell spacing	1.415$\AA$		1.413$\AA$		1.515$\AA$	
Theoretical Column Ratio	0.155		0.883		2.205	
Atomic Column	III	V	III	V	III	V
Atomic Number, Z	13	33	31	33	49	33
Atom RMS Displacement	0.078$\AA$	0.090$\AA$	0.091$\AA$	0.094$\AA$	0.130 $\AA$	0.111$\AA$

Table 3.4 – The parameters used in the simulations for the III-V crystal structures. The details of InAs are included in this table as these parameters are used in the simulations in chapter 7.

required the original software to be modified significantly. These modifications were necessary to reduce both the computation and subsequent processing time. The main modifications are detailed in section 3.2. The processing software that was used to manipulate the simulation output is detailed in section 3.4. The calculated HAADF and EELS signals from an interfacial structure can be complex. This required the calculation of the HAADF and EELS signals from single crystal III-V materials. These single crystal calculations, detailed in section 3.6, are used as a direct comparison for interfacial measurements in the following chapters.

Chapter 4

Debye Waller Factor Validation

4.1 Background Theory

The atoms within a crystal structure are not stationary, but rather vibrate about their equilibrium positions. The magnitude of the vibration is dependent on both the chemistry and temperature of the material [75, 26]. These quantised modes of vibration, called phonons, can also be excited when an incident electron transfers energy to the crystal lattice. An electron-phonon interaction is therefore inelastic and results in typical energy losses of less than 0.1eV [89].

There are three major features apparent in diffraction patterns which are the Kikuchi bands, the thermal diffuse background and the higher-order Laue zone (HOLZ) ring. Thermal vibrations are responsible for the Kikuchi banding and the thermal diffuse background. They also reduce the intensity in the HOLZ ring [72, 45]. The frozen phonon technique was introduced as a means of including the effects of thermal vibrations into the multislice calculations (described in section 3.1.3) [45]. The TDS contribution is significant for incoherent high angle scattering and is therefore an important inclusion when simulating HAADF images [64].

For low angle scattering, the inter-planar spacing parallel to the incident beam is considerably greater than the amplitude of the thermal vibrations. As as a result low angle scattering is dominated by coherent phase effects [86]. As the scattering angle increases, the apparent inter-planar spacing becomes comparable to the amplitude of the thermal motion until the electrons no longer 'see' a regular array of atoms and scattering becomes incoherent [91]. TDS causes the intensity in the Bragg beams to be reduced and redistributed as a diffuse background. It is this reduction in intensity

that can be described using the Debye Waller Factor (DWF) in equation 4.1.

$$DWF = e^{-2M} \tag{4.1}$$

where M is given by

$$M = 8\pi^2 < u^2 > \left[\frac{sin(\theta)}{\lambda}\right]^2 \tag{4.2}$$

M is a function of scattering angle, θ, and incident electron wavelength, λ. The parameter $< u^2 >$ is the mean square displacement of the atomic position perpendicular to the Bragg beam. This parameter is dependent on the atomic species and the temperature of the material [92, 72, 75].

The mean square displacement is a parameter that can be varied in the multislice simulations. The effect of this parameter can be assessed by comparing the simulated CBED patterns to experimental energy filtered CBED patterns. The multislice software simulates elastic scattering and before a direct comparison can be made the experimental images must be zero loss filtered. This filtering removes electrons that have lost a measurable energy loss through interaction with the specimen. A comparison is then made by measuring the ratio of the scattered intensity in First Order Laue Zone (FOLZ) to the intensity in the TDS background. This relationship was investigated as a function of specimen thickness allowing $< u^2 >$ to be systematically varied in the simulations and then compared to the experimental measurements.

The experimental energy filtered images were taken using a Gatan Image Filter fitted to the Tecnai T20 (see sec. 2.4.1.1 on page 31). The specimens were formed from a [001] grown GaAs wafer and prepared using the cross-section method outlined in section 2.5.1. The GIF is capable of imaging an angular range just below $4\mathring{A}^{-1}$ at a camera length of 125mm. This sets a limitation for imaging the full FOLZ ring of specific crystallographic orientations.

The radius of the FOLZ is related to the lattice spacing parallel to the beam direction, H, which can be calculated for specific beam directions $[UVW]$ (i.e. the [310] direction) using equation 4.3.

$$\frac{1}{H_{theoretical}} = \frac{a_0(U^2 + V^2 + W^2)^{\frac{1}{2}}}{P} \tag{4.3}$$

In equation 4.3 a_0 is the lattice parameter, and for fcc materials $P = 1$ for U+V+W odd and $P = 2$ for U+V+W even. For GaAs the lattice parameter is $5.6533\AA$ which allows the angular radius of the FOLZ ring, G, to be calculated using equation 4.4 where λ is the wavelength of illumination.

$$\frac{1}{H_{experimental}} = \frac{1}{2}G^2\lambda \tag{4.4}$$

These equations give calculated FOLZ radius of $4.4673\AA^{-1}$ for the [110] orientation and indicate that the full FOLZ cannot be imaged using the GIF. An initial investigation was therefore performed using the [310] orientation which has a smaller FOLZ radius of $2.9875\AA^{-1}$. Figure 4.1 shows a line trace through the center of an experimental energy filtered CBED pattern taken using the T20 and a [310] orientated sample confirming the expected radius of the FOLZ.

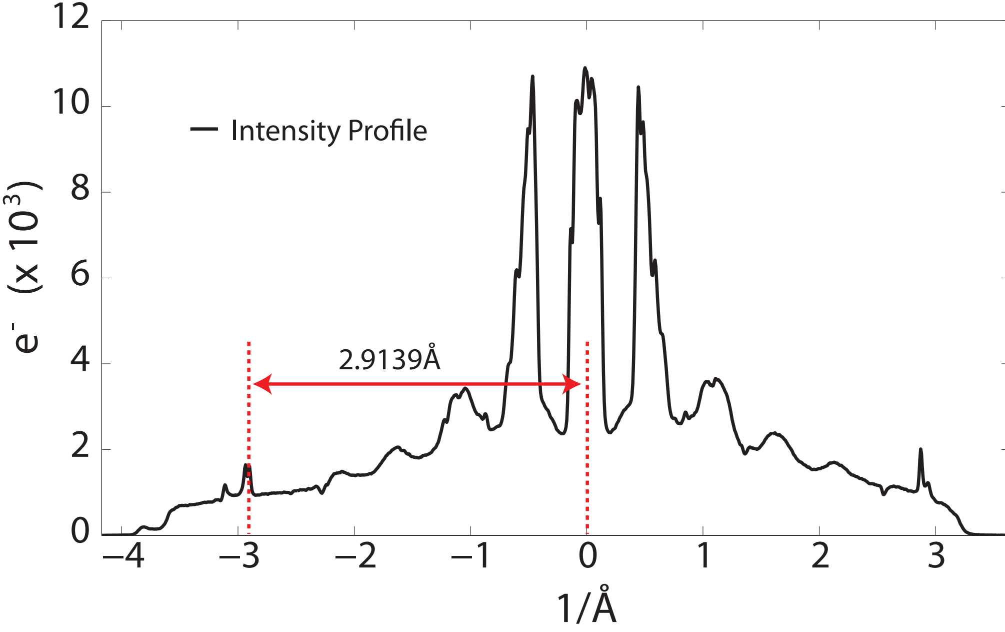

Figure 4.1 – The plot shows a line profile through the center of the energy filtered CBED pattern of a [310] orientated GaAs sample at 200kV. The radius of the FOLZ gives a direct measure of the lattice spacing parallel to the beam direction.

The vibrational modes of GaAs are anisotropic and the CBED intensity measurements from one crystallographic direction may give different results to those obtained from another direction. Therefore, after the initial investigation of the [310] orientation, a procedure was developed that utilised a combination of beam and sample tilts allowing a section of the [110] FOLZ to be imaged while using the central diffraction disks as a reference. This process ensures that the correct diffraction conditions were

maintained. A schematic of the microscope conditions for the [310] and [110] orientations are shown in figure 4.2 and the corresponding energy filtered images shown in figure 4.3. To image the [110] orientation, a short camera length was required which increased the electron flux onto the GIF. However, with a small spot size and a short integration time, it was possible to record the CBED patterns without damage to the camera. The small spot size required multiple images to be averaged together to improve the overall signal to noise ratio. Table 4.1 contains the microscope parameters used when collecting the energy filtered CBED images and the t/λ measurements.

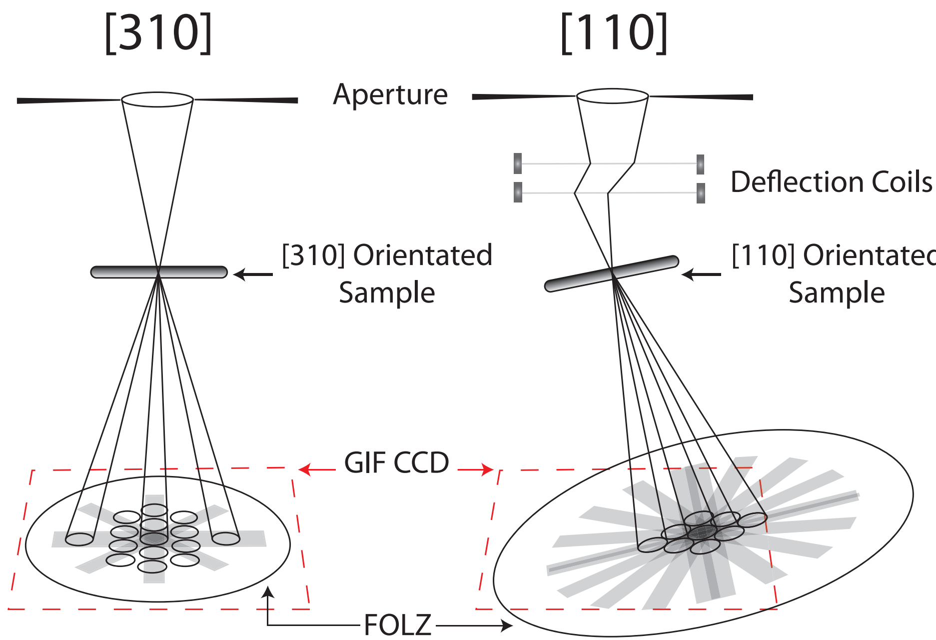

Figure 4.2 – The acceptance angles of the GIF allow the complete [310] FOLZ to be imaged, this is shown in the schematic on the left hand side. To record the [110] FOLZ requires a combination of sample and beam tilts where the central CBED pattern is required to ensure that the crystal remains orientated on zone after tilting. It is possible to image the central disks and the FOLZ for [110] orientated GaAs using a short camera length ($140mm$).

4.2 Specimen Thickness Measurement

An accurate simulation of an experimental image requires the knowledge of the specimen thickness at the area used to form the image. The thickness of a sample can be measured using a convergent two-beam condition to an accuracy of $<5\%$ [59]. However, tilting the sample to the two-beam condition can significantly change the probe position affecting the measured sample thickness. Alternatively, the GIF can be used to take a t/λ measurement without tilting the sample. This measurement can be con-

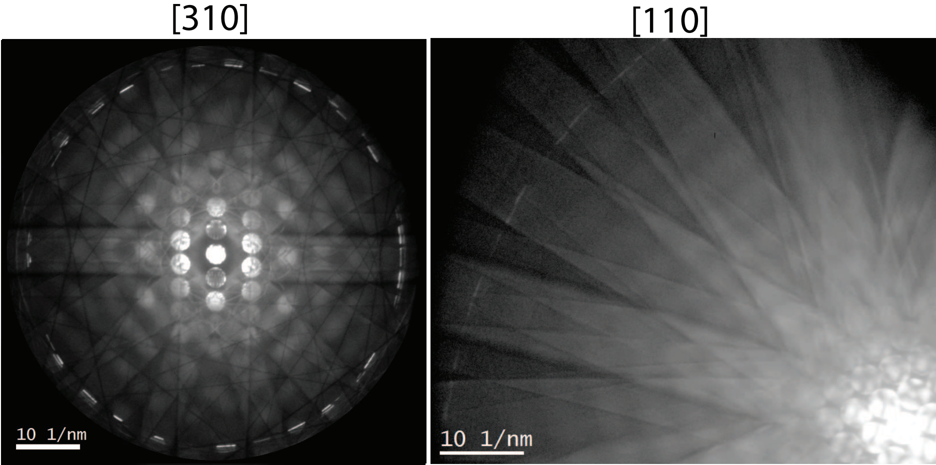

Figure 4.3 – The energy filtered CBED images for the [310] and [110] orientated GaAs (both are shown on a log scale). The [110] CBED image requires both sample and illumination tilt to image both the central CBED disks and the FOLZ on the GIF CCD.

Energy Filtered CBED Parameters:	
Incident Electron Energy	$200kV$
Convergence Angle, α	$50\mu m$
	$1.89\pm$ $0.05mrad$
Collection Aperture, β	$3mm$
	$79.9mrad$
Spot Size	$FWHM$ $58nm$ (10)
Camera Length	$140mm$
EELS Parameters:	
Incident Electron Energy	$200kV$
Convergence Angle, α	$30\mu m$
	$1.19\pm$ $0.05mrad$
Collection Aperture, β	$2mm$
	$53.3mrad$
Spot Size	10, $FWHM$ $18nm$
Camera Length	$150mm$
EFTEM	on
Dispersion	$0.5eV/pixel$
t/λ collection time	$10sec$

Table 4.1 – The tables above indicate the experimental parameters used for taking the Energy Filtered CBED Images (top) and t/λ measurements (bottom).

verted to an absolute thickness using the mean free path, λ. The mean free path can, however, vary significantly depending on the microscope parameters and the diffraction conditions used. The error in the thickness measurement can also be up to 20% using this technique. A combination of both these measurement methods can be used to measure the local thickness without requiring significant tilts. This requires the measurement of the mean free path for the specific set of microscope conditions used in the acquisition of the energy filtered CBED images. The MFP was calculated by taking a two-beam image and a t/λ measurement close to the zone axis for a range of specimen thicknesses. The thickness measurement from the two-beam image is used to calculate the MFP for the crystal orientation and microscope parameters used. This calculated λ can then be used in subsequent t/λ measurements when recording the on zone CBED images. An outline of the two-beam and t/λ measurements are given in sections 4.2.1 and 4.2.2. The resulting MFP measurements are detailed in section 4.2.4.

4.2.1 Two-Beam Condition

A method for measuring the thickness of a specimen using the intensity oscillations in CBED diffraction disks was first described by Kelly et al. [59]. The method involves tilting the sample to a two-beam condition, where parallel intensity oscillations in the 000 beam and the diffracted beam contain information on the local specimen thickness.

For both the [110] and the [310] orientations the two-beam condition was set up using the 000 and 400 reflections as seen in figure 4.4.

This method of thickness determination utilises the two-beam dynamical theory in the form equation 4.5.

$$\left(\frac{s_i}{n_k}\right)^2 + -\frac{1}{\xi_g^2}\left(\frac{1}{n_k^2}\right) = \frac{1}{t^2} \tag{4.5}$$

In equation 4.5, ξ_g is the extinction distance of the particular excited reflection, n_k is an integer and t is the thickness of the specimen [46]. The central bright fringe in the 400 disk corresponds to the Bragg condition where the deviation parameter is exactly zero. s_i is the deviation of the ith minimum from the exact Bragg condition and can be measured directly from the two-beam image (see figure 4.5) [62, 61]. This is done by measuring θ_i which is the distance from the central fringe to the ith minima, s_i is

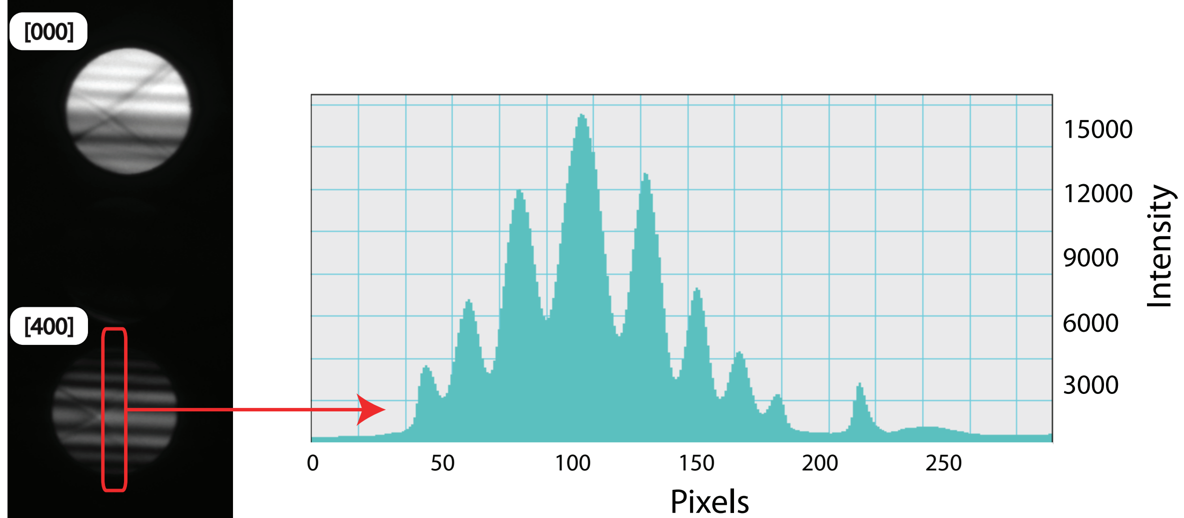

Figure 4.4 – For the GaAs substrate sample the two-beam condition was set up using the 000 and 400 reflections (left), a line trace through the 400 reflection (right) allows the intensity oscillations to be measured.

then defined in equation 4.6.

$$s_i = \lambda \frac{\theta_i}{2\theta_B d^2} \tag{4.6}$$

In this expression θ_B & d are the Bragg angle and the inter-planar spacing of the reflecting planes.

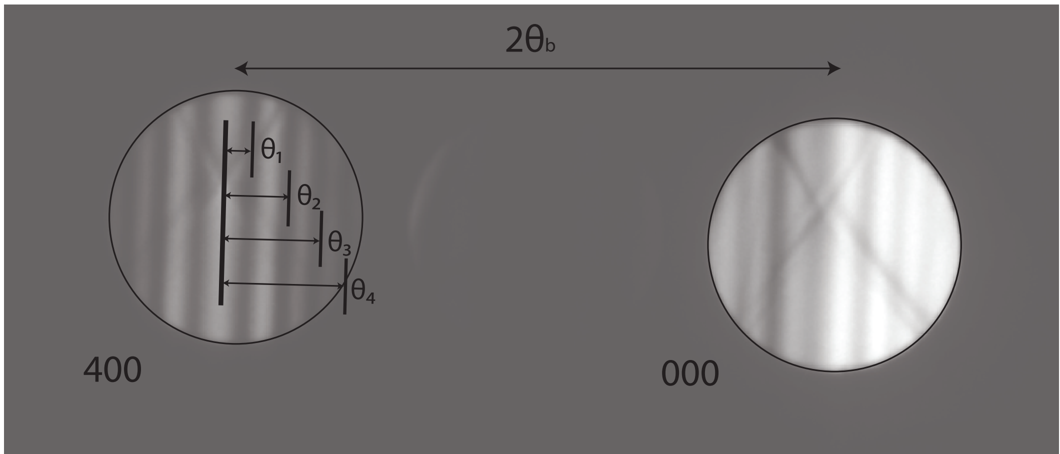

Figure 4.5 – Measurements for θ_i is taken as the distance from the central intensity peak to the ith fringe, while $2\theta_B$ is twice the Bragg angle.

A graphical method of thickness determination can be used by inspecting the graph of $\left(\frac{s_i}{n_i}\right)^2 vs. \left(\frac{1}{n_i}\right)^2$ which should reveal a straight line with the y intercept at $\frac{1}{t^2}$ [62]. The integer value n_i is varied in sequence until the fitted line produces a correlation coefficient nearest to unity, which indicates the correct specimen thickness.

Figure 4.6 shows an example of the fitting procedure for one of the two-beam

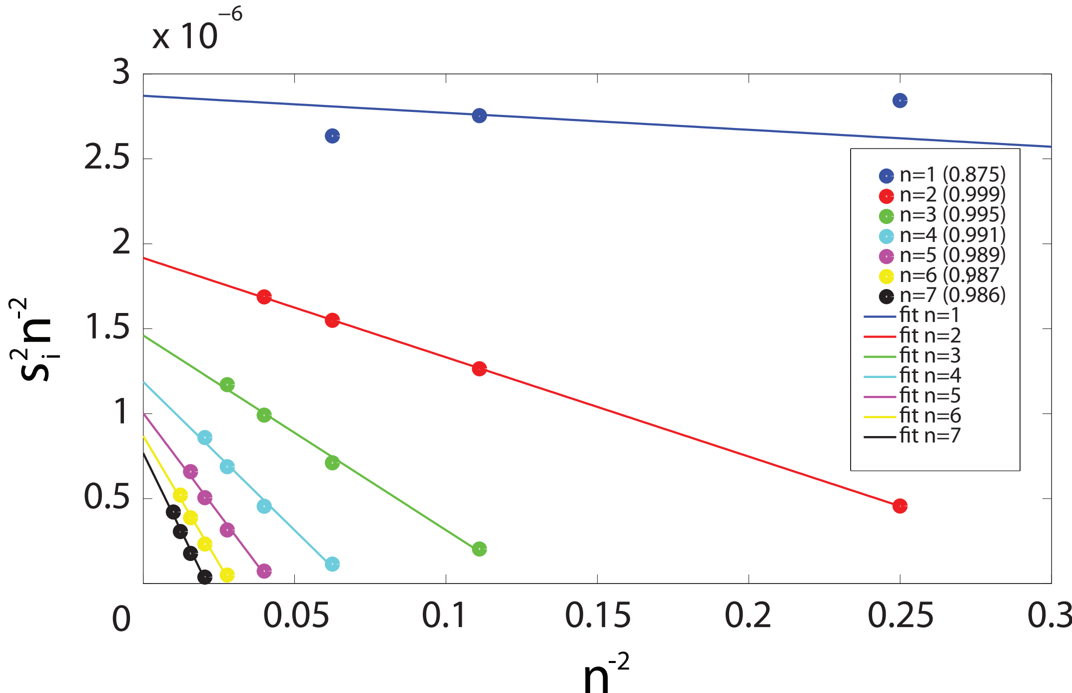

Figure 4.6 – The specimen thickness can be calculated by plotting $(\frac{s_i}{n_i})^2 vs.(\frac{1}{n_i})^2$ and then systematically varying the integer n. The fit with a correlation coefficient closest to unity corresponds to the correct selection of the parameter. These coefficients are indicated in the legend in brackets and show $n = 2$ corresponds to the optimum fit.

images taken. The measured values are represented by the circular markers and the corresponding fit as the solid line. The legend indicates the integer value of n used for each fit and the corresponding correlation coefficient is shown in brackets. From figure 4.6 it is clear that $n = 2$ yields to the optimum fit. A linear regression intercepts the y-axis at 1.9165×10^{-6} resulting in a calculated specimen thickness of $722 \pm 36\mathring{A}$.

This method of thickness determination is one of the most accurate and the reported error can be as low as a few percent [59]. This measurement method is, however, suitable only for crystalline materials. It therefore does not account for any surface amorphous material that may be at the specimen entrance or exit face (from either sample preparation or surface oxidisation). This can result in an error when calculating the mean free path [62, 59, 61].

A study by Barna investigated the amorphisation and surface morphology development of GaAs after ion milling at low kV. The resulting TEM images indicated that a final low kV polish reduces any surface amorphisation ($<<1nm$) [71]. Furthermore, by storing the specimen under vacuum, any surface oxidisation can be minimised. The calculated error for the MFP will, therefore, be minimal. An amorphous layer of $0.5nm$ will result in an error typically less than $\pm 1\%$.

4.2.2 t/λ Measurement

Thickness information about the specimen can be obtained from the energy-loss spectrum as the probability of inelastic scattering events increase with increasing specimen thickness [40]. The sample thickness can be estimated by measuring the intensity under the zero loss peak, I_0, and the intensity under the entire spectrum, I_t (indicated in figure 4.7). In practice a large fraction of the total intensity is in the low loss region of the spectrum and so if the measured spectrum is $> 50eV$ then this can be approximated to the total spectrum intensity. The ratio of $ln(I_0/I_t)$ is a measurement of t/λ and the specimen thickness is defined by equation 4.7.

$$t = \lambda ln(\frac{I_t}{I_0}) \tag{4.7}$$

The parameters used to collect the t/λ measurements are detailed in Table 4.1.

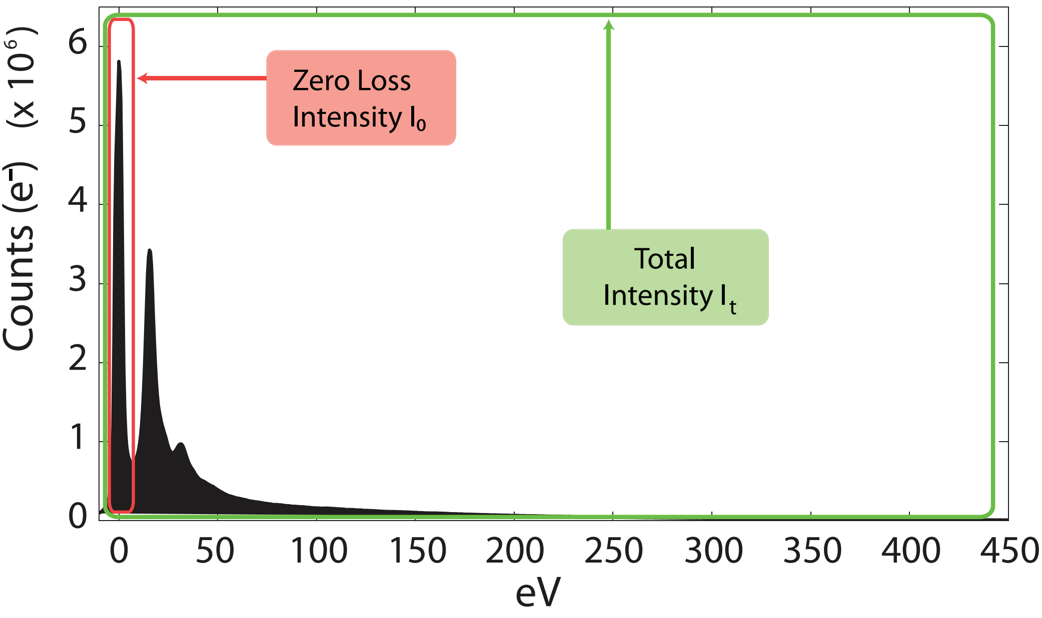

Figure 4.7 – The thickness of the specimen can be determined from the EELS spectrum, this relationship is defined in Equation 4.7.

4.2.3 Mean Free Path Approximation

An approximation for the mean free path was described by Malis et al. [93] and can be estimated using equation 4.8. In this approximation, $E_m = 7.6Z^{0.36}$ and is a material

dependent average energy loss. E_0 is the incident electron energy and is expressed in kV and β is the collection angle in mrad.

$$\lambda \approx (106nm) \frac{F\left(\frac{E_0}{E_m}\right)}{In\left(2\beta \frac{E_0}{E_m}\right)} \tag{4.8}$$

$$F = (106nm) \frac{1 + (E_0/1022)}{(1 + (E_0/511))^2} \tag{4.9}$$

The variable F in 4.8 is a relativistic factor and is 0.61762 for 200kV & 0.76789 for 100kV electrons. For III-V compounds an effective atomic number can be substituted for Z (equation 4.10, where f_i is the atomic fraction) allowing the expression to estimate the expected mean free paths for the III-V materials listed in table 4.2. This expression will also allow a comparison to the experimentally measured mean free paths in section 4.2.4.

$$Z_{effective} = \frac{\sum_i f_i Z_i^{1.3}}{\sum_i f_i Z_i^{0.3}} \tag{4.10}$$

Equation 4.8 also assumes the illumination is parallel and that the mean free path saturates at a particular convergence angle, α. However, if the collection angle $\beta \gg \alpha$ then the approximation holds.

Compound	$Z_{effective}$	Estimated Mean Free Path, λ ($\mathring{A}$)
AlP	14.3	1245±249
InP	29.8	1007±201
GaAs	32.3	983±196
InAs	44.1	930±186
InSb	49.7	866±173

Table 4.2 – Using Equation 4.8 the mean free path can be estimated for III-V materials. These approximations are shown in the table above for common binary III-V compounds.

4.2.4 Mean Free Path Determination for GaAs

4.2.4.1 Mean Free Path Measurement for GaAs [310]

This section details the results for the measurement of the mean free path for a [310] orientated GaAs crystal. A plot of t/λ as a function of crystal thickness can be seen in figure 4.8. This plot shows a linear relationship over the full range of thicknesses. The

linear fit can be used to calculate an "average" mean free path of $1045 \pm 64\mathring{A}$. This is somewhat more than the $983\mathring{A}$ predicted by the approximation calculated using Equation 4.8, but does fall within the error estimation.

Identical microscope conditions were used to record the [310] orientated CBED images in section 4.3 and so this calculated MFP will be used to calibrate the t/λ measurements for the CBED images recorded at the [310] crystal orientation.

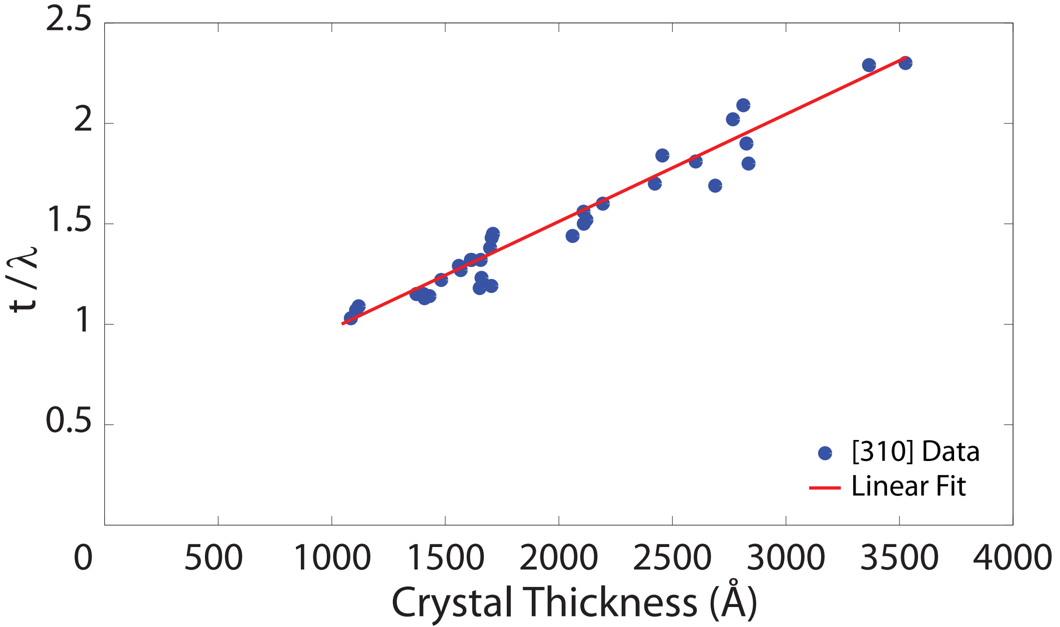

Figure 4.8 – A plot of t/λ as a function of the crystal thickness measured using CBED for the [310] crystallographic orientation of GaAs.

4.2.4.2 Mean Free Path Measurement for GaAs [110]

This section details the results for the measurement of the mean free path for a [110] orientated GaAs crystal. A plot of t/λ as a function of crystal thickness for the [110] orientation can be seen in figure 4.9. This plot also indicates that a linear relationship is present. The average mean free path was calculated to be $788 \pm 39\mathring{A}$ which is less than the $983\mathring{A}$ predicted by Equation 4.8. Again an identical microscope setup was used during the acquisition of the [110] orientated CBED patterns in section 4.3. A MFP measurement of $788\mathring{A}$ will therefore be used to calibrate all the t/λ measurements for the [110] orientation.

The measured mean free path is different for the [310] and [110] orientations which may be related to the difference in the atomic spacing in the z-direction. For the [110] orientation the z-spacing in the atomic column is smaller which will increase

the probe channelling effect and the inelastic interaction will be high. For the [310] orientation the atomic spacing in the z-direction is considerably larger which will reduce the overall inelastic interaction of the column. However, if the measurement procedure is consistently applied then the thickness measurement will be accurate.

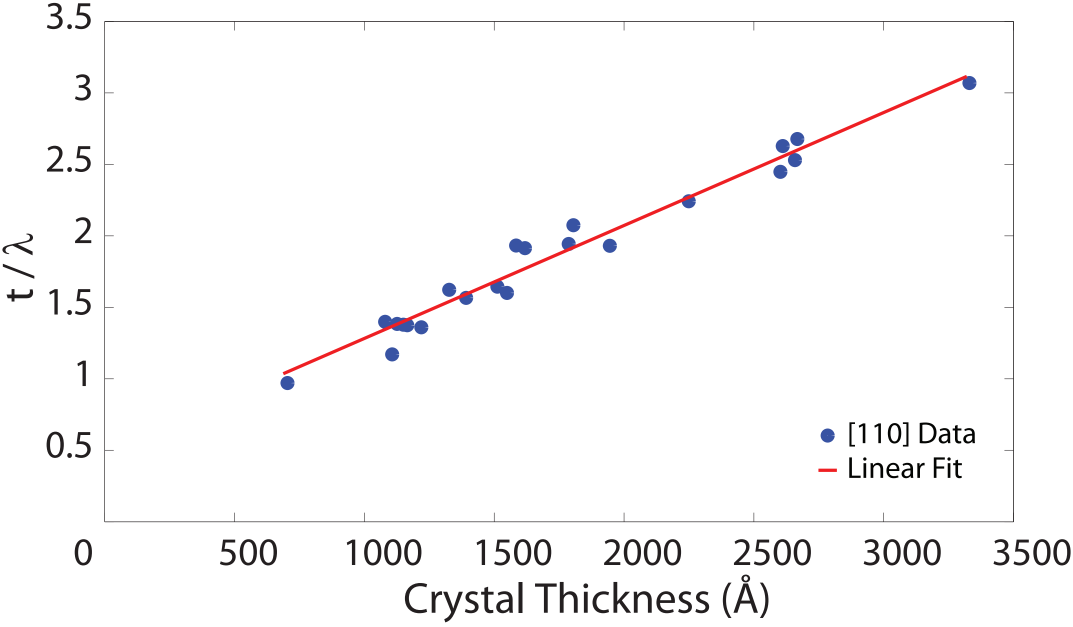

Figure 4.9 – A plot of t/λ as a function of the crystal thickness measured using CBED for the [110] crystallographic orientation of GaAs.

4.3 Experimentally Derived Mean Square Displacement

This section investigates how the scattered intensity in the convergent beam diffraction patterns varies with specimen thickness. In particular, the intensity in the FOLZ ring and the surrounding background is measured and compared. The overall aim is to optimise the mean square displacement parameter, $< u^2 >$, to fit the intensity measurements taken from the experimental images. Firstly, a series of energy filtered CBED images are recorded over a large thickness range. For each experimental image the intensity in the FOLZ and the background is measured and then compared to a series of simulations. In these simulations $< u^2 >$ is systematically varied from 15% below the currently used $< u^2 >$ to 15% above. The measured intensity in the experimental image can then be directly compared to each simulation. This allows the optimum $< u^2 >$ to be ascertained. The last stage is to evaluate the effect of $< u^2 >$

on the HAADF signal and Column Ratio for the aberration corrected SuperSTEM 1 probe.

The mean free path measurements calculated in section 4.2.4 were used to calibrate the t/λ measurements for the acquired on-zone energy filtered CBED patterns. This calibration provides a measurement of the specimen thickness for each CBED image without having to tilt the specimen from the on-zone position. Furthermore, the initial calibration is made with the same microscope conditions used to collect the on-zone images.

The multislice simulation method is outlined in section 3.1 and the GaAs [110] unit cell used is defined in section 3.6.1. The GaAs [310] unit cell is shown in figure 4.10 and consists of 20 atoms arranged into ten repeating layers with a Δz of $0.894\mathring{A}$. This orientation forms a structure that is similar to the [110] direction, in both cases each atomic column contains only one type of atom. However, unlike the dumbbells formed in the [110] orientation, the [310] direction forms a series of evenly spaced atomic rows.

The upper section of figure 4.11 shows an experimental energy filtered [310] CBED pattern. The red box indicates the section that was used to calculate the FOLZ ratio. This ratio was calculated by firstly taking an averaged line trace over the first order Laue zone. The section used is parallel to the 004 vertical Kikuchi band and the line trace is taken across the $\bar{5}\,17\,1$ reflection . This line trace allows both the peak (I_{FOLZ}) and the background ($I_{Background}$) signal values to be calculated. The upper right section of figure 4.11 shows the averaged line trace and the measurement of the I_{FOLZ} and $I_{Background}$. The background intensity is estimated by interpolating two points on either side of the first order Laue zone. The ratio is then calculated using equation 4.11. The lower half of figure 4.11 shows the simulated energy filtered CBED pattern which has good visual agreement with the Kikuchi banding. Furthermore, the first order Laue ring and Zero order disks are accurately reproduced.

$$FOLZ_{ratio} = \frac{I_{FOLZ} - I_{Background}}{I_{Background}} \tag{4.11}$$

The FOLZ ratio was calculated for the GaAs [310] crystal over a range of specimen thicknesses. The experimental ratio is plotted in figure 4.12 using the black diamond markers. The FOLZ ratio shows a pseudo-linear decrease with thickness and drops from ~ 7 to 2.5 over the experimental thickness range. The mean square displacement

parameters used in the initial calculations are detailed in table 3.4 and are labelled "Current DWF" in figure 4.12. The parameter $< u^2 >$ was then changed sequentially by ±5%, ±10% and ±15% and for each set of simulations and the FOLZ ratio was re-calculated. Figure 4.12 shows the variation of the FOLZ with thickness and gives a clear indication of how the parameter $< u^2 >$ affects the FOLZ Ratio. The graph indicates that a small reduction (-5%) in the currently used DWF would reproduce the experimental data more accurately.

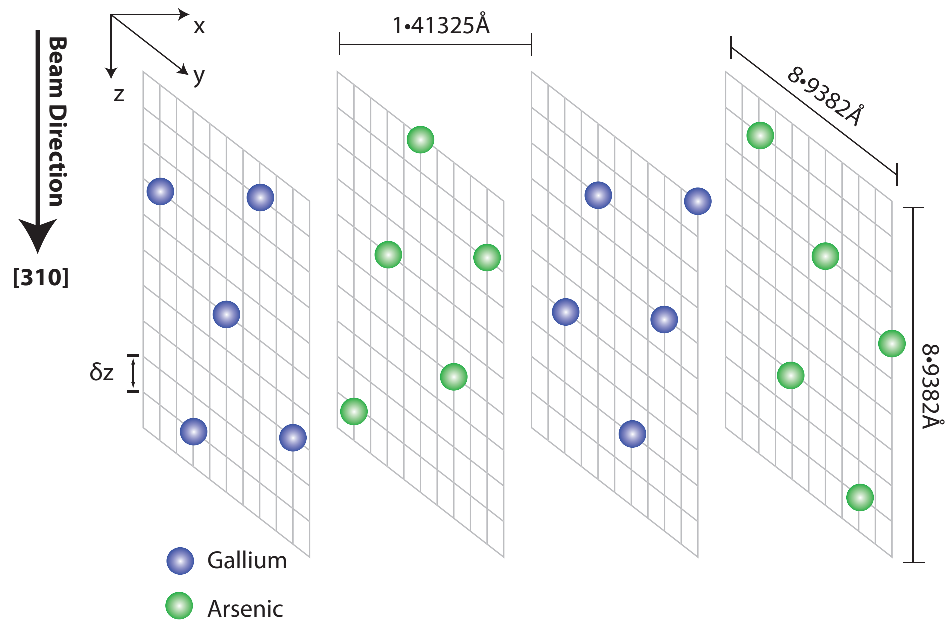

Figure 4.10 – The unit cell for GaAs [310] forms a series of four repeating atomic rows where each row contains only one species of atom. For the multislice simulation the unit cell is split into ten repeating slices in the z direction. The 10 x 10 x 4 grid in the image above indicates the relative position of the gallium (blue) and the arsenic (green) atoms within the unit cell.

This process can now be applied to the [110] orientation with the addition of the tilting step described in section 4.1. The tilting step allows both a section of the [110] FOLZ and the central CBED disks to be imaged simultaneously using the GIF. Figure 4.13 shows the experimental [110] FOLZ ratio data calculated over a range of specimen thicknesses and is represented by the black diamond markers. These experimental calculations are overlaid onto the simulation data. The calculations were performed firstly using the currently published mean square displacement parameters. The parameter $< u^2 >$ was then changed by ±5%, ±10% and ±15%. Figure 4.13 shows the simulated FOLZ over a range of specimen thicknesses for the various $< u^2 >$. The figure also indicates that the optimum $< u^2 >$ requires a small reduction of $< u^2 >_{current}$ by 10% to find good agreement with the experimental FOLZ ratio.

Energy Filtered CBED Image:

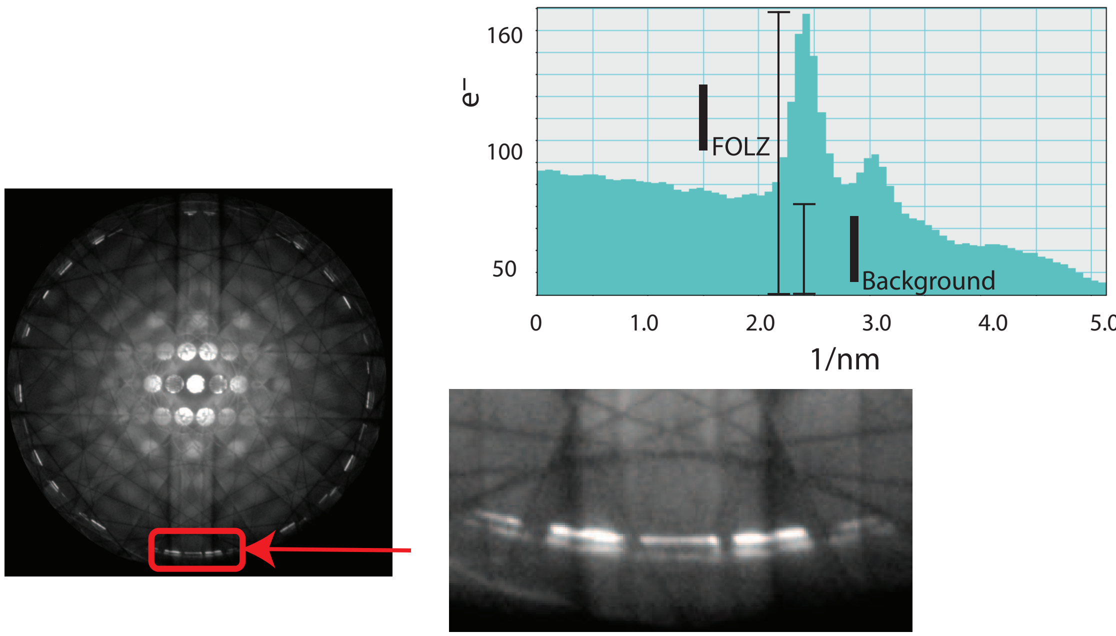

Multislice Simulation:

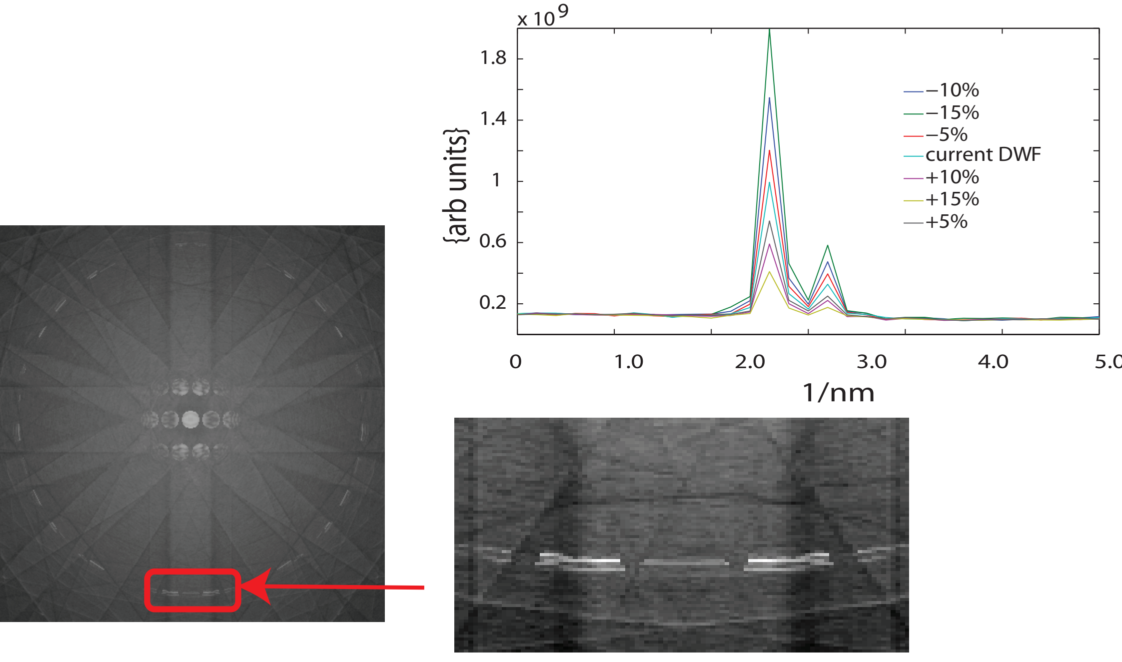

Figure 4.11 – A comparison of the experimental GaAs [310] EF-CBED pattern (upper left) to an equivalent simulated image (lower left) indicates that the main features of the pattern are replicated. The section of the FOLZ that is used for the calculation of the FOLZ ratio is indicated by the red box. From each pattern an averaged line profile through this section of the FOLZ ring is taken.

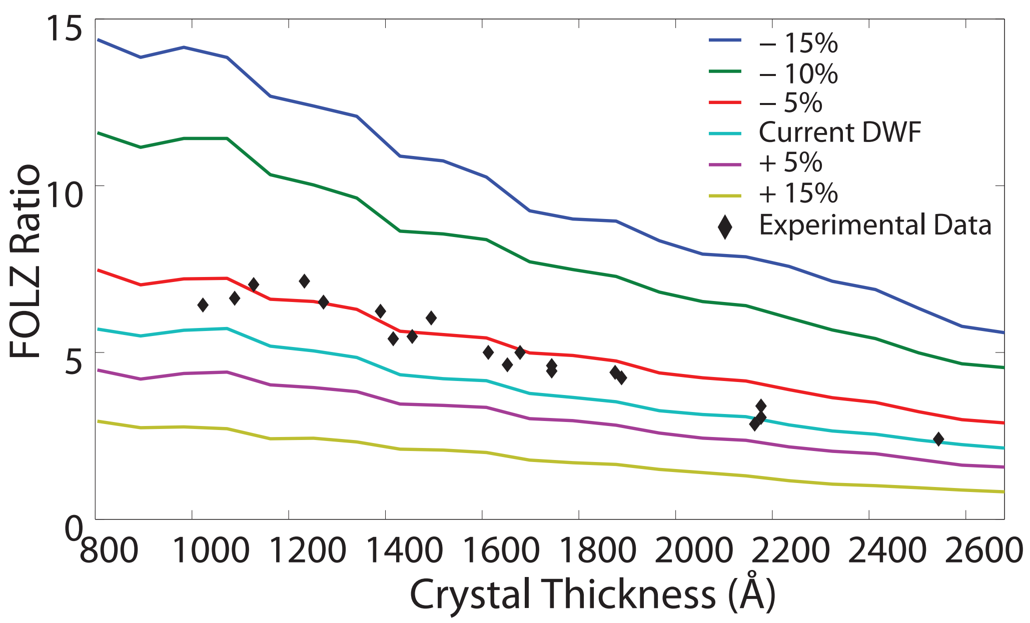

Figure 4.12 – The simulated and experimental FOLZ_{ratio} for the [310] orientation, the ratio is $[I_{FOLZ} - I_{Background}]/I_{Background}$. The variable parameter, $< u^2 >$, is the mean square displacement found in equation 4.1 which is varied in steps of 5%.

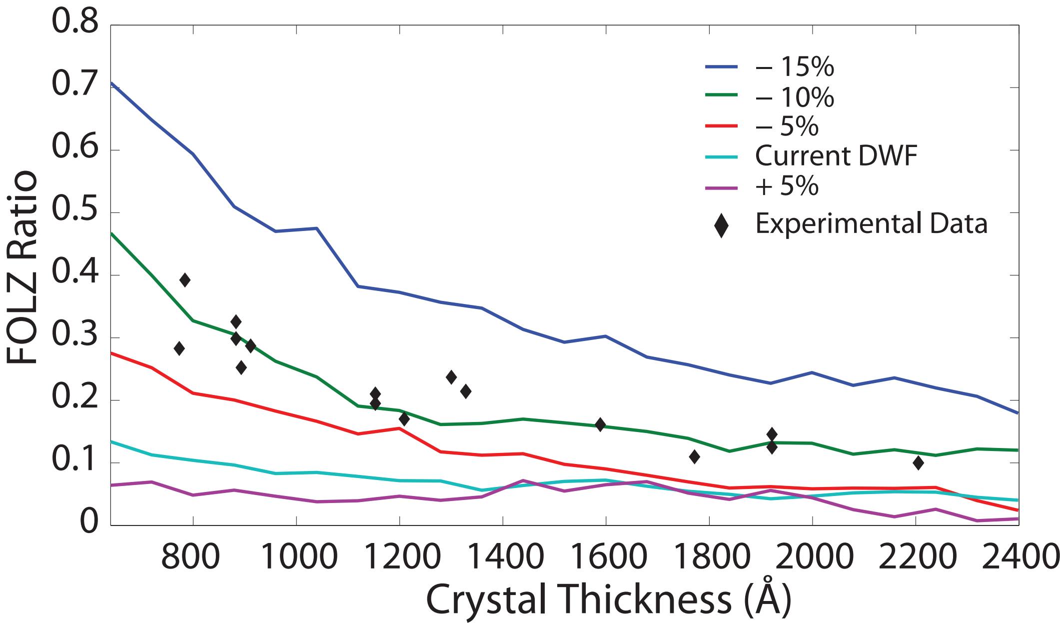

Figure 4.13 – The simulated and experimental FOLZ_{ratio} for the [110] orientation, the ratio is $[I_{FOLZ} - I_{Background}]/I_{Background}$. The variable parameter, $< u^2 >$, is the mean square displacement found in equation 4.1 which is varied which is varied in steps of 5%.

4.4 Effect of $< u^2 >$ on HAADF Signal

Section 4.3 described the method used to calculate the optimum value for the mean square displacement parameter $< u^2 >$ for both the [110] and [310] crystallographic orientations. Figure 4.12 showed that for the [310] orientation, a good agreement between the simulated and experimental $FOLZ_{ratio}$ can be achieved by reducing $< u^2 >_{current}$ by 5%. Likewise, figure 4.13 indicated that for the [110] orientation, a reduction of 10% was necessary to achieve a good match between the simulated and experimental results.

4.4.1 T20 Probe

The aim of this section is to explore the effect of changing the parameter $< u^2 >$ on the expected HAADF signal from the simulated T20 probe for both the [310] and the [110] orientations. Figure 4.14 shows the variation of the integrated HAADF signal for the T20 probe incident on a [110] orientated GaAs crystal. The HAADF signal was integrated over a solid angle of 70 - 210 mrad for an mean square displacement of $< u^2 >_{current-10\%}$, $< u^2 >_{current}$ and $< u^2 >_{current+10\%}$ and each calculation was averaged over 100 phonon configurations. Figure 4.14 shows a plot of the HAADF signal as a function of crystal thickness. The graph also indicates the signal variation as a percentage shown using the black broken line (right hand axis) which indicates that as $< u^2 >$ is changed from $< u^2 >_{current-10\%}$ to $< u^2 >_{current+10\%}$ the variation in HAADF signal is never greater than 6%. Furthermore, the maximum variation occurs at very small crystal thicknesses of than 100Å. For typical specimen thicknesses of 300-600Å, the variation in the total integrated HAADF signal is consistently less than 4%. This graph clearly shows that a variation of ±10% in the mean square displacement parameter does not have a significant impact on the total integrated HAADF signal when using the T20 probe. Figure 4.15 shows the same graph for the [310] GaAs orientation, however the variation in $< u^2 >$ is this time ±5% which corresponds to the FOLZ measurements shown in figure 4.12. Figure 4.15 also indicates that the variation of the HAADF signal produced from a 5% change in the mean square displacement is small for the T20 probe and is less than 3% for crystal thicknesses greater than 300Å. These results indicate that for the T20 probe the currently used mean square displacements detailed in table 3.4 are sufficiently accurate to reproduce

the intensity found in the energy-filtered CBED patterns for [110] and [310] orientated gallium arsenide single crystals.

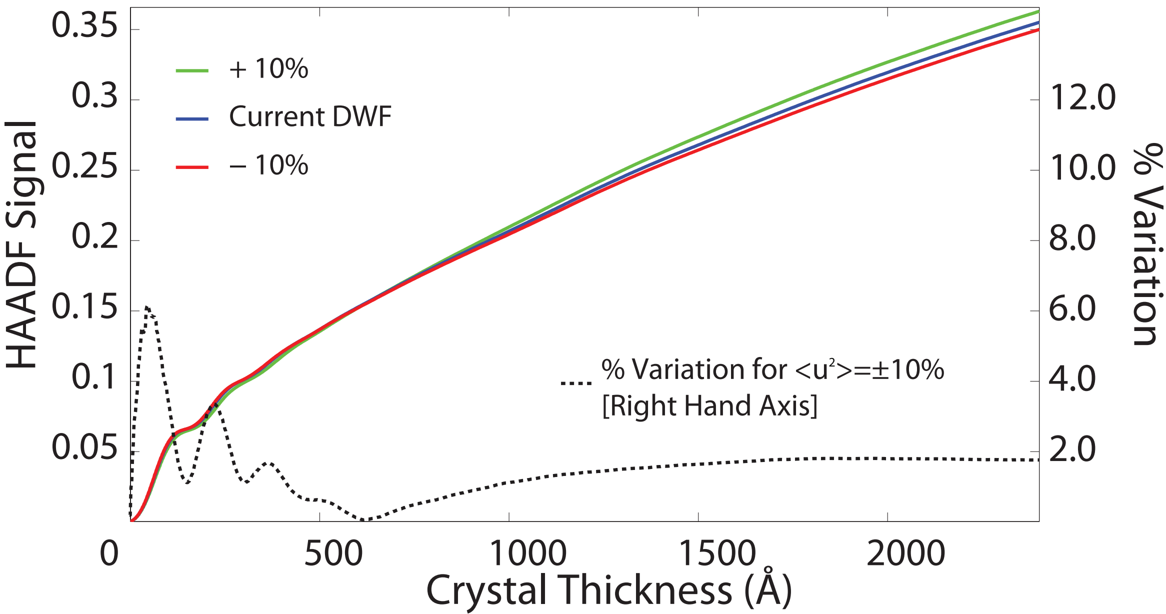

Figure 4.14 – The resulting HAADF signal from the [110] orientated GaAs crystal for the T20 probe showing the dependence on the mean square displacement parameter $< u^2 >$.

4.4.2 SuperSTEM Probe

The next consideration is the effect of a 10% change in $< u^2 >$ when using an aberration corrected 24mrad SuperSTEM 1 probe. This is investigated for a [110] orientated GaAs crystal. The starting probe conditions are identical to those detailed in tables 3.2 and 3.3 and three probe positions are calculated corresponding to the probe focused on the Type-3 column, the Type-5 column and the background position. The HAADF signal was again integrated over a solid angle of 70 to 210mrad. The mean square displacement used in the calculations were set to $< u^2 >_{current-10\%}$, $< u^2 >_{current}$ and $< u^2 >_{current+10\%}$ and averaged over 100 phonon configurations.

Figure 4.16 shows the integrated HAADF signal as a function of specimen thickness where the solid lines correspond to the calculation using $< u^2 >_{current}$. The data plotted with the "+" markers was generated using an mean square displacement of $< u^2 >_{current+10\%}$ and the data with the "-" markers using an mean square displacement of $< u^2 >_{current-10\%}$. The "red" data corresponds to the probe positioned between the dumbbells and behaves as expected. A reduction in the mean square displacement

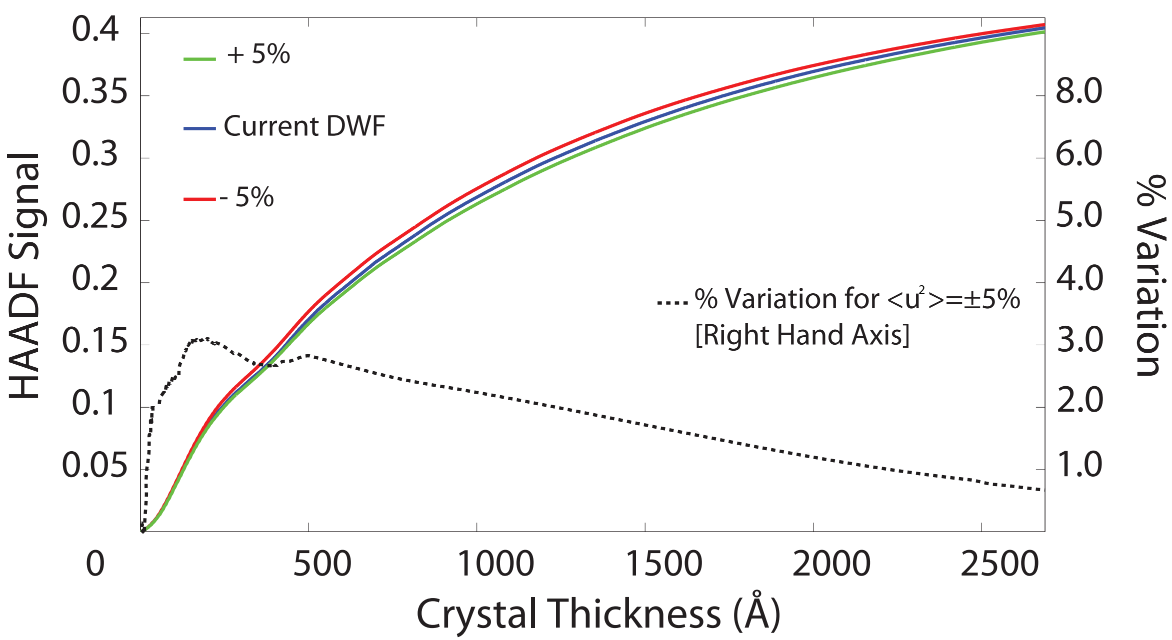

Figure 4.15 – The resulting HAADF signal from the [310] orientated GaAs crystal for the T20 probe showing the dependence on the mean square displacement parameter $< u^2 >$.

reduces the overall HAADF signal and an increase in the mean square displacement increases the overall HAADF signal. However, when the probe is positioned on the atomic columns, the behavior is more complex. This is probably due to the channelling effects within the top 300Å of the crystal. Equation 3.5 described how the HAADF signals are used to calculate the column ratio. These generated HAADF signals can be used to calculate the column ratio as a function of specimen thickness, using the three mean square displacement values ($< u^2 >_{current-10\%}$, $< u^2 >_{current}$ and $< u^2 >_{current+10\%}$). Figure 4.17 shows this calculated column ratio where $< u^2 >_{current}$ is shown as the solid lines, $< u^2 >_{current-10\%}$ is represented by the $-$ marker and $< u^2 >_{current+10\%}$ is represented by the $+$ marker. The plot clearly indicates that increasing the DWF by 10% changes the measured column ratio in the top $20nm$ of the crystal. This is most likely an effect caused by the channelling in the top region of the atomic column. However, figure 4.17 indicates that reducing the DWF by 10% has no significant effect on the measured column ratio for single crystal GaAs.

4.5 Discussion and Conclusions

The aim of this chapter was to evaluate the effect of the mean square displacement parameter $< u^2 >$ on the multislice calculations. This was done by comparing a series

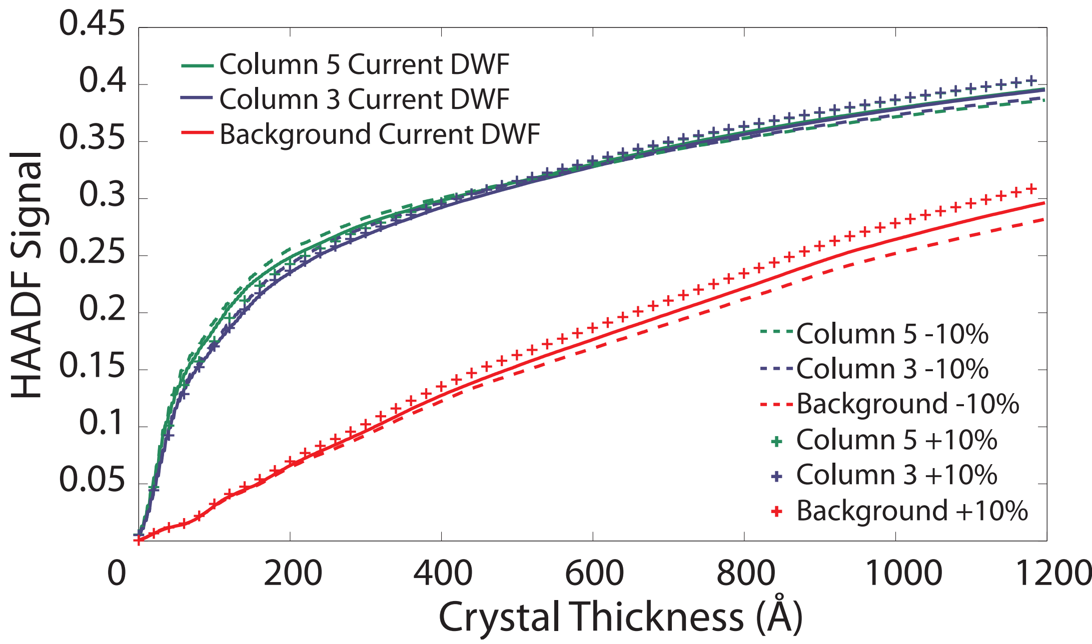

Figure 4.16 – The Column 5, Column 3 and Background HAADF signals from the [110] orientated GaAs crystal as a function of thickness. This graph shows how the HAADF signal varies depending on the mean square displacement parameter $< u^2 >$ and indicates that a 10% change from the currently used $u$makes little difference to the overall HAADF signals.

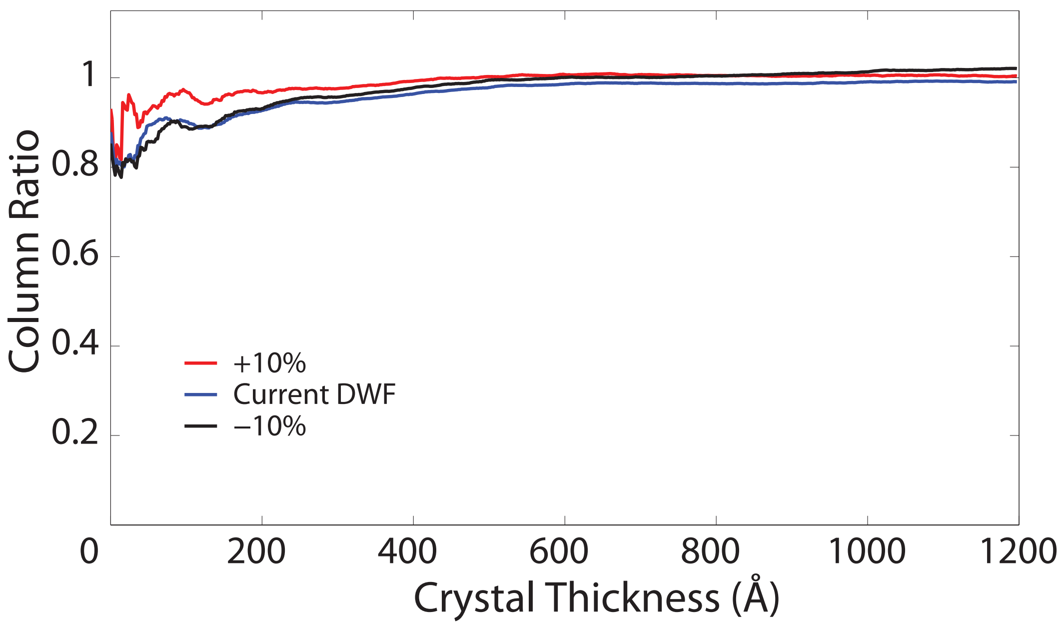

Figure 4.17 – The Column Ratio from the [110] orientated GaAs crystal as a function of thickness. This graph shows how the column ratio depends on the mean square displacement parameter $< u^2 >$ and is calculated using the HAADF signal data used to create figure 4.16.

of simulated and experimental CBED patterns over a range of thicknesses. Section 4.2 outlined the method used to measure the experimental sample thicknesses using a two beam condition and a t/λ measurement. This allowed the mean free path to be calculated for each orientation. This then allowed a calibration of the subsequent t/λ measurements.

A range of (zero-loss) energy filtered CBED patterns were recorded and the t/λ measurements were used to measure the specimen thickness. Each CBED pattern was then compared to a series of multislice simulations where the mean square displacement parameter was systematically varied. Comparing the FOLZ ratio from the experimental image and the multislice series, an "effective" mean square displacement was calculated from the simulated data that best represented the experimental CBED pattern. This optimum $< u^2 >$ was calculated to be be 5-10% lower than the currently used mean square displacement value. Section 4.4 then investigated the effect of changing this parameter on the generated HAADF signals from bulk GaAs for both the Tecnai T20 and the SuperSTEM probes. This gives a clear indication that $< u^2 >_{current}$ satisfactorily reproduces the thermal diffuse scattering observed experimentally and that changes in $< u^2 >$ of the order of $\pm 10\%$ have no significant impact on the HAADF signal for these operating conditions used at SuperSTEM 1.

This apparent variation of $< u^2 >$ may however be due to the anisotropic vibration of the atoms in the GaAs crystal. The simulated mean square displacement is isotropic and therefore has an equal $< u^2 >$ in all directions. However, in single crystal GaAs the crystal structure is anisotropic which results in anisotropic vibrations. Figure 4.18 shows the integrated intensity within the GaAs [310] FOLZ ring as a function of angle. The upper image indicates the angular section, $\delta\theta$, integrated at position θ within the CBED image. The lower plot shows the normalised intensity variation for both the experimental and simulated FOLZ rings. The pattern and the magnitude of the intensity oscillations in the experimental data can be investigated using the simulated data as a reference. The plot in figure 4.18 clearly indicates that the integrated intensity has directional dependence, in some directions there is a good agreement between the experimental and simulated intensity. However, in other directions there is only an agreement of the intensity oscillation pattern, but not the magnitude of the intensity. This may be an indication of the anisotropic mean square displacement in GaAs and could account for the difference in the FOLZ ratio measured in section 4.3 above.

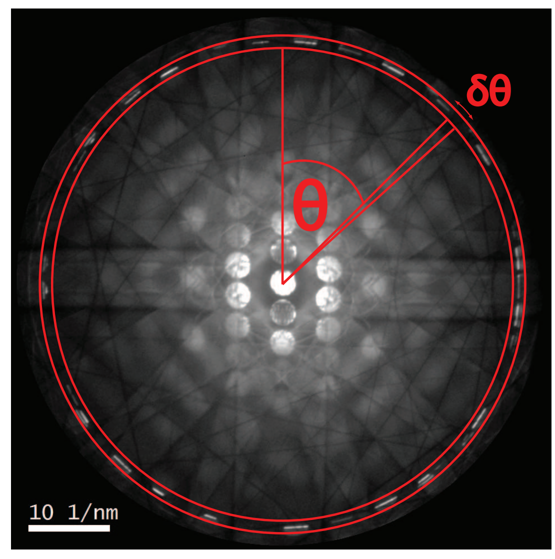

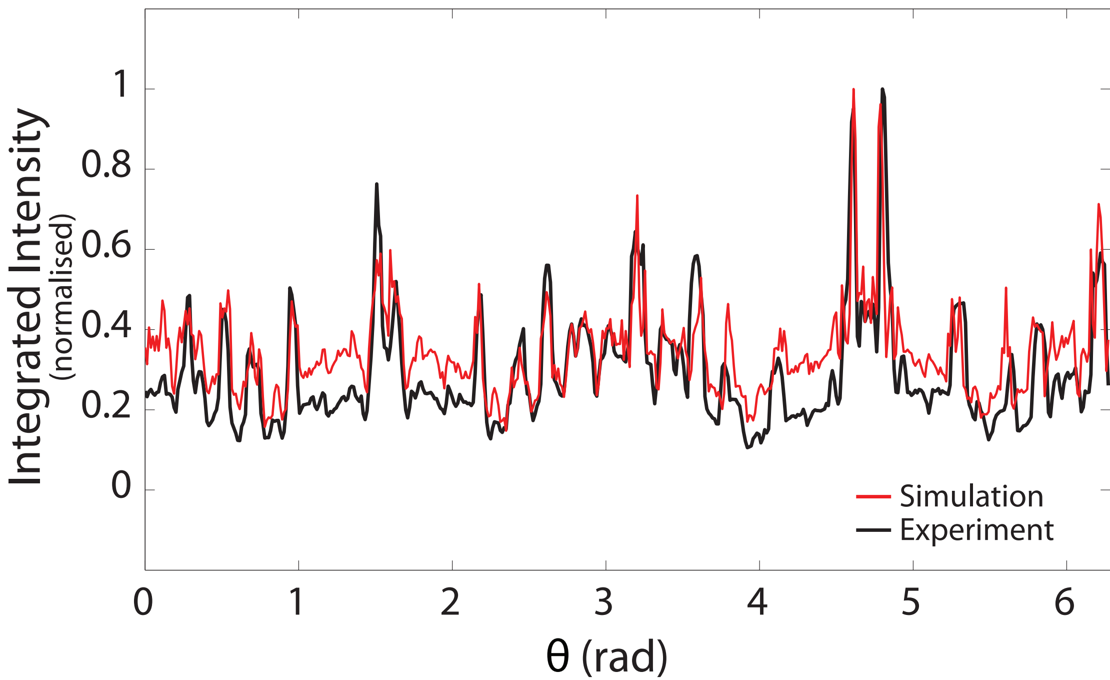

Figure 4.18 – A comparison of the simulated and experimental integrated FOLZ intensity as a function of angle, θ for GaAs orientated to a [310] direction.

Chapter 5

Experimental GaAs - AlAs Interface

5.1 Introduction

The ability to accurately control MBE growth is vital for the development of sophisticated semiconductor devices. MBE techniques can currently produce very thin abrupt layers with good control over parameters such as layer thickness, composition and doping. Chapter 1 described the benefits of being able to characterise MBE grown materials at the atomic scale. With the advent of aberration correction it is now possible to form sub-Ångström electron probes and study interfacial structure at the atomic level. SuperSTEM can typically form an electron probe with a FWHM of $1\AA$ which can be used to resolve the atomic columns of a [110] orientated GaAs/AlAs interface. SuperSTEM was used to characterise the GaAs - AlAs interfaces from a thickness series of HAADF images [23]. This study highlighted complexities in image interpretation when interfaces are comprised of materials with different atomic numbers. The aim of this chapter, is to firstly describe an investigation into the image processing method used to extract the HAADF image data. The process is called Column Ratio Mapping and the process is described in section 5.2 [94]. Section 5.3 then describes how the interface width and interface position is measured using the extracted HAADF data through the fitting of an analytical function. This measurement process is then used on a series of experimental SuperSTEM images and the results are described in section 5.4.

5.2 Column Ratio Mapping

An atomic resolution image processing technique was developed by Robb et al. [94] which provides a consistent method for the extraction of high-resolution atomic column information from HAADF images. This technique provides an automated approach allowing objective extraction of the HAADF image data while also providing a statistical analysis and estimation of errors. The HAADF signal is a function of the probe position which in turn depends on the specimen composition, orientation and thickness. The upper diagram of figure 5.1 shows a HAADF image of a [110] orientated GaAs - AlAs interface with a schematic of the crystal structure is partially overlaid. A common method of analysing this type of image involves taking an averaged intensity line profile through the atomic columns, indicated by the red box. These line profiles are then investigated in order to ascertain characteristics such as interfacial sharpness and growth defects. The lower plot of figure 5.1 shows the average line profile of the HAADF signal, consisting of the high-resolution atomic column signal modulated by a background signal (broken red). To investigate the scattering from each atomic column it is necessary to remove this background modulation. This results in the background subtracted HAADF signal (shown as the broken black line in figure 5.1). The procedure for the measurement and removal of the background HAADF signal is detailed in section 5.2.1. The process used for extracting the atomic column signal is described in section 5.2.2.

5.2.1 Background HAADF Signal Removal

The STEM probe, formed from a convergent electron beam focused at the entrance to the sample, produces a divergent probe wavefunction within the sample. The probe interaction volume is, in a simple approximation, cone shaped. Therefore, a probe focused onto an atomic column will result in a HAADF signal that is formed from the primary column signal and the delocalised scattering from other non-primary columns. This total HAADF signal, will be approximately proportional to the square of the average atomic number contained within this interaction volume, $Z_{average}$. For a sample containing repeating GaAs and AlAs layers (with the interfaces orientated to the beam direction) the overall background signal can vary significantly with probe position. Furthermore, for a repeating superlattice structure the background signal can extend

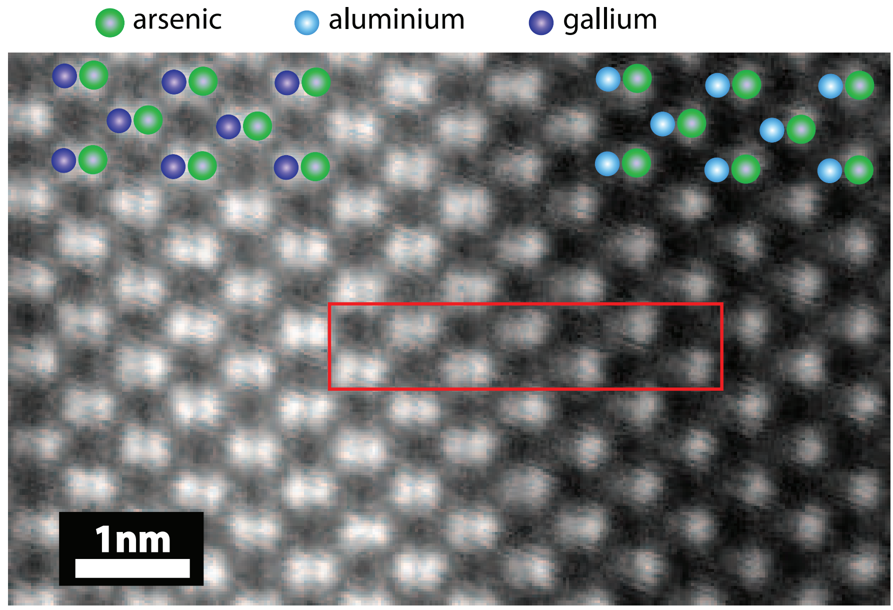

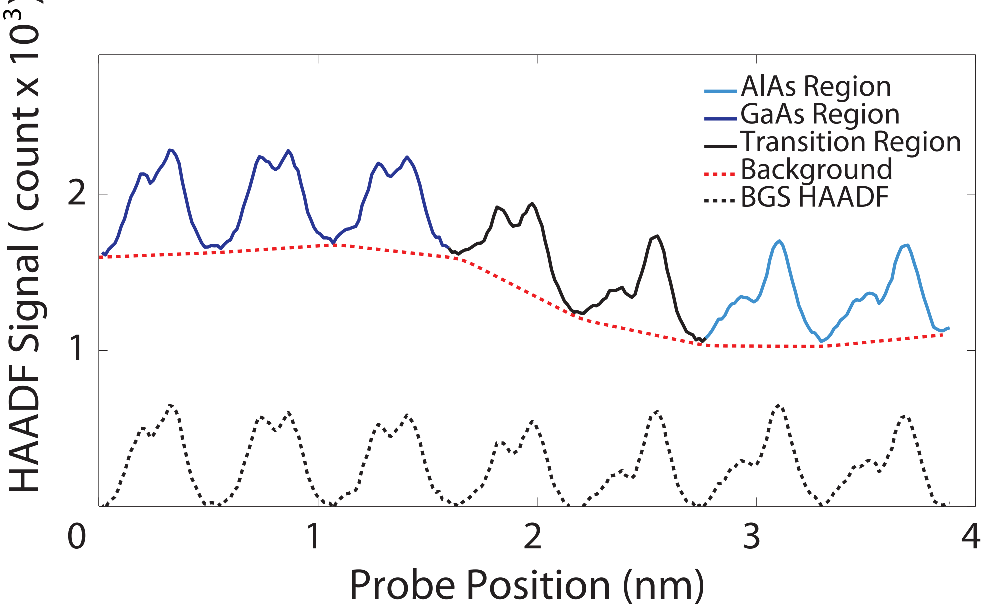

Figure 5.1 – A HAADF image of a [110] orientated GaAs - AlAs interface (top) at a thickness of 42nm. An averaged line trace (bottom) taken from the red box in the image shows that the atomic column signals are modulated by a background signal which must be removed before analysis.

significantly into adjacent layers. For example, a probe positioned in the center of an AlAs layer can have a significant background signal contribution from the two adjacent GaAs layers. This can affect the analysis of such a signal, complicating interpretation. In addition, if a series of images are required at increasing thicknesses the background contribution can vary significantly.

To allow an investigation of the HAADF signal generated from the primary columns the background signal must be removed. An exact measurement of the background HAADF signal generated when the probe is placed on an atomic column cannot be made and so the background signal must be estimated for each atomic column in the image. Two different methods that can be used to measure the background HAADF signal are discussed in sections 5.2.1.1 and 5.2.1.2.

5.2.1.1 Frequency Filter Method

The simplest method to extract the background signal is by masking the low frequency spatial information in the Fourier Transform (FT) of the HAADF image. The FT of the HAADF image reveals the spatial frequencies contained within the image. For a structured superlattice, the FT will contain the high frequency lattice reflections and a low frequency background modulation. The center of the FT corresponds to the low frequency image information and can be isolated and removed by using a pass-band mask. The central mask should be large enough to envelope the central low frequency disk, but small enough that the lowest frequency lattice reflections are not removed. The lattice reflections contain the high-resolution dumbbell information and it is vital that this information remains in the image. The edge of the mask should also be smoothed to reduce image artifacts. After the application of the (smoothed) low frequency mask, the inverse FT produces an image where the low frequency 'background' modulation is removed. The mask, however, also removes the FT's central scaling pixel which refers to the total integrated intensity in the original HAADF image. The effect of this is clear when the inverse FT is taken and the total integrated intensity sums to zero. The signal between the dumbbells are now not averaging about zero. They are instead, averaging about some negative value and an appropriate constant must therefore be added to the image to ensure that the signal between the dumbbells averages to zero. This process produces a background subtracted image containing the high spatial frequency dumbbell information.

While this method of background subtraction is straightforward and reproducible it does have some drawbacks. The extracted background often is not a true representation of the ideal localised background. For the case of a GaAs - AlAs superlattice the extracted background values using this method can deviate by as much as 10% when referenced to the intensity at the 'true' background position (i.e. the position between the dumbbells in the original HAADF image). The upper diagram in figure 5.2 shows the Fourier Transform of a GaAs -AlAs superlattice HAADF image. Indicated on the FT are a series of pass-band masks used to remove the low frequency background signal ranging from 0.5 nm^{-1} - 1.9 nm^{-1}. The effectiveness of the background removal process can be evaluated by investigating the signal between the dumbbells in the final processed image. After background removal the signal should ideally fall to zero between all of the atomic columns.

The lower plot in figure 5.2 shows four averaged line traces through the same atomic row for each of the four mask sizes used. In each profile the variation in background HAADF signal can be clearly seen (i.e. between the columns). The residual background difference is indicated by the red arrows and remains regardless of the mask size used. Using **only** this filtering method for background removal can therefore cause the background signal to be over, or more typically, under estimated. While this residual background component is not consistently present in all regions of the processed image, it is particularly prevalent at interfacial regions. This can contribute to artifacts when measuring the atomic column signals.

5.2.1.2 Positional Mask Method

Another method for extracting the background HAADF signal, is to mask off an integration window at the background position for the dumbbell in the HAADF image. The left side of figure 5.3 shows a single background mask placement adjacent to the dumbbell (perpendicular to the growth direction). As any compositional changes in this structure are perpendicular to the interface, this background position should be approximately consistent with the scattering under the adjacent dumbbell and so a common background position is used for both atomic columns. However, using a single background position in the calculation of atomic column intensities can lead to inaccurate results due to the gradient of the background under the atomic columns. The gradient on the background will have the effect of increasing the signal of one

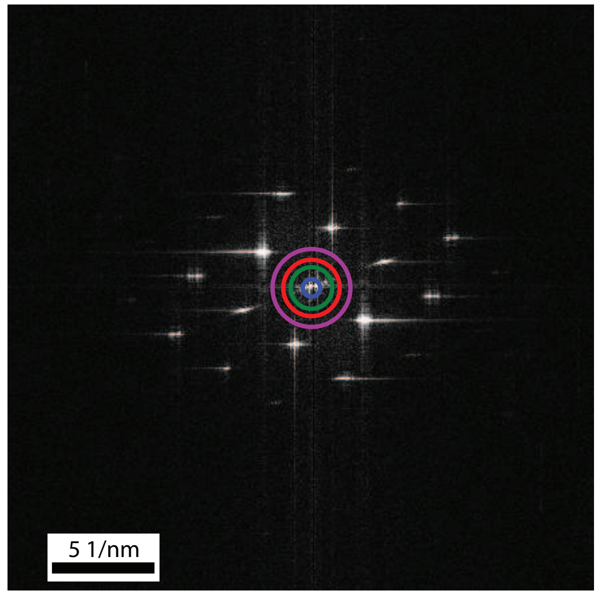

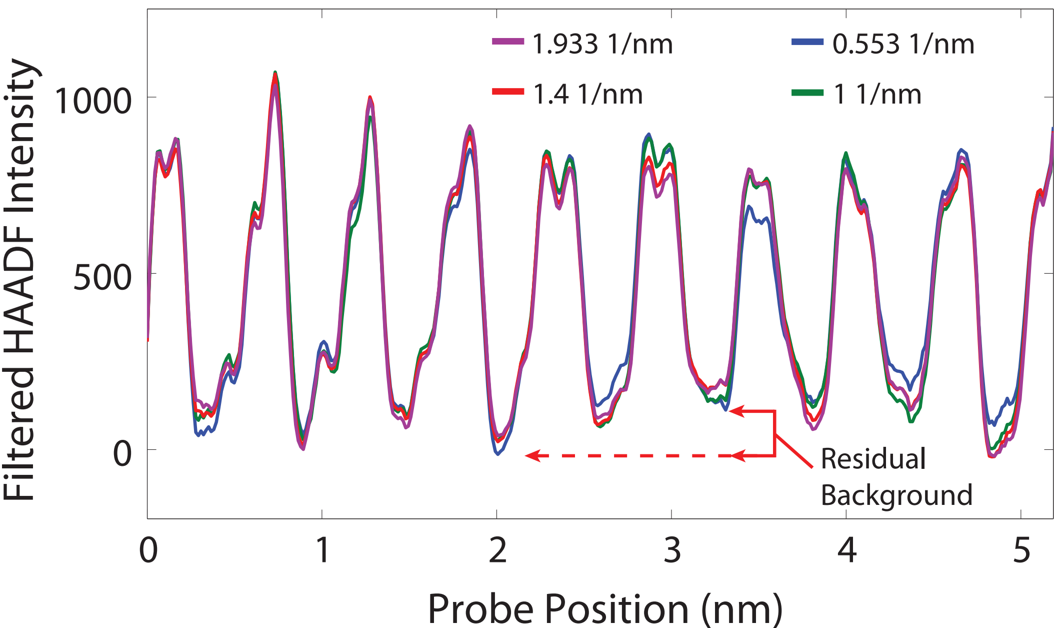

Figure 5.2 – The top image shows the FT of the image from figure 5.1. Indicated on the FT are the positions of a series of masks used to remove the central low frequency background modulation. The masks span a range of spatial frequencies. The lower plot shows the line traces through the dumbbells at the interface. The colour of the line profiles indicate the mask that was used and clearly show that in each case there is a residual background remaining after using this method.

column while reducing the other. The magnitude of this effect will be dependent on the gradient of the background.

Rather than using a single background position, two background positions can be measured which are collinear with the atomic column positions. These background measurements can then be used to extrapolate to the background beneath the atomic column positions. This method is detailed in the lower right section of figure 5.3. The background signal for each atomic column (for a [110] orientated zinc-blende structure) is found using equation 5.1.

$$BG_{Type-3} = \frac{3}{8}(BG_2 - BG_1) + BG_1 \quad BG_{Type-5} = \frac{5}{8}(BG_2 - BG_1) + BG_1 \qquad (5.1)$$

Figure 5.4 shows the calculated column ratio profile from an experimental GaAs - AlAs superlattice at a thickness of 95nm. The green data displays the column ratio using a single background position adjacent to the measured dumbbell. The blue data indicates the column ratio when the background is interpolated to the correct location under the atomic columns. The red circles indicate where the column ratio is affected most. This occurs at the interfacial regions where the background gradient is greatest. There is a positive gradient edge effect where the gradient is positive and the dumbbell orientation is such that the Type-5 column intensity is increased while the Type-3 column is reduced. This causes the measured column ratio to be decreased. At the opposite interface, the background signal gradient is negative and the reverse effect occurs, causing the measured column ratio to be increased. The most extreme effects are observed at the interfacial region. However, in a short repeating superlattice the column ratio values within the layer can also be affected. The resulting compositional analysis of the column ratio profile extracted using a single background position could lead to incorrect compositional interpretation. The interpolated background signal at the atomic column position will produce a closer estimation of the "true" background signal. However, the signal under the columns is unlikely to be linear. Therefore, a combination of both the FT and the interpolation methods are employed to remove the background signals from the experimental images.

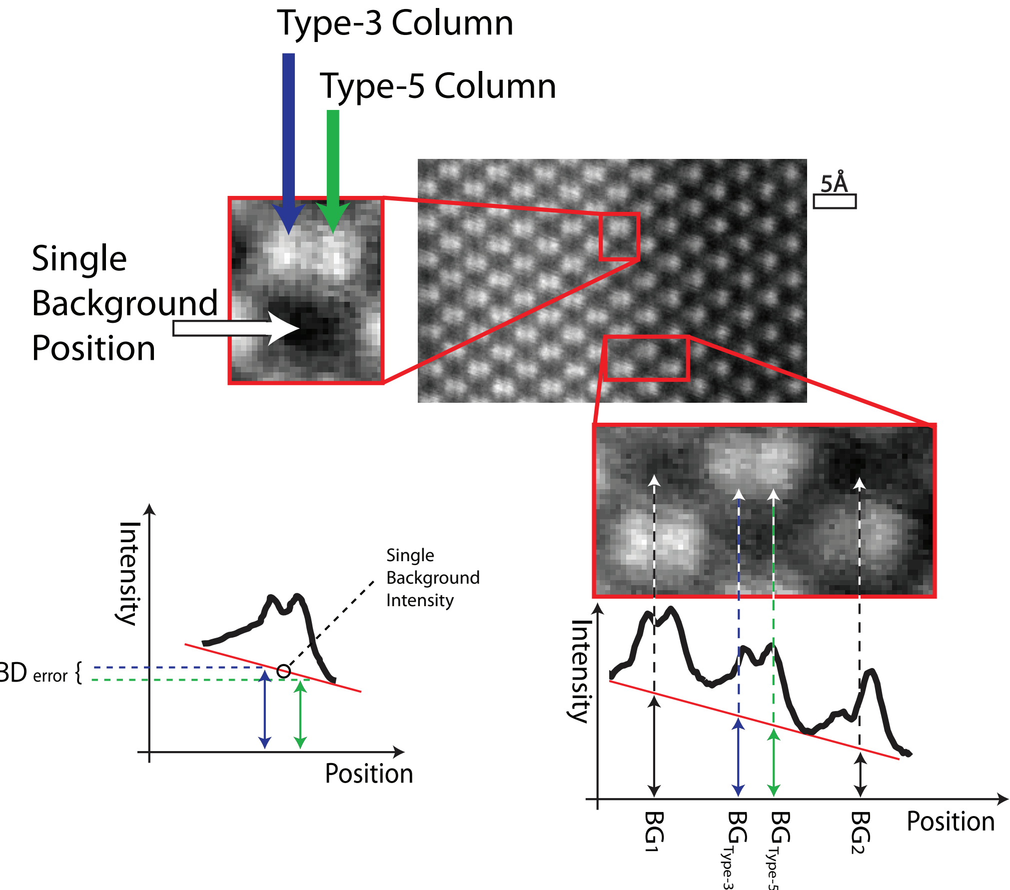

Figure 5.3 – This diagram shows the original HAADF image of a GaAs - AlAs interface. The diagram on the left shows the single background location and indicates the possible error that occurs from using a common background position for each atomic column (this error is larger for interfaces with a larger background gradient). The lower right detail shows that by using an interpolated background the error in the background removal process is minimised.

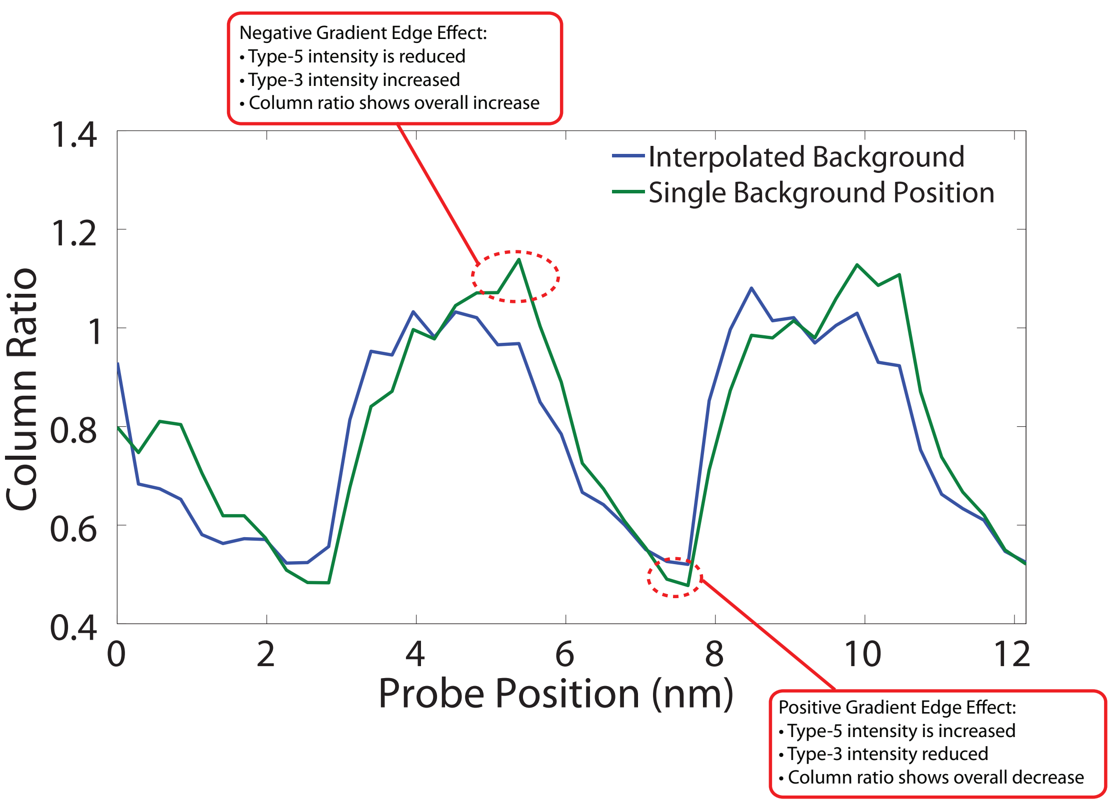

Figure 5.4 – The green data is the column ratio using a single background value while the blue is interpolated to the atomic column position. The column ratio is affected most where the background gradient is greatest (i.e. at the interfacial mid point).

5.2.2 Automated Signal Measurement

A typical GaAs - AlAs HAADF image contains over 1000 dumbbells. It would therefore be prohibitive to process each dumbbell by hand. An automated approach was required to accurately extract the background signal as well as the atomic column signal from each image. Given the location of an atomic dumbbell in the image, the approximate location of an adjacent dumbbell can be described using a set of translation vectors. The HAADF image is, however, often distorted by scan noise, hysteresis in the scan coils or image magnification changes. The extraction process therefore requires a form of pattern matching to locate the atomic columns accurately. This section describes the development of a Matlab script used to extract the HAADF data from each image.

The script operates on an FFT filtered, background subtracted HAADF image which is then rotated to align the interface vertically. From this rotated image a section is identified that is free from obvious image artifacts and is used to define a subsection detailing the total number of rows and columns of dumbbells to be processed. The top of figure 5.5 shows a sub-section of a HAADF image that was rotated ready for processing. The average translation vector can then be defined such that the applied shift moves from the center of one dumbbell to an adjacent dumbbell in the same row. This vector is defined at runtime and is measured directly from the rotated image. The location of the first dumbbell to be processed is also defined at this point. A sub-section around this first dumbbell is identified and compared to the "expected" form of the dumbbell. This expected form consists of two Gaussian peaks with a separation of the typical dumbbell spacing. The form of the Gaussian peaks can be varied using two parameters. These are the peak separation and the vertical skew and are shown in figure 5.5. A comparison between this expected form and the experimental image sub-section is calculated using a cross-correlation. This cross-correlation is calculated over a range of parameter variations (separation and skew) and is recorded for each parameter combination. By assessing the correlation coefficient, the optimum parameter combination can be found. This enables the location of the atomic columns in the image subset to be found. The lower graph in figure 5.5 shows how the correlation coefficient varies as a function of the skew and separation parameters. The optimum parameters are found from the maximum correlation coefficient. A similar method is used to locate the minimum background positions around each dumbbell.

The interpolation process, described in section 5.3, is applied to calculate the background under the atomic column positions. With the locations of the atomic columns and the background calculated, each signal intensity can be integrated over a suitable window. The atomic column positions are then used to estimate the central position of the dumbbell. Then the translation vector is applied to move to the next dumbbell position. Locating the dumbbell position after each step provides a degree of image drift correction. However, a visual cross check of the extraction process is required during processing.

The integrated signal intensity around the atomic columns are used to calculate the column ratio for each processed dumbbell. For a [110] orientated zinc-blende structure, an image containing 20 x 20 dumbbells will convert into a column ratio map containing 40 x 20 pixels. The map replicates the relative positions of the dumbbells which form a chess board distribution. An example of a processed image can be seen in figure 5.6 for the GaAs - AlAs superlattice. The repeating layered structure is clearly evident with the variation of the column ratio indicating the change in composition. This data set can now be manipulated in a variety of ways to assist the interpretation of the column ratio maps. Section 5.3 describes the methods that can be used to measure the width of the interface regions.

5.3 Interface Width Measurement

The column ratio map gives an overview of the compositional changes across the HAADF image. For the case shown in figure 5.6 the image is orientated such that the growth direction is left to right. This allows the column ratio values to be averaged along the y-axis producing a column ratio line profile. This profile can then be used to measure specific characteristics from the superlattice such as the interfacial width, the layer width and the interface position. Furthermore, each point of the profile is created from a range of “equivalent” dumbbells, therefore the standard deviation will give a measure of the variability of the MBE growth. Two techniques were considered when measuring the interface widths of interfacial regions from the column ratio line-traces. These methods can be applied consistently to both experimental and simulated linetraces and are detailed below in sections 5.3.1 & 5.3.2.

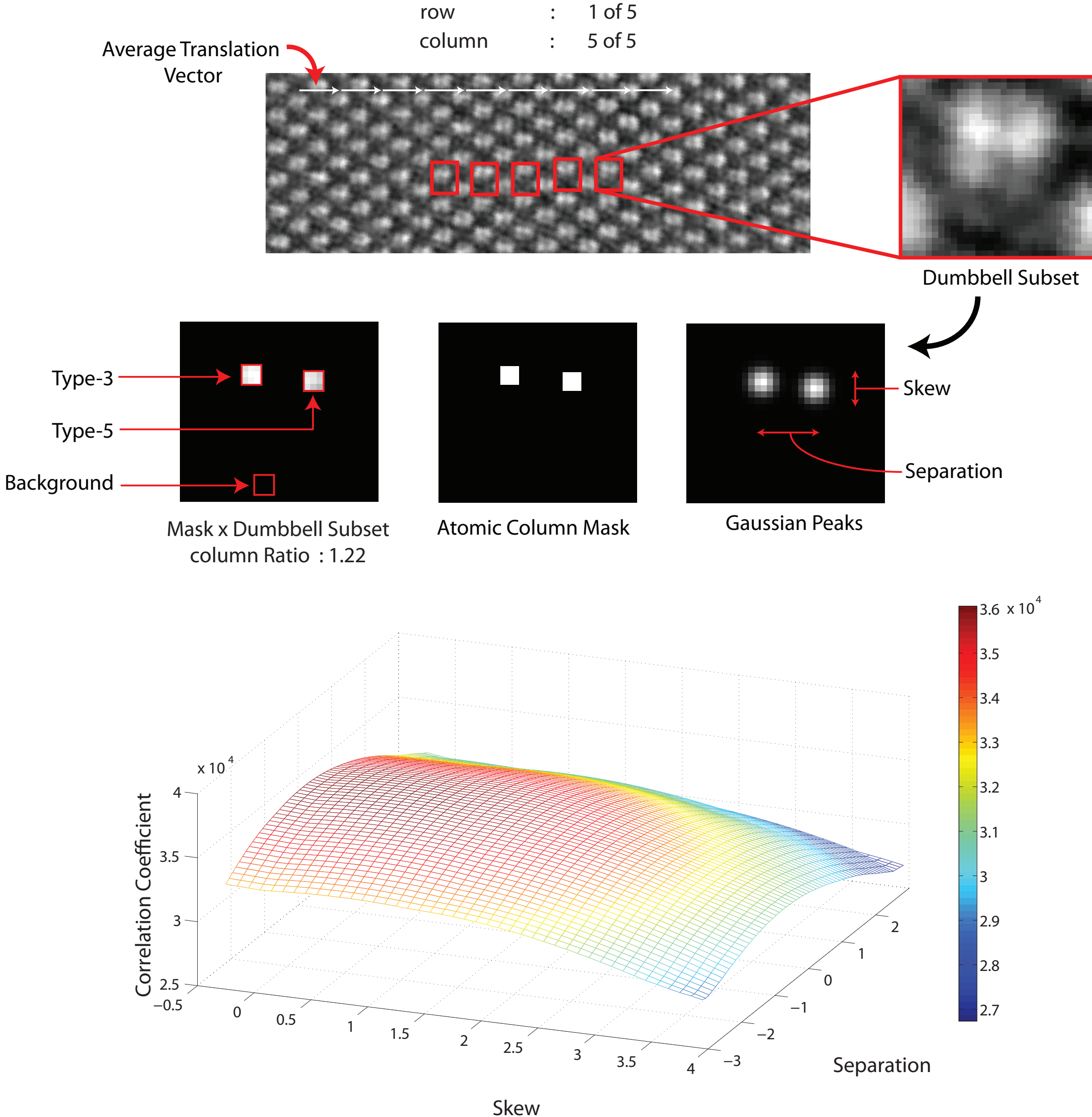

Figure 5.5 – The upper image shows a section of the HAADF image. A sub-section around each dumbbell location is isolated and compared to the "expected" form of the dumbbell structure. The automated script fits two Gaussian peaks to the dumbbell positions with the "peak separation" and "skew" as fitting parameters. The cross-correlation is calculated over a range of parameter values and the maximum correlation coefficient gives the optimum fit. The maxima of the Gaussian peaks locate the atomic columns and the signal intensity can be integrated over a specified number of pixels.

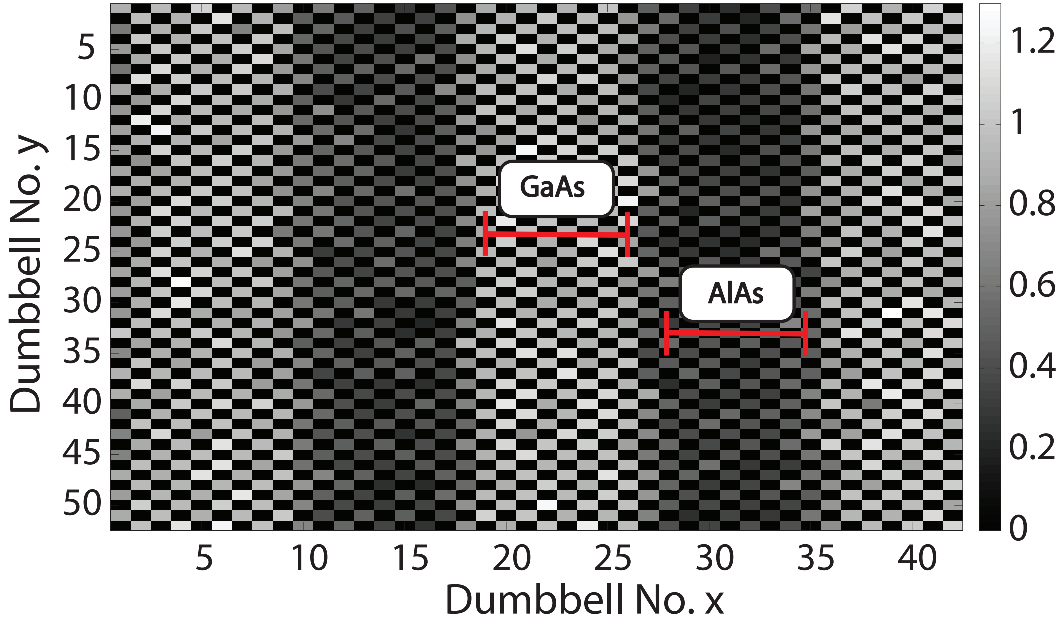

Figure 5.6 – The column ratio map replicates the relative positions of the dumbbells from the [110] orientated zinc-blende structure which forms a chess board distribution. The resulting column ratio map gives immediately interpretable results where each pixel in the image corresponds to the column ratio at a particular dumbbell position. A line trace through the interface can be produced by averaging the image perpendicular to the interface, this allows the standard error to be obtained.

5.3.1 Column Ratio Threshold

The width of the interfacial region can be measured directly from the column ratio profile by counting the number of dumbbells that are not part of the bulk GaAs or bulk AlAs regions. An example of this method can be seen in Figure 5.7 which shows an experimental column ratio profile from the deep superlattice at a thickness of 53nm. A straightforward method of deciding if the dumbbell in question is transitional (i.e. part of the interface) is to apply two thresholds corresponding to the column ratio values in the bulk GaAs and AlAs regions. The threshold can be set to the standard error of the bulk regions. Figure 5.7 shows this method where the horizontal broken lines indicate the limits that separate a bulk dumbbell from one that is considered to be part of the interfacial region. The dumbbells contributing to this interfacial region can be counted to estimate the interfacial width. This width, for a single interface, is indicated in figure 5.7 by the solid vertical red lines. However, this method can produce inconclusive results when analyzing experimental superlattice data. This is because it can be difficult to extract enough dumbbells from the experimental images to reduce the statistical error to a level where a suitable threshold can be applied. The resulting

measurement can also depend on which dumbbells are considered to be part of the bulk material which in turn affects the threshold levels.

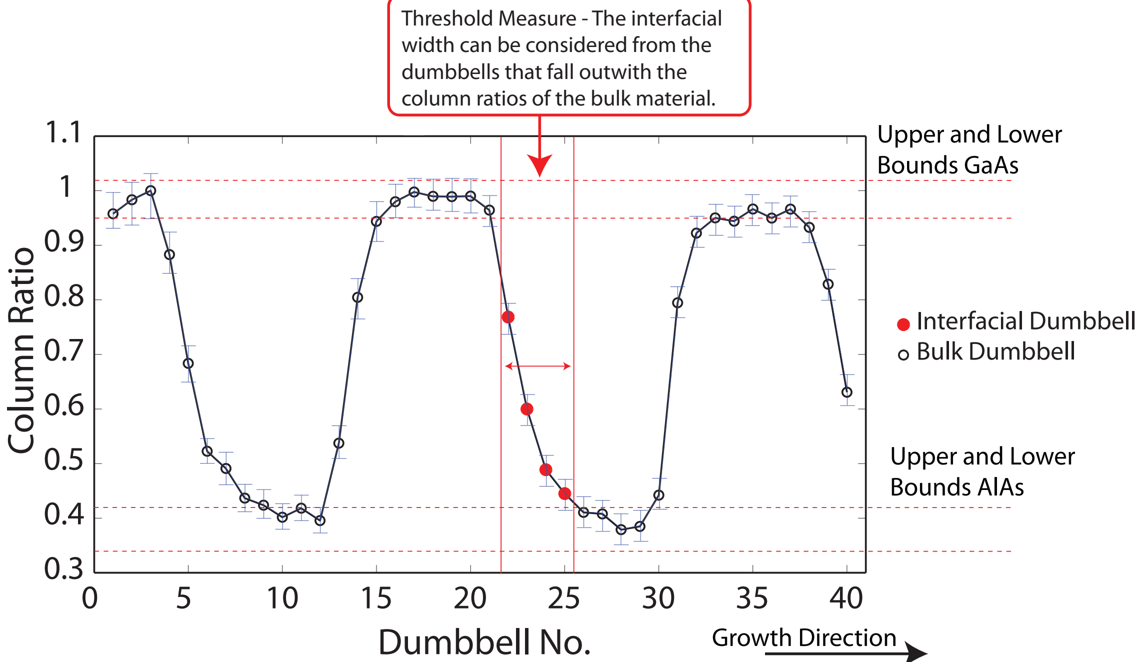

Figure 5.7 – A threshold for the bulk GaAs and AlAs regions corresponding to the standard error is indicated by the red horizontal broken lines. Any column ratio out with this threshold is considered to be a transitional dumbbell. This gives an estimation of the interfacial width which is indicated by the vertical solid lines. In this case corresponding to a width of 4 dumbbells.

5.3.2 Analytical Function Fitting

The averaged column ratio line profile represents the average compositional change across the interfacial region. This profile generally exhibits a smooth transition of column ratio values from the bulk GaAs to the bulk AlAs region. The transition can be approximated to an error function which allows the interfacial width to be measured from the analytical function rather than the experimental data. Figure 5.8 shows the same experimental data used in figure 5.7. In figure 5.8 the data indicates that the smooth variation of column ratios across the interfacial region correspond well to the error function.

The error function defined in equation 5.2 has three parameters (a, b & c) corresponding to the function amplitude, width and lateral position. These parameters can be manipulated to accurately fit the function to the column ratio data. The optimum fit of the error function to the experimental data can be achieved using a *least squares*

method. The Matlab *Curve Fitting Toolbox*[1] was used for the fitting procedure. This toolbox utilises a least squares formulation where some initial estimates of the starting parameters were supplied assisting the convergence of the algorithm.

$$erf\,(x) = \frac{2a}{\sqrt{\pi}} \int_0^{b(x-c)} e^{-t^2} \mathrm{d}t \qquad (5.2)$$

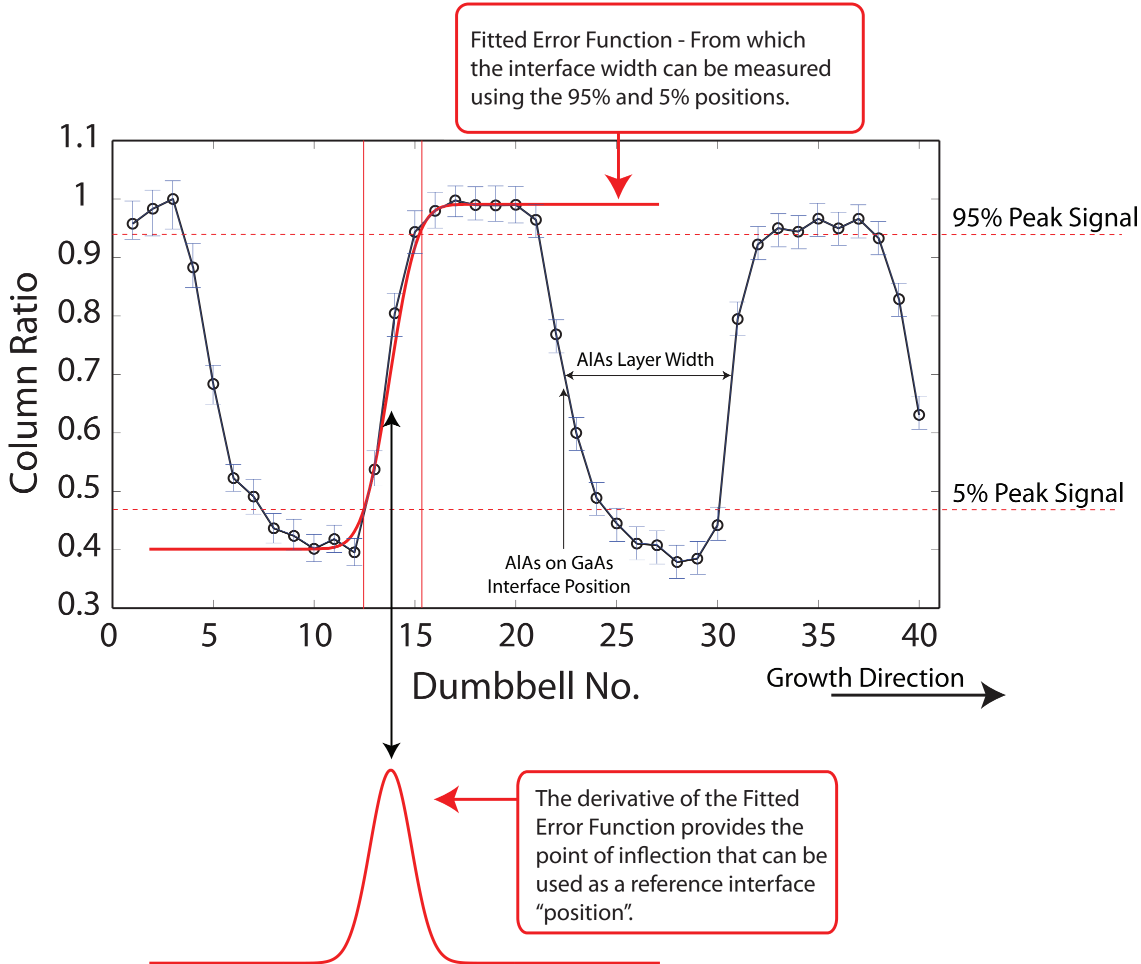

Figure 5.8 – The smooth transition of column ratios across the interface naturally lends itself to the fitting of an error function curve. The width of the interface can be measured from a particular percentage of the curve's maximum and minimum values. The interfacial "position" can also be estimated from the point of inflection of the function.

The width of the interface can then be defined using a variety of measures, one of which is the distance between the 95% and 5% points on the range of the error function curve. These limits are indicated by the solid vertical red lines in figure 5.8. From the fitted curve, the point of inflection can also be used as a measure of

[1]The MathWorks inc.

the interface "position". This measure can be applied and compared consistently to a range of interfaces. Unlike the threshold procedure this method can give width measurements in fractional values of a dumbbell. An interface width of $2\frac{1}{4}$ dumbbells can be interpreted as the average roughness when a number of rows from an image have been averaged together.

5.4 Experimental SuperSTEM Images

SuperSTEM has been used to characterise MBE grown GaAs-AlAs heterostructures as part of an ongoing project investigating III-V materials [23]. A growth map of the specimen is detailed in figure 5.9 and shows the [001] orientated GaAs substrate at the base followed by layers of $Al_X Ga_{1-X} As$, wide layers of AlAs and GaAs and then a series of superlattices with $Al_X Ga_{1-X} As$ $(for\ X = 0,\ 0.25,\ 0.5,\ 0.75\ \&\ 1)$.

The superlattices are composed of 20 repeated units of 9ML $Al_x Ga_{1-x} As$ / 9ML $GaAs$ and were grown at a substrate wafer temperature of $908K$. The wafer rotation was set to 50 rpm. During the growth process, the temperature of the Ga oven was fixed at $1233K$ and the temperature of the Al oven was $1352K$. The As oven was set at a temperature of $414K$ and the As shutter was open continuously during the whole growth process.

The right side of figure 5.9 show a series of column ratio maps formed from the interfaces between the wide AlAs and GaAs layers and also the deep AlAs - GaAs superlattice. The alternating structure of the superlattice allowed the investigation of two types of interfaces. The first is an AlAs layer grown onto an GaAs surface (Type-A Interface). The second interface type is formed when GaAs is grown on a AlAs surface (Type-G Interface). The isolated interfacial region also allowed an isolated Type-A interface and an isolated Type-G interface to be imaged. From each region a series of images were recorded over a wide range of sample thicknesses. This gives a dynamical perspective of the interfaces. The thickness series allows the measurement of characteristics that may not be observed with a single image such as changes in the interfacial width in the [110] beam direction.

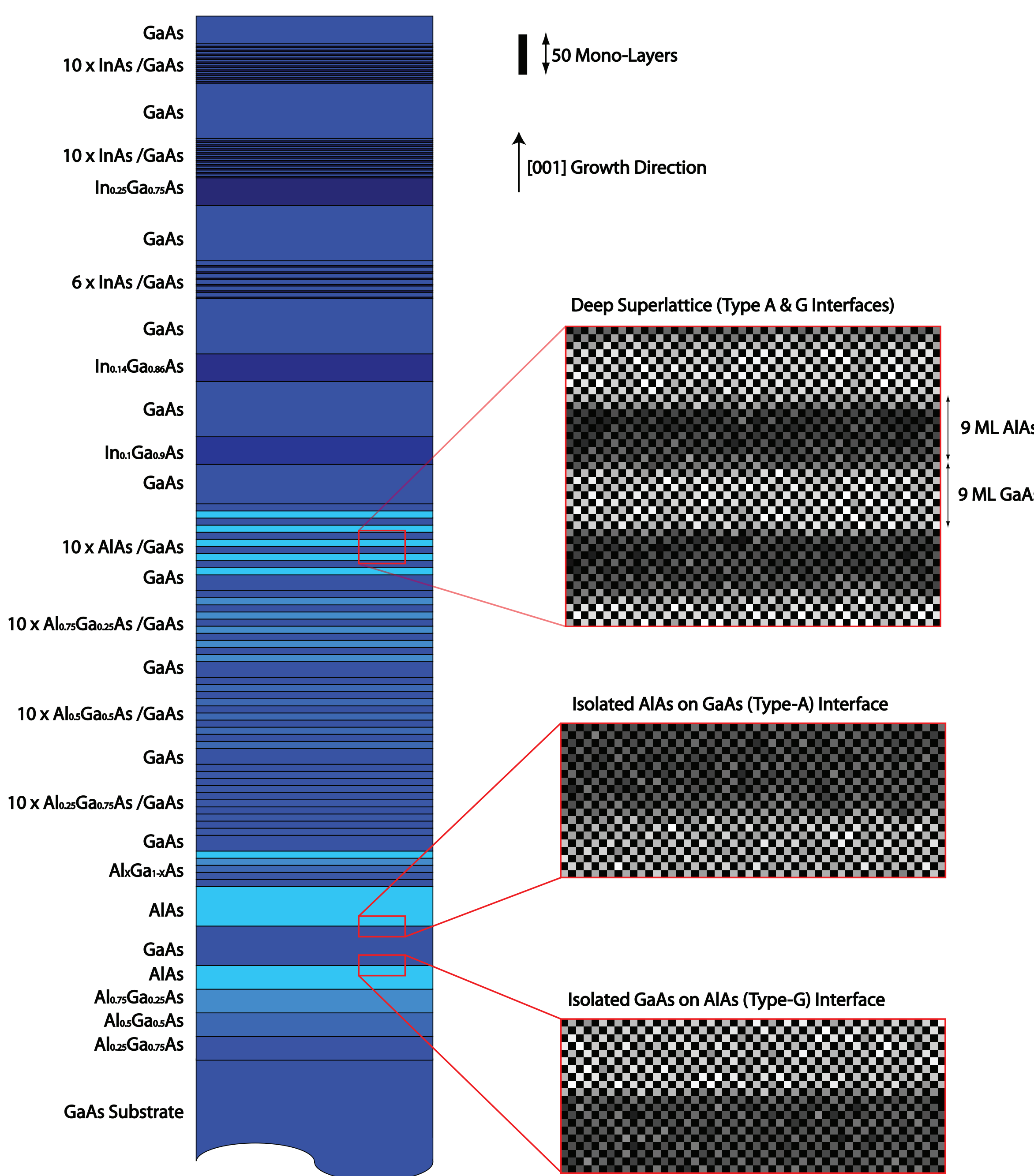

Figure 5.9 – Details of the MBE grown sample C102. The column ratio maps indicate the regions from the sample corresponding to the deep superlattice and the isolated interfaces.

5.4.1 Local Roughness

The measurement methods outlined in section 5.3 can be used to ascertain the interfacial width. These measurements are taken from an averaged column ratio line profile. However, each atomic row from the image will correspond to a different atomic configuration within the sample. While the averaging of these rows together gives a global overview of the interfacial region, it contains little information about any localised roughness across the image. This localised roughness can be characterised by processing the image row by row. This process builds up a picture of how each row differs from the next. The row by row analysis can be used when measuring both the interface width and the interface position. This section describes an investigation into the variability of the interface positions across a series of HAADF images.

The position of the interface can be described as the point of inflection of the fitted analytical function. However, this section uses the last atomic column that is consistent with a bulk GaAs column as a reference point. This atomic column was used as a reference. Using this dumbbell as a reference clearly highlights the end of the bulk GaAs region and the start of the interfacial region when overlaid onto the column ratio maps. Furthermore, the location of this dumbbell should be unaffected by the overall width of the interface.

Figure 5.10 shows an image of the GaAs - AlAs superlattice with 9ML repeating layers of each compound. A region of interest is defined within this image containing a single GaAs - AlAs interface with 18 mono-layers. This area is indicated by the red box in figure 5.10. This single interface has an overall average line profile that will give a measure of the average interface width. This averaged line profile is in turn compared to each row of the image. The average line profile is fitted to each row using a least squares fitting method and when the location of the best fit is found a vertical red line is used to indicate the position. Figure 5.11 shows the column ratio map with these dumbbell locations indicated. The overall roughness of the interface can be quantified by collecting the distribution of these fitted positions in a histogram and then using a Gaussian to measure the overall distribution width. The width of the Gaussian can be used as a direct measure of the distribution width. This gives an indication of the relative interfacial roughness of each interface. Furthermore, this is a measure that is independent of the interfacial width. This method was used to

compare the distribution of fitted profiles at different specimen thicknesses. Figure 5.13 shows a plot of the measured Gaussian width for each type of interface over a range of specimen thicknesses. These results indicate that the AlAs-on-GaAs interface is in general rougher than the GaAs-on-AlAs interface which is visually apparent on inspection of the column ratio maps. However, there are no immediate trends in the measured roughness and the distributions do not appear to depend on the specimen thickness in any consistent manner. Moreover, this indicates that the averaging of the column ratio maps is not masking any identifiable trends in the interface growth.

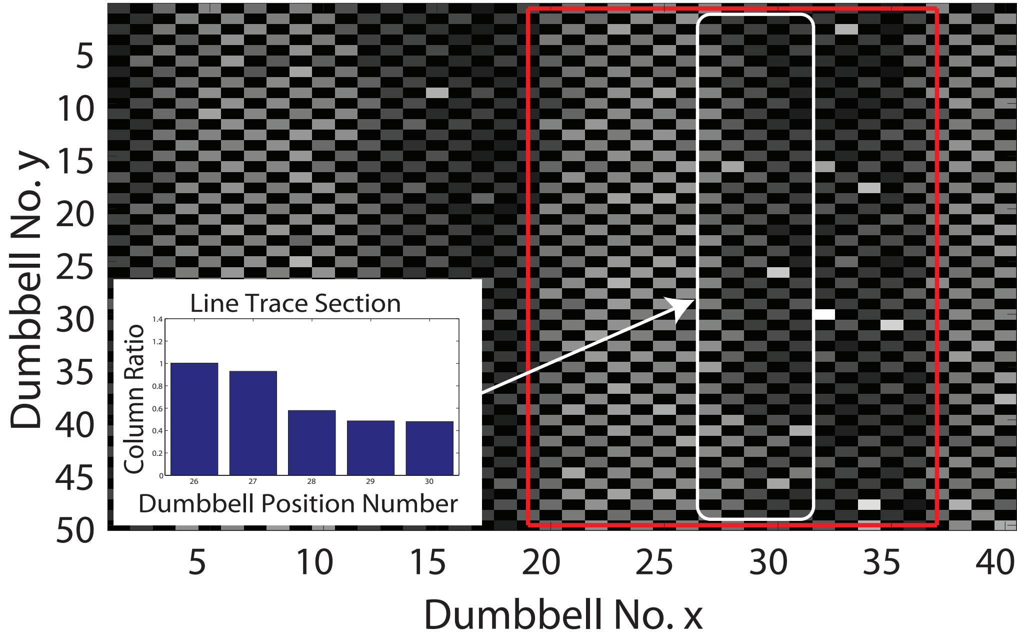

Figure 5.10 – The red section defines the section of the superlattice that is of interest, the average profile is taken from a smaller region across the interface (inset), this profile is then fitted to each row in turn to ascertain the variation of the local profile to the overall average.

5.4.2 Experimental Measurements

Section 5.4.1 investigated the lateral roughness in each of the deep superlattice HAADF images. This highlighted that there is no observable trend in this type of roughness over the image series. The next stage is to measure the MBE growth characteristics of both the deep superlattice region and the isolated interfaces. For the deep superlattice, the width of the interfaces and the interface positions were measured. This was acheved by using the analytical function fitting method outlined in section 5.3.2. For the isolated layers, only the interface widths were measured.

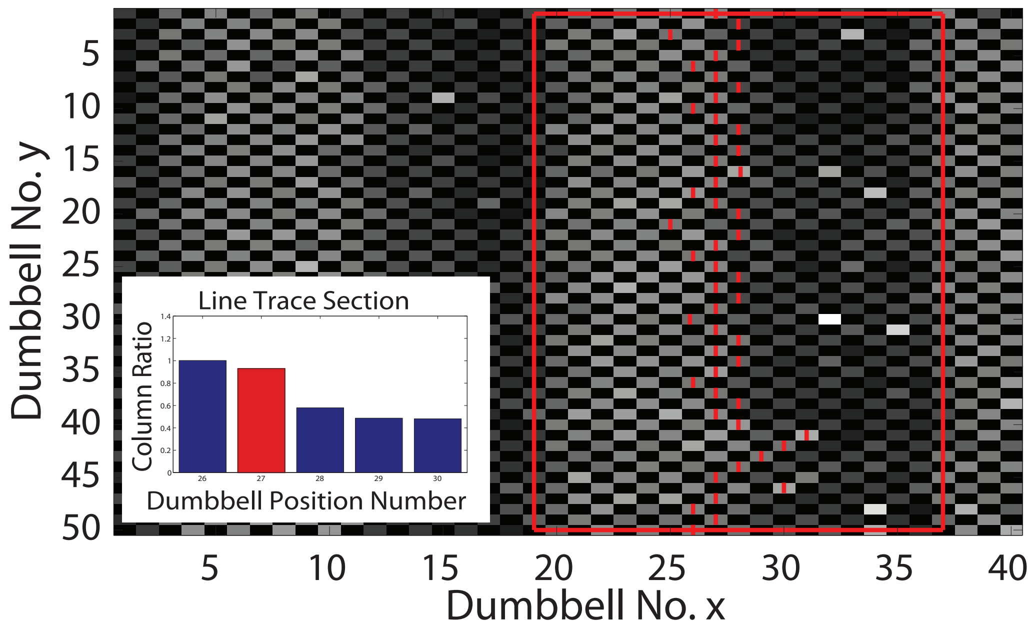

Figure 5.11 – Column ratio map with averaged line profile fit, the red line indicates the position of the last GaAs like dumbbell before a transition region.

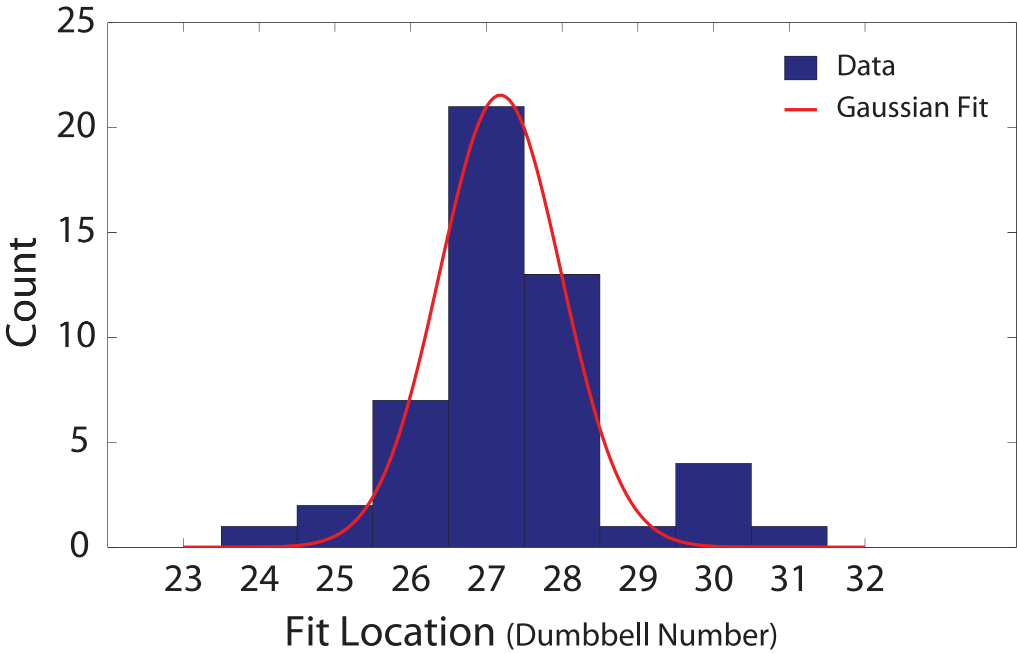

Figure 5.12 – Histogram of best fit positions gives an indication of the local variation. The FWHM of the fitted Gaussian gives a relative measure of the roughness width.

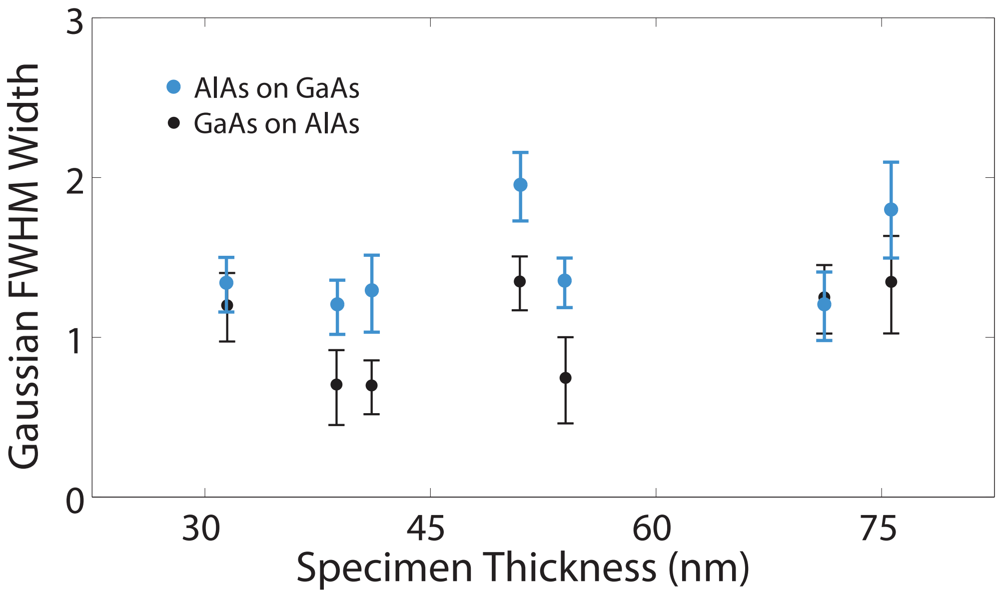

Figure 5.13 – Histogram of best fit positions gives an indication of the local variation. The FWHM of the fitted Gaussian gives a relative measure of the roughness width.

The process of fitting the function to the interface data gives the location of three distinct measures. The first is the point of inflection of the error function. This can be used as a point of reference defining the interface "position". The remaining two measures correspond to the 95% and 5% positions of the analytical function. From these three positions, two important characteristics can be measured from the images which are detailed below.

Interface Width - is defined as the separation of the 95% and 5% positions of the range of the analytical function. The interface is uniquely defined using the growth direction. The Type-A interface is formed when AlAs is grown on a GaAs surface during MBE. The Type-G interface is formed when GaAs is grown on an AlAs surface.

Layer Width - is measured as the separation of the interface positions. The width of the GaAs layer would be the separation of the Type-G interface position and the Type-A interface position that bounds the layer.

The analysis of the column ratio data can be performed on the averaged column ratio map by creating the column ratio profile. This is done by averaging all the atomic rows together before fitting the analytical function to the data. A typical column ratio

map will consist of 50 interleaving atomic rows, 40 dumbbells wide. The single line profile is created by averaging each alternate atomic row together to produce a single line trace, giving an overview of the average characteristics of the interfacial region.

The analysis of the column ratio data can also be performed on a row by row basis which allows the variability across the image to be monitored. This can be valuable as each atomic row can have a different atomic configuration. Therefore, the row by row approach provides additional information on the spread of measurements within any given image.

Figure 5.15 shows the measured interface widths[2] for the Type-A (AlAs grown on GaAs) and Type-G (GaAs grown on AlAs) interfaces from both the deep superlattice and the isolated interfacial regions. The widths are measured from the averaged column ratio line profile and are plotted as a function of specimen thickness. The graphs highlight that, while the width of the Type-G interface is independent of specimen thickness, the width of the Type-A interface increases with increasing specimen thickness.

Figures 5.16 and 5.17 show the same average width measurements represented by the black circles for the Type-A and Type-G interface respectively. The distribution below each point now indicates the spread of width measurements that combine to make each average measurement. The distribution below each point is a histogram of the row by row analysis. This gives a clear indication that each row in the column ratio maps has a different level of sharpness. The addition of the colour bar at the right of the plot indicates the number of counts contributing to each distribution.

The interface positions can also be monitored as a function of specimen thickness. Figure 5.14 shows three column ratio line profiles at thicknesses of $32nm$, $53nm$ and $76nm$. These profiles have been aligned so that the left side of the GaAs layer is located in the same position for each trace. It is clear from the profiles that as the specimen thickness increases the apparent interface position of the Type-A interface shifts to the right. The profiles are taken from different images and it is not unambiguous whether the interface motion is from the Type-A or Type-G interface. However, the change in the interfacial position affects the measurement of the GaAs layer width. This can be used as a characteristic measurement. The GaAs layer width increases by $2\frac{1}{2}$ dumbbells over the entire image series.

[2]first reported in [23]

These results show that the measured interface width and layer width depend on both the growth orientation and the specimen thickness in an unusual way. Figures 5.15 and 5.14 suggest that changes of composition are being detected by the probe deep within the crystal at the AlAs on GaAs (Type-A) interface which affects the measured widths. However, these effects are not observed at the GaAs on AlAs (Type-G) interface. While these effects may be due to differences in the composition in the projected Z direction it is unclear why the measurements are asymmetrical. To aid the interpretation of these results a series of interfacial models were developed and investigated using the multislice code. The model development and simulation results are detailed in chapter 6.

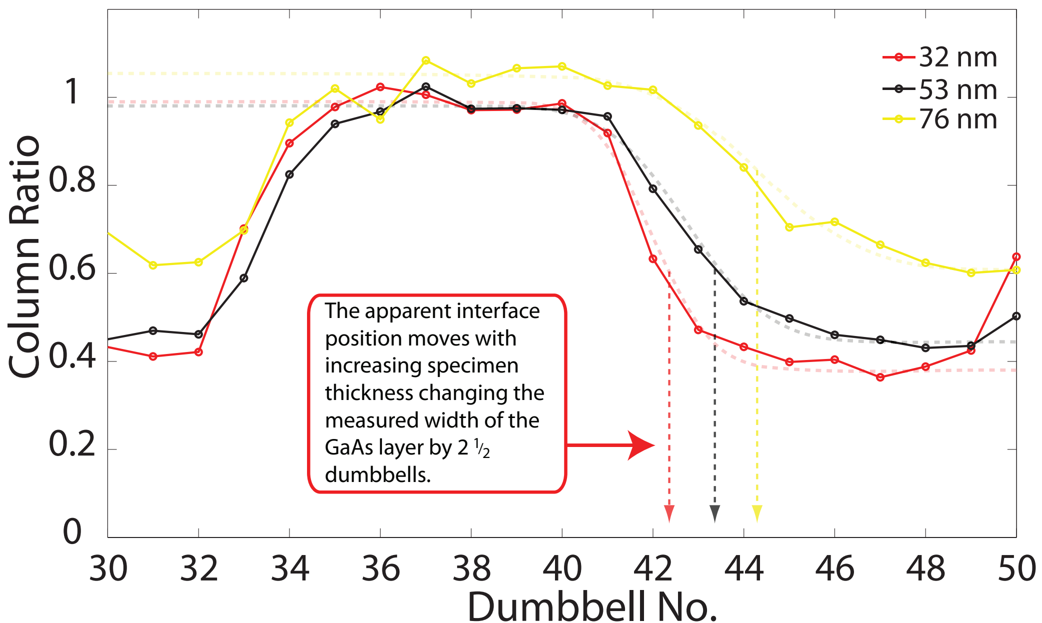

Figure 5.14 – The figure shows a column ratio profile across a GaAs layer from the deep superlattice. The profiles are at specimen thicknesses of $32nm$, $53nm$ and $76nm$ and indicate that the width of the GaAs layer increases with increasing specimen thickness.

5.5 Background Signal Analysis

The above analysis of the SuperSTEM 1 HAADF images was performed using the high resolution information from the atomic columns in the superlattice region. The line profile in figure 5.1 reveals that the intensity variation is a function of position and takes the form of high spatial resolution peaks associated with the dumbbell locations

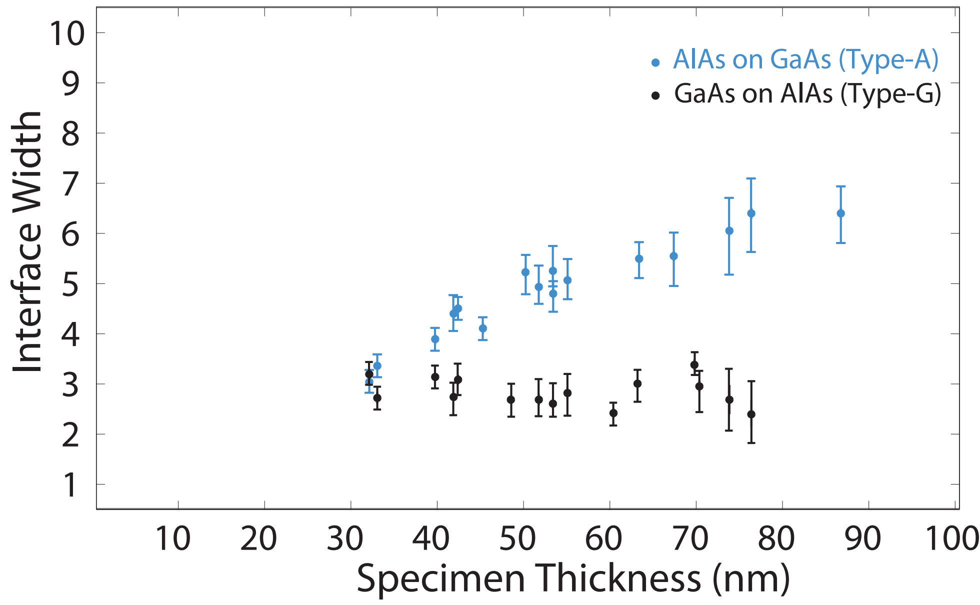

Figure 5.15 – This graph shows the measured interface width as a function of specimen thickness for the Type-A and Type-G interfaces. It is clear that the Type-G interface remains constant with thickness while the Type-A interface increases with thickness.

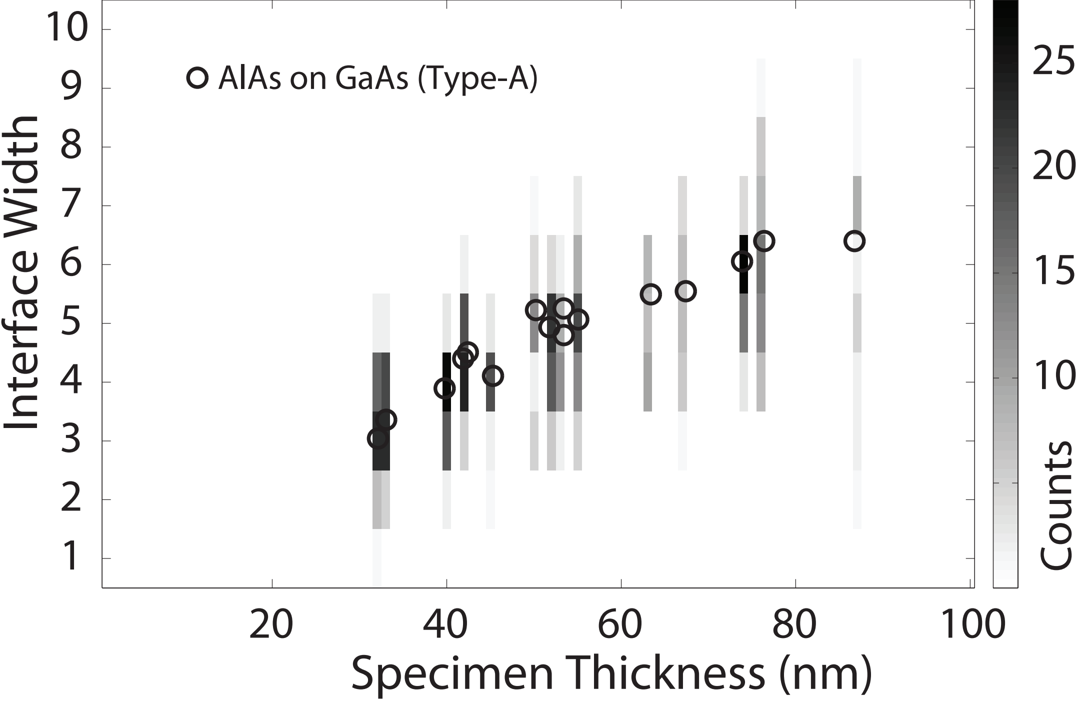

Figure 5.16 – The average data for the Type-A interface can be graphed with the distribution of widths from each line of the image. This distribution analysis gives an indication of the overall roughness of the interface at each thickness.

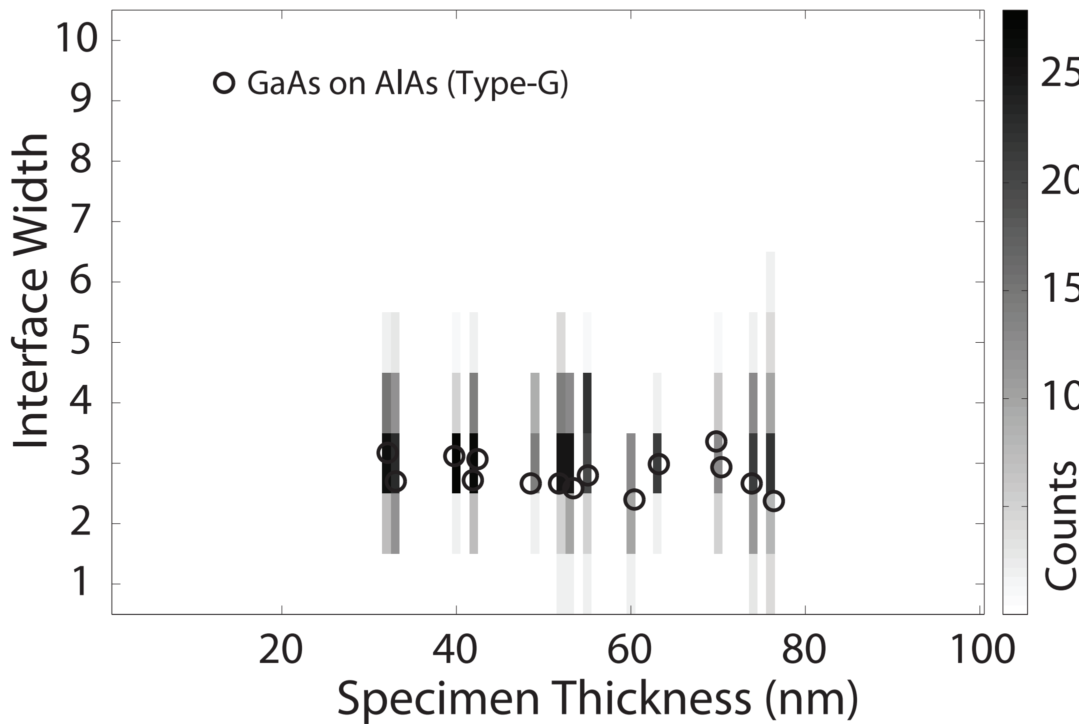

Figure 5.17 – The average data for the Type-G interface can be graphed with the distribution of widths from each line of the image. This distribution analysis gives an indication of the overall roughness of the interface at each thickness.

modulated by a background. The upper plot in figure 5.18 shows the background HAADF signal from an isolated Type-A GaAs - AlAs interface at a specimen thickness of $45nm$. The high background signal, on the left, is associated with the higher average Z GaAs region. Likewise the lower background signal, on the right, is associated with the lower average Z AlAs region. Between these regions the background signal varies smoothly across the interface. The vertical broken red lines indicate the 95% and 5% positions of the signal. The estimation of the interface width using the background signal can be complicated by two issues.

The first issue is that for an isolated interface, the width of the background signal varies with specimen thickness due to beam spreading. Beam spreading in turn depends on the composition of the structure and the convergence of the probe. However, this background variation can be modelled using a simple geometrical probe spreading argument which can allow an estimation of the interface width.

The second issue is found when imaging a superlattice structure. In a superlattice the background from the GaAs region can extend significantly into the AlAs region. The lower diagram of figure 5.18 shows the background signal (solid black) from the

isolated interface overlaid onto a schematic of the superlattice structure. From this diagram it is clear that the variation in the background signal extends beyond the center of the AlAs layer. Therefore a probe placed in the center of the AlAs layer will have a background signal contribution from the GaAs layer on the left and the GaAs layer on the right. This will in turn affect the measured position of the 5% location of this signal from the Type-A and Type-G interfaces. This is due to the background signal in the center of the AlAs layer is being affected by both adjacent GaAs layers. Furthermore, as the specimen thickness increases, the background contributions will increase, greatly limiting the ability to accurately characterise the interfacial structure. Figure 5.19 shows the measured interface width as a function of specimen thickness for the Type-A and Type-G interfaces using only the background HAADF signal. It is clear from the plot that many of the characteristics of the interface structure are lost. While the Type-A interface is generally wider than the Type-G interface there is very little variation in the interface width with increasing thickness. This indicates a significant problem when attempting to investigate the interfacial structure within a superlattice using the background signal alone.

5.6 Discussion and Conclusions

The aim of this chapter was the investigation of the column ratio mapping technique used to process high resolution STEM HAADF images. This technique was developed to separate the high resolution information relating to the atomic columns from the background signal that is associated with scattering from non-primary columns. Section 5.2 describes a method that can be used to isolated the background signal and details a method that minimises the generation of image artifacts at the interfacial regions. Section 5.2.2 describes an automated method for quickly extracting the dumbbell data using a pattern matching method. This process consists of fitting a two dimensional Gaussian function to the atomic column data. A number of free parameters are used to ensure that the Gaussian peaks are fitted to appropriate areas of the image. The extracted intensity data can then be used to form a column ratio map that indicates the changes in composition as a function of dumbbell location.

These column ratio maps are then used to measure a number of characteristics related to the structure of the growth layers such as the interface position, layer width

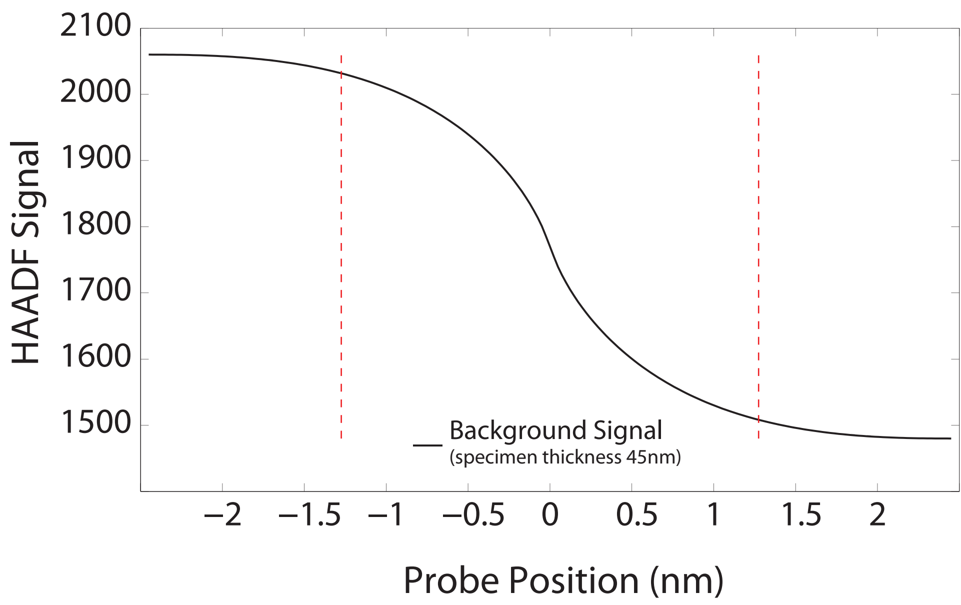

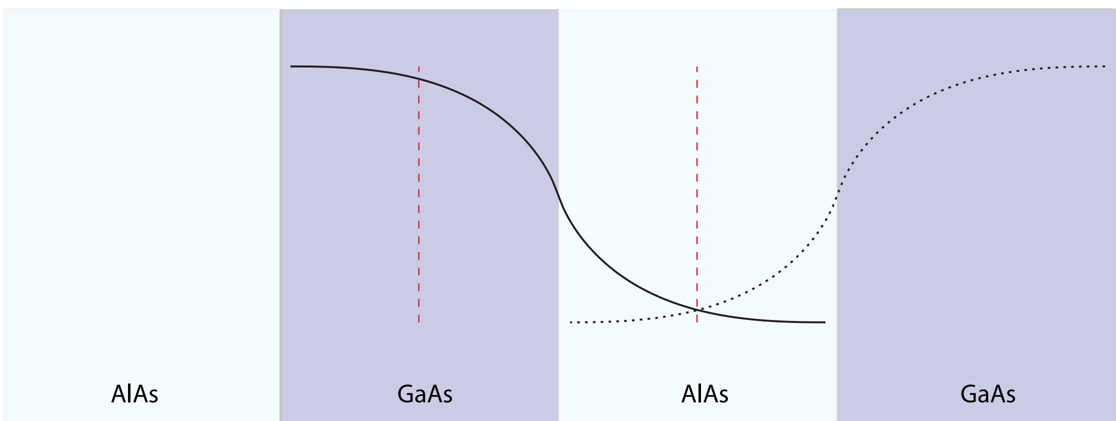

Figure 5.18 – The upper plot shows the background HAADF signal across an isolated Type-A interface at a thickness of 45nm. The vertical broken lines indicate the 95% and 5% locations. The lower schematic shows this background signal overlaid onto a diagram of the superlattice. This schematic indicates that a probe placed in the center of the AlAs layer will have contributions from the GaAs layers on either side. As the thickness of the specimen increases the contribution will grow.

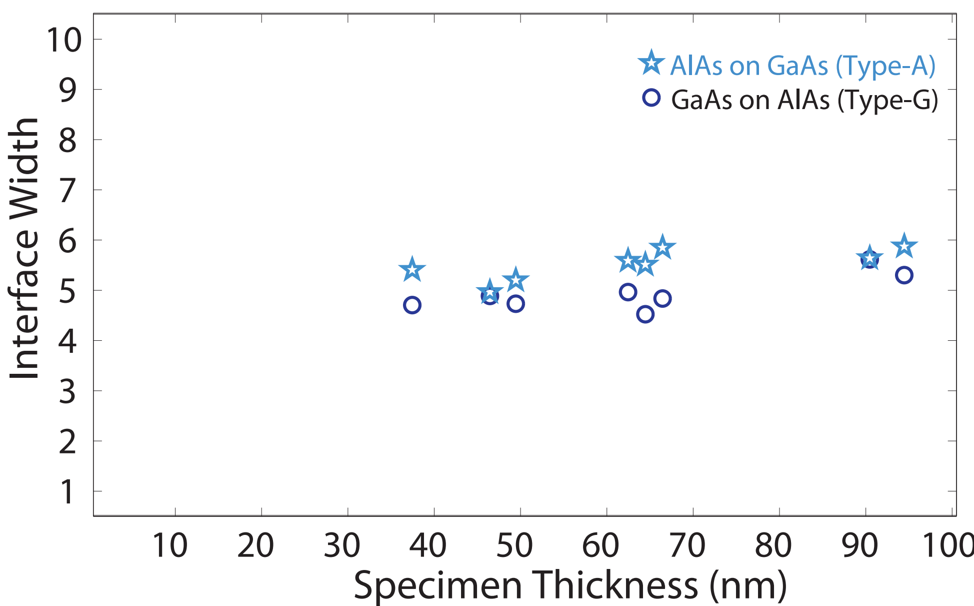

Figure 5.19 – This graph shows the measured interface width as a function of specimen thickness for the Type-A and Type-G interfaces from the deep superlattice region using the background HAADF signal.

and interface width. These characteristics can be measured for the averaged column ratio map which gives a general overview across the entire map. However, a line by line approach can also be performed which provides details on localised changes across the column ratio map. Section 5.4.2 showed the measured characteristics using both the line by line and averaged analysis. The results indicate a distinct difference between the two interfaces studied. The measured Type-G interface width remains between $2-3$ dumbbells over the full range of specimen thickness investigated. At a specimen thickness of $32nm$, the measurements indicate that the width of the Type-G and Type-A interfaces are equivalent. However, as the specimen thickness increases, the width of the Type-A interface increases by approximately $3\frac{1}{2}$ dumbbells. Furthermore, the apparent GaAs layer width changes with specimen thickness by approximately $2\frac{1}{2}$ dumbbells. The aim of the following chapter is to describe the interfacial structures that would result in these types of characteristic measurements. This is achieved by first forming a series of simple interface structures and simulating the resulting HAADF images. An evaluation of the measured characteristics can be achieved using the same methods applied to the experimental images. The model data will therefore provide an indication of the possible structures present in this GaAs - AlAs specimen.

Chapter 6

Simulated GaAs - AlAs Interface

6.1 Modelling Proposals

The interface width and position measurements from section 5.4 indicate a distinct difference in interfacial characteristics of the Type-A (AlAs grown on GaAs) and the Type-G (GaAs grown on AlAs) interfaces. To develop a greater understanding of the types of interfaces that would generate these characteristics, a series of models were developed.

The first consideration for the model development are the mechanisms that are present during MBE growth of the Type-A and Type-G interfaces. Several studies have been carried out with the aim of achieving high-quality AlAs - GaAs superlattices [95, 96, 97]. Therefore, many characterisation techniques which measure the interfacial step structures on the atomic scale have been developed [14, 98, 99, 100, 101]. The characterisation of interfacial structures has been attempted using techniques such as reflection high-energy electron diffraction (RHEED) [14, 98, 99] and photo-luminescence measurements [101, 100]. The RHEED measurements provide information on the morphology of the growing surfaces which, in turn, determines the morphology of the interfaces. However, these measurements do not provide information about the characteristics of each interfacial step. Information such as the straightness and height of the step edge, or the distance from neighboring steps can be obtained using high resolution transmission electron microscopy (HR-TEM) which allows atomic-scale observation of the structure [102]. A study of this interfacial stepping using CTEM revealed that of the stepping on a Type-A interface, those parallel to the $[1\bar{1}0]$ direction are typically greater than $55nm$ in length [102]. However, the step length parallel to the [110] di-

rection was found to be typically less then 15nm in length [102]. This same study also suggests that the Type-A interface is atomically abrupt and that the Type-G interface has a degree of inter-diffusion [102].

A separate study, investigating surface segregation at III-V interfaces using a chemical potential model, found Type-3 atom segregation at both the Type-A and Type-G interfaces. However, the width of the Type-A interface was calculated to be considerably larger than that of the Type-G interface [103]. The surface segregation model was developed using a 10 x 10 monolayer GaAs - AlAs superlattice and the CTEM study performed on a GaAs - AlAs superlattice grown under very similar conditions to sample C102 detailed in figure 5.9. The results from both of these studies were considered during the model development process.

The second consideration for the model development are the conditions under which the images are taken. In particular, the effect that the different materials have on the STEM probe. Section 3.6 reported on the scattering of a sub-Ångström probes in single crystal III-V materials and showed the difference in the probe channelling depth. The channelling depth is a measure of the depth into the crystal that the probe will stay on the primary column. It is within this depth that compositional changes of the primary column can be detected. These calculations showed that the primary column HAADF signal was limited to the top 20nm of the crystal for GaAs. For AlAs this channelling depth was considerably deeper.

The range of possible interface structures is therefore vast. The conditions above are used to limit the probable structures to a range that can be investigated within a suitable time frame. From the possible structures five simple models were developed and explored using the multislice code. These models are detailed below.

A model of a **perfect interface** was initially investigated where the interface was abrupt over one monolayer and the interface normal was orientated to [001]. This simple structure provided a basic understanding of the HAADF signal when a probe is scanned across an ideal interface. This provides details of the background and primary column signals and also served as a comparison for the subsequent models.

It has been reported that during MBE growth **terraced interface** structures can form in the [001] growth direction, described in reference [99]. When orientated to [110] this

type of structure could form a repeating stepped interface. A simple model was created where the repeating step length was varied from a short step length (approximately the channelling depth of GaAs, 20nm) to a long repeat length of 110nm.

The MBE substrates are also polished to a tolerance of $\pm\frac{1}{2}^{\circ}$. A superlattice grown on a substrate at one of these extremes would form an orientated **vicinal interface**. For a sample $120nm$ thick a $\frac{1}{2}^{\circ}$ projected interface would be approximately 4 dumbbells wide and at the interface the STEM probe would project through one material before the other. Two types of models were explored, the first model consisted of GaAs at the entrance face of the specimen (GaAs projection). The second model consisted of AlAs at the entrance face of the specimen (AlAs projection).

A **simplified diffusion model** was also considered where the interface width was due to intermixing of the Type-3 atoms. A distribution was considered where the composition was linearly varied across a wide interface giving a broad overview of the HAADF signal generated from a partially populated Al_xGa_{1-x} column.

An **accurate diffusion model** was also formed from data obtained from modelling of surface segregation during the MBE growth of GaAs - AlAs heterostructures under similar growth conditions [103].

For each of these models, the generated HAADF signals were calculated and averaged over 100 phonon configurations. The interface width and position was evaluated using the same method that was applied to the experimental images. This process therefore allows the objective measurement of the interface characteristics allowing the models and experimental results to be compared. The simulation results are presented below in section 6.2.

6.2 Simulated GaAs - AlAs Interface

6.2.1 Model Configuration

The atomic co-ordinate file for each interface was constructed using a Matlab script and was formed within a supercell of 14 x 12 x 300 unit cells. The supercell can be seen in figure 6.1 and is split into three distinct sections. The upper and lower sections consist of single crystal GaAs and AlAs respectively. The composition of the central section is varied depending on the type of interfacial structure required. The script provides control over the composition of each atomic column within the interfacial region and allows the formation of a perfect, diffuse or stepped interface. The HAADF signals for sixteen dumbbells are calculated for each simulation. These dumbbells are numbered 1 to 16. Dumbbell 1 is in the bulk GaAs region and the line profile is calculated across the interface region and ends at dumbbell 16 in the bulk AlAs region. For each dumbbell the Type-3, Type-5 and background HAADF signal is calculated and the positions of the dumbbells within the supercell are indicated in figure 6.1.

A diffuse interface can be generated by specifying the fractional content of each atomic species for each column within the interfacial region. The crystal structure is generated one unit cell at a time and a random number generator is employed to select the atomic species for each of the Type-3 atoms. The bulk crystal regions are then created resulting in the formation of the entire supercell.

A randomly stepped interface is formed in a similar way. However, the random number generator is this time used to select both the step length, in the [110] beam direction, and the step direction. The step direction can be either in the [001] or [$00\bar{1}$] direction (i.e. perpendicular to the beam direction). The step length is chosen from a Gaussian distribution with a mean of $5nm$ and a variance of $100nm$ for step lengths greater than zero only (see figure 6.71 in section 6.2.6). This step distribution is consistent with HRTEM observations of step lengths in the [001] direction at a GaAs - AlAs interface [102]. The supercell is created by allocating each Type-3 atom depending on which side of the interface the atom falls.

In addition to these interface structures the angle of the interface can also be defined and introduced at the point of creating the supercell. This provides the flexibility to create a perfectly abrupt vicinal interface at a specified angle. However, it also allows the formation of a diffuse vicinal interface or a randomly stepped vicinal interface. The

vicinal angle is applied using a shift in the atomic columns that is dependent on the unit cell size. For example, an abrupt vicinal GaAs - AlAs interface of 0.5° requires a lateral shift in the interface position of roughly one atomic column as the depth of the specimen increases by $30nm$. This shift in the interfacial position can, therefore, be applied to the stepped or diffuse interface structures to introduce a degree of vicinality.

For clarity in the following sections, data generated from a Type-5 column will be indicated using green. Data from a Type-3 column from bulk GaAs will be in dark blue. Data from the Type-3 column from bulk AlAs in light blue. The background signals will be shown in red. Data from the Type-3 column from interfacial region will be displayed in black. All data from the interfacial regions are shown using a broken line, while the bulk regions are shown using a solid line. This allows data from the interfacial columns and data from the bulk material to be shown on the same graphs.

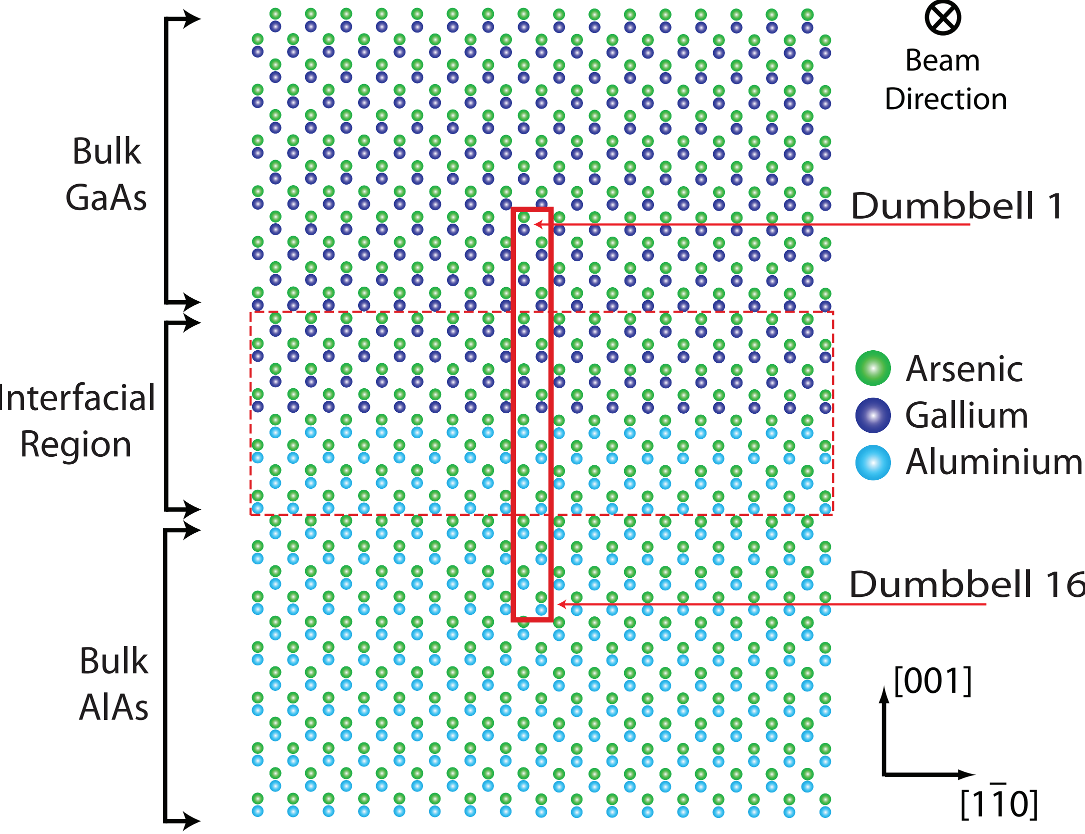

Figure 6.1 – The configuration of the model is outlined in the figure above, the green columns correspond to the position of the arsenic atoms, dark blue are gallium and light blue aluminium. The broken red rectangle indicates the interfacial region where the composition can be varied, the solid red rectangle indicates the dumbbell columns that relate to the probe positions 1 thru 16. To calculate the column ratio for a single dumbbell requires three probe positions, the Type-3, Type-5 and background positions. The location of the probe positions within a dumbbell is shown in figure 3.6.

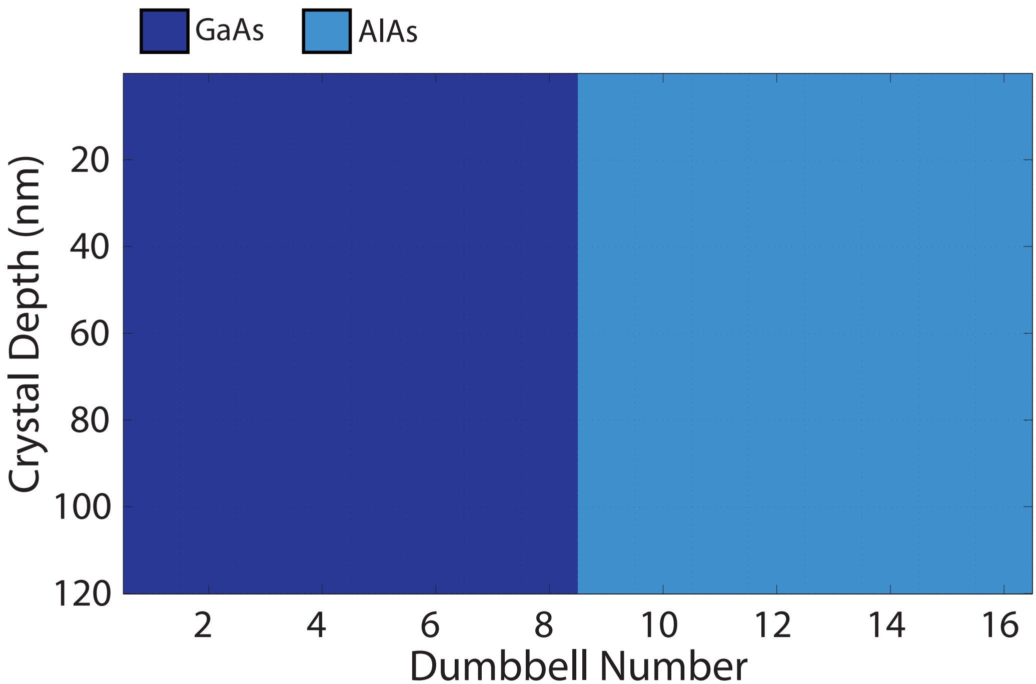

Figure 6.2 – An overview of the ideal interface used in the simulation. The interface is abrupt and located between dumbbells 8 (GaAs) and 9 (AlAs) with the change in composition occurring over one mono-layer. The interface normal is also orientated parallel to the [001] growth direction.

6.2.2 Perfect Interface

The first model calculated was also the simplest and consisted of an ideal interface. The change in composition from GaAs to AlAs was abrupt over one mono-layer in the [001] growth direction. Figure 6.2 shows a side view schematic of the ideal interface used in the simulation and indicates that the change in composition from GaAs to AlAs occurs between dumbbells 8 (GaAs) and 9 (AlAs) consistently throughout the supercell. The interface normal is also orientated parallel to the [001] growth direction (i.e. 0° vicinality). This ideal interface provides a basic understanding when interpreting the results from interfaces with increasing complexity. This model also provides evidence that the observed experimental effects (detailed in section 5.4.2) do not arise simply from beam spreading across an ideal interface.

The HAADF signal was calculated for each probe position and was averaged over 100 phonon configurations. This number of phonons was required to bring the error in the column ratio calculation to less than the measured experimental error from the column ratio maps. The signals generated from the dumbbells at either side of the interface (dumbbells 8 and 9) are important. The signal from these dumbbells will indicate if the proximity of the interface modifies the measured column ratio. Figure

6.3 is a comparison plot of the HAADF signals from dumbbell 8 and the HAADF signals from a dumbbell in the bulk GaAs region. This graph allows the effect of the interface to be ascertained by comparing each signal in turn.

The Type-3 signal from dumbbell 8 is the broken black line and can be compared to the Type-3 signal from bulk GaAs which is the solid blue line. For the first $20nm$ the two signals are indistinguishable and exhibit identical characteristics. However, for crystal thicknesses greater than $20nm$ the signal from dumbbell 8 deviates from that of the bulk GaAs region. The Type-5 signal from dumbbell 8 is indicated by the broken green line while the Type-5 signal from bulk GaAs is the solid green line. This shows a similar pattern where the signals are identical from 0 to $20nm$ after which the signal from dumbbell 8 deviates from that of the bulk GaAs region. This type of behavior is not unexpected. Section 3.6.1 detailed the results for a GaAs single crystal and found that in the top $20nm$ of the crystal the HAADF signal is predominantly generated from the primary column.

Figure 6.4 shows that the intensity on the primary column of dumbbell 8 is very similar to a bulk GaAs dumbbell therefore the generated HAADF signal should also be very similar while there is significant intensity on the primary column. After 20nm, however, the probe has dechanneled from the primary columns and the resulting HAADF signal will be generated from the columns adjacent to the probe position. The drop in HAADF signal from dumbbell 8 can be attributed to the reduction in the background signal and figure 6.3 shows that the background signal from dumbbell 8 is clearly lower than in bulk GaAs. However figure 6.3 shows another difference in the generated signals. For bulk GaAs (solid lines) the Type-3 and Type-5 signals tend to the same magnitude for crystal thicknesses greater than $\sim 60nm$. Whereas, the Type-3 signal generated from dumbbell 8 is consistently lower than the Type-5 signal. Figure 6.4 shows the primary column intensity for dumbbell 8 where the primary column intensity for bulk GaAs are the solid lines and the primary column intensity for dumbbell 8 are indicated by the broken lines. Clearly the primary column intensity for dumbbell 8 is identical to the intensity of bulk GaAs and therefore the on-column intensity can not account for the differences observed in the HAADF signal.

This effect is a result of the close proximity of the probe to the interface and can be understood from the atomic configuration local to dumbbell 8. The left side of figure 6.5 shows a schematic of the atomic columns around dumbbell 8. The upper

diagram details the probe placed on the Type-3 column (red circle) and the lower diagram shows the configuration when the probe is placed on the Type-5 column. At a crystal depth greater than $20nm$, the HAADF signal will no longer be generated predominately from the primary column. Instead the six nearest atomic columns will be generating a significant percentage of the total signal. When the probe is placed on the Type-3 column (upper diagram) the six nearest atomic columns consist of two arsenic, two gallium and two aluminium which are enclosed in the red box. For the case when the probe is placed on the Type-5 column the six nearest atomic columns consist of two gallium and four arsenic which are again within the red box. In the case of the Type-3 signal, the generated HAADF signal will therefore be reduced as two arsenic columns are replaced by two aluminium columns.

These diagrams are overlaid onto the real space intensity maps at a crystal thickness of approximately $60nm$. In these maps, darker regions indicate areas with a high electron intensity and lighter areas correspond to a lower electron intensity. These maps show the electron distribution at a specific depth within the crystal and give an indication of the atomic columns that are contributing to the HAADF signal. For the Type-3 probe position there is significant intensity around the AlAs columns below dumbbell 8 indicating that these columns within the AlAs region are attracting the electrons. Whereas, in the case of the Type-5 probe position the electron intensity is drawn to the two GaAs columns above dumbbell 8. This gives a clear indication that the generated HAADF signal from the adjacent columns will be higher in the Type-5 probe position which accounts for the differences shown in figure 6.3.

For dumbbell 9 a similar set of comparisons can be made and figure 6.6 shows a comparison plot of the HAADF signals from dumbbell 9 and from the bulk AlAs region. The Type-3 signal from dumbbell 9 is the broken black line and can be compared to the Type-3 signal from bulk AlAs which is the solid blue line. In this case, the HAADF signal from dumbbell 9 is consistently higher than that of the bulk AlAs region. This is also true for the background and Type-5 signals. However, figure 6.6 shows that the increased signal generated from the Type-3 probe position has not increased to the same extent as the background and Type-5 probe positions. This again can be attributed to the atomic configuration around the primary columns as the right side of figure 6.5 now shows. The upper diagram corresponds to the probe positioned on the Type-3 column and the red box again indicates the six nearest atomic columns. The

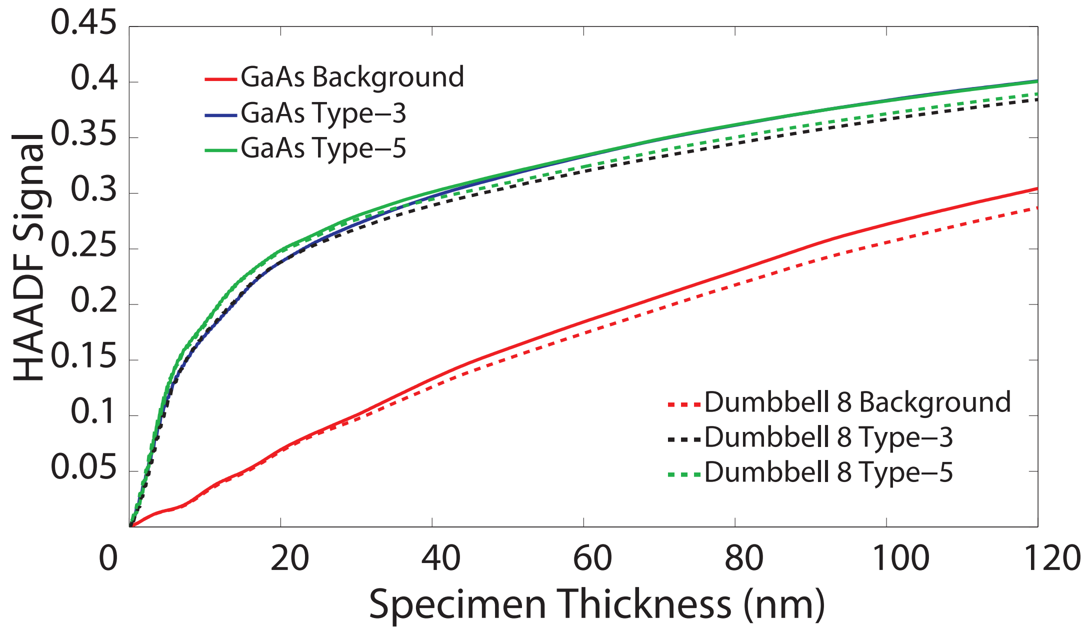

Figure 6.3 – The HAADF signal generated from the Type-3, Type-5 and background probe positions for bulk GaAs are the solid lines. The HAADF signal generated from the Type-3, Type-5 and background probe positions for dumbbell 8 are the broken lines. Dumbbell 8 is the last GaAs dumbbell before the interface.

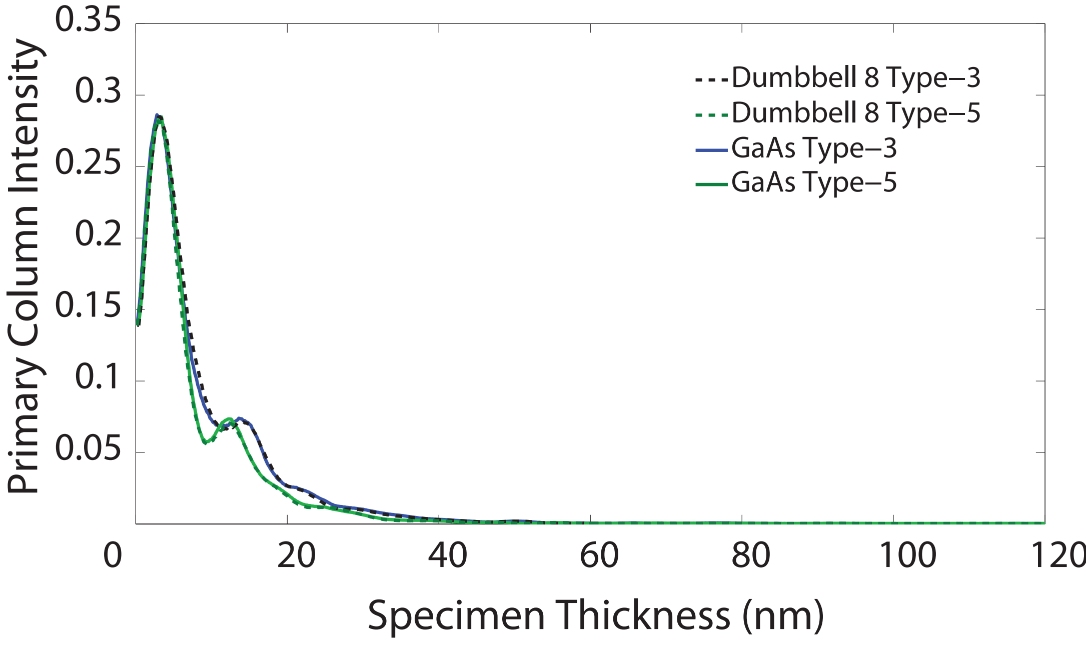

Figure 6.4 – The Primary Column Intensity on the Type-3, Type-5 probe positions for bulk GaAs are the solid lines. The Primary Column Intensity on the Type-3, Type-5 probe positions for dumbbell 8 are the broken lines. Dumbbell 8 is the last GaAs dumbbell before the interface.

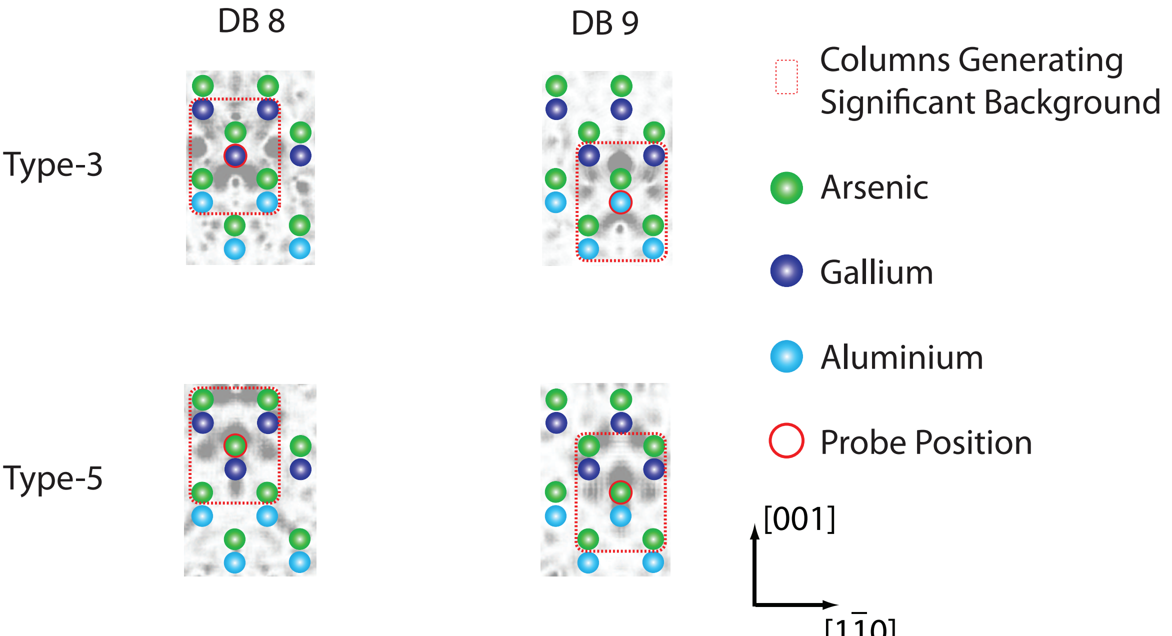

Figure 6.5 – The schematic above shows the probe positioning for dumbbells 8 and 9. The left side shows the probe positioning (red circle) for dumbbell 8 for the Type-3 column (upper diagram) and Type-5 column (lower diagram). In each case the surrounding 7 atomic columns are highlighted indicating a difference in the average Z in the immediate vicinity of the STEM probe. The right side shows the probe positioning for dumbbell 9 where the upper diagram is the Type-3 probe position and the lower is the Type-5 probe position. The schematic of the atomic columns are overlaid onto a real space intensity map where the darker regions correspond to a higher electron density.

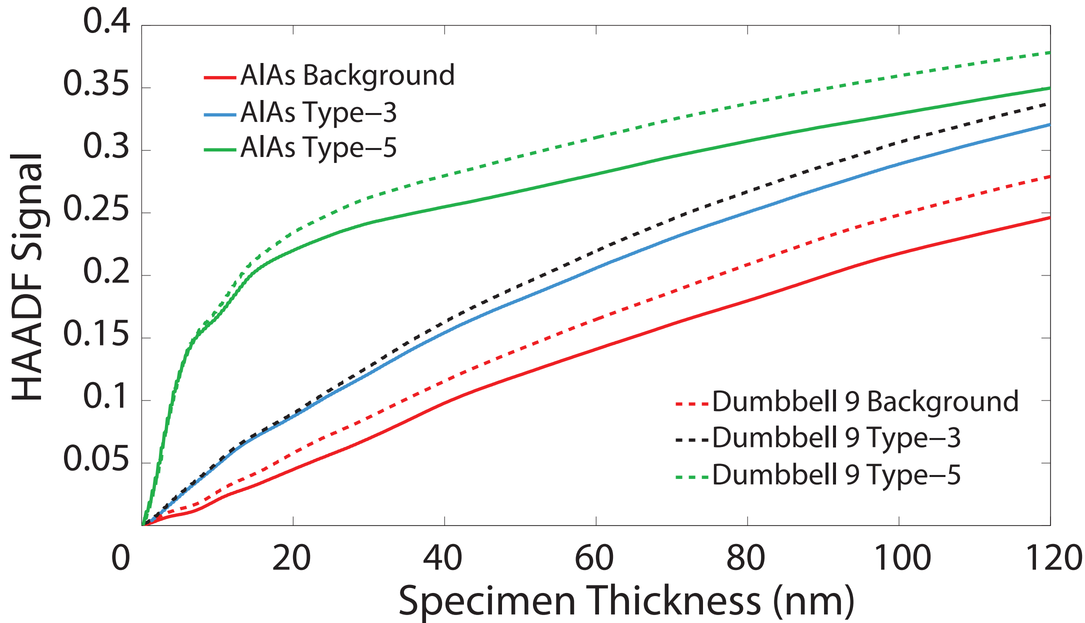

Figure 6.6 – The HAADF signal generated from the Type-3, Type-5 and background probe positions for bulk AlAs are the solid lines. The HAADF signal generated from the Type-3, Type-5 and background probe positions for dumbbell 9 are the broken lines. Dumbbell 9 is the first AlAs dumbbell after the interface.

intensity map indicates that a proportion of the intensity is drawn towards the upper two gallium columns, however, intensity also remains within the AlAs region by being drawn down towards the two adjacent AlAs columns. In the Type-5 probe position case (lower right) a significant fraction of the electron intensity has been drawn into the GaAs region. This atomic configuration would therefore account for the smaller increase in the Type-3 HAADF signal for dumbbell 9.

The proximity of the interface has an impact on the generated HAADF signal by not only modifying the background signal but changing the dynamical scattering processes in adjacent atomic columns. This will, in turn, affect the measured column ratio and figure 6.7 shows how the proximity of the interface affects the overall column ratio as a function of specimen thickness. The green and blue lines represent the column ratios generated from a bulk GaAs and AlAs dumbbell respectively. The column ratios generated from dumbbells 8 and 9 are also indicated on this figure by the black broken lines. In both cases the column ratio for crystal thicknesses less than $10nm$ are relatively unaffected by the interface position. However, for thicknesses greater than this, the close proximity of the interface causes a reduction in the measured column ratio. This effect is clear in figure 6.7 but can also be seen in figure 6.8 which shows a series of column ratio line profiles calculated at a series of specimen thicknesses. At a thickness

of $10nm$ dumbbells 8 and 9 are indistinguishable to the bulk GaAs and AlAs regions respectively. At a thickness of $30nm$ and $50nm$ the drop in column ratio is apparent and by $120nm$ there is a significant drop in the column ratio values of dumbbell 8, 9. Furthermore, at this depth, dumbbells 7 and 10 are beginning to be affected also.

The column ratio profiles in figure 6.8 allows the interfacial width to be measured for each specimen thickness using the same fitting procedure detailed in section 5.3.2. Figure 6.9 shows the interface width of the perfect interface in red and is overlaid onto the experimental width data for a direct comparison. It is clear from figure 6.8 that the simulated perfect interface appears abrupt over one monolayer over the full simulation range (i.e. $0-120nm$). This is reflected in the width measurements in figure 6.9 where a constant interfacial width of slightly less than one dumbbell is measured. The measured interfacial width reflects the issue of fitting an analytical function to discreet data and although the interface is abrupt measuring the distance between the 95 and 5 percent position on the function will result in a finite width.

The column ratio data from figure 6.8 also allows the interfacial position to be measured and in particular how the interface position changes with increasing specimen thickness. Figure 6.10 shows the results of the interface position measurement and the position is overlaid onto the model overview giving a direct comparison of the "actual" interface position to the measured interface position. Figure 6.10 indicates that there is very little movement in the measured interfacial position. It remains fixed between dumbbells 8 and 9 as the thickness of the specimen increases. These results clearly indicate that a perfectly abrupt interface with a normal orientated to the [001] growth direction does not exhibit any of the interfacial characteristics observed experimentally in section 5.4.2. The data obtained from this ideal interface will serve as a comparison for the interfacial models developed in the following sections.

6.2.3 Sawtooth Interface

MBE growth is an epitaxial process involving the reaction of one or more thermal beams of atoms with a crystal surface [1]. The process can achieve accurate growth of multilayer systems but requires accurate control over parameters such as effusion cell temperature, substrate temperature and substrate holder rotation. Under certain conditions the growth material can form terracing which can produce a stepped inter-

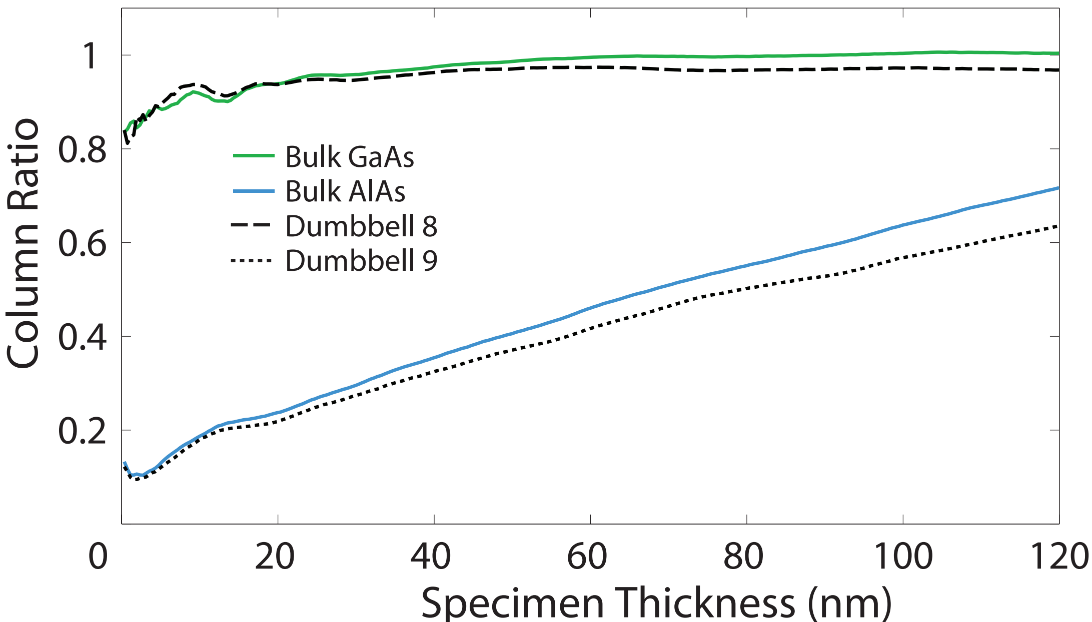

Figure 6.7 – The graph above shows the column ratio as a function of specimen thickness for bulk GaAs (green) and bulk AlAs (blue). The column ratio from the (ideal interface) dumbbell 8 (dashed) and dumbbell 9 (dotted) are also plotted. For a thin specimen thickness ($\sim 20nm$) the column ratio from dumbbell 8 matches a bulk GaAs dumbbell. Likewise for a thin specimen the column ratio from dumbbell 9 matches bulk AlAs. However as the specimen thickness increases the measured column ratio deviated from bulk material. This is due to the proximity of the interface affecting the background signal of both dumbbells 8 and 9.

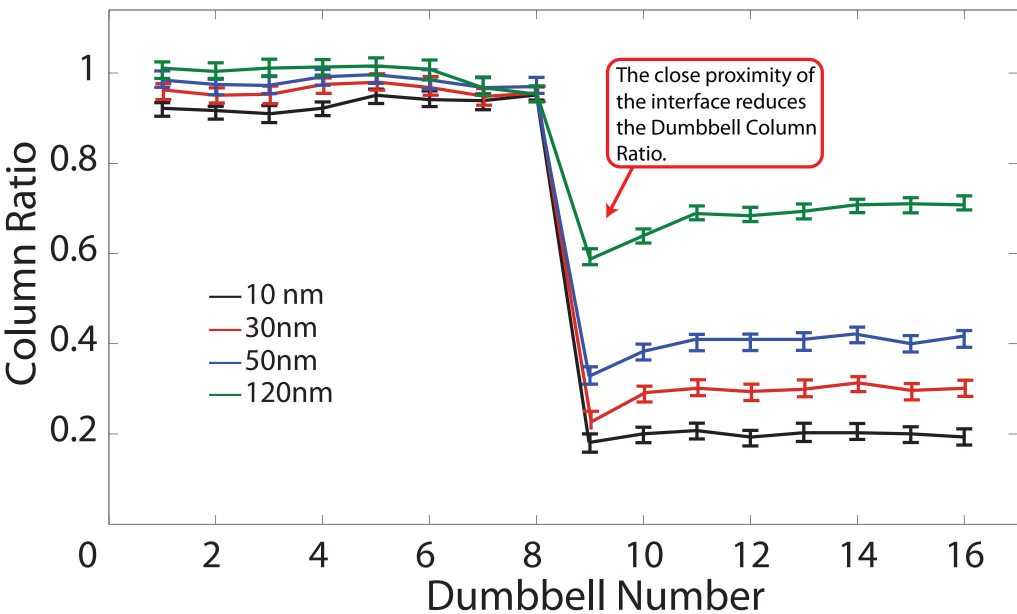

Figure 6.8 – The graph above shows a column ratio profile for the ideal interface for a crystal thickness of $10nm$, $30nm$, $50nm$ and $120nm$. The column ratio of dumbbell 9 drops below bulk AlAs due to the proximity of the interface modifying the background signal.

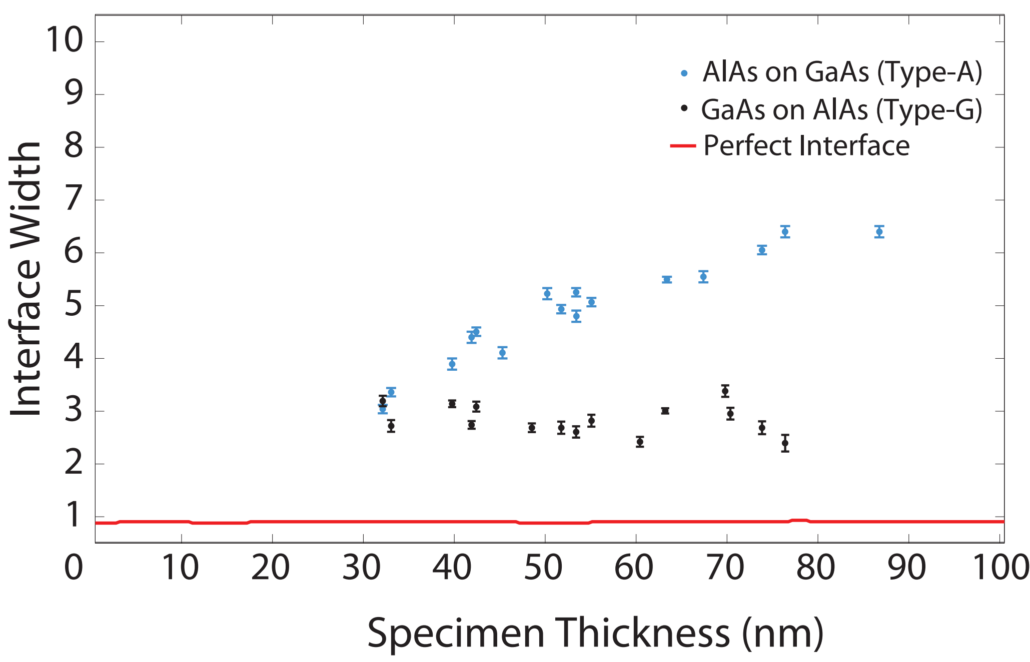

Figure 6.9 – The graph above shows the measured interface width as a function of specimen thickness for the ideal interface. The measured data from the model is overlaid onto the experimental width measurements from figure 5.15 on page 118.

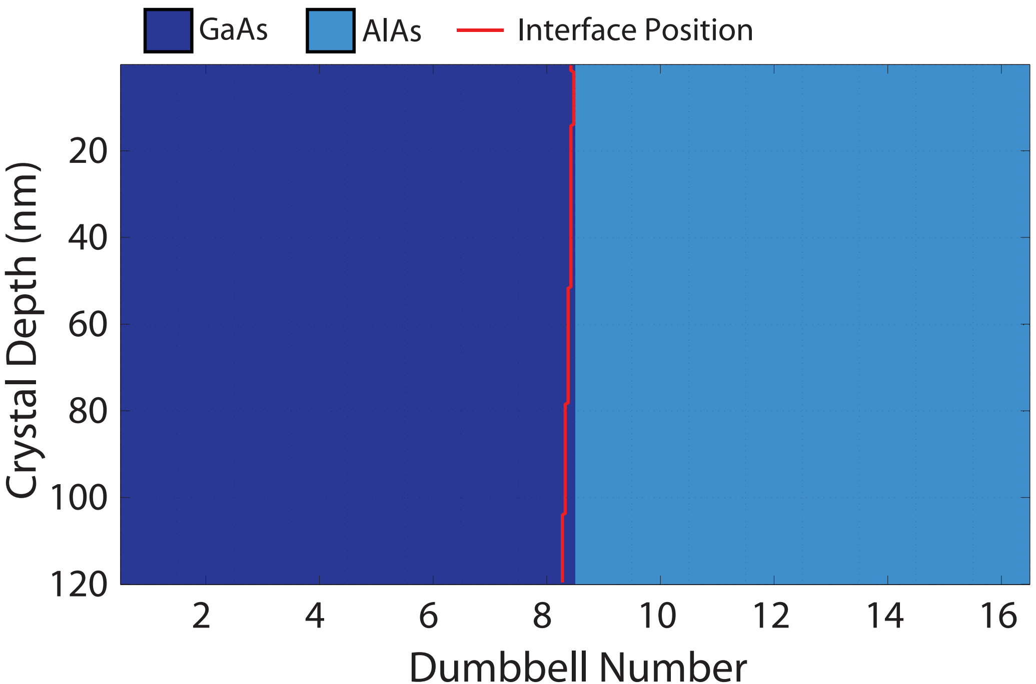

Figure 6.10 – A schematic of the ideal interface used in the simulation with the measured interface position overlaid in red. The interface position is positioned between dumbbells 8 and 9 and the measured interface position remains between these dumbbells over the full range of specimen thicknesses.

face between layers. When orientated in the [110] direction, these terraces can form a sawtooth structure, the morphology of which can be simplified and described using a characteristic step length (the distance from one step to the next) and a characteristic repeat length (the length over which the stepping pattern is repeated). The repeat and step lengths can be varied giving a range of models that can be interrogated to obtain a clear picture of how these structures would affect the interfacial measurements. The characteristic repeat length was explored for a short repeat length (18nm), which was comparable to the channelling depth of a fully populated gallium column, and a long repeat length (110nm), approximately equal to the full simulation depth. The step length was chosen to be 7.2nm which is consistent with a typical step length in the [110] direction. These step lengths were measured using HRTEM for a GaAs - AlAs interface grown in a [001] orientation under similar conditions [102].

6.2.3.1 110nm Repeat Length (AlAs Projection)

A schematic of a sawtooth interface with a 110nm repeat length can be seen in figure 6.11. The first feature of this model is the AlAs at the entrance face of the specimen from dumbbells 6-12. The Type-3 columns of these dumbbells are partially populated with aluminium and partially populated with gallium and the compositional changes depend on both the crystal thickness and the probe position. However, for these interfacial columns aluminium is the initial element at the entrance face of the Type-3 columns and therefore this type of orientation can be described as an AlAs projection.

Figure 6.12 shows a series of column ratio line profiles for this model at specimen thicknesses of 10nm, 30nm, 50nm and 120nm. The plot shows that both the interface width and the interface position change significantly as the specimen thickness increases. From the schematic in figure 6.11, it is apparent that at a depth of 10nm dumbbells 1-5 are fully populated GaAs columns and dumbbells 7-16 are fully populated AlAs columns. Whereas, dumbbell 6 has a change of composition at a depth of 7.2nm from AlAs to GaAs. This is reflected in the column ratio profile data. At 10nm (black line) the data indicates the interface width is 1 dumbbell wide with only dumbbell number 6 contributing to the interfacial region. The compositional change within dumbbell 6 is reflected in the measured value of the column ratio at that thickness (~ 0.47) which is clearly between bulk GaAs and AlAs. Furthermore, as the thickness increases to 30nm dumbbells 6, 7 and 8 form the interface. However, looking at the

column ratio line trace only dumbbells 7 and 8 appear to form part of the interface. The column ratio of dumbbell 6 has increased significantly and now appears to be part of the GaAs bulk region. This "saturation" effect has caused the apparent interface position to shift to the right towards the bulk AlAs region. As the thickness of the specimen is increased the interface position continues to move towards the bulk AlAs region.

Figure 6.13 plots this change in the measured interface position as a function of thickness. The measured interface position is overlaid onto the schematic indicating how the perceived interface position varies from the "average" interface position. The data indicates that the interface position starts near dumbbell 5 but gradually moves towards the bulk AlAs region with increasing thickness. It remains at a position near dumbbell 12 after a specimen thickness of $57nm$. From this point on, the interface position remains constant. This effect can be understood from the channelling depth of the aluminium column in AlAs. Section 3.6.2.2 showed that a significant fraction of the probe remains on the Al column to depths of greater than 120nm. Therefore, compositional changes from aluminium to gallium in the top section of this crystal can be detected. The measured interface position accurately tracks the gallium content in the atomic columns.

For specimen thicknesses above $57nm$ the interface position remains constant. At this point the interface is beginning to step back in the opposite direction, however, the changes in composition at these depths are not detected. These compositional changes are not detected as there in not a sufficient density of electrons around the primary columns. The change in HAADF signal at these depths is from background scattering only. The results from section 3.6.1.2 showed that only $25nm$ of gallium was required to scatter most of the electron intensity off the primary column. With no electrons on the primary column any compositional changes can not be detected and, in this sawtooth model, the projected overhang of the structure is sufficient to scatter a significant fraction of the probe intensity off of the primary columns.

One interesting feature from the column ratio profiles are column ratio values for dumbbells number 6 and 7. The column ratio from these dumbbells appear to deviate from the surrounding dumbbells. At a specimen thickness of $50nm$ and above, dumbbell 6 and dumbbell 7 both show a column ratio value that is significantly different from the surrounding dumbbells. This effect appears to be specific to the depth at which

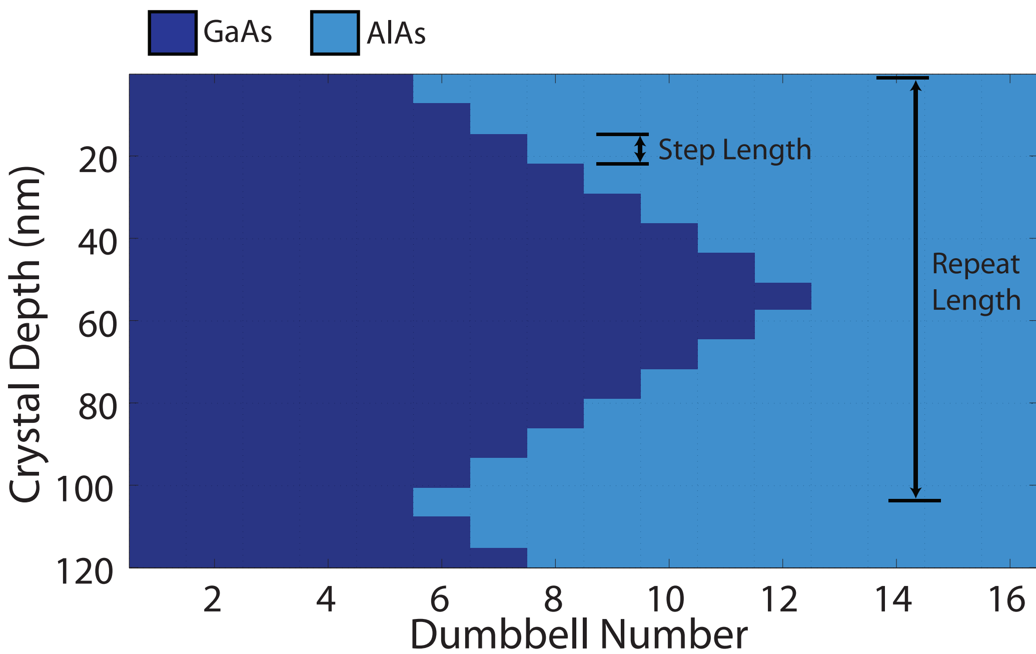

Figure 6.11 – This diagram shows the schematic of the (AlAs projection) sawtooth interface where the characteristic repeat length is $110nm$. The step length was chosen to be $7.2nm$ to be consistent with step length measurements from a HRTEM study into MBE grown GaAs - AlAs heterostructures [102].

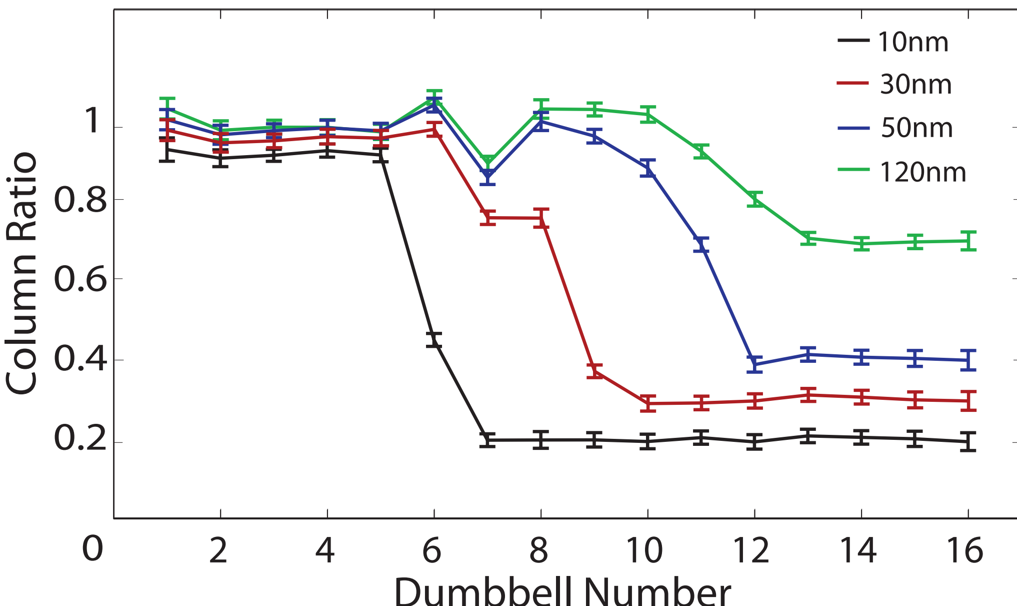

Figure 6.12 – A series of column ratio line profiles at specimen thicknesses of $10nm$, $30nm$, $50nm$ and $120nm$. The line profiles show the interface position gradually shift towards the bulk AlAs region with increasing thickness. Another feature are the deviation of the column ratio values of dumbbells 6 and 7 from the surrounding dumbbells. Dumbbell 6 has increased greater than bulk GaAs and dumbbell 7 is significantly below bulk GaAs.

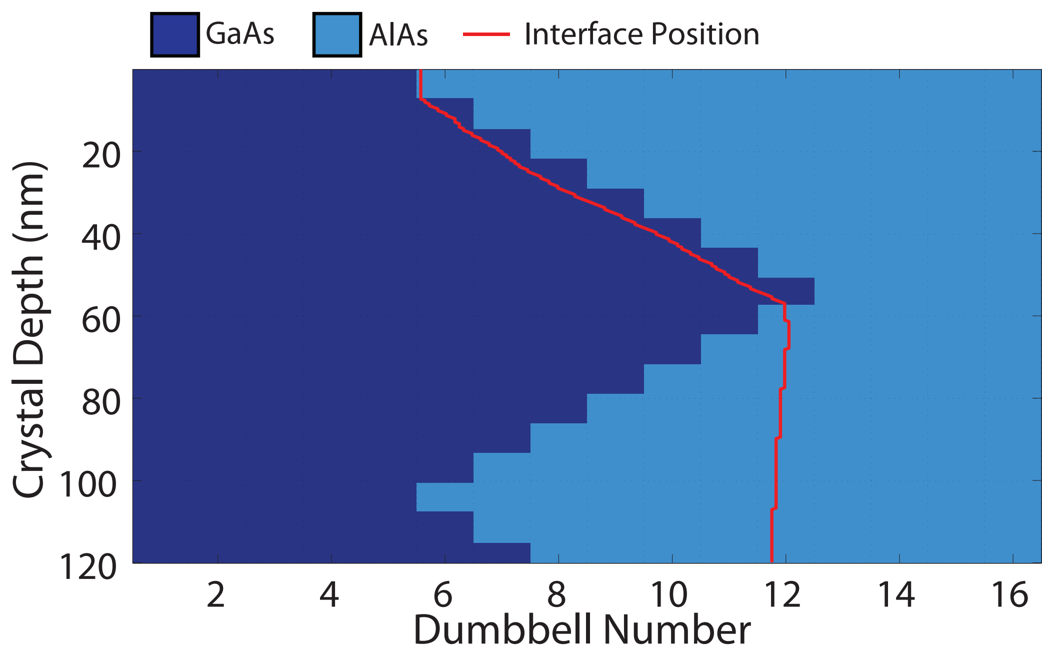

Figure 6.13 – The measured interface position is overlaid onto the model schematic indicating that the interface position tracks the gallium content of the atomic columns. Furthermore at a depth of 55nm the actual interface steps back towards the bulk GaAs region causing an overhang. This overhanging structure is, however, not detected due to the low primary column intensity at these depths.

the compositional changes occur.

The graph in figure 6.15 shows the electron intensity on the primary Type-3 column for dumbbell 6 (broken black) and figure 6.17 shows the electron intensity on the primary Type-3 column for dumbbell 7 (broken black). Both of these graphs also show the electron intensity from a complete gallium column from bulk GaAs (dark blue) and a complete aluminium column from bulk AlAs (light blue). The positions of the compositional change from Al to Ga is indicated by the change of background colour. The first change in composition for dumbbell 6 (figure 6.15) occurs at a depth of 7.2nm and until this depth the intensity is consistent with a fully populated aluminium column. At this point, the Type-3 column changes from aluminium to gallium and over the next 25nm the intensity on the column drops significantly. By a depth of 32nm, the intensity on the primary column has dropped to less than 5% of the peak value. The change in composition for dumbbell 7 (figure 6.17), occurs at a depth of 14.4nm and until this depth the intensity is again consistent with a fully populated aluminium column. By 38nm the on column intensity has dropped to below 5% of the peak value. This is consistent with the findings in section 3.6 that 25nm of gallium would scatter 95% of the peak primary column intensity.

The graphs in figure 6.14 shows the background subtracted HAADF signal generated from the primary Type-3 columns for dumbbell 6. Figure 6.16 shows the background subtracted HAADF signal generated from the primary Type-3 columns for dumbbell 7. The solid blue lines represents the bulk gallium (dark blue) and bulk aluminium (light blue) primary columns. The black broken line is the data from the interfacial dumbbells where the background colour indicates the compositional changes. The first compositional change occurs at a depth of $7.2nm$ for dumbbell 6 and $14.4nm$ for dumbbell 7. The HAADF signal from dumbbell 6 (figure 6.14) changes from appearing like an aluminium column to a gallium column over a specimen thickness of $7.2 - 32nm$. At thicknesses of greater than $34nm$, the scattering from dumbbell 6 is greater than a fully populated gallium column. Likewise, the HAADF signal from dumbbell 7 (figure 6.16) changes significantly at the compositional change depth. However, in this case the column signal does not reach the same level of scattering as the complete gallium column.

This effect can be understood from the primary column intensity which is shown figures 6.15 and 6.17 for dumbbells 6 and 7 respectively. Figure 6.15 shows the intensity data from dumbbell 6, from inspection, the depth of the compositional change from aluminium to gallium occurs when the electron intensity on the primary column is high. With a high electron density on the primary column, the compositional change from a lower Z material to a higher Z material will result in a significant increase in the HAADF signal. Figure 6.17 shows the intensity data from dumbbell 7. Now the first compositional change occurs where the intensity on the primary column is reduced due to scattering off of the primary column. The compositional change at this depth results in reduced scattering from the atomic column which is apparent from the HAADF signal. The effect on the column ratio is clear from figure 6.12 where columns 6 and 7 deviate from the bulk GaAs at depths greater than $50nm$.

The final stage is to measure how the interface width varies with thickness for this model. Figure 6.18 details the width measurements made from the column ratio line profiles. The data has again been overlaid onto the experimental width measurements for the Type-A and Type-G interface types to allow a direct comparison. Figure 6.18 shows that the measured interface width in the top $30nm$ of the crystal and is a fair representation of the model configuration as at least two steps are observed. However at crystal thicknesses greater than $30nm$ the atomic columns begin to suffer from column

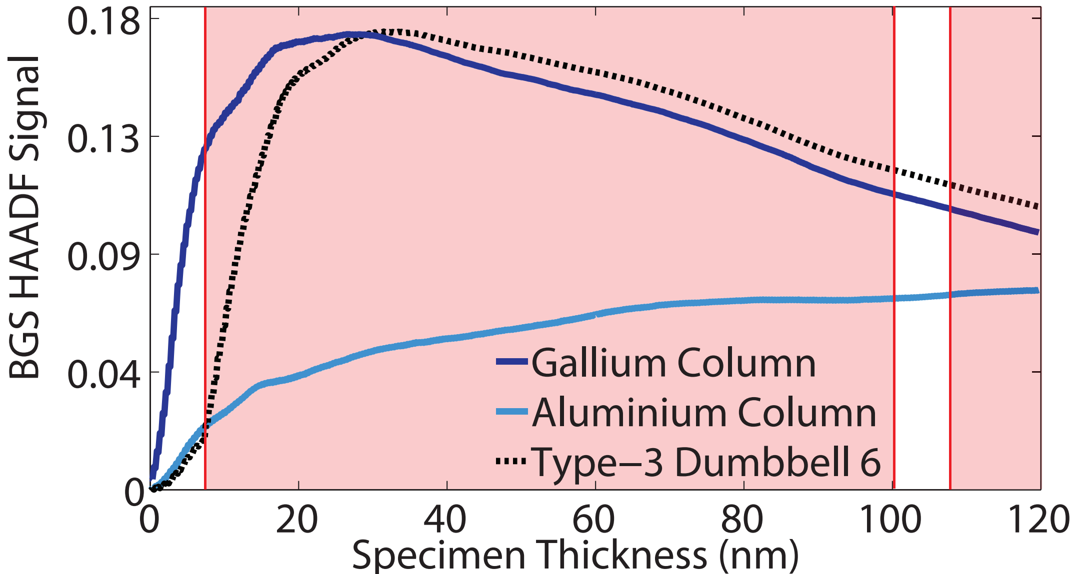

Figure 6.14 – The solid blue lines represents the background subtracted HAADF signal from the gallium (dark blue) and aluminium (light blue) primary columns. The black broken line is the data from the interfacial dumbbells and the background indicates the depth of the first compositional change from AlAs to GaAs which occurs at $7.2nm$. The HAADF signal from dumbbell 6 changes from appearing like an aluminium column to a gallium column from a specimen thickness of $7.2 - 32nm$ while at thicknesses of greater than $34nm$ the scattering from dumbbell 6 is greater than a fully populated gallium column.

ratio saturation. This saturation effect means that atomic dumbbells with a significant amount of gallium (i.e. $\sim 25nm$) will appear as a fully populated gallium column. The result of this effect is evident as the interfacial width does not increase after $30nm$ but instead tends to a constant width of 3 dumbbells. In reality, for thicknesses greater than $30nm$ the position of the interface appears to shift towards the bulk AlAs region and the interfacial width remains almost constant.

6.2.3.2 110nm Repeat Length (GaAs Projection)

The next model has again the same sawtooth structure with an identical repeat length of $110nm$ and an identical step length of $7.2nm$. However, the stepping pattern is shifted such that the material at the entrance face is now GaAs which produces an initial GaAs overhang. Figure 6.19 shows the schematic of the model which indicates the AlAs terracing now protrudes into the GaAs region. The model was then evaluated and the interface position and interface width was calculated for each slice of the structure. The interface position is overlaid onto the schematic in figure 6.19 and is indicated in red.

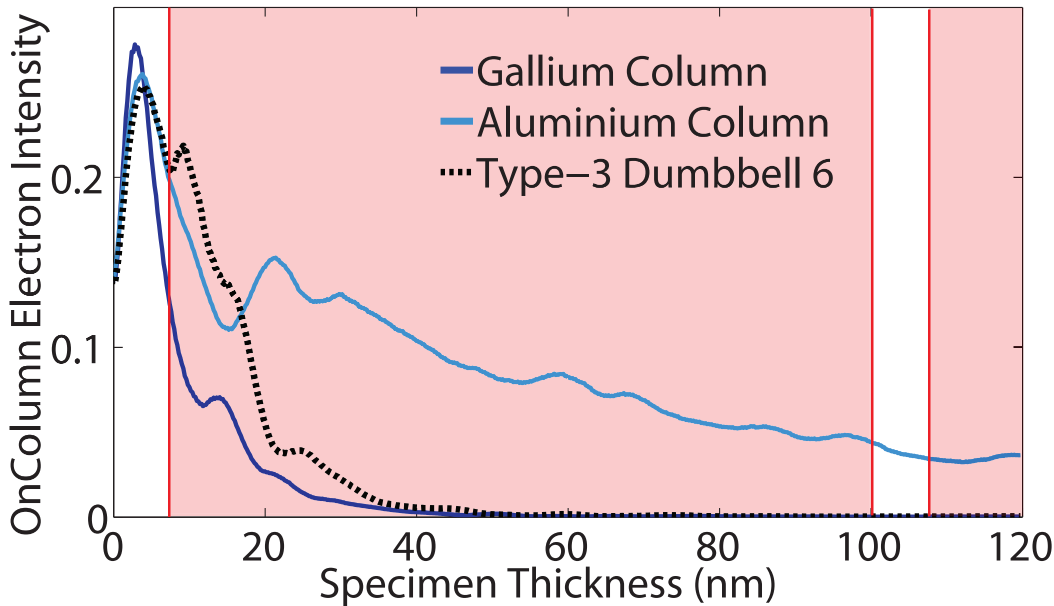

Figure 6.15 – The change in composition for dumbbell 6 occurs at a depth of $7.2nm$ and until this depth the intensity is consistent with a fully populated aluminium column. At this point the Type-3 column changes from aluminium to gallium and over the next $25nm$ the intensity on the column drops significantly. By a depth of $32nm$ the intensity on the primary column has dropped to less than 5% of the peak value

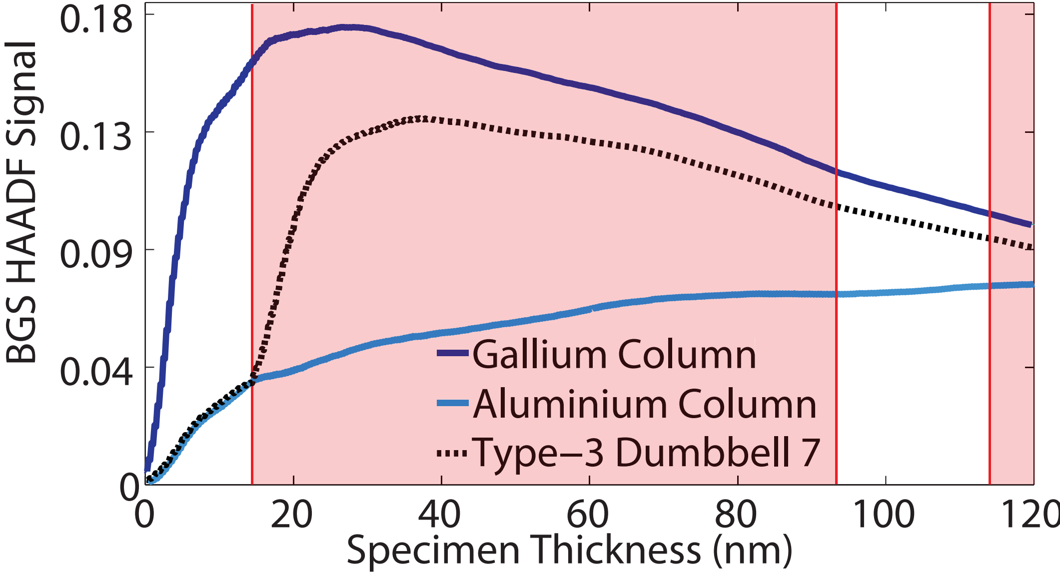

Figure 6.16 – The solid blue lines represents the bulk gallium (dark blue) and bulk aluminium (light blue) primary column intensity. The black broken line is the data from the interfacial dumbbells and the background indicates the depth of the first compositional change from AlAs to GaAs which occurs at $14.4nm$. The HAADF signal from dumbbell 7 changes significantly at the compositional change depth, however, the column signal does not increase to match the scattering from a complete gallium column.

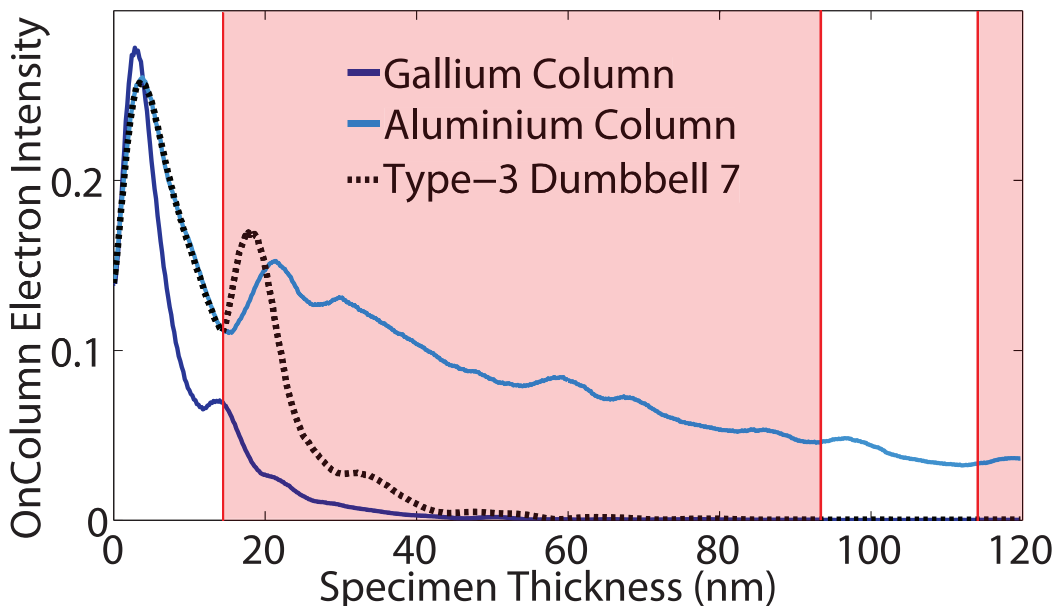

Figure 6.17 – The change in composition for dumbbell 7 occurs at a depth of $14.4nm$ and until this depth the intensity is again consistent with a fully populated aluminium column. By $38nm$ the on column intensity has dropped to below 5% of the peak value. This is consistent with the findings in section 3.6 that $\sim 25nm$ of gallium would scatter 95% of the peak primary column intensity.

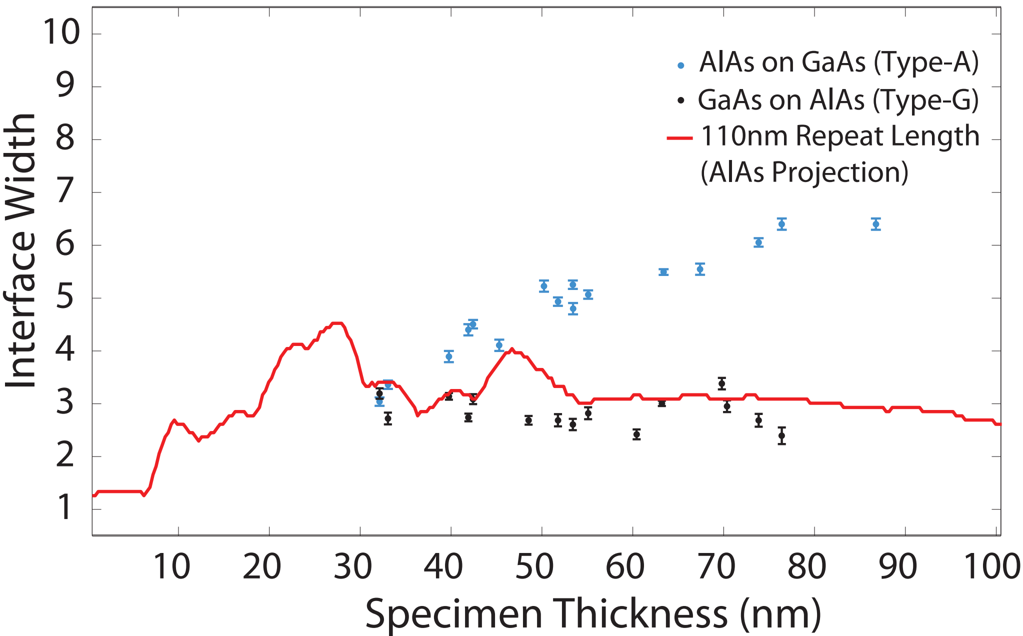

Figure 6.18 – This graph shows the measured interface width as a function of specimen thickness (red). The measured interface width from the model is overlaid onto the experimental measurements from figure 5.15 for comparison. The interface width increases over the first $30nm$ of the specimen thickness at which point the measured width drops to ~ 3 dumbbells and remains almost constant for the remainder of the model.

The schematic shows that for a specimen thickness of less than the step length (i.e. $<7.2nm$) the interface is abrupt and is located between dumbbells 11 and 12. This is reflected in the measured position of the interface in figure 6.20 which is also positioned between dumbbells 11 and 12 at depths of less than $7.2nm$. The position of the interface is also apparent in the column ratio line profiles shown in figure 6.21 which only shows the profiles at depths of $7nm$, $50nm$ and $120nm$ for clarity. The profile at $7nm$ (black) shows the interface position is located firmly between dumbbells 11 and 12, as should be the case. At a depth of $50nm$, it can be seen from the schematic that dumbbells 6-10 form the interface. However, the measured interface position is located between dumbbells 10 and 11. The column ratio profiles at this depth indicates that only dumbbells 9, 10 and 11 appear to form the interface and dumbbells 6, 7 and 8 have saturated and appear to form part of the bulk GaAs region. Section 3.6.1.2 detailed that the channelling depth of the gallium column was approximately $25nm$ which explains the reason that dumbbells 6, 7 and 8 are saturated and dumbbells 9, 10 and 11 are not. Dumbbells 6, 7 and 8 have $43.2nm$, $36nm$ and $28.8nm$ of gallium at the top of the Type-3 atomic columns respectively which are all greater than the channelling depth of gallium. Dumbbells 9, 10 and 11 have $21.6nm$, $14.4nm$ and $7.2nm$ of gallium at the top of the Type-3 atomic columns respectively which are all less than the channelling depth of gallium.This being the case the compositional changes in dumbbells 9, 10 and 11 can therefore be detected accounting for the shift in the interface position with increasing thickness. Figure 6.20 shows the measured interface width as a function of specimen thickness which is plotted with the experimental interface width measurements for comparison. The plot shows that the changes in the interface width are only an accurate representation of the actual interface width in the top $25nm$ of the crystal.

One interesting feature of this model is the difference in the dynamics of dumbbells 10 and 11. The schematic shown in figure 6.19 indicates that dumbbell 10 has a higher gallium concentration than dumbbell 11. This is clear also from the line profiles in figure 6.21 where at $7nm$ the scattering from dumbbell 10 is similar to that of dumbbell 11 which should be the case as the interface is abrupt at this point and the specimen is thin enough that the proximity of the interface is not an issue. At $50nm$ the line profiles show that the column ratio from dumbbell 10 is again higher than that of dumbbell 11 due to the higher gallium content at the entrance of dumbbell 10. However the issue

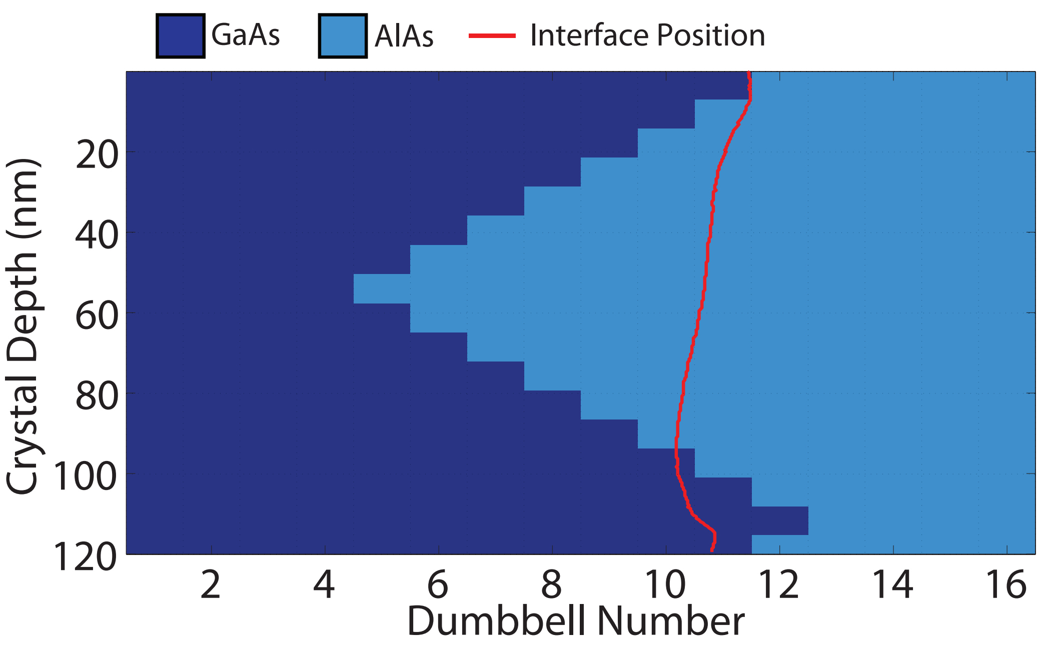

Figure 6.19 – This diagram shows the schematic of the (GaAs projection) sawtooth interface where the characteristic repeat length is 110nm. The step length was chosen to be 7.2nm to be consistent with step length measurements from a HRTEM study into MBE grown GaAs - AlAs heterostructures [102]. The measured interface position is overlaid onto the model schematic.

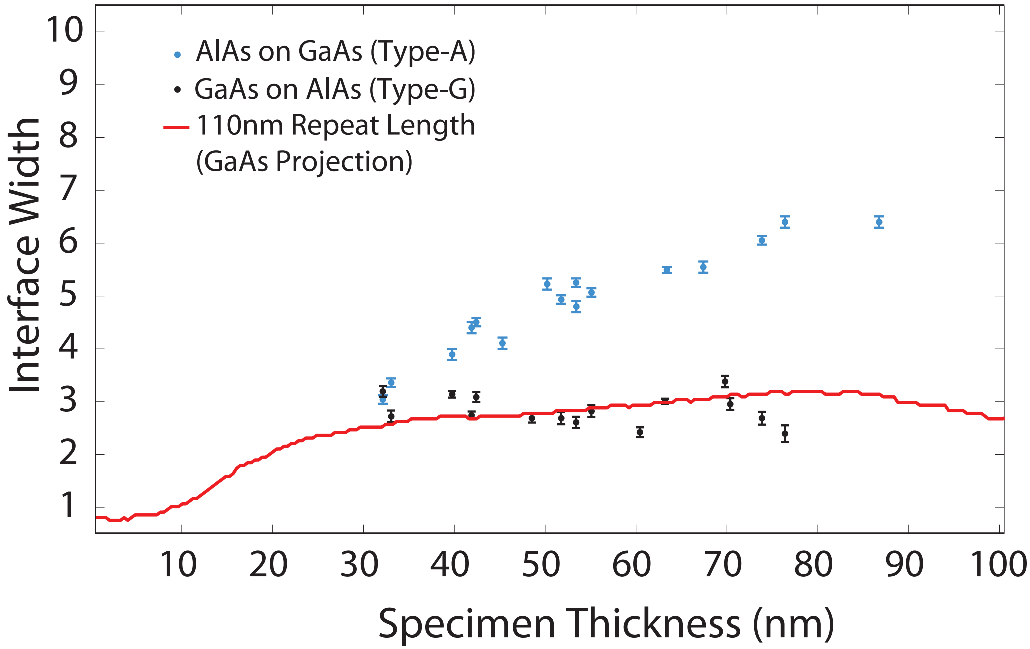

Figure 6.20 – This graph shows the measured interface width as a function of specimen thickness (red). The measured interface width from the model is overlaid onto the experimental measurements from figure 5.15 for comparison. The interface width increases over the first 25nm of the model after which the increase is gradual to a depth of 80nm.

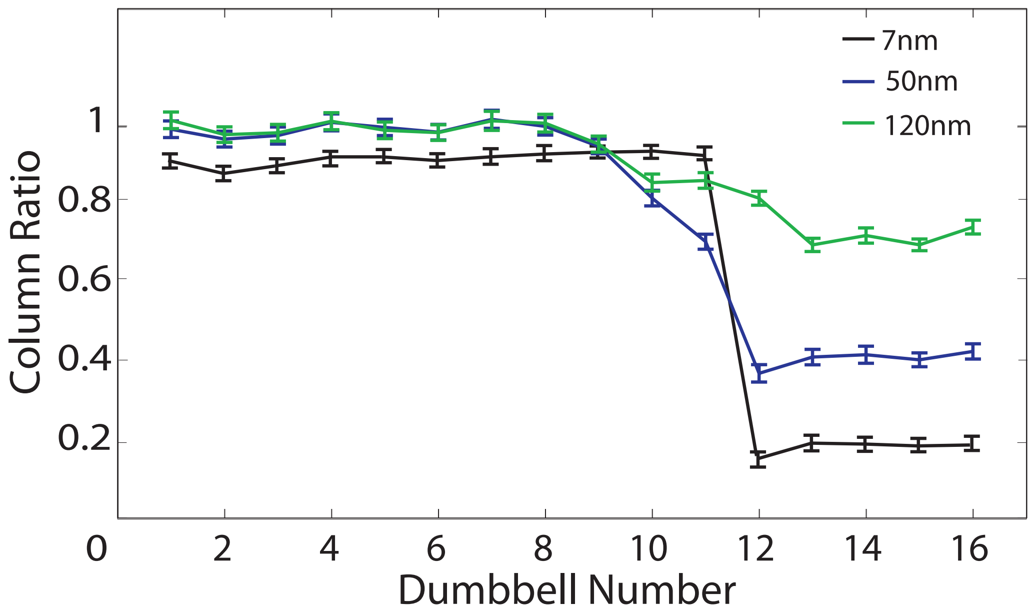

Figure 6.21 – A series of column ratio line profiles at specimen thicknesses of $7nm$, $50nm$ & $120nm$. The line profiles show the interface position gradually shift towards the bulk GaAs region with increasing thickness. This shift is due in part to the compositional changes of dumbbells 10 and 11 that occur near the crystal surface and in part to the change in background scattering due to the change of structure under the GaAs overhang.

arises for the profile at a depth of $120nm$ which now indicates that the column ratio of dumbbells 10 and 11 are almost identical. The overall GaAs content of dumbbells 10 and 11 are now 36% and 24% respectively but the column ratios do not indicate this difference.

This difference can be understood by again investigating the electron intensity down each of the Type-3 atomic columns for dumbbell 10 and 11. The graph in figure 6.23 shows the primary Type-3 column intensity (broken black) for dumbbell 10 along with the electron intensity down a fully populated gallium (dark blue) and aluminium (light blue) column. This column contains two compositional changes which are indicated by the vertical red lines. The first compositional change from GaAs to AlAs is at a depth of $14.4nm$ and the second compositional change is from AlAs back to GaAs and occurs at a depth of $93.6nm$. The graph shows that in the top section of the on-column intensity of dumbbell 10 is equivalent to a fully populated gallium column. However, after the first compositional change a residual amount of electron intensity remains on the column and channels down the aluminium section of the column. This residual electron intensity is then scattered when it reaches the second compositional change to

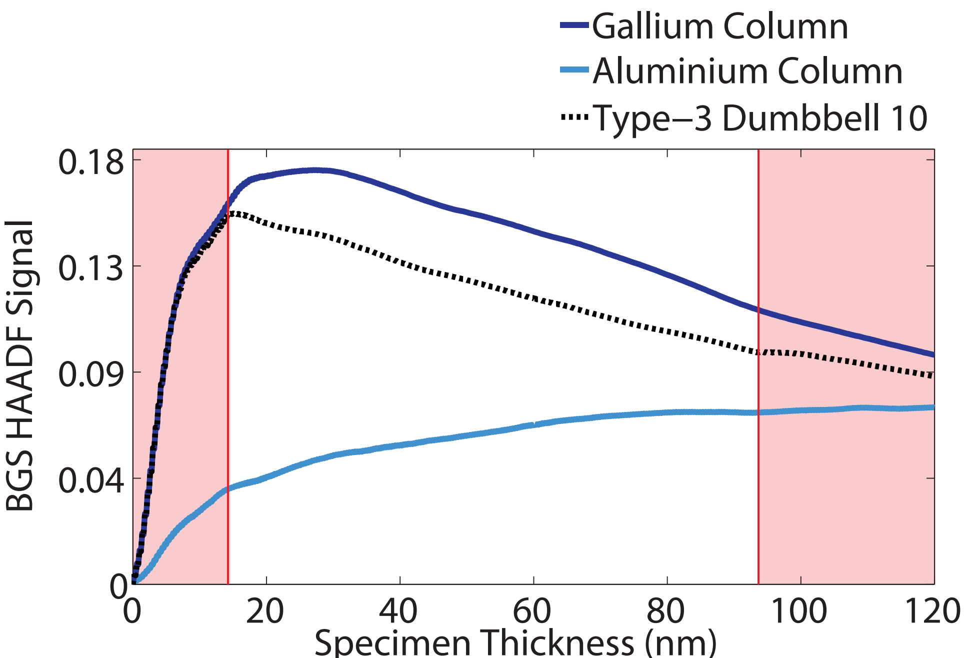

Figure 6.22 – A graph of the generated HAADF signal from the Type-3 column of dumbbell 10 (broken black). The background indicates the change in composition from the high Z material (red) to the low Z material (white). The HAADF signals from the Type-3 columns of single crystal GaAs (dark blue) and AlAs (light blue) are also shown for comparison.

gallium at the exit face of the crystal.

Figure 6.22 shows the background subtracted HAADF signal generated from the Type-3 column of dumbbell 10 (broken black) and again is overlaid onto the equivalent signals from a fully populated gallium and aluminium column. The plot also indicates the depths of the compositional changes down the atomic column by the change in background colour where the red region is the higher Z material. It is clear that at a thickness of less than $14nm$ the signal generated from the Type-3 column of dumbbell 10 is equivalent to a fully populated gallium column. At the first compositional change (GaAs to AlAs) the background subtracted signal from dumbbell 10 drops and has a negative gradient which is an indication that a significant percentage of the probe intensity is scattered off the primary column and that most of the HAADF signal (at that depth) is being generated from the background scattering. There is also a small change in the generated signal at the second compositional change (AlAs to GaAs) at a depth of $93.6nm$ as the remaining intensity on the primary column is scattered.

The graph in figure 6.25 shows the primary column intensity on the Type-3 column of dumbbell 11 which is again overlaid onto the primary column intensity for a fully populated gallium and aluminium column. The compositional changes are also

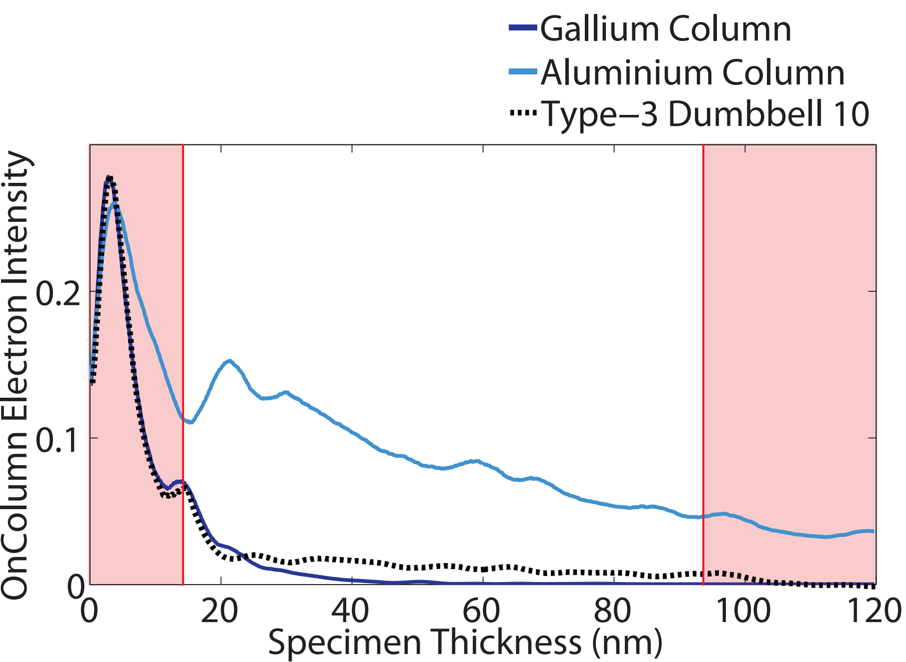

Figure 6.23 – A graph of the primary column intensity on the Type-3 column of dumbbell 10 (broken black). The background indicates the change in composition from the high Z material (red) to the low Z material (white). The primary column intensities on the Type-3 columns of single crystal GaAs (dark blue) and AlAs (light blue) are also shown for comparison.

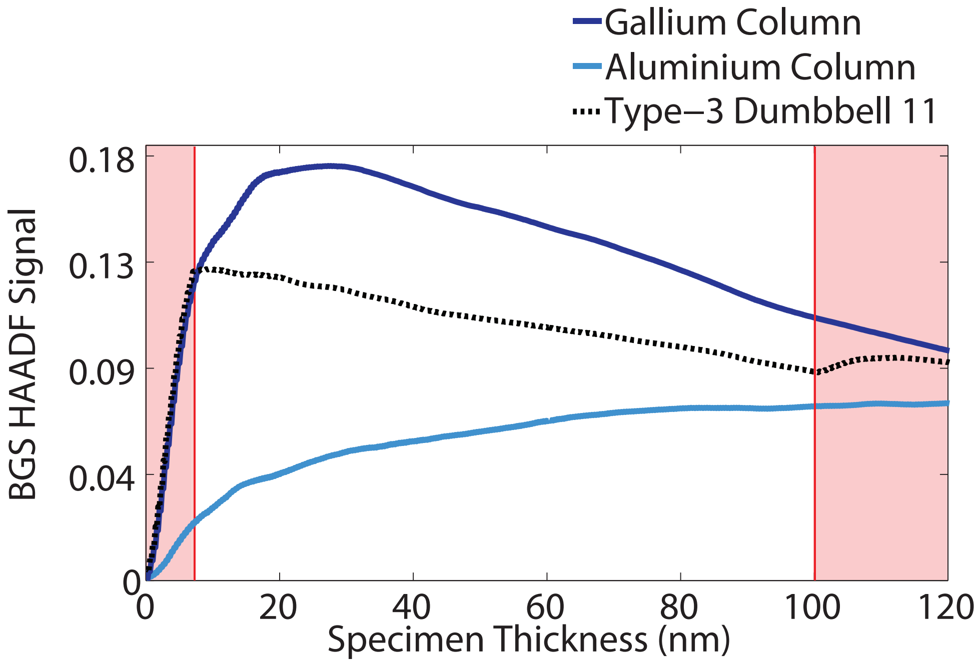

Figure 6.24 – A graph of the generated HAADF signal from the Type-3 column of dumbbell 11 (broken black). The background indicates the change in composition from the high Z material (red) to the low Z material (white). The HAADF signals from the Type-3 columns of single crystal GaAs (dark blue) and AlAs (light blue) are also shown for comparison.

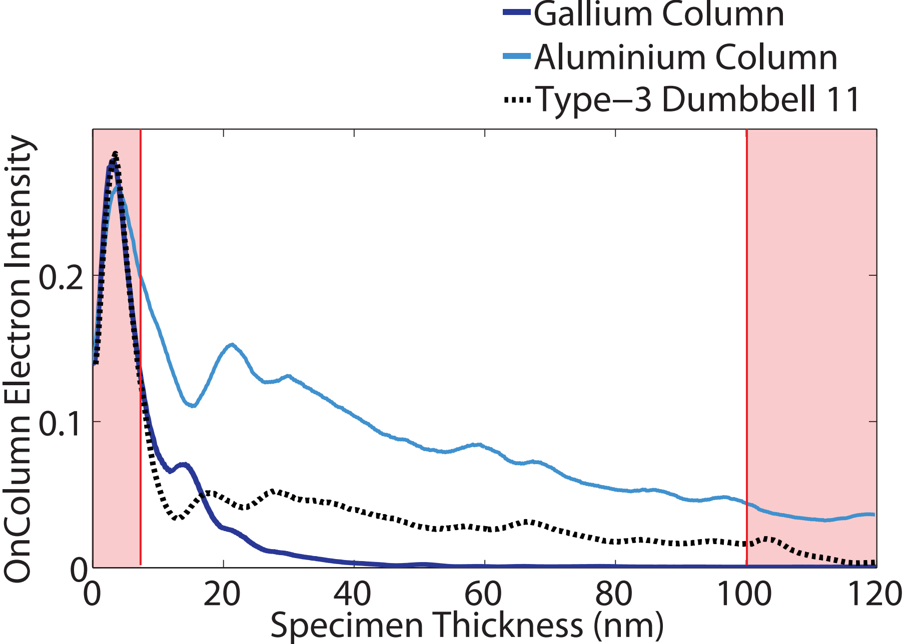

Figure 6.25 – A graph of the primary column intensity on the Type-3 column of dumbbell 10 (broken black). The background indicates the change in composition from the high Z material (red) to the low Z material (white). The primary column intensities on the Type-3 columns of single crystal GaAs (dark blue) and AlAs (light blue) are also shown for comparison.

indicated by the red vertical lines and this time the first compositional change from GaAs to AlAs is at a depth of $7.2nm$ and the second compositional change from AlAs to GaAs occurs at a depth of $101nm$. In this case there is a smaller amount of gallium at the top of the Type-3 column and therefore at the first compositional change there is a larger percentage of the probe still on the primary column. This is evident from the graph which shows more intensity channelling down the AlAs region of the column. This electron intensity is also scattered by the second change in composition (AlAs to GaAs) at the exit face of the column. The plot in figure 6.24 shows the background subtracted HAADF signal generated form dumbbell 11 again overlaid onto the background subtracted HAADF signals from a fully populated gallium and aluminium column. In the section of the column from $0 - 7.2nm$ the scattering from the column is again equivalent to a fully populated gallium column. At the compositional change the signal also drops and shows a negative gradient. However, the magnitude of the gradient is not as large as the case for dumbbell 10. This indicates that the intensity on the primary column is larger and the proportion of scattering coming from the primary column is also larger. The effect of having a larger percentage of the probe intensity on the primary column is evident at the second compositional change of $101nm$. In

this case there is a significant increase in the scattering from the primary column of dumbbell 11 to such an extent that by $120nm$ the scattering from dumbbells 10 and 11 are equivalent.

This is a clear indication that while compositional changes at the entrance face of a crystal are important, multiple compositional changes within a single atomic column can produce scattering effects that are counter intuitive.

6.2.3.3 18nm Repeat Length (AlAs Projection)

The next sawtooth interface structure is shown in the left of figure 6.26 where the repeat length is comparable to the channelling depth of gallium. The relative position of the repeat pattern was selected to form an AlAs projection (i.e. the probe is first projecting through AlAs). The characteristics of this interface are similar to the long repeat length AlAs projection interface in section 6.2.3.1 in that the measured interface position (shown in red over the schematic) indicates that the location of the interface also tracks the gallium content in the Type-3 columns. The measured interface position shifts from between dumbbells 5 and 6 to a position past dumbbell 10 in the top $10nm$ of the structure. As the repeat length is comparable to the channelling depth of gallium the change of composition below the first terrace is detected which occur as at a depth between $10-20nm$. This change in composition causes the measured interface position to move back towards dumbbell 10. The second terrace also affects the interface position and a shift in position is measured at a depth of $\sim 25nm$. However, as the probe is projecting through GaAs at this depth the measured interface position is a poor representation of the average interface position. The measured interface width is shown in figure 6.26 and reflects the rapid change in interface width due to the first terrace. From $0 - 10nm$ the measured interface width is a reasonable representation of the actual interface width. However, as the thickness of the crystal increases and becomes comparable to the channelling depth of the Type-3 column the ability to differentiate between the composition of the columns becomes impossible. Figure 6.28 shows the column ratio profiles for this model at depths of $4nm$, $10nm$, $50nm$ and $120nm$ and shows the rapid motion of the measured interface position in the top $10nm$ of the model.

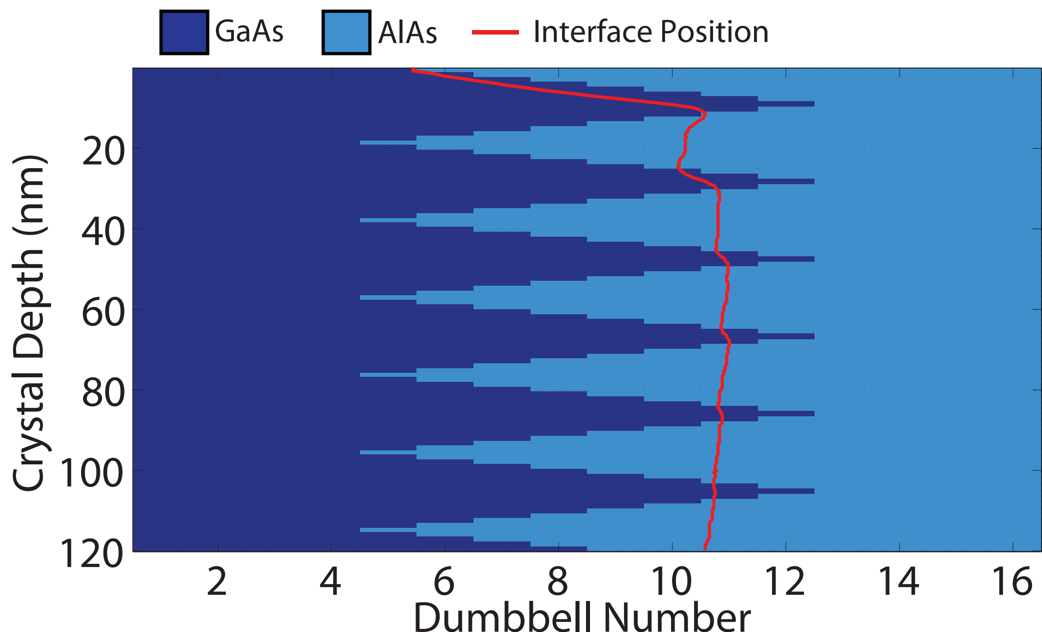

Figure 6.26 – This diagram shows the schematic of the (AlAs projection) sawtooth interface where the characteristic repeat length is 18nm. The step length was chosen so that the repeat length was comparable to the channelling depth of GaAs. The measured interface position is overlaid onto the model schematic indicating that the interface position starts between dumbbells 5 and 6 and quickly moves to a position near dumbbell 10 by a depth of 10nm. As the thickness of the sample increases the measured interface position remains between dumbbells 10 and 11.

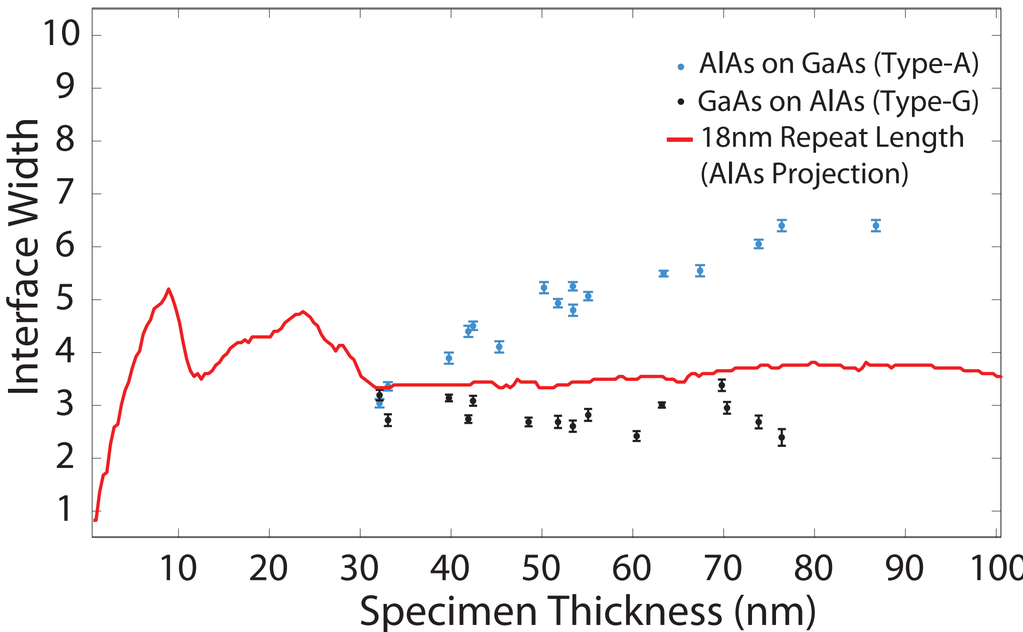

Figure 6.27 – This graph shows the measured interface width as a function of specimen thickness (red). The measured interface width from the model is overlaid onto the experimental measurements from figure 5.15 for comparison. The measured interface width increases dramatically in the first 10nm of this model. In the top 30nm there are some fluctuations of the measured width, however at depths greater than 30nm the measured width remains between 3 and 4 dumbbells.

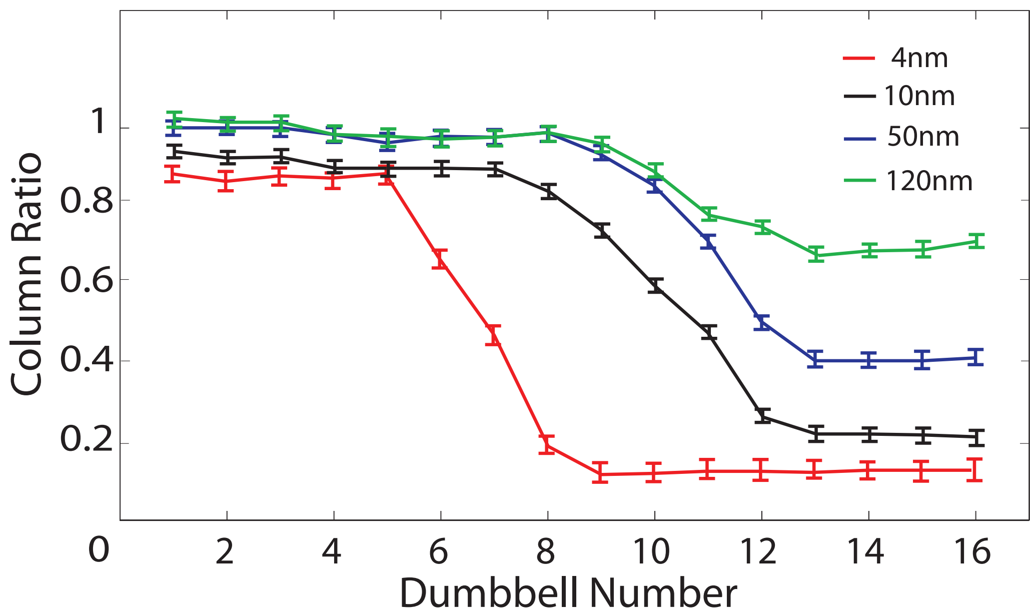

Figure 6.28 – A series of column ratio line profiles at specimen thicknesses of 4*nm*, 10*nm*, 50*nm* & 120*nm*. The line profiles show the interface position quickly shift towards the bulk AlAs region with increasing thickness. This quick change in the interface position is due to the short repeat length of the model which has the first repeating terrace within the top 20*nm* of the model.

6.2.3.4 18nm Repeat Length (GaAs Projection)

By shifting the repeat pattern depth, a GaAs projection can be formed. The schematic for this type of model can be seen in figure 6.29. The measured characteristics from this model are, however, very different to the AlAs projection which is apparent from the overlaid interface position in figure 6.29. This plot shows that the perceived interface position is initially located near to the bulk AlAs region between dumbbells 11 and 12 and gradually moves towards the bulk GaAs region with increasing thickness. The measured interface width also exhibits a distinct difference from the AlAs projection model and figure 6.30 shows that the maximum interface width for this model is considerably larger. Furthermore, the measured interface width also appears wider over a larger range of depths than in the AlAs projection case. The difference in the measured interface position and the measured interface width can be attributed to the small amounts of GaAs at the entrance face of this model. The resulting high angle scattering from an atomic column is very sensitive to compositional changes in the top few *nm*, particularly when the change of composition is from a high Z to low Z material. Figure 6.31 shows the column ratio profile and gives an indication of the

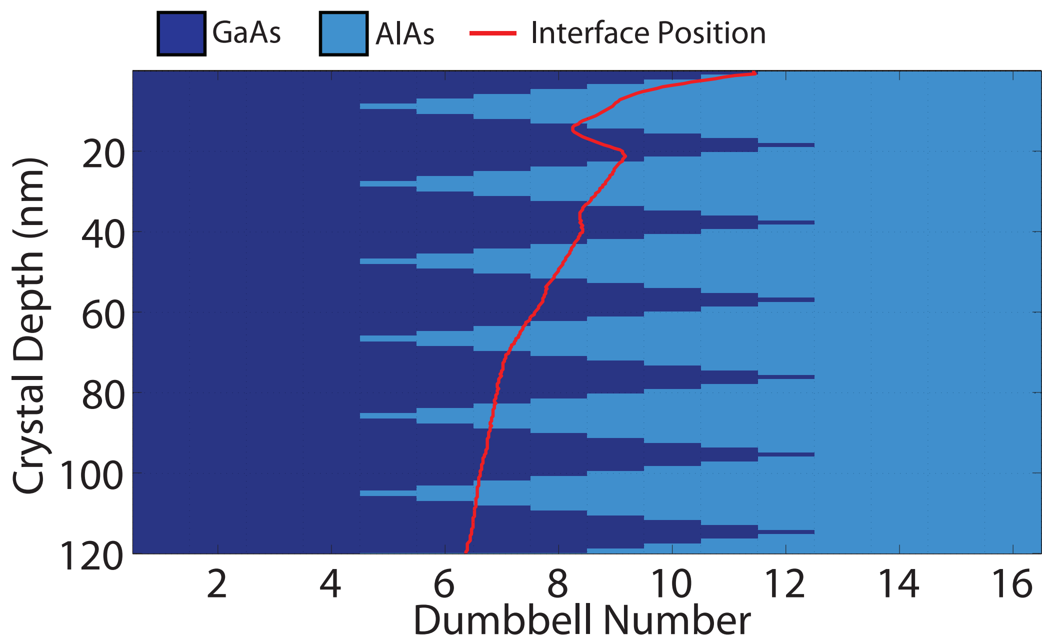

Figure 6.29 – This diagram shows the schematic of the (GaAs projection) sawtooth interface where the characteristic repeat length is $18nm$. The measured interface position is overlaid onto the model schematic indicating that the interface position starts between dumbbells 11 and 12 and quickly moves to a position near dumbbell 8 by a depth of $20nm$ and as the thickness of the sample increases it continues to shift towards the bulk GaAs. This is in contrast to the AlAs projection in figure 6.26.

difference in scattering from each of the dumbbells. For instance, from the schematic in figure 6.29, dumbbell 5 consists mainly of GaAs but has 6 sections within the columns consisting of AlAs. From the column ratio profile in figure 6.31, dumbbell 5 appears like a fully populated GaAs dumbbell over the entire simulation depth ($0 - 120nm$). This behavior is confirmed by plotting the generated HAADF signal from the Type-3 column of dumbbell 5 which can be seen in the plot of figure 6.32. This plot shows the compositional changes that occur down the atomic column where the red sections of the graph correspond to depths where the higher Z material is located. The six sections of AlAs can clearly be seen in this plot. However, the AlAs regions are small and do not significantly affect the overall scattering from the atomic column and the signal is comparable to a fully populated gallium column (dark blue).

An interesting feature of this model is the column ratio values for dumbbells 6, 7 and 8. The column ratio profile in figure 6.31 shows that from a specimen thickness of $10nm$ to $120nm$ the variation of the column ratio for these dumbbells is very small. This is a direct result of the compositional change from gallium to aluminium in the first few nm of the Type-3 columns. For a fully populated gallium column, this is where

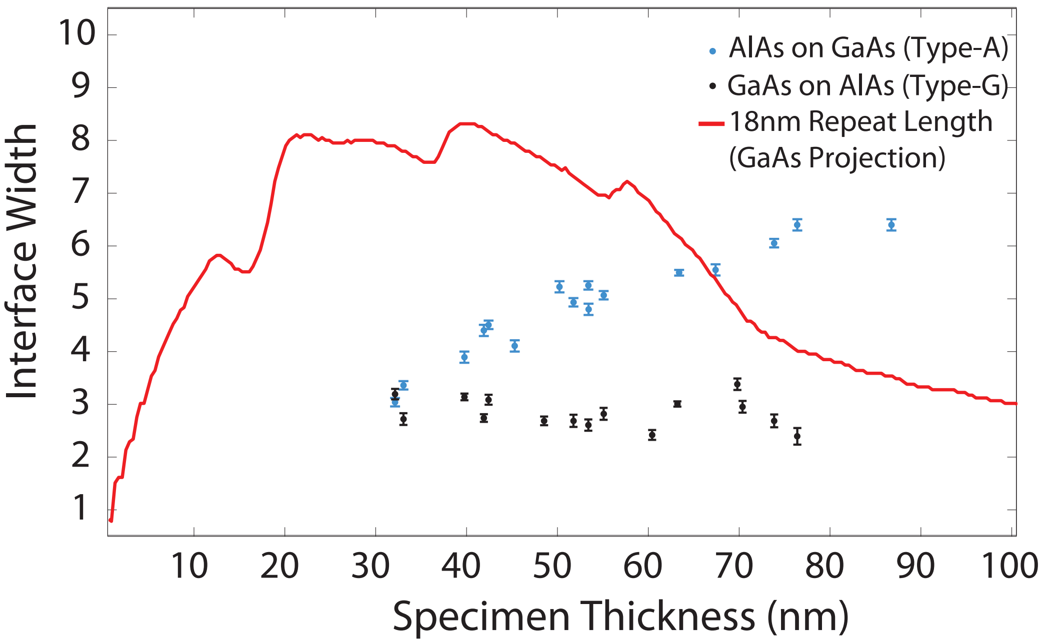

Figure 6.30 – This graph shows the measured interface width as a function of specimen thickness (red). The measured interface width from the model is overlaid onto the experimental measurements from figure 5.15 for comparison. The measured interface width increases dramatically in the first 25nm of this model to a width of ~ 8 dumbbells. However, as the thickness of the specimen increases beyond 40nm the measured width begins to drop (due to atomic column saturation) which is again different to the AlAs projection shown in figure 6.27.

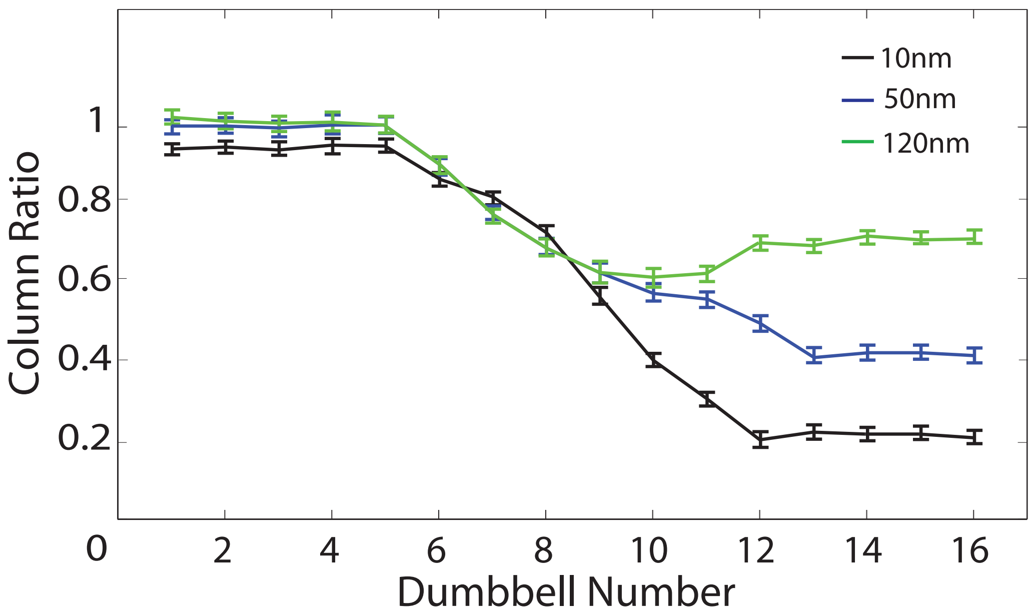

Figure 6.31 – A series of column ratio line profiles at specimen thicknesses of 10nm, 50nm & 120nm. The line profiles show the interface position gradually move towards the bulk GaAs region with increasing thickness. The column ratio profile for the GaAs projection is very different to that seen in the AlAs projection column ratio profiles (figure 6.28).

a significant amount of the HAADF signal is generated from the primary column. It is in this region that there are strong dynamical scattering effects as the probe scatters between the primary atomic column and the adjacent columns. A compositional change from a high-Z material to a low-Z material in this region affects this scattering and as a result changes the generated HAADF signal. Figure 6.33 shows the HAADF signal from dumbbell 7 and indicates that there is a compositional change at a depth of 6nm which is in this region of strong dynamical scattering. Unlike the compositional change within dumbbell 5 (figure 6.32) which does not affect the HAADF signal significantly, the compositional changes within dumbbell 7 greatly reduce the signal generated by this atomic column.

For dumbbells 9, 10 and 11 this effect is so significant that for a 120nm thick crystal the scattering from the Type-3 atomic column is *less* than that of a fully populated aluminium column. This can be seen in the column ratio line profile of figure 6.31 where the 120nm profile (green) show that the column ratio for these dumbbells (9, 10 & 11) is less than those from the bulk AlAs region (13, 14, 15 & 16). The generated HAADF signal from dumbbell 10 can be seen in figure 6.34. This plot clearly shows that, at depths of 80nm and greater, the scattering from the Type-3 column of dumbbell 10

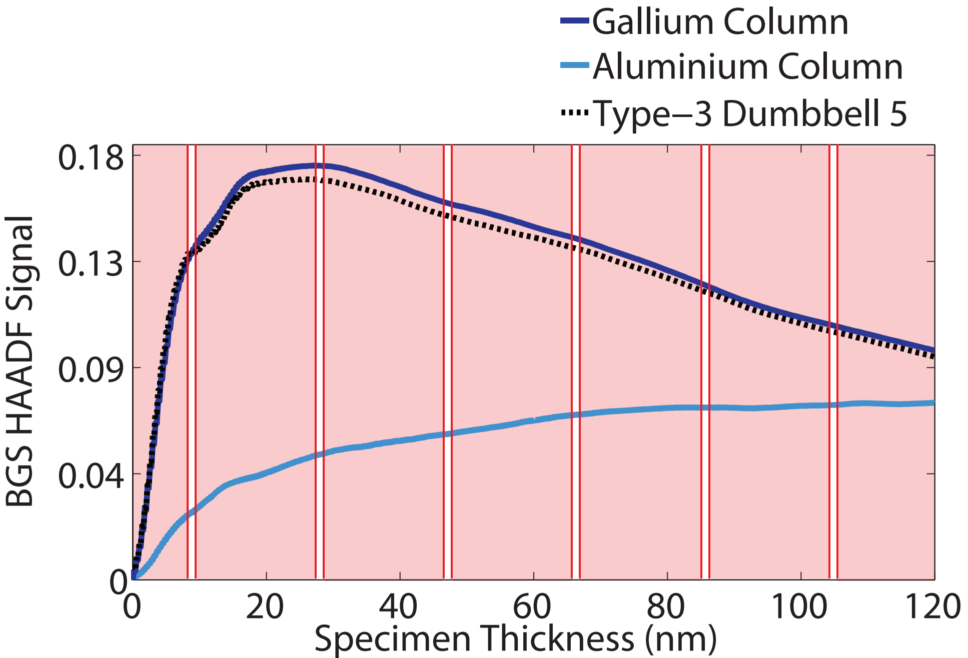

Figure 6.32 – A graph of the generated HAADF signal from the Type-3 column of dumbbell 5 (broken black). The background indicates the change in composition from the high Z material (red) to the low Z material. The HAADF signals from the Type-3 columns of single crystal GaAs (dark blue) and AlAs (light blue) are also shown for comparison.

drops to below that of a fully populated aluminium column.

The resulting HAADF signal is therefore very sensitive to the exact composition of the atomic column at the entrance of the specimen and it is this sensitivity that causes these short repeat length models to have very different characteristics. However, of the stepped interfacial structures investigated, none of the models exhibit interface characteristics that are consistent with the experimental measurements from section 5.4.2.

6.2.4 Diffused Interface

Diffusion occurs in the presence of a chemical potential gradient and, in general, the atoms will move in such a way as to remove the gradient. If the atom jumps are random, the flux of atoms is proportional to the concentration gradient. For a GaAs - AlAs interface inter-diffusion occurs so that the Type-3 atoms are redistributed resulting in a diffuse interface. Two distinct models for inter-diffusion were developed the first of which uses a linear concentration gradient from the bulk GaAs to the bulk AlAs region. The second model is formed using data taken from a detailed study of diffusion

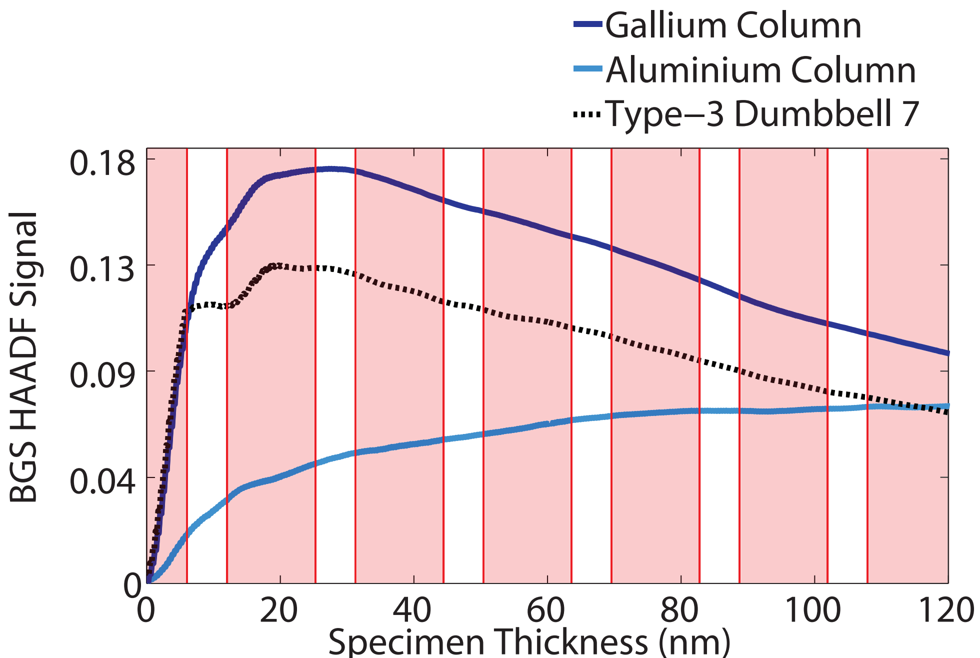

Figure 6.33 – A graph of the generated HAADF signal from the Type-3 column of dumbbell 7 (broken black). The background indicates the change in composition from the high Z material (red) to the low Z material. The HAADF signals from the Type-3 columns of single crystal GaAs (dark blue) and AlAs (light blue) are also shown for comparison.

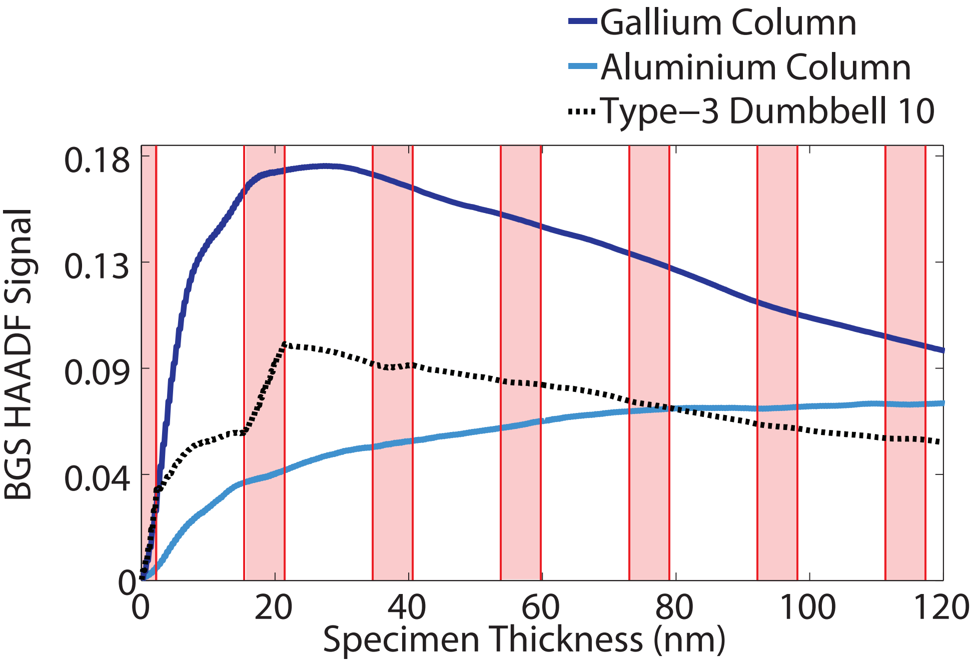

Figure 6.34 – A graph of the generated HAADF signal from the Type-3 column of dumbbell 10 (broken black). The background indicates the change in composition from the high Z material (red) to the low Z material. The HAADF signals from the Type-3 columns of single crystal GaAs (dark blue) and AlAs (light blue) are also shown for comparison.

in III-V superlattices. In this study, concentration profiles of GaAs - AlAs interfaces were calculated using a surface segregation model which is described in section 6.2.4.2.

6.2.4.1 Linear Diffusion Model

The first type of diffused interface that was considered consisted of a linear concentration gradient of the Type-3 atomic columns between the bulk GaAs and AlAs regions. Figure 6.35 shows the details of the gallium and aluminium concentrations for interfacial dumbbells 1 to 16.

The atomic species within each interfacial column was varied using a random number generator to obtain the required concentration. A series of ten models with the same concentrations were created and calculated. The calculation results from these ten models were then averaged together which is the equivalent of averaging together the atomic rows in the column ratio maps. Figure 6.36 shows a schematic for the diffuse interface. While this linear model is not physically accurate it provides a simple starting point to investigate partially populated atomic columns. Furhtermore, it will give a broad overview of the resulting HAADF signals from such configurations.

The gradual change in composition across the diffuse interface is reflected in the column ratio profiles shown in figure 6.37. A series of profiles are shown for thicknesses of $10nm$, $30nm$, $50nm$ and $120nm$. These profiles give an indication of the overall change in the interfacial characteristics as the specimen thickness increases. At a thickness of 10nm, the gradual change in composition forms a wide interface where all eight interfacial dumbbells contribute to the interface width. As the thickness is increased the columns containing higher concentrations of gallium begin to saturate causing the apparent interface position to shift towards the bulk AlAs region. This change in interface position is shown in figure 6.38 with the interface position starting near dumbbell 8 for a very thin crystal and gradually moving across to dumbbell 12 with increasing thickness. For this linear diffusion model, the interface width is initially wide and the atomic columns progressively saturate. This causes the apparent interface width to narrow with increasing thickness. This effect can be seen in figure 6.39 where the interface width is initially wide for thicknesses of less than $10nm$ and then progressively narrows with increasing thickness and tends towards a width of less than 2 dumbbells for very large specimen thicknesses.

The column ratio profiles also indicate the limitations when detecting partially

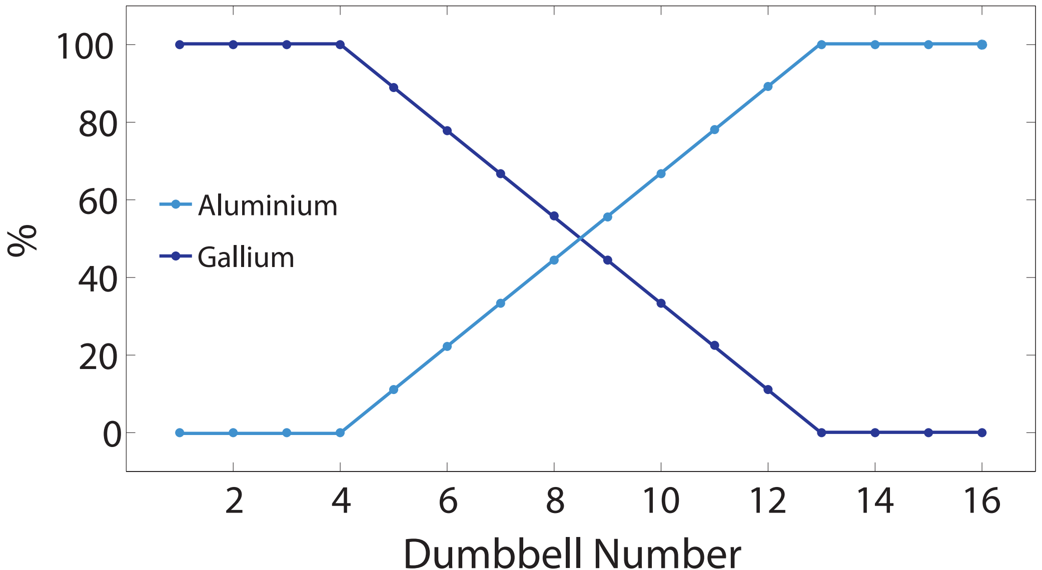

Figure 6.35 – The Type-3 atomic column gallium and aluminium concentration for the linear diffusion model. While this is not a physically accurate diffusion model it provides a basic understanding of the HAADF signal generated from partially populated atomic columns.

populated atomic columns. In particular dumbbell 12 has a gallium concentration of $\sim 11\%$ and the column ratio profile (figure 6.37) indicates that over a large thickness range this will be detectable as an interfacial dumbbell as the column ratio always falls between that of bulk GaAs and AlAs. However, for typical TEM specimen thicknesses of $30nm$ atomic columns containing up to 55% Al (i.e. dumbbells 5-8) will have a column ratio that is comparable with bulk GaAs. This indicates a significant complication when attempting to characterise this type of diffuse interface from a single HAADF image using a thin specimen.

6.2.4.2 Segregation Model

The broadening of an interface during its formation at moderate temperatures is generally described by thermodynamical models based on the difference of the bulk and surface chemical potentials. McLean's equation describes a quantitative model involving balancing the systems entropy and chemical potential [104, 105]. However, for III-V binary and ternary compounds, the surface region has a natural parameter which is different from the substrate because of the compositional difference. The resulting strain therefore requires an additional elastic constant term. This extended relation is described by Moison et al. [103] and was used to develop a model of surface segregation

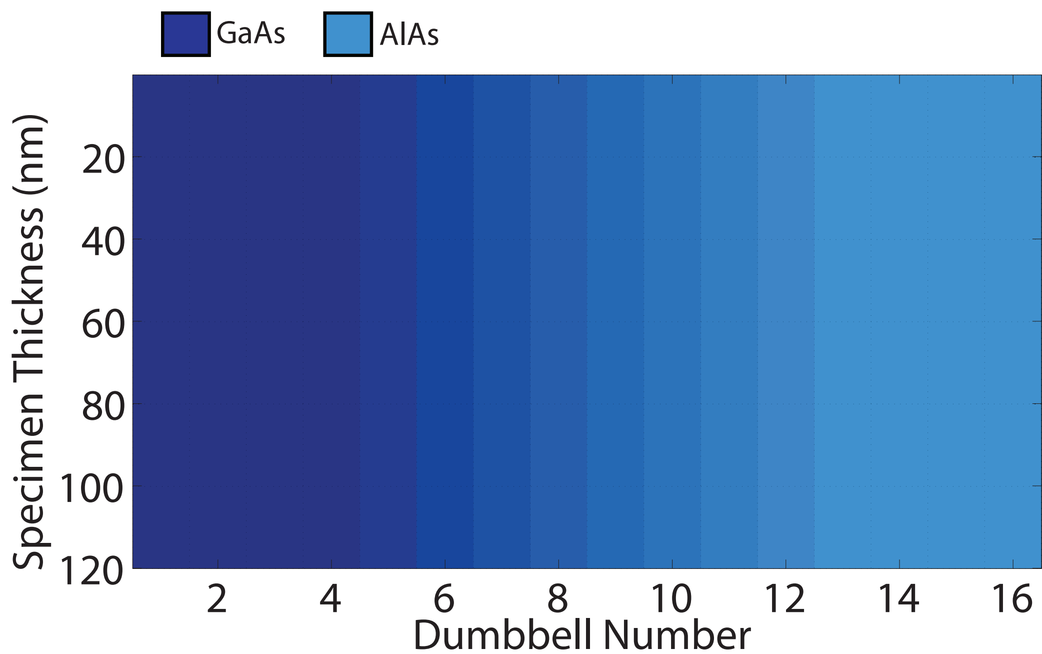

Figure 6.36 – The model schematic for the linear diffusion model. The atomic configuration for this model was generated using a random number generator. The concentration of each interfacial dumbbell can be specified using a fraction of the segregation species. Ten random atomic configurations were calculated and the results averaged together.

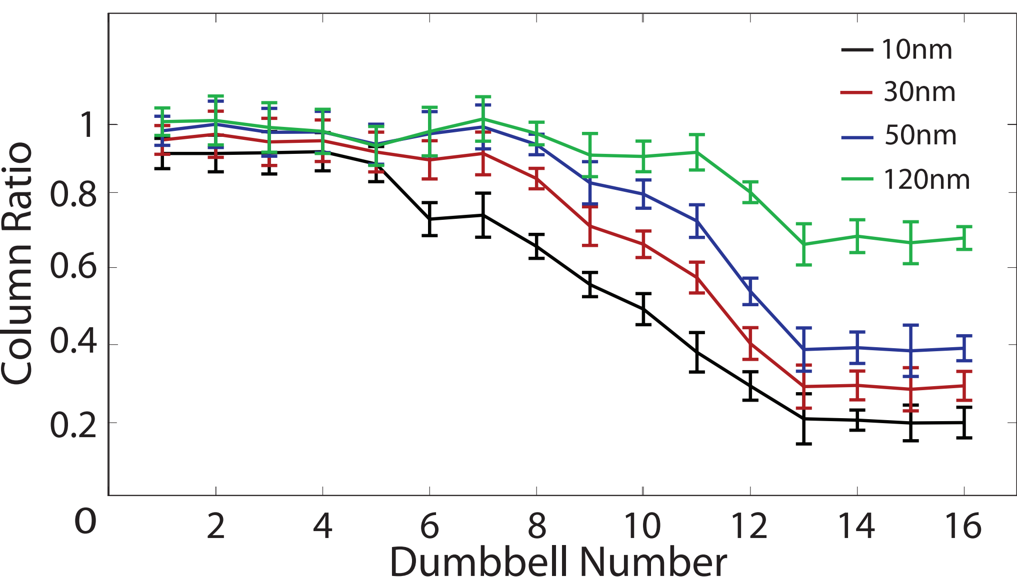

Figure 6.37 – A series of column ratio profiles for the linear diffusion model at a specimen thicknesses of $10nm$, $30nm$, $50nm$ & $120nm$. The profiles reveal that the measured interface position moves towards the bulk AlAs region which is due to the dumbbells with a higher gallium concentration saturating.

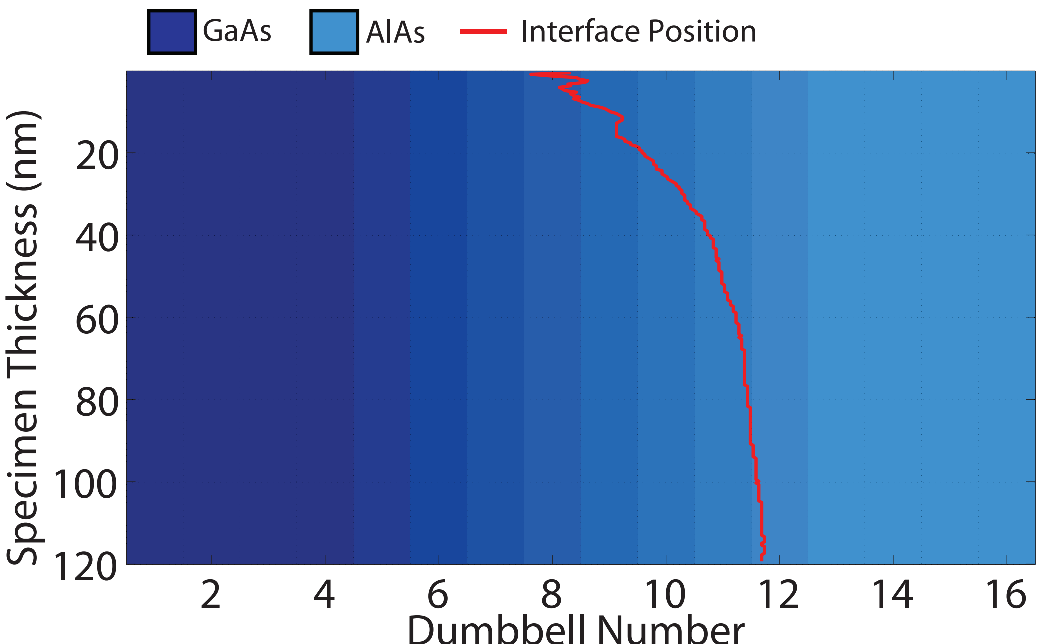

Figure 6.38 – This diagram shows the schematic of the linear diffusion model. The measured interface position (red) is overlaid onto the model schematic indicating that the interface position starts between dumbbells 7 and 8 and moves towards the bulk AlAs region finishing at a position near dumbbell 12 at a depth of $120nm$. This gradual motion of the measured interface position is due to the column ratio saturation.

in III-V heterostructures. Furthermore, this model was used to develop concentration profiles of a MBE grown GaAs - AlAs short-period superlattice (10ML x 10ML) grown on a GaAs substrate (@ $800K$). From this model, the two types of interfaces behaved differently and the Type-A interface exhibited a gradual change in composition over 8 monolayers. The model for the Type-G interface showed an abrupt compositional change over no more than 4 dumbbells. The compositional change profile for the Type-A interface can be seen in figure 6.40 and the profile for the Type-G interface is shown in figure 6.45.

The segregation model conditions are similar to the growth conditions of sample C102 which are detailed in section 5.4. These study results can therefore serve as a model for diffusion within a GaAs - AlAs superlattice such as that in sample C102. The multislice simulation results for the Type-A and Type-G models are detailed in the following sections.

Type A Interface The Type-A interface is formed when AlAs is grown on a GaAs surface. The concentration profile developed from the segregation model can be seen in figure 6.40. When AlAs is deposited on a GaAs surface, the Type-3 atom segregation

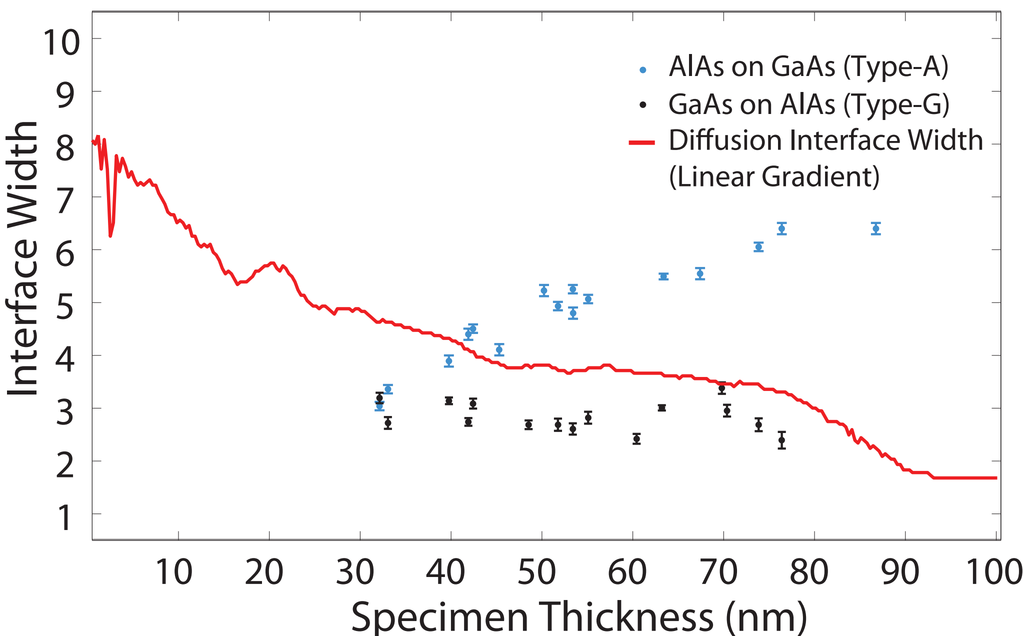

Figure 6.39 – This graph shows the measured interface width as a function of specimen thickness (red). The measured interface width from the model is overlaid onto the experimental measurements from figure 5.15 for comparison. For a thin specimen the gradual variation of the gallium concentration across the interface is detectable and the interface width spans the full 8 dumbbells. As the thickness of the specimen increases the columns with a high gallium content (>50%) saturate and appear like a fully populated GaAs dumbbell. This causes a shift in the apparent interface position and a reduction of the measured interface width.

causes diffusion over many mono-layers. These concentration values were used when forming the crystal input files and 10 random configurations using these concentrations were generated. The calculation results of each configuration were averaged together. The schematic for this Type-A diffusion model is shown in figure 6.41. Figure 6.42 shows a series of column ratio line profiles at $10nm$, $30nm$, $50nm$ and $120nm$. These indicate some clear differences from the linear diffusion model. The first difference is that at $10nm$ the change in composition from dumbbell 4 to 5 is clear and the column ratio value shows a distinct drop. The column ratio of dumbbells 6, 7, 8 and 9 then show a gradual sweeping drop until dumbbell 10 onwards appears like bulk AlAs. This is not unexpected as dumbbell 10 has a gallium content of $\sim 4\%$ and at $10nm$ that corresponds to (on average) a single gallium atom within the Type-3 atomic column. As the number of gallium atoms within the Type-3 column increases the column ratio increases accordingly. However, the gradual change in composition results in a narrow interfacial width measurement at $10nm$ of ~ 2.3 dumbbells. At $30nm$, the interfacial width has increased and likewise the interfacial position has moved slightly towards the bulk AlAs region. This trend continues as the specimen thickness increases, in that the measured interface width increases and the measured interface position shifts towards the bulk AlAs region.

The interfacial width increases with thickness due to the random population of the Type-3 columns. For example, at a thickness of 40nm, an atomic dumbbell with a 1% gallium concentration will typically contain a single gallium atom. Therefore, at $10nm$ only one in four atomic columns will contain any gallium. However, as the thickness of the specimen is increased so too does the probability that the atomic column will contain a gallium atom. It is therefore the small gallium concentrations within dumbbells 7-12 that cause the measured interfacial width to change with specimen thickness.

Figure 6.43 shows the change in interface position with specimen thickness which is overlaid onto the model schematic. For a very thin crystal thickness the interfacial position is measured between dumbbells 4 and 5. As the thickness is increased, the interface position shifts towards the bulk AlAs region. At a thickness of $80nm$ onwards the interface position is located between dumbbells 6 and 7. The interfacial width is shown in figure 6.44 and is overlaid onto the experimental width measurements for comparison. This figure clearly shows the increase in interfacial width with specimen thickness. Furthermore, there is good agreement between the model and the

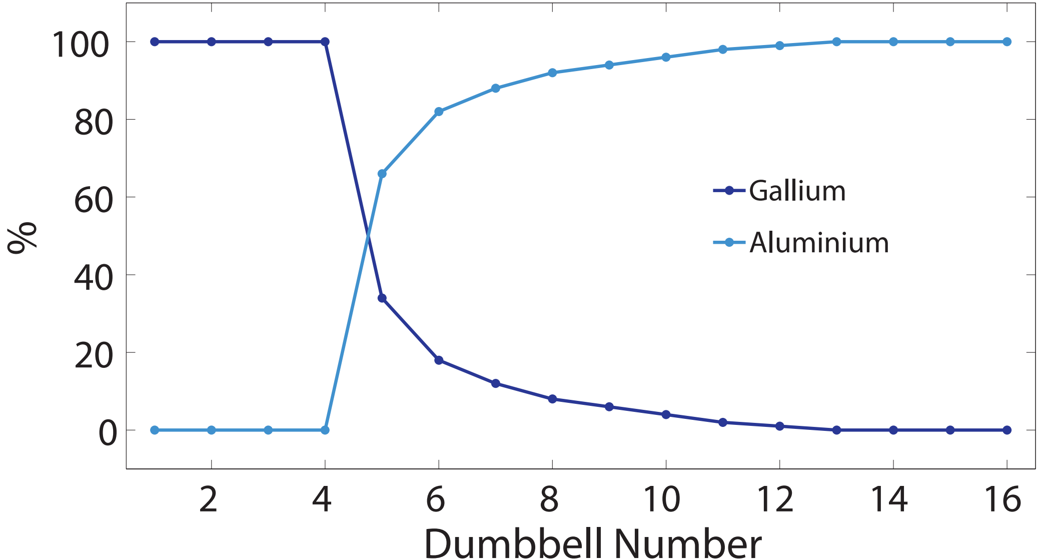

Figure 6.40 – The Type-3 atomic column gallium and aluminium concentration for the Type-A diffusion model. This Type-A model (AlAs grown on GaAs) was formed using a model of surface segregation in III-V heterostructures developed by Moison et al. [103].

experimental measurements in this case.

Type-G Interface The model developed by Moison et al. [103] indicates a different level of interfacial diffusion at the Type-G (GaAs on AlAs) interface. The calculated concentrations are shown in figure 6.45 indicating that the gallium segregation into the AlAs layer is this time significantly reduced. Moreover, only two atomic dummbells have significant amounts of gallium. This results in a significantly narrower interfacial region. The corresponding schematic for this concentration profile is shown in figure 6.46. These concentration profiles were again used to form the crystal structures that were then used in the multislice calculations. The interface position as a function of specimen thickness was calculated and is plotted in figure 6.47. This indicates, what may be expected, that the narrower diffuse interface results in a smaller shift in the measured interface position.

The measured interface width was also recorded and can be seen in figure 6.48. Clearly the concentration levels of gallium can have a significant effect on the measured characteristics of the interface. For the Type-A interface the interface width increases with thickness while in this case, the Type-G model, the measured interface width appears to remain constant with thickness. This indicates that there is a possibility of

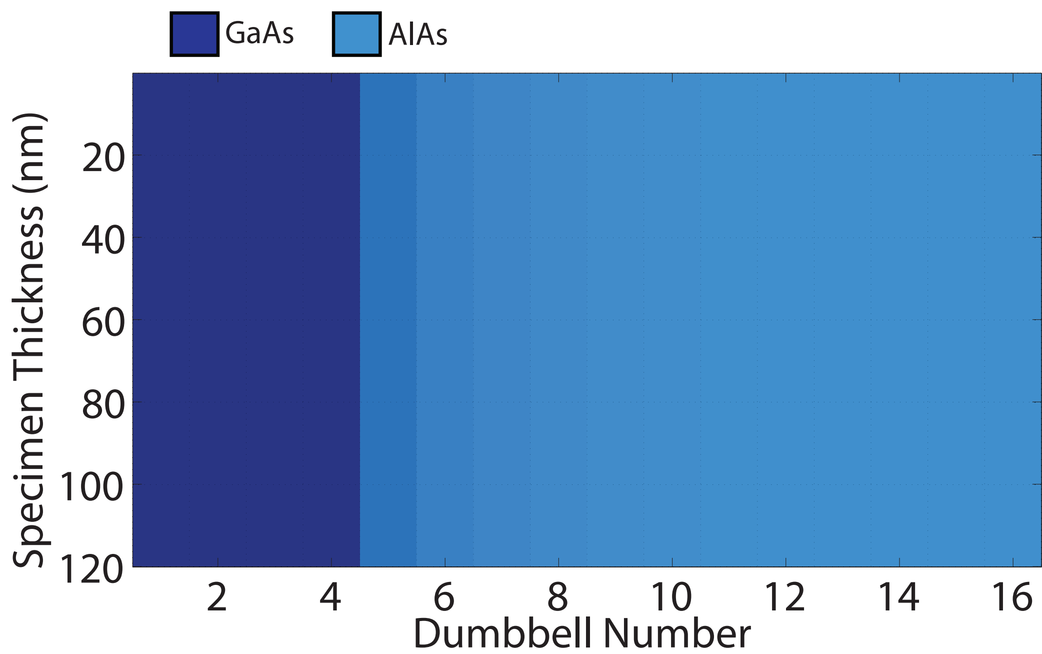

Figure 6.41 – The model schematic for the Type-A diffusion model. The concentrations for this Type-A model (AlAs grown on GaAs) were formed using a model of surface segregation in III-V heterostructures developed by Moison et al. [103].

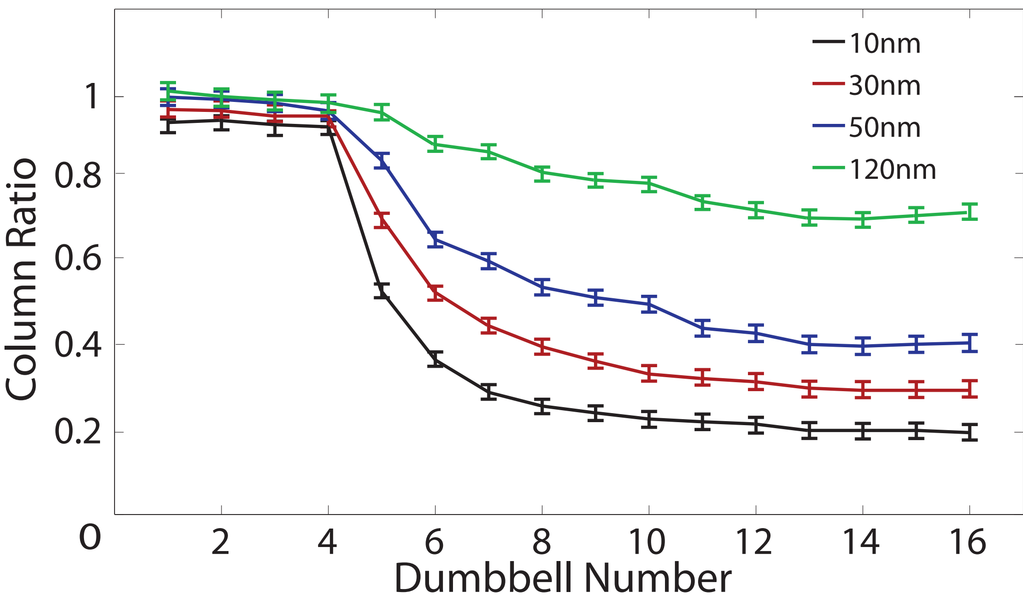

Figure 6.42 – A series of column ratio profiles for the Type-A diffusion model at a specimen thicknesses of $10nm$, $30nm$, $50nm$ & $120nm$. The profiles reveal the gradual move of the measured interface position towards the bulk AlAs region.

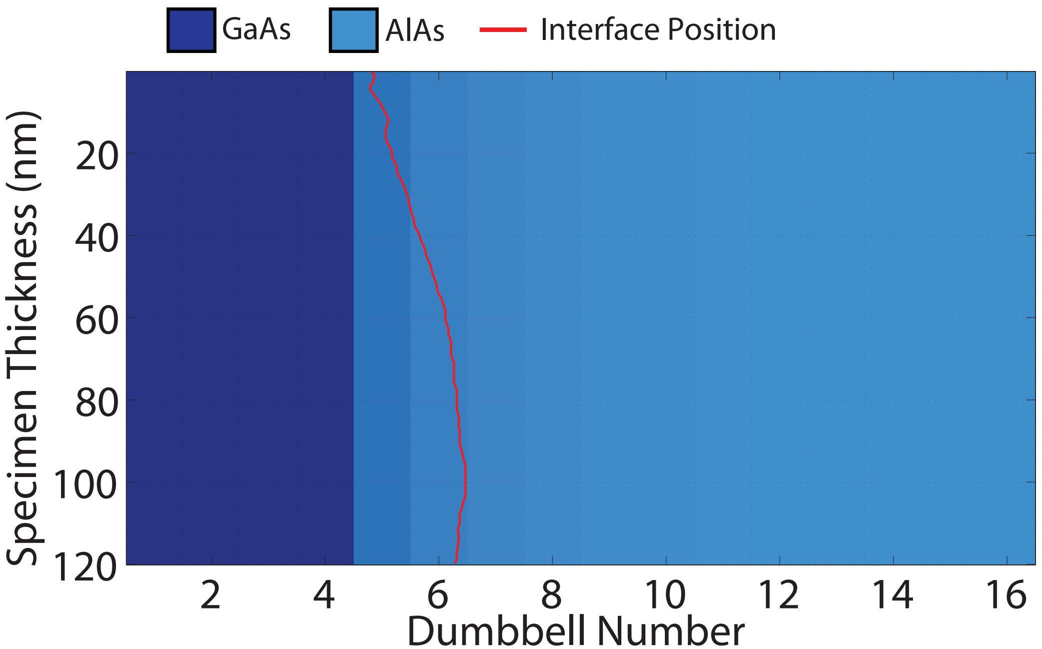

Figure 6.43 – This diagram shows the schematic of the Type-A diffusion model. The measured interface position is overlaid onto the model schematic indicating that the interface position starts at dumbbell 5 and moves towards the bulk AlAs region finishing at a position between dumbbell 6 and dumbbell 7 at a depth of $120nm$.

differentiating between the different levels of diffusion at a basic level.

There is clearly good agreement between the measured characteristics of the Type-A and Type-G diffusion models with the experimental measurements. However, the measured characteristics of this model may not be unique and a further investigation into vicinal structures is detailed in the following sections.

6.2.5 Simple Vicinal Interface

Experimentally, the superlattice is grown on a polished [001] orientated GaAs substrate and the polishing tolerance is precise to $\pm\frac{1}{2}^{\circ}$. An inclined substrate would force the growth layers to the same angle of inclination. In this case, when the sample is prepared in a [110] orientation, the interface would not be parallel to the beam direction. Instead, a degree of vicinality will have been introduced, this results in a stepped interface. A schematic of a simple vicinal interface can be seen in figure 6.49 where the interface lies at angles of $+\theta$ (right) and $-\theta$ (left) to the [110] direction. Depending on the substrates initial orientation (and the subsequent specimen orientation in the microscope) θ may be positive or negative. From the growth direction indicated in figure 6.49, both cases are a Type-A interface where AlAs is grown onto a GaAs substrate. However, the case

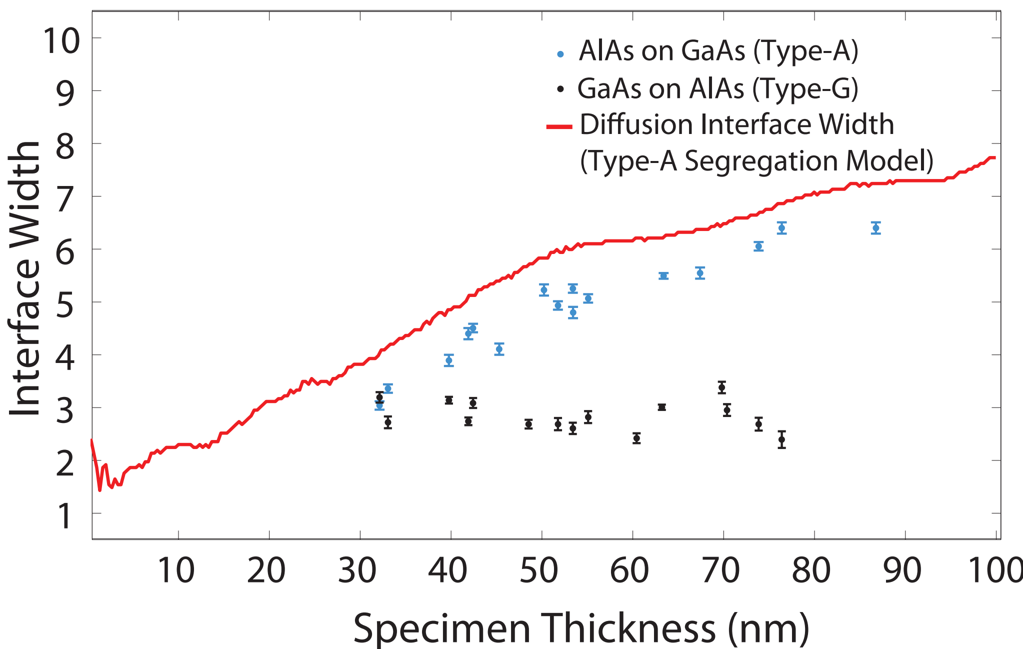

Figure 6.44 – This graph shows the measured interface width as a function of specimen thickness (red). The measured interface width from the model is overlaid onto the experimental measurements from figure 5.15 for comparison. At thin specimen thicknesses some columns will *typically* have no gallium in the atomic columns. However as the specimen thickness increases the number of columns that will contribute to the interface increases. For a $120nm$ sample there are approximately 300 atoms in each atomic column and if the gallium concentration is 1% this equates to 3 gallium atoms. At $12nm$ only one in three atomic columns will contain any gallium. In this case as the specimen thickness increases the apparent width will increase as the gallium content of the atomic columns increases.

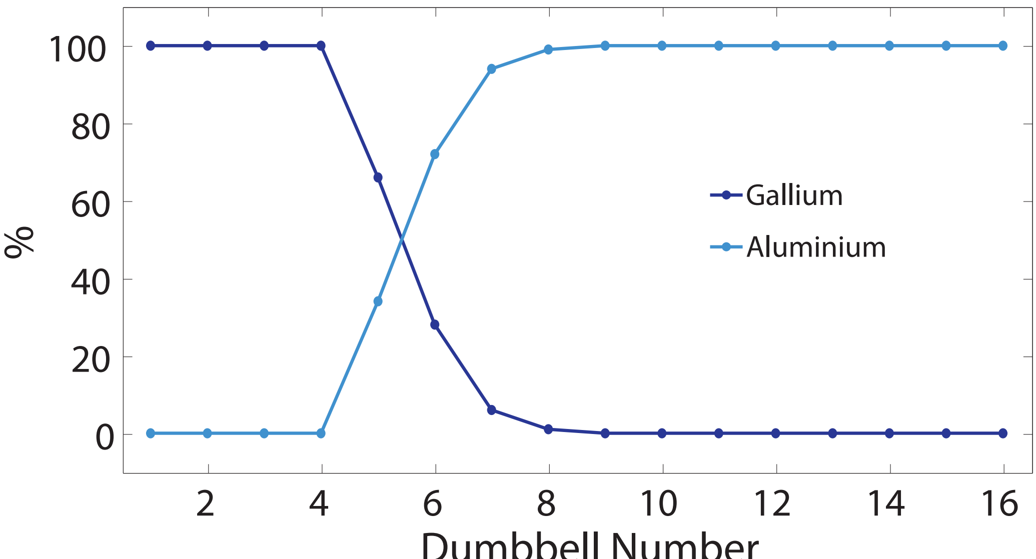

Figure 6.45 – The Type-3 atomic column gallium and aluminium concentration for the Type-G diffusion model. This Type-G model (GaAs grown on AlAs) was formed using a model of surface segregation in III-V heterostructures developed by Moison et al. [103].

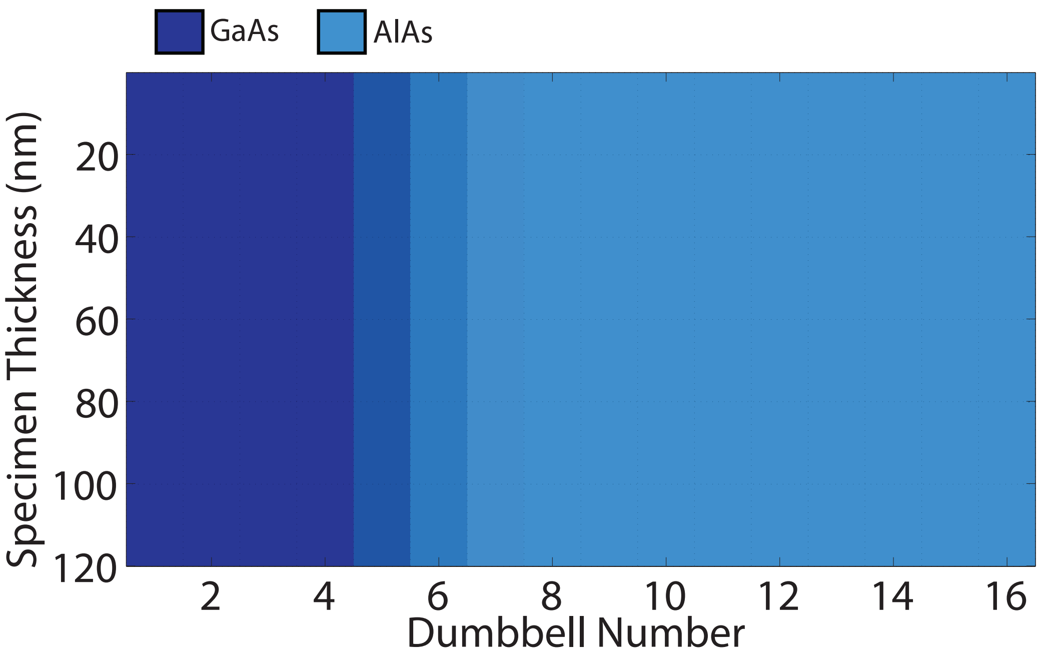

Figure 6.46 – The model schematic for the Type-G diffusion model. The concentrations for this Type-G model (GaAs grown on AlAs) were formed using a model of surface segregation in III-V heterostructures developed by Moison et al. [103].

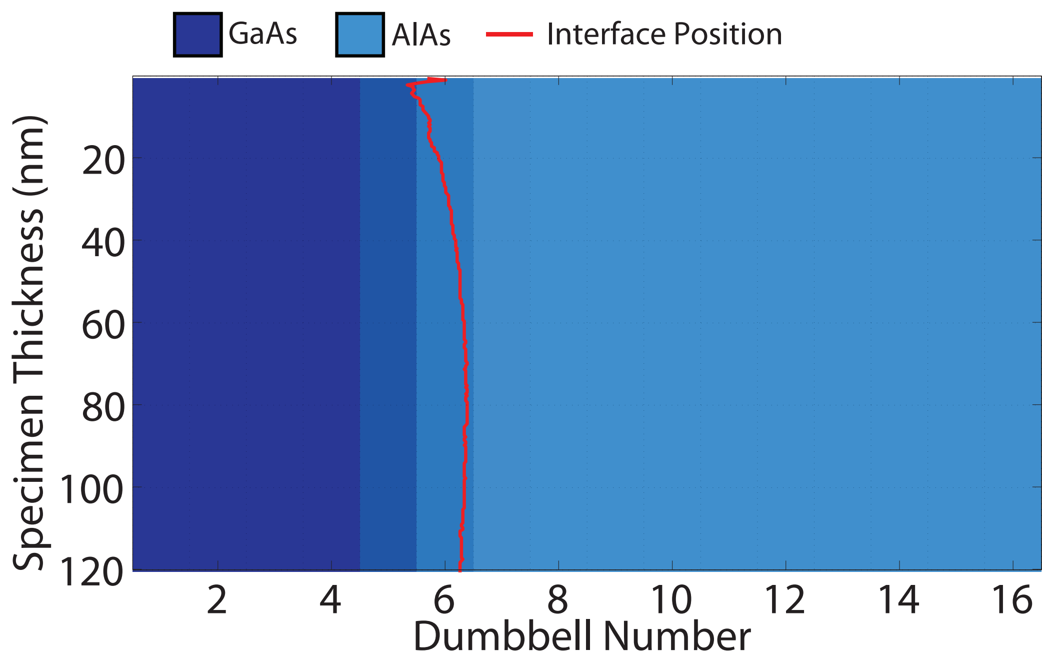

Figure 6.47 – This diagram shows the schematic of the Type-G diffusion model. The measured interface position is overlaid onto the model schematic indicating that the motion of interface position is small as it starts near dumbbell 5 and moves towards, and then past, dumbbell 6.

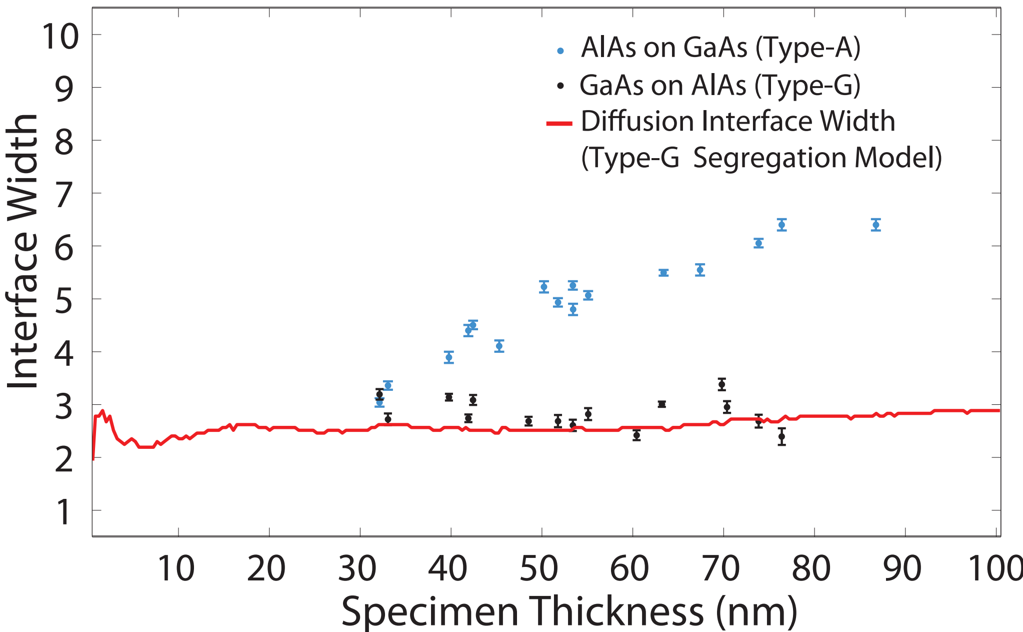

Figure 6.48 – This graph shows the measured interface width as a function of specimen thickness (red). The measured interface width from the model is overlaid onto the experimental measurements from figure 5.15 for comparison. The concentration levels in this model are such the as the specimen thickness increases the measured interface width remains between 2 and 3 dumbbells.

shown on the left of figure 6.49 shows negative θ and is such that a probe placed at the interface would first project through AlAs before GaAs (AlAs projection). The ratio of aluminium to gallium within a particular Type-3 atomic column will therefore be dependent on the probe position and interface angle. The next case is shown on the right of figure 6.49 and shows the opposite orientation where a probe placed at the interface will first project through GaAs before AlAs (GaAs projection).

The interface position in the simple vicinal model steps across like a staircase with a regular step length. The step length is constant and dependent on the angle of the interface. However, when the sample is prepared, the entrance face of the specimen can be formed at any position within the first step, as indicated in figure 6.49. The red arrows indicate possible positions of the specimen surface and for each position the depth of the first step is different. To fully understand this model, a variety of 1° vicinal interfaces were created for both positive and negative θ, the first step length was varied also to ascertain any effects that this might have.

A simple vicinal model was created where the crystal depth was $120nm$ and to create a 1° interface a step length of 37 unit cells ($\sim 15nm$) was chosen. Thus, for every 37 unit cells in the [110] direction, the interface position will shift by one dumbbell in the [001] growth direction. While an interfacial angle of 1° is greater than the polished tolerance of the substrate, this model will produce an interface with a large number of steps and should therefore give a good overview of the behavior of this type of stepped structure.

6.2.5.1 AlAs Projection

The first orientation is shown in figure 6.50 and corresponds to the case where AlAs is projected through before GaAs at the entrance face of the specimen and therefore forms an AlAs projection (i.e. θ is negative). Six AlAs into GaAs interfaces were modelled with initial entry steps of $2nm$, $4nm$, $6nm$, $8nm$, $10nm$ and $12nm$.

Figure 6.50 shows a side view schematic for the $8nm$ entry step. The arrow indicates the first step at the entrance face of the specimen. Figure 6.51 shows a series of column ratio line profiles for this model. The plot contains profiles at specimen thicknesses of 10, 30, 50, 80 and $120nm$ and shows the progression of the interface width and interface position as the specimen thickness increases. Using the schematic as a reference (figure 6.50), the small entry step is located at dumbbell 5 and the compositional change occurs

Vicinal Interface

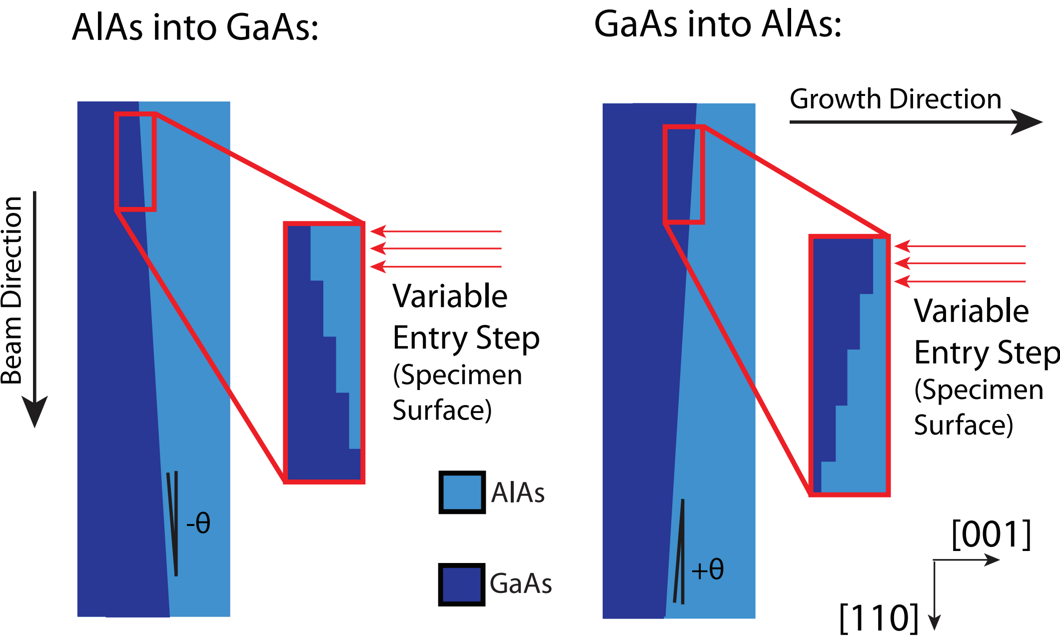

Figure 6.49 – The two cases for a simple vicinal interface. With the [001] growth direction defined both these interfaces are AlAs grown on GaAs (i.e. 'AlAs on GaAs'). However, a probe placed at the interface will project through one material before the other. The left image shows the 'AlAs projection' case where a probe at the interface first projects through AlAs. The right image shows the 'GaAs projection' case where a probe at the interface projects through GaAs first. Depending on the specimen preparation the first step can be at a variety of depths.

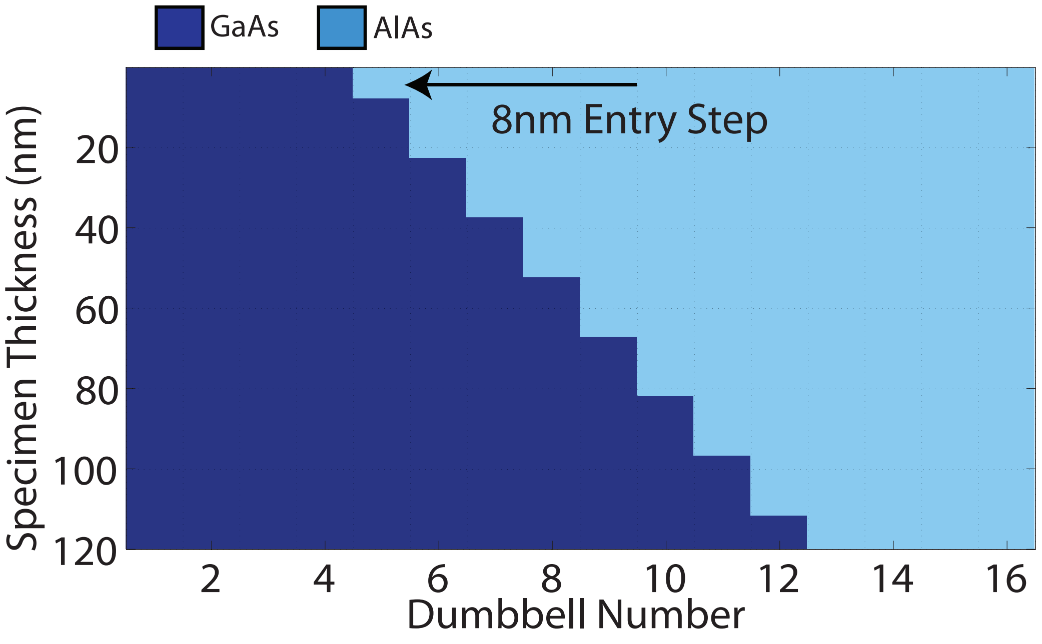

Figure 6.50 – An overview of the Vicinal Interface (AlAs projection) 8nm entry step schematic where a probe at the interface first projects through AlAs then through GaAs. The first 8nm step at the interface is indicated with the arrow.

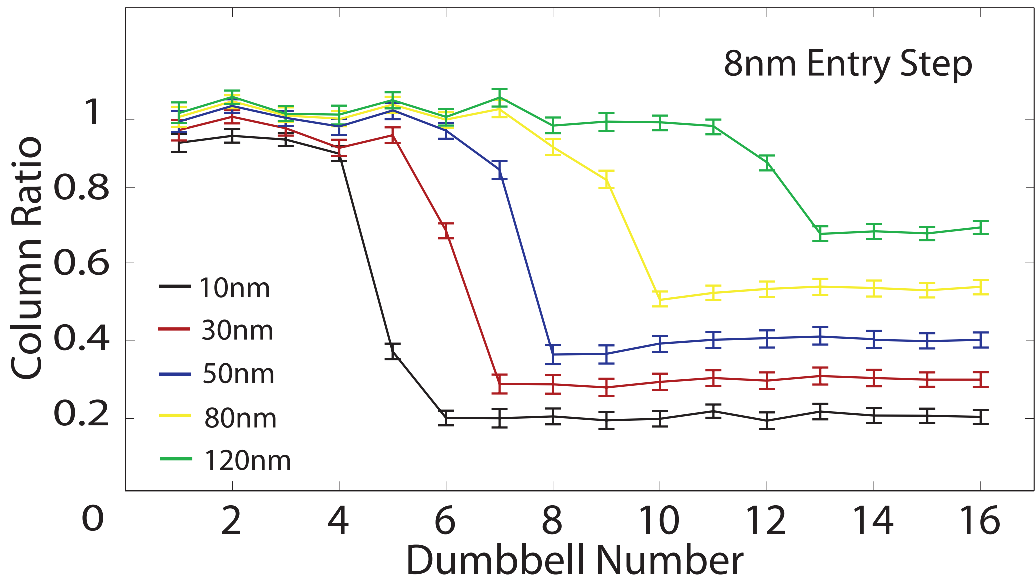

Figure 6.51 – The column ratio profile for this vicinal AlAs into GaAs 8*nm* entry step model shows that as the specimen thickness increases the interface position moves quickly towards the bulk AlAs region.

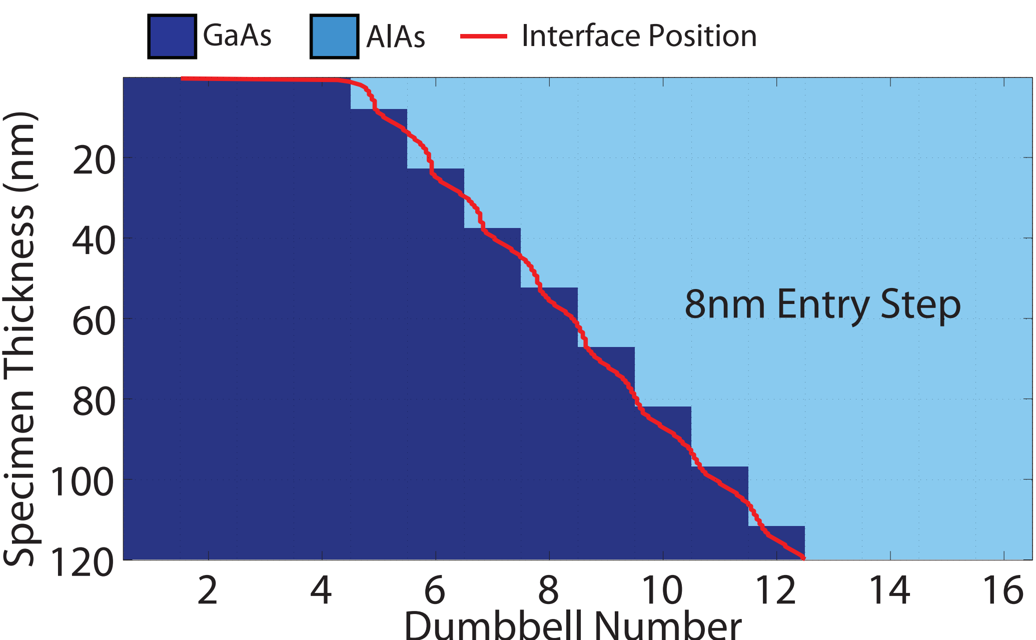

Figure 6.52 – The measured interface position tracks the gallium content in the atomic columns over the full simulation depth for this 8*nm* entry step model. This results in a shift in the measured interface position as the specimen thickness increases.

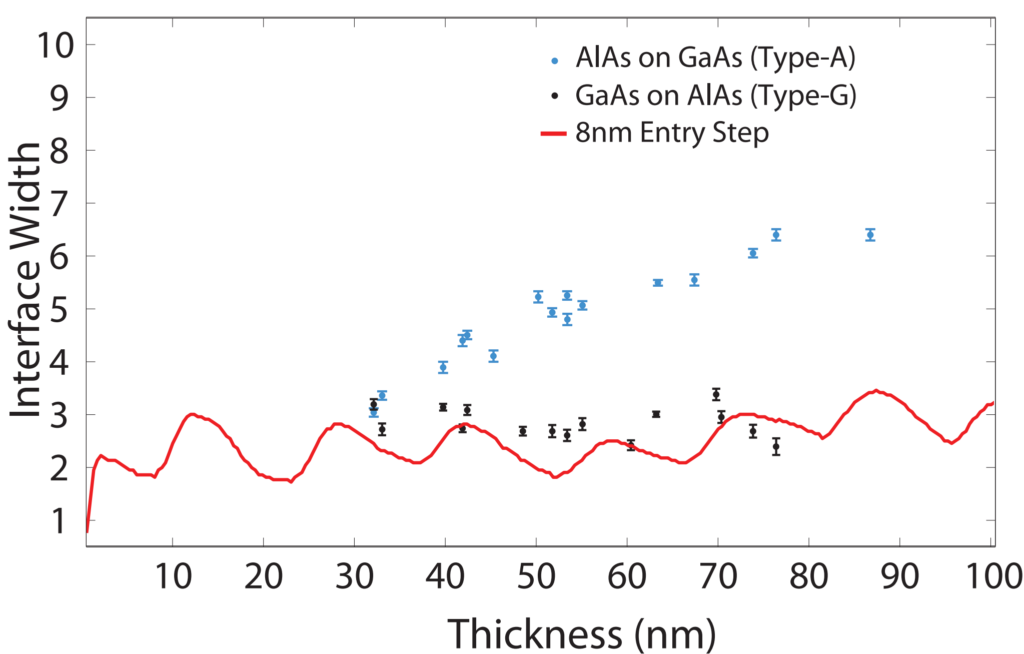

Figure 6.53 – This graph shows the measured interface width as a function of specimen thickness (red). The measured interface width from the model is overlaid onto the experimental measurements from figure 5.15 for comparison. For this model the overall interface width again oscillates as the specimen thickness increases.

at a depth of $8nm$ within the Type-3 column. The column ratio profile plot shows that at $10nm$ (black) dumbbell 5 appears like a interfacial column as the column ratio value lies between that of bulk GaAs and bulk AlAs. This is consistent with the schematic which indicates that at a thickness of $10nm$ the Type-3 column of dumbbell 5 will consist of $8nm$ of aluminium followed by $2nm$ of gallium. It is the gallium at the base of the atomic column that has forced an increase in the column ratio. At this thickness, the "apparent" interface position is located between dumbbells 4 and 5. At $30nm$ dumbbells 5 and 6 have saturated and appear to be part of the bulk GaAs region. However, dumbbell 7 now has an amount of gallium at the base of the Type-3 atomic column which is reflected in the measured column ratio value. At this depth, the interfacial width does not appear any wider, but the interface position has shifted towards the bulk AlAs region and is now located near to dumbbell 6. This pattern continues with increasing thickness where each column in turn forms part of the apparent interfacial region and then quickly saturates pushing the interfacial position towards the bulk AlAs region. Furthermore, figure 6.52 shows the measured interface position overlaid onto the model schematic. This clearly indicates that the measured interface position does not represent the average interface position. Instead, the measured interface position

tracks the gallium content in the atomic columns. Figure 6.52 shows how the systematic saturation of the dumbbells cause the interface position to shift dramatically. The interface position is initially located between dumbbells 4 and 5. As the thickness of the specimen increases the interface position shifts until it is located between dumbbells 12 and 13. The saturation of the dumbbells also has a distinct effect on the interface width. Figure 6.53 shows the interfacial width as a function of thickness again overlaid onto the experimental width measurements for comparison. The plot indicates that the interface width oscillates with thickness. Each oscillation corresponds to a particular step in the interface. So, if a particular AlAs column has GaAs at the exit face, the change in composition will only be measurable between a thickness t and $t + \delta t$ that corresponds to the column ratio changing from "AlAs like" to "GaAs like" after which the column will appear like a bulk GaAs column. This causes the overall interface width to oscillate as the specimen thickness increases instead of increasing, as might have been expected.

Figure 6.54 shows a side view schematic for the $2nm$ entry step, the arrow indicates the first step at the entrance face of the specimen. Figure 6.55 shows the column ratio line profile for this model and the plot again contains profiles at specimen thicknesses of $10nm$, $30nm$, $50nm$, $80nm$ and $120nm$. Using the schematic as a reference (figure 6.54), the small entry step is located at dumbbell 5 and the compositional change occurs at a depth of $2nm$ within the Type-3 column. It is clear from the column ratio line profile that at $10nm$ (black) dumbbell 5 appears like a fully populated GaAs column. At this depth, the interface appears abrupt between dumbbells 5 and 6. At $30nm$, dumbbell 6 has a small amount of GaAs at the exit face of the crystal (which is reflected in the column ratio value) which causes a widening of the interface width. This pushes the interface position towards the bulk AlAs region. By $50nm$ dumbbells 5, 6 and 7 have significant amounts of GaAs within the columns and are beginning to saturate (i.e. appear like a fully populated GaAs column) and dumbbell 8 has a small amount at the exit face of the specimen. This again changes the interfacial width and shifts the interface position towards the bulk AlAs region. The same pattern continues with increasing thickness where each column in turn forms part of the apparent interfacial region in the column ratio line profile but quickly saturates pushing the interfacial position towards the bulk AlAs region. Figure 6.56 shows the measured interface position overlaid onto the model schematic and indicates that the behavior is similar

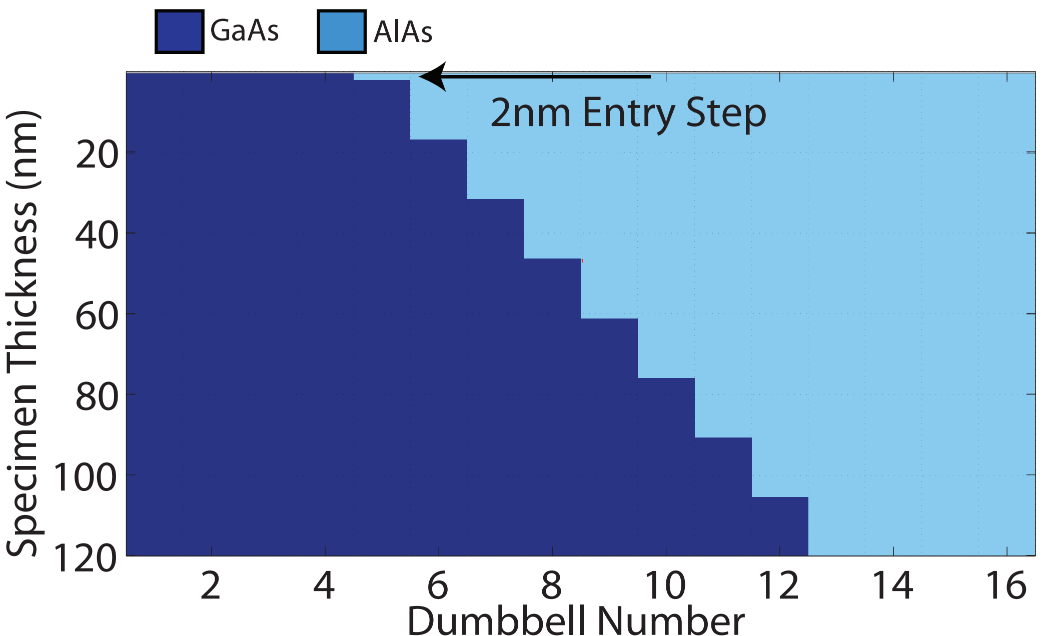

Figure 6.54 – An overview of the Vicinal Interface (AlAs projection) $2nm$ entry step schematic where a probe at the interface first projects through AlAs then through GaAs. The first $2nm$ step at the interface is indicated with the arrow.

to the $8nm$ entry step case with the interface position starting between dumbbells 4 and 5 and quickly shifts towards the bulk AlAs region ending between dumbbells 12 and 13. Figure 6.57 also shows that the interface width of this model oscillates with increasing thickness.

The behavior of these interfaces is very similar to the sawtooth interfaces modelled in section 6.2.3. This is not surprising, a simple vicinal interface of this type is a special case of the sawtooth interface where the repeat length is considerably longer than the specimen thickness.

One significant difference that the size of the entry step makes is evident from the column ratio profiles in figures 6.51 and 6.55. The general form and behavior of the interfaces are similar in both cases. However, in each case dumbbell 6 shows a marked difference at thicknesses of $50nm$, $80nm$ and $120nm$. For the $8nm$ entry step model, dumbbell 6 appears to form part of the bulk GaAs region at these depths while for the $2nm$ entry step model, dumbbell 6 consistently remains below bulk GaAs. This is related to the depth of the compositional change within the Type-3 atomic columns. In the case of the 2nm entry step the composition changes from aluminium to gallium at a depth of $\sim 16nm$. For the 8nm entry step the composition changes at a depth of $22nm$.

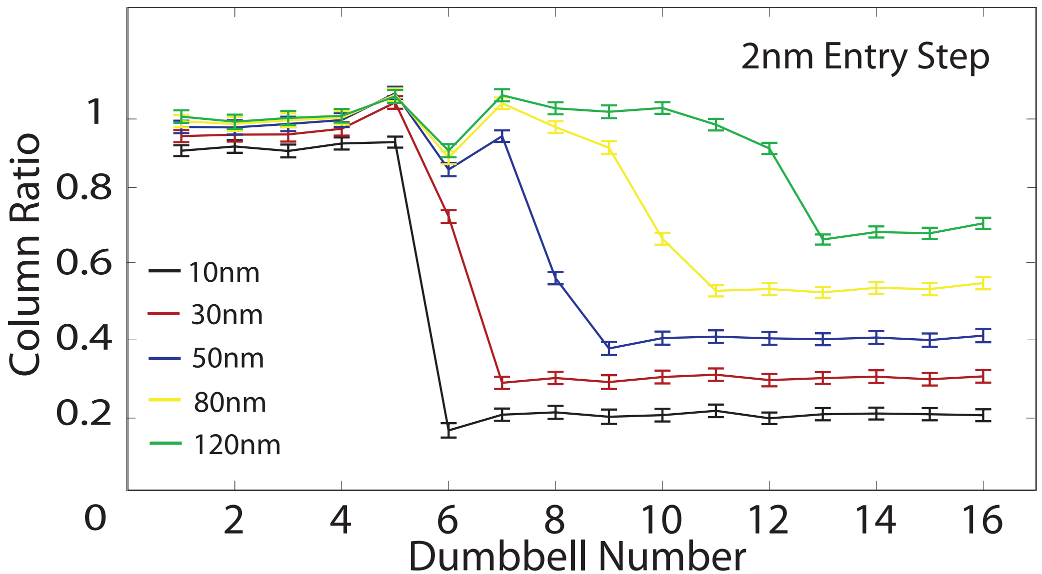

Figure 6.55 – The column ratio profile for this vicinal AlAs into GaAs 2nm entry step model. The profiles show that as the specimen thickness increases the interface position moves quickly towards the bulk AlAs region. However one interesting feature of this model is the column ratio values of dumbbells 5 and 6. As the thickness increases the scattering from these dumbbells deviates from the surrounding dumbbells significantly. The column ratio of dumbbell 5 is greater than the surrounding dumbbells while dumbbell 6 is lower than the surrounding dumbbells.

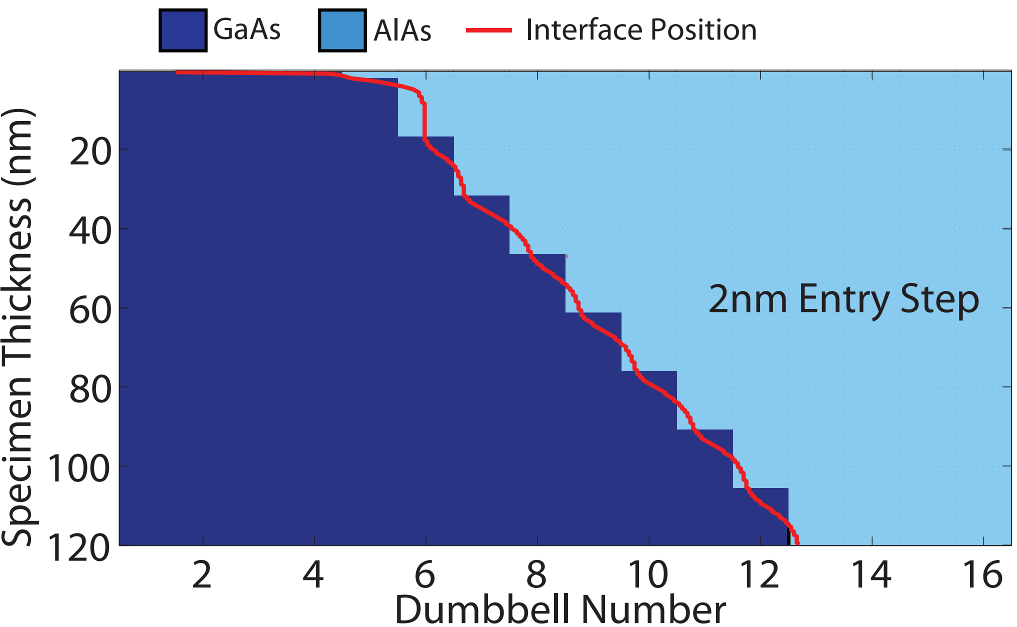

Figure 6.56 – It is apparent from the schematic that the measured interface position tracks the gallium content in the atomic columns over the full simulation depth. This results in a shift in the measured interface position as the specimen thickness increases.

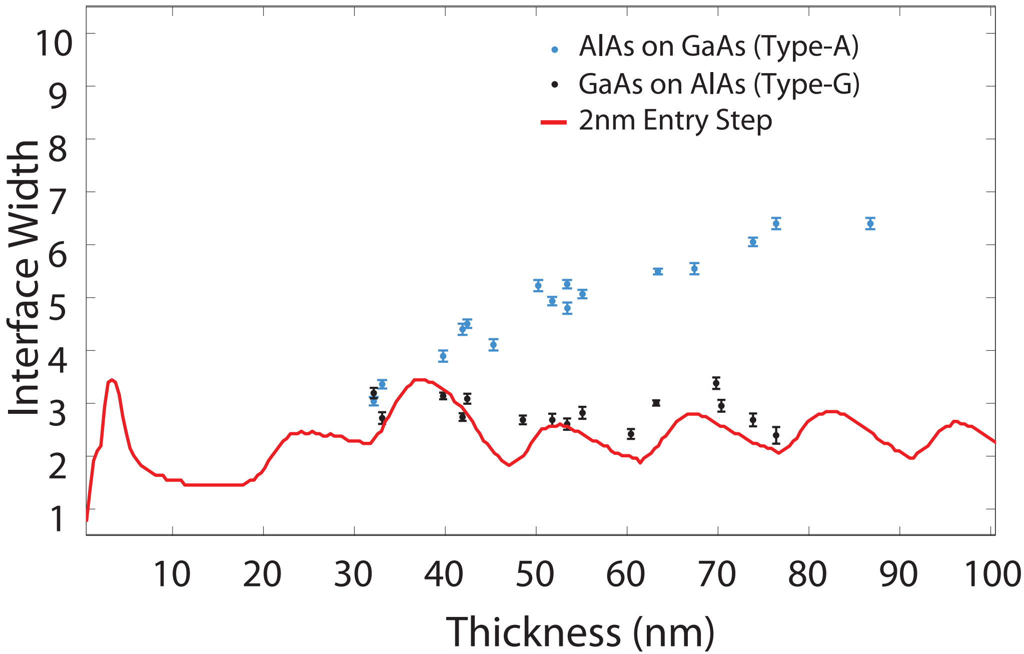

Figure 6.57 – This graph shows the measured interface width as a function of specimen thickness (red). The measured interface width from the model is overlaid onto the experimental measurements from figure 5.15 for comparison. For this model the overall interface width oscillates as the specimen thickness increases. This is due to the atomic columns containing large amounts of gallium quickly saturating and so instead of the interface width increasing there is a shift in the measured interface position.

To look at this in more detail, figure 6.58 shows the calculated column ratio values (broken black) from dumbbell 6 for the $2nm$ entry step case. The graph also shows the column ratio for bulk GaAs (dark blue) and bulk AlAs (light blue) and the intensity on the primary column of a Type-3 AlAs dumbbell (solid black). The compositional change from aluminium to gallium occurs at a depth of $16nm$ which coincides with a minima in the primary column intensity. The depth of the compositional change is indicated by the red and white regions of the plot where the red region is the higher-Z material (in this case GaAs). The change in the atomic column potential affects the scattering in such a way that the scattering from the Type-3 column never reaches the same intensity as the Type-5 column. This is reflected in a column ratio that is consistently below 1.

Figure 6.59 shows the calculated column ratio value as a function of thickness from dumbbell 6 for the $8nm$ entry step case. The plot also shows the bulk GaAs, bulk AlAs and Type-3 primary column intensity. However now the compositional change from aluminium to gallium occurs where the intensity on the primary column is a local maxima at a depth of $22nm$. As the specimen thickness increases beyond $22nm$, the column ratio steadily climbs until the scattering from both the Type-3 and Type-5 columns are equal. This is a clear indication that the measured column ratio from a dumbbell is dependent not only on the composition of the atomic columns but also the distribution of atoms.

6.2.5.2 GaAs Projection

The next orientation is for a positive interface angle, $+\theta$. This model is shown in figures 6.60 and 6.61 where a probe at the interface projects first through GaAs before AlAs. Six different models were evaluated where the first entry step was varied from $2nm$, $4nm$, $6nm$, $8nm$, $10nm$ and $12nm$. Figure 6.60 shows a side schematic of the model with the $2nm$ entry step. Figure 6.61 shows the schematic of the model with a $12nm$ entry step. The column ratio profiles for both of these models are shown in figures 6.62 and 6.63 for the $2nm$ and $12nm$ entry step interfaces respectively. The column ratio plots contain profiles at specimen thicknesses of $10nm$, $30nm$, $50nm$, $80nm$ and $120nm$ and show the progression of the interface width and interface position as the specimen thickness increases. These profiles indicate that the interface position does not change significantly with thickness and in both cases the interfacial position starts

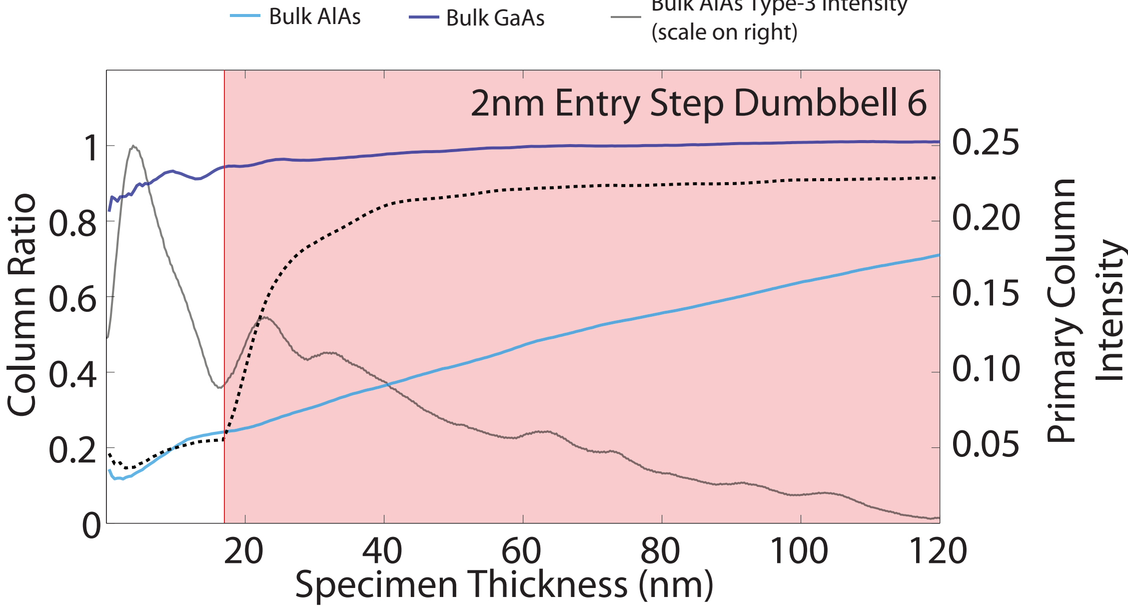

Figure 6.58 – A graph of the column ratio as a function of specimen thickness dumbbell 6 (broken black) from the 2nm entry step model. The background indicates the change in composition from the low Z material to the high Z material (red). The column ratio of single crystal GaAs (dark blue) and AlAs (light blue) are also shown for comparison. The primary column intensity from the Type-3 column of single crystal AlAs is also shown which indicates the electron intensity on the Type-3 column of dumbbell 6 at the depth of the compositional change.

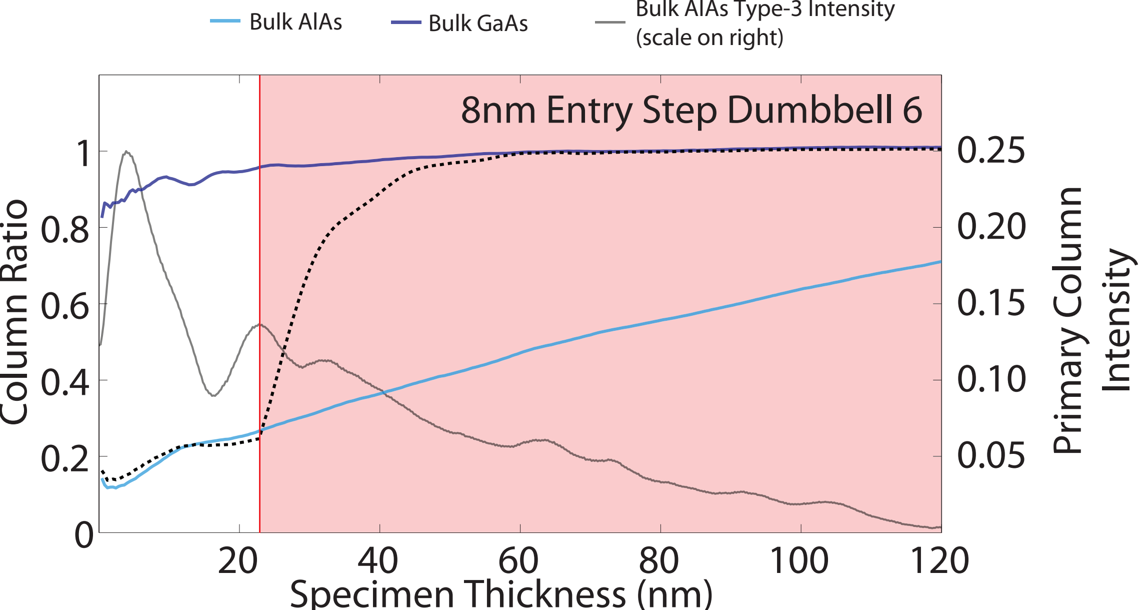

Figure 6.59 – A graph of the column ratio as a function of specimen thickness of dumbbell 6 (broken black) from the 8nm entry step model. The background indicates the change in composition from the low Z material to the high Z material (red). The column ratio of single crystal GaAs (dark blue) and AlAs (light blue) are also shown for comparison. The primary column intensity from the Type-3 column of single crystal AlAs is also shown which indicates the electron intensity on the Type-3 column of dumbbell 6 at the depth of the compositional change.

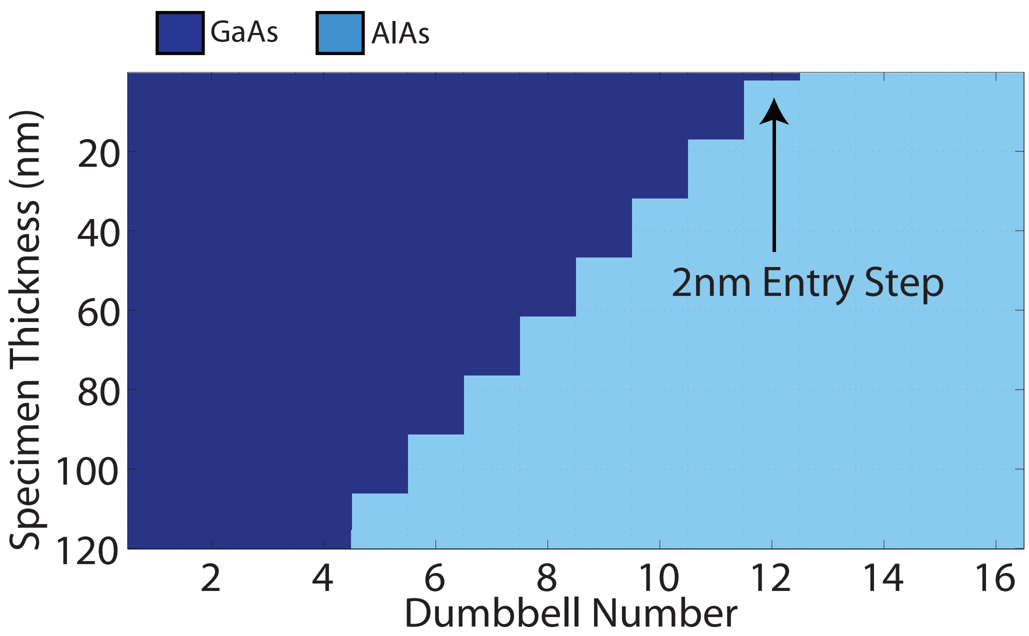

Figure 6.60 – An overview of the Vicinal Interface (GaAs projection) $2nm$ entry step schematic where a probe at the interface first projects through GaAs then through AlAs. The first $2nm$ step at the interface is indicated with the arrow.

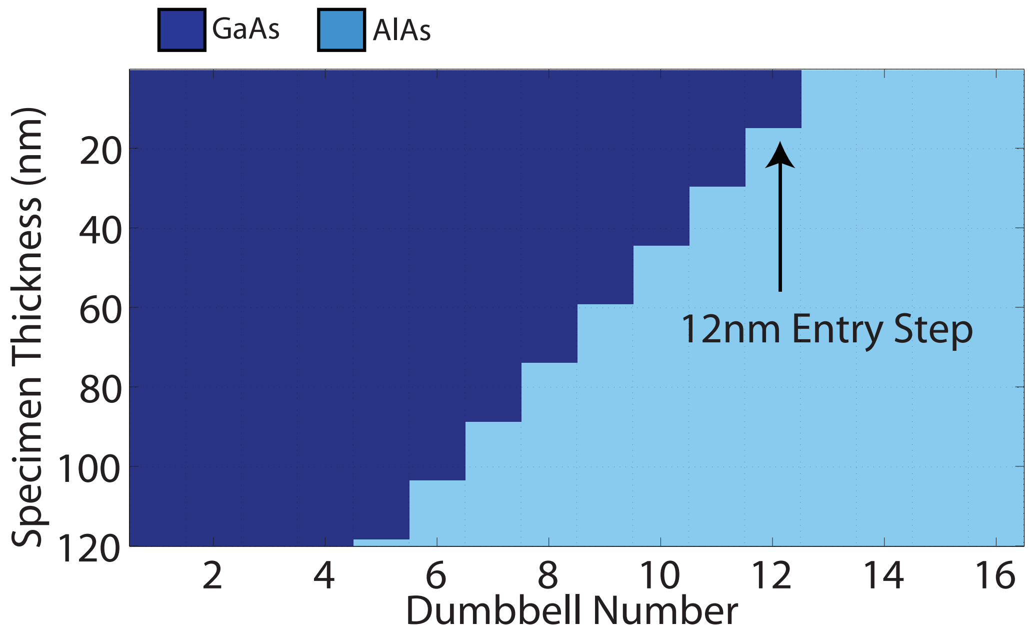

Figure 6.61 – An overview of the Vicinal Interface (GaAs projection) $12nm$ entry step schematic where a probe at the interface first projects through AlAs then through GaAs. The first $12nm$ step at the interface is indicated with the arrow.

between dumbbells 12 and 13. For the case of the $2nm$ entry step model, the interface position shifts towards the bulk GaAs region and finishes between dumbbells 11 and 12. For the case of the $12nm$ entry step model, the interface position remains located between dumbbells 12 and 13 over the full simulation range from $0-120nm$. This subtle difference is apparent from the column ratio line profiles in figure 6.62, in particular from the behavior of dumbbell 12.

Considering the $12nm$ entry step model first (figure 6.63), at $10nm$ (black line) dumbbell 12 consists of a complete gallium column and the column ratio is consistent with bulk GaAs. The compositional change then occurs at a depth of $12nm$ which is shorter than the channelling depth of the gallium column and so the compositional change is detected and at $30nm$ the column ratio of dumbbell 12 is between bulk GaAs and bulk AlAs. This dumbbell continues to appear like an interfacial dumbbell as the thickness increases and the interfacial position remains between dumbbells 12 and 13.

For the $2nm$ entry step case (figure 6.62), at $10nm$ dumbbell 12 consists of $2nm$ of GaAs followed by $8nm$ of AlAs and appears like an interfacial dumbbell. However, as the specimen thickness increases the column ratio of dumbbell 12 begins to drop. At $80nm$ the line profile indicates that the column ratio of dumbbell 12 has dropped below that of a fully populated AlAs column. By $120nm$ dumbbell 12 is significantly below bulk AlAs causing the apparent interface position to shift to a location between dumbbells 11 and 12.

Figure 6.64 shows the shift in interface position for the $2nm$ entry step model (overlaid onto the model schematic) which clearly indicates that the interface position starting between dumbbells 12 and 13 and progressively shifting towards the bulk GaAs region to finish between dumbbells 11 and 12. It is also clear that although dumbbells 5 through to 12 are interfacial and contain compositional changes these are not detected and the measured interface position gives no information regarding the 'average' interface position. In this model, compositional changes below $25nm$ cannot be detected due to the electron intensity scattering off of the primary column and therefore the interface position and width remains constant for all specimen thicknesses.

Figure 6.65 shows the measured interface positions for the $12nm$ entry step model which again is overlaid onto the model schematic. This plot also indicates that the interface position remains between dumbbells 11 and 12. The measured interface width is shown in figure 6.66 for the $2nm$ model and figure 6.67 for the $12nm$ entry step

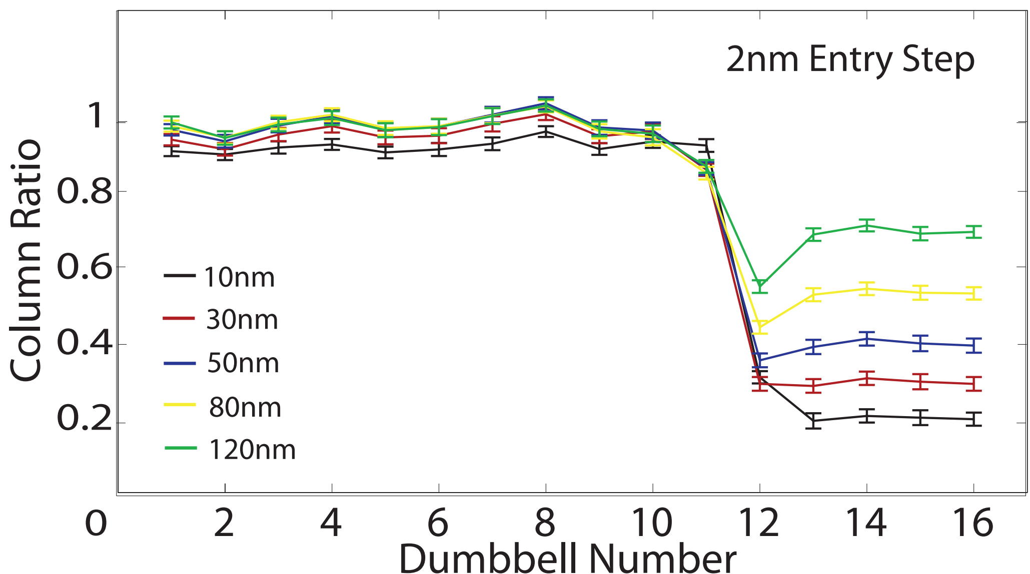

Figure 6.62 – The column ratio profile for this vicinal GaAs into AlAs $2nm$ entry step model. The profiles show that as the specimen thickness increases the interface position remains close to the bulk AlAs region. However one interesting feature of this model is the column ratio value of dumbbell 12. As the thickness increases the scattering from this dumbbell drops below the bulk AlAs columns. At thicknesses of $80nm$ and above the scattering from the Type-3 column of dumbbell 12 is less than a fully populated aluminium column even though the average Z is higher.

model. These plots confirm that apart from the width fluctuations in the top $10nm$ of the specimen the measured interface width remains consistently between 2 and 3 dumbbells in both cases.

Both of these models exhibit very similar characteristics. However, the measured column ratio can again be significantly affected by compositional changes at the entrance face of the specimen. In particular this effect is seen in figure 6.62 where the column ratio of dumbbell 12 shows a significant difference with the change in composition in the top $20nm$ of the crystal.

The drop in the column ratio value of dumbbell 12 in the $2nm$ entry step model can be explained by investigating how the primary column intensity and column ratio change with specimen thickness. This data is shown in figure 6.68 which indicates the column ratio from dumbbell 12 (broken black), the light and dark blue data corresponds to the column ratio from bulk AlAs and GaAs respectively. The red background indicates the GaAs section of the atomic column and the solid black line shows the primary column intensity down the Type-3 column of bulk GaAs (i.e. the gallium column).

The data from the $2nm$ entry step case is shown in figure 6.68 and in the top $2nm$

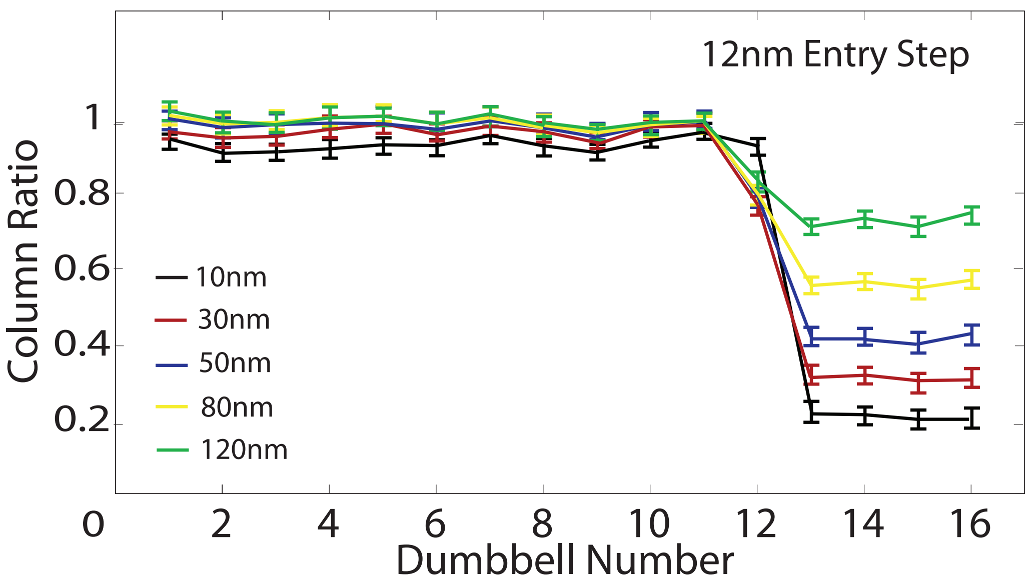

Figure 6.63 – The column ratio profile for this vicinal GaAs into AlAs 12nm entry step model. The profiles show that as the specimen thickness increases the interface position remains close to the bulk AlAs region. However the column ratio of dumbbell 12 is considerably different to the behavior seen in the vicinal GaAs into AlAs 2nm entry step model.

of the crystal the column ratio from dumbbell 12 appears like bulk GaAs (dark blue). After the compositional change at 2nm the column ratio quickly drops and by 30nm the column ratio is comparable with that of bulk AlAs (light blue). However as the specimen thickness increases beyond 30nm the column ratio continues to drop below bulk AlAs and by 120nm is significantly below. Figure 6.68 shows that for dumbbell 12 the compositional change from gallium to aluminium occurs where there is a peak in the primary column intensity which affects the scattering in such a way as to significantly reduce the scattering from the remainder of the atomic column. This significant drop in the column ratio can be compared to the 12nm entry step case. This is shown in figure 6.69. The column ratio of dumbbell 12 is again shown by the broken black line and can be compared to that of bulk GaAs (dark blue) and bulk AlAs (light blue). In this case the drop in column ratio is not nearly as large and the column ratio always remains between that of bulk GaAs and Bulk AlAs. This results in the dumbbell consistently appearing like an interfacial dumbbell below the compositional change.

Small amounts of gallium at the entrance face of an aluminium column can have a significant effect on the column scattering for thicker crystals. Therefore, the measured column ratio depends not only on the compositional content of the atomic columns but

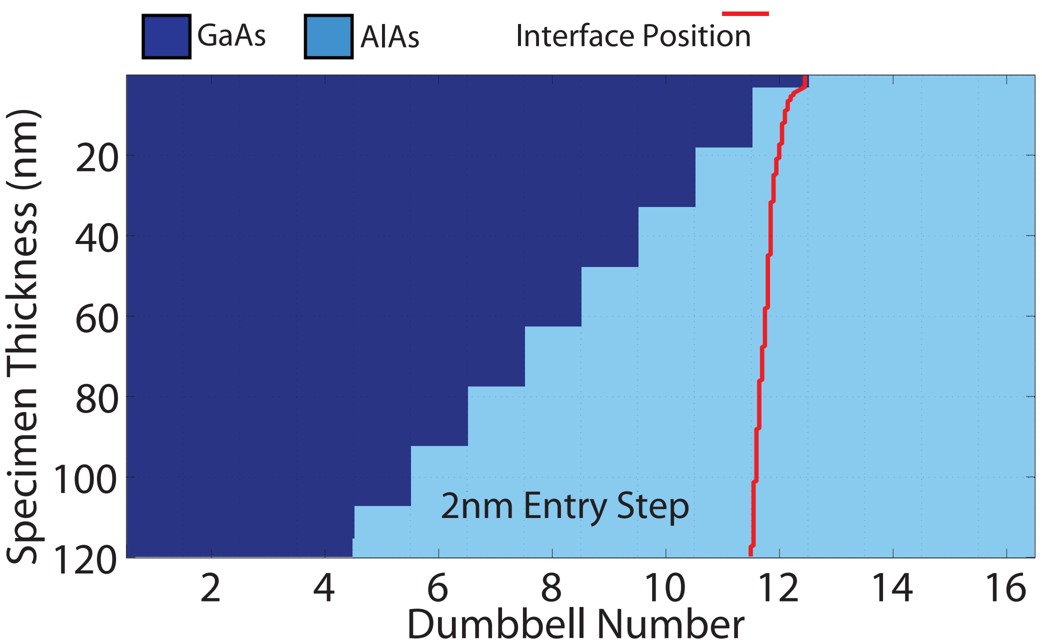

Figure 6.64 – The measured interface position for this GaAs projection model starts between dumbbells 12 and 13 for a very thin crystal and shifts slightly towards the bulk GaAs region. This shift is due to the column ratio of dumbbell 12 dropping with increasing thickness.

also on the form of the distribution. For example, a crystal $100nm$ thick consisting of bulk AlAs would produce a column ratio of 0.64, whereas an AlAs column with $2nm$ of GaAs at entrance face would have a column ratio of nearer 0.49. So in this case, the Type-3 atomic column partially populated with gallium, having a higher average Z, produces a smaller HAADF signal than the fully populated aluminium column.

The results from this section indicate that a simple stepping vicinal model could not be used to describe the effects observed in the experimental data. The data showed that an interface with positive theta (i.e. AlAs at the crystal surface projecting into GaAs) produces interface width that oscillates with thickness and an interfacial position that steadily shifts towards the bulk AlAs region tracking the gallium content of the Type-3 columns. For an interface with negative theta (i.e. GaAs at the crystal surface projecting into AlAs), the interface width remained constant with thickness and the interfacial position also remained constant with thickness. These effects were primarily caused by the HAADF signals from the primary atomic columns saturating. Specifically, where dumbbells contain a significant amount of gallium the column ratio quickly increases as the specimen thickness increases making the dumbbell appear like a fully populated GaAs column.

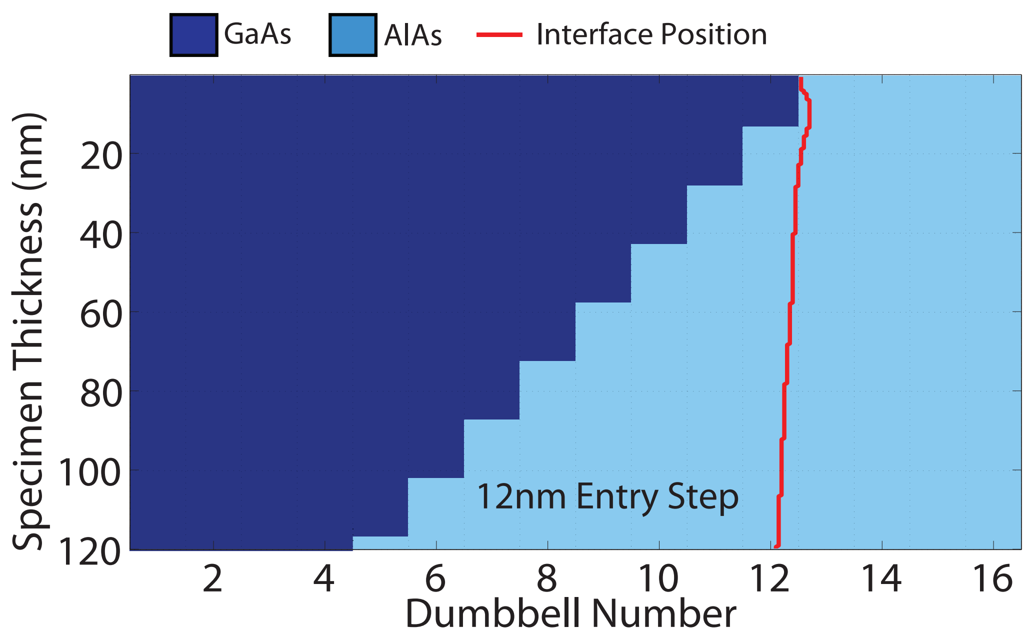

Figure 6.65 – The measured interface position for this model remains between dumbbells 12 and 13 over the full simulation depth.

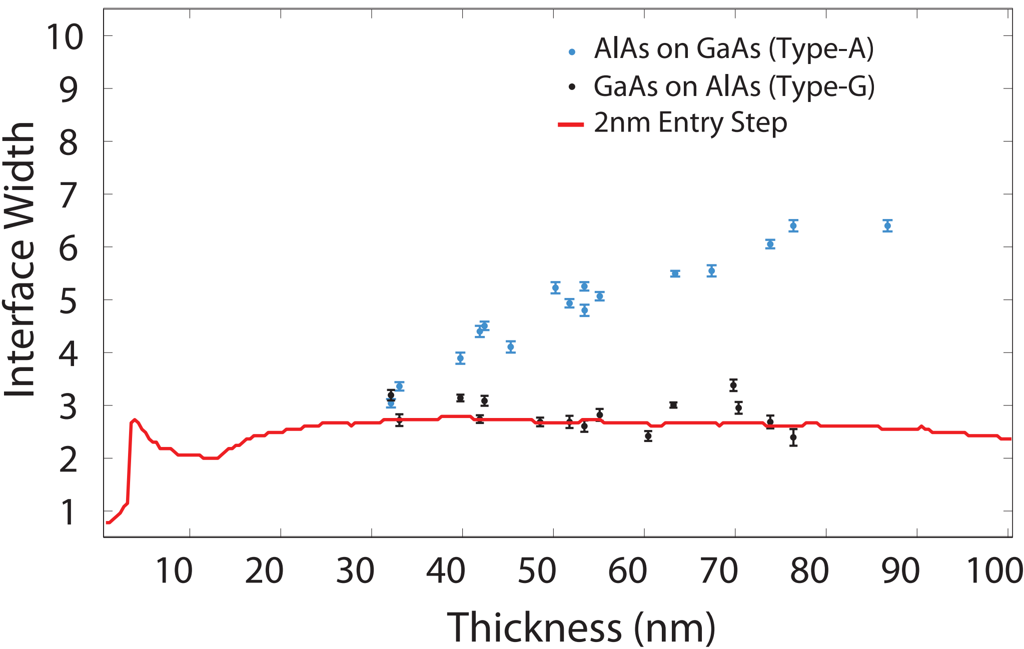

Figure 6.66 – This graph shows the measured interface width as a function of specimen thickness (red). The measured interface width from the model is overlaid onto the experimental measurements from figure 5.15 for comparison. There is a degree of variability in the measured interface width in the top $20nm$ of the model after which the width remains between 2-3 dumbbells.

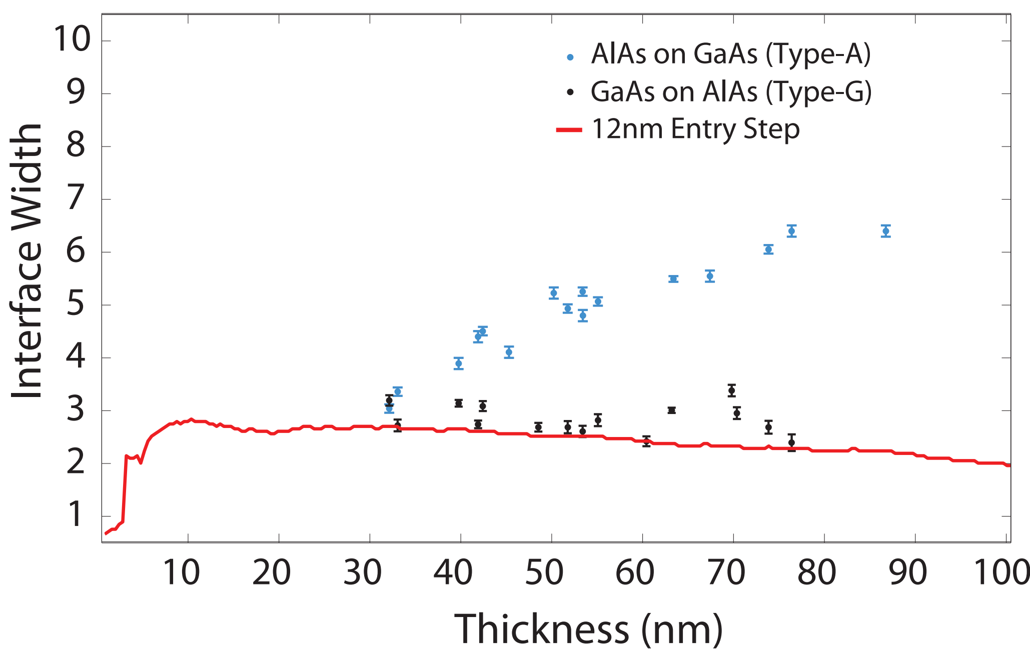

Figure 6.67 – This graph shows the measured interface width as a function of specimen thickness (red). The measured interface width from the model is overlaid onto the experimental measurements from figure 5.15 for comparison. There is a degree of variability in the measured interface width in the top $10nm$ of the model after which the width remains between 2-3 dumbbells, showing a gradual reduction in the measured interface width with increasing thickness.

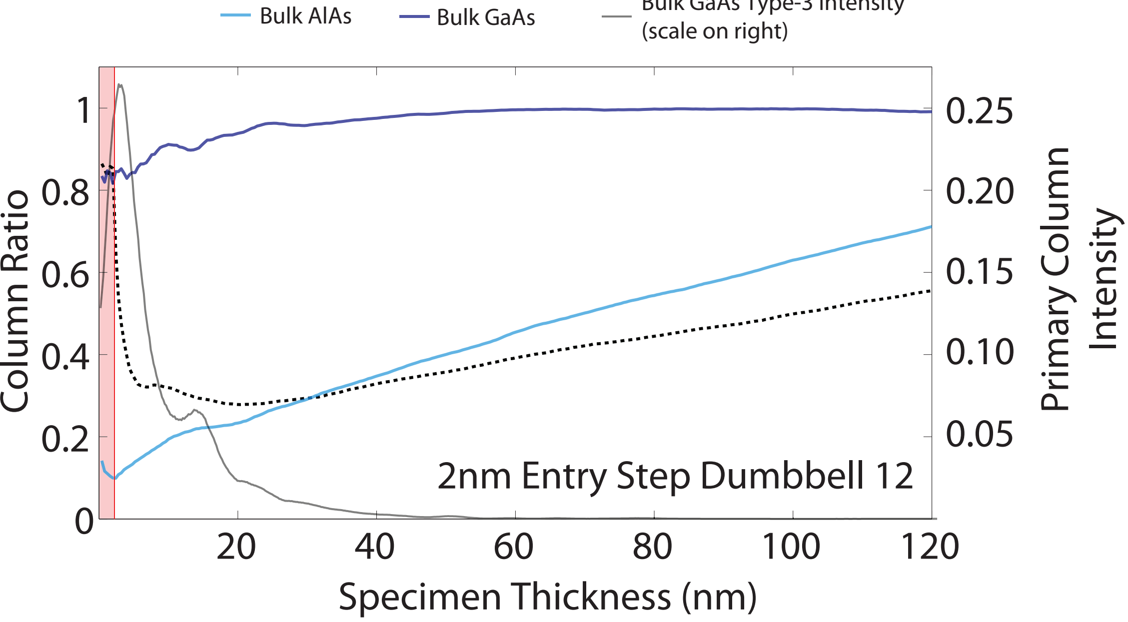

Figure 6.68 – A graph of the column ratio as a function of specimen thickness of dumbbell 12 (broken black) from the $2nm$ entry step model. The background indicates the change in composition from the high Z material (red) to the low Z material. The column ratio of single crystal GaAs (dark blue) and AlAs (light blue) are also shown for comparison. The primary column intensity from the Type-3 column of single crystal GaAs is also shown which indicates the electron intensity on the Type-3 column of dumbbell 12 at the depth of the compositional change.

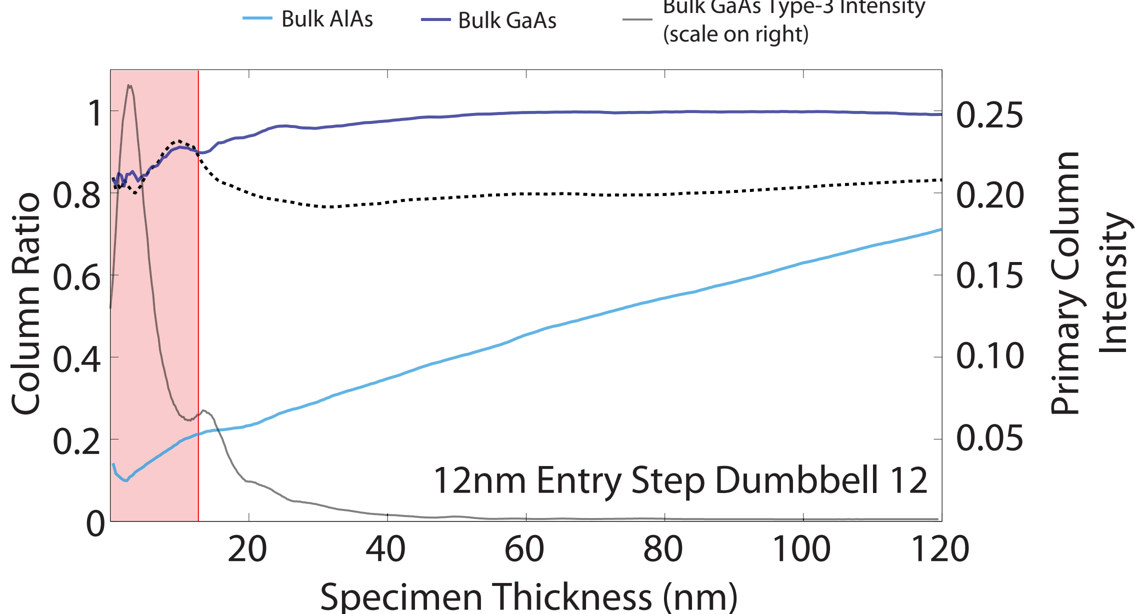

Figure 6.69 – A graph of the column ratio as a function of specimen thickness of dumbbell 12 (broken black) from the 12nm entry step model. The background indicates the change in composition from the high Z material (red) to the low Z material. The column ratio of single crystal GaAs (dark blue) and AlAs (light blue) are also shown for comparison. The primary column intensity from the Type-3 column of single crystal GaAs is also shown which indicates the electron intensity on the Type-3 column of dumbbell 12 at the depth of the compositional change.

6.2.6 Random Step Vicinal Interface

The simple vicinal models were created using a regular and consistent step length. While this structure gives an indication of the characteristics of a vicinal interface such a regular structure would be unlikely to form during MBE growth. A study by Ikarashi et al. reported on the stepping structures that formed during the MBE growth of GaAs - AlAs superlattices. This study provided information on the step intervals and straightness of step edges of both the Type-A and Type-G interfaces. In particular, they observed that while the Type-A interface was atomically abrupt there was a significant amount of interfacial stepping. Furthermore, the step lengths were predominantly short (i.e. $< 20nm$). Another observation was that microscopic diffusion occurs at the Type-G interface due to mixing of the Type-3 atoms. This occurred over a few monolayers [102]. This form of interfacial stepping and diffusion can be integrated into the vicinal models allowing the investigation of a configuration that may be more typical of an MBE grown interface.

Type-A By considering the experimental measurements and the simulation results so far the possible structures for each type of interface can be narrowed. From the experimental width measurements (figure 5.16), the Type-A interface width continues to increase as the specimen thickness increases from $30nm$ to $80nm$. To detect compositional changes at this depth, the interface angle must be orientated such that the probe is projecting through AlAs before GaAs. This orientation can be combined with the interfacial stepping measured by Ikarashi et al. to create a model for the Type-A interface.

Figure 6.70 shows a schematic of ten different random configurations of this type of structure and shows the random stepping overlaid onto a vicinal interface. The random step distribution can be formed using a Gaussian with a mean of $5nm$ and a variance of $100nm$ (for step lengths $\geqslant 0$ only).The distribution is consistent with HRTEM observations of step lengths of a $[\bar{1}10]$ orientated GaAs - AlAs interface [102]. The distribution can be seen in figure 6.71 and was used to select the random step length when forming the vicinal interface models of the Type-A interface. As the interface is now formed using random stepping it is vital to average several configurations together to ensure the results are not sensitive to any one configuration and instead give an overview of the model characteristics. Furthermore, averaging many configurations together is equivalent to averaging the column ratio line profiles together from the experimental images. The following four sections details the Type-A interface configurations where theta (the interface angle) was varied from 0.2 - 0.8 degrees which allowed the resulting interfacial positions and widths to be measured.

6.2.6.1 Type-A ($\theta = 0.2°$)

The schematic of the first Type-A model can be seen in figure 6.72 and consists of a $0.2°$ interface orientated to have an AlAs projection (i.e. probe projects through AlAs before GaAs). The model was calculated for ten random step configurations and the resulting column ratio profiles were averaged together before the interface position and widths were measured. The schematic shows a projection through all ten atomic configurations. The vicinal angle forces a single step in the model at a typical depth of $60nm$ and it is over this single vicinal step that the random stepping is applied. The schematic in figure 6.72 shows all ten profiles averaged together and the measured interfacial position is overlaid in red. The measured interface position corresponds well

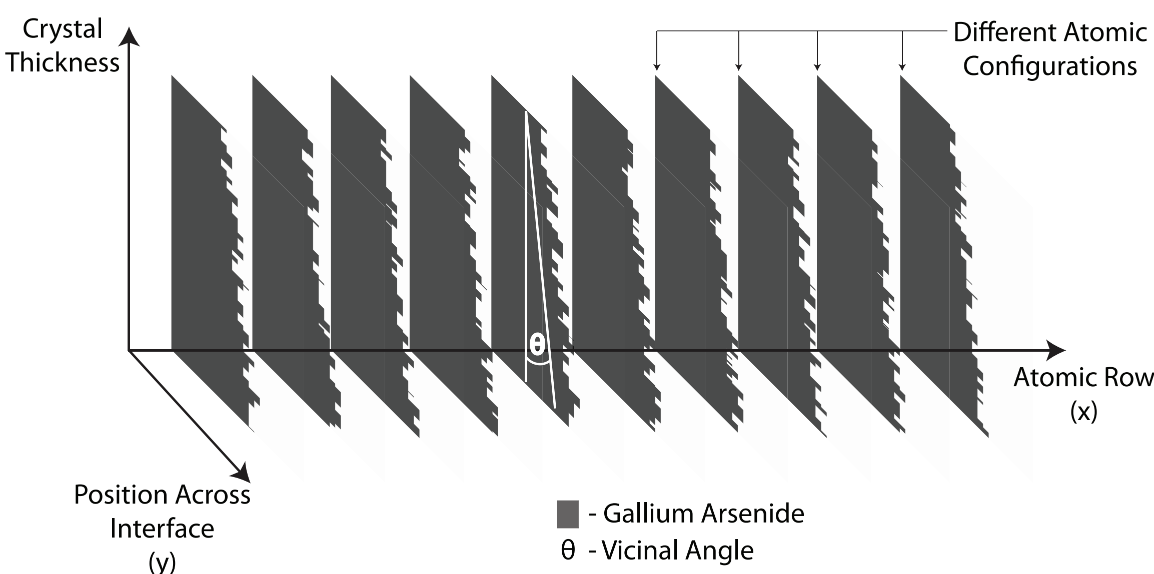

Figure 6.70 – This Type-A vicinal model was created using a random distribution of step lengths. These step lengths were generated using a Gaussian distribution to match experimental TEM measurements recorded by Ikarashi et al. [102]. This random stepping formed the interface between the AlAs grown on GaAs (Type-A) layers at a specified vicinal angle. Ten different atomic configurations were calculated and the results averaged together to replicate the averaging used in the column ratio mapping technique.

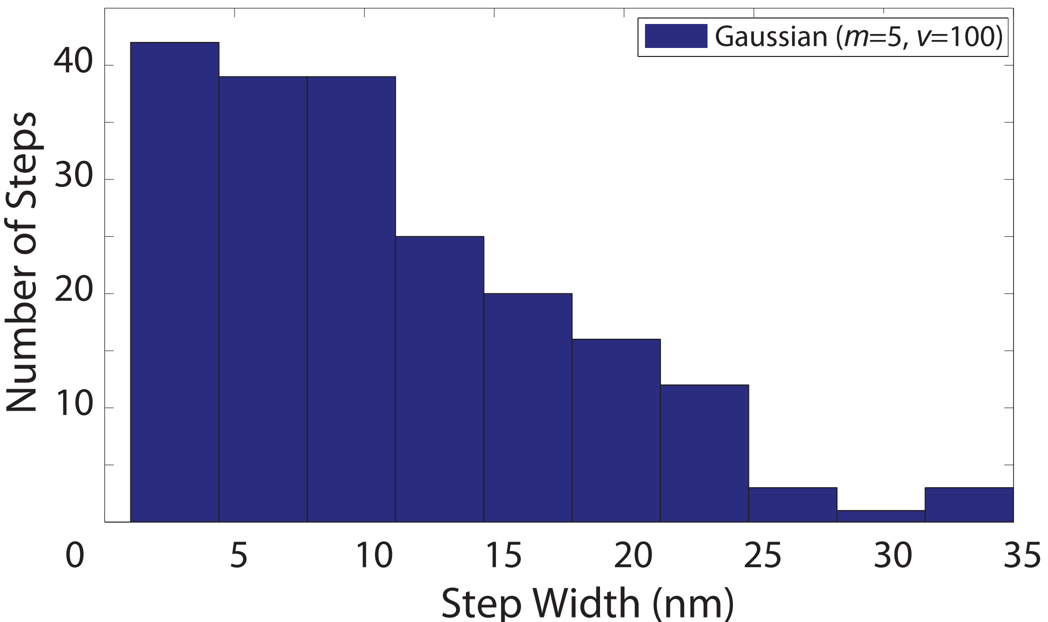

Figure 6.71 – The step length is chosen from a Gaussian distribution with a mean (m) of $5nm$ and a variance (v) of $100nm$ for step lengths > 0 only. The distribution is consistent with HRTEM observations of step lengths of a $[\bar{1}10]$ orientated GaAs - AlAs interface [102].

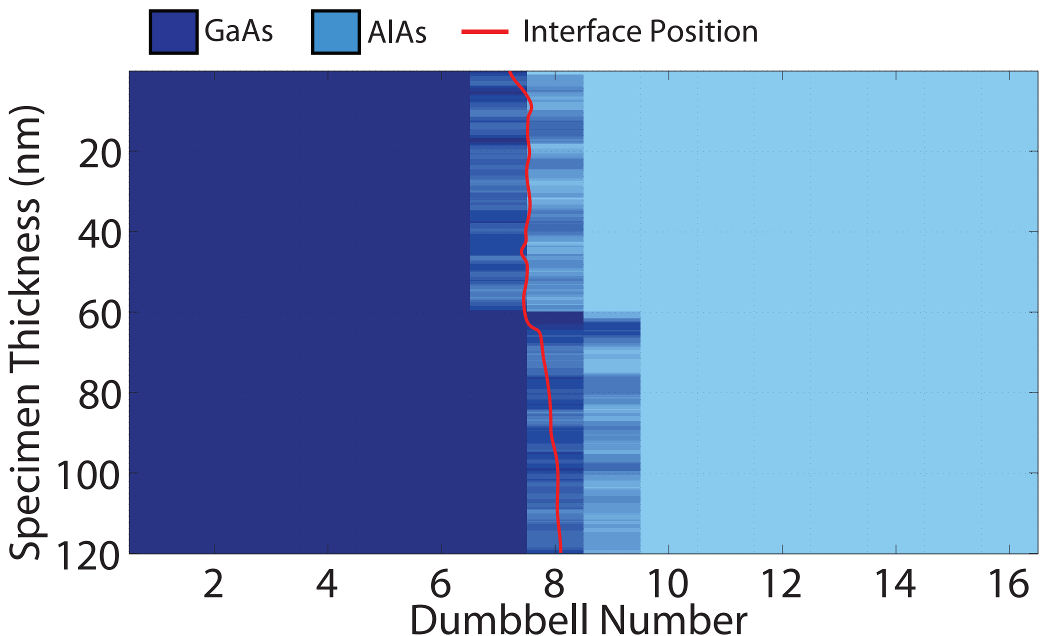

Figure 6.72 – This graph shows the schematic for the Type-A random vicinal interface where $\theta = 0.2°$ with the measured interface position (red) overlaid. Initially the measured interface position is located between dumbbells 7 and 8. At the depth of the first step, $\sim 60nm$ the interface position begins to move towards dumbbell 8.

to the location of the "averaged" interface and for a thin crystal is positioned between dumbbells 7 and 8. As the thickness of the model increases the interface position moves due to the vicinal step which produces a shift of less than one dumbbell. The measured interface width is shown in figure 6.73 and indicates that the width increases after the vicinal step at a depth of $60nm$.

The results from the 0.2° vicinal model indicates that the step below $60nm$ is detectable as there is a measurable change in the interface position and interface width. The relative change in interface position and the increase in width do not correspond to those measured from the experimental Type-A interface. This 0.2° model does, however, indicate that an increase in θ may produce characteristics that are consistent with the experimental measurements.

6.2.6.2 Type-A ($\theta = 0.3°$)

The next model is formed in an identical way to the first with ten random configurations calculated independently. For this model the angle of the interface is changed to 0.3°. The schematic of this model is shown in figure 6.74 where now the overall vicinal angle forces two steps at depths of $40nm$ and $80nm$ and the random stepping is then applied over the interface. The measured interface position is overlaid in red

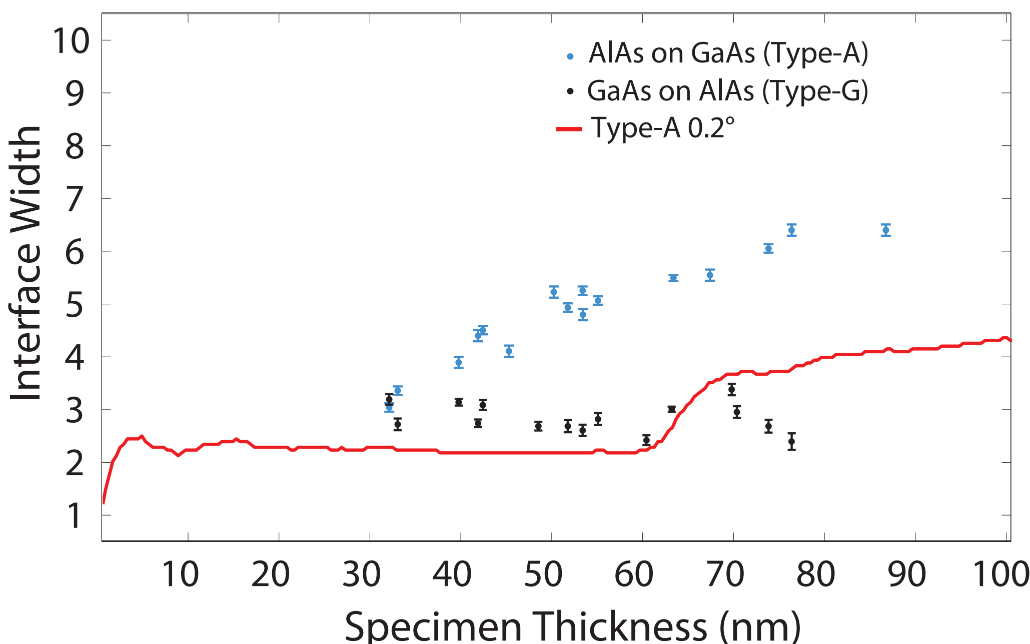

Figure 6.73 – This graph shows the measured interface width for the Type-A random vicinal interface where $\theta = 0.2°$ (red). The measured interface width from the model is overlaid onto the experimental measurements from figure 5.15 for comparison. As with other AlAs projection models the measured interface width reflects the change in composition, which in this case is at a depth of 60nm.

and indicates that the apparent location of the interface steps towards the bulk AlAs region approximately one dumbbell as the thickness of the interface increases. It also indicates that the measured interface position is a reasonable representation of the actual (average) interface position for the upper half of the model. Figure 6.75 shows the measured interface width overlaid onto the experimental data and indicates that the interfacial steps are detected at both $40nm$ and $80nm$. This model clearly indicates that an increase of $0.1°$ produces a measurable change in the interface position and in the measured interface width. However, the resulting shift in interface position and the change in interface width are less than those measured for the experimental Type-A interface.

6.2.6.3 Type-A ($\theta = 0.6°$)

By increasing the angle of the vicinal interface it should therefore be possible to tailor the model to match the experimental measurements. This would give a clear indication of the type of vicinal model that could be used to describe the experimental structures. One of the issues with increasing the interfacial angle is that by doing so the depth of

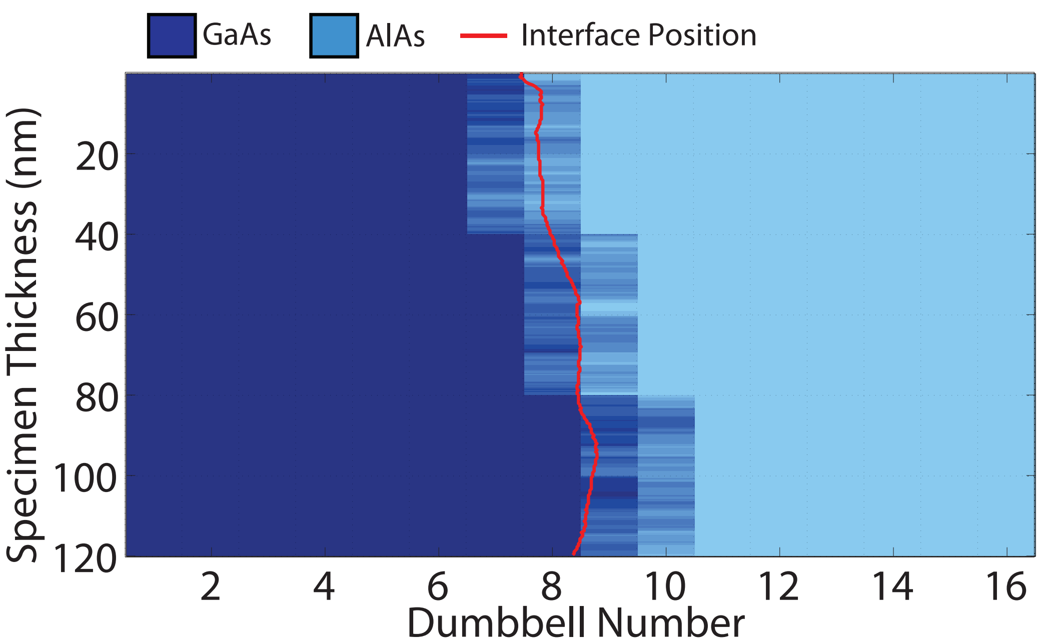

Figure 6.74 – This graph shows the schematic for the Type-A random vicinal interface where $\theta = 0.3°$ with the measured interface position (red) overlaid. Initially the measured interface position is located between dumbbells 7 and 8 and as the thickness of the specimen is increased the position moves towards dumbbell 8. The final step at a depth of $\sim 80nm$ does not, however, affect the measured interface position.

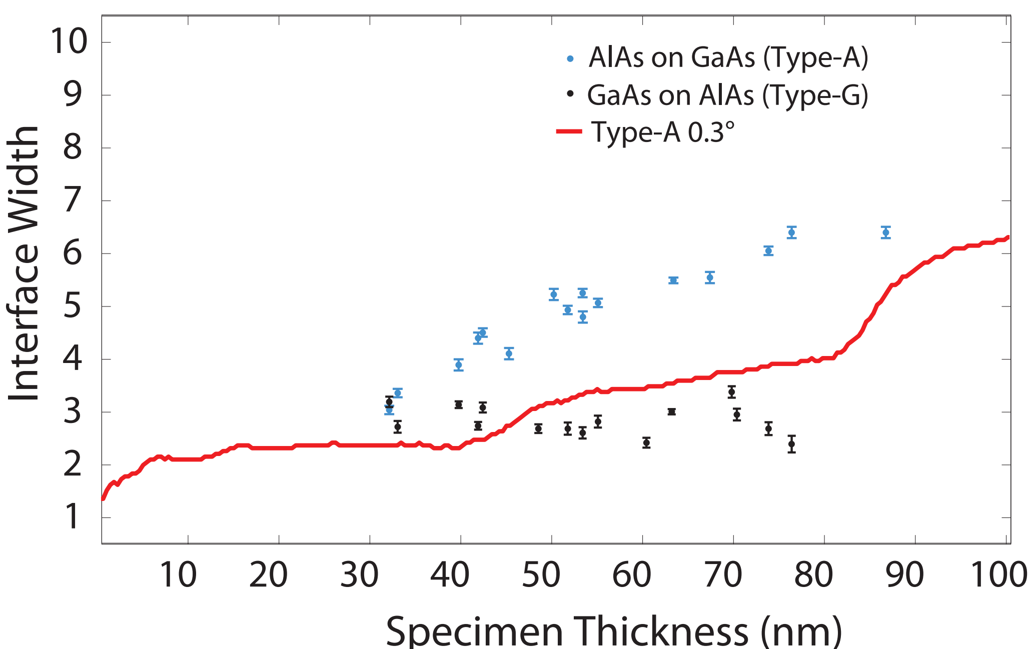

Figure 6.75 – This graph shows the measured interface width for the Type-A random vicinal interface where $\theta = 0.3°$ (red). The measured interface width from the model is overlaid onto the experimental measurements from figure 5.15 for comparison. As with other AlAs projection models the measured interface width reflects the gallium content of the atomic columns. In this case the change of composition (interface steps) occur at depths of $40nm$ and $82nm$.

the first vicinal step is reduced. For example in the $\theta = 0.2°$ model the first vicinal step occurred at a depth of $\sim 60nm$, when the value of theta is increased to $\theta = 0.6°$ the first vicinal step occurs at $\sim 20nm$. A schematic of the $\theta = 0.6°$ model can be seen in figure 6.76 and the dumbbell with this first vicinal step can be seen at dumbbell 5. As these columns now have a significant amount of gallium near to the entrance of the atomic columns the resulting measured column ratio quickly saturates. This saturation will produce a similar effect to the sawtooth models where instead of a gradual widening of the interface the interface position will quickly shift towards the bulk AlAs region. This is the case for this $\theta = 0.6°$ model and the interface position is shown over the schematic in figure 6.76. The position of the interface moves from between dumbbells 5 and 6 for a thin crystal to near dumbbell 10 for a crystal at 120nm. This saturation of the column ratio has the effect of reducing the overall measured interface width. The atomic columns with significant quantities of gallium appear to form part of the bulk GaAs region as the thickness increases. A plot of the measured interface width can be seen in figure 6.77 which indicates that the rate of change of the interface width is larger than that of the $\theta = 0.3°$ model. However, the measured width of the model is still below that of the experimental Type-A interface. This is a clear indication that simply increasing the vicinal angle of the model interface does not change the measured interface width in a predictable way.

Type-G Each Type-A interface from the preceding section can be paired to another model which corresponds to the interface at the other face of the growth layer. For example, an AlAs layer grown on a vicinal GaAs substrate will form a Type-A interface that will necessarily have the same angle of inclination as the substrate. The growth of a further GaAs layer will form a Type-G interface which would again have the same vicinal angle as the Type-A interface and so on. When these interfaces are orientated to a [110] direction one interface will form an AlAs projection and the other a GaAs projection. The Type-A model from section 6.2.6.1 formed a 0.2° vicinal AlAs projection which can be paired with a 0.2° Type-G GaAs projection model. The following two sections detail the results from a 0.2° and a 0.6° Type-G interfaces where the interfacial roughness is incorporated via gallium diffusion [1, 4, 102, 103]. This form of roughness at a Type-G interface was identified in the study by Ikarashi et al. [102]. The concentration distribution of the diffuse interface is identical to that shown

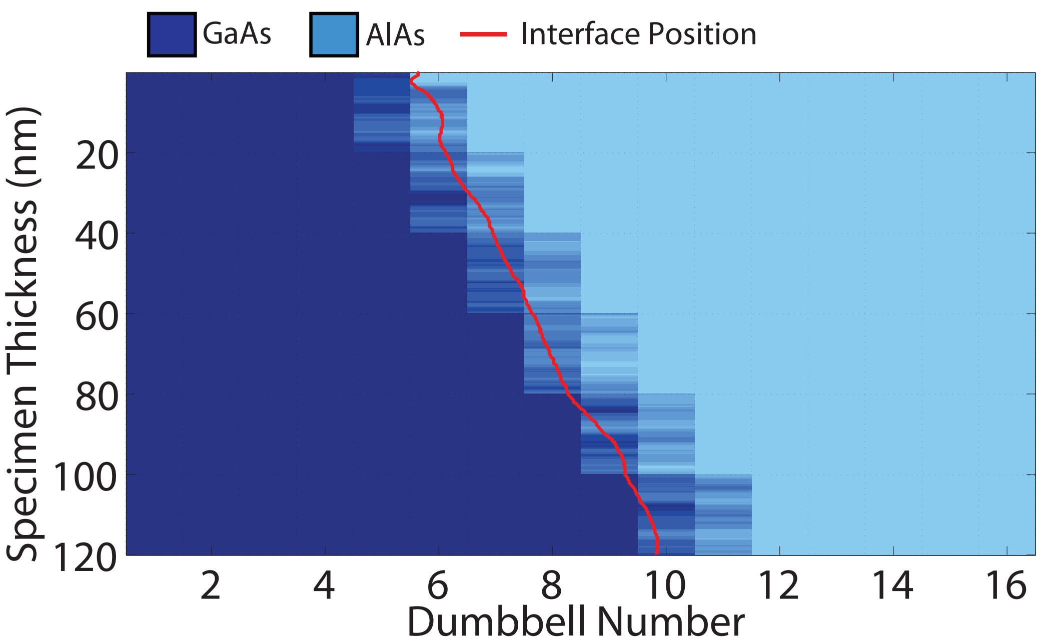

Figure 6.76 – This graph shows the schematic for the Type-A random vicinal interface where $\theta = 0.6°$ with the measured interface position (red) overlaid. Initially the measured interface position is located at dumbbell 6. As the thickness of the specimen is increased the location of the measured interface gradually shifts towards the bulk AlAs region and at a depth of $120nm$ the interface position is located at dumbbell 10.

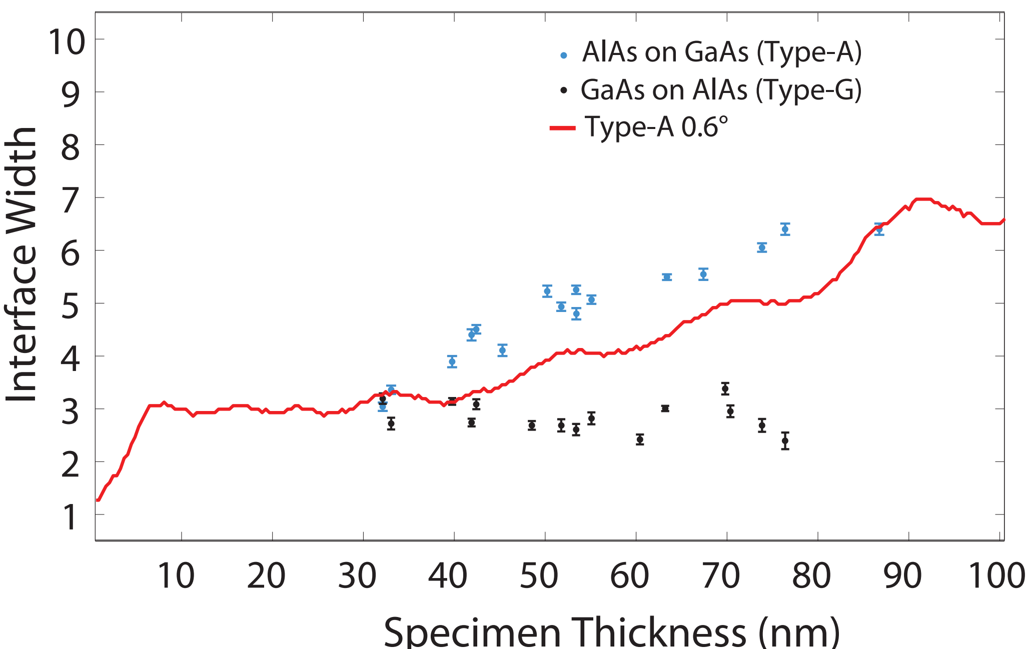

Figure 6.77 – This graph shows the measured interface width for the Type-A random vicinal interface where $\theta = 0.6°$. The measured interface width from the model is overlaid onto the experimental measurements from figure 5.15 for comparison. This model exhibits a gradual change in the interface width as a function of thickness which is comparable to the measurements taken experimentally from the Type-A interface.

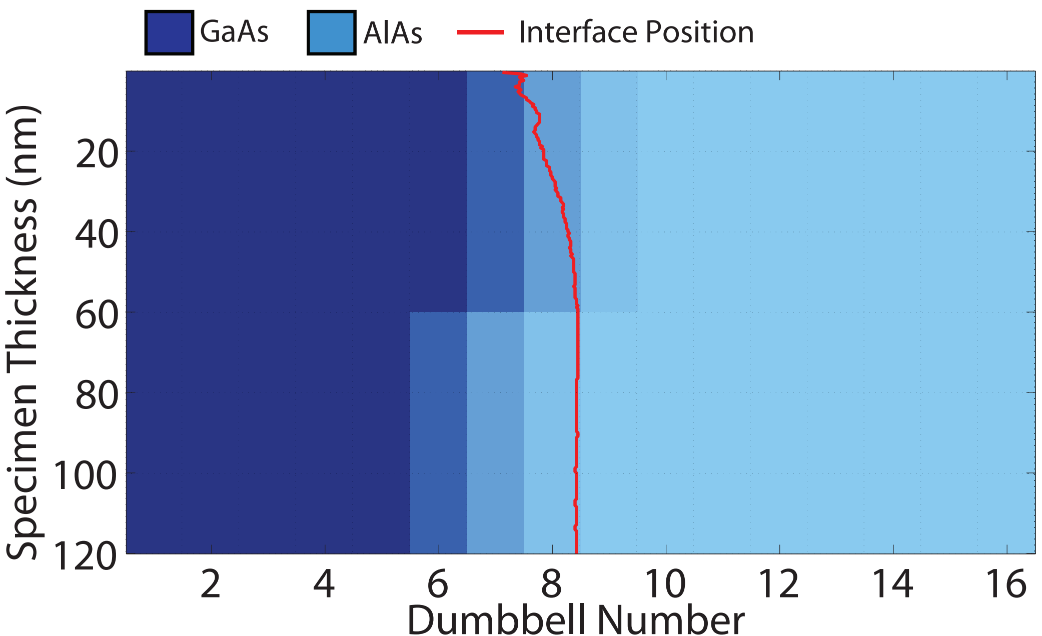

Figure 6.78 – This graph shows the schematic for the Type-G diffuse vicinal interface where $\theta = 0.6°$ with the measured interface position (red) overlaid. Initially the measured interface position is located between dumbbells 7 and 8. As the thickness of the specimen is increased the location of the measured interface gradually shifts to between dumbbells 8 and 9.

in figure 6.45 on page 169 with the addition of the overall vicinality.

6.2.6.4 Type-G ($\theta = 0.2°$)

The vicinal angle was chosen to match the Type-A model from section 6.2.6.1 and set to 0.2° with a GaAs projection. A schematic of the configuration can be seen in figure 6.78 and the interfacial region spans from dumbbells 6 to 10. The schematic shows a single vicinal step at a depth of $60nm$. The schematic also shows the measured interface position in red and indicates that the location of the interface starts between dumbbells 7 and 8 at the crystal surface. As the specimen thickness increases, the interface position gradually moves to a position between dumbbells 8 and 9. The interfacial step makes little difference to the measured interface position as it is below the GaAs overhang. The measured interface width (shown in figure 6.79) shows an increase in the interfacial width in the first $15nm$ of the model and then a gradual decline in width over the remainder of the simulation depth.

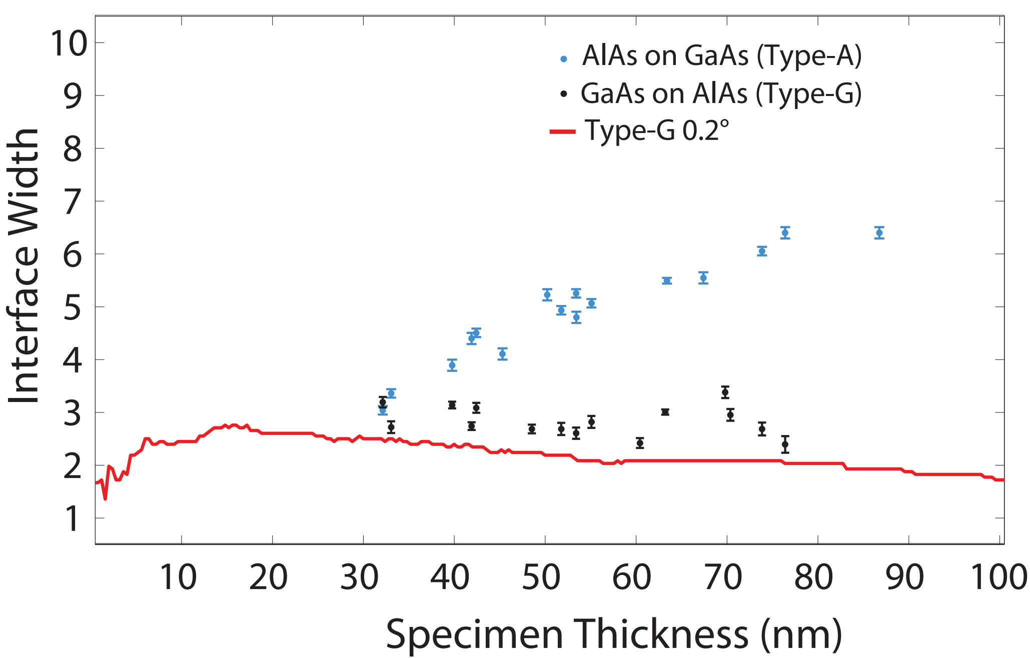

Figure 6.79 – This graph shows the measured interface width for the Type-G diffuse vicinal interface where $\theta = 0.2°$. The measured interface width from the model is overlaid onto the experimental measurements from figure 5.15 for comparison. This measured interface width for this model increases from $0 - 15nm$ and then gradually drops with increasing thickness. The maximum measured width does not increase to greater than 3 dumbbells.

6.2.6.5 Type-G ($\theta = 0.6°$)

The vicinal angle was then increased to 0.6° to match the Type-A model from section 6.2.6.3. A schematic of this model can be seen in figure 6.80 and shows the increased vicinal angle which now produces a significant GaAs projected interface. The model schematic shows five vicinal steps over the $120nm$ simulation depth. The measured interface position in also shown in red. For this model, the interfacial position starts between dumbbells 8 and 9 and initially moves towards the bulk AlAs region until the first vicinal step at a depth of $20nm$ after which there is a gradual shift back towards the bulk GaAs region. The measured width of the interface is also indicated in figure 6.81 which shows little variation over the simulation depth. The width gradually increases over the first $20nm$ of the model and then remains constant at a width of 3 dumbbells for the remainder of the model.

The results from these randomly stepped vicinal interfaces indicate that some of the experimental characteristics can be reproduced. Furthermore, the increase in the measured Type-A interfacial width can be accounted for using the 0.6° Type-A vicinal

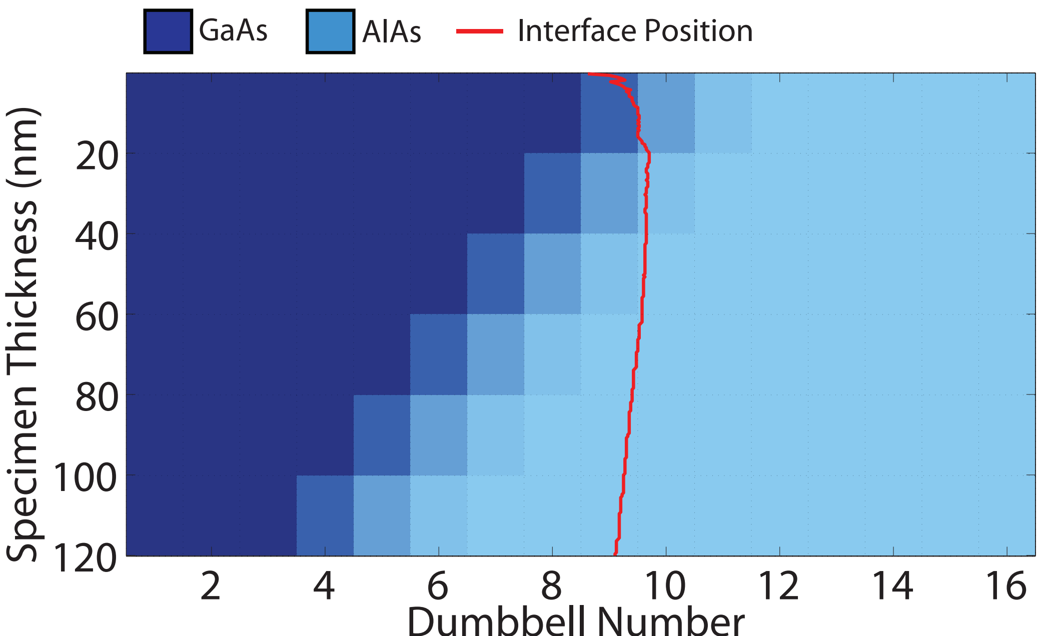

Figure 6.80 – This graph shows the schematic for the Type-G diffuse vicinal interface where $\theta = 0.6°$ with the measured interface position (red) overlaid. Initially the measured interface position is located between dumbbells 8 and 9. The position follows a curved path which is due to both the diffusion in the top region of the crystal and also the AlAs under the overhang affecting the background signal.

model. However, all of the characteristics of the experimental measurements are not reproduced. For example, the measured GaAs layer for the 0.6° Type-A vicinal model would appear to increase significantly with increasing specimen thickness. This is not observed in the experimental images and, therefore, it is unlikely that the interfaces in sample C102 are vicinal.

6.3 Discussion and Conclusions

The aim of this chapter was to develop a series of models that could describe the experimental measurements taken from the MBE grown GaAs -AlAs superlattice. Table 6.1 provides a summary of the main characteristics measured from each model. The table gives details of the model name, the section containing the results, a schematic of the interface is also shown with the change in interface width, ΔI_W, and interface position,ΔI_P, (in dumbbells) that occurs over 30-100nm. A positive shift in the interface position corresponds to a shift towards the bulk AlAs region.

The model development began with a broad range of simple structures that were investigated using the multislice code. The first model consisted of a perfectly abrupt

Model	Section	Schematic	ΔI_W	ΔI_P
Perfect Interface	6.2.2		0	0
Sawtooth Interface				
Long Repeat Length				
- AlAs Projection	6.2.3.1		+2	+6
- GaAs Projection	6.2.3.2		+2	-1
Short Repeat Length				
- AlAs Projection	6.2.3.3		+2	0
- GaAs Projection	6.2.3.4		+2	-2
Diffused Interface				
- Linear Diffusion Model	6.2.4.1		-5	+1.5
Segregation Model				
- Type-A	6.2.4.2		+3	+2
- Type-G	6.2.4.2		0	+1
Simple Vicinal Interface				
- AlAs Projection	6.2.5.1		+1	+5
- GaAs Projection	6.2.5.2		0	0
Random Vicinal Interface				
Type-A				
- 0.2°	6.2.6.1		+1	+1
- 0.3°	6.2.6.2		+2	+1.5
- 0.6°	6.2.6.3		+3	+4
Type-G				
- 0.2°	6.2.6.4		0	+1
- 0.6°	6.2.6.5		0	0

Table 6.1 – This table gives a summary of the interfacial models discussed in the sections above. The table shows the model name and section reference. A schematic of the interface is also shown with the change in interface width, ΔI_W, and interface position, ΔI_P, (in dumbbells) that occurs over 30-100nm. A positive shift in the interface position corresponds to a shift towards the bulk AlAs region.

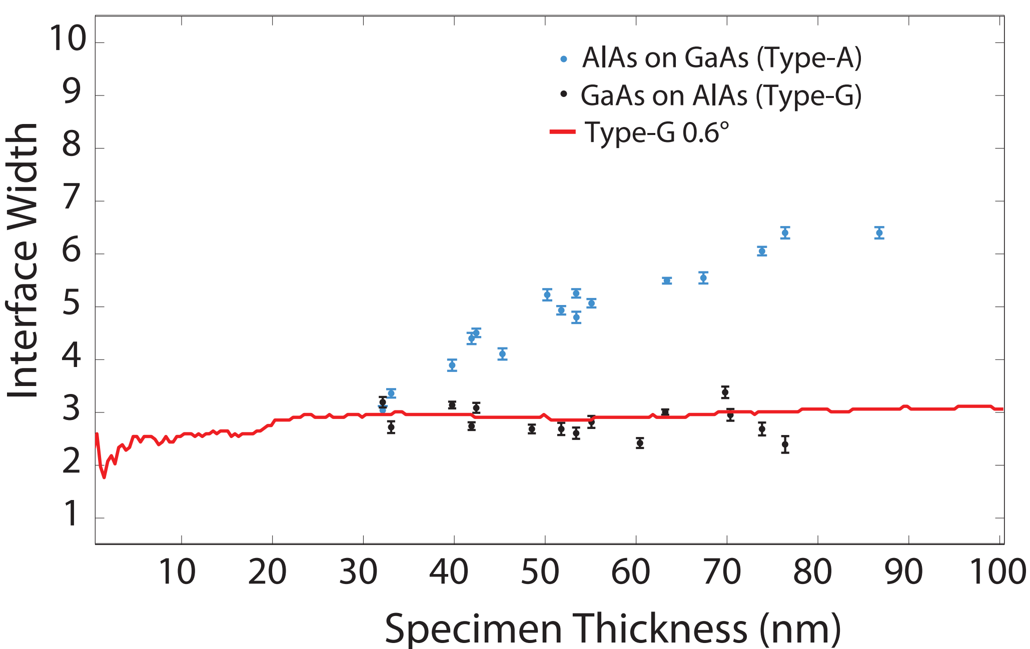

Figure 6.81 – This graph shows the measured interface width for the Type-G diffuse interface where $\theta = 0.6°$. The measured interface width from the model is overlaid onto the experimental measurements from figure 5.15 for comparison. The vicinal angle of this interface is greater than the $\theta = 0.3°$ case, however the vicinal angle causes a GaAs projection and therefore the compositional changes are not detected below the overhanging interface.

AlAs - GaAs interface. This model provided an understanding of how effects such a beam broadening affected the measured characteristics of the interface. The results from this model indicated that both the interface width and position remained constant with increasing thickness. However, the proximity of the interface was found to affect the measured column ratio as a result of the background scattering of the probe.

The next set of models consisted of a range of terrace structures that formed a repeating sawtooth pattern in the z-direction. While these models exhibited many of the characteristics observed in the experimental data, it was clear that none of the models met all of the constraints imposed by the experimental measurements. However, the results of the sawtooth models indicated the possibility that a vicinal interface of some description could describe the experimental data.

Two simple vicinal models were initially formed, the angle of the interfaces was chosen to be $+1°$ and then $-1°$. The positive interface angle formed a GaAs projection where the probe was projecting through GaAs at the entrance of the specimen. The negative interface angle formed an AlAs projection where the probe would project through AlAs first. The results from these simple vicinal interfaces indicated that the

column ratio quickly saturates in the case of the AlAs projection and the apparent shift in interface position can be significant because of this effect. Furthermore, the GaAs projection indicated that both the measured interface position and interface width remain constant with thickness.

The next development for this type of vicinal model was the introduction of a degree of stepping at the interface which reduced the saturation effect. The results indicated that an interface with a vicinality of $0.6°$ and a degree of interfacial roughness could be used to describe some of the experimental results. For example, the upper graph in figure 6.82 shows the measured interface width as a function of specimen thickness for both the Type-A and Type-G interfaces. While the measured interface width from this vicinal model was consistent with the experimentally measured interface widths, the measured interface position was not. The lower schematic of figure 6.82 shows the measured change in layer width that would be measured from the model vicinal interface structure. The measurements indicate that the change in width of the GaAs layer would be 4 dumbbells which is greater than the $2\frac{1}{2}$ dumbbells measured experimentally.

The diffused model described in section 6.2.4 found the best agreement with the experimental data. This model was developed using model concentration profiles that were calculated using a segregation model for III-V materials [103]. This indicates that both the measured characteristics of the simulated Type-A (AlAs on GaAs) and Type-G (GaAs on AlAs) interfaces were in good agreement with the experimental measurements of chapter 5. The upper graph in figure 6.83 shows the measured interface width as a function of specimen thickness for the experimental interfaces. The Type-A and Type-G diffusion model results are overlaid indicating good agreement between the two data sets. Furthermore, the lower schematic in figure 6.83 shows the apparent change in the GaAs layer that would occur from this diffusion model. In this diffusion case, the apparent increase in the GaAs layer would be consistent with the experimentally measured layer widths.

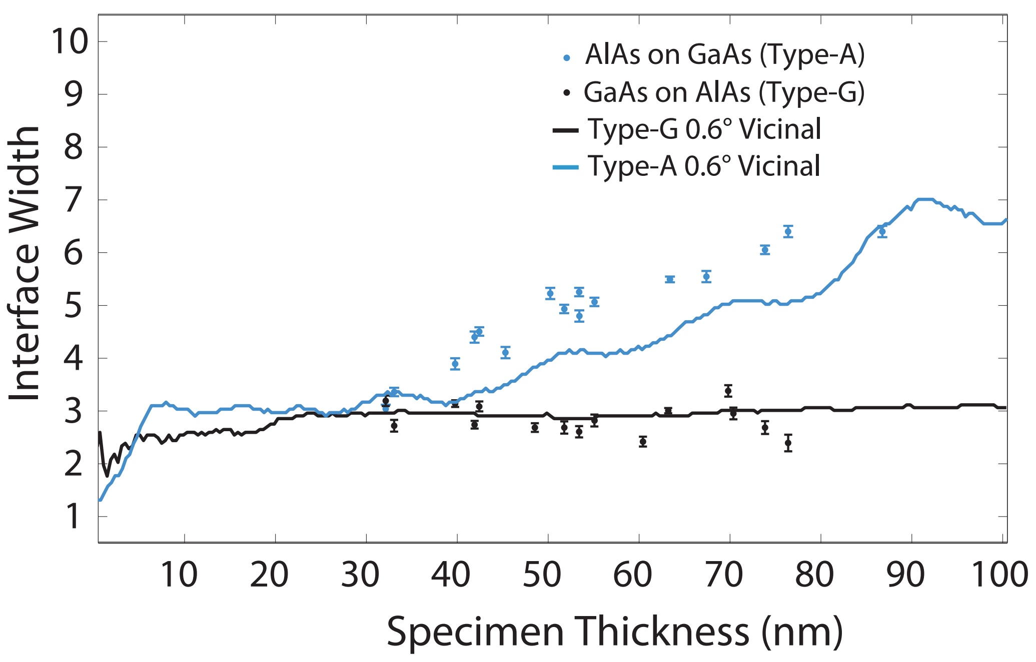

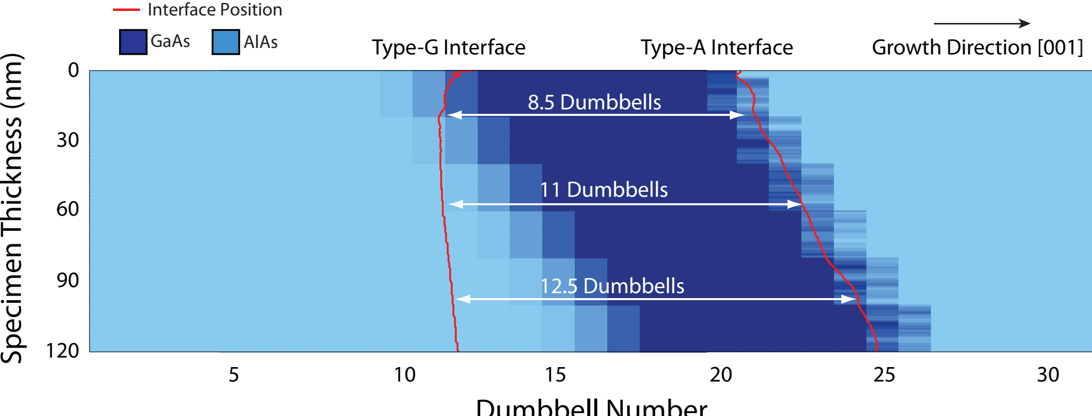

Figure 6.82 – The upper graph shows the measured interface width as a function of specimen thickness for both the Type-A and Type-G interfaces. While the measured interface width from the vicinal model was consistent with the experimentally measured interface widths, the measured interface position was not. The lower schematic shows the measured change in layer width that would be expected from this type of vicinal interface structure. This vicinal model indicates that the change in width of the GaAs layer would be 4 dumbbells which is greater than the $2\frac{1}{2}$ dumbbells measured experimentally.

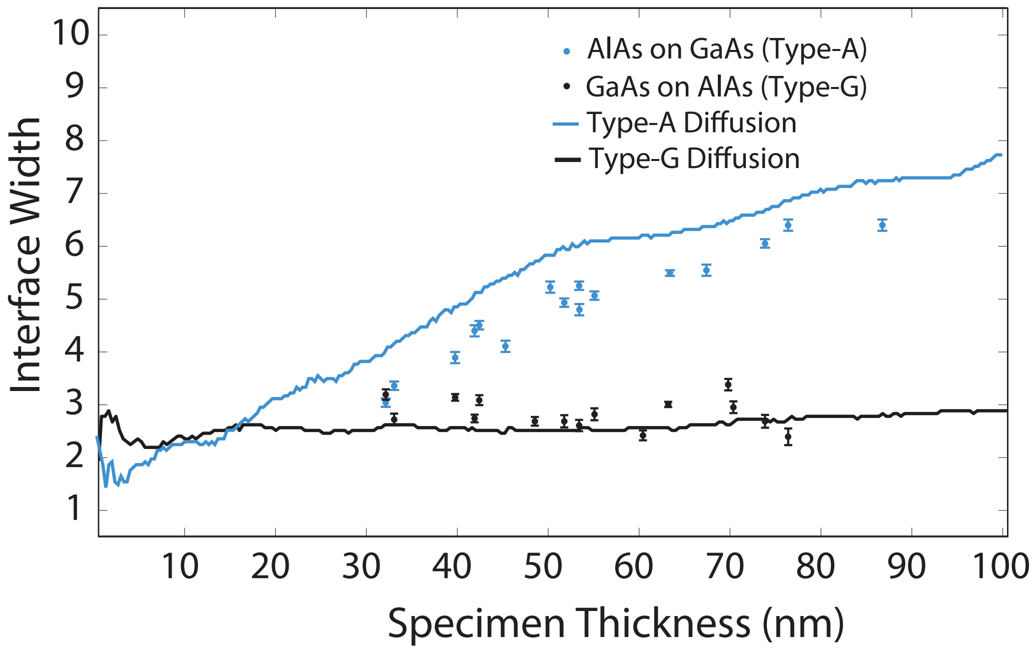

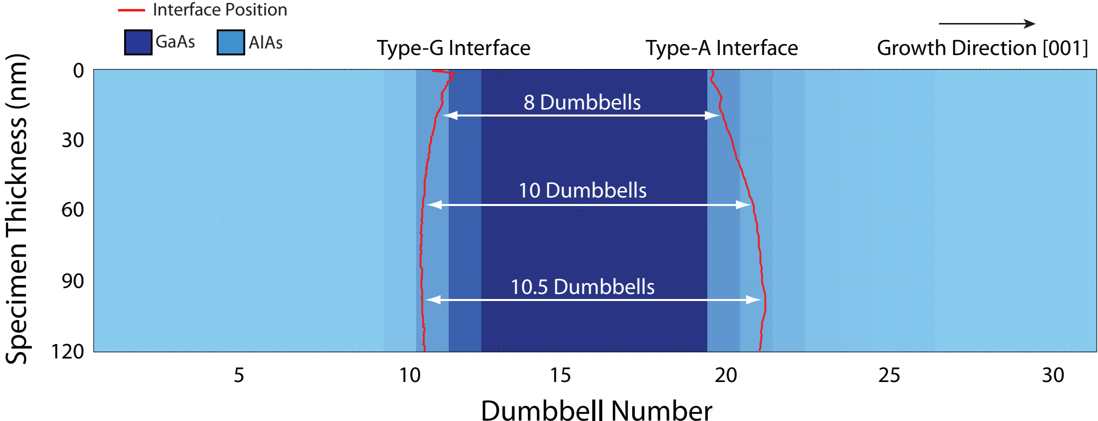

Figure 6.83 – The upper graph represents the model that can be used to describe the change in the measured interface width observed experimentally. The interface width measurements indicate that the experimental interfaces are diffuse. Furthermore, the gallium diffusion at the Type-A interface extends many monolayers into the AlAs layer while the aluminium diffusion at the Type-G interface is more contained. The lower schematic represents the diffusion model that can be used to describe the change in GaAs layer width observed experimentally. The results indicate that the experimental interfaces are diffuse resulting in a change in the measured GaAs layer of approximately $2\frac{1}{2}$ dumbbells. This very similar to the measured change in the GaAs layer width described in section 5.4.2.

Chapter 7

Atomic Column Scattering

The ability to interpret atomic resolution HAADF images intuitively is dependent on the assumption that the image intensity variations correspond directly to changes of composition within the sample. The multislice calculations from chapter 6 have, however, indicated that the scattering that is generated from an atomic column depends not only on the composition of the column but also on the depths at which the compositional changes occur.

Section 3.6 showed the comparison of experimental and simulated column ratio data from bulk GaAs and bulk AlAs. This data indicated that the measured value of the column ratio varied with thickness in a predictable manner. For example, the multislice simulations allow the column ratio value for single crystal GaAs and AlAs to be predicted for a sample of known thickness. This allowed an initial assumption that dumbbells with a column ratio between bulk GaAs and bulk AlAs are interfacial and consist of a Type-3 column that is partially populated with gallium and partially populated with aluminium.

Section 6.2.4.1 showed the results from the linear diffusion model where a diffuse interface was located between bulk GaAs and AlAs. The gallium concentration was varied linearly across the interface and the following calculations indicated that interfacial dumbbells were identifiable up until the point of saturation. Until saturation the measured column ratio value of an interfacial dumbbell fell between those of bulk GaAs and bulk AlAs. Therefore the linear diffusion model supports the assumption that the column ratio data is directly interpretable.

The results from the vicinal AlAs projection model from section 6.2.5.1 showed that when the compositional changes within an atomic column have a specific configuration

the column ratio values changed in an unpredictable way. For example, the column ratio profile in figure 6.55 showed the results from an AlAs projected interface where dumbbells 5 and 6 consisted of atomic columns with small amounts of aluminium at the top of a gallium column. The results for this model indicated that at a thickness of $50nm$ the generated HAADF signal from dumbbell 5 resulted in a column ratio greater than a fully populated gallium column. However, if the depth of the compositional change is varied as in the case of dumbbell 6 this can considerably reduced the overall scattering from the column. Furthermore, the results from section 6.2.5.2 showed a GaAs projection model where dumbbell 12 consisted of a Type-3 column with a small amount of gallium at the top of an aluminium column. In this case, the generated HAADF signal from dumbbell 12 resulted in a column ratio that was considerably less than a fully populated aluminium column for thick crystals.

A typical TEM specimen is thin ($<30nm$) and these counter intuitive effects are not as prominent. However, the investigation of an interface requires a series of images to be processed over a large range of thickness. It is therefore important to understand how the generated HAADF signal changes with specimen thickness. This is especially important when the composition of the atomic columns are changing with depth, which is typically the case at an interfacial region.

The aim of this chapter is to systematically investigate compositional changes within atomic columns and, in particular, the effect that the compositional change has on the HAADF signal. Two simplifications were used when creating the crystal structures, both simplifications are related to the change in lattice parameter that occurs at an interface between two lattice mismatched materials.

During MBE growth, when the growth material changes typically the lattice parameter also changes. The lattice misfit is then accommodated by elastic strain which is shown in the upper diagram of figure 7.1. The strained layer is able to expand at the free surfaces of the sample which leads to a distortion of the lattice parameter near the interface. Furthermore, the strain may cause the formation of dislocations at the interfacial region. The upper diagram in figure 7.1 shows the case where the interface that is formed between the lattice mismatched material is perfect. The interface may, however, have a degree of roughness which is indicated in the diagram below which is labeled as a "Strained Stepped Interface". In this case the upper section of the indicated atomic column is formed from a different atomic species from the lower section

(the beam direction is indicated by the arrow). To simulate an interface of this type would require a calculation of the strain at the interface and the resulting deformation of the two crystal lattices. A new strain calculation would be required as the depth of the step was changed and a simplification is therefore necessary. The first simplification is to form a crystal where each atomic column is a replica of the primary atomic column. This simplification can be seen in the next diagram below labeled "Strained Simplification". In this case the depth of the compositional change is constant for all of the atomic columns in the supercell. This simplification therefore does not take into account the proximity of the interface.

The second simplification is to ignore the effects of strain at the depth of the composition change which can be seen in the last diagram labeled "Simulation". This simplification maintains the change in lattice parameter at the compositional change depth, however, the resulting strain and formation of dislocations are ignored.

These two simplifications will however have an effect on the scattering from the atomic column. However, the effect of the proximity of the interface was studied in section 6.2.2. The results indicated that the effect of the interface was predictable to an extent as it modifies the overall background scattering. For a GaAs - AlAs interface this reduced the measured column ratio of the atomic dumbbells adjacent to the interface. Therefore, the effect from the interfacial region can be estimated. The second simplification is the effect of strain at the interface. Yu et al. studied the effects of strain at the interfaces formed in silicon [106]. Their findings indicated that strain fields cause the probe to de-channel. This results in a increased scattering to small angles. However, for HAADF imaging the effect was minimal. Therefore, the results obtained using these simplifications will give an indication of the scattering behavior that can be expected from atomic columns at the interfacial region.

The simulation supercell is constructed so that the central dumbbell columns are aligned, this is indicated by the arrow in the lower right diagram in figure 7.1. It is this central dumbbell that is used as the primary dumbbell for the multislice calculation. These simplifications allow a range of models to be constructed in a consistent manner and the simulation results are detailed in the following sections. Each model in the following section describes a set of conditions where the measured effects are at their greatest. The measured signals are shown in each case for the interfacial dumbbell and for single crystal materials allowing a detailed comparison. A simple hypothesis is

then formed and the validity of this model is explored in an attempt to describe these results.

7.1 AlAs - GaAs

The first series of models investigated consisted of an upper section of AlAs and a lower section of GaAs. In each consecutive model the depth of the compositional change was changed by one unit cell and the generated HAADF signal, primary column intensity and total integrated intensity was calculated for each slice to a depth of $120nm$. The series of models therefore allowed a detailed examination of the effect that the depth of the compositional change has on these measured signals. The overall aim is to gain a deeper understanding of the generated HAADF signal and in particular explain some of the counter intuitive results found in chapter 6. The results in the following sections can be compared to single crystal simulations for GaAs (section 3.6.1) and AlAs (section 3.6.2).

7.1.1 AlAs - GaAs $_{4.3nm}$

The graphs in figure 7.2 show the results from the model where the compositional change was at a depth of $4.3nm$ which corresponds to 11 unit cells of AlAs followed by 289 unit cells of GaAs. The lowest of the three graphs shows the change in column ratio as a function of crystal thickness. The graph contains column ratio data from the compositional change model and column ratio data from GaAs and AlAs single crystals. The data from the bulk GaAs crystal is represented by a solid dark blue line and the data from the AlAs crystal is shown as a broken light blue line for clarity. The column ratio data from the $AlAs-GaAs_{4.3nm}$ model is shown in black and the depth of the compositional change is indicated by the change in colour of the graph background. The AlAs region is shown in white and the change of composition to GaAs is indicated by the change in background to red. The data in the graph indicates that in the upper section of the model the measured column ratio corresponds to that of bulk AlAs. At the depth of the compositional change the column ratio begins to increase and at a depth of $18nm$ the column ratio from the model is comparable to that of bulk GaAs. However as the thickness of the crystal increases the column ratio continues to rise and peaks at a value of 1.14 at a depth of $60nm$.

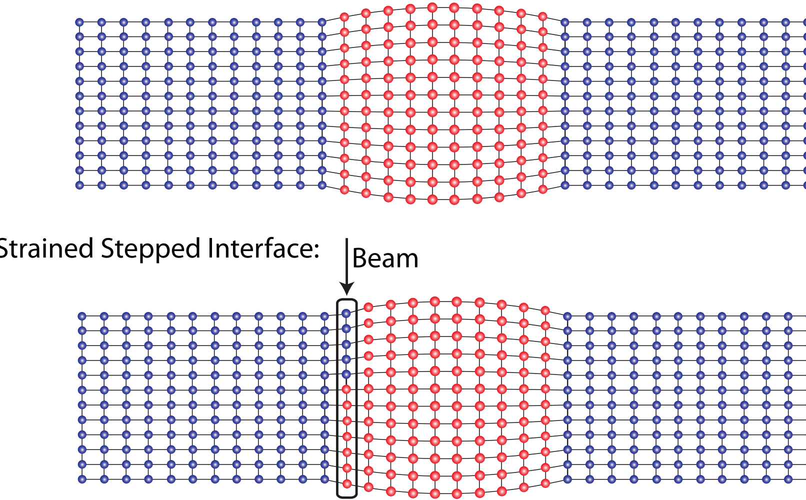

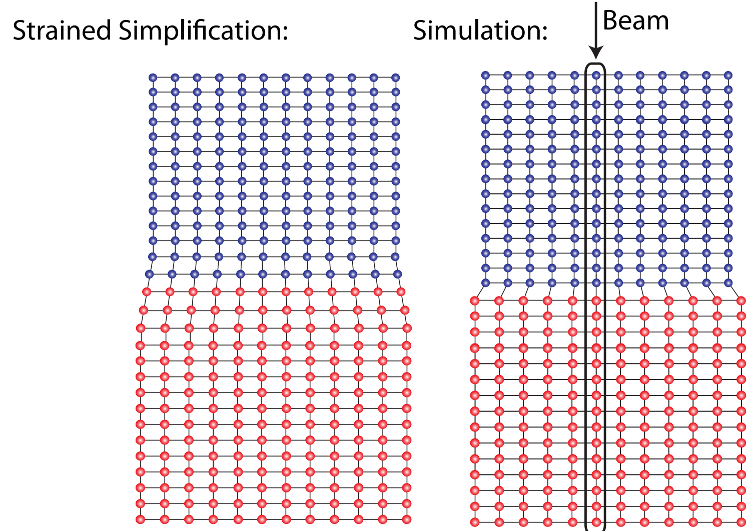

Figure 7.1 – The difference in lattice parameter at a heterojunction is accommodated by elastic strain which is shown in the top diagram (labeled: Strained Perfect Interface). The diagram below this shows an interfacial dumbbell with a compositional change at a specific depth (labeled: Strained Stepped Interface). The effect of this compositional change on the generated HAADF signal can be calculated using the multislice code. A simplified structure can be modeled where the compositional change is only in the beam direction and is shown in the lower left diagram (labeled: Strained Simplification). This model can be further simplified by ignoring the strain at the compositional depth as shown in the lower right diagram (labeled: Simulation). It is this simplified "Simulation" model that is used for the calculation in this chapter.

The background subtracted (BGS) HAADF signal can be seen in the upper of the three plots. This shows the signal from the $AlAs - GaAs_{4.3nm}$ model and the signal that is generated from a fully populated gallium column in single crystal GaAs. The graph indicates that in the upper AlAs region the generated HAADF signal is considerably lower than that from the fully populated gallium column. At the change of composition the HAADF signal from the $AlAs - GaAs_{4.3nm}$ model increases and at a depth of $\sim 18nm$ the scattering is comparable to the fully populated gallium column. The generated signal continues to rise and peaks at a depth of $\sim 32nm$ which is deeper than that of the fully populated gallium column.

This model clearly indicates a set of conditions where the scattering from the Type-3 atomic column is greater than the scattering from the Type-5 atomic column for depths greater than $20nm$ and the increase in scattering from the Type-3 column of the $AlAs-GaAs_{4.3nm}$ model is a direct result of the depth of the compositional change. The middle graph of figure 7.2 indicates the intensity on the Type-3 primary column of the $AlAs - GaAs_{4.3nm}$ model (black). For comparison the Type-3 primary column intensity is shown for bulk AlAs (broken light blue) and GaAs (solid dark blue). This graph clearly indicates that the change in composition coincides with a peak in the on-column intensity which significantly affects the scattering from the column. This model represents the atomic configuration that results in maximum scattering from the partially populated Type-3 (gallium-aluminium) column.

7.1.2 AlAs - GaAs $_{14.3nm}$

The next model consists of a crystal where the AlAs - GaAs change occurs at a depth of $14.3nm$ ($AlAs-GaAs_{14.3nm}$). Figure 7.3 shows an identical set of graphs and the lower of the three shows the column ratio variation as a function of specimen thickness. The graph shows the column ratio from bulk GaAs, bulk AlAs and the $AlAs - GaAs_{14.3nm}$ model. For the top $14nm$ of the model the scattering from the atomic column within the dumbbells are consistent with that of the fully populated AlAs crystal. The depth of the compositional change within the Type-3 column is again indicated by the change in the background colour. At this depth the column ratio begins to increase as the scattering from the Type-3 column increases, however, in this model the column ratio value never reaches 1 and remains below bulk GaAs. This behavior is reflected in

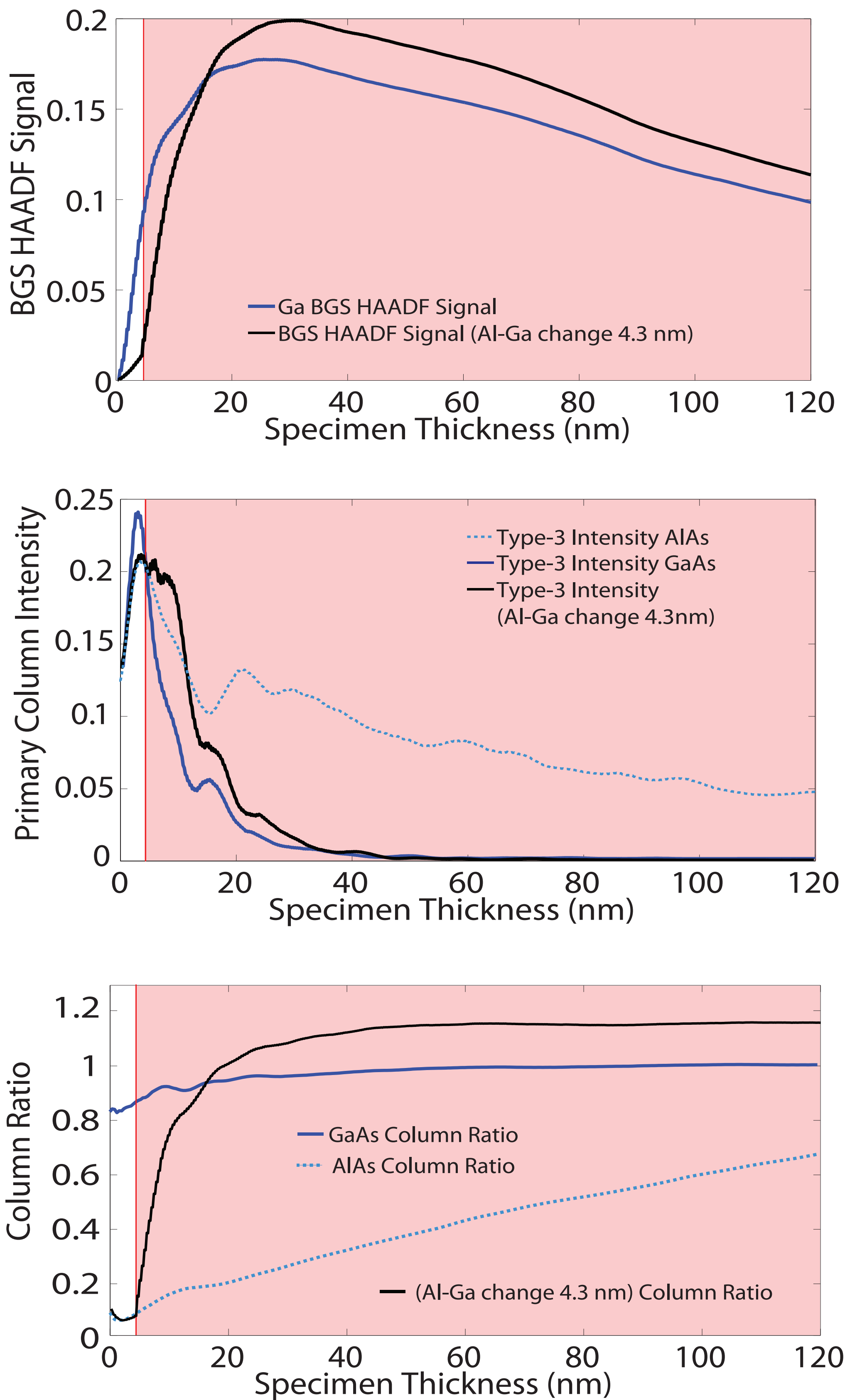

Figure 7.2 – These graphs show the HAADF signal (top), primary column intensity (middle) and the column ratio (bottom) for the AlAs into GaAs model where the compositional change is at a depth of $4.3nm$. The data from the model is shown in black and the data from the single crystal GaAs is shown by the solid blue line and single crystal AlAs by the broken blue line (for clarity).

the background subtracted HAADF signals which are shown in the top plot of figure 7.3 and the signal from the $AlAs - GaAs_{14.3nm}$ model remains below that of a fully populated gallium column over the full $120nm$ range of the simulation. The interesting feature is the depth of the compositional change in relation to the intensity oscillations down the Type-3 atomic column. The middle graph of figure 7.3 shows the Type-3 on-column intensity for bulk AlAs, bulk GaAs and the $AlAs - GaAs_{14.3nm}$ model. In this case the change in composition coincides with a minima in the intensity oscillations.

The primary column intensity plots correspond to the integrated intensity within $0.2\mathring{A}$ of the primary column and the data is used to estimate the possible EELS signal generated from a particular atomic column. However, a contribution to the HAADF signal may be generated from regions outwith this integration window. The projected atomic potential for gallium and aluminium is still significant outside of this region, as at a distance of $0.2\mathring{A}$ from the atomic column, the potential has dropped to approximately 10% of the peak value in both cases. It is therefore instructive to obtain an overview of the scattering in the form of an integrated intensity map. This map displays the radial distribution of intensity as a function of both radial distance and crystal thickness. Each slice of the simulation is processed by integrating the intensity contained within a given radius and then normalising to the total probe intensity as shown in figure 7.4. Each slice contributes to a row of data in the map which is shown in figure 7.5. The integration map is reflected over the ordinate to highlight the change in integrated intensity in the top $20nm$ of the crystal. The abscissa indicates the integration distance from the atomic column, the ordinate is the crystal thickness and the normalised intensity is colour coded corresponding to the colour bar shown on the right side of the plot. This map gives an overview of the distribution of electrons in the top $50nm$ of an AlAs crystal when the probe is placed onto the Type-3 column. This section of the map is integrated out to a distance of 10 Ångströms from the atomic column and clearly shows that the probe is drawn into the atomic column in the top $5nm$ of the crystal. The map indicates that in this region the intensity distribution of the probe intensifies around the atomic column.

The horizontal broken lines that are overlaid onto the map indicate the depths of the compositional change for the $AlAs-GaAs_{4.3nm}$ and the $AlAs-GaAs_{14.3nm}$ models. In the first case the compositional change of the $AlAs - GaAs_{4.3nm}$ model at a depth of $4.3nm$ which occurs where the electron intensity distribution is concentrated on the

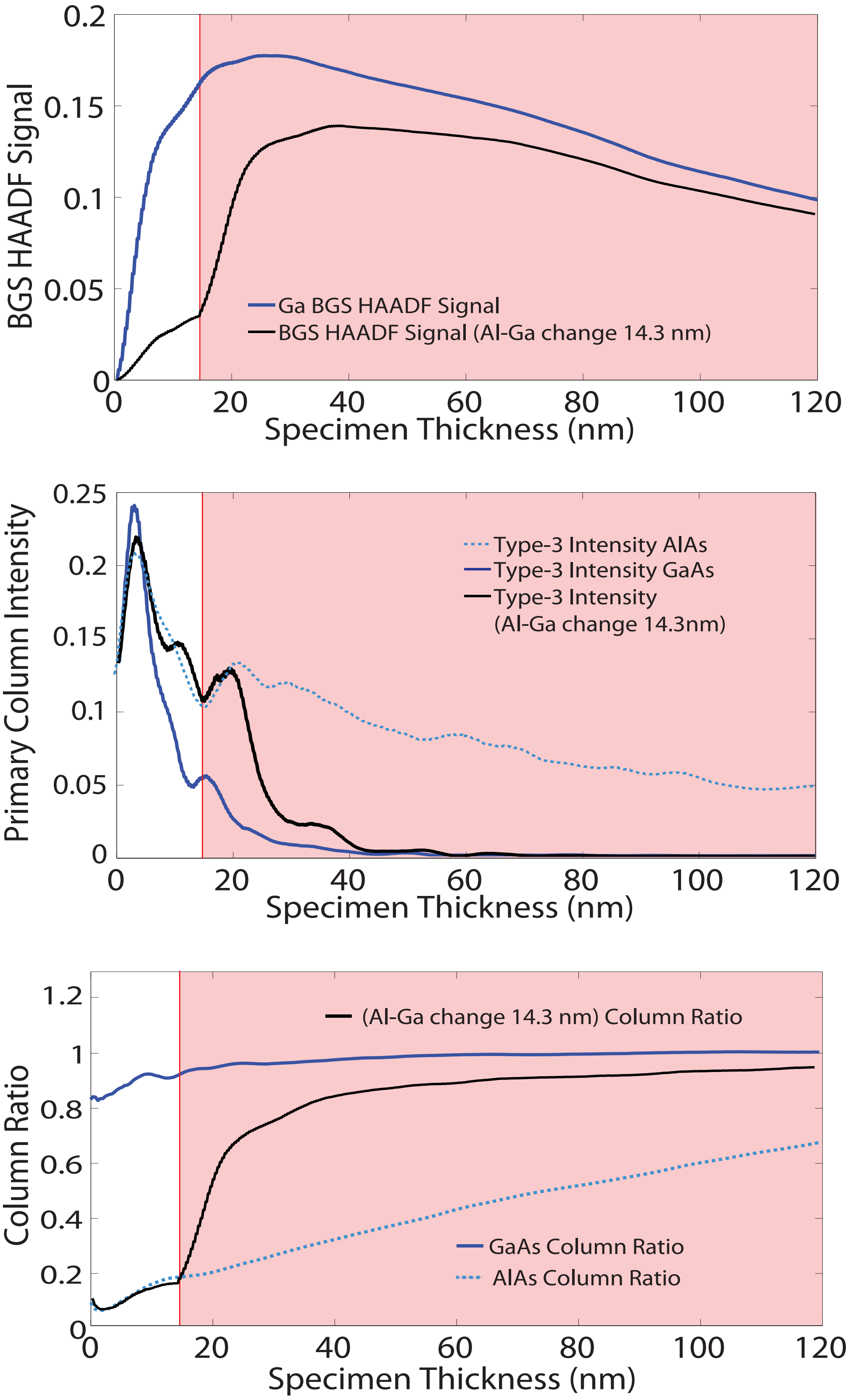

Figure 7.3 – These graphs show the HAADF signal (top), primary column intensity (middle) and the column ratio (bottom) for the AlAs into GaAs model where the compositional change is at a depth of 14.3nm. The data from the model is shown in black and the data from the single crystal GaAs is shown by the solid blue line and single crystal AlAs by the broken blue line (for clarity).

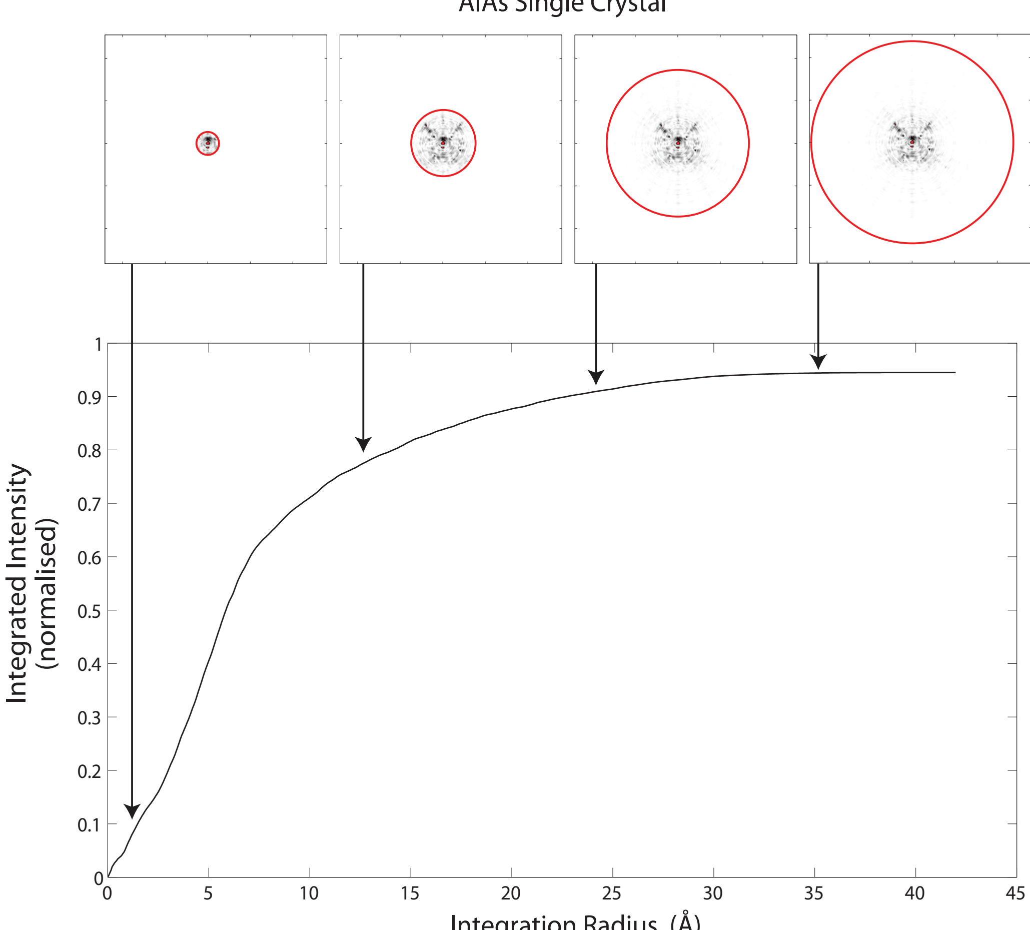

Figure 7.4 – This diagram shows the method for integrating the intensity distribution for each slice of the simulation. The top four images show the intensity distribution from a single specimen thicknesses where the integration radius increases from left to right. The total integrated intensity can be graphed as a function of the radius, show in the lower graph. This integration profile shows the distribution of scattering within the slice of the specimen.

atomic column. The compositional change of the $AlAs - GaAs_{14.3nm}$ model occurs when the electron intensity is considerably lower and the dark blue and light blue regions (which correspond to the 0-30% and 30-40% regions respectively) are located further from the atomic column.

7.1.3 AlAs - GaAs $_{30.8nm}$

The intensity around the atomic column is, however, not the only consideration as the following model demonstrates. The compositional change for this model occurs at a depth of $\sim 31nm$ and figure 7.6 shows three plots containing the column ratio, HAADF signal and primary column intensity data. The lower plot shows the column ratio changing as a function of thickness for a AlAs single crystal, GaAs single crystal

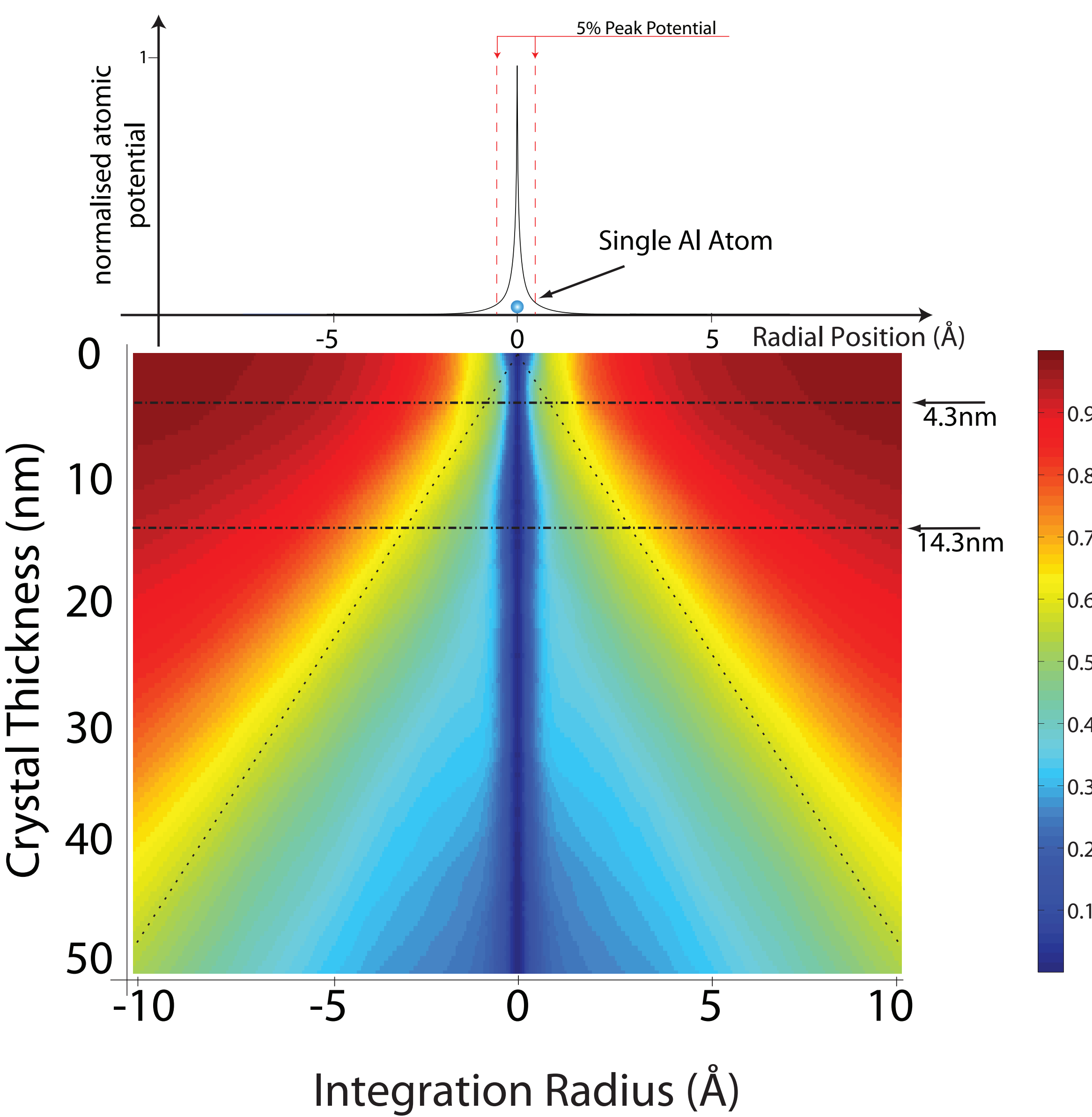

Figure 7.5 – The intensity map above shows the radial integrated intensity within each slice of the simulation from $0 - 50nm$ for single crystal AlAs when the probe is placed on the Type-3 column. Each row in the map is calculated from the intensity distribution profile from a single slice of the simulation (shown in figure 7.4). The diverging broken lines indicate geometrical spreading at an angle of 24mrad.

and the $AlAs - GaAs_{30.8nm}$ model and the compositional change is again indicated by the change in background colour. In the upper section of the $AlAs - GaAs_{30.8nm}$ model the column ratio is identical to that of single crystal AlAs. At the compositional change depth the column ratio begins to increase and at a depth of $50nm$ the column ratio has increased to a value of 1. Beyond this thickness the column ratio continues to increase and peaks at a depth of $120nm$ at a value of 1.17. The middle plot of figure 7.6 shows the primary Type-3 column intensity for the $AlAs - GaAs_{30.8nm}$ model, single crystal GaAs and single crystal AlAs. In the upper section of the crystal the on column intensity is identical to single crystal AlAs. At the compositional change depth the primary column intensity exhibits a peak followed by a rapid drop in intensity that is caused by the change in atomic potential of the column. The intensity distributions for this model and for that of the $AlAs - GaAs_{14.3nm}$ model are similar at the depth of the compositional change. However, in this case, the change in column ratio is significantly different.

This difference is again due to the depth of the compositional change in the Type-3 column, but more specifically it is the relationship between the scattering from the Type-3 column compared to that of a fully populated gallium column. The upper plot in figure 7.6 shows the background subtracted HAADF signals for the Type-3 column from the $AlAs - GaAs_{30.8nm}$ model and the background subtracted HAADF signal from a fully populated gallium column. For the fully populated gallium column the background subtracted HAADF signal peaks at a depth of approximately $25nm$ after which the magnitude of the signal begins to drop. The drop in the signal is due to the re-scattering of electrons outwith the solid angle of the detector. For the $AlAs - GaAs_{30.8nm}$ model the increased scattering at a depth of $31nm$ occurs where the scattered intensity from the fully populated gallium column is already dropping. As a result, the background subtracted HAADF signal from the $AlAs - GaAs_{30.8nm}$ model is greater than the fully populated gallium column at crystal thicknesses greater than $55nm$.

7.1.4 AlAs - GaAs $_{100nm}$

The last AlAs - GaAs model highlights the effect of re-scattering on the measured column ratio for a thick crystal. The compositional change for this model occurs deep

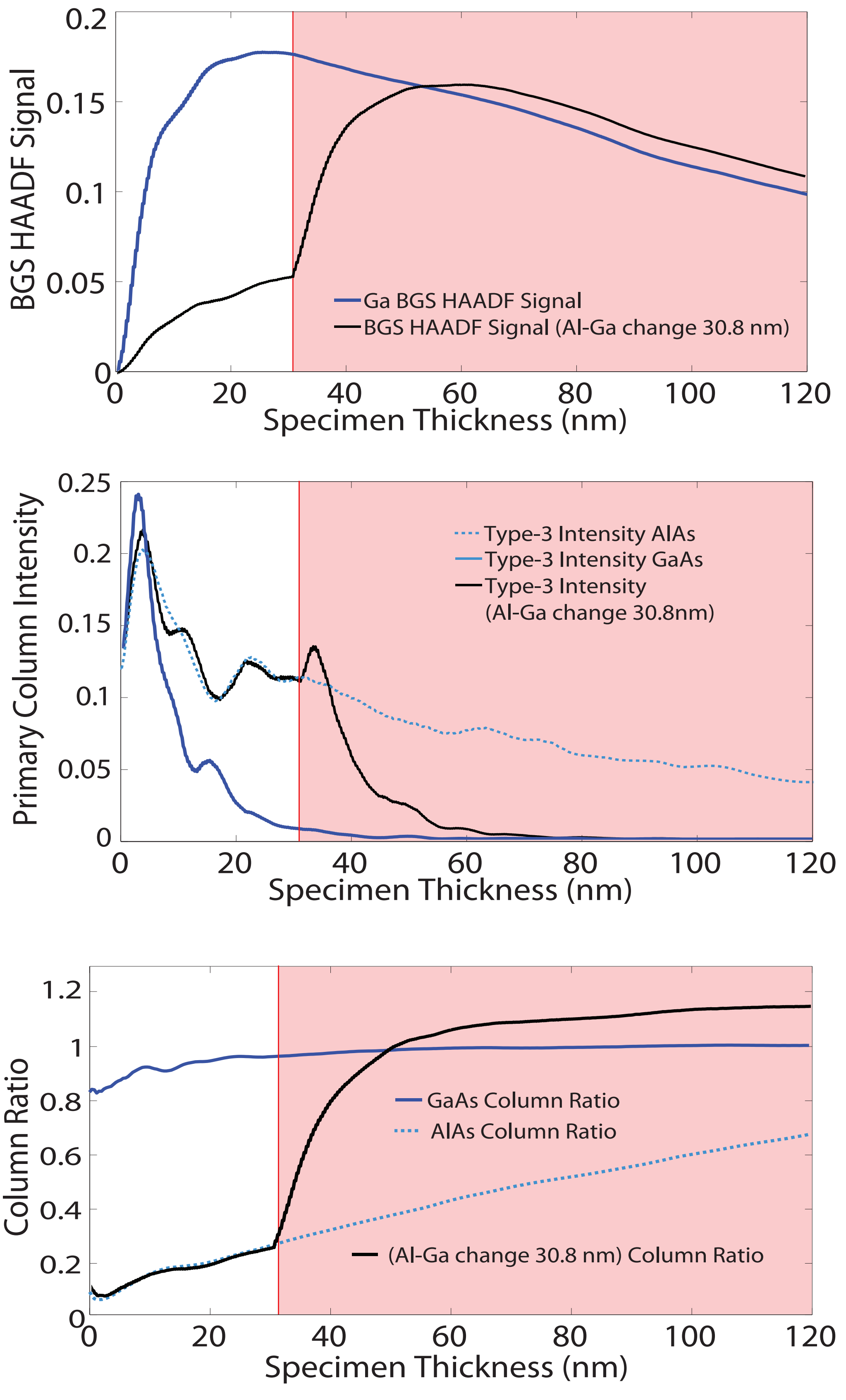

Figure 7.6 – These graphs show the HAADF signal (top), primary column intensity (middle) and the column ratio (bottom) for the AlAs into GaAs model where the compositional change is at a depth of $30.8nm$.

within the atomic column at $100nm$. The middle graph of figure 7.7 shows the Type-3 column intensity as a function of specimen thickness for the $AlAs - GaAs_{100nm}$ model and also for a fully populated gallium column. This plot indicates that at a depth of $100nm$ the intensity on the primary column for the $AlAs - GaAs_{100nm}$ model has dropped to $\sim 22\%$ of the peak column intensity. Furthermore, at the exit face of the specimen, the on-column intensity has not fully scattered and fallen to zero.

The upper graph in figure 7.7 shows the variation of the background subtracted HAADF signal for the $AlAs-GaAs_{100nm}$ model (black) and the background subtracted HAADF signal from a fully populated gallium column (dark blue). In the case of the $AlAs - GaAs_{100nm}$ model the HAADF signal gradually builds in the AlAs region (top $100nm$) of the model and therefore the re-scattering of the electrons from the upper section of the model is not as significant. The compositional change at $100nm$ produces a change in the generated HAADF signal which increases and, by the exit face of the crystal, the generated signal from the $AlAs - GaAs_{100nm}$ Type-3 column and the fully populated gallium column are identical. The lower graph in figure 7.7 shows the overall effect on the column ratio and indicates that for thick crystals compositional change at the exit face of an atomic column can have a significant effect on the measured column ratio. These re-scattering effects could have a significant impact on the ability to accurately characterise structures at the entrance face of crystal structures using HAADF imaging. However, attributing these effects to electron re-scattering is an assumption that can be tested through a simple model. The development of this simple model is described in the following section.

7.1.5 Electron Re-Scattering

Figure 7.8 shows a schematic of the crystal model simulated in this section where the upper structure is AlAs and the lower section is GaAs. The left side of the diagram shows that the model can be broken down into a number of slices. As the probe propagates through each slice the atomic potential of the atoms in each slice will scatter the probe and the measured HAADF signal will increase. The right side of the diagram shows that as the thickness of the model increases scattering from the nth slice must traverse through an increasing number of layers before reaching exit face of the structure. The central graph indicates that the contribution to the HAADF signal

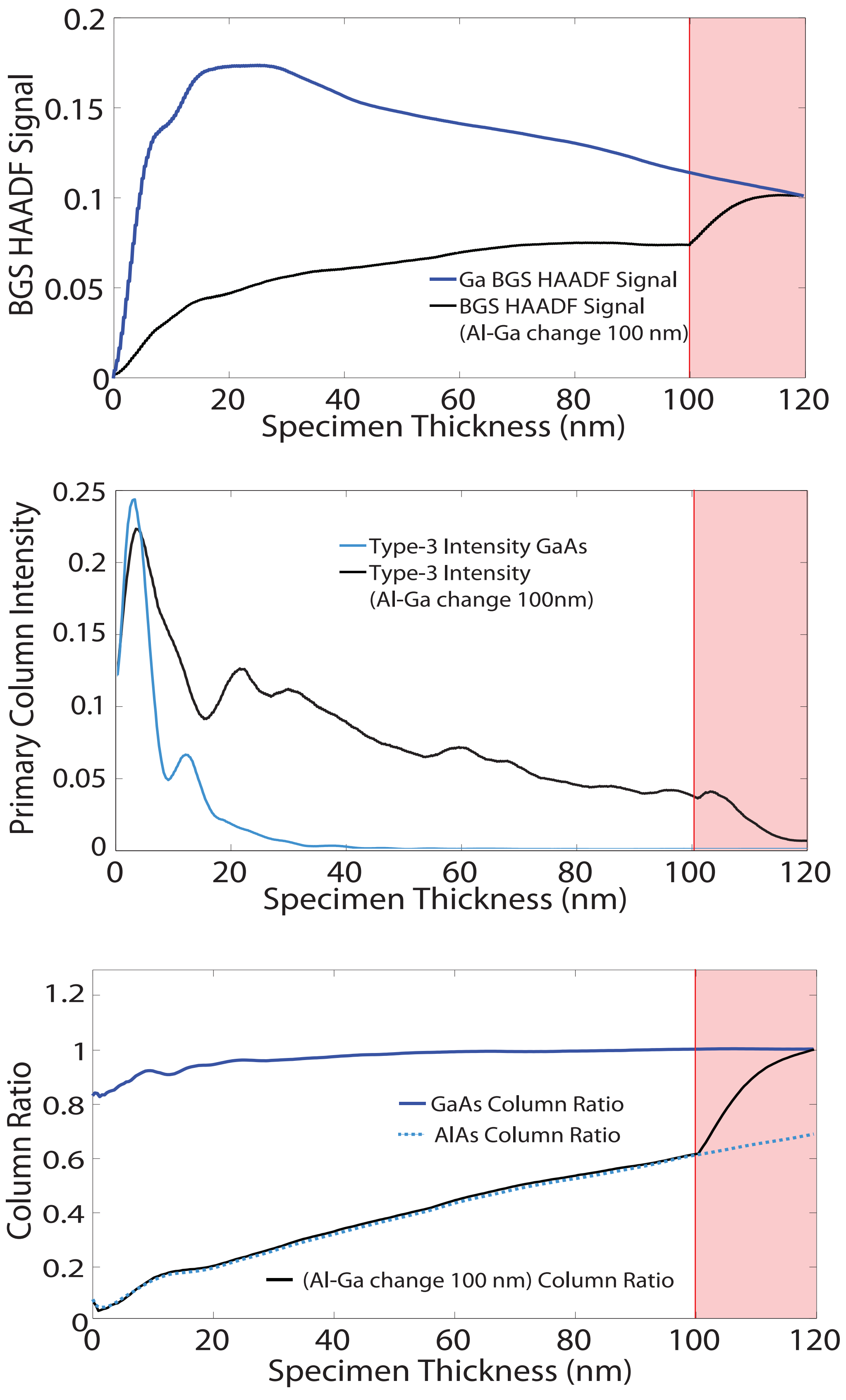

Figure 7.7 – These graphs show the HAADF signal (top), primary column intensity (middle) and the column ratio (bottom) for the AlAs into GaAs model where the compositional change is at a depth of $100nm$.

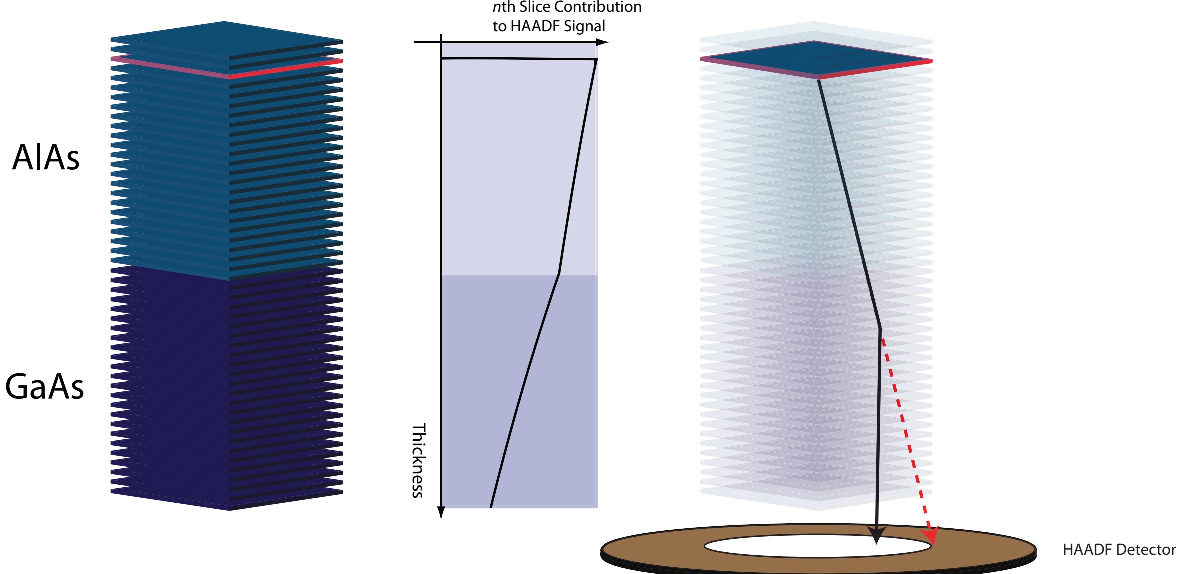

Figure 7.8 – The schematic above describes the effect of re-scattering. The left side of the diagram shows an AlAs into GaAs structure with an atomic slice highlighted in red near to the crystal surface. The middle graph shows the total contribution of the nth slice to the HAADF signal for various crystal thicknesses. The right side of the diagram shows that electrons scattered by this slice will have to traverse the remainder of the structure to be detected by the HAADF detector. The probability of the electron being re-scattered depends on not only the number of slices between the nth slice and the exit face of the crystal but also on the average Z of these slices.

from the nth layer will drop as a function of the remaining crystal thickness. The rate of signal drop off will also be dependent on the average Z of each slice and re-scattering will be higher in regions of the model with a higher average Z. To evaluate the contribution to the total HAADF signal from the nth slice, the re-scattering from all slices from the $(n+1)$th slice to the slice at the exit face of the model must be taken into account.

The effect of re-scattering can be evaluated through the development of a simple scattering model with the aim of determining whether a combination of re-scattering and a Z^η model can describe the changes in HAADF signal observed in the preceding sections.

The first stage is to integrate the intensity localised to all of the atomic positions in each slice of the multislice calculation. Each atom is considered in turn and the size of the integration mask that is used is dependent on the atomic species. The radius around each atom position is chosen to correspond with where the atom potential drops to 5% of the peak. This is however, a simplification and a more accurate method would be to consider the resulting phase change from the atomic potential. However,

for this initial investigation, the simplification will be sufficient. The intensity located in the masked region of the atom position is then weighted using a free parameter, η, as an index. This process is repeated for each atom in the slice and the total weighted intensity is then recorded. A total integrated intensity is then calculated for each slice of the multislice calculation which gives an estimation of the scattered probe intensity into the solid angle of the HAADF detector.

The effect of re-scattering can then be applied to this data and so, for a crystal one monolayer thick, the estimated HAADF signal would simply be the integrated (weighted) intensity of the first slice. For a crystal two monolayer thick the estimated HAADF signal would be the full integrated intensity of slice two added to the scaled integrated intensity from slice one and so on. This scaling takes the form of equation 7.1 where N_X is the number of atoms of atom species X and Z_X is the atomic number of atoms of species X. The other two parameters (α and η) are then selected to fit the integrated intensity data to the HAADF signal data for bulk GaAs and AlAs.

$$\alpha[N_{Al}Z_{Al}^{\eta} + N_{Ga}Z_{Ga}^{\eta} + N_{As}Z_{As}^{\eta}] \tag{7.1}$$

The process of scaling the integrated intensity from each slice can then be simplified by calculating a re-scattering matrix which is shown in figure 7.9. The matrix is shown as a two dimensional map and details the contribution of each given slice in the simulation to the final HAADF signal. The appearance of the map will depend on the number and species of atoms in each slice of the model. The map in figure 7.9 corresponds to an AlAs into GaAs model where the compositional change occurs at a depth of $40nm$. The x-axis details the crystal depth in nm and the y-axis corresponds to the slice within the model. Each row of the map corresponds to the contribution of a specific slice to the final HAADF signal where the colour relates to the colour bar on the right. For example, slice number 140 is indicated on the y-axis and is located at a depth of $28nm$ indicated by the vertical arrow. For a crystal thickness of $30nm$, most of the integrated intensity from slice 140 would contribute to the HAADF signal. As the crystal thickness increases the contribution from this slice drops (as indicated by the colour change along the horizontal broken line) and, for a crystal $120nm$ thick, the contribution from this slice has dropped to 60% of the original integrated intensity from that slice. Therefore, for a given specimen thickness, the columns within the map

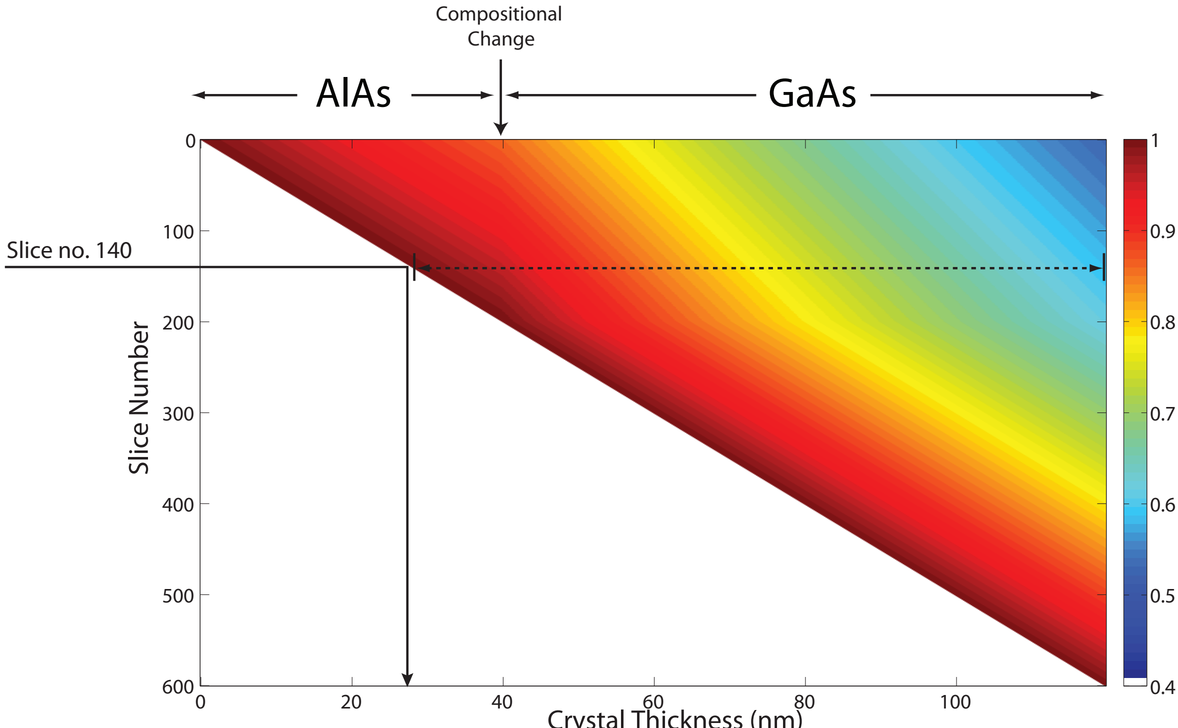

Figure 7.9 – The re-scattering matrix shown above allows the contribution to the final HAADF signal from each slice to be calculated. For example slice number 140 is indicated on the y-axis which is located at a depth of $28nm$ indicated by the vertical arrow. For a crystal thickness of $30nm$, most of the integrated intensity from slice 140 would contribute to the HAADF signal. As the crystal thickness increases the contribution from this slice drops (as indicated by the colour change along the horizontal broken line) and, for a crystal $120nm$ thick, the contribution from this slice has dropped to 60% of the original integrated intensity from that slice. Therefore, for a given specimen thickness, the columns of the map correspond to the contributions from each slice which can be easily evaluated.

correspond to the contributions from each slice and can be easily evaluated.

The parameters α and η were evaluated using single crystal GaAs and AlAs by manually comparing the background subtracted HAADF signal to the integrated intensity over the full range of thicknesses. The upper graph in figure 7.10 shows the background subtracted HAADF signal from single GaAs and the upper graph in figure 7.11 shows the background subtracted HAADF signals for single crystal AlAs. The corresponding integrated intensity graphs are shown in the lower graphs of figures 7.10 and 7.11. An optimum value for both parameters (α and η) was found by adjusting the parameters so that the form of the integrated intensity graphs matched the HAADF signal graphs for both bulk GaAs and bulk AlAs. Using this method a good agreement was found for $\alpha = 6 \times 10^{-9}$ and $\eta = 1.85$.

The evaluation of this re-scattering model using the single crystal materials pro-

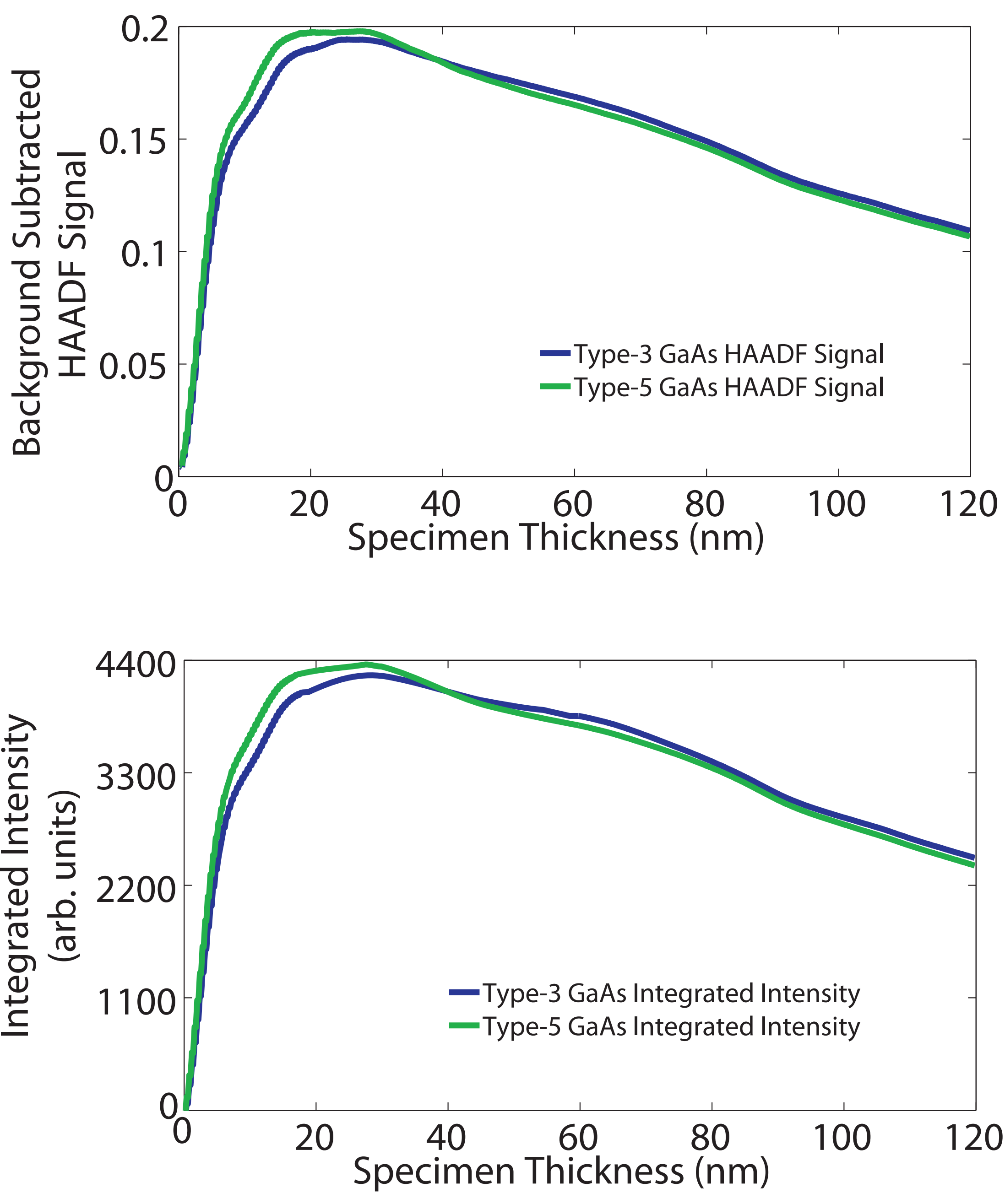

Figure 7.10 – The top graph shows the background subtracted HAADF signal from the Type-3 and Type-5 columns of single crystal GaAs. The lower graph shows the integrated intensity where re-scattering of the electrons is accounted for.

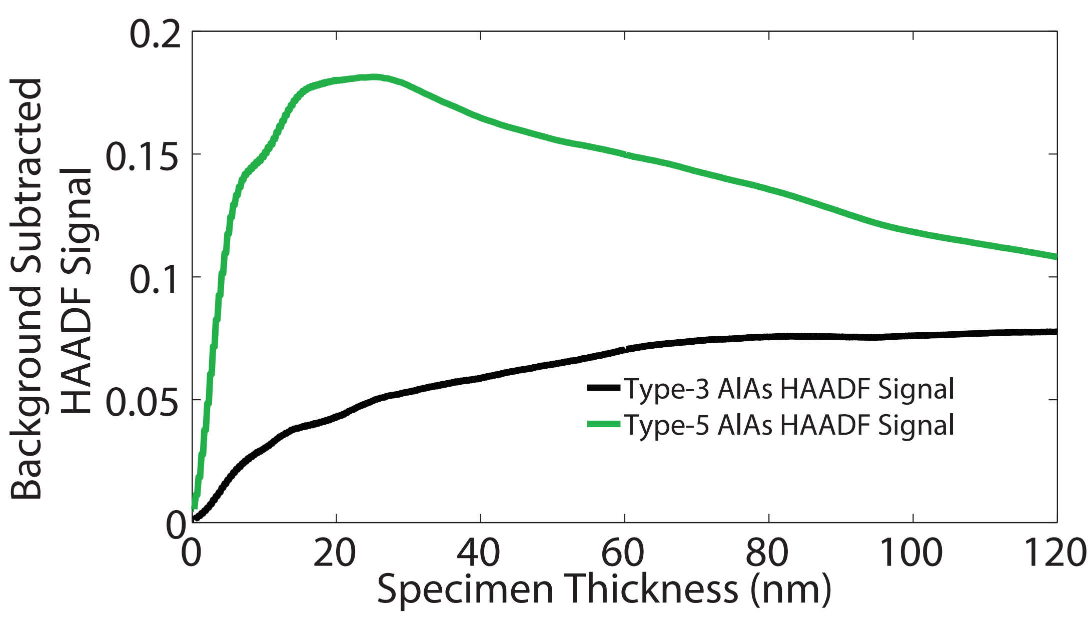

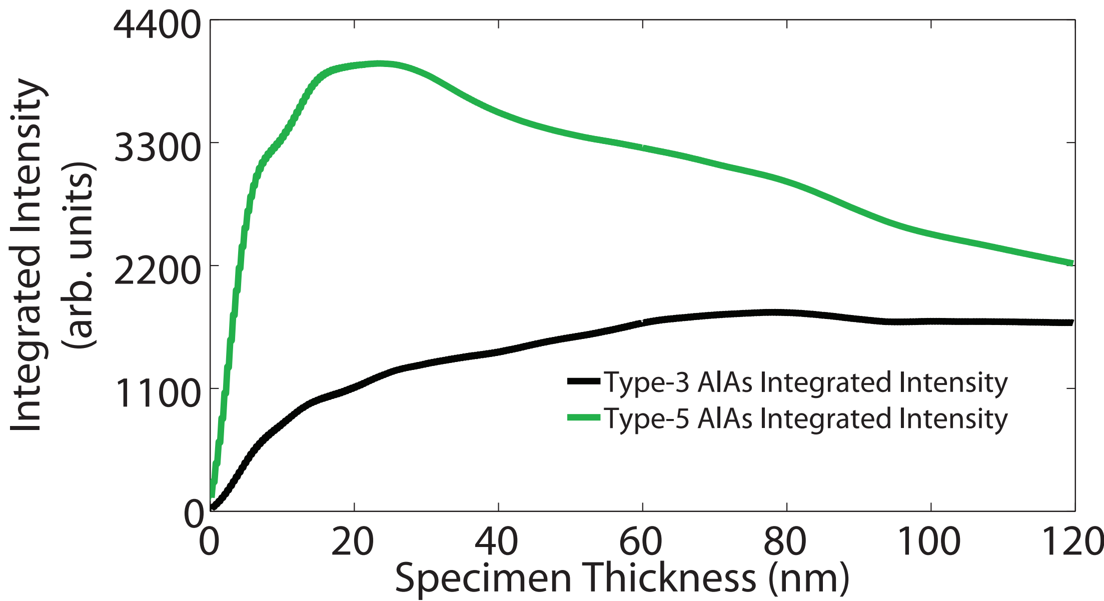

Figure 7.11 – The top graph shows the background subtracted HAADF signal from the Type-3 and Type-5 columns of single crystal AlAs. The lower graph shows the integrated intensity where re-scattering of the electrons is accounted for.

duces good agreement between the HAADF data and the integrated intensity data. The same comparison can then be made on the AlAs into GaAs structures that were investigated in sections 7.1.1 to 7.1.4. The comparison graphs for these models can be seen in figures 7.12, 7.13, 7.14 and 7.15.

Figure 7.12 shows the graphs that correspond to the AlAs into GaAs model where the compositional change occurs at a depth of 4.3nm, $AlAs - GaAs_{4.3nm}$. The upper graph in figure 7.12 shows the graph of the background subtracted HAADF signals for the Type-3 and Type-5 probe positions. The lower graph in figure 7.12 shows the corresponding integrated intensity for the same model and clearly indicates that all of the features present in the HAADF signal are reproduced in the integrated intensity signal.

Figure 7.13 corresponds to the $AlAs - GaAs_{14.3nm}$ model where again the upper graph shows the HAADF signal variation with specimen thickness and the lower graph shows the integrated intensity model. The integrated intensity for this model again reproduces the features of the HAADF signal. The HAADF signal and integrated intensity plots for the $AlAs - GaAs_{30.8nm}$ model are shown in figure 7.14 and the HAADF signal and integrated intensity plots for the $AlAs - GaAs_{100nm}$ model are shown in figure 7.15. For each of these models the integrated intensity model reproduces the HAADF signal faithfully.

In each case there is good agreement between the integrated intensity model and the HAADF signal data, this indicates that the characteristics observed in sections 7.1.1 to 7.1.4 can be accounted for using a model that firstly assumes that the scattering is proportional to $Z^{1.85}$ and secondly accounts for electron re-scattering.

This section presented an investigation into the generated HAADF signals from partially populated atomic columns. In these models the upper material was AlAs and the lower material was GaAs. It was found that the generated HAADF signal from a partially populated column depends on two factors. The first is the electron intensity around the atomic column and the second is the depth within the atomic column that the HAADF signal is being generated. Figures 7.12 to 7.15 indicate that the scattered intensity from the Type-3 column can be counter intuitive and that atomic columns with a lower average Z can produce a higher signal than a column with a higher average Z.

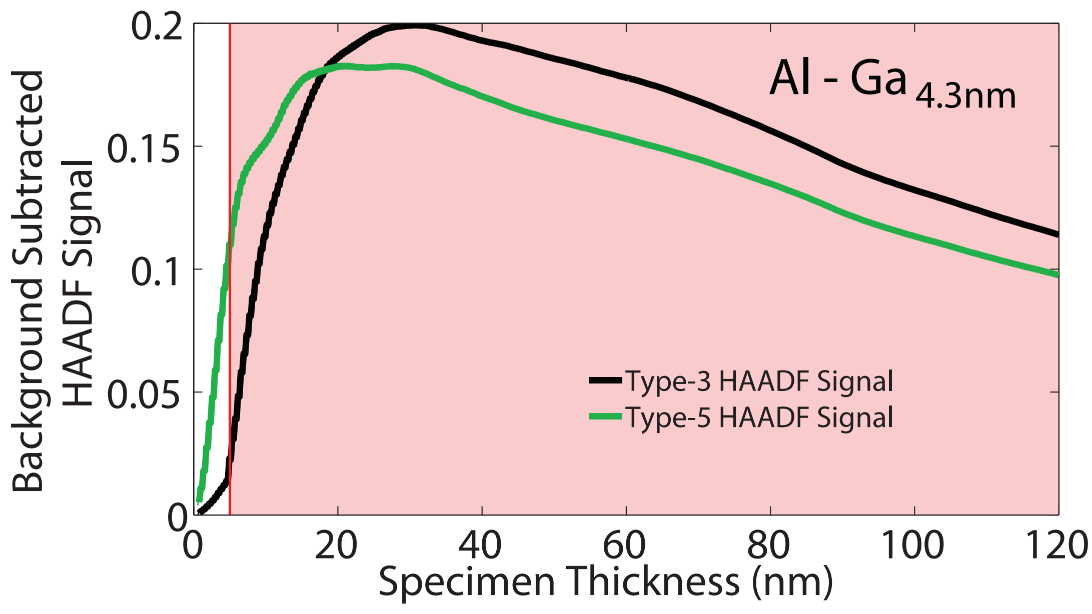

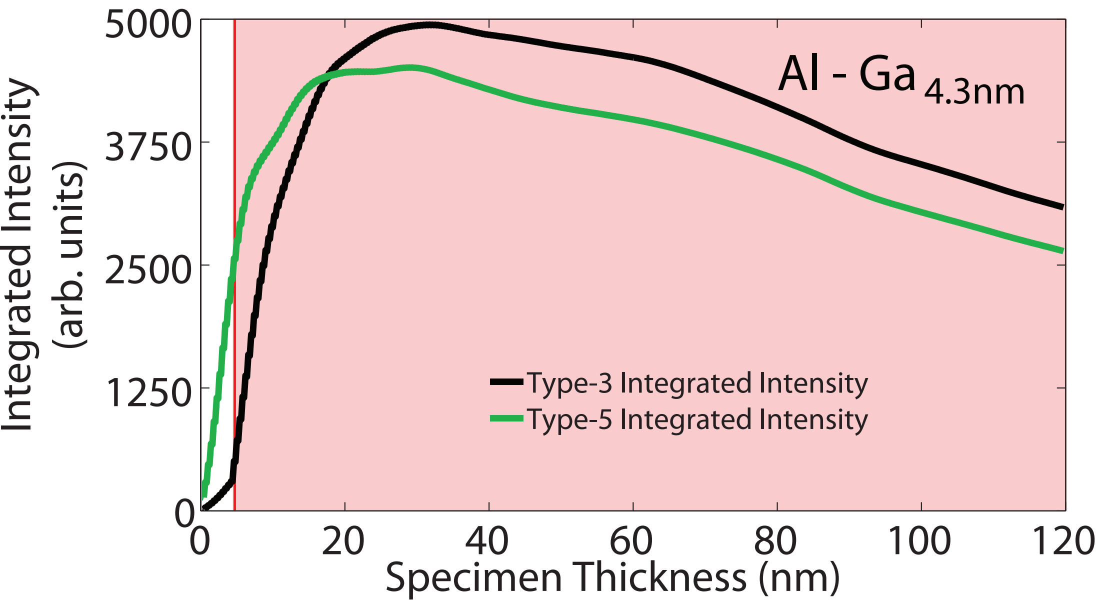

Figure 7.12 – The top graph shows the background subtracted HAADF signal from the Type-3 and Type-5 columns of the AlAs into GaAs 4.3nm model. The lower graph shows the integrated intensity where re-scattering of the electrons is accounted for.

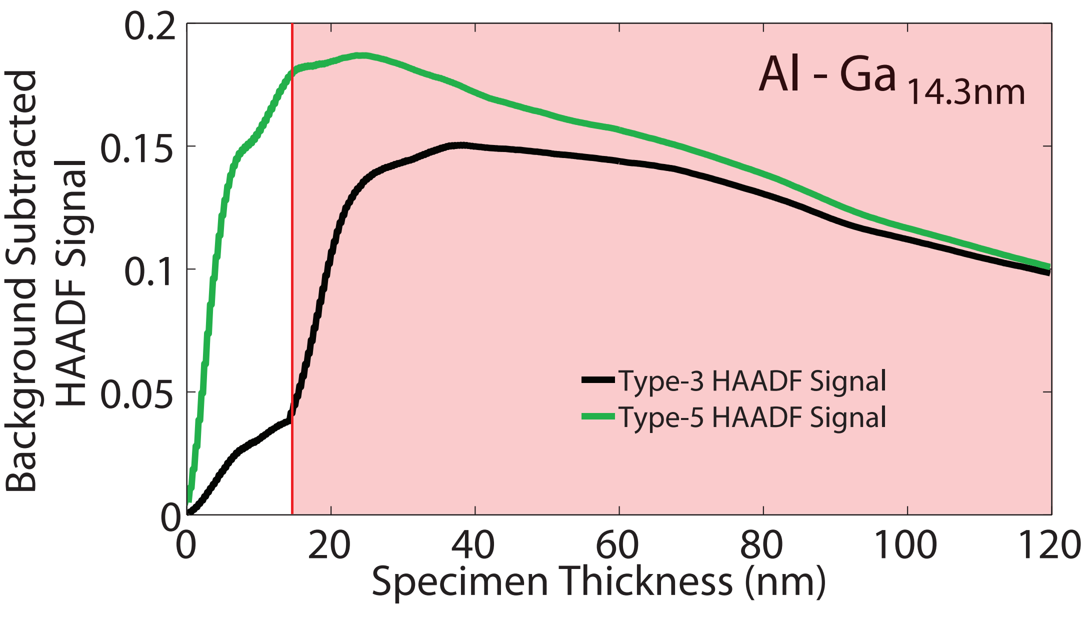

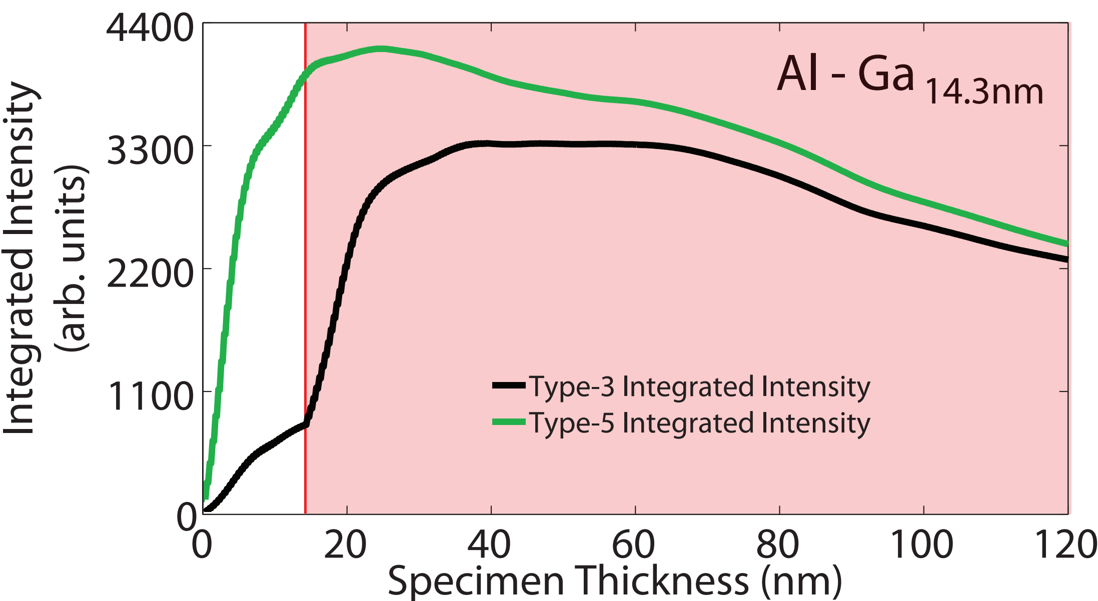

Figure 7.13 – The top graph shows the background subtracted HAADF signal from the Type-3 and Type-5 columns of the AlAs into GaAs 14.3nm model. The lower graph shows the integrated intensity where re-scattering of the electrons is accounted for.

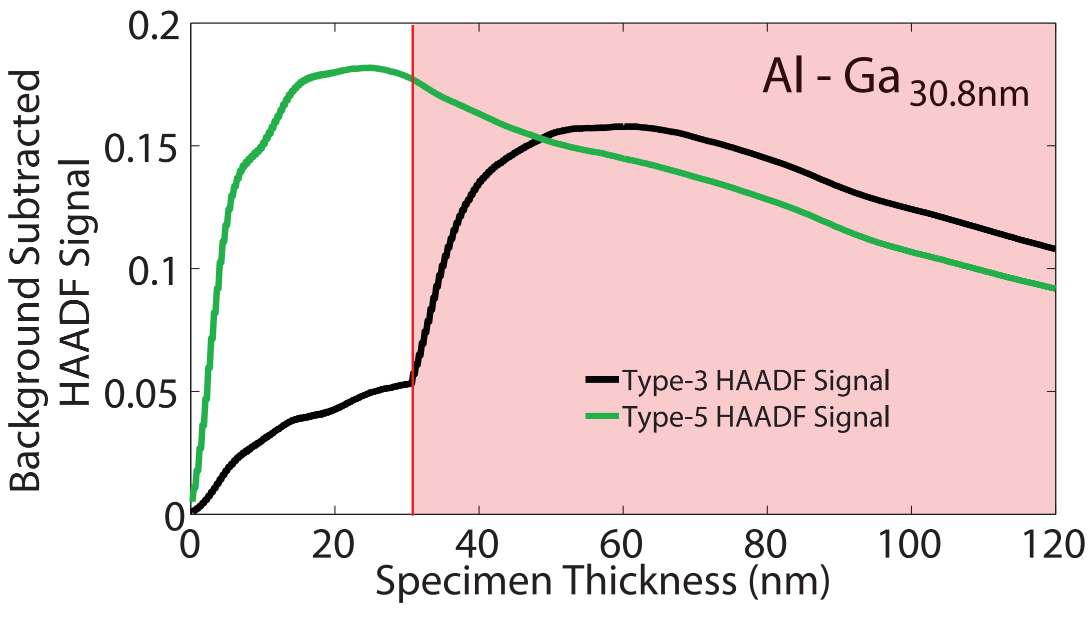

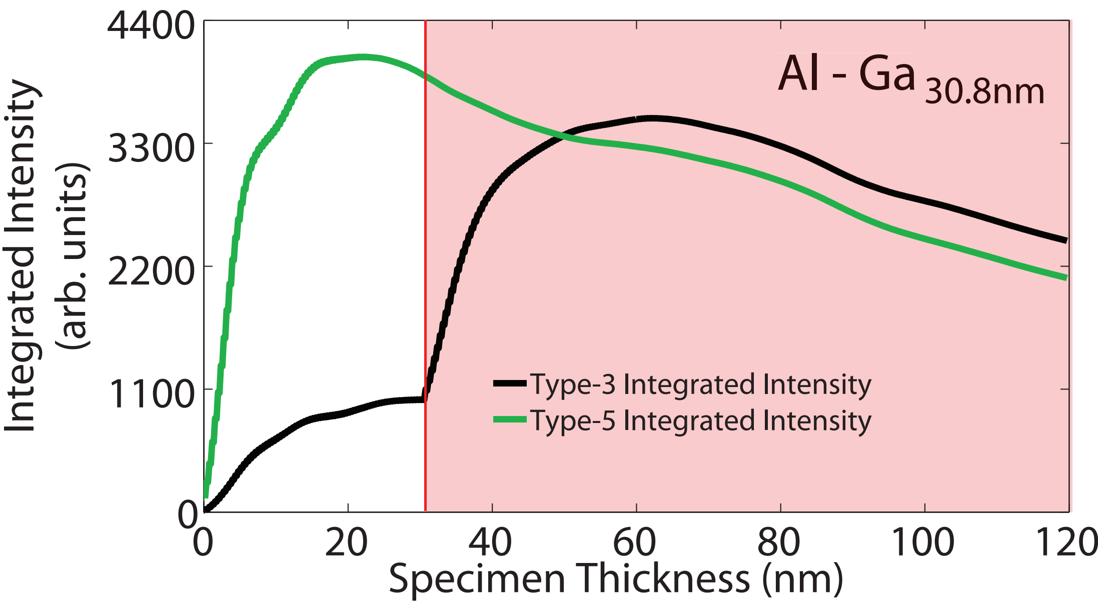

Figure 7.14 – The top graph shows the background subtracted HAADF signal from the Type-3 and Type-5 columns of the AlAs into GaAs 30.8nm model. The lower graph shows the integrated intensity where re-scattering of the electrons is accounted for.

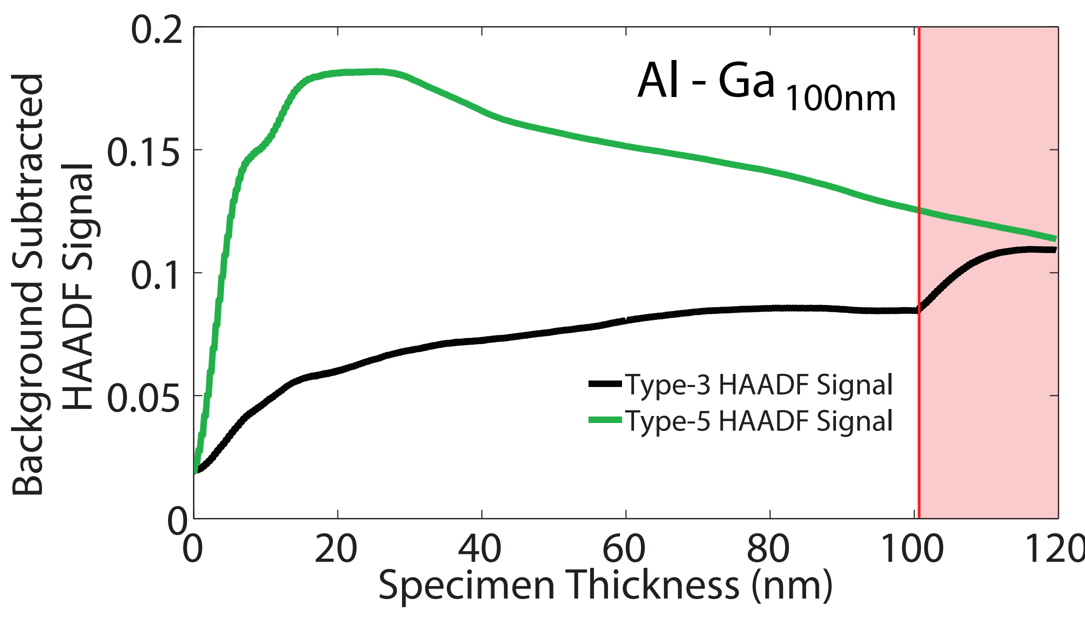

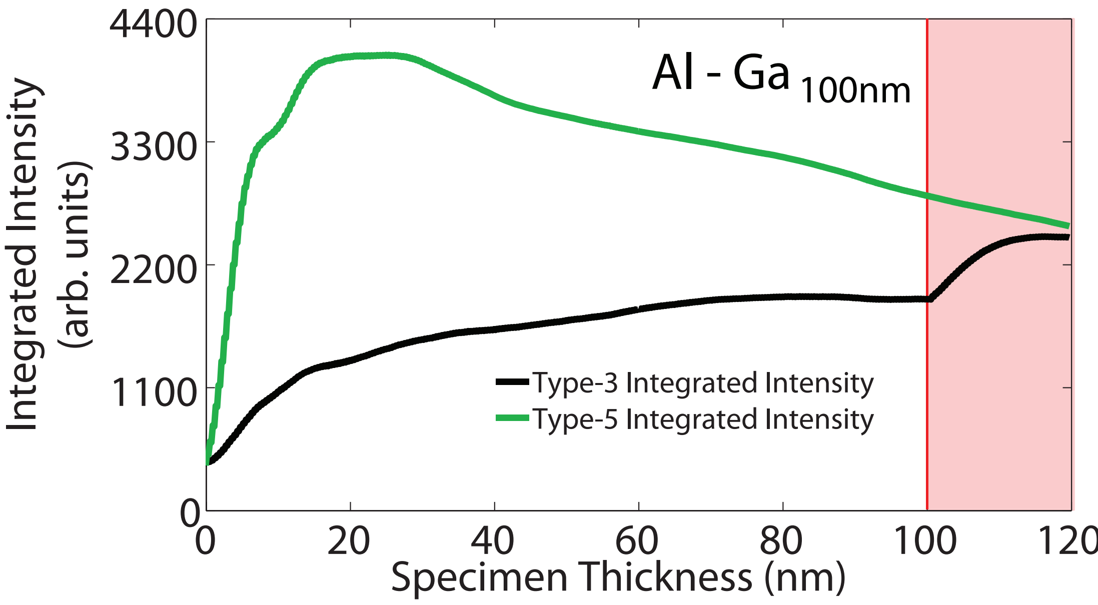

Figure 7.15 – The top graph shows the background subtracted HAADF signal from the Type-3 and Type-5 columns of the AlAs into GaAs 100nm model. The lower graph shows the integrated intensity where re-scattering of the electrons is accounted for.

7.2 GaAs - AlAs

The next series of models investigated consisted of an upper section of GaAs and a lower section of AlAs. The depth of the compositional change was varied for each model in steps of one unit cell and the generated HAADF signal, primary column intensity and total integrated intensity was calculated. The series of models allowed a detailed examination of the effect that the depth of the compositional change has on these measured signals. The results in this sections can be compared to single crystal simulations for GaAs (3.6.1 on page 60) and AlAs (3.6.2 on page 66).

Figure 7.16 shows the integrated distribution of the STEM probe on the Type-3 column of single crystal GaAs. This map was formed in the same manner as for the AlAs case in figure 7.5. The scattering from the Type-3 column in this case shows a considerable difference due to the significantly higher Z of the atomic column. In the top $5nm$ of the crystal, the probe is again drawn in by the atomic potential of the column. At a depth of approximately $4nm$ the intensity around the atomic column reaches a maximum. As the probe continues to propagate through the crystal a considerable amount of scattering disperses the probe intensity and the intensity on the primary column quickly drops. Above the intensity distribution map is the normalised potential of a single gallium atom and the radial position that the potential drops to 5% of the peak value is also indicate by the vertical broken lines. This map will be used when considering the model in section 7.2.1 below.

7.2.1 GaAs - AlAs $_{3.9nm}$

An interesting effect can occur when a STEM probe is focused onto an atomic column where the column composition changes from high Z to a lower Z material. This is the case for this model where the top $3.9nm$ of the model is GaAs and the lower section consists of AlAs. Figure 7.17 shows three graphs the lower of which shows the change in column ratio as a function of thickness for this model. For comparison the column ratio of single crystal GaAs (dark blue) and AlAs (light blue) are also shown and the compositional change from GaAs to AlAs is indicated with the graph background colour. In this instance for the top $3.9nm$ of the model the column ratio is consistent with single crystal GaAs. At the compositional change depth the column ratio drops significantly as the Type-3 column composition changes from gallium to aluminium.

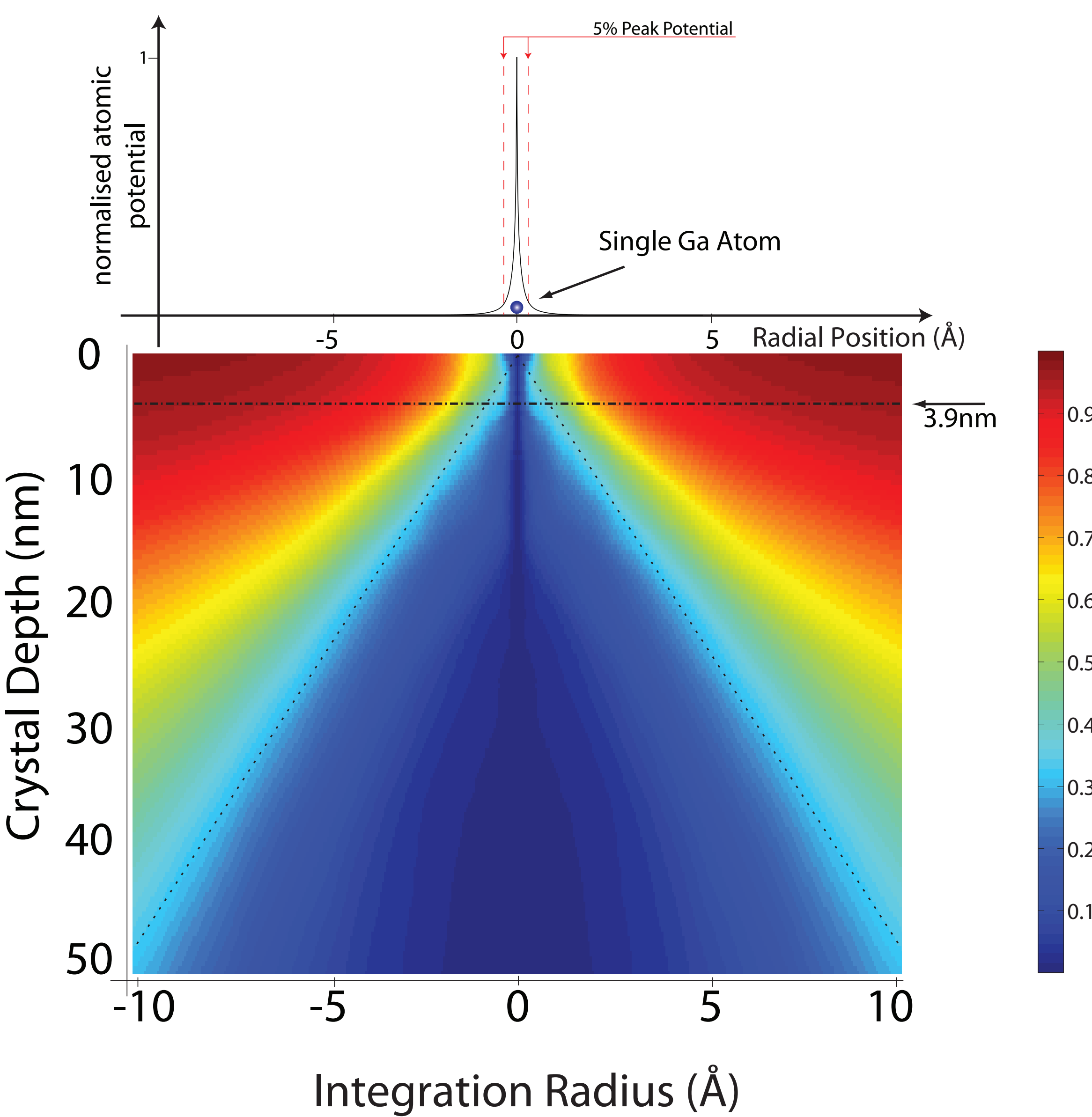

Figure 7.16 – The intensity map above shows the radial integrated intensity within each slice of the simulation from $0 - 50nm$ for single crystal GaAs when the probe is placed on the Type-3 column. The diverging broken lines indicate geometrical spreading at an angle of 24mrad.

At a crystal thickness of $28nm$ the column ratio of the dumbbell is consistent with single crystal AlAs. However as the thickness of the crystal increases the column ratio continues to drop below bulk AlAs. The depth of this compositional change is indicated on the intensity integration map in figure 7.16 and is located in a position below the strong scattering region. The on column intensity at this position has therefore interacted with the atomic potential of the Type-3 column and is beginning to be strongly scattered when the change in composition occurs. This is confirmed by the primary column intensity plot shown in the middle graph of figure 7.17. This graph shows the intensity on the primary column for a Type-3 AlAs column and the primary column intensity for the Type-3 column of the $GaAs - AlAs_{3.9nm}$ model. The graph indicates that the gallium at the entrance of the Type-3 column causes the overall intensity down the atomic column to drop below that of a fully populated aluminium column.

The top plot in figure 7.17 shows the background subtracted HAADF signals generated from the Type-3 columns of single crystal AlAs and GaAs and from the $GaAs - AlAs_{3.9nm}$ model. This graph gives an indication why the column ratio of the $GaAs - AlAs_{3.9nm}$ model drops below single crystal AlAs at depths of greater than $30nm$. In the case of the fully populated aluminium column the contribution to the HAADF signal builds over the top $30nm$ of the crystal and then continues to increase over the remainder of the atomic column. In the case of the $GaAs - AlAs_{3.9nm}$ model a significant portion of the HAADF signal is generated in the top $10nm$ of the model. This being the case, the re-scattering of this signal intensity causes the total measured signal to be less at thicknesses of greater than $30nm$. The overall effect is that an atomic column with a higher average Z can generate a lower level of scattering depending on the specific configuration of the atoms at the top of the column. Furthermore, this model corresponds to the atomic configuration that results in the minimum scattering from a partially populated Type-3 (gallium-aluminium) column.

7.3 InAs - AlAs

Moving to a III-V material with a higher average Z will allow both the re-scattering model and the variability of the column ratio to be investigated further. For InAs the Type-3 material is replaced with indium which has $Z = 49$ which changes the probe

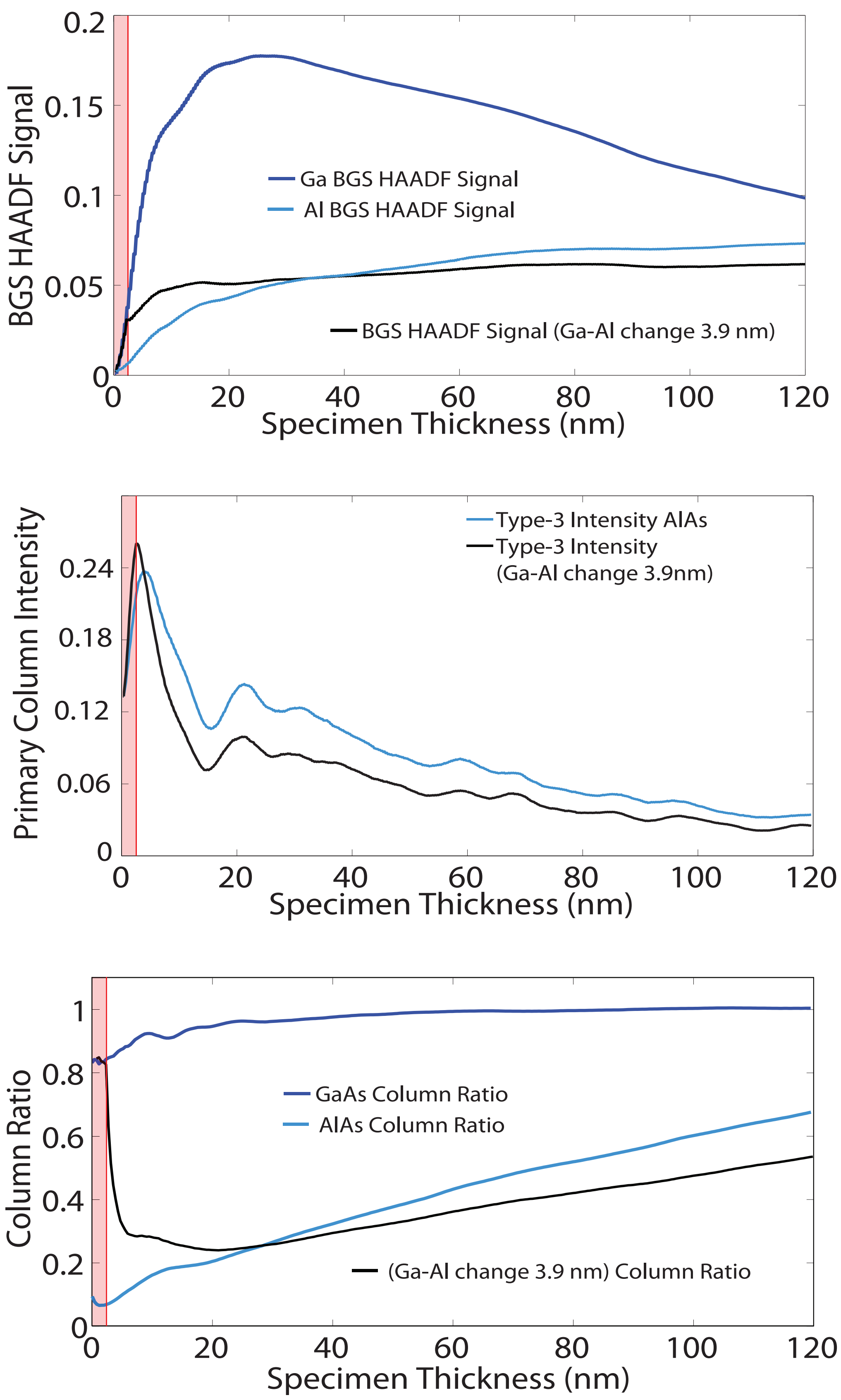

Figure 7.17 – The three graphs above show the HAADF signal (top), primary column intensity (middle) and the column ratio (bottom) for the GaAs into AlAs model where the compositional change is at a depth of $3.9nm$.

interaction with the Type-3 column and changes the resulting column ratio measurements. Figure 7.18 shows three graphs containing the column ratio, background subtracted HAADF signal and the primary column intensity for single crystal InAs and table 3.4 on page 71 details the simulation parameters used in this calculation. The lower of the three graphs shows the variation in column ratio as a function of thickness for single crystal InAs. Also indicated on the graph are the simple Z^2 theory for the column ratio of InAs alongside the column ratio variation for single crystal GaAs and AlAs for comparison. An interesting feature is that, at no thickness, does the column ratio of InAs equate to the simple Z^2 theory. This may again be due to the re-scattering effect as the HAADF signal from the Type-3 column in InAs is generated in the top $15nm$ of the crystal. This can be seen from the primary column intensity plot shown in the middle graph of figure 7.18 where the primary column intensities for both the Type-3 (red) and the Type-5 (green) columns are indicated. In the case of the indium column the on-column intensity peaks at a depth of $\sim 2nm$ and rapidly drops over the following $10nm$ of the atomic column until at a depth of $15nm$ the on-column intensity has dropped to less than 5% of the peak signal. The high rate scattering from the Type-3 column is also evident from the background subtracted HAADF signal plot shown in the top graph of figure 7.18. In this case the background subtracted HAADF signal from the Type-3 column peaks at a depth of $13nm$ at which point re-scattering causes the total signal to quickly drop with increasing thickness. In the case of the Type-5 HAADF signal the peak signal occurs at a depth of $26nm$ and it is apparent from the graph that the rate of re-scattering is the same in each case. However, the depth of the peak signal is deeper in the case of the Type-5 column and as a result the overall signal generated from this column is higher at thicknesses greater that $\sim 17nm$. A combination of the high rate of scattering from the Type-3 column and the re-scattering effect causes the column ratio of single crystal InAs to deviate from the simple Z^2 prediction.

Furthermore, the re-scattering effect greatly complicates the image interpretation for InAs based structures as for typical TEM specimen thicknesses the measured column ratio from an InAs dumbbell is comparable to that of a GaAs dumbbell. This complication is evident from previous HAADF studies of InAs - GaAs structures [23] where HAADF imaging was used to characterise the growth of InAs in a GaAs - InAs superlattice. The fine InAs - GaAs superlattice is shown at the top of figure 5.9 and

consisted of repeats of 1ML InAs / 6ML GaAs and also a different section with repeats of 1ML InAs / 3ML GaAs. Both sections were studied using SuperSTEM and each case the column ratio maps indicated that the superlattice was considerably less well defined than the AlAs / GaAs superlattice. As a result, the analysis from the InAs region of the superlattice produced inconclusive results.

7.3.1 InAs - AlAs $_{1.7nm}$

Section 7.2.1 detailed the results from projecting through a small amount of gallium at the top of a aluminium column and found that the scattering from the atomic column onto the HAADF detector can be reduced with certain atomic configurations. For the case of indium at the top of a aluminium column this effect can be magnified. The results from the following model, $InAs - AlAs_{1.7nm}$, are shown in figure 7.19 where the upper material in InAs and a compositional change to AlAs occurs at a depth of $1.7nm$. The top graph shows the HAADF signal generated from the Type-3 column of the $InAs - AlAs_{1.7nm}$ model. A significant portion of the HAADF signal is generated in the upper high-Z section of the atomic column. In this case the initial HAADF signal is generated closer to the entrance surface of the specimen increasing the path length to the exit face of the crystal. The effect on the column ratio can be seen in the lower graph in figure 7.19 which indicates that at a depth of 42nm the column ratio drops below bulk AlAs. Therefore, in this case a smaller quantity of indium at the entrance face of the Type-3 column causes a reduction in the column ratio for thick crystals that is more significant than in the case of the $GaAs - AlAs_{3.9nm}$ model. This will be in part due to the additional re-scattering from the HAADF signal generated in the top region of the crystal. However, it is primarily due to the higher Z material greatly reducing the on-column intensity. This can be seen from the primary column intensity graph in the middle of figure 7.19. In the case of the $GaAs - AlAs_{3.9nm}$ model there was still a significant fraction of intensity propagating down the atomic column in the lower region of the specimen. In this case the on-column intensity has almost dropped to zero at a depth of $40nm$. Therefore in this case it is only the top $40nm$ of the atomic column that will be generating the primary column HAADF signal.

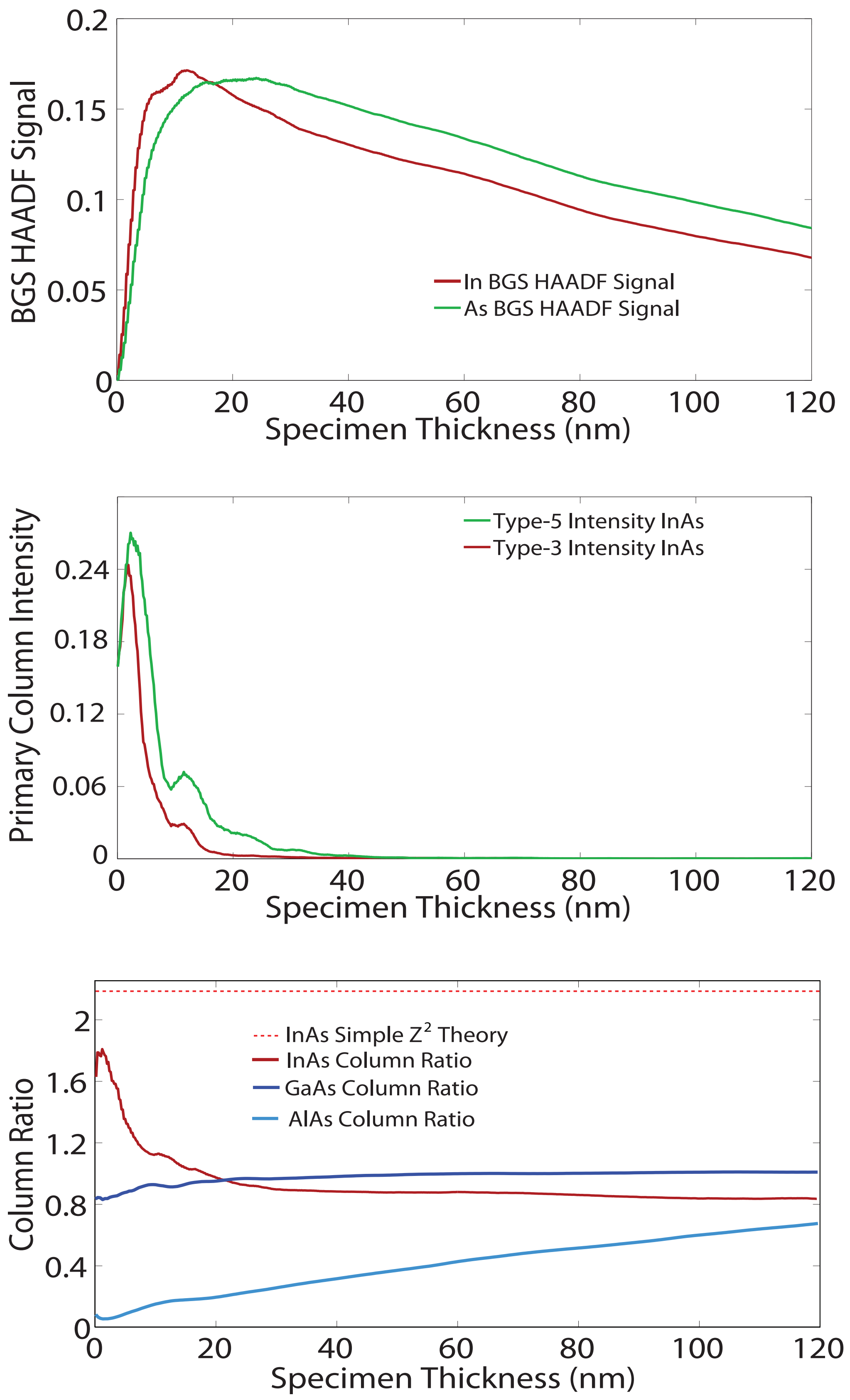

Figure 7.18 – The three graphs above show the HAADF signal (top), primary column intensity (middle) and the column ratio (bottom) for single crystal InAs.

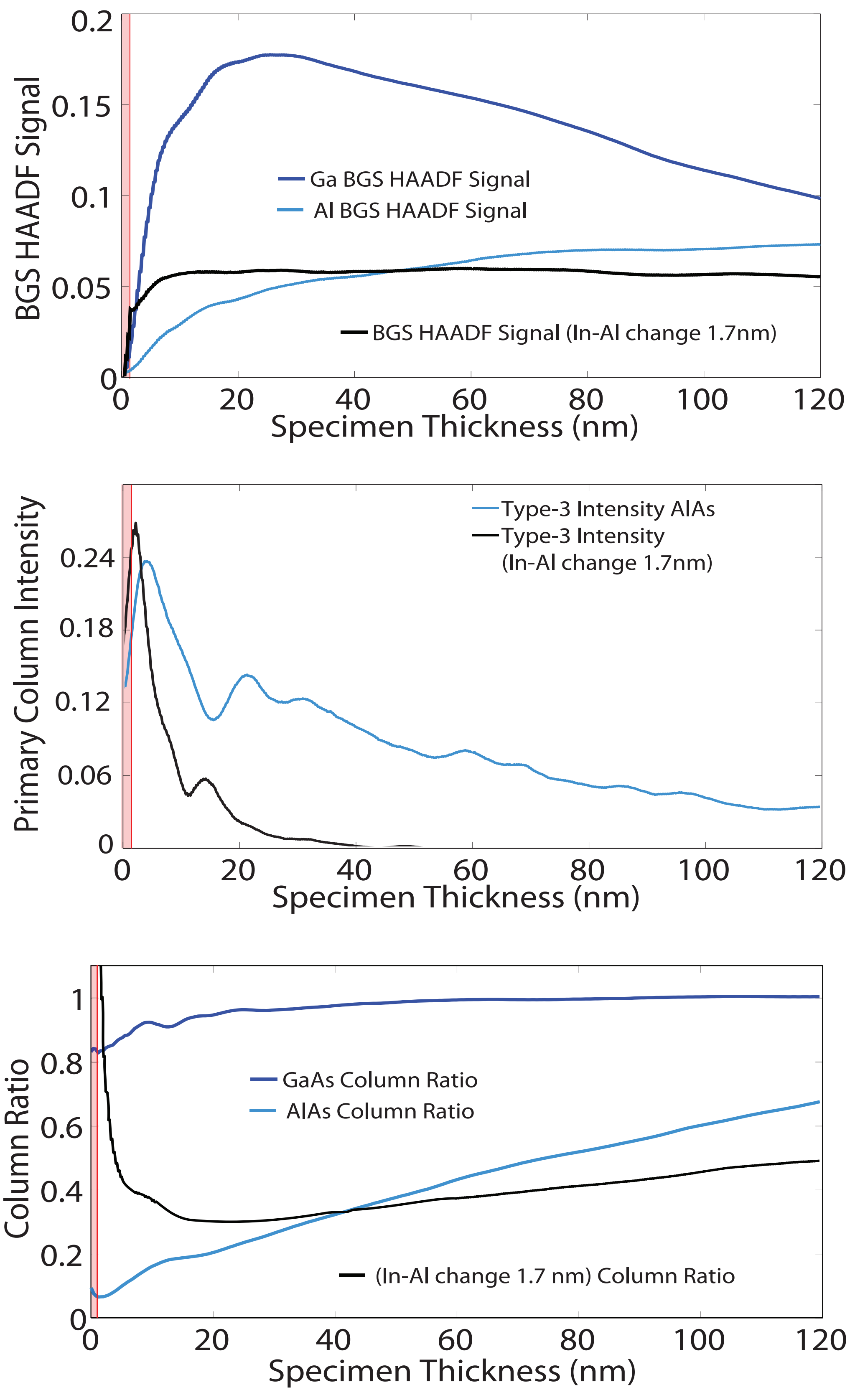

Figure 7.19 – The three graphs above show the HAADF signal (top), primary column intensity (middle) and the column ratio (bottom) for the InAs into AlAs model where the compositional change is at a depth of 1.7nm.

7.4 Implications for Quantitative HAADF Imaging

7.4.1 Quantitative HAADF Imaging

HAADF imaging can provide atomic structure images with atomic-number sensitivity and has been used in the past to determine the precise location of individual atoms in clusters [17, 107, 108]. However, a qualitative interpretation gives only an indication of the structure. Current research [66] has indicated that experimental HAADF images can be placed on an absolute scale by normalising the image intensity to that of the incident beam. The measurement of the incident beam intensity is possible using a HAADF detector with single electron collection sensitivity and an output voltage that is directly proportional to the incident electron intensity. The uniformity of the detector size, shape and response must also be characterised. This allows the images to be quantitatively compared with multislice calculations. Instead of comparing ratios of intensities (such as the column ratio) the normalised image allow image intensities to be compared directly.

The overall aim is to allow quantified measurements of the atomic columns in the structure being investigated. However, sections 7.1, 7.2 and 7.3 above detailed that there is a complex relationship between the composition of the atomic column and the resulting HAADF signal. The results from the preceding section described some of the complications associated with changes of atomic species within an atomic column. Many of the effects were observed when the compositional change occurred near either the entrance or exit surface of the specimen. This type of compositional change can occur when studying MBE grown interfacial layers such as in this project. However, HAADF imaging is also used to study other structures such as III-V quantum dots which can form at the interface between two growth layers. The size and shape of these structures depend greatly on the growth conditions and chemistry of the materials and the quantification and characterisation of these structures could be complicated by the effects described above. The following section summarises the cases where quantitative measurements are complicated by the specific configuration of the atomic columns. These cases are showed graphically for a typical thin TEM sample thickness of $30nm$ and a thicker sample thickness of $60nm$.

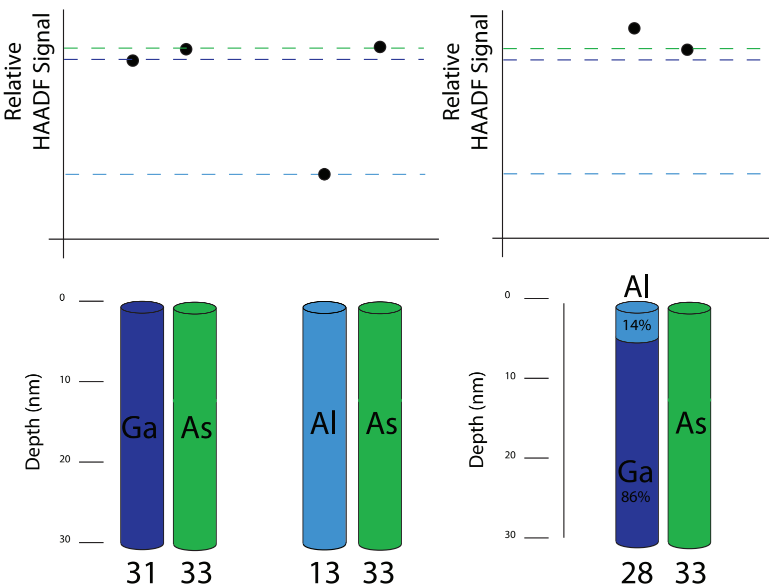

Figure 7.20 – This diagram summarises the counter intuitive scattering effects that can complicate image interpretation for typical TEM specimen thicknesses ($\sim 30nm$). The compositional change is from a low Z to a high Z material.

7.4.1.1 Thin Specimen - 30nm

The left side of figure 7.20 shows a schematic for single crystal GaAs and AlAs. The lower half indicates the atomic columns, the relative thickness of the columns in this case is $30nm$ and the average Z of the column is also indicated along with the atomic species population as a percentage. Above this diagram is a graph showing the relative HAADF signal from each column and the relative signals from bulk GaAs and bulk AlAs are highlighted using the horizontal colour coded broken lines. The diagram on the left consists of the single crystals which are used as a reference for the diagram on the right. In figure 7.20 the diagram on the right shows a partially populated Type-3 column where the entrance of the column is aluminium followed by gallium. Figure 7.20 shows the case where an atomic column with a lower average Z produces a higher HAADF signal.

The second case is shown in figure 7.21 where again the left side shows the single crystal dumbbell signals and the right diagram indicates an atomic column with gallium at the top of the column and aluminium in the lower section. In this case the overall scattering from the Type-3 column is lower than the scattering for a fully populated aluminium column. This case clearly indicates that an atomic column with a higher average Z can result in a lower overall HAADF signal.

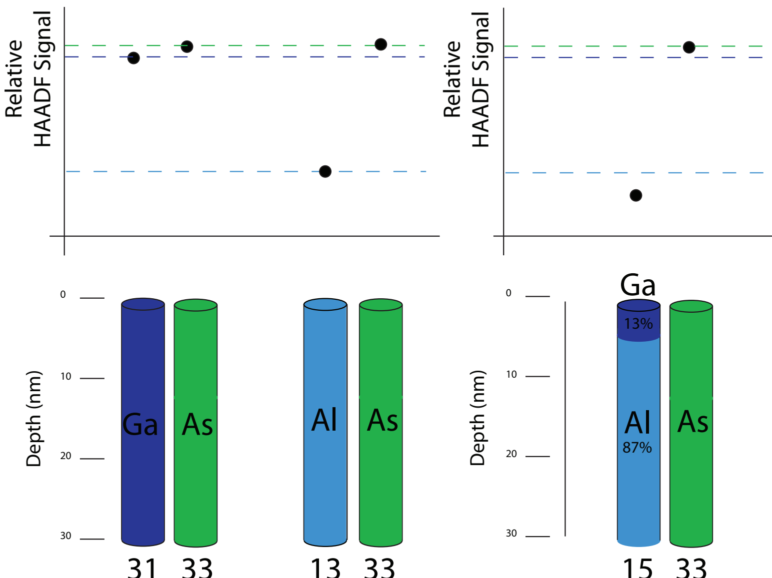

Figure 7.21 – This diagram summarises the counter intuitive scattering effects that can complicate image interpretation for typical TEM specimen thicknesses ($\sim 30nm$). The compositional change is from a high Z to a low Z material.

7.4.1.2 Thick Specimen - 60nm

This section details the relative diagrams for a thicker specimen at $60nm$. Figure 7.22 again indicates the fully populated single crystal case on the left. The right side of figure 7.22 shows how the scattering from a partially populated Al/Ga column can vary depending on the depth of the compositional change. From left to right the aluminium content is increasing and therefore the average Z of the Type-3 column is dropping. However, the scattering does not follow a simple Z^{η} model and the first and last configurations produce scattering that is greater than a fully populated gallium column. Figure 7.23 also summarises the case where an atomic column with a higher average Z produces a lower HAADF signal. Using the single crystal models as a reference, the right diagram in figure 7.23 indicates that having small amounts of a high-Z material at the top of an atomic column can drastically reduce the HAADF signal that is generated. This could have implications when imaging interfaces which require a thickness series and also when imaging quantum structures embedded at the surface of a III-V crystal.

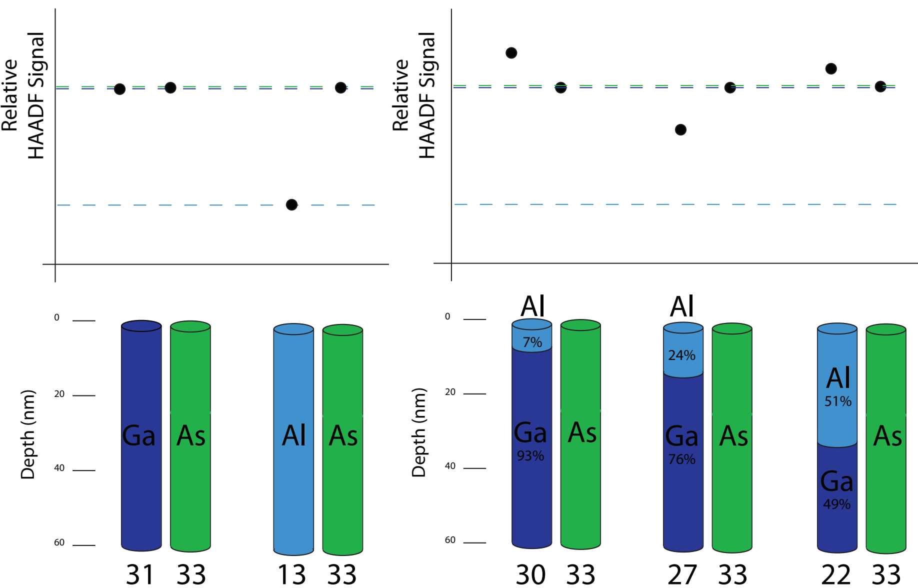

Figure 7.22 – This diagram summarises the counter intuitive scattering effects that can complicate image interpretation for larger TEM specimen thicknesses ($\sim 60nm$). The compositional change is from a low Z to a high Z material.

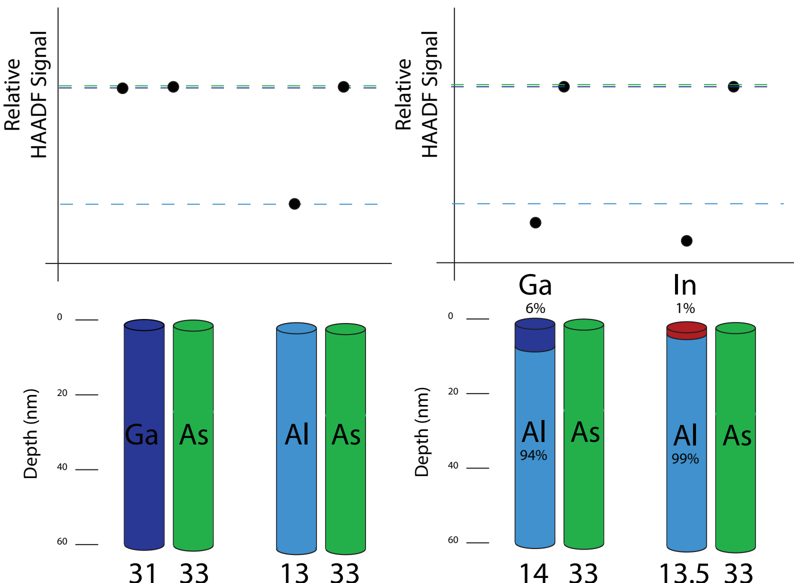

Figure 7.23 – This diagram summarises the counter-intuitive scattering effects that can complicate image interpretation for larger TEM specimen thicknesses ($\sim 60nm$). The compositional change is from a high Z to a low Z material.

7.5 Discussion and Conclusions

Presented within this chapter are the results from a detailed investigation into the effect of compositional changes within an atomic column on the generated HAADF signal. The first series of models investigated consisted of an upper section of AlAs and a lower section of GaAs and were discussed in section 7.1. In this section conditions were explored where an atomic column with a lower average Z can produce a higher HAADF signal as a direct result of the distribution of atoms within the atomic column. The investigation found a strong correlation between the primary column intensity and the generated HAADF signal. However, the primary column intensity alone was insufficient to describe all of the effects observed in the HAADF signals. In section 7.1.5 a simple electron re-scattering model was developed. The first stage of the model was to integrate the intensity localised to all of the atomic positions within each slice of the simulation. The integrated intensity was weighted depending on the atomic species. The next stage scaled the contribution from each slice depending on its depth within the crystal. This re-scattering model found good agreement with the observed HAADF signals and can be used to accurately describe the variability of the HAADF signals. Sections 7.2 and 7.3 then describe conditions where an atomic column with a higher average Z can produce a lower HAADF signal as a result of the distribution within the atomic column. The results indicated that under certain conditions the scattering from the atomic columns can be counter-intuitive. Section 7.4 then discussed the implications that these results have for quantitative HAADF measurements. This section also gives a summary of these implications and how they would affect HAADF measurements for thin and thick samples.

Chapter 8

Conclusions and Future Work

8.1 Introduction

The aim of this project was to improve the understanding and interpretation of high resolution HAADF-STEM images. In particular the study focused on images obtained using SuperSTEM 1 which were used to analyse several MBE grown III-V semiconductor structures. The images were taken as part of a previous investigation into the composition and quality of the various MBE grown layers and interfaces. The aim of the original SuperSTEM investigation by Robb et al. [23] was to obtain information on the accuracy of the MBE growth techniques. During the project, a process for extracting the high resolution information from the HAADF-STEM images was developed. This process provided a consistent method that could be applied to the STEM images to extract the high resolution atomic column information. The process is called column ratio mapping [94] and to assist in the interpretation of these column ratio maps an extensive modelling project into the scattering of Ångström sized STEM probes was undertaken for single crystal III-V materials [23].

The results from the modelling project indicated that the experimentally measured column ratio from single crystal III-V materials was accurately reproduced by the simulations. However, the scattering of the Ångström sized STEM probe within a partially populated atomic column was unknown. Therefore, it was unclear how the generated HAADF signals at a complex interface would vary from those generated within single III-V crystal structures. As a result, the interpretation of the experimental images was not fully understood.

The aim of the current project was to investigate the effect that the interfacial

structure has on the scattering of the Ångström sized STEM probe. More specifically, the investigation focused on how the interfacial characteristics, such as interface width and position, varied depending on the type of interface structure being imaged.

The investigation started with the column ratio mapping method. In particular, the process used to separate the high resolution column signals from the background signal. This separation process was important as the atomic resolution information is generated by the primary column while the background signal is a result of scattering from the de-localised probe. An automated approach was developed that accurately extracted the atomic column data. Moreover, possible sources of error were identified and the developed process ensured the minimisation of image artifacts. An objective process was developed to characterise the interface data from a thickness series of HAADF images. This process allowed the measurement of the interface position and interface width for each atomic row in the image. A range of simple models were formed and explored using the multislice code in an attempt to understand the experimental interfacial structure. The same objective measurement process was applied to the models allowing a direct comparison to the experimental data. The further development of the simulated models allowed a detailed evaluation of the structure of the MBE grown interfaces.

The final investigation looked into the relationship between the scattering of the Ångström sized probe within single atomic columns and systematically studied the variability of the resulting HAADF signal. A simple electron re-scattering model was developed that can be used to describe the observed scattering effects when the atomic column is partially populated with multiple atomic species.

Section 8.2 below summarises the conclusions from the preceding chapters and section 8.3 describes future experimental and modelling work that could be performed to clarify some remaining issues associated with HAADF imaging.

8.2 Conclusions

Thermal diffuse scattering contributes significantly to the measured HAADF signal and is incorporated into the multislice calculation using the frozen phonon approximation. The contribution of phonon scattering is controlled using a single parameter in the simulations and the effect of this parameter, $< u^2 >$, was investigated in Chapter 4.

By comparing a series of simulated and experimental CBED patterns over a range of thicknesses a mean free path was calculated for the crystallographic orientation and the microscope conditions used. This mean free path was then used as a calibration for the subsequent EELS t/λ measurements recorded at the position of each energy filtered CBED pattern. The experimental CBED patterns were compared to multislice simulations where the mean square displacement parameter was systematically varied. By comparing the intensity in the FOLZ, an "effective" mean square displacement was calculated to be be 5-10% lower than the currently used mean square displacement value. However, it was found that a variation of this magnitude has only a minimal effect on the resulting HAADF signal. Furthermore, the 5-10% reduction may simply be due to the anisotropic vibration of the atoms in the GaAs crystal structure. Therefore, the currently used mean square displacement, $< u^2 >_{current}$, was found to satisfactorily reproduce the thermal diffuse scattering observed experimentally and was used for the simulations in chapters 6 and 7. This investigation was limited to single crystal GaAs where the Type-3 and Type-5 atomic columns have a similar atomic number. It is possible that for other materials such as AlAs, where the Type-3 and Type-5 atomic columns have significantly different atomic numbers, that this effect could be more significant.

Experimental HAADF images must be processed to first separate the high resolution information generated by the atomic columns from the background signal generated by delocalised scattering from the non-primary columns. Chapter 5 described a method for background separation that minimises image artifacts. An automated method using pattern recognition was described which allowed large areas of the HAADF image to be processed accurately and quickly. An analytical function was fitted to the HAADF data using a least squares fitting method resulting in an objective measure of the image characteristics. The measured characteristics consisted of the interface width and interface position which were measured as a function of specimen thickness. The measurements indicated a difference between the Type-A interface (AlAs grown on GaAs) and Type-G interface (GaAs grown on AlAs). While the width of the Type-G interface was independent of specimen thickness the Type-A interface width increased with increasing specimen thickness. Furthermore, the apparent width of the GaAs layer also increased with increasing specimen thickness.

The multislice calculations for single crystal III-V materials in section 3.6 indicated

that a large number of phonon configurations were required (typically > 80) to reduce the error in the simulated column ratio to a level that was consistent with the measured experimental error. The simulation of an interface requires many probe positions and increased the computational time by an order of magnitude. If the interface structure then consists of a random structure such as stepping or diffusion then a number of random configurations have to be averaged together, which again greatly increases the time required for the calculation. The complexity and range of models investigated required the use of large scale computing resource called the GRID, part of which is based at Glasgow University.

The model development in chapter 6 began with a broad range of simple structures that were investigated using the multislice code. The first of which was a perfectly abrupt AlAs - GaAs interface (section 6.2.2) which indicated that both the interface width and position remained constant with increasing thickness. However, this model indicated that the proximity of the interface can affect the measured column ratio. This was a direct result of the change in the background signal which varied depending on the composition of the atomic columns surrounding the primary column. This result indicates that the method used to estimate the background signal under the atomic columns is inaccurate. This is a result of the difference in the generated background when the probe is placed on an atomic column and when the probe is placed between the atomic columns. The main difference is the channelling that occurs when the probe is placed on the atomic columns which does not occur at the background probe position.

A range of terrace structures, forming a repeated sawtooth pattern, were then investigated. While these models exhibited many of the characteristics observed in the experimental data it was clear that none of the models met all of the constraints imposed by the experimental measurements. The models did, however, indicate that the measured characteristics for such structures can vary greatly depending on the compositional orientation at the entrance face of the specimen. Furthermore, the measured characteristics of these structures were only apparent when compared over a range of specimen thicknesses. The results of the sawtooth models also indicated the possibility that a vicinal interface could describe the experimental data.

Two simple vicinal models were initially formed where the angle of the interface, θ, was chosen to be $+1°$ and then $-1°$. The positive θ interface angle formed a GaAs

projection where the probe was projecting through GaAs at the entrance of the specimen. The negative θ interface angle formed an AlAs projection where the probe would project through AlAs first. The results from these interfaces indicated that the column ratio would quickly saturate in the case of the AlAs projection resulting in a shift of the apparent interface position. This resulted in measured characteristics that were unlike those observed experimentally. The next development of this type of model was the introduction of a degree of stepping at the interface which reduced the saturation effect. The results indicated that an interface with a vicinality of $0.6°$ and a degree of interfacial roughness could be used to describe some of the experimental results. However, the diffused model described in section 6.2.4 found the best agreement with the experimental data. This model was developed using model concentration profiles that were calculated using a segregation model for III-V materials [103]. This indicates that both the measured characteristics of the simulated Type-A (AlAs on GaAs) and Type-G (GaAs on AlAs) interfaces are in good agreement with the experimental measurements of chapter 5.

The results of chapter 6 also indicated that the column ratio measured from the interface depends on the specific configuration of atoms within the atomic columns and often varied in an unpredictable way. Chapter 7 describes an investigation into the dependence of the generated HAADF signal on compositional changes within an atomic column. The models investigated were a simplification of the atomic columns that could form at a III-V heterojunction. This simplification ignored the proximity of the interface and the strain at the interface produced from the change in lattice parameter where the change in composition was limited to the z-direction. The results indicated that there was a strong correlation between the HAADF signal and the intensity around the atomic columns. The intensity around the atomic column was integrated and weighted by Z^{η}. When re-scattering of the electrons was accounted for good agreement between the HAADF signal and the integrated intensity was found. Furthermore, this simple model accounted for the changes in the column ratios observed at the interface models from the preceding sections.

Section 7.3 also presented an investigation into Ångström sized probe scattering within single crystal InAs. The results indicated that the column ratio of InAs varied in a complex way with increasing thickness and did not follow the simple Z^{η} theory at any specimen thickness. Furthermore, at specimen thicknesses greater than 20nm

the column ratio of InAs fell below that of single crystal GaAs. This means that at thicknesses greater than 20nm the scattering from the higher Z Type-3 column will be less than that of the lower Z Type-5 column. This counter initiative atomic column scattering would complicate both image interpretation and quantitative measurements. Furthermore, the ability to characterise InAs structures grown in a GaAs lattice using the atomic column information would be complicated.

This complication was apparent when an attempt to characterise InAs - GaAs structures using SuperSTEM [23]. In this investigation column ratio maps were produced from a InAs - GaAs superlattice. However, the compositional identification and interfacial characterisation was inconclusive. The problems associated with InAs - GaAs interfacial characterisation could be a result of indium diffusion. However, this result could also be associated with the problems associated with distinguishing a partially populated indium - gallium atomic column at the interface from either a bulk indium column or a bulk gallium column.

These results indicate issues that will occur when attempting to take quantitative measurements from HAADF images. The final section of chapter 7 described how these scattering effects could potentially affect quantitative measurements from HAADF images taken from both thin and thicker crystalline samples. The generated HAADF signal from an atomic column depends on many factors. The atomic columns surrounding the primary column, the composition of the primary atomic column, the distribution of atoms within the atomic column and the atomic species within the atomic column all affect the measured signal. Furthermore, the HAADF signal generated from columns with a similar average atomic number can vary significantly depending on one or other of these factors. Likewise, atomic columns with a very different average atomic number can generate the same HAADF signal.

These issues with quantitative measurements are significant, however, techniques that can achieve depth sensitivity are being developed. Many issues with image interpretation arise because images are a result of the illumination projecting through many atomic layers. Techniques such as confocal STEM can produce a focused probe at a specific depth within the crystal [109, 110]. With these techniques it may be possible to detect the compositional changes within an atomic column as a function of depth. This would allow the complete characterisation of an interfacial structure where the species and location of each atom can be mapped in three dimensions. These techniques are,

however, very new and a full understanding of how this type of illumination interacts with the interfacial structure is still required.

8.3 Future Work

The comparison of the FOLZ intensity in chapter 4 show that there is an angular dependence on the intensity in the FOLZ ring. The anisotropic vibration of the atoms in single crystal GaAs has been studied in great detail and a comparison of the directional motion of the atoms to the intensity profile in figure 4.18 would indicate whether the angular dependence is related to the mean square displacement anisotropy. This investigation could be expanded to include other III-V materials. Furthermore, parameters such as the specimen temperature could be investigated and modeled to form a full picture of the relationship between the HAADF signal and thermal diffuse scattering.

The experimental SuperSTEM images that were recorded consisted of a thickness series in one orientation only, [110]. By taking a number of images in different orientations many of the possible interface structures could have been eliminated. For example, if the interface structure is vicinal, this can be confirmed by flipping the sample orientation in the specimen holder. A vicinal interface would be apparent from the change in the measured interface position over the image thickness series. Furthermore, by creating two samples one in the [110] orientation and another in the $[1\bar{1}0]$ orientation the vicinality of the interface may be apparent. In both orientations the images would be formed from a projection through many layers. However, it may be possible to image any terracing that has occurred during MBE growth.

The results from the diffused interface indicate that, for the Type-A interface, the measured width would increase as a function of specimen thickness. This increase in measured interface width was a direct result of the gallium concentration levels in the atomic columns. The relationship between the concentration levels and the HAADF signal could be investigated further using the multislice code. Diffusion levels have been measured using a variety of techniques for MBE growth and, with further study, the characteristics measured from the HAADF image such as the interface position and width could be used to provide an estimation of the diffusion levels at superlattice interfaces. This is, however, a clear indication that it is not possible to estimate interfacial diffusion using a single HAADF image from a thin sample.

The calculations from a perfect interface in section 6.2.2 showed that the proximity of the interface has an effect on the measured column ratio. This effect is directly related to the background scattering and, in particular, the difference between the scattering when the probe is placed on the atomic column and at the background position. The simple scattering model that was developed in section 7.1.5 could be used to study the difference between these background signals using the integrated intensity. The integrated intensity can be measured for all of the non-primary columns when the probe is placed on an atomic column and compared to the integrated intensity when the probe is placed at the background position. This may allow an improvement in the estimated background signal which would in turn give a better estimation of the primary column intensity from the experimental images.

Another interesting area to investigate would be the analytical signal generated from an interface. Using the multislice code, the probe conditions could be optimised for a given specimen thickness. For example, the probe divergence changes with the convergence angle and, while a larger convergence angle can produce a smaller probe at the entrance face of the specimen, the divergence of the probe within the specimen can result in a poorer analytical signal resolution. The multislice code can be used to estimate the EDX and EELS signal for a specific set of probe conditions. The probe convergence angle can be varied systematically allowing a degree of optimisation. Furthermore, it may be the case that the aberrations used to optimise the imaging probe can also be optimised for an analytical probe which would result in an improved analytical signal. This optimisation is increasingly important as atomic-resolution analytical analysis has become achievable through aberration correction.

The re-scattering model that was described in section 7.1.5 indicated that the measured HAADF signal is dependent on many factors such as the depth at which the signal is generated, the thickness of the specimen and the average Z of the structure. This will, therefore, have significant implications when attempting to characterise nanostructures within a bulk crystalline sample. For example, Z-contrast imaging is commonly used to measure the characteristics of burried quantum structures [111]. For this type of measurement, the depth and composition of the structures will affect the images using this technique. However, taking these effects into account the imaging conditions can be optimised ensuring accurate characterisation.

The effect of re-scattering could also affect other imaging techniques. For example,

techniques have been developed that use an aberration corrected STEM probe focused within the crystal structure in an attempt to detect dopant atoms within the bulk sample [112]. These investigations were performed at very thin sample thicknesses, $\sim 16nm$. However, for typical TEM sample thicknesses, $\sim 30nm$, the effects from re-scattering may significantly affect the ability to detect dopant atoms at the entrance face of the specimen. Therefore, an investigation into these effects may prove insightful.

The studies in this project focused on the microscope conditions used in SuperSTEM 1 with an Ångström sized probe. With current developments in aberration correction the ability to form sub-Ångström probes is available. The objective lens aberrations can be corrected to fifth order allowing the probe convergence angle to be greatly increased. This increase in convergence angle will reduce the depth of atomic column channelling and increase the probe divergence within the crystal structure. This may have significant implications when considering the re-scattering of electrons as the HAADF signal from an atomic column will be generated from a smaller region at the entrance face of the specimen. Therefore, the study of sub-Ångström probes in III-V materials is essential. This type of investigation would highlight the limitations and provide optimum imaging conditions when using probes with large convergence angles.

Bibliography

[1] S. M. Sze. *Physics of Semiconductor Devices.* Wiley, New York, 2 edition, 1981.

[2] A. S. Grove. *Physics and Technology of Semiconductor Devices.* Wiley, New York, 1967.

[3] E. H. Nicollian and J. R. Brews. *MOS Physics and Technology.* Wiley, New York, 1982.

[4] S. M. Sze. *High-Speed Semiconductor Devices.* Wiley Interscience, 1990.

[5] R. A. Smith. *Ssemiconductors.* Cambridge University Press, Cambridge, 1978.

[6] K. Eberl. Low dimensional structures prepared by epitaxial growth or regrowth on patterned substrates. *Series E: Applied Sciences*, 298, 1995.

[7] E. F. Schubert. *Doping in III- V semiconductors.* Cambridge University Press, 1993.

[8] R.A. Stradling and P.C. Klipstein. *Growth and characterisation of semiconductors.* Aam Hilger, 1991.

[9] G. Bauer, F. Kuchar, and H. Henrich. *Two dimensional systems, Heterojunctions and superlattices.* Springer-Verlag, Berlin, 1984.

[10] Y. Fu, Y.-M. Mu, and M. Willander. Effect of interface roughness on III-V relation of AlGaAs/GaAs heterojunction field effect transistor. *Superlattices Microstruct.*, 23(2):502, 1998.

[11] J. R. Brews, W. Fichtner, E. H. Nicollain, and S. M. Sze. Generalized Guide for MOSFET Miniaturisation. *IEEE Int. Electron Devices Meeting Digest*, page 384, 1983.

[12] G. Turner, B. Nechay, and S. Eglash. Frequency-Domain Analysis of Time Dependent Reflection High-Energy Electron Diffraction Intensity Data. *J. Vac. Sci. Tech. B*, 8:283 – 287, 1990.

[13] P. Cohen, P. Pukite, J. van Hove, and C. Lent. Reflection High Energy Electron Diffraction Studies of Epitaxial Growth on Semiconductor Surfaces. *J. Vac. Sci. Tech. B*, 3:1251 – 1258, 1986.

[14] J. H. Neave, B. A. Joyce, P. J. Dobson, and N. Norton. Convergent beam RHEED calculations of a 'forbidden reflection' from the Si (111) surface. *Appl. Phys.*, A31:631, 1983.

[15] Y. Peng, P. D. Nellist, and S. J. Pennycook. HAADF-STEM imaging with sub-Angstrom probes. *J. Electron Microsc.*, 53(3):257 – 266, 2004.

[16] A. Bleloch and A. Lupini. Imaging at the picoscale. *Nature*, 2004.

[17] P. M. Voyles, J. L. Grazul, and D. A. Muller. Imaging individual atoms inside crystals with ADF-STEM. *Ultramicroscopy*, 96:251 – 273, 2003.

[18] O. Scherzer. The theoretical resolution limit of the electron microscope. *J. Appl. Phys.*, 20:20 – 29, 1949.

[19] O. L. Krivanek, N. Dellby, and A. R. Lupini. Towards sub-A electron beams. *Ultramicroscopy*, 78:1, 1999.

[20] L. M. Brown. A Synchrotron in a Microscope. *Institute of Physics Conference Series*, 153(153):17 – 22, 1997.

[21] A. Bleloch, L. M. Brown, R. Brydson, A. Craven, P. Goodhew, and C. Kiely. The superSTEM: An Aberration Corrected Analytical Microscopy Facility. *Microsc. Microanal.*, 1, 2002.

[22] A. L. Bleloch, M. Brown, R. Brydson, A. Craven, M. Falke, U. Falke, P. Goodhew, and G. Tatlock. First results from the UK superSTEM Laboratory. *Microsc. Microanal.*, 4, 2003.

[23] P. Robb. *A study of MBE grown III-V structures using SuperSTEM.* PhD thesis, University of Glasgow, University Avenue, Glasgow, 2007.

[24] L. M. Peng. Electron atomic scattering factors, Debye-Waller factors and the optical potential for high-energy electron diffraction. *J. Electron Microsc.*, 54(3):199 – 207, 2005.

[25] L. M. Peng. Anisotropic Thermal Vibrations and Dynamical Electron Diffraction by Crystals. *Acta Cryst.*, A53:663 – 672, 1997.

[26] C. E. Hall. *Introduction to Electron Microscopy.* McGraw Hill, New York, 1953.

[27] L. de Broglie. *Ann. de Physiques*, 3(22), 1925.

[28] G. Davisson and L. H. Germer. *Phys. Rev.*, 30:705, 1927.

[29] M. Knoll and E. Ruska. *Z. Physik*, 78:318, 1932.

[30] P. Grivet. *Electron Optics.* Pergamon Press, New York, 1972.

[31] P. W. Hawkes. *Magnetic Electron Lenses.* Springer-Verlag, New York, 1982.

[32] O. L. Krivanek, P. D. Nellist, N. Dellby, M. F. Murfitt, and Z. Szilagyi. Towards sub-0.5 A electron beams. *Ultramicroscopy*, 96:229 – 237, 2003.

[33] P. B. Hirsch, A. Howie, R. B. Nicholson, D. W. Pashley, and M. J. Wheelan. *Electron Microscopy of Thin Crystals.* Krieger Huntington, New York, second edition, 1977.

[34] D. B. Williams and C. B. Carter. *Transmission Electron Microscopy.* Springer, New York, first edition, 1996.

[35] R. F. Egerton, F. Wang, and P. A. Crozier. Beam-Induced Damage to Thin Specimens in an Intense Electron Probe. *Microsc. Microanal.*, 12:65 – 71, 2006.

[36] M. H. Loretto. *Electron Beam Analysis of Materials.* Chapman and Hall, 19981984.

[37] M. H. Loretto. *Electron beam analysis of materials.* Chapman and Hall, New York, second edition, 1994.

[38] J. W. Steeds. *Introduction to analytical electron microscopy.* Plenum, New York, 1979.

[39] D. Kyser. *Electron-Beam Specimen Interactions for Microscopy.* SAMF O'Hare, Illinois, 1984.

[40] L. Reimer. *Transmission electron microscopy.* Springer-Verlag, New York, third edition, 1993.

[41] J. A. Belk. Electron microscopy and microanalysis of crystalline materials. *Microsc. Microanal.*, 1978.

[42] K. W. Andrews and D. J. Dyson. *Electron Diffraction Patterns.* IOP, Bristol, 1967.

[43] C. J. Rossouw, L. J. Allen, S. D. Findlay, and M. P. Oxley. *96*, 96:299 – 312, 2003.

[44] S. D. Findlay, L. J. Allen, M. P. Oxley, and C. J. Rossouw. *Ultramicroscopy*, 96:65 – 81, 2003.

[45] R. F. Loane, P. Xu, and J. Silcox. Thermal vibrations in convergent-beam electron diffraction. *Acta Cryst*, A47:267–278, 1991.

[46] M. V. C. Riglos and A. Tolley. A method for thin foil thickness determination by transmission electron microscopy. *Microsc. Microanal.*, 254:420 – 424, 2007.

[47] V. J. Keast, A. J. Scott, R. Brydson, D. B. Williams, and J. Bruley. *Journal of Microscopy*, 203(0):135 – 175, 2001.

[48] N. A. Dyson. *X-ray analysis and nuclear physics.* Longman, Harlow, 1973.

[49] C. C. Chang. *Analytical Auger Electron Spectroscopy.* Plenum, New York, 1974.

[50] R. F. Egerton, P. Li, and M. Malac. Radiation damage in the TEM and SEM. *Radiat. Res.*, 35:399 – 409, 2004.

[51] F. J. Bryant and A. F. J. Cox. Atomic displacement energies for binary semiconductors. *J . PHYS.*, 1(2):1734–1736, 1968.

[52] P. W. Hawkes. *Advances in optical and electron microscopy.* 1978.

[53] P. Goodhew and A. Bleloch. SuperSTEM-the microscope with glasses. *Materials World*, 11:23 – 24, 2003.

[54] P. W. Hawks. *Electron optics and electron micriscopy.* Taylor and Francis Ltd, London, 1972.

[55] L. E. Murr. *Electron optical applications in material science.* McGraw Hill, New York, 1970.

[56] I. M. Watt. *The principles and practice of electron microscopy.* Cambridge University Press, New York, 1985.

[57] O. L. Krivanek. *Microsc. Microanal. Microstruct*, 2:2, 1991.

[58] J. C. H. Spence. *Electron Microdiffraction.* Plenuml, New York, first edition, 1992.

[59] P. M. Kelly, A. Jostons, R.G Blake, and J. G. Napier. *Phys. stat. sol.*, A31:771, 1975.

[60] S. M. Allen. *Phil. Mag.*, A43 - 2:325 – 335, 1981.

[61] D. Mitchell. Determination of mean free path for energy loss and surface oxide film thickness using convergent beam electron diffraction and thickness mapping. *Journal of Microscopy*, 224:187, 2006.

[62] Y. Berta, C. Ma, and Z. L. Wang. Nanobelt Thickness and Mean-free Path Determination by CBED and PEELS. *Mater. Sci.*, pages 30332 – 30245, 2002.

[63] A. V. Crewe, J. Wall, and J. Langmore. Visibility of single atoms. *Science*, 168:1338, 1970.

[64] S. J. Pennycook and L. A. Boatner. *Nature*, 336:565, 1988.

[65] J. C. H. Spence. *High-Resolution Transmission Electron Microscopy.* Oxford University Press, Oxford, 3 edition, 2003.

[66] J. M. LeBeau, S. D. Findlay, L. J. Allen, and S. Stemmer. Quantitative Atomic Resolution Scanning Transmission Electron Microscopy. *Physical Review Letters*, 100(68):206101, 2008.

[67] D. C. Joy. *Principles of analytical electron microscopy.* Plenum Press, New York, 2 edition, 1986.

[68] R. F. Egerton. Electron Energy Loss Spectroscopy in the Electron Microscope. 1996.

[69] P. E. Batson, N. Dellby, and O. L. Krivanek. Sub-ångstrom resolution using aberration corrected electron optics. *Nature*, 418:617 – 620, 2002.

[70] C. P. Scott. TEM cross- section preparation with minimal ion milling time. *Journal of Microscopy*, 182(3):186 – 191, 1996.

[71] A. Barna, B. PCcz, and M. Menyhard. Amorphisation and surface morphology development at low-energy ion milling. *Ultramicroscopy*, 70:161 – 171, 1998.

[72] E. J. Kirkland. *Advanced computing in electron microscopy.* Plenum Press, New York, 1998.

[73] C. Dwyer and J. Etheridge. Scattering of Angstrom scale electron probes in silicon. *Ultramicroscopy*, 96:343 – 360, 2003.

[74] M. Finnie, A. J. Craven, and P. D. Robb. A HAADF Investigation of AlAs GaAs interfaces using SuperSTEM. *Journal of Physics: EMAG conference series*, 2009.

[75] E. Kirkland, R. F. Loane, and J. Silcox. *Ultramicroscopy*, 23:77, 1987.

[76] J. M. Cowley and A. F. Moodie. *Acta Crystallogr*, 10:609, 1957.

[77] A. I. Kirkland and R. Meyer. Indirect High-Resolution Transmission Electron Microscopy: Aberration Measurement and Wavefunction Reconstruction. *Microsc. Microanal.*, 10:401 – 413, 2004.

[78] C. Dwyer. Multislice Theory of Atomic Inner-Shell Ionization. *Microsc. Microanal.*, 78(1999):1 – 12, 2007.

[79] D. K. Saldin and P. Rez. Multislice theory of fast electron scattering. *Philos. Mag.*, B - 55:481, 1987.

[80] C. J. Rossouw and V. W. Maslen. *Philos. Mag.*, 49:743, 1984.

[81] E. C. Cosgriff, M. P. Oxley, L. J. Allen, and S. J. Pennycook. The spatial resolution of imaging using core loss spectroscopy in the scanning transmission microscope. *Ultramicroscopy*, 102:317–326, 2005.

[82] N. Dellby, O. L. Krivanek, P. D. Nellist, P. E. Batson, and A. R. Lupini. Progress in aberration-corrected scanning transmission electron microscopy. *J. Electron Microsc.*, 50:177, 2001.

[83] Z. L. Wang and J. M. Cowley. Imaging elastic strains in HAADF STEM. *Ultramicroscopy*, 31:437, 1989.

[84] D. E. Jesson and S. J. Pennycook. Incoherent imaging of crystals using thermally scattered electrons. *Proc. Roy. Soc. London*, 449:273, 1995.

[85] P. L. Taylor and O. Heinonen. *A quantum approach to condensed matter physics.* Cambridge University Press, 2002.

[86] D. A. Muller, B. Edwards, E. J. Kirkland, and J. Silcox. Simulation of thermal diffuse scattering including a detailed phonon dispersion curve. *Ultramicroscopy*, 86:371 – 380, 2001.

[87] J. M. Cowley. Diffraction Physics. *Elsevier Science*, 1995.

[88] R. J. Glauber. *Phys. Rev.*, 98:1692, 1955.

[89] C. Dinges and H. Rose. Simulation of transmission and scanning transmission electron microscopic images considering elastic and thermal diffuse scattering. *Scanning Microscopy International*, 11:277 – 286, 1997.

[90] J. Li. *Modelling Simul. Mater. Sci. Eng.*, 11:173, 2003.

[91] P. D. Nellist and S. J. Pennycook. Incoherent imaging using dynamically scattered coherent electrons. *Ultramicroscopy*, 78:111, 1999.

[92] J. S. Reid. Debye- Waller factors of zinc- blende structure materials- a lattice dynamical comparison. *Acta Crystallographica Section A*, A39:1 – 13, 1983.

[93] T. Malis, S. C. Cheng, and R. F. Egerton. EELS log-ratio technique for specimen thickness in the TEM. *Journal of Electron Microscopy*, 8:193, 1988.

[94] P. D. Robb and A. J. Craven. Column ratio mapping: a processing technique for atomic resolution high angle annular dark field (HAADF) images. *Ultramicroscopy*, 2008.

[95] H. Sakaki and M. T. Yoshino. High resolution TEM of AlAs-GaAs semiconductor superlattices. *ibid.*, 24:417, 1985.

[96] T. Sakamoto, H. Eunabashi, K. Ohta, T. Nakagawa, N. J. Kawai, and T. Kojima. RHEED intensity oscillations in the growth of Ag/Fe/Au. *Jpn. J. Appl. Phys.*, 23:657, 1984.

[97] T. Fukunaga, K. L. I. Kobayashi, and H. Nakashima. High resolution TEM of AlAs-GaAs semiconductor superlattices. *ibid.*, 24:510, 1985.

[98] B. A. Joyce, P. J. Dobson, J. H. Neave, and J. Zhang. Statistical treatment of dynamical electron diffraction from growing surfaces. *Surf. Sci.*, 1:174, 1986.

[99] P. R. Pukite, G. S. Petrich, S. Batra, and P. I. Cohen. A reflection high-energy electron diffraction study of growth processes at step edges during molecular beam epitaxy of GaAs and AlAs. *J. Cryst. Growth*, 95:95, 1989.

[100] L. Goldstein, Y. Horikoshi, S. Tarucha, and H. Okamoto. Interface disorder in GaAs/AlGaAs quantum wells grown by MBE. *Jpn. J. Appl. Phys.*, 22:1489, 1983.

[101] M. Tanaka and H. Sakaki. Effects of growth interruption on structure of MBE grown GaAs/AlAs interfaces. *J. Cryst. Growth*, 81:153, 1987.

[102] N. Ikarashi and K. Ishida. High-resolution transmission electron microscopy of AIAs-GaAs semiconductor superlattices. *J. Mater. Sci. - Mater. Electron.*, 7(295):285, 1996.

[103] J. M. Moison, C. Guille, F. Houzay, F. Berthe, and M. Van Rompay. Surface segregation of third-column atoms in group III-V arsenide compounds. *Physical Review B*, 40(9), 1989.

[104] G. A. Chadwick and D. A. Smith. *Grain Boundary Structure and Properties.* Academic, London, 1975.

[105] J. Benard. *Adsorption on Metal Surfaces.* Elsevier, New York, 1983.

[106] Z. Yu, D. A. Muller, and J. Silcox. *J. Appl. Phys.*, 95:3362, 2004.

[107] P. M. Voyles, D. A. Muller, J. L. Grazul, P. H. Citrin, and H. J. L. Gossmann. Atomic-scale imaging of individual dopant atoms and clusters in highly n-type bulk Si. *Nature*, 416:826, 2002.

[108] A. Singhal, J. C. Yang, and J. M. Gibson. Atomic-scale imaging of individual dopant atoms and clusters in highly n-type bulk Si. *Ultramicroscopy*, 67:191, 1997.

[109] P.D.Nellist, G.Behan, A.I.Kirkland, and C.J.D.Hetherington. Confocal operation of a transmission electron microscope with two aberration correctors. *Applied Physics Letters*, 89, 2006.

[110] P.D.Nellist, G.Behan, A.I.Kirkland, and C.J.D.Hetherington. Imaging modes for scanning confocal electron microscopy in a double aberration corrected TEM. *Microscopy and Microanalysis*, 14:82–88, 2008.

[111] P. Wang, A. L. Bleloch, M. Falke, and P. J. Goodhew. Direct measurement of composition of buried quantum dots using aberration-corrected scanning transmission electron microscopy. *Appl. Phys. Lett.*, 89, 2006.

[112] A. Y. Borisevich, A. R. Lupini, S. Travaglini, and S. J. Pennycook. Depth sectioning of aligned crystals with the aberration-corrected scanning transmission electron microscope. *J. Electron Microsc.*, 55(1):7 – 12, 2006.

Index

Z^2 Approximation, 66

Aberrations, 25
AlAs Projection, 136, 170, 245
AlAs Single Crystal, 66
Analytical Function Fitting, 108
Anisotropic Vibration, 93, 247
Atomeye, 56
Atomic Column Scattering, 203

Background Signal Analysis, 117
Background subtracted HAADF signal, 69
Balancing Aberrations, 28
Bash, 51
Beam Damage, 20
Beam Specimen Interaction, 14
Bragg Condition, 78
Bragg Scattering, 18

CBED, 33, 74
Characteristic Repeat Length, 136
Characteristic Step Length, 136
Coherent scattering, 19
Column Ratio, 65, 66, 70
Column Ratio Mapping, 96
Column Ratio Threshold, 107
Contrast Transfer Function, 28
Convergent Beam Electron Diffraction, 33
Cross Sectioning Method, 39

Debye Phonon Model, 47
Debye Waller Factor, 19, 46, 73, 74
Deep Superlattice, 113
DeviationParameter, 79
Device Growth, 2
Diffused Interface, 125, 157
Displacement Energy, 21

EELS, 36, 46, 49, 62, 66, 210, 248
Einstein Phonon Model, 47
Elastic Scattering, 15
Electron Intensity Distribution, 45
Electron Lenses, 24
Electron Microscopy, 8, 22
Electron Re-scattering, 216
Electron Sources, 22
Error Function, 109

Field Effect Transistor, 3
Field-Emission Sources, 23
First Order Laue Zone, 74
Frequency Filter Background Removal, 98
Frozen Phonon Method, 46, 73
Future Work, 247

GaAs, 75
GaAs - AlAs Interface, 95, 123
GaAs Projection, 144, 179, 244
GaAs Single Crystal, 60
Gatan Dimple Grinder, 40
Gatan ENFINA Spectrometer, 35

Gatan Image Filter, 31, 74
Gatan Precision Ion Polishing System, 40
GRID, 51, 244

HAADF, 16, 36, 42, 45, 46, 49, 63, 66, 85, 96
High-k, 6
Higher Order Aberrations, 27
HRTEM, 126

Inelastic Scattering, 18
Information Limit, 29
Intensity Map, 213, 229
Interface Proximity, 132
Interface Width Measurement, 105
Interfacial Roughness, 8

Kikuchi bands, 73

Laue Equation, 17
Linear Diffusion Model, 157
Linear Interpolation, 101
Local Roughness, 112

Matlab, 51, 54, 109, 125
MaximumTransferEnergy, 21
MBE Growth, 95
Mean Free Path, 36, 78, 81, 82, 243
mean square Displacement, 84
MODFET, 6
MOSFET, 3
Multislice, 48
Multislice Simulation, 42

Optical Transfer Function, 29

Perfect Interface, 124, 127
Phonon, 18, 46, 73
Plasmon, 18
Positional Mask Background Removal, 99
Probe Wavefunction, 44, 48, 56

Quantitative HAADF Imaging, 236

Random Step Vicinal Interface, 184
Rayleigh Criterion, 26
RHEED, 123

Sample C102, 110, 124
Sample Preparation, 39
Sawtooth Interface, 124, 134
Scattering Cross Section, 15
Scherzer, 25, 29
Scherzer Defocus, 28
ScotGrid, 53
ScreeningParameter, 16
Segregation Model, 162
Semiconductor, 1
Semiconductor Device Development, 1
Simple Vicinal Interface, 169
Single Electron Scattering, 20
Specimen Thickness Measurement, 76
Spherical Aberration, 25
SuperSTEM, 9, 30, 37, 58, 90, 95, 110, 241
Surface Segregation Model, 124

Technoorg Linda Gentle Mill, 40
Tecnai T20, 31, 56, 74, 89
Tecnai TF20, 34
Thermal Diffuse Scattering, 46, 73, 242
Thermionic Sources, 23
Thesis Outline, 11

TransferEnergy, 21

Transmission Function, 43

Two-Beam Condition, 34, 78

Type-3, 61

Type-5, 61

Type-A Interface, 110, 124, 162, 243

Type-G Interface, 110, 124, 163, 243

Vicinal Interface, 125

X-ray Emission, 20

Appendix A: Modified C Source

This appendix contains the main modified C-source files that were developed throught this project (both of these programs were originally written by E. J. Kirkland). The first program is the modified probe generating software that has been updated to include higher order aberrations up to and including fifth order. The code is written specifically to generate a SuperSTEM 24mrad probe and begins on page 263 below. The next modified program is the multislice code which was changed to integrate the intensity around the atomic columns, calculated the HAADF signal and the intensity around the primary probe position and the modified program begins on page 267 below. The modified source code calls subroutines from slicelib.c, tiffsubs.c, memory.c and fft2dc.c which are available on the supplimental disk supplied with "Advanced computing in electron microscopy" [72].

Modified Probe Code

This modified version of the probe code requires user input and requests the dumbbell number (i.e. 1-16) and the dumbbell position (i.e Column3, Column5 or BD). This is for the naming of the output file only and the probe position in Ångströms is also required. The script then generates a probe wavefunction for a 24mrad SuperSTEM 1 probe. The image size, sampling and parameters are scaled to work with the multislice code (autoslic_interface.c) detailed below.

```
1  /*  ***  probe.c  ***
2
3  /*------------ Modified Code: M.P. Finnie ------------------*/
4  This is the final working copy of the probe code that includes
      higher order aberrations up to fifth order.  The code is written
        to generate a SuperSTEM 24mrad probe.
5
6
7
8  /*------------ Original Code: E.J.Kirkland ------------------*/
9
10 ANSI-C version
11 Calculate a focused probe wavefunction in real space
```

```
12 this file is formatted for a tab size of 8 characters
13 rewritten in C 6-dec-1995 ejk fixed sign error in aberration
      function 1-mar-1997 ejk removed commas from keyboard input 3-oct
      -1997 ejk */
14
15
16 /*-------------------- Include Files ------------------------*/
17 #include <stdio.h> /* ANSI-C libraries */ #include <stdlib.h> #
      include <string.h> #include <math.h> #include <time.h> #include
      <complex.h>
18 #include "fft2dc.h" /* FFT's */ #include "memory.h" /* memory
      allocation routines */ #include "slicelib.h" /* define parameter
      offsets */ #include "tiffsubs.h" /* file I/O libraries */
19 #define NCMAX 132 /* characters per line to read featom.tab */ #
      define NPARAM 64 /* number of parameters */
20
21 /*---------------------- Parameters --------------------------*/
22 void main() { char fileout[NCMAX]; char pixkthetaout[NCMAX]; char
      pixkphiout[NCMAX]; char testimageout[NCMAX]; int ix, iy, nx, ny,
      ixmid, iymid, i, ismoth; float rmin, rmax, aimin, aimax; float
      *param, **pixr, **pixi;
23 double kx, ky, ky2, k2, k2max, v0, wavlen, ax, by, rx2, ry2, pi, dx
      , dy, scale, pixel, Cs, df, chi1, chi2, sum, chi, time, qmax;
      double tiltKx, tiltKy, alpha;
24 float c2, a22, phi22, a31, phi31, a33, phi33, c4, a42, phi42, a44,
      phi44, a51, phi51, a53, phi53, a55, phi55, c6, a62, phi62, a64,
      phi64, a66, phi66;
25 float c1, c12a, c12b, c21a, c21b, c23a, c23b, c3, c32a, c32b, c34a,
      c34b, c41a, c41b, c43a, c43b, c45a, c45b, c5, c52a, c52b, c54a,
      c54b, c56a, c56b;
26 float kphi, ktheta, ktm; /* Echo version date */
27 printf( "c-probe version dated 3-oct-1997 ejk\n\nTo create a
      SuperSTEM Probe 24 mrad with Batson Conditions\n\n");
28
29 /*------------------- Input Parameters ----------------------*/
30 /* printf("Name of file to get focussed probe wavefunction:\n");
      scanf("%s", fileout ); */
31 strcpy(fileout,"Super_STEM_Probe_24_mrad.tif");
32 /* printf("Desired size of output image in pixels Nx,Ny:\n"); scanf
      ("%d %d", &nx, &ny ); */
33 nx=1024; ny=1024;
34 if( (nx != powerof2(nx)) || (ny != powerof2(ny)) ) { printf("Nx=%d,
      Ny=%d must be a power of 2,\n" "try again.\n", nx, ny); exit( 0
      ); }
35 printf("Size of output image in Angstroms ax,by:\n"); scanf("%lf %
      lf", &ax, &by );
36 /* ax=54.6700; by=54.6700; */
37 /* printf("Beam voltage in kilovolts:\n"); scanf("%lf", &v0 ); */
38 v0=100;
39 /* printf("Spherical aberration in mm.:\n"); scanf("%lf", &Cs ); Cs
      = Cs * 1.0e7;
40 */ printf("Defocus in Angstroms (8.4 - df) :\n"); scanf("%lf", &df
```

```
        ); /* printf("Aperture in mrad:\n"); scanf("%lf", &k2max ); */
41  k2max=24.00;
42  k2max = k2max * 0.001; alpha=k2max; /* printf("Type 1 for smooth
        aperture:\n"); scanf("%d", &ismoth );
43  */
44  ismoth=0;
45  printf("Probe position in Angstroms:\n"); scanf("%lf %lf", &dx, &dy
        );
46
47  /*--------------------- Coefficients ----------------------------*/
48  c1= 8.4-df; c12a= 3.7; c12b= 0.5; c21a= 308; c21b= -3736; c23a=
        -483; c23b= -973; c3= -199448; c32a= -66272; c32b= -8710; c34a=
        -65613; c34b= 69533; c41a= -1007440; c41b= 12199870; c43a=
        1576470; c43b= 3177760; c45a= 232570; c45b= 145810; c5=
        440365700; c52a= 140835390; c52b= 18510170; c54a= 186631310;
        c54b= -197781720; c56a= -5748520; c56b= 47644720;
49  c2=c1; a22= sqrt(c12a*c12a+c12b*c12b); phi22= atan2(c12b,c12a); a31
        = sqrt(c21a*c21a+c21b*c21b); phi31= atan2(c21b,c21a); a33= sqrt(
        c23a*c23a+c23b*c23b); phi33= atan2(c23b,c23a); c4=c3; a42= sqrt(
        c32a*c32a+c32b*c32b); phi42= atan2(c32b,c32a); a44= sqrt(c34a*
        c34a+c34b*c34b); phi44= atan2(c34b,c34a); a51= sqrt(c41a*c41a+
        c41b*c41b); phi51= atan2(c41b,c41a); a53= sqrt(c43a*c43a+c43b*
        c43b); phi53= atan2(c43b,c43a); a55= sqrt(c45a*c45a+c45b*c45b);
        phi55= atan2(c45b,c45a); c6=c5; a62= sqrt(c52a*c52a+c52b*c52b);
        phi62= atan2(c52b,c52a); a64= sqrt(c54a*c54a+c54b*c54b); phi64=
        atan2(c54b,c54a); a66= sqrt(c56a*c56a+c56b*c56b); phi66= atan2(
        c56b,c56a);
50  printf("c(2)= 8.4; : %f\n", c1); printf("a(2,2)= 3.733630941; : %f\
        n", a22); printf("phi(2,2)= 0.134321442; : %f\n", phi22); printf
        ("a(3,1)= 3748.674432; : %f\n", a31); printf("phi(3,1)=
        -1.488541227; : %f\n", phi31); printf("a(3,3)= 1086.286334; : %f
        \n", a33); printf("phi(3,3)= -2.031562099; : %f\n", phi33);
        printf("c(4)= -199448; : %f\n", c4); printf("a(4,2)=
        66841.91861; : %f\n", c2); printf("phi(4,2)= -3.010913586; : %f\
        n", phi42); printf("a(4,4)= 95602.8444; : %f\n", a44); printf("
        phi(4,4)= 2.327196953; : %f\n", phi44); printf("a(5,1)=
        12241395.48; : %f\n", a51); printf("phi(5,1)= 1.653187317; : %f\
        n", phi51); printf("a(5,3)= 3547311.134; : %f\n", a53); printf("
        phi(5,3)= 1.110277809; : %f\n", phi53); printf("a(5,5)=
        274498.3807; : %f\n", a55); printf("phi(5,5)= 0.56000107; : %f\n
        ", phi55); printf("c(6)= 440365700; : %f\n", c6); printf("a(6,2)
        = 142046589.1; : %f\n", a62); printf("phi(6,2)= 0.1306822; : %f\
        n", phi62); printf("a(6,4)= 271935386.9; : %f\n", a64); printf("
        phi(6,4)= -0.814396359; : %f\n", phi64); printf("a(6,6)=
        47990257.62; : %f\n", a66); printf("phi(6,6)= 1.690869794; :
        %15.12f\n", phi66);
51
52
53  /*-------------- Calculate misc constants --------------------*/
54  time = cputim( ); pi = 4.0 * atan( 1.0 );
55  rx2 = 1.0/ax; rx2 = rx2 * rx2; ry2 = 1.0/by; ry2 = ry2 * ry2; ixmid
        = nx/2; iymid = ny/2; wavlen = 12.26/ sqrt( v0*1.e3 + v0*v0
```

```
    *0.9788 ); chi1 = pi*wavlen; chi2 = 0.5 * Cs * wavlen*wavlen;
    k2max = k2max/wavlen; k2max = k2max * k2max;
56 param = float1D( NPARAM, "probe-param" ); for( i=0; i<NPARAM; i++)
    param[i] = 0.0F; pixr = float2D( 2*nx, ny, "pixr" ); pixi = pixr
     + nx;
57 /* Calculate MTF NOTE zero freg is in the bottom left corner and
    expandes into all other corners - not in the center this is
    required for FFT
58 PIXEL = diagonal width of pixel squared if a pixel is on the
    apertur boundary give it a weight of 1/2 otherwise 1 or 0 */
    pixel = ( rx2 + ry2 );
59 qmax = sin(alpha)/wavlen;
60 printf("qmax: %f\n", qmax);
61 for( iy=0; iy<ny; iy++) { ky = (double) iy; if( iy > iymid ) ky = (
    double) (iy-ny); ky2 = ky*ky*ry2; for( ix=0; ix<nx; ix++) { kx =
     (double) ix; if( ix > ixmid ) kx = (double) (ix-nx); k2 = kx*kx
    *rx2 + ky2;
62
63 /*---------- Calculate Aberration Function ------------------*/
64 if ( k2 <= k2max ) {
65 ktheta = casinf(sqrt(k2)*wavlen); kphi = atan2(ky,kx);
66 chi=2*pi/wavlen*(0.5*(a22*cos(2*(kphi-phi22))+c2)*ktheta*ktheta
    +(0.3333)*(a33*cos(3*(kphi-phi33))+a31*cos(1*(kphi-phi31)))*
    ktheta*ktheta*ktheta+(0.25)*(a44*cos(4*(kphi-phi44))+a42*cos(2*(
    kphi-phi42))+c4)*ktheta*ktheta*ktheta*ktheta+(0.2)*(a55*cos(5*(
    kphi-phi55))+a53*cos(3*(kphi-phi53))+a51*cos(1*(kphi-phi51)))*
    ktheta*ktheta*ktheta*ktheta*ktheta+(0.166667)*(a66*cos(6*(kphi-
    phi66))+a64*cos(4*(kphi-phi64))+a62*cos(2*(kphi-phi62))+c6)*
    ktheta*ktheta*ktheta*ktheta*ktheta*ktheta) - 2.0F*pi*( (dx*kx/ax
    ) + (dy*ky/by) );
67 /* chi= chi1*k2* (chi2*k2-df) - 2.0F*pi*( (dx*kx/ax) + (dy*ky/by) )
    ;
68 */ pixr[ix][iy]= (float) cos(chi); pixi[ix][iy]= (float) -sin(chi);
69 } else {
70 pixr[ix][iy] = pixi[ix][iy] = 0.0F;
71 } } }
72 fft2d( pixr, pixi, nx, ny, -1);
73
74
75 /*------- Normalize probe intensity to unity ---------------*/
76 sum = 0.0; for( ix=0; ix<nx; ix++) for( iy=0; iy<ny; iy++) sum +=
    pixr[ix][iy]*pixr[ix][iy] + pixi[ix][iy]*pixi[ix][iy];
77 scale = 1.0 / sum; scale = scale * ((double)nx) * ((double)ny);
    scale = (double) sqrt( scale );
78 for( ix=0; ix<nx; ix++) for( iy=0; iy<ny; iy++) { pixr[ix][iy] *= (
    float) scale; pixi[ix][iy] *= (float) scale; }
79
80 /*----------------- Output Files ---------------------*/
81 /* Output results and find min and max to echo remember that
    complex pix are stored in the file in FORTRAN order for
    compatability */
82 rmin = pixr[0][0]; rmax = rmin; aimin = pixi[0][0]; aimax = aimin;
```

Line of input text:	Required for:
Phonon_50_Column5_16	Append output filename with this string
xyz_file.xyz	input xyz structure filename
14	replicate structure in x
1	replicate structure in y
1	replicate structure in z
output.tif	output wavefunction name (not used in current version)
n	partial coherence y/n?
y	start from a previous result?
d:/sims/GaAs/Input_Files/Probes... .../Interface_16_Column5.tif	path and filename of starting wavefunction
0	tilt in x
0	tilt in y
1.99875	slice thickness
n	include real space intensity y/n?
y	include phonons y/n?
300	temperature (in Kelvin)
y	output intensity integration y/n?
0.25	size of integration site around atom positions in Å
y	output HAADF data y/n?

Figure 8.1 – Input Parameters for autoslic_interface.c

```
    for( iy=0; iy<ny; iy++) { for( ix=0; ix<nx; ix++) { if( pixr[ix
    ][iy] < rmin ) rmin = pixr[ix][iy]; if( pixr[ix][iy] > rmax )
    rmax = pixr[ix][iy]; if( pixi[ix][iy] < aimin ) aimin = pixi[ix
    ][iy]; if( pixi[ix][iy] > aimax ) aimax = pixi[ix][iy]; } }
83 param[pRMAX] = rmax; param[pIMAX] = aimax; param[pRMIN] = rmin;
    param[pIMIN] = aimin; param[pDEFOCUS]= (float) df; param[pDX]= (
    float) (ax / nx); param[pDY]= (float) (by / ny); param[pENERGY]=
     (float) v0; param[pWAVEL]= (float) ( sqrt(k2max) * wavlen);
    param[pCS]= (float) Cs; param[27]= (float) dx; param[28]= (float
    ) dy;
84 if( tcreateFloatPixFile( fileout, pixr, (long) (2*nx), (long) ny,
    2, param ) != 1 );
85 printf( "Pix range %15.7g to %15.7g real,\n" " and %15.7g to %15.7g
     imaginary\n", rmin, rmax, aimin, aimax ); time = cputim() -
    time; printf("\nCPU time = %f sec\n", time );
86 } /* end main() */
```

Modified Multislice Code

The modified multislice code below requires user input detailed in table 8.1:

```
1  /* *** autoslic_interface.c ***
2  /*----------- Modified Code: M.P. Finnie ----------------*/
3  This is the final working copy integrating CBED intensity on the
       HAADF detector, can use different sizes for ax and by Integrates
        the intensity around each atom site (follows wobble of atoms)
       for a given radial integration distance Integrates down the
       probe position, reading in the probe position co-ordinates from
       the probe image file Writes all the above to text files, doesn't
       output any images. All the above are written as functions....
4
5  /*----------- Original Code: E.J.Kirkland ----------------*/
6
7
8  ANSI C and TIFF version
9  Transmit an electron wave through a specimen using the multislce
       method with automatic slicing. Read in the (x,y,z) coordinates
       of the whole specimen and break into slices on-the-fly.
10 started 24-july-1996 E. Kirkland working 19feb-1997 ejk last
       revised 19-feb-1997 ejk added look-up-table vzatomLUT() for 3X-4
       X increase in speed 23-may-1997 ejk put bandwith limit inside
       trlayer() 1-oct-1997 ejk added Gaussian thermal displacements 1-
       oct-1997 ejk removed /sqrt(3) from Thermal rms displacements to
       be consistent with Int'l X-ray tables 22-dec-1997 ejk corrected
       zmin/max error with thermal displac. 24-dec-1997 ejk fixed small
        aliasing problem 5-jan-1998 ejk added unit cell replication
       option and moved ReadXYZcoord() into slicelib.c 11-jan-1998 ejk
       added astigmatism and modify to use different set of random
       offsets on each illum. angle with partial coherence 5-feb-1998
       ejk fix typo in z range message with partial coherence and
       thermal vibrations 9-july-1998 ejk
11 ax,by,cz = unit cell size in x,y BW = Antialiasing bandwidth limit
       factor acmin = minimum illumination angle acmax = maximum
       illumination angle Cs = spherical aberration coeficient df0 =
       defocus (mean value) sgmaf = defocus spread (standard deviation)
        dfdelt = sampling interval for defocus integration this file is
        formatted for a TAB size of 8 characters */
12
13 /*---------------- Include Section ---------------------*/
14 #include <stdio.h> /* ANSI C libraries */ #include <stdlib.h> #
       include <string.h> #include <math.h> #include <time.h>
15 #include "fft2dc.h" /* FFT routines */ #include "memory.h" /*
       memory allocation routines */ #include "slicelib.h" /* misc.
       routines for multislice */ #include "tiffsubs.h" /* file I/O
       routines in TIFF format */
16 #define BW (2.0F/3.0F) /* bandwidth limit */ #define ABERR 1.0e-4
       /* max error for a,b */
17 #define NSMAX 1000 /* max number of slices */ #define NPARAM 64 /*
       number of parameters */
18 #define NCMAX 256 /* max characters in file names */
19 #define NZMAX 103 /* max atomic number Z */ #define NRMAX 100 /*
       number of in look-up-table in vzatomLUT */ #define RMIN 0.01 /*
       r (in Ang) range of LUT for vzatomLUT() */ #define RMAX 5.0
```

```
20 /* spline interpolation coeff. */ int splineInit=0, *nspline;
     double *splinx, **spliny, **splinb, **splinc, **splind;
21 /* define functions at end of this file (i.e. so main can be 1st)
     */
22 void trlayer( const float x[], const float y[], const float occ[],
     const int Znum[], const int natom, const float ax, const float
     by, const float kev, float **transr, float **transi, const long
     nx, const long ny, double *phirms, long *nbeams, const float
     k2max ); double vzatomLUT( int Z, double r ); void sortByZ(
     float x[], float y[], float z[], float occ[], int Znum[], int
     natom );
23
24 /*---------- Define new HAADF Function here ------------*/
25 int detect_inner=70, detect_outer=210;
26 double HAADF_create(float** HAADF_create_mask,const int nx, const
     int ny, const float ax, const float by, const float wavlen,
     const int detect_inner, const int detect_outer);
27 double HAADF_integrate(float** HAADF_create_mask, float** waver,
     float** wavei, const int nx, const int ny, float**
     HAADF_cbed_waver , float** HAADF_cbed_wavei);
28
29 /*-------- Define new Intensity Function here ----------*/
30 void Intensity_mask_create( const float x[], const float y[], const
      float occ[], int Znum[], const int natom, const float ax, const
      float by, const float kev, float **As_mask, float **Ga_mask,
     float **Al_mask, float **ProbePosition_mask, const long nx,
     const long ny, double *phirms, long *nbeams, const float k2max,
     const float integrate_radius, const float ProbePosition_x, const
      float ProbePosition_y);
31 double Intensity_mask_apply(float **Species_mask, float** waver,
     float** wavei, const int nx, const int ny );
32
33 /*----------- global data for trlayer() -------------*/
34 float *kx2, *ky2;
35 FILE *HAADF_file, *INTENSITY_file, *EELS_file;
36 int main() { char filein[NCMAX], fileout[NCMAX], filestart[NCMAX],
     filebeam[NCMAX], datetime[20], description[NCMAX];
37 int lstart=0, lpartl=0, lbeams=0, lwobble=0; int ix, iy, nx, ny,
     ixmid, iymid, i, nslic0, islice, nacx,nacy, iqx, iqy, npix, ndf,
      idf, nbout, ib, nbits[3], samples, ncellx, ncelly, ncellz; int
     *hbeam, *kbeam; int natom, *Znum, *Znum2, istart, na; long nxl,
     nyl, nbeams, nillum; long ltime; unsigned long iseed;
38 float *x, *y, *z, *occ, *wobble; float *x2, *y2, *z2, *occ2; float
     wmin, wmax, xmin,xmax, ymin, ymax, zmin, zmax, cbed_sum;
39 float *kx, *ky, *xpos, *ypos, *param, *sparam; float k2, k2max,
     scale, v0, mm0, wavlen, rx, ry, ax, by, cz, pi, rmin, rmax,
     aimin, aimax, rx2,ry2, ctiltx, ctilty, tctx, tcty, acmin, acmax,
      Cs, df, df0, sigmaf, dfdelt, aobj, qx, qy, qy2, q2, q2min,
     q2max, sumdf, pdf, k2maxo, temperature, dfa2, dfa2phi, dfa3,
     dfa3phi;
40 float tr, ti, wr, wi;
41 float **waver, **wavei, **transr, **transi, *propxr, *propxi, *
```

```
    propyr, *propyi, **tempr, **tempi, **pix, **HAADF_create_mask,
    **HAADF_cbed_wavei, **HAADF_cbed_waver;
42  double sum, timer, xdf, chi, chi1, chi2, phi, t, zslice, deltaz,
    phirms;
43  float HAADF_data_yn;
44  float integrate_intensity_yn, **As_mask, **Ga_mask, **Al_mask, **
    ProbePosition_mask, integrate_radius; float As_intensity,
    Ga_intensity, Al_intensity, ProbePosition_x, ProbePosition_y,
    ProbePosition_intensity;
45  FILE *fp1;
46
47
48  /*----- echo version date and get input file name -------*/
49  printf("autoslic(e)␣version␣dated␣9-Jul-1998␣ejk\n␣modified␣2009␣
    mpf␣\n\n"); pi = (float) (4.0 * atan( 1.0 )); param = float1D(
    NPARAM, "param" ); sparam = float1D( NPARAM, "sparam" );
50  printf("Name␣of␣file␣with␣input␣atomic␣" "potential␣in␣x,y,z␣format
    :\n"); scanf("%s", filein );
51
52  /*--------------- get simulation options ---------------*/
53  printf("Replicate␣unit␣cell␣by␣NCELLX,NCELLY,NCELLZ␣:\n"); scanf("%
    d␣%d␣%d", &ncellx, &ncelly, &ncellz); if( ncellx < 1 ) ncellx =
    1; if( ncelly < 1 ) ncelly = 1; if( ncellz < 1 ) ncellz = 1;
54  printf("Name␣of␣file␣to␣get␣binary␣output␣of␣multislice␣result:\n")
    ; scanf("%s", fileout );
55  lpartl = askYN("Do␣you␣want␣to␣include␣partial␣coherence");
56  if( lpartl == 1 ) { printf("Illumination␣angle␣min,␣max␣in␣mrad:\n"
    ); scanf("%f␣%f", &acmin, &acmax); acmin = acmin * 0.001F; acmax
     = acmax * 0.001F; printf("Spherical␣aberration␣(in␣mm.):\n");
    scanf("%g", &Cs); Cs = Cs * 1.0e7F; printf("Defocus,␣mean,␣
    standard␣deviation,␣and" "␣sampling␣size␣(in␣Angstroms)␣=\n");
    scanf("%f␣%f␣%f", &df0, &sigmaf, &dfdelt); printf("Objective␣
    aperture␣(in␣mrad)␣=\n"); scanf("%f", &aobj); aobj = aobj *
    0.001F; printf( "Magnitude␣and␣angle␣of␣2-fold␣astigmatism" "␣(
    in␣Ang.␣and␣degrees):\n"); scanf( "%f␣%f", &dfa2, &dfa2phi);
    dfa2phi = dfa2phi * pi /180.0F; printf( "Magnitude␣and␣angle␣of␣
    3-fold␣astigmatism" "␣(in␣Ang.␣and␣degrees):\n"); scanf( "%f␣%f"
    , &dfa3, &dfa3phi); dfa3phi = dfa3phi * pi /180.0F; lstart = 0;
    } else { printf("NOTE,␣the␣program␣image␣must␣also␣be␣run.\n");
    lstart = askYN("Do␣you␣want␣to␣start␣from␣previous␣result"); }
57  if ( lstart == 1 ) { printf("Name␣of␣file␣to␣start␣from:\n"); scanf
    ("%s", filestart); } else { printf("Incident␣beam␣energy␣in␣kev
    :\n"); scanf("%g", &v0); printf("Wavefunction␣size␣in␣pixels,␣Nx
    ,Ny:\n"); scanf("%d␣%d", &nx, &ny ); }
58  printf("Crystal␣tilt␣x,y␣in␣mrad.:\n"); scanf("%f␣%f", &ctiltx, &
    ctilty); ctiltx = ctiltx /1000; ctilty = ctilty /1000;
59  /* remember that the slice thickness must be > atom size to use
    projected atomic potential */ printf("Slice␣thickness␣(in␣
    Angstroms):\n"); scanf("%lf", &deltaz ); if( deltaz < 1.0 ) {
    printf("WARNING:␣this␣slice␣thickness␣is␣probably␣too␣thin" "␣
    for␣autoslice␣to␣work␣properly.\n"); }
60  if( lpartl == 0 ) { lbeams = askYN("Do␣you␣want␣to␣record␣the␣(real
```

```
    ,imag) value\n" " of selected beams vs. thickness"); if( lbeams
    == 1 ) { printf("Name of file for beams info:\n"); scanf("%s",
    filebeam ); printf("Number of beams:\n"); scanf("%d", &nbout);
    if( nbout<1 ) nbout = 1; hbeam = int1D( nbout, "hbeam" ); kbeam
    = int1D( nbout, "kbeam" ); for( ib=0; ib<nbout; ib++) { printf("
    Beam %d, h,k=\n", ib+1); scanf("%d %d", &hbeam[ib], &kbeam[ib] )
    ; } } }
61 lwobble = askYN("Do you want to include thermal vibrations"); if(
    lwobble == 1 ) { printf( "Type the temperature in degrees K:\n")
    ; scanf( "%g", &temperature ); /* get random number seed from
    time if available otherwise ask for a seed */ if( lwobble == 1 )
     { ltime = (long) time( NULL ); iseed = (unsigned) ltime; if(
    ltime == -1 ) { printf("Type initial seed for random number
    generator:\n"); scanf("%ld", &iseed); } else printf( "Random
    number seed initialized to %ld\n", iseed ); } } else temperature
     = 0.0F;
62 integrate_intensity_yn = askYN("Do you want to output EELS
    Intensity data?"); if( integrate_intensity_yn == 1 ) { printf("
    Radius in Angstroms for atom site integration: \n"); scanf("%f",
     &integrate_radius); }
63 HAADF_data_yn = askYN("Do you want to output HAADF data?");
64 /* start timing the actual computation just for fun */
65 timer = cputim();
66 /* get starting value of transmitted wavefunction if required (this
     can only be used in coherent mode) remember to save params for
    final output pix */
67 if ( lstart == 1 ) { if( topenFloat( filestart ) != 1 ) { printf("
    Cannot open input file: %s .\n", filestart ); exit( 0 ); } tsize
    ( &nxl, &nyl, nbits, &samples ); nx = (int) nxl; ny = (int) nyl;
68 waver = float2D( nx, ny, "waver" ); nx = nx/2; wavei = waver + nx;
    if( treadFloatPix( waver, nxl, nyl, &npix, datetime, sparam ) !=
     1 ) { printf("Cannot read input file %s.\n", filestart); exit
    (0); } tclose(); if( npix != 2 ) { printf("Input file %s must be
     complex, can't continue.\n", filestart ); exit( 0 ); } if( (nx
    != powerof2(nx)) || (ny != powerof2(ny)) ) { printf("Nx=%d, Ny=%
    d must be a power of 2\n" "problem in starting image, try again
    .\n", nx, ny); exit( 0 ); } ProbePosition_x=sparam[27];
    ProbePosition_y=sparam[28];
69 ProbePosition_x=ProbePosition_x+2*sparam[pDX]; ProbePosition_y=
    ProbePosition_y+6*sparam[pDY];
70 printf("Probe Position x=%g y=%g Angstroms\n", ProbePosition_x,
    ProbePosition_y); ax = sparam[pDX] * nx; by = sparam[pDY] * ny;
    v0 = sparam[pENERGY]; nslic0 = (int) sparam[pNSLICES]; printf("
    Starting pix range %g to %g real\n" " %g to %g imag\n", sparam[
    pRMIN], sparam[pRMAX], sparam[pIMIN], sparam[pIMAX] ); printf("
    Beam voltage = %g kV\n", v0); printf("Old crystal tilt x,y = %g,
     %g mrad\n", 1000.*sparam[pXCTILT], 1000.*sparam[pYCTILT]);
71 } else {
72 nslic0 = 0;
73 } /* end if( lstart...) */
74
75 /*- calculate relativistic factor and electron wavelength -*/
```

```
76 mm0 = 1.0F + v0/511.0F; wavlen = (float) wavelength( v0 ); printf("electron wavelength = %g Angstroms\n", wavlen);
77
78 /* read in specimen coordinates and scattering factors */
79 natom = ReadXYZcoord( filein, ncellx, ncelly, ncellz, &ax, &by, &cz, &Znum, &x, &y, &z, &occ, &wobble, description, NCMAX );
80 printf("%d atomic coordinates read in\n", natom ); printf("%s", description );
81 printf("Size in pixels Nx, Ny= %d x %d = %d beams\n", nx,ny, nx*ny); printf("Lattice constant a,b = %12.4f, %12.4f\n", ax,by);
82 /* calculate the total specimen volume and echo */ xmin = xmax = x[0]; ymin = ymax = y[0]; zmin = zmax = z[0]; wmin = wmax = wobble[0];
83 for( i=0; i<natom; i++) { if( x[i] < xmin ) xmin = x[i]; if( x[i] > xmax ) xmax = x[i]; if( y[i] < ymin ) ymin = y[i]; if( y[i] > ymax ) ymax = y[i]; if( z[i] < zmin ) zmin = z[i]; if( z[i] > zmax ) zmax = z[i]; if( wobble[i] < wmin ) wmin = wobble[i]; if( wobble[i] > wmax ) wmax = wobble[i]; } printf("Total specimen range is\n %g to %g in x\n" " %g to %g in y\n %g to %g in z\n", xmin, xmax, ymin, ymax, zmin, zmax ); if( lwobble == 1 ) printf("Range of thermal rms displacements (300K) = %g to %g\n", wmin, wmax );
84 /* calculate spatial frequencies and positions for future use */
85 rx = 1.0F/ax; rx2= rx*rx; ry = 1.0F/by; ry2= ry*ry; ixmid = nx/2; iymid = ny/2; nxl = nx; nyl = ny;
86 kx = float1D( nx, "kx" ); kx2 = float1D( nx, "kx2" ); xpos = float1D( nx, "xpos" ); freqn( kx, kx2, xpos, nx, ax );
87 ky = float1D( ny, "ky" ); ky2 = float1D( ny, "ky2" ); ypos = float1D( ny, "ypos" ); freqn( ky, ky2, ypos, ny, by );
88
89 /* allocate some more arrays and initialize wavefunction */
90 transr = float2D( nx, ny, "transr" ); transi = float2D( nx, ny, "transi" );
91 if( HAADF_data_yn == 1 ) { HAADF_create_mask = float2D( nx, ny, "HAADF_create_mask" ); HAADF_cbed_waver = float2D( nx, ny, "HAADF_cbed_waver" ); HAADF_cbed_wavei = float2D( nx, ny, "HAADF_cbed_wavei" ); }
92
93
94 /*------------- create intensity mask arrays -------------*/
95 if( integrate_intensity_yn == 1 ) {
96 As_mask = float2D( nx, ny, "As_mask" ); Ga_mask = float2D( nx, ny, "Ga_mask" ); Al_mask = float2D( nx, ny, "Al_mask" ); ProbePosition_mask = float2D( nx, ny, "ProbePosition_mask" );
97 }
98 if( lstart == 0 ) { waver = float2D( 2*nx, ny, "waver" ); wavei = waver + nx; for( ix=0; ix<nx; ix++) for( iy=0; iy<ny; iy++) { waver[ix][iy] = 1.0F; wavei[ix][iy] = 0.0F; } }
99
100 /*------------- calculate propagator function -------------*/
101 k2max = nx/(2.0F*ax); tctx = ny/(2.0F*by); if( tctx < k2max ) k2max = tctx; k2max = BW * k2max; printf("Bandwidth limited to a real
```

```
    ␣space␣resolution␣of␣%f␣Angstroms\n", 1.0F/k2max); printf("␣(=␣
    %.2f␣mrad)␣for␣symmetrical␣anti-aliasing.\n", wavlen*k2max
    *1000.0F); k2max = k2max*k2max;
102 tctx = (float) (2.0 * tan(ctiltx)); tcty = (float) (2.0 * tan(
    ctilty));
103 propxr = float1D( nx, "propxr" ); propxi = float1D( nx, "propxi" );
     propyr = float1D( ny, "propyr" ); propyi = float1D( ny, "propyi
    " );
104 scale = pi * ((float)deltaz);
105 for( ix=0; ix<nx; ix++) { t = scale * ( kx2[ix]*wavlen - kx[ix]*
    tctx ); propxr[ix] = (float) cos(t); propxi[ix] = (float) -sin(t
    ); } for( iy=0; iy<ny; iy++) { t = scale * ( ky2[iy]*wavlen - ky
    [iy]*tcty ); propyr[iy] = (float) cos(t); propyi[iy] = (float) -
    sin(t); }
106
107 /*------------ iterate the multislice algorithm ------------*/
108 /* iterate the multislice algorithm proper
109 NOTE: zero freg is in the bottom left corner and expandes into all
    other corners - not in the center this is required for the FFT -
     don't waste time rearanging
110 partial coherence method force the integrals to include the origin
    and to be symmetric about the origin and to have the same
    periodic boundary conditions as the sampling grid */ if( lpartl
    == 1 ) {
111 printf("Illumination␣angle␣sampling␣(in␣mrad)␣=␣%f,␣%f\n\n", 1000.*
    rx*wavlen, 1000.*ry*wavlen);
112 pix = float2D( nx, ny, "pix" ); for( ix=0; ix<nx; ix++) for( iy=0;
    iy<ny; iy++) pix[ix][iy] = 0.0F;
113 tempr = float2D( nx, ny, "tempr" ); tempi = float2D( nx, ny, "tempi
    " );
114 ndf = (int) ( ( 2.5F * sigmaf ) / dfdelt );
115 nacx = (int) ( ( acmax / ( wavlen * rx ) ) + 1.5F ); nacy = (int) (
     ( acmax / ( wavlen * ry ) ) + 1.5F );
116 q2max = acmax / wavlen; q2max = q2max*q2max;
117 q2min = acmin / wavlen; q2min = q2min*q2min;
118 k2maxo = aobj / wavlen; k2maxo = k2maxo*k2maxo;
119 chi1 = pi * wavlen; chi2 = 0.5 * Cs * wavlen *wavlen; nillum = 0;
120 x2 = float1D( natom, "x2" ); /* for Monte Carlo stuff */ y2 =
    float1D( natom, "y2" ); z2 = float1D( natom, "z2" ); occ2 =
    float1D( natom, "occ2" ); Znum2 = int1D( natom, "Znum2" );
121 if( lwobble == 0 ) sortByZ( x, y, z, occ, Znum, natom );
122
123
124 /*-------- integrate over the illumination angles ----------*/
125 for( iqy= -nacy; iqy<=nacy; iqy++) { qy = iqy * ry; qy2 = qy * qy;
126 for( iqx= -nacx; iqx<=nacx; iqx++) { qx = iqx * rx; q2 = qx*qx +
    qy2;
127 if( (q2 <= q2max) && (q2 >= q2min) ) { nillum += 1; for( ix=0; ix<
    nx; ix++) for( iy=0; iy<ny; iy++) { t = 2.0*pi*( qx*xpos[ix] +
    qy*ypos[iy] ); waver[ix][iy] = (float) cos(t); wavei[ix][iy] = (
    float) sin(t); } /* add random thermal displacements scaled by
    temperature if requested remember that initial wobble is at 300K
```

```
    for each direction */ if( lwobble == 1 ){ scale = (float) sqrt(
    temperature/300.0) ; for( i=0; i<natom; i++) { x2[i] = x[i] + (
    float)(wobble[i]*rangauss(&iseed)*scale); y2[i] = y[i] + (float)
    (wobble[i]*rangauss(&iseed)*scale); z2[i] = z[i] + (float)(
    wobble[i]*rangauss(&iseed)*scale); occ2[i] = occ[i]; Znum2[i] =
    Znum[i]; } printf( "Sorting atoms by depth...\n"); sortByZ( x2,
    y2, z2, occ2, Znum2, natom ); zmin = z2[0]; /* reset zmin/max
    after wobble */ zmax = z2[natom-1]; printf("Thickness range with
     thermal displacements" " is %g to %g (in z)\n", zmin, zmax ); }
     else for( i=0; i<natom; i++) { x2[i] = x[i]; y2[i] = y[i]; z2[i
    ] = z[i]; occ2[i] = occ[i]; Znum2[i] = Znum[i]; }
128 zslice = zmin + deltaz; istart = 0;
129 while( istart < natom ) {
130 /* find range of atoms for current slice */ na = 0; for(i=istart; i
    <natom; i++) if( z2[i] < zslice ) na++; else break;
131 
132 /*------------ calculate transmission function ---------------*/
133 trlayer( &x2[istart], &y2[istart], &occ2[istart], &Znum2[istart],na
    , ax, by, v0, transr, transi, nxl, nyl, &phirms, &nbeams, k2max
    );
134 transmit( waver, wavei, transr, transi, nx, ny );
135 /* remember: prop needed here to get anti-aliasing right */ fft2d(
    waver, wavei, nx, ny, +1); propagate( waver, wavei, propxr,
    propxi, propyr, propyi, kx2, ky2, k2max, nx, ny ); fft2d( waver,
     wavei, nx, ny, -1);
136 zslice += deltaz; istart += na;
137 } /* end while(zslice<=..) */
138 scale = 1.0F / ( ((float)nx) * ((float)ny) ); sum = 0.0; for( ix=0;
     ix<nx; ix++) for( iy=0; iy<ny; iy++) sum += waver[ix][iy]*waver
    [ix][iy] + wavei[ix][iy]*wavei[ix][iy]; sum = sum * scale;
139 printf("Illumination angle = %7.3f, %7.3f mrad", 1000.*qx*wavlen,
    1000.*qy*wavlen); printf(", integrated intensity= %f\n", sum );
140 /* integrate over +/- 2.5 sigma of defocus */
141 fft2d( waver, wavei, nx, ny, +1); sumdf = 0.0F;
142 for( idf= -ndf; idf<=ndf; idf++) { df = df0 + idf*dfdelt;
143 for( ix=0; ix<nx; ix++) for( iy=0; iy<ny; iy++) { k2 = kx2[ix] +
    ky2[iy]; if( k2 <= k2maxo ) { phi = atan2( ky[iy], kx[ix] ); chi
     = chi1*k2* ( chi2*k2 - df + dfa2*sin( 2.0*(phi-dfa2phi) ) + 2.0
    F*dfa3*wavlen*sqrt(k2)* sin( 3.0*(phi-dfa3phi) )/3.0 ); tr = (
    float) cos(chi); ti = (float) -sin(chi); wr = waver[ix][iy]; wi
    = wavei[ix][iy]; tempr[ix][iy] = wr*tr - wi*ti; tempi[ix][iy] =
    wr*ti + wi*tr; } else { tempr[ix][iy] = 0.0F; tempi[ix][iy] =
    0.0F; } }
144 fft2d( tempr, tempi, nx, ny, -1);
145 xdf = (double) ( (df - df0) /sigmaf ); pdf = (float) exp( -0.5F *
    xdf*xdf ); sumdf += pdf;
146 for( ix=0; ix<nx; ix++) for( iy=0; iy<ny; iy++) { wr = tempr[ix][iy
    ]; wi = tempi[ix][iy]; pix[ix][iy] += pdf* ( wr*wr + wi*wi ); }
147 }/* end for(idf..) */ }/* end if( q2...) */
148 } /* end for( iqx..) */ } /* end for( iqy..) */
149 printf("Total number of illumination angle = %ld\n", nillum);
    printf("Total number of defocus values = %d\n", 2*ndf+1); scale
```

```
    = 1.0F / ( ((float)nillum) * sumdf ); rmin = pix[0][0] * scale;
    rmax = rmin; aimin = 0.0F; aimax = 0.0F;
150 for( ix=0; ix<nx; ix++) for( iy=0; iy<ny; iy++) { pix[ix][iy] = pix
    [ix][iy] * scale; if( pix[ix][iy] < rmin ) rmin = pix[ix][iy];
    if( pix[ix][iy] > rmax ) rmax = pix[ix][iy]; }
151
152
153 /*------------ start coherent method ------------*/
154 } else {
155 if( lbeams ==1 ) { fp1 = fopen( filebeam, "w" ); if( fp1==NULL) {
    printf("can't open file %s\n", filebeam); exit(0); } fprintf(
    fp1, " (h,k) = ", nbout); for(ib=0; ib<nbout; ib++) fprintf(fp1,
    " (%d,%d)", hbeam[ib], kbeam[ib]); fprintf( fp1, "\n" ); fprintf
    ( fp1, "nslice, (real,imag) (real,imag) ...\n\n"); for( ib=0; ib
    <nbout; ib++) { if( hbeam[ib] < 0 ) hbeam[ib] = nx + hbeam[ib];
    if( kbeam[ib] < 0 ) kbeam[ib] = ny + kbeam[ib]; if( hbeam[ib] <
    0 ) hbeam[ib] = 0; if( kbeam[ib] < 0 ) kbeam[ib] = 0; if( hbeam[
    ib] > nx-1 ) hbeam[ib] = nx-1; if( kbeam[ib] > ny-1 ) kbeam[ib]
    = ny-1; } }
156 /* add random thermal displacements scaled by temperature if
    requested remember that initial wobble is at 300K for each
    direction */ if( lwobble == 1 ){ scale = (float) sqrt(
    temperature/300.0) ; for( i=0; i<natom; i++) { x[i] += (float) (
    wobble[i] * rangauss( &iseed ) * scale); y[i] += (float) (wobble
    [i] * rangauss( &iseed ) * scale); z[i] += (float) (wobble[i] *
    rangauss( &iseed ) * scale); } zmin = z[0]; /* reset zmin/max
    after wobble */ zmax = z[natom-1]; printf("Thickness range with
    thermal displacements" " is %g to %g (in z)\n", zmin, zmax ); }
157 printf( "Sorting atoms by depth...\n"); sortByZ( x, y, z, occ, Znum
    , natom );
158 scale = 1.0F / ( ((float)nx) * ((float)ny) );
159 zslice = zmin + deltaz/2; /* ??? */ /*??? zslice = zmin + deltaz;
    */ istart = 0; islice = 1;
160 while( (istart < natom) && ( zslice < (zmax+deltaz) ) ) {
161 /* find range of atoms for current slice */ na = 0; for(i=istart; i
    <natom; i++) if( z[i] < zslice ) na++; else break;
162 /* calculate transmission function and bandwidth limit */ trlayer(
    &x[istart], &y[istart], &occ[istart], &Znum[istart], na, ax, by,
     v0, transr, transi, nxl, nyl, &phirms, &nbeams, k2max );
163
164
165 /*------------ apply masks to wavefunction ------------*/
166 if( integrate_intensity_yn == 1 ) {
167 Intensity_mask_create( &x[istart], &y[istart], &occ[istart], &Znum[
    istart], na, ax, by, v0, As_mask, Ga_mask, Al_mask,
    ProbePosition_mask, nxl, nyl, &phirms, &nbeams, k2max ,
    integrate_radius, ProbePosition_x, ProbePosition_y);
168 As_intensity=Intensity_mask_apply(As_mask, waver, wavei, nx, ny);
    Ga_intensity=Intensity_mask_apply(Ga_mask, waver, wavei, nx, ny)
    ; Al_intensity=Intensity_mask_apply(Al_mask, waver, wavei, nx,
    ny); ProbePosition_intensity=Intensity_mask_apply(
    ProbePosition_mask, waver, wavei, nx, ny);
```

```
169 EELS_file=fopen("EELS_data.txt","a"); fprintf(EELS_file,"%f %f %f\n
       ",As_intensity, Ga_intensity, Al_intensity); fclose(EELS_file);
170 INTENSITY_file=fopen("INTENSITY_PP_data.txt","a"); fprintf(
       INTENSITY_file,"%f\n", ProbePosition_intensity); fclose(
       INTENSITY_file);
171 }
172 /*??? printf("average atompot comparison = %g\n", phirms/(wavlen*
       mm0) ); */
173 transmit( waver, wavei, transr, transi, nx, ny );
174 fft2d( waver, wavei, nxl, nyl, +1); if( lbeams== 1 ) { fprintf( fp1
       , "%5d", islice); for( ib=0; ib<nbout; ib++) fprintf(fp1, "%10.6
       f %10.6f", scale*waver[hbeam[ib]][kbeam[ib]], scale*wavei[hbeam[
       ib]][kbeam[ib]]); fprintf( fp1, "\n"); } /* remember: prop
       needed here to get anti-aliasing right */ propagate( waver,
       wavei, propxr, propxi, propyr, propyi, kx2, ky2, k2max, nx, ny )
       ; fft2d( waver, wavei, nxl, nyl, -1);
175 sum = 0.0; for( ix=0; ix<nx; ix++) for( iy=0; iy<ny; iy++) sum +=
       waver[ix][iy]*waver[ix][iy] + wavei[ix][iy]*wavei[ix][iy]; sum =
        sum * scale;
176 printf("z= %f A, %ld beams, %d coord., \n" " aver. phase= %f, total
        intensity = %f\n", zslice, nbeams, na, phirms, sum );
177 if( HAADF_data_yn == 1 ) { HAADF_create(HAADF_create_mask, nx, ny,
       ax, by, wavlen, detect_inner, detect_outer); cbed_sum=
       HAADF_integrate(HAADF_create_mask, waver, wavei, nx, ny,
       HAADF_cbed_waver, HAADF_cbed_wavei);
178 printf("cbed_sum: %f\n",cbed_sum );
179 HAADF_file=fopen("HAADF_data.txt","a"); fprintf(HAADF_file,"%f\n",
       cbed_sum); fclose(HAADF_file); }
180 zslice += deltaz; istart += na; islice++;
181 } /* end while(istart<natom..) */
182 rmin = waver[0][0]; rmax = rmin; aimin = wavei[0][0]; aimax = aimin
       ;
183 for( ix=0; ix<nx; ix++) for( iy=0; iy<ny; iy++) { wr = waver[ix][iy
       ]; wi = wavei[ix][iy]; if( wr < rmin ) rmin = wr; if( wr > rmax
       ) rmax = wr; if( wi < aimin ) aimin = wi; if( wi > aimax ) aimax
        = wi; }
184 } /* end else .. coherent section */
185 /* output results and find min and max to echo remember that
       complex pix are stored in the file in FORTRAN order for
       compatability if( lstart == 1 ) for( ix=0; ix<NPARAM; ix++ )
       param[ix] = sparam[ix]; else for( ix=0; ix<NPARAM; ix++ ) param[
       ix] = 0.0F; param[pRMAX] = rmax; param[pIMAX] = aimax; param[
       pRMIN] = rmin; param[pIMIN] = aimin; param[pXCTILT] = ctiltx;
       param[pYCTILT] = ctilty; param[pENERGY] = v0; param[pDX] = (
       float) ( ax/((float)nx) ); param[pDY] = (float) ( by/((float)ny)
        ); param[pWAVEL] = wavlen; param[pNSLICES] = 0.0F; ??? if (
       lpartl == 1 ) { param[pDEFOCUS] = df0; param[pOAPERT] = aobj;
       param[pCS] = Cs; param[pCAPERT] = acmax; param[pDDF] = sigmaf; }
186 if ( lpartl == 1 ) i = tcreateFloatPixFile( fileout, pix, (long) nx
       , (long) ny, 1, param ); else i = tcreateFloatPixFile( fileout,
       waver, (long) (2*nx), (long) ny, 2, param );
187 if( i != 1 ) printf( "autoslice cannot write TIF file %s\n",
```

```
    fileout ); printf( "pix range %g to %g real,\n" " %g to %g imag\
    n", rmin,rmax,aimin,aimax ); */ printf("Total CPU time = %f sec
    .\n", cputim()-timer );
188 } /* end main() */
189
190
191 /*---------------- functions detailed below ------------------*/
192
193 /*---------------- Intensity_mask_create() ------------------*/
194 /* create masks around the atomic sites for each atomic species
195 x[],y[] = real array of atomic coordinates occ[] = real array of
    occupancies Znum[] = array of atomic numbers natom = number of
    atoms ax, by = size of transmission function in Angstroms kev =
    beam energy in keV transr = 2D array to get real part of
    specimen transmission function transi = 2D array to get imag
    part of specimen transmission function nx, ny = dimensions of
    transmission functions *phirms = average phase shift of
    projected atomic potential *nbeams = will get number of Fourier
    coefficients k2max = square of max k = bandwidth limit
196 */ void Intensity_mask_create( const float x[], const float y[],
    const float occ[], int Znum[], const int natom, const float ax,
    const float by, const float kev, float **As_mask, float **
    Ga_mask, float **Al_mask, float **ProbePosition_mask, const long
     nx, const long ny, double *phirms, long *nbeams, const float
    k2max, const float integrate_radius, const float ProbePosition_x
    , const float ProbePosition_y) { int idx, idy, i, ixo, iyo, ix,
    iy, ixw, iyw, nx1, nx2, ny1, ny2, rad_x, rad_y; float k2; int
    ir_pix_x, ir_pix_y; double r, rx2, vz, rmin, sum, scale; int
    probe_position_pix_x, probe_position_pix_y; const double rmax
    =3.0; /* max atomic radius in Angstroms */
197 probe_position_pix_x= (int) (nx*ProbePosition_x/ax);
    probe_position_pix_y= (int) (ny*ProbePosition_y/by);
198 ir_pix_x= (int) (nx*integrate_radius/ax); ir_pix_y= (int) (ny*
    integrate_radius/by);
199 idx = (int) ( nx*rmax/ax ) + 1; idy = (int) ( ny*rmax/by ) + 1;
200 for( ix=0; ix<nx; ix++) for( iy=0; iy<ny; iy++){ As_mask[ix][iy] =
    0.0F; Ga_mask[ix][iy] = 0.0F; Al_mask[ix][iy] = 0.0F;
    ProbePosition_mask[ix][iy] = 0.0F;}
201 /* probe position mask */
202 for (rad_x=probe_position_pix_x-ir_pix_x; rad_x<
    probe_position_pix_x+ir_pix_x+1;rad_x++) for (rad_y=
    probe_position_pix_y-ir_pix_y; rad_y<probe_position_pix_y+
    ir_pix_y+1;rad_y++) {
203 if (rad_x<0 )rad_x=0; if (rad_x>nx )rad_x=nx; if (rad_y<0 )rad_y=0;
     if (rad_y>ny )rad_y=ny;
204 ProbePosition_mask[rad_x][rad_y] = 1.0; }
205 /* Atomic species masks*/
206 for( i=0; i<natom; i++) { ixo = (int) ( nx*x[i]/ax ); iyo = (int) (
     ny*y[i]/by );
207 if (ixo<0 )ixo=0; if (ixo>nx )ixo=nx;
208 if (iyo<0 )iyo=0; if (iyo>ny )iyo=ny;
209 if (Znum[i]==33.0) for (rad_x=ixo-ir_pix_x; rad_x<ixo+ir_pix_x+1;
```

```
    rad_x++) for (rad_y=iyo-ir_pix_y; rad_y<iyo+ir_pix_y+1;rad_y++)
    {
210 if (rad_x<0 )rad_x=0; if (rad_x>nx )rad_x=nx; if (rad_y<0 )rad_y=0;
     if (rad_y>ny )rad_y=ny;
211 As_mask[rad_x][rad_y] = 1.0; }
212 if (Znum[i]==31.0) for (rad_x=ixo-ir_pix_x; rad_x<ixo+ir_pix_x+1;
    rad_x++) for (rad_y=iyo-ir_pix_y; rad_y<iyo+ir_pix_y+1;rad_y++)
    {
213 if (rad_x<0 )rad_x=0; if (rad_x>nx )rad_x=nx; if (rad_y<0 )rad_y=0;
     if (rad_y>ny )rad_y=ny;
214 Ga_mask[rad_x][rad_y] = 1.0; }
215 if (Znum[i]==13.0) for (rad_x=ixo-ir_pix_x; rad_x<ixo+ir_pix_x+1;
    rad_x++) for (rad_y=iyo-ir_pix_y; rad_y<iyo+ir_pix_y+1;rad_y++)
    {
216 if (rad_x<0 )rad_x=0; if (rad_x>nx )rad_x=nx; if (rad_y<0 )rad_y=0;
     if (rad_y>ny )rad_y=ny;
217 Al_mask[rad_x][rad_y] = 1.0; }
218 /* end for(iy... */ /* end for(ix... */
219 } /* end for(i=0... */
220 return;
221 } /* end I_m_c() */
222
223 /*------------- Intensity_mask_apply() -----------------*/
224 /* function to apply the Intensity masks to the wave function and
    return the */
225 double Intensity_mask_apply(float **Species_mask, float** waver,
    float** wavei, const int nx, const int ny ) { float
    sum_intensity; int ix, iy;
226 sum_intensity=0.0;
227 for( ix=0; ix<nx; ix++) for( iy=0; iy<ny; iy++) { sum_intensity +=
    (waver[ix][iy]*Species_mask[ix][iy])*(waver[ix][iy]*Species_mask
    [ix][iy]) + (wavei[ix][iy]*Species_mask[ix][iy])*(wavei[ix][iy]*
    Species_mask[ix][iy]); }
228 float normal_nxny=(float)nx*(float)ny;
229 sum_intensity=sum_intensity/normal_nxny;
230 return(sum_intensity); }
231
232 /*--------------- HAADF_integrate() ------------------*/
233 /* function to take the wavefunction at a particular slice and
    integrate the intensity falling onto the HAADF detector,
    normalise it and return the summed Intensity value */
234 double HAADF_integrate(float** HAADF_create_mask, float** waver,
    float** wavei, const int nx, const int ny, float**
    HAADF_cbed_waver , float** HAADF_cbed_wavei) { int ix, iy; float
     cbedsum;
235 /*copy wavefunction to temp array*/
236 for( ix=0; ix<nx; ix++) for( iy=0; iy<ny; iy++) { HAADF_cbed_waver[
    ix][iy] = waver[ix][iy]; HAADF_cbed_wavei[ix][iy] = wavei[ix][iy
    ];
237 }
238 /* take fft to move to freq space*/ fft2d( HAADF_cbed_waver,
    HAADF_cbed_wavei, nx, ny, +1);
```

```
239 float normal_nxny=(float)nx*(float)nx*(float)ny*(float)ny;
240 /* Integrate the HAADF signal across the detector */
241 cbedsum=0.0F;
242 for( ix=0; ix<nx; ix++) for( iy=0; iy<ny; iy++) { cbedsum=cbedsum
        +(((HAADF_cbed_waver[ix][iy]*HAADF_cbed_waver[ix][iy]+
        HAADF_cbed_wavei[ix][iy]*HAADF_cbed_wavei[ix][iy])*
        HAADF_create_mask[ix][iy])/(normal_nxny)); }
243 return(cbedsum);
244 } /* end HAADF_integrate() */
245 /* function to create a HAADF mask used to integrate the electron
        intensity from the CBED pattern */
246 double HAADF_create(float** HAADF_create_mask,const int nx, const
        int ny, const float ax, const float by, const float wavlen,
        const int detect_inner, const int detect_outer)
247 {
248 float *param; int ix, iy; float kxx, kyy, alpha_square,
        alpha_square_min, alpha_square_max;
249 float image_dkx, image_dky, image_kx_max, image_ky_max, alpha_max_x
        , alpha_max_y; float one_pix_x, one_pix_y, detect_pix_min_x,
        detect_pix_min_y, alpha_square_min_x, alpha_square_min_y,
        alpha_square_max_x, alpha_square_max_y; float detect_pix_max_x,
        detect_pix_max_y; char HAADF_mask[NCMAX];
250 param = float1D( NPARAM, "param" );
251 /* Calculate constants */
252 image_dkx=1.0/(ax*(1e-10)); //% kx-value per pixel image_dky=1.0/(
        by*(1e-10)); //% ky-value per pixel
253 image_kx_max=(nx/2.0)*image_dkx; //% maaximum posiible kx in image
        image_ky_max=(ny/2.0)*image_dky; //% maaximum posiible ky in
        image
254 alpha_max_x=(wavlen*1e-10)*image_kx_max*1000.0; //% convergence
        angle at image edge x-dir (in mrad) alpha_max_y=(wavlen*1e-10)*
        image_ky_max*1000.0; //% convergence angle at image edge y-dir (
        in mrad)
255 one_pix_x=(alpha_max_x/(nx/2.0)); // %one_pix el in x direction =
        mrad; one_pix_y=(alpha_max_y/(ny/2.0)); // %one_pix el in x
        direction = mrad;
256 alpha_square_min=detect_inner*detect_inner; alpha_square_max=
        detect_outer*detect_outer;
257 /* printf( "ax %f\n", HC_ax ); printf( "by %f\n", HC_by ); printf(
        "nx %d\n", HC_nx ); printf( "ny %d\n", HC_ny ); printf( "wavlen
        %f\n", HC_wavlen ); printf( "detect_inner %i\n", detect_inner );
         printf( "detect_outer %i\n", detect_outer );
258 printf( "image_dkx %f\n", image_dkx ); printf( "image_dkx %f\n",
        image_dky );
259 printf( "image_kx_max %f\n", image_kx_max ); printf( "image_ky_max
        %f\n", image_ky_max );
260 printf( "alpha_max_x %f\n", alpha_max_x ); printf( "alpha_max_y %f\
        n", alpha_max_y );
261 printf( "one_pix_x %f\n", one_pix_x ); printf( "one_pix_y %f\n",
        one_pix_y );
262 printf( "alpha_square_min %f\n", alpha_square_min ); printf( "
        alpha_square_max %f\n", alpha_square_max ); */
```

```
263 /* ensure HAADF_create_mask is zero*/
264 for ( ix=0; ix<(nx); ix++ ) for ( iy=0; iy<(ny); iy++ )
265 { {HAADF_create_mask[ix][iy] = 0.0F;} }
266 /* set mask >inner radius & <outer radius to one */ /*top left*/
      for ( ix=0; ix<(nx/2); ix++ ) for ( iy=0; iy<(ny/2); iy++ )
267 { kyy = iy*one_pix_y; kxx =ix*one_pix_x; alpha_square=kxx*kxx+kyy*
      kyy; if (alpha_square<alpha_square_min) {HAADF_create_mask[ix][
      iy] = 0.0F;} else if (alpha_square>alpha_square_max) {
      HAADF_create_mask[ix][iy] = 0.0F;} else {HAADF_create_mask[ix][
      iy] = 1.0F;} }
268 /*top right*/ for ( ix=nx/2; ix<(nx); ix++ ) for ( iy=0; iy<(ny/2);
      iy++ ) { kyy = iy*one_pix_y; kxx =(nx-ix)*one_pix_x;
      alpha_square=kxx*kxx+kyy*kyy; if (alpha_square<alpha_square_min)
      {HAADF_create_mask[ix][iy] = 0.0F;} else if (alpha_square>
      alpha_square_max) {HAADF_create_mask[ix][iy] = 0.0F;} else {
      HAADF_create_mask[ix][iy] = 1.0F;} }
269 /* bottom right*/ for ( ix=nx/2; ix<(nx); ix++ ) for ( iy=ny/2; iy
      <(ny); iy++ )
270 { kyy = (ny-iy)*one_pix_y; kxx =(nx-ix)*one_pix_x; alpha_square=kxx
      *kxx+kyy*kyy; if (alpha_square<alpha_square_min) {
      HAADF_create_mask[ix][iy] = 0.0F;} else if (alpha_square>
      alpha_square_max) {HAADF_create_mask[ix][iy] = 0.0F;} else {
      HAADF_create_mask[ix][iy] = 1.0F;} }
271 /*bottom left*/ for ( ix=0; ix<(nx/2); ix++ ) for ( iy=ny/2; iy<(ny
      ); iy++ ) { kyy = (ny-iy)*one_pix_y; kxx =ix*one_pix_x;
      alpha_square=kxx*kxx+kyy*kyy; if (alpha_square<alpha_square_min)
      {HAADF_create_mask[ix][iy] = 0.0F;} else if (alpha_square>
      alpha_square_max) {HAADF_create_mask[ix][iy] = 0.0F;} else {
      HAADF_create_mask[ix][iy] = 1.0F;}
272 }
273 /* strcpy(HAADF_mask,"HAADF_mask.tif");
274 for( ix=0; ix<NPARAM; ix++ ) param[ix] = 0.0F;
275 param[pRMAX] = 1; param[pIMAX] = 1; param[pRMIN] = 0; param[pIMIN]
      = 0; param[pXCTILT] = 0; param[pYCTILT] = 0; param[pENERGY] = 0;
      param[pDX] = 0; param[pDY] = 0; param[pWAVEL] = 0; param[
      pNSLICES] = 0;
276 tcreateFloatPixFile( HAADF_mask, HAADF_create_mask, (long) (nx), (
      long) ny, 1, param ); */ return;
277 } /* end HAADF_create() */
278
279 /*-------------------- sortByZ() --------------------*/
280 /* sort atom info by coordinate z (Shell sort)
281 x[], y[], z[] = atom coordinates occ[] = occupancy of each atom
      Znum[] = atomic number of each atom natom = number of atoms */
282 void sortByZ( float x[], float y[], float z[], float occ[], int
      Znum[], int natom ) { int i, j, k, m; void iswap( int *i, int *j
      ); void fswap( float *a, float *b );
283 m = 1; j = 2; do{ m+=1; j*=2;} while( j <= natom ); m = j / 2;
284 do{ /* ??? not most efficient stride but it works */ k = natom - m;
      for( j=0; j<k; j++) for( i=j; i>=0; i-=m) { if( z[i+m] < z[i] )
      { fswap( &x[i], &x[i+m] ); fswap( &y[i], &y[i+m] ); fswap( &z[i
      ], &z[i+m] ); fswap( &occ[i], &occ[i+m] ); iswap( &Znum[i], &
```

```
    Znum[i+m] ); } } m = m/2; } while( m > 0 );
285 /* Test sort routine -- DELETE this after awhile */ for( i=1; i<
    natom; i++) if( z[i-1] > z[i] ) printf("Bad sort !\n");
286 } /* end sortByZ() */
287
288 /*-------------------- trlayer() --------------------*/
289 /* Calculate complex specimen transmission function for one layer
    using real space projected atomic potentials
290 x[],y[] = real array of atomic coordinates occ[] = real array of
    occupancies Znum[] = array of atomic numbers natom = number of
    atoms ax, by = size of transmission function in Angstroms kev =
    beam energy in keV transr = 2D array to get real part of
    specimen transmission function transi = 2D array to get imag
    part of specimen transmission function nx, ny = dimensions of
    transmission functions *phirms = average phase shift of
    projected atomic potential *nbeams = will get number of Fourier
    coefficients k2max = square of max k = bandwidth limit
291 */ void trlayer( const float x[], const float y[], const float occ
    [], const int Znum[], const int natom, const float ax, const
    float by, const float kev, float **transr, float **transi, const
    long nx, const long ny, double *phirms, long *nbeams, const
    float k2max ) { int idx, idy, i, ixo, iyo, ix, iy, ixw, iyw, nx1
    , nx2, ny1, ny2; float k2; double r, rx2, vz, rmin, sum, scale;
292 const double rmax=3.0; /* max atomic radius in Angstroms */
293 scale = sigma( kev ) / 1000.0; /* in 1/(volt-Angstroms) */
294 /* min radius to avoid singularity */ rmin = ax/((double)nx); r =
    by/((double)ny); rmin = 0.25 * sqrt( 0.5*(rmin*rmin + r*r) );
295 idx = (int) ( nx*rmax/ax ) + 1; idy = (int) ( ny*rmax/by ) + 1;
296 for( ix=0; ix<nx; ix++) for( iy=0; iy<ny; iy++) transr[ix][iy] =
    0.0F;
297 for( i=0; i<natom; i++) { ixo = (int) ( nx*x[i]/ax ); iyo = (int) (
    ny*y[i]/by ); nx1 = ixo - idx; nx2 = ixo + idx; ny1 = iyo - idy
    ; ny2 = iyo + idy;
298 /* add proj. atomic potential at a local region near its center
    taking advantage of small range of atomic potential */
299 for( ix=nx1; ix<=nx2; ix++) { rx2 = x[i] - ((double)ix)*ax/nx; rx2
    = rx2 * rx2; ixw = ix; while( ixw < 0 ) ixw = ixw + nx; ixw =
    ixw % nx; for( iy=ny1; iy<=ny2; iy++) { r = y[i] - ((double)iy)*
    by/ny; r = sqrt( rx2 + r*r ); if( r <= rmax ) { iyw = iy; while(
    iyw < 0 ) iyw = iyw + ny; iyw = iyw % ny; if( r < rmin ) r =
    rmin; /* vz = occ[i] * scale * vzatom( Znum[i], r ); slow */ vz
    = occ[i] * scale * vzatomLUT( Znum[i], r ); transr[ixw][iyw] +=
    (float) vz; } } /* end for(iy... */ } /* end for(ix... */
300 } /* end for(i=0... */
301 /* convert phase to a complex transmission function */ sum = 0; for
    ( ix=0; ix<nx; ix++) for( iy=0; iy<ny; iy++) { vz = transr[ix][
    iy]; sum += vz; transr[ix][iy] = (float) cos( vz ); transi[ix][
    iy] = (float) sin( vz ); }
302 *phirms = sum / ( ((double)nx)*((double)ny) );
303 /* bandwidth limit the transmission function */ *nbeams = 0; fft2d(
    transr, transi, nx, ny, +1); for( ix=0; ix<nx; ix++) for( iy=0;
    iy<ny; iy++) { k2 = ky2[iy] + kx2[ix]; if (k2 < k2max) *nbeams
```

```
    += 1; else transr[ix][iy] = transi[ix][iy] = 0.0F; } fft2d(
    transr, transi, nx, ny, -1);
304 return;
305 } /* end trlayer() */
306
307 /*------------------------- iswap() --------------------------*/
308 /* Swap 2 int's (for sorting) Can also be used for reals (via
    equivalence) */ void iswap( int *i, int *j ) { int it; it = *i;
    *i = *j; *j = it; return; } /* end iswap() */
309
310 /*------------------------- fswap() --------------------------*/
311 /* Swap 2 int's (for sorting) Can also be used for reals (via
    equivalence) */ void fswap( float *a, float *b ) { float t; t =
    *a; *a = *b; *b = t; return; } /* end fswap() */
312
313 /*-------------- vzatomLUT() ------------------------------*/
314 /* return the (real space) projected atomic potential for atomic
    number Z at radius r (in Angstroms)
315 this mimics vzatom() in slicelib.c but uses a look-up-table with
    cubic spline interpolatoin to make it run about 2X-4X faster
316 started 23-may-1997 E. Kirkland fix Z range to allow Hydrogen 1-jan
    -1998 ejk
317 Z = atomic number 1 <= Z <= 98 r = radius in Angstroms */
318 double vzatomLUT( int Z, double r ) { int i, iz; double dlnr, vz;
319 if( splineInit == 0 ) { splinx = (double*) malloc( NRMAX * sizeof(
    double ) ); spliny = (double**) malloc( NZMAX * sizeof( double*
    ) ); splinb = (double**) malloc( NZMAX * sizeof( double* ) );
    splinc = (double**) malloc( NZMAX * sizeof( double* ) ); splind
    = (double**) malloc( NZMAX * sizeof( double* ) ); if( (splinx==
    NULL) || (spliny==NULL) || (splinb==NULL) || (splinc==NULL) || (
    splind==NULL) ) { printf( "Cannot allocate spline pointer" "in 
    vzatomLUT()\n"); exit( 0 ); }
320 /* generate a set of logarithmic r values */ dlnr = log(RMAX/RMIN)
    /(NRMAX-1); for( i=0; i<NRMAX; i++) splinx[i] = RMIN * exp( i *
    dlnr ); printf( "fit from r= %g to r= %g\n", splinx[0], splinx[
    NRMAX-1] );
321 nspline = int1D( NZMAX, "nspline" ); for( i=0; i<NZMAX; i++)
    nspline[i] = 0; splineInit = 1; /* remember that this has been
    done */ }
322 iz = Z - 1; /* convert atomic number to array index */ if( (Z < 1)
    || ( Z > NZMAX) ) { printf("Bad atomic number %d in vzatomLUT()\
    n", Z); exit( 0 ); }
323 /* if this atomic number has not been called before generate the
    spline coefficients */ if( nspline[iz] == 0 ) { spliny[iz] =
    double1D( NRMAX, "spliny" ); splinb[iz] = double1D( NRMAX, "
    splinb" ); splinc[iz] = double1D( NRMAX, "splinc" ); splind[iz]
    = double1D( NRMAX, "splind" );
324 for( i=0; i<NRMAX; i++) spliny[iz][i] = vzatom( Z, splinx[i] );
    nspline[iz] = NRMAX; splinh( splinx, spliny[iz], splinb[iz],
    splinc[iz], splind[iz], NRMAX); }
325 /* now that everything is set up find the scattering factor by
    interpolation in the table */
```

```
326 vz = seval( splinx, spliny[iz], splinb[iz], splinc[iz], splind[iz],
        nspline[iz], r );
327 return( vz );
328 }
329 /* end vzatomLUT() */
```

Appendix B: Matlab Scripts

This appendix contains the main Matlab scripts that were developed during the course of this project. These scripts were developed to interregate the data generated from the simulations and the first of which checks the status of the currently running interface simulation. The script begins on page 284 and graphically displays the completed jobs for each phonon iteration and each probe position. Once the simulation data has been sucessfully generated the Sim-Read script can be used to average all of the valid phonon configurations together to produce a series of matlab matrices that contain the HAADF and Intensity data. The Sim-Read script begins on page 287. Having generated the simulation data and averaged the phonons together the data set can now be interrogated and the interface characteristics measured using the Interface Interpolate script. This script begins on page 292 and measures the interface position and width by fitting an analytical function to the simulated data. To interrogate specific column data the script on page 296 can be used. This script plots the HAADF and intensity data as a function of speciemn thickness for a given dumbbell. Likewise the script on page 297 can be used to plot a line profile of the column ratio data for a give specimen thickness.

These scripts allow the large datasets to be processed and visualised in detail and can be used as the basis for further investigations into large interfacial structures by simply copying the code into the *Matlab Editor*[1].

Sim-Status

```
1 %%/*------------ Original Code: M.P.Finnie ----------------*/
2 Copyright March 2010 Michael P. Finnie
3 The computer code and or data in this file is provided for
    demonstration purposes only with no guarantee or warranty of any
     kind that it is correct or produces correct results. By using
    the code and or data in this file the user agrees to accept all
    risks and liabilities associated with the code and or data. The
    computer code and or data in this file may be copied (and used)
    for non-commercial academic or research purposes only, provided
    that this notice is included. This file or any portion of it may
     not be resold, rented or distributed without the written
    permission of the author.
```

[1]The MathWorks Inc.

```
4  %%/*---------------------- Sim-Status --------------------------*/
5
6
7
8  %%/*-------- Model directory and folder details -----------*/
9  directory_path='G:\mfinnie\Matlab\DATA\Final_Model\GRID\'; model='
       Vicinal_0_point_3_degree_Random_Step_7UC_config_5';
10 no_of_phonons=50;  % maximum number of phonons
11
12 %%/*------------------ Pre-allocate matrices ------------------*/
13 EELS_Grid_BD=zeros(16,no_of_phonons); EELS_Grid_Column3=zeros(16,
       no_of_phonons); EELS_Grid_Column5=zeros(16,no_of_phonons);
14 HAADF_Grid_BD=zeros(16,no_of_phonons); HAADF_Grid_Column3=zeros(16,
       no_of_phonons); HAADF_Grid_Column5=zeros(16,no_of_phonons);
15 INTENSITY_PP_Grid_BD=zeros(16,no_of_phonons);
       INTENSITY_PP_Grid_Column3=zeros(16,no_of_phonons);
       INTENSITY_PP_Grid_Column5=zeros(16,no_of_phonons);
16
17
18 %%/*---- Check EELS dataset for available phonons --------*/
19 Data_Set='EELS';
20 for phonon_no=1:no_of_phonons; for Probe_position_counter=1:3;
               if Probe_position_counter==1  Probe_position=('BD');
       end              if Probe_position_counter==2 Probe_position=('
       Column3'); end                          if Probe_position_counter==3
       Probe_position=('Column5'); end                    for
       Dumbbell_counter=1:16    Dumbbell=num2str(Dumbbell_counter);
21 eval(sprintf('pathname=(''%s\\%s\\Dumbbell_%s_%s\\Phonon_%s_%s_%s_%
       s_data.txt'');',directory_path,model,Dumbbell,Probe_position,
       num2str(phonon_no),Probe_position,Dumbbell,Data_Set))
       %   Where multislice images are stored
22 if exist(pathname,'file');
23 % check file size fid = fopen(pathname); fseek(fid, 0, 'eof');
                              filesize = ftell(fid); fclose(fid);
24 if strcmp(Data_Set,'EELS')  && (filesize>16000)  && (filesize
       <17000)      A=1; else     A=0;      end
25 else      A=0; end                                  eval(sprintf('%
       s_Grid_%s(Dumbbell_counter,phonon_no)=␣␣␣A;',Data_Set,
       Probe_position));
26 end end end
27
28 %%/*---- Check HAADF dataset for available phonons -------*/
29 Data_Set='HAADF';
30 for phonon_no=1:no_of_phonons; for Probe_position_counter=1:3;
               if Probe_position_counter==1  Probe_position=('BD');
       end              if Probe_position_counter==2 Probe_position=('
       Column3'); end                          if Probe_position_counter==3
       Probe_position=('Column5'); end                    for
       Dumbbell_counter=1:16    Dumbbell=num2str(Dumbbell_counter);
31 eval(sprintf('pathname=(''%s\\%s\\Dumbbell_%s_%s\\Phonon_%s_%s_%s_%
       s_data.txt'');',directory_path,model,Dumbbell,Probe_position,
       num2str(phonon_no),Probe_position,Dumbbell,Data_Set))
```

```
    %   Where multislice images are stored
32 if exist(pathname, 'file');
33 % check file size fid = fopen(pathname); fseek(fid, 0, 'eof');
                              filesize = ftell(fid); fclose(fid);
                            % INTENSITY_PP filesize = 6000 % HAADF =
    6000 % EELS = 16800
34 if strcmp(Data_Set, 'HAADF') && (filesize >5900) && (filesize <6100)
       A=1; else     A=0;      end else      A=0; end
                                    eval(sprintf('%s_Grid_%s(
    Dumbbell_counter,phonon_no)=␣␣␣A;',Data_Set,Probe_position));
35 end end end
36
37 %%/*--- Check Intensity dataset for available phonons ---*/
38 Data_Set='INTENSITY_PP';
39 for phonon_no=1:no_of_phonons; for Probe_position_counter=1:3;
             if Probe_position_counter==1  Probe_position=('BD');
    end           if Probe_position_counter==2 Probe_position=('
    Column3'); end                  if Probe_position_counter==3
    Probe_position=('Column5');  end              for
    Dumbbell_counter=1:16   Dumbbell=num2str(Dumbbell_counter);
40 eval(sprintf('pathname=(''%s\\%s\\Dumbbell_%s_%s\\Phonon_%s_%s_%s_%
    s_data.txt'');',directory_path,model,Dumbbell,Probe_position,
    num2str(phonon_no),Probe_position,Dumbbell,Data_Set))
    %   Where multislice images are stored
41 if exist(pathname, 'file');
42 % check file size fid = fopen(pathname); fseek(fid, 0, 'eof');
                              filesize = ftell(fid); fclose(fid);
                            % INTENSITY_PP filesize = 6000 % HAADF =
    6000 % EELS = 16800
43 if strcmp(Data_Set, 'INTENSITY_PP') && (filesize >5900) && (filesize
    <6100)     A=1; else     A=0; end else     A=0; end
                                    eval(sprintf('%s_Grid_%s(
    Dumbbell_counter,phonon_no)=␣␣␣A;',Data_Set,Probe_position));
44 end end end
45 clear A Dumbbell Dumbbell_counter Probe_position
    Probe_position_counter ans fid filesize  clear Data_Set
    directory_path model no_of_phonons pathname phonon_no
46
47
48 %%/*------------ Plot complete phonon data ---------------*/
49 % Plot EELS Data:
50 subplot(3,3,1);
51 imagesc(EELS_Grid_BD); figure(gcf) title('EELS␣Grid␣BD'); xlabel('
    Phonon␣no.'); xlabel('Dumbbell␣no.');
52 subplot(3,3,2);
53 imagesc(EELS_Grid_Column3); figure(gcf) title('EELS␣Grid␣Column3');
     xlabel('Phonon␣no.'); xlabel('Dumbbell␣no.');
54 subplot(3,3,3);
55 imagesc(EELS_Grid_Column5); figure(gcf) title('EELS␣Grid␣Column5');
     xlabel('Phonon␣no.'); xlabel('Dumbbell␣no.');
56
57 % Plot HAADF Data:
```

```
58 subplot(3,3,4);
59 imagesc(HAADF_Grid_BD); figure(gcf) title('HAADF Grid BD'); xlabel(
       'Phonon no.'); xlabel('Dumbbell no.');
60 subplot(3,3,5);
61 imagesc(HAADF_Grid_Column3); figure(gcf) title('HAADF Grid Column3'
       ); xlabel('Phonon no.'); xlabel('Dumbbell no.');
62 subplot(3,3,6);
63 imagesc(HAADF_Grid_Column5); figure(gcf) title('HAADF Grid Column5'
       ); xlabel('Phonon no.'); xlabel('Dumbbell no.');
64
65 % Plot Intensity Data:
66 subplot(3,3,7);
67 imagesc(INTENSITY_PP_Grid_BD); figure(gcf) title('INTENSITY_PP Grid
       BD'); xlabel('Phonon no.'); xlabel('Dumbbell no.');
68 subplot(3,3,8);
69 imagesc(INTENSITY_PP_Grid_Column3); figure(gcf) title('INTENSITY_PP
       Grid Column3'); xlabel('Phonon no.'); xlabel('Dumbbell no.');
70 subplot(3,3,9);
71 imagesc(INTENSITY_PP_Grid_Column5); figure(gcf) title('INTENSITY_PP
       Grid Column5'); xlabel('Phonon no.'); xlabel('Dumbbell no.');
```

Sim-Read

```
1 %%/*------------ Original Code: M.P.Finnie ---------------*/
2 Copyright March 2010 Michael P. Finnie
3 The computer code and or data in this file is provided for
      demonstration purposes only with no guarantee or warranty of any
       kind that it is correct or produces correct results. By using
      the code and or data in this file the user agrees to accept all
      risks and liabilities associated with the code and or data. The
      computer code and or data in this file may be copied (and used)
      for non-commercial academic or research purposes only, provided
      that this notice is included. This file or any portion of it may
       not be resold, rented or distributed without the written
      permission of the author.
4
5 %%/*---------------------- Sim-Read ----------------------*/
6
7
8 %%/*------- Model directory and folder details ----------*/
9 directory_path='G:\mfinnie\Matlab\DATA\Final_Model\GRID\'; model='
      Vicinal_0_point_2_degree_Random_Step_7UC_config_1';
10 no_of_phonons=50; % maximum number of phonons
11
12 %%/*--------------- Pre-allocate matrices ---------------*/
13 EELS_Grid_BD=zeros(16,no_of_phonons); EELS_Grid_Column3=zeros(16,
      no_of_phonons); EELS_Grid_Column5=zeros(16,no_of_phonons);
14 HAADF_Grid_BD=zeros(16,no_of_phonons); HAADF_Grid_Column3=zeros(16,
      no_of_phonons); HAADF_Grid_Column5=zeros(16,no_of_phonons);
15 INTENSITY_PP_Grid_BD=zeros(16,no_of_phonons);
      INTENSITY_PP_Grid_Column3=zeros(16,no_of_phonons);
```

```
    INTENSITY_PP_Grid_Column5=zeros(16,no_of_phonons);
16
17 %%/*---- Check EELS dataset for available phonons --------*/
18 Data_Set='EELS';
19 for phonon_no=1:no_of_phonons; for Probe_position_counter=1:3;
              if Probe_position_counter==1  Probe_position=('BD');
    end             if Probe_position_counter==2 Probe_position=('
    Column3'); end                         if Probe_position_counter==3
    Probe_position=('Column5');  end       for Dumbbell_counter=1:16
      Dumbbell=num2str(Dumbbell_counter);
20 eval(sprintf('pathname=(''%s\\%s\\Dumbbell_%s_%s\\Phonon_%s_%s_%s_%
    s_data.txt'');',directory_path,model,Dumbbell,Probe_position,
    num2str(phonon_no),Probe_position,Dumbbell,Data_Set))
    %   Where multislice images are stored
21 if exist(pathname,'file');
22 % check file size
23 fid = fopen(pathname); fseek(fid, 0, 'eof');
                                filesize = ftell(fid); fclose(fid);
                    % STANDARD SIMULATION FILE SIZES: % INTENSITY_PP
    filesize = 6000 % HAADF = 6000 % EELS = 16800
24 if strcmp(Data_Set,'EELS')  && (filesize >16000)  && (filesize
    <17100)     A=1; else     A=0;      end
25 else      A=0; end                              eval(sprintf('%
    s_Grid_%s(Dumbbell_counter,phonon_no)=␣␣␣A;',Data_Set,
    Probe_position));
26 end end end
27
28 %%/*---- Check HAADF dataset for available phonons -------*/
29 Data_Set='HAADF';
30 for phonon_no=1:no_of_phonons; for Probe_position_counter=1:3;
              if Probe_position_counter==1  Probe_position=('BD');
    end             if Probe_position_counter==2 Probe_position=('
    Column3'); end                          if Probe_position_counter==3
    Probe_position=('Column5');  end                 for
    Dumbbell_counter=1:16    Dumbbell=num2str(Dumbbell_counter);
31 eval(sprintf('pathname=(''%s\\%s\\Dumbbell_%s_%s\\Phonon_%s_%s_%s_%
    s_data.txt'');',directory_path,model,Dumbbell,Probe_position,
    num2str(phonon_no),Probe_position,Dumbbell,Data_Set))
    %   Where multislice images are stored
32 if exist(pathname,'file');
33 % check file size fid = fopen(pathname); fseek(fid, 0, 'eof');
                                filesize = ftell(fid); fclose(fid);
34 if strcmp(Data_Set,'HAADF') && (filesize >5900) && (filesize <6100)
      A=1; else     A=0;      end else     A=0; end
                                   eval(sprintf('%s_Grid_%s(
    Dumbbell_counter,phonon_no)=␣␣␣A;',Data_Set,Probe_position));
35 end end end
36
37
38 %%/*-- Check Intensity dataset for available phonons ----*/
39 Data_Set='INTENSITY_PP';
40 for phonon_no=1:no_of_phonons; for Probe_position_counter=1:3;
```

```
            if Probe_position_counter==1  Probe_position=('BD');
    end            if Probe_position_counter==2 Probe_position=('
    Column3'); end                         if Probe_position_counter==3
    Probe_position=('Column5');  end                 for
    Dumbbell_counter=1:16    Dumbbell=num2str(Dumbbell_counter);
41  eval(sprintf('pathname=(''%s\\%s\\Dumbbell_%s_%s\\Phonon_%s_%s_%s_%
    s_data.txt'');',directory_path,model,Dumbbell,Probe_position,
    num2str(phonon_no),Probe_position,Dumbbell,Data_Set))
    %   Where multislice images are stored
42  if exist(pathname,'file');
43  % check file size fid = fopen(pathname); fseek(fid, 0, 'eof');
                                filesize = ftell(fid); fclose(fid);
44  if strcmp(Data_Set,'INTENSITY_PP') && (filesize>5900) && (filesize
    <6100)      A=1; else      A=0; end else      A=0; end
                                      eval(sprintf('%s_Grid_%s(
    Dumbbell_counter,phonon_no)=   A;',Data_Set,Probe_position));
45  end end end
46  clear A Dumbbell Dumbbell_counter Probe_position
    Probe_position_counter ans fid filesize
47
48
49  %%/*-------- total number of phonons available ----------*/
50  No_of_Phonons_EELS_Grid_BD=sum(EELS_Grid_BD');
    No_of_Phonons_EELS_Grid_Column3=sum(EELS_Grid_Column3');
    No_of_Phonons_EELS_Grid_Column5=sum(EELS_Grid_Column5');
51  No_of_Phonons_HAADF_Grid_BD=sum(HAADF_Grid_BD');
    No_of_Phonons_HAADF_Grid_Column3=sum(HAADF_Grid_Column3');
    No_of_Phonons_HAADF_Grid_Column5=sum(HAADF_Grid_Column5');
52  No_of_Phonons_INTENSITY_PP_Grid_BD=sum(INTENSITY_PP_Grid_BD');
    No_of_Phonons_INTENSITY_PP_Grid_Column3=sum(
    INTENSITY_PP_Grid_Column3');
    No_of_Phonons_INTENSITY_PP_Grid_Column5=sum(
    INTENSITY_PP_Grid_Column5');
53
54  %%/*---------- Process data into averaged dataset --------*/
55  for Probe_position_counter=1:3;          if Probe_position_counter
    ==1  Probe_position=('BD');  end              if
    Probe_position_counter==2 Probe_position=('Column3'); end
                           if Probe_position_counter==3 Probe_position
    =('Column5');  end              for Dumbbell_counter=1:16
    Dumbbell=num2str(Dumbbell_counter);
    eval(sprintf('pathname=(''%s\\%s\\Dumbbell_%s_%s\\'');',
    directory_path,model,Dumbbell,Probe_position))              %
    Where multislice images are stored
56  no_of_slices=600;
57  arrayname=sprintf('HAADF_Data_array_%s_%s',Dumbbell,Probe_position)
    ; eels_arrayname_As=sprintf('EELS_As_Data_array_%s_%s',Dumbbell,
    Probe_position); eels_arrayname_Ga=sprintf('EELS_Ga_Data_array_%
    s_%s',Dumbbell,Probe_position); eels_arrayname_Al=sprintf('
    EELS_Al_Data_array_%s_%s',Dumbbell,Probe_position);
    INTENSITY_PP_arrayname=sprintf('INTENSITY_PP_Data_array_%s_%s',
    Dumbbell,Probe_position);
```

```
58 eval(sprintf('%s=zeros(no_of_slices,No_of_Phonons_HAADF_Grid_%s(1,%
     i));',arrayname,Probe_position,Dumbbell_counter)); eval(sprintf(
     '%s=zeros(no_of_slices,No_of_Phonons_EELS_Grid_%s(1,%i));',
     eels_arrayname_As,Probe_position,Dumbbell_counter)); eval(
     sprintf('%s=zeros(no_of_slices,No_of_Phonons_EELS_Grid_%s(1,%i))
     ;',eels_arrayname_Ga,Probe_position,Dumbbell_counter)); eval(
     sprintf('%s=zeros(no_of_slices,No_of_Phonons_EELS_Grid_%s(1,%i))
     ;',eels_arrayname_Al,Probe_position,Dumbbell_counter)); eval(
     sprintf('%s=zeros(no_of_slices,No_of_Phonons_INTENSITY_PP_Grid_%
     s(1,%i));',INTENSITY_PP_arrayname,Probe_position,
     Dumbbell_counter));
59 eval(sprintf('Phonon_Array_%s=find(HAADF_Grid_%s(Dumbbell_counter
     ,:));',Probe_position,Probe_position));
60 eval(sprintf('haadf_temp_array=Phonon_Array_%s;',Probe_position));
      haadf_temp_counter=1;
61
62
63 %%/*------------------- Process HAADF array ------------------*/
64 % Process HAADF array using available phonon files:
65 for k=haadf_temp_array      phonon_count=num2str(k);
66   fname=sprintf('Phonon_%s_%s_%s_HAADF_data.txt',phonon_count,
       Probe_position,Dumbbell);    fid=fopen(fname, 'rb');
                 magic_str1=[    'HAADF_data=dlmread(''',pathname,'',
       fname,''');'     ];       eval(magic_str1);
67     for line_counter=1: no_of_slices
                                              eval(sprintf('%s(
       line_counter,haadf_temp_counter)=HAADF_data(line_counter,1);
       ',arrayname));
68     end haadf_temp_counter=haadf_temp_counter+1; end
69
70 %%/*---------------- Process Intensity array ----------------*/
71 % Process Intensity array using available phonon files:
72 eval(sprintf('Phonon_Array_%s=find(INTENSITY_PP_Grid_%s(
     Dumbbell_counter,:));',Probe_position,Probe_position));
73 eval(sprintf('intensity_temp_array=Phonon_Array_%s;',Probe_position
     ));   intensity_temp_counter=1;
74 for k=intensity_temp_array      phonon_count=num2str(k);
     intensity_name=sprintf('Phonon_%s_%s_%s_INTENSITY_PP_data.txt',
     phonon_count,Probe_position,Dumbbell);    fid=fopen(fname, 'rb');
                         magic_str3=[    'INTENSITY_PP_data=dlmread(''',
     pathname,'',intensity_name,''');'     ];        eval(magic_str3);
75     for line_counter=1: no_of_slices
76 eval(sprintf('%s(line_counter,intensity_temp_counter)=
     INTENSITY_PP_data(line_counter,1);',INTENSITY_PP_arrayname));
        end intensity_temp_counter=intensity_temp_counter+1; end
77
78 %%/*------------------- Process EELS array -------------------*/
79 eval(sprintf('Phonon_Array_%s=find(EELS_Grid_%s(Dumbbell_counter,:)
     );',Probe_position,Probe_position));
80 eval(sprintf('eels_temp_array=Phonon_Array_%s;',Probe_position));
     eels_temp_counter=1;
81 for k=eels_temp_array      phonon_count=num2str(k);          eels_name
```

```
    =sprintf('Phonon_%s_%s_%s_EELS_data.txt',phonon_count,
    Probe_position,Dumbbell);    fid=fopen(eels_name, 'rb');
              magic_str2=[    'EELS_data=dlmread(''',pathname,'',
    eels_name,''');'    ];     eval(magic_str2);
82     for line_counter=1: no_of_slices
83 eval(sprintf('%s(line_counter,eels_temp_counter)=EELS_data(
    line_counter,1);',eels_arrayname_As)); eval(sprintf('%s(
    line_counter,eels_temp_counter)=EELS_data(line_counter,2);',
    eels_arrayname_Ga)); eval(sprintf('%s(line_counter,
    eels_temp_counter)=EELS_data(line_counter,3);',eels_arrayname_Al
    ));
84     end eels_temp_counter=eels_temp_counter+1; end
85 average_phonon_number=(length(eels_temp_array)+length(
    intensity_temp_array)+length(haadf_temp_array))/3;    eval(
    sprintf('Std_Err_%s=(std(%s'')./(sqrt(average_phonon_number)))''
    ;',arrayname,arrayname));      eval(sprintf('Average_%s=(mean(%s
    ''))'';',arrayname,arrayname));      eval(sprintf('clear %s',
    arrayname));
86 eval(sprintf('Std_Err_%s=(std(%s'')./(sqrt(average_phonon_number)))
    '';',eels_arrayname_As,eels_arrayname_As));      eval(sprintf('
    Average_%s=(mean(%s''))'';',eels_arrayname_As,eels_arrayname_As)
    );      eval(sprintf('clear %s',eels_arrayname_As));
87 eval(sprintf('Std_Err_%s=(std(%s'')./(sqrt(average_phonon_number)))
    '';',eels_arrayname_Ga,eels_arrayname_Ga));      eval(sprintf('
    Average_%s=(mean(%s''))'';',eels_arrayname_Ga,eels_arrayname_Ga)
    );      eval(sprintf('clear %s',eels_arrayname_Ga));
88 eval(sprintf('Std_Err_%s=(std(%s'')./(sqrt(average_phonon_number)))
    '';',eels_arrayname_Al,eels_arrayname_Al));      eval(sprintf('
    Average_%s=(mean(%s''))'';',eels_arrayname_Al,eels_arrayname_Al)
    );      eval(sprintf('clear %s',eels_arrayname_Al));
89 eval(sprintf('Std_Err_%s=(std(%s'')./(sqrt(average_phonon_number)))
    '';',INTENSITY_PP_arrayname,INTENSITY_PP_arrayname));      eval(
    sprintf('Average_%s=(mean(%s''))'';',INTENSITY_PP_arrayname,
    INTENSITY_PP_arrayname));      eval(sprintf('clear %s',
    INTENSITY_PP_arrayname));
90 eval(sprintf('display(''Probe Position: %s  Dumbbell: %s  
    no_of_phonons: %i'')',Probe_position,Dumbbell,
    average_phonon_number));
91 end end
92
93 %%/*-------------------------- Cleanup --------------------------*/
94 clear fid fname magic_str1 k no_of_phonons pathname phonon_count
    HAADF_data HAADF_Data_array clear no_of_slices i Dumbbell
    arrayname Probe_position magic_str2 EELS_data eels_name
    eels_arrayname_Ga clear eels_arrayname_As eels_arrayname_Al
    INTENSITY_PP_arrayname INTENSITY_PP_data intensity_name clear
    line_counter magic_str3 intensity_temp_array
    intensity_temp_counter model phonon_no clear
    average_phonon_number directory_path eels_temp_array
    eels_temp_counter haadf_temp_array haadf_temp_counter  clear
    Probe_position_counter Phonon_Array_Column5 Phonon_Array_Column3
     Phonon_Array_BD clear Data_Set Dumbbell_counter
```

Interface Interpolate

```
1  %%/*---------- Original Code: M.P.Finnie ---------------*/
2  Copyright March 2010 Michael P. Finnie
3  The computer code and or data in this file is provided for
       demonstration purposes only with no guarantee or warranty of any
        kind that it is correct or produces correct results. By using
       the code and or data in this file the user agrees to accept all
       risks and liabilities associated with the code and or data. The
       computer code and or data in this file may be copied (and used)
       for non-commercial academic or research purposes only, provided
       that this notice is included. This file or any portion of it may
        not be resold, rented or distributed without the written
       permission of the author.
4
5
6  %%/*--------------- Interface-Interpolate -------------*/
7
8
9  %%/*------- Model directory and folder details ----------*/
10 load('G:\mfinnie\Matlab\DATA\Terraced_Interface\
       Terraced_GaAs_Into_AlAs_18uc\Terraced_GaAs_Into_AlAs_18uc.mat');
11
12 directory_path=''; interface_type=('Terraced GaAs into AlAs');
13
14 %%/*------------- Pre-allocate matrices ---------------*/
15 dumbbell_width=zeros(1,300); Interface_Position=zeros(1,300);
16
17
18 %%/*---------- Calculate column ratio data --------------*/
19 cmax=0; for Dumbbell_counter=1:16 eval(sprintf('Column_Ratio_%
       i_temp=(Average_HAADF_Data_array_%i_Column3-
       Average_HAADF_Data_array_%i_BD)./(Average_HAADF_Data_array_%
       i_Column5-Average_HAADF_Data_array_%i_BD);',Dumbbell_counter,
       Dumbbell_counter,Dumbbell_counter,Dumbbell_counter,
       Dumbbell_counter));
20 end
21 for Dumbbell_counter=1:16      for i=1:300 eval(sprintf('
       Column_Ratio_%i(i,1)=Column_Ratio_%i_temp(2*i,1);',
       Dumbbell_counter,Dumbbell_counter)); eval(sprintf('if
       Column_Ratio_%i(i,1)>cmax; cmax=Column_Ratio_%i(i,1); end',
       Dumbbell_counter,Dumbbell_counter));      end end
22 for Dumbbell_counter=1:16 eval(sprintf('clear Column_Ratio_%s_temp'
       ,num2str(Dumbbell_counter))); end
23 for Dumbbell_counter=1:16 eval(sprintf('Error_Column_Ratio_%i_temp
       (:,1)=sqrt((Std_Err_HAADF_Data_array_%i_Column3./(
       Average_HAADF_Data_array_%i_Column3-Average_HAADF_Data_array_%
       i_BD)).^2+((Std_Err_HAADF_Data_array_%i_BD./(
       Average_HAADF_Data_array_%i_Column5-Average_HAADF_Data_array_%
       i_BD))-(Std_Err_HAADF_Data_array_%i_BD./(
       Average_HAADF_Data_array_%i_Column3-Average_HAADF_Data_array_%
```

```
    i_BD))).^2+(Std_Err_HAADF_Data_array_%i_Column5./(
    Average_HAADF_Data_array_%i_Column5-Average_HAADF_Data_array_%
    i_BD)).^2);',Dumbbell_counter,Dumbbell_counter,Dumbbell_counter,
    Dumbbell_counter,Dumbbell_counter,Dumbbell_counter,
    Dumbbell_counter,Dumbbell_counter,Dumbbell_counter,
    Dumbbell_counter,Dumbbell_counter,Dumbbell_counter,
    Dumbbell_counter)); end
24 for Dumbbell_counter=1:16     for i=1:300 eval(sprintf('
    Error_Column_Ratio_%i(i,1)=Error_Column_Ratio_%i_temp(2*i,1);',
    Dumbbell_counter,Dumbbell_counter));     end end
25 for Dumbbell_counter=1:16 eval(sprintf('clear Error_Column_Ratio_%
    s_temp',num2str(Dumbbell_counter))); end
26
27
28 %%/*------------ Process each slice in turn ---------------*/
29 for slice=1:300;
30     % create line trace of first slice:
31 depth=round(0.199875*slice); depth=num2str(round(0.199875*slice));
    eval(sprintf('title_1=''%s %snm'';',interface_type,depth));
32 for line_trace_counter=1:16     eval(sprintf('line_trace(%i)=
    Column_Ratio_%i(%i);',line_trace_counter,line_trace_counter,
    slice)); end
33 for line_trace_counter=1:16     eval(sprintf('line_trace_error(%i)=
    Error_Column_Ratio_%i(%i);',line_trace_counter,
    line_trace_counter,slice)); end
34
35 % Interpolate to 300 point line trace
36 x = 1:16;  y = line_trace;  xi = 1:(15/300):15.99;  yi = interp1(x,
    y,xi);  interp_line_trace=yi;
37
38 % Create plot of datasets and fits
39 a_max=2*0.7; b_max=2*16; c_max=2*16; d_max=2*11;
40
41 % Set up figure to receive datasets and fits
42 legh_ = []; legt_ = {};   % handles and text for legend xlim_ = [
    Inf -Inf];       % limits of x axis
43
44   % --- Plot data originally in dataset "yi vs. xi" xi = xi(:); yi
      = yi(:);
45 xlim_(1) = min(xlim_(1),min(xi)); xlim_(2) = max(xlim_(2),max(xi));
46 legt_{end+1} = 'yi vs. xi';
47
48 % --- Create fit "fit 1" fo_ = fitoptions('method','
    NonlinearLeastSquares', 'Lower',[-a_max -b_max -c_max -d_max],'
    Upper',[a_max b_max c_max d_max]);
49 ok_ = isfinite(xi) & isfinite(yi); if ~all( ok_ )     warning( '
    GenerateMFile:IgnoringNansAndInfs', ...         'Ignoring NaNs 
    and Infs in data' ); end st_ = [-0.36 7.50 -0.52 3.60 ]; set(fo_
    ,'Startpoint',st_); ft_ = fittype('a*erf(b*(x-d))-c',...      '
    dependent',{'y'},'independent',{'x'},...      'coefficients',{'a
    ', 'b', 'c', 'd'});
50
```

```
51 % Fit this model using new data [cf_ , gof] = fit(xi(ok_), yi(ok_),
      ft_ , fo_);
52 % Or use coefficients from the original fit: if 0    cv_ = { 0.22,
      -1.43, -0.76, 9.25};      cf_ = cfit(ft_ , cv_{:}); end
53 legt_{end+1} = 'fit␣1';
54
55 % Extract width coefficient and error from fitted data
56 coeffvalues(cf_); ci=confint(cf_); a=ans(1); b=ans(2); c=ans(3); d=
      ans(4);
57
58
59 %%/*-------------------- cleanup ----------------------*/
60 clear xlim_ ans ax2_ ax_ cf_ f_ fo_ ft_ h_ i_  legh_
      leginfo_ legrh_  clear legrt_ legt_     ok_ res_ st_ x_
      x_1
61 % Fit and std error   for x=1:16 fn(x)=a*erf(b*(x-d))-c; end
62 for x=1:16 fn_upper(x)=fn(x)+gof.rmse; end
63 for x=1:16 fn_lower(x)=fn(x)-gof.rmse; end
64 coe=[a b c d];
65
66 % Create figure to plot data
67 subplot(3,1,1);
68
69 %%/*------------- Find 5 and 95 positions ---------------*/
70 % Calculate interface width from 95 and 5 percent positions on
      error function
71 threshold_percentage=0.1; width_x_axis=1:15/299:16; width_f_n=coe
      (1)*erf(coe(2)*(width_x_axis-coe(4)))-coe(3); plot(width_x_axis,
      width_f_n, 'DisplayName', 'width_f_n', 'YDataSource', 'width_f_n
      ','color','green');  eval(sprintf('title(''%s␣␣␣␣Crystal␣Depth:␣
      %snm'');',interface_type,depth));  axis([0 17 0 1.3]); range_u_l
      =abs(width_f_n(300)-width_f_n(1)); range_percent=
      threshold_percentage*range_u_l; upper_percent=width_f_n(1)-
      range_percent; lower_percent=width_f_n(300)+range_percent;
72 hold on        errorbar(line_trace,line_trace_error, 'DisplayName',
      'line_trace', 'YDataSource', 'line_trace'); hold off
73 legend('fit','data')                    ylabel('Column␣Ratio');
                     xlabel('Dumbbell␣Number');                % Find
      location of 5 and 95 percent                    peak_finder=1./((
      width_f_n-upper_percent).^2); [peak_value,upper_peak_position] =
       max(peak_finder);
74 peak_finder=1./((width_f_n-lower_percent).^2); [peak_value,
      lower_peak_position] = max(peak_finder);
75 pixel_width=abs(lower_peak_position-upper_peak_position);
      dumbbell_width(slice)=(pixel_width/300)*16;
76 % mark 5 and 95 percent location on figure
77 line([0 17],[upper_percent upper_percent],[0 0],'Color','red','
      LineStyle',':', 'LineWidth',1, 'MarkerSize',12); line([0 17],[
      lower_percent lower_percent],[0 0],'Color','red','LineStyle',':'
      , 'LineWidth',1, 'MarkerSize',12);
78 line([width_x_axis(upper_peak_position) width_x_axis(
      upper_peak_position)],[0 1.3],[0 0],'Color','red','LineStyle',':
```

```
    ', 'LineWidth',1, 'MarkerSize',12); line([width_x_axis(
    lower_peak_position) width_x_axis(lower_peak_position)],[0
    1.3],[0 0],'Color','red','LineStyle',':', 'LineWidth',1, '
    MarkerSize',12);
79  line([0.5*(width_x_axis(upper_peak_position)+width_x_axis(
    lower_peak_position)) 0.5*(width_x_axis(upper_peak_position)+
    width_x_axis(lower_peak_position))],[0 1.3],[0 0],'Color','red',
    'LineStyle',':', 'LineWidth',1, 'MarkerSize',12);
80  Interface_Position(slice)=0.5*(width_x_axis(upper_peak_position)+
    width_x_axis(lower_peak_position));
81
82
83  %%/*------------ Plot the interface width ---------------*/
84  subplot(3,1,2); x_axis=0:2*0.199875:2*300*0.199875-0.199875; plot(
    x_axis,dumbbell_width, 'DisplayName', 'dumbbell_width', '
    YDataSource', 'dumbbell_width'); xlabel('Crystal␣Thickness␣nm')
    ; ylabel('Interface␣Width␣(Dumbbells)'); title(interface_type);
    figure(gcf)
85  % Plot the interface position at this slice depth
86  subplot(3,1,3); plot(Interface_Position,x_axis, 'DisplayName', '
    Interface_Position', 'YDataSource', 'Interface_Position'); xlim
    ([0 17]) ylim([0 120]) xlabel('Dumbbell␣No.'); ylabel('Depth');
    set(gca,'YDir','reverse') figure(gcf)
87  end
88
89  % Create final interface width figure figure1 = figure('PaperSize
    ',[20.98 29.68]);
90  % Create final interface width axes set(gca,'Parent',figure1,... '
    fontsize',32);
91  % Plot interface width
92  plot(x_axis,dumbbell_width, 'DisplayName', 'dumbbell_width', '
    YDataSource', 'dumbbell_width','linewidth',2); xlabel('Crystal␣
    Thickness␣nm'); ylabel('Interface␣Width␣(Dumbbells)'); legend('
    Error␣Function␣Method','location','NW'); axis([0 120 0 8]);
93  title(interface_type);
94
95  % Overlay the experimntntal interface width measurements
96  hold Experimental_xaxis=[42 51 54 67 71 95 99];
    AlAs_On_GaAs_Experimental=[3.04,3.92,3.28,4.40,3.68,6.40,5.28;]
97  plot(Experimental_xaxis,AlAs_On_GaAs_Experimental, 'DisplayName', '
    experimental_AlAs_on_GaAs', 'YDataSource', '
    experimental_AlAs_on_GaAs','marker','o'); xlim([0.5 100.5])
    ylim([0.5 10.5])
98  % Create final interface position figure figure1 = figure('
    PaperSize',[20.98 29.68]);
99  % Create final interface position axes axes('Parent',figure1,'YDir
    ','reverse');
100 box('on'); hold('all');
101 plot(Interface_Position,x_axis, 'DisplayName', 'Interface_Position'
    , 'YDataSource', 'Interface_Position'); figure(gcf) xlim([0.5
    16.5])
```

Dataset Interrogation

HAADF & Intensity Column-Data

```
1  %%/*———————— Original Code: M.P. Finnie ————————————*/
2  Copyright March 2010 Michael P. Finnie
3  The computer code and or data in this file is provided for
      demonstration purposes only with no guarantee or warranty of any
       kind that it is correct or produces correct results. By using
      the code and or data in this file the user agrees to accept all
      risks and liabilities associated with the code and or data. The
      computer code and or data in this file may be copied (and used)
      for non-commercial academic or research purposes only, provided
      that this notice is included. This file or any portion of it may
       not be resold, rented or distributed without the written
      permission of the author.
4
5  %%/*————————— HAADF & Intensity Column Data ————————*/
6
7  % HAADF & Intensity Column Data
8
9  %%/*————— Model directory and folder details ————————*/
10 load('D:\Users\mfinnie\Matlab\DATA\AlAs_into_GaAs_25uc_offset\
      AlAs_into_GaAs_25uc_offset.mat'); interface_type=('Vicinal GaAs
      AlAs Interface (25uc offset)');
11
12
13 %%/*——————————————— Dumbbell Number ———————————————*/
14 Dumbbell_counter=5
15
16 %%/*———————————————— Create figure ————————————————*/
17 figure1 = figure('PaperSize',[20.98 29.68]);
18 % Create axes set(gca,'Parent',figure1,... 'fontsize',32);
19 %% Plot Data:
20 x_axis=0:0.199875:119.8; eval(sprintf('plot(x_axis,
      Average_HAADF_Data_array_%s_Column5, ''DisplayName'', ''
      Average_HAADF_Data_array_%s_Column5'', ''YDataSource'', ''
      Average_HAADF_Data_array_%s_Column5'',''linewidth'',3); hold all
      ; plot(x_axis,Average_HAADF_Data_array_%s_Column3, ''DisplayName
      '', ''Average_HAADF_Data_array_%s_Column3'', ''YDataSource'', ''
      Average_HAADF_Data_array_%s_Column3'',''linewidth'',3); plot(
      x_axis,Average_HAADF_Data_array_%s_BD, ''DisplayName'', ''
      Average_HAADF_Data_array_%s_BD'', ''YDataSource'', ''
      Average_HAADF_Data_array_%s_BD'',''linewidth'',3); hold off;
      figure(gcf)',num2str(Dumbbell_counter),num2str(Dumbbell_counter)
      ,num2str(Dumbbell_counter),num2str(Dumbbell_counter),num2str(
      Dumbbell_counter),num2str(Dumbbell_counter),num2str(
      Dumbbell_counter),num2str(Dumbbell_counter),num2str(
      Dumbbell_counter)));
21 eval(sprintf('Title(''%s    [Dumbbell: %2.0f ]'');',interface_type,
      Dumbbell_counter)); xlabel('Crystal Depth nm'); ylabel('HAADF
```

```
    Signal'); legend('Column5','Column3','BD','location','SE');
22  figure2 = figure('PaperSize',[20.98 29.68]);
23
24  % Create axes set(gca,'Parent',figure2,... 'fontsize',32);
25  eval(sprintf('plot(x_axis,Average_INTENSITY_PP_Data_array_%
    s_Column5, ''DisplayName'', ''Average_INTENSITY_PP_Data_array_%
    s_Column5'', ''YDataSource'', ''Average_INTENSITY_PP_Data_array_
    %s_Column5'',''linewidth'',3); hold all; plot(x_axis,
    Average_INTENSITY_PP_Data_array_%s_Column3, ''DisplayName'', ''
    Average_INTENSITY_PP_Data_array_%s_Column3'', ''YDataSource'', '
    'Average_INTENSITY_PP_Data_array_%s_Column3'',''linewidth'',3); 
     hold off; figure(gcf)',num2str(Dumbbell_counter),num2str(
    Dumbbell_counter),num2str(Dumbbell_counter),num2str(
    Dumbbell_counter),num2str(Dumbbell_counter),num2str(
    Dumbbell_counter))); eval(sprintf('Title(''%s    [Dumbbell: %2.0
    f ]'');',interface_type,Dumbbell_counter)); xlabel('Crystal 
    Depth nm'); ylabel('On Column Electron Intensity'); legend('
    Column5','Column3','BD','location','Ne');
```

Column Ratio Slice-Data

```
1   %%/*———————— Original Code: M.P. Finnie ——————————*/
2   Copyright March 2010 Michael P. Finnie
3   The computer code and or data in this file is provided for
    demonstration purposes only with no guarantee or warranty of any
     kind that it is correct or produces correct results. By using
    the code and or data in this file the user agrees to accept all
    risks and liabilities associated with the code and or data. The
    computer code and or data in this file may be copied (and used)
    for non-commercial academic or research purposes only, provided
    that this notice is included. This file or any portion of it may
     not be resold, rented or distributed without the written
    permission of the author.
4
5   %%/*—————————— Column Ratio Slice Data —————————*/
6
7   % Column Ratio Slice Data
8
9   %%/*————— Model directory and folder details ———————*/
10  load('D:\Users\mfinnie\Matlab\DATA\AlAs_into_GaAs_25uc_offset\
    AlAs_into_GaAs_25uc_offset.mat'); interface_type=('Vicinal GaAs 
    AlAs Interface (25uc offset)');
11
12
13  %%/*————————————— Crystal Depth ——————————————*/
14  thickness=100;        % thickness of crystal in nm (max: 120)
15
16
17  %%/*———————————— Convert HAADF data ———————————*/
18  cmax=0;
19  for Dumbbell_counter=1:16 eval(sprintf('Column_Ratio_%i_temp=(
    Average_HAADF_Data_array_%i_Column3-Average_HAADF_Data_array_%
```

```
    i_BD)./(Average_HAADF_Data_array_%i_Column5-
    Average_HAADF_Data_array_%i_BD);',Dumbbell_counter,
    Dumbbell_counter,Dumbbell_counter,Dumbbell_counter,
    Dumbbell_counter));
20 end
21 for Dumbbell_counter=1:16       for i=1:300 eval(sprintf('
    Column_Ratio_%i(i,1)=Column_Ratio_%i_temp(2*i,1);',
    Dumbbell_counter,Dumbbell_counter)); eval(sprintf('if
    Column_Ratio_%i(i,1)>cmax; cmax=Column_Ratio_%i(i,1); end',
    Dumbbell_counter,Dumbbell_counter));       end end
22 for Dumbbell_counter=1:16 eval(sprintf('clear Column_Ratio_%s_temp'
    ,num2str(Dumbbell_counter))); end
23 for Dumbbell_counter=1:16 eval(sprintf('Error_Column_Ratio_%i_temp
    (:,1)=sqrt((Std_Err_HAADF_Data_array_%i_Column3./(
    Average_HAADF_Data_array_%i_Column3-Average_HAADF_Data_array_%
    i_BD)).^2+((Std_Err_HAADF_Data_array_%i_BD./(
    Average_HAADF_Data_array_%i_Column5-Average_HAADF_Data_array_%
    i_BD))-(Std_Err_HAADF_Data_array_%i_BD./(
    Average_HAADF_Data_array_%i_Column3-Average_HAADF_Data_array_%
    i_BD))).^2+(Std_Err_HAADF_Data_array_%i_Column5./(
    Average_HAADF_Data_array_%i_Column5-Average_HAADF_Data_array_%
    i_BD)).^2);',Dumbbell_counter,Dumbbell_counter,Dumbbell_counter,
    Dumbbell_counter,Dumbbell_counter,Dumbbell_counter,
    Dumbbell_counter,Dumbbell_counter,Dumbbell_counter,
    Dumbbell_counter,Dumbbell_counter,Dumbbell_counter,
    Dumbbell_counter)); end
24 for Dumbbell_counter=1:16       for i=1:300 eval(sprintf('
    Error_Column_Ratio_%i(i,1)=Error_Column_Ratio_%i_temp(2*i,1);',
    Dumbbell_counter,Dumbbell_counter));       end end
25 for Dumbbell_counter=1:16 eval(sprintf('clear Error_Column_Ratio_%
    s_temp',num2str(Dumbbell_counter))); end
26
27
28
29 %%/*--------------- 1d column ratio profile ------------------*/
30 %% Calculate the 1d column ratio image for a given thickness %(line
     profile)
31 subplot(2,1,2); slice=round(thickness/(2*0.199875));
    column_ratio_linetrace=zeros(1,16); error_column_ratio_linetrace
    =zeros(1,16);
32 for Dumbbell_counter=1:16 eval(sprintf('column_ratio_linetrace(1,%i
    )=Column_Ratio_%i(slice,1);',Dumbbell_counter,Dumbbell_counter))
    ; eval(sprintf('error_column_ratio_linetrace(1,%i)=
    Error_Column_Ratio_%i(slice,1);',Dumbbell_counter,
    Dumbbell_counter)); end
33 errorbar(column_ratio_linetrace,error_column_ratio_linetrace); axis
    ([0 17 0 cmax+0.1*cmax]);   eval(sprintf('title(''Column Ratio   
    [thickness: %5.0f nm]'');',thickness)); figure(gcf);
34 subplot(2,1,1);
35
36 %%/*--------------- 2d column ratio profile ------------------*/
37 %% Calculate the 2d column ratio image for a given thickness %(
```

```
    Checkered profile)
38 column_ratio_image=zeros(2,16);
39 for Dumbbell_counter=1:16 eval(sprintf('column_ratio_image((1+rem(
    Dumbbell_counter,2)),%i)=Column_Ratio_%i(slice,1);',
    Dumbbell_counter,Dumbbell_counter)); end
40 imagesc(column_ratio_image); daspect([1 1 1]); caxis([0 cmax]);
    colormap gray; colorbar('SouthOutside'); eval(sprintf('title(''
    Column Ratio   [thickness: %5.0f nm]'');',thickness)); figure(
    gcf);   set(gca,'fontsize',14)
```